K. Busch, S. Lölkes, R. B. Wehrspohn,
and H. Föll (Eds.)

Photonic Crystals

Advances in Design, Fabrication,
and Characterization

Photonic Crystals. Edited by K. Busch, S. Lölkes, R. B. Wehrspohn and H. Föll
Copyright © 2004 Wiley-VCH Verlag GmbH & Co. KGaA
ISBN: 3-527-40432-5

Edited by
K. Busch, S. Lölkes , R. B. Wehrspohn, and H. Föll

Photonic Crystals

Advances in Design, Fabrication, and Characterization

WILEY-VCH Verlag GmbH & Co. KGaA

Editors

Kurt Busch
University of Central Florida, USA
e-mail: kbusch@physics.ucf.edu

Stefan Lölkes
Christian-Albrechts-Universität zu Kiel, Germany
e-mail: stl@tf.uni-kiel.de

Ralf B. Wehrspohn
Universität Paderborn, Germany
e-mail: wehrspohn@mpi-halle.de

Helmut Föll
Christian-Albrechts-Universität zu Kiel, Germany
e-mail: hf@tf.uni-kiel.de

Coverpicture
(Main picture) Simulation of field distribution in a photonic crystal (PhC) waveguide with integrated beam splitter. (Background) SEM picture of an electrochemically etched 3D PhC with a full photonic bandgap in the IR. (Foreground) Emission spectrum of a PhC laser.

This book was carefully produced. Nevertheless, editors, authors, and publisher do not warrant the information contained therein to be free of errors. Readers are advised to keep in mind that statements, data, illustrations, procedural details or other items may inadvertently be inaccurate.

Library of Congress Card No.: applied for
British Library Cataloging-in-Publication Data:
A catalogue record for this book is available from the British Library

Bibliographic information published by Die Deutsche Bibliothek
Die Deutsche Bibliothek lists this publication in the Deutsche Nationalbibliografie; detailed bibliographic data is available in the Internet at <http://dnb.ddb.de>.

© 2004 WILEY-VCH Verlag GmbH & Co. KGaA, Weinheim

All rights reserved (including those of translation into other languages). No part of this book may be reproduced in any form – nor transmitted or translated into machine language without written permission from the publishers. Registered names, trademarks, etc. used in this book, even when not specifically marked as such, are not to be considered unprotected by law.

Printed in the Federal Republic of Germany
Printed on acid-free paper

Cover Design Petra Beissert, conimago
Composition Uwe Krieg, Berlin
Printing Druckhaus Darmstadt GmbH, Darmstadt
Bookbinding Großbuchbinderei J. Schäffer GmbH & Co. KG, Grünstadt
ISBN 3-527-40432-5

Contents

Preface **XIII**

About the editors **XV**

List of contributors **XVI**

1 On the solid-state theoretical description of photonic crystals
(*K. Busch, M. Diem, M. Frank, A. Garcia-Martin, F. Hagmann, D. Hermann, S. Mingaleev, S. Pereira, M. Schillinger, and L. Tkeshelashvili*) **1**
1.1 Introduction . . . 1
1.2 Photonic band structure computation . . . 2
1.2.1 Density of states . . . 4
1.2.2 Group velocity and group velocity dispersion . . . 5
1.3 Nonlinear photonic crystals . . . 6
1.4 Finite structures . . . 8
1.5 Defect structures in photonic crystals . . . 12
1.5.1 Maximally localized photonic Wannier functions . . . 13
1.5.2 Wannier description of defect structures . . . 15
1.5.3 Localized cavity modes . . . 16
1.5.4 Dispersion relations of waveguides . . . 17
1.5.5 Light propagation through photonic crystal circuits . . . 19
1.6 Conclusions . . . 20
References . . . 21

2 Spontaneous emission in photonic structures: Theory and simulation
(*G. Boedecker, C. Henkel, Ch. Hermann, and O. Hess*) **23**
2.1 Introduction . . . 23
2.2 Basic concepts . . . 24
2.2.1 Fermi's Golden Rule . . . 24
2.2.2 Beyond the simple picture . . . 27
2.2.3 Coherent tuning of spontaneous decay . . . 28
2.2.4 QED in a structured continuum . . . 29
2.3 Simulations . . . 33
2.3.1 Frequency domain . . . 33
2.3.2 Time domain . . . 36
2.4 Concluding remarks . . . 38
References . . . 40

3 Semiconductor optics in photonic crystal structures

(*T. Meier and S. W. Koch*) **43**
3.1 Introduction 43
3.2 Semiclassical theory 44
  3.2.1 Light–matter coupling 44
  3.2.2 Generalized Coulomb potential 44
  3.2.3 Hamilton operator 48
  3.2.4 Equations of motion 49
3.3 Numerical results 51
  3.3.1 Linear exciton absorption 51
  3.3.2 Coherently excited inhomogeneous populations 54
  3.3.3 Quasi-equilibrium inhomogeneous populations and nonlinear absorption 55
  3.3.4 Coherent wave packet dynamics versus dephasing and thermalization 58
3.4 Summary and outlook 61
References 62

4 Electrochemically-prepared 2D and 3D photonic crystals

(*R.B. Wehrspohn, J. Schilling, J. Choi, Y. Luo, S. Matthias, S. L. Schweizer, F. Müller, U. Gösele, S. Lölkes, S. Langa, J. Carstensen, and H. Föll*) **63**
4.1 Introduction 63
4.2 Materials 64
  4.2.1 Porous silicon 64
  4.2.2 Porous alumina 67
  4.2.3 Porous III–V semiconductors 68
4.3 Application to photonic crystals 69
  4.3.1 Introduction 69
  4.3.2 2D photonic crystals made of macroporous silicon 70
  4.3.3 Photonic defects in electrochemically–prepared 2D photonic crystals 73
  4.3.4 3D photonic crystals made of macroporous silicon 75
  4.3.5 2D photonic crystals made of porous alumina 78
  4.3.6 1D photonic crystals made of InP 78
  4.3.7 2D photonic crystals made of InP 79
  4.3.8 3D photonic crystals made of InP and GaAs 81
4.4 Summary 81
References 82

5 Optical properties of planar metallo–dielectric photonic crystals

(*A. Christ, S. Linden, T. Zentgraf, K. Schubert, D. Nau, S.G. Tikhodeev, N.A. Gippius, J. Kuhl, F. Schindler, A.W. Holleitner, J. Stehr, J. Crewett, J. Lupton, T. Klar, U. Scherf, J. Feldmann, C. Dahmen, G. von Plessen, and H. Giessen*) **85**
5.1 Introduction 85
5.2 Optical characterization of individual gold nanodisks 86
5.3 Observation of Rayleigh anomalies in metallo-dielectric nanostructures . . . 87
  5.3.1 Metallic nanoparticle arrays 87
  5.3.2 Metallic nanowire arrays 90

5.4 Waveguide–plasmon polaritons: Strong coupling in a metallic photonic crystal 94
  5.4.1 Metallic nanoparticle arrays on dielectric waveguide substrates 94
  5.4.2 Metallic nanowire arrays on dielectric waveguide substrates 97
  5.4.3 Ultrafast dynamics of waveguide-plasmon polaritons 101
5.5 A polymer DFB laser based on a metal nanoparticle array 103
5.6 Summary 106
References 107

6 Preparation of 3D photonic crystals from opals
(*M. Egen, R. Zentel, P. Ferrand, S. Eiden, G. Maret, and F. Caruso*) **109**
6.1 Introduction 109
6.2 Preparation of monodisperse colloids 110
  6.2.1 General methods 110
  6.2.2 Preparation of functional core shell structures 115
6.3 Crystallization into opaline structures 120
  6.3.1 Sedimentation 120
  6.3.2 Crystallization mediated by the magnetic field 120
  6.3.3 Two dimensional crystallization to photonic crystal films 121
6.4 Structured photonic crystals 125
  6.4.1 Lateral patterning 125
  6.4.2 Preparation of heterostructures from different colloids 125
6.5 Replica from opaline structure 127
References 128

7 Light emitting opal–based photonic crystal heterojunctions
(*S. G. Romanov, N. Gaponik, A. Eychmüller, A. L. Rogach, V. G. Solovyev, D. N. Chigrin, and C. M. Sotomayor Torres*) **132**
7.1 Introduction 132
7.2 Experimental techniques and material preparation 135
  7.2.1 Measurement techniques 135
  7.2.2 Preparation of hetero–opals 136
  7.2.3 Selective impregnation of hetero–opals with luminescent nanocrystals 138
7.3 Reflectance and transmission spectra of hetero–opals 140
  7.3.1 Observation of two Bragg band gaps 140
  7.3.2 The interface gap 141
7.4 Light emission in hetero–opals 145
  7.4.1 Anisotropy of photoluminescence in hetero–opals 145
  7.4.2 Emission modification at the interface 147
References 151

8 Three–dimensional lithography of Photonic Crystals
(*A. Blanco, K. Busch, M. Deubel, C. Enkrich, G. von Freymann, M. Hermatschweiler, W. Koch, S. Linden, D.C. Meisel, and M. Wegener*) **153**
8.1 Introduction 153
8.2 Holographic lithography 154

8.2.1 The photoresist . . . 155
8.2.2 The crystallography of multiple-beam interference patterns . . . 155
8.2.3 Experimental realization . . . 158
8.2.4 Optical properties of the photoresist structures . . . 160
8.3 Direct laser writing . . . 161
8.3.1 Multi–photon polymerization . . . 162
8.3.2 Experimental realization . . . 164
8.3.3 Direct laser writing of three–dimensional photonic crystals . . . 165
8.3.4 Optical characterization . . . 167
8.4 Templates infiltration . . . 168
8.4.1 Silicon CVD . . . 169
8.4.2 Electrochemical deposition . . . 171
8.5 Conclusions . . . 172
References . . . 172

9 Tunable photonic crystals using liquid crystals
(*H.–S. Kitzerow and J.P. Reithmaier*) **174**
9.1 Introduction: Concepts of tunable photonic crystals . . . 174
9.2 Properties of liquid crystals . . . 178
9.3 Spatially periodic LCs and colloidal crystals . . . 180
9.3.1 Periodic liquid crystals . . . 180
9.3.2 Colloidal crystals containing LCs . . . 182
9.3.3 Polymer–dispersed liquid crystals . . . 185
9.4 Microstructured semiconductors . . . 186
9.4.1 Macroporous silicon . . . 186
9.4.2 Group III–V semiconductors . . . 187
9.5 Summary and perspectives . . . 192
9.5.1 Possible applications of macroporous silicon . . . 192
9.5.2 Possible applications for tunable planar III/V–semiconductor photonic crystals . . . 193
References . . . 194

10 Microwave modelling of photonic crystals
(*W. Freude, G.–A. Chakam, J.–M. Brosi, and Ch. Koos*) **198**
10.1 Fundamentals . . . 198
10.1.1 Maxwell's equations and scaling laws . . . 199
10.1.2 Numerical tools . . . 202
10.2 Microwave measurements . . . 202
10.2.1 Scattering matrix . . . 202
10.2.2 Microwave equipment . . . 203
10.2.3 Coupling of coaxial metallic to dielectric strip waveguide . . . 204
10.3 Loss measurement of waveguide resonator . . . 207
10.4 Experimental results . . . 209
10.4.1 2D infinite–height PhC . . . 210
10.4.2 2D finite–height PhC with line–defect waveguide . . . 210
References . . . 212

11 Scanning near-field optical studies of photonic devices
(*V. Sandoghdar, B. Buchler, P. Kramper, S. Götzinger, O. Benson, and M. Kafesaki*) **215**
11.1 Introduction 215
11.2 Scanning near-field optical microscopy (SNOM) 215
  11.2.1 Brief historical background 215
  11.2.2 The operation principle of SNOM 216
  11.2.3 Instrumentation 217
  11.2.4 Various modes of SNOM operation 218
11.3 Imaging photonic devices with SNOM 219
  11.3.1 The evanescent field on a prism 219
  11.3.2 SNOM on whispering–gallery resonators 220
  11.3.3 Interferometric SNOM measurements 222
  11.3.4 Photonic crystals 224
11.4 Manipulating photonic devices with SNOM 233
11.5 Conclusion 234
References 235

12 Application of photonic crystals for gas detection and sensing
(*R.B. Wehrspohn, S. L. Schweizer, J. Schilling, T. Geppert, C. Jamois, R. Glatthaar, P. Hahn, A. Feisst, and A. Lambrecht*) **238**
12.1 Principle 238
12.2 Realizations with 3D photonic crystals 241
12.3 Conclusion 245
References 245

13 Polymeric photonic crystal lasers
(*K. Forberich, S. Riechel, S. Pereira, A. Gombert, K. Busch, J. Feldmann, and U. Lemmer*) **247**
13.1 Introduction 247
13.2 Fabrication of microstructured surfaces by interference lithography 247
  13.2.1 Interference lithography 248
  13.2.2 Replication and subsequent substrate processing 250
13.3 Active materials for organic photonic crystal lasers 252
13.4 Lasing in two dimensional polymeric photonic crystals 254
13.5 Semiclassical theory of lasing in surface relief structures 256
  13.5.1 Semiclassical laser theory in structured media 257
  13.5.2 Effective 2D model for surface relief structures 260
  13.5.3 Discussion of lasing behavior in surface relief structures 261
13.6 Conclusions 263
References 264

14 Photonic crystal fibers
(*J. Kirchhof, J. Kobelke, K. Schuster, H. Bartelt, R. Iliew, C. Etrich, and F. Lederer*) **266**
14.1 Introduction 266
14.2 Modeling of photonic crystal fibers 267

14.2.1 Plane wave expansion methods 269
14.2.2 The localized functions method 271
14.2.3 The finite element method (FEM) 272
14.2.4 The multipole method 272
14.2.5 Propagation methods 273
14.3 Fiber technology 275
14.3.1 Preparation of photonic crystal fibers 275
14.3.2 Fluid–dynamic aspects in the preparation of photonic crystal fibers . . 276
14.4 Special properties of photonic crystal fibers 278
14.4.1 Spectral transmission 278
14.4.2 Variation of the numerical aperture and the mode profil 280
14.4.3 Dispersion properties 282
14.4.4 Mechanical properties 283
14.5 Overview of applications 284
14.6 Conclusions 286
References 286

15 Photonic crystal optical circuits in moderate index materials
(*M. Augustin, G. Böttger, M. Eich, C. Etrich, H.-J. Fuchs, R. Iliew, U. Hübner, M. Kessler, E.–B. Kley, F. Lederer, C. Liguda, S. Nolte, H.G. Meyer, W. Morgenroth, U. Peschel, A. Petrov, D. Schelle, M. Schmidt, A. Tünnermann, and W. Wischmann*) **289**
15.1 Motivation 289
15.2 Design of the PhC films 291
15.3 Photonic crystal waveguides in niobiumpentoxide 292
15.4 Photonic crystals in polymer films 297
15.5 Conclusions 304
References 306

16 Planar high index-contrast photonic crystals for telecom applications
(*R. März, S. Burger, S. Golka, A. Forchel, C. Hermann, C. Jamois, D. Michaelis, and K. Wandel*) **308**
16.1 Introduction and motivation 308
16.2 Waveguide losses 309
16.3 Efficient analysis of photonic crystals 312
16.4 Patterning of photonic crystals 314
16.5 Sources for multi-channel WDM–transmitters 318
16.6 Photonic crystal superprisms for WDM–applications 320
16.7 PhC–based dispersion compensator 323
16.8 Fiber–to–chip coupling of photonic crystals 325
References 327

17 Photonic crystal based active optoelectronic devices
(*M. Kamp, T. Happ, S. Mahnkopf, A. Forchel, S. Anand, and G.–H. Duan*) **329**
17.1 Introduction 329
17.2 Waveguide based 2D photonic crystals 330

17.3 Semiconductor lasers with photonic crystal mirrors 332
    17.3.1 Fabrication 333
    17.3.2 Device performance 336
    17.3.3 Single mode photonic crystal based lasers 336
17.4 All photonic crystal lasers 339
17.5 Tunable photonic crystal lasers 342
17.6 Conclusion 345
References 346

Appendix

A List of abbreviations 347

B Conventions 348

Index 349

Preface

The semiconductor revolution, that began in the late 1940's, enabled profound and unanticipated improvements in our standard of living. These artificial electronic materials, that control the flow of electrons on a microscopic scale, remain a centerpiece of today's micro-electronics industry. Likewise, the invention of the laser in the early 1960's, inspired the development of artificial materials that mold the flow of light. The photonics industry has irrevocably enhanced the way we transmit information, through the replacement of electronic signals in wires, with laser pulses in optical fibers. Along this course of scientific and technological progress, it is tempting to ask whether there exists a photonic analogue of the electronic semiconductor micro-chip. This requires the design and fabrication of practical photonic materials that can localize light and mold its flow on an equivalently microscopic scale. The collection of articles in this book describes significant research developments in Germany towards this objective.

Photonic band gap (PBG) materials are a novel class of photonic crystals that carry the concept of molding the flow of light to the most microscopic level allowed by the laws of physics. Consisting of dielectric microstructures with periodicity of roughly half the wavelength of light, PBG materials scatter photons in a manner similar to the scattering of electrons by the crystalline array of atoms in a semiconductor. The resulting gap in the electromagnetic spectrum provides a unique environment in which unwanted pathways for electromagnetic wave propagation are removed and desired ones can be selectively engineered, through defects in the photonic crystal lattice. In this way, a PBG material provides a robust platform for the integration of passive optical circuitry and active light emitting devices onto a compact optical micro-chip. Moreover, the electromagnetic density of states on the optical micro-chip can be engineered through suitable crystal defect architectures. This enables highly frequency selective changes in the rate of spontaneous emission of light from atoms whose resonance frequency lies within the engineered electromagnetic vacuum. This provides a new frontier in the field of quantum optics. The possibilities outlined above have inspired a worldwide effort to design, fabricate, and characterize a variety of different types of photonic crystals.

Research efforts in Germany have played a leading role in the worldwide effort to realize the promise of photonic band gap materials. These include the fabrication of two-dimensional and three-dimensional photonic crystals of unprecedented aspect ratio, in single crystal semiconductors such as silicon, using photo-electrochemical etching. These crystals have provided a platform for pioneering optical experiments both within Germany and internationally. Other novel photonic band gap architectures may soon be achieved through direct optical "writing" using two-photon absorption and holographic lithography in a polymer-based template, followed by replication (inversion) of the template with polycrystalline semiconductors. On the theoretical side, efficient modeling of electromagnetic wave propagation in complex defect architectures is an essential prerequisite to the design and fabrication process. This prominent role for theory is made possible through the essentially perfect applicability of Maxwell's equations to the optical properties of photonic crystals, without additional complicating interactions such as electron-electron and electron-phonon interactions that arise in the electronic properties of solids. Nevertheless the complex geometries of photonic crystal defect architectures and their concomitant light localization effects, call for the development of novel computational approaches. One of these, described in this book, is the introduction of Wannier functions (the optical analogue of localized atomic orbitals in solid state physics) as the basis functions for electromagnetic wave propagation. These localized basis functions may be indispensable for efficiently describing optical propagation within optical circuit architectures of three-dimensional PBG materials. Finally, a number of practical applications of photonic crystals is beginning to appear. Two particularly interesting and unique developments are the use of photonic crystals as mirrors and couplers for practical III-V semiconductor based lasers and the integration of a number of such lasers within a photonic crystal micro-chip.

It is clear from the above illustrations that photonic crystal research in Germany has provided a number of important, first-of-its-kind in the world, achievements. This book provides the reader with a valuable introduction to a number of these developments and an overview of a number of other emerging research directions.

Sajeev John

Toronto, December 2003

About the editors

Kurt Busch has been an Associate Professor at the Department of Physics and the School of Optics: CREOL & FPCE at the University of Central Florida (Orlando, USA) since January 2004. He received his undergraduate (Dipl.-Phys.; 1993) and postgraduate training (Dr. rer. nat.; 1996) at the University of Karlsruhe (Germany) and partly at the Iowa State University (Ames, USA). His professional experience included working at Iowa State University (Ames, USA), the University of Toronto (Canada; 1997-1999) and leading a junior research group within the Emmy-Noether program of the Deutsche Forschungsgemeinschaft at the University of Karlsruhe (Germany; 2000-2003). His research interests lie in light-matter interactions and wave propagation in strongly scattering materials and Photonic Crystals.

Stefan Lölkes graduated in semiconductor physics at the Technical University of Munich, Germany, in 2000. In 2001, he started his Ph.D. thesis on “Electrochemical etching of Photonic Crystals” at the Chair for General Materials Science at the Christian-Albrechts-University of Kiel, Germany. In parallel, he co-organized already several national symposia on Photonic Crystals in the framework of the DFG priority program 1113 “Photonic Crystals”.

Ralf B. Wehrspohn received his diploma degree in physics at the University of Oldenburg in 1995. He then carried out a Ph.D. at the Ecole Polytechnique in France about thin film technology and electrochemistry. In 1998 he joined the Philips Research Laboratories in Redhill, U.K., to work on thin film transistors for AMLCD. From end of 1999 to March 2003 he has been responsible for the activities on photonic crystals and self-ordered porous materials at the Max-Planck-Institute of Microstructure Physics in Halle. Since April 2003 he is full professor in experimental physics at the University of Paderborn where he leads the activities on nanophotonic materials. R. B. Wehrspohn has been awarded with the Heinz Maier-Leipnitz award of the DFG and the TR100 innovation price of the MIT in 2003.

Helmut Föll received his Ph.D. degree in Physics in 1976 from the University of Stuttgart in conjunction with the Max-Planck-Institute for Metal Research in Stuttgart. After postdoctorial work at the Department of Materials Science and Engineering at Cornell University and a position as guest scientist at the T.J. Watson Res. Center of IBM in Yorktown Heights, he joined Siemens in 1980, working in the newly founded Solar Energy Department of Central Research in Munich. After various senior positions in microelectronics development, in 1991 he accepted an offer of the Christian-Albrechts-University of Kiel to become the founding dean of the newly established Faculty of Engineering, where he also holds the Chair for General Materials Science. Since 1998 he is back to research, with particular interest in solar cell technology and the electrochemistry of semiconductors. He is one of the pioneers in the field of porous semiconductors and has coauthored more than 150 papers and 20 patents.

Photonic Crystals: Advances in Design, Fabrication, and Characterization.
Edited by Kurt Busch, Stefan Lölkes, Ralf B. Wehrspohn, Helmut Föll
Copyright © 2004 Wiley-VCH Verlag GmbH & Co. KGaA
ISBN: 3-527-40432-5

List of contributors

- *Srinivasan Anand (Ch. 17)*

  Royal Institute of Technology (KTH),
  Electrum 229,
  16440 Kista, Sweden

- *Markus Augustin (Ch. 15)*

  Institut für Angewandte Physik,
  Friedrich–Schiller–Universität Jena,
  Max–Wien–Platz 1,
  07743 Jena, Germany

- *Hartmut Bartelt (Ch. 14)*

  Institute for Physical High Technology,
  Albert–Einstein–Straße 9,
  07745 Jena, Germany
  e-mail: bartelt@ipht-jena.de

- *Oliver Benson (Ch. 11)*

  Humboldt–Universität zu Berlin,
  Institut für Physik,
  Hausvogteiplatz 5–7,
  10117 Berlin, Germany

- *Alvaro Blanco (Ch. 8)*

  Institut für Nanotechnologie,
  Forschungszentrum Karlsruhe
  in der Helmholtz–Gemeinschaft,
  76021 Karlsruhe, Germany

  and

  DFG–Center for Functional Nanostructures (CFN)

- *Geesche Boedecker (Ch. 2)*

  Institut für Physik,
  Universität Potsdam,
  Am Neuen Palais 10,
  14469 Potsdam, Germany

- *Gummar Böttger (Ch. 15)*

  Materials in Electrical Engineering
  and Optics,
  Technische Universität Hamburg-Harburg,
  Eissendorfer Strasse 38,
  20173 Hamburg, Germany

- *Jan–Michael Brosi (Ch. 10)*

  High–Frequency and Quantum Electronics Laboratory,
  University of Karlsruhe,
  Kaiserstr. 12,
  76128 Karlsruhe, Germany

- *Ben Buchler (Ch. 11)*

  Laboratorium für Physikalische Chemie,
  Eidgenossische Technische Hochschule (ETH),
  CH-8093 Zurich, Switzerland

- *Sven Burger (Ch. 16)*

  Konrad-Zuse-Zentrum
  für Informationstechnik Berlin (ZIB),
  Takustraße 7,
  14195 Berlin

Photonic Crystals: Advances in Design, Fabrication, and Characterization.
Edited by Kurt Busch, Stefan Lölkes, Ralf B. Wehrspohn, Helmut Föll
Copyright © 2004 Wiley-VCH Verlag GmbH & Co. KGaA
ISBN: 3-527-40432-5

- *Kurt Busch (Ch. 1, 8, and 13)*

  Institut für Theorie
  der Kondensierten Materie,
  Universität Karlsruhe,
  76128 Karlsruhe, Germany
  e-mail: kbusch@physics.ucf.edu

  and

  DFG–Center for Functional Nanostructures (CFN)

  and

  Department of Physics and School of Optics,
  CREOL&FPCE,
  University of Central Florida,
  Orlando, FL 32816, USA

- *Jürgen Carstensen (Ch. 4)*

  Faculty of Engineering,
  Christian–Albrechts–University of Kiel,
  Kaiserstr. 2,
  24143 Kiel, Germany

- *Frank Caruso (Ch. 6)*

  Max Planck Institute
  of Colloids and Interfaces,
  Potsdam, Germany

  present address:

  Department of Chemical and Biomolecular Engineering,
  The University of Melbourne, Australia

- *Guy–Aymar Chakam (Ch. 10)*

  High–Frequency and Quantum Electronics Laboratory,
  University of Karlsruhe,
  Kaiserstr. 12,
  76128 Karlsruhe, Germany

- *Dmitri Chigrin (Ch. 7)*

  Institute of Materials Science & Department
  of Electrical and Information Engineering,
  University of Wuppertal,
  42097 Wuppertal, Germany

- *Jinsub Choi (Ch. 4)*

  Max Planck Institute
  of Microstructure Physics,
  Weinberg 2,
  06120 Halle, Germany

- *Andre Christ (Ch. 5)*

  Max–Planck–Institut
  für Festkörperforschung,
  Heisenbergstr. 1,
  70569 Stuttgart, Germany

- *Jana Crewett (Ch. 5)*

  Photonics and Electronics Group,
  Ludwig-Maximilians–University,
  Amalienstr. 54,
  80799 München, Germany

- *Christian Dahmen (Ch. 5)*

  1. Physikalisches Institut,
  RWTH–Aachen,
  Huyskensweg,
  52074 Aachen, Germany

- *Markus Deubel (Ch. 8)*

  Institut für Angewandte Physik,
  Universität Karlsruhe (TH),
  Wolfgang–Gaede–Straße 1,
  76131 Karlsruhe, Germany

  and

  DFG–Center for Functional Nanostructures (CFN)

- *Marcus Diem (Ch. 1)*

  Institut für Theorie
  der Kondensierten Materie,
  Universität Karlsruhe,
  76128 Karlsruhe, Germany

- *Guang–Hua Duan (Ch. 17)*

  Opto+,
  Route de Nozay,
  91461 Marcoussis, France

- *Marc Egen (Ch. 6)*

  Institute of Organic Chemistry,
  Johannes Gutenberg-University,
  Duesbergweg 10–14,
  55099 Mainz, Germany

- *Manfred Eich (Ch. 15)*

  Materials in Electrical Engineering
  and Optics,
  Technische Universität Hamburg-Harburg,
  Eissendorfer Strasse 38,
  20173 Hamburg, Germany
  e-mail: m.eich@tu-harburg.de

- *Stefanie Eiden (Ch. 6)*

  Department of Physics,
  University of Konstanz,
  Box M 621,
  78457 Konstanz, Germany

- *Christian Enkrich (Ch. 8)*

  Institut für Angewandte Physik,
  Universität Karlsruhe (TH),
  Wolfgang–Gaede–Straße 1,
  76131 Karlsruhe, Germany

  and

  DFG–Center for Functional Nanostructures (CFN)

- *Christoph Etrich (Ch. 14 and 15)*

  Institute of Solid State Theory and Theoretical Optics,
  Friedrich–Schiller–Universität Jena,
  Max–Wien–Platz 1,
  07743 Jena, Germany

- *Alexander Eychmüller (Ch. 7)*

  Institute of Physical Chemistry,
  University of Hamburg,
  20146 Hamburg, Germany

- *Arno Feisst (Ch. 12)*

  Fraunhofer–Institut
  für Physikalische Messtechnik,
  Heidenhofstr. 8,
  79110 Freiburg, Germany

- *Jochen Feldmann (Ch. 5 and 13)*

  Photonics and Electronics Group,
  Center for NanoScience (CENS),
  Ludwig–Maximilians–University,
  Amalienstr. 54,
  80799 München, Germany

- *Patrick Ferrand (Ch. 6)*

  Institute of Materials Science and Department of Electrical and Information Engineering,
  University of Wuppertal,
  Gaußstr. 20,
  42097 Wuppertal, Germany

- *Karen Forberich (Ch. 13)*

  Freiburger Materialforschungszentrum,
  Universität Freiburg,
  79104 Freiburg, Germany

- *Helmut Föll (Ch. 4)*

  Faculty of Engineering,
  Christian–Albrechts–University of Kiel,
  Kaiserstr. 2,
  24143 Kiel, Germany

- *Alfred Forchel (Ch. 16 and 17)*

  Technical Physics,
  University of Würzburg,
  Am Hubland,
  97074 Würzburg, Germany

- *Meikel Frank (Ch. 1)*

  Institut für Theorie
  der Kondensierten Materie,
  Universität Karlsruhe,
  76128 Karlsruhe, Germany

- *Wolfgang Freude (Ch. 10)*

  High–Frequency and Quantum Electronics Laboratory,
  University of Karlsruhe,
  Kaiserstr. 12,
  76128 Karlsruhe, Germany
  e-mail: W.Freude@etec.uni-karlsruhe.de

- *Georg von Freymann (Ch. 8)*

  Institut für Nanotechnologie,
  Forschungszentrum Karlsruhe
  in der Helmholtz–Gemeinschaft,
  76021 Karlsruhe, Germany

  and

  DFG–Center for Functional Nanostructures (CFN)

- *Hans–Jörg Fuchs (Ch. 15)*

  Institut für Angewandte Physik,
  Friedrich–Schiller–Universität Jena,
  Max–Wien–Platz 1,
  07743 Jena, Germany

- *Nikolai Gaponik (Ch. 7)*

  Institute of Physical Chemistry,
  University of Hamburg,
  20146 Hamburg, Germany

  On leave from

  Belarussian State University,
  Minsk, Belarus

- *Antonio Garcia-Martin (Ch. 1)*

  Institut für Theorie
  der Kondensierten Materie,
  Universität Karlsruhe,
  76128 Karlsruhe, Germany

  and

  Instituto de Microelectronica de Madrid,
  Consejo Superior de Investigaciones Cientificas,
  Issac Newton, 8 (PTM), 28760 - Tres Cantos,
  Madrid, Spain

- *Torsten Geppert (Ch. 12)*

  Max Planck Institute
  of Microstructure Physics,
  06120 Halle, Germany

  and

  Department of Physics,
  University Paderborn,
  33095 Paderborn, Germany

- *Harald Giessen (Ch. 5)*

  Institute of Applied Physics,
  University of Bonn, Wegelerstr. 8,
  53115 Bonn, Germany
  e-mail: giessen@iap.uni-bonn.de

- *Nikolai A. Gippius (Ch. 5)*

  General Physics Institute RAS,
  Vavilova 38,
  Moscow 119991, Russia

  and

  Max–Planck–Institut
  für Festkörperforschung,
  Heisenbergstr. 1,
  70569 Stuttgart, Germany

- *Regine Glatthaar (Ch. 12)*

  Fraunhofer–Institut
  für Physikalische Messtechnik,
  Heidenhofstr. 8,
  79110 Freiburg, Germany

- *Ulrich Gösele (Ch. 4)*

  Max Planck Institute
  of Microstructure Physics,
  Weinberg 2,
  06120 Halle, Germany

- *Stephan Götzinger (Ch. 11)*

  Humboldt–Universität zu Berlin,
  Institut für Physik,
  Hausvogteiplatz 5–7,
  10117 Berlin, Germany

- *Sebastian Golka (Ch. 16)*

  Fraunhofer Institute for Telecommunications,
  Heinrich-Hertz Institut,
  Einsteinufer 3,
  10587 Berlin, Germany

- *Andreas Gombert (Ch. 13)*

  Fraunhofer Institute for Solar Energy Systems ISE,
  Heidenhofstr.2,
  79110 Freiburg, Germany

- *Frank Hagmann (Ch. 1)*

  Institut für Theorie
  der Kondensierten Materie,
  Universität Karlsruhe,
  76128 Karlsruhe, Germany

- *Peter Hahn (Ch. 12)*

  Fraunhofer–Institut
  für Physikalische Messtechnik,
  Heidenhofstr. 8,
  79110 Freiburg, Germany

- *Thomas Happ (Ch. 17)*

  Technische Physik,
  Am Hubland,
  97074 Würzburg, Germany

- *Carsten Henkel (Ch. 2)*

  Institut für Physik,
  Universität Potsdam,
  Am Neuen Palais 10,
  14469 Potsdam, Germany
  e-mail: carsten.henkel@quantum.physik.uni-potsdam.de

- *Christian Hermann (Ch. 2 and 16)*

  Theoretical Quantum Electronics,
  Institute of Technical Physics,
  Deutsches Zentrum für Luft– und Raumfahrt (DLR),
  Pfaffenwaldring 38–40,
  70569 Stuttgart, Germany

- *Daniel Hermann (Ch. 1)*

  Institut für Theorie
  der Kondensierten Materie,
  Universität Karlsruhe,
  76128 Karlsruhe, Germany

- *Martin Hermatschweiler (Ch. 8)*

  Institut für Theorie
  der Kondensierten Materie,
  Universität Karlsruhe
  76128 Karlsruhe, Germany

  and

  DFG–Center for Functional Nanostructures (CFN)

- *Ortwin Hess (Ch. 2)*

  Theoretical Quantum Electronics,
  Institute of Technical Physics,
  Deutsches Zentrum für Luft– und Raumfahrt (DLR),
  Pfaffenwaldring 38–40,
  70569 Stuttgart, Germany

  and

  Advanced Technology Institute,
  School of Electronics and Physical Sciences,
  University of Surrey,
  Guildford, Surrey GU2 7XH, UK

- *Alexander W. Holleitner (Ch. 5)*

  Photonics and Electronics Group,
  Ludwig-Maximilians–University,
  Amalienstr. 54,
  80799 München, Germany

- *Uwe Hübner (Ch. 15)*

  Abt. Kryoelektronik,
  Institut für Physikalische Hochtechnologie Jena e.V.,
  Winzerlaer Str. 10,
  07745 Jena, Germany

- *Rumen Iliew (Ch. 14 and 15)*

  Institute of Solid State Theory and Theoretical Optics,
  Friedrich–Schiller–Universität Jena,
  Max–Wien–Platz 1,
  07743 Jena, Germany

- *Cecile Jamois (Ch. 12 and 16)*

  Max Planck Institute
  of Microstructure Physics,
  06120 Halle, Germany

- *Maria Kafesaki (Ch. 11)*

  Research Center of Crete,
  Heraklion,
  Crete, Greece

- *Martin Kamp (Ch. 17)*

  Technische Physik,
  Am Hubland,
  97074 Würzburg, Germany
  e-mail: martin.kamp@physik.uni-wuerzburg.de

- *Marcus Kessler (Ch. 15)*

  Alcatel Research Center Stuttgart,
  Alcatel SEL AG,
  Lorenzstr. 10,
  70435 Stuttgart, Germany

- *Johannes Kirchhof (Ch. 14)*

  Institute for Physical High Technology,
  Albert–Einstein–Straße 9,
  07745 Jena, Germany

- *Heinz–Siegfried Kitzerow (Ch. 9)*

  Department of Chemistry, Faculty of Science
  University of Paderborn
  Warburger Str. 100
  33098 Paderborn, Germany
  e-mail: kitzerow@chemie.upb.de

- *Thomas Klar (Ch. 5)*

  Photonics and Electronics Group,
  Ludwig-Maximilians–University,
  Amalienstr. 54,
  80799 München, Germany

- *Ernst–Bernhard Kley (Ch. 15)*

  Institut für Angewandte Physik,
  Friedrich–Schiller–Universität Jena,
  Max–Wien–Platz 1,
  07743 Jena, Germany

- *Jens Kobelke (Ch. 14)*

  Institute for Physical High Technology,
  Albert–Einstein–Straße 9,
  07745 Jena, Germany

- *Wolf–Peter Koch (Ch. 8)*

  Institut für Angewandte Physik,
  Universität Karlsruhe (TH),
  Wolfgang–Gaede–Straße 1,
  76131 Karlsruhe, Germany

  and

  DFG–Center for Functional Nanostructures (CFN)

- *Stephan W. Koch (Ch. 3)*

  Department of Physics and Material Sciences Center,
  Philipps University,
  Renthof 5,
  35032 Marburg, Germany

- *Christian Koos (Ch. 10)*

  High–Frequency and Quantum Electronics Laboratory,
  University of Karlsruhe,
  Kaiserstr. 12,
  76128 Karlsruhe, Germany

- *Peter Kramper (Ch. 11)*

  CNRS/LPN,
  route de Nozay,
  91460 Marcoussis, France

- *Jürgen Kuhl (Ch. 5)*

  Max–Planck–Institut
  für Festkörperforschung,
  Heisenbergstr. 1,
  70569 Stuttgart, Germany

- *Armin Lambrecht (Ch. 12)*

  Fraunhofer–Institut
  für Physikalische Messtechnik,
  Heidenhofstr. 8,
  79110 Freiburg, Germany

- *Sergiu Langa (Ch. 4)*

  Faculty of Engineering,
  Christian–Albrechts–University of Kiel,
  Kaiserstr. 2,
  24143 Kiel, Germany

- *Falk Lederer (Ch. 14 and 15)*

  Institute of Solid State Theory and Theoretical Optics,
  Friedrich–Schiller–Universität Jena,
  Max–Wien–Platz 1,
  07743 Jena, Germany

- *Uli Lemmer (Ch. 13)*

  Lichttechnisches Institut,
  Universität Karlsruhe,
  76128 Karlsruhe, Germany
  e-mail: uli.lemmer@lti.uni-karlsruhe.de

- *Christian Liguda (Ch. 15)*

  Materials in Electrical Engineering
  and Optics,
  Technische Universität Hamburg-Harburg,
  Eissendorfer Strasse 38,
  20173 Hamburg, Germany

- *Stefan Linden (Ch. 5 and 8)*

  Institut für Nanotechnologie,
  Forschungszentrum Karlsruhe
  in der Helmholtz–Gemeinschaft,
  76021 Karlsruhe, Germany

  and

  DFG–Center for Functional Nanostructures (CFN)

  and

  Max–Planck–Institut
  für Festkörperforschung,
  Heisenbergstr. 1,
  70569 Stuttgart, Germany

- *Stefan Lölkes (Ch. 4)*

  Faculty of Engineering,
  Christian–Albrechts–University of Kiel,
  Kaiserstr. 2,
  24143 Kiel, Germany

- *Yun Luo (Ch. 4)*

  Max Planck Institute
  of Microstructure Physics,
  Weinberg 2,
  06120 Halle, Germany

- *John Lupton (Ch. 5)*

  Photonics and Electronics Group,
  Ludwig-Maximilians–University,
  Amalienstr. 54,
  80799 München, Germany

- *Reinhard März (Ch. 16)*

  Infineon Technologies AG,
  Corporate Research,
  Otto-Hahn-Ring 6,
  81739 München, Germany

- *Sven Mahnkopf (Ch. 17)*

  Technische Physik,
  Am Hubland,
  97074 Würzburg, Germany

- *Georg Maret (Ch. 6)*

  Department of Physics,
  University of Konstanz,
  Box M 621,
  78457 Konstanz, Germany

- *Sven Matthias (Ch. 4)*

  Max Planck Institute
  of Microstructure Physics,
  Weinberg 2,
  06120 Halle, Germany

- *Torsten Meier (Ch. 3)*

  Department of Physics and Material Sciences Center,
  Philipps University,
  Renthof 5,
  35032 Marburg, Germany

- *Daniel C. Meisel (Ch. 8)*

  Institut für Nanotechnologie,
  Forschungszentrum Karlsruhe
  in der Helmholtz–Gemeinschaft,
  76021 Karlsruhe, Germany

  and

  DFG–Center for Functional Nanostructures (CFN)

- *Hans–Georg Meyer (Ch. 15)*

  Abt. Kryoelektronik,
  Institut für Physikalische Hochtechnologie Jena e.V.,
  Winzerlaer Str. 10,
  07745 Jena, Germany

- *Dirk Michaelis (Ch. 16)*

  Fraunhofer-Institute for Applied Optics and Precision Engineering (IOF),
  Albert-Einstein-Str. 7,
  07745 Jena, Jena

- *Sergei Mingaleev (Ch. 1)*

  Institut für Theorie
  der Kondensierten Materie,
  Universität Karlsruhe,
  76128 Karlsruhe, Germany

  and

  Bogolyubov Institute
  for Theoretical Physics,
  03143 Kiev, Ukraine

- *Wolfgang Morgenroth (Ch. 15)*

  Abt. Kryoelektronik,
  Institut für Physikalische Hochtechnologie Jena e.V.,
  Winzerlaer Str. 10,
  07745 Jena, Germany

- *Frank Müller (Ch. 4)*

  Max Planck Institute
  of Microstructure Physics,
  Weinberg 2,
  06120 Halle, Germany

- *Dietmar Nau (Ch. 5)*

  Institute of Applied Physics,
  University of Bonn, Wegelerstr. 8,
  53115 Bonn, Germany

- *Stefan Nolte (Ch. 15)*

  Institut für Angewandte Physik,
  Friedrich–Schiller–Universität Jena,
  Max–Wien–Platz 1,
  07743 Jena, Germany

- *Suresh Pereira (Ch. 1 and 13)*

  Institut für Theorie
  der Kondensierten Materie,
  Universität Karlsruhe,
  76128 Karlsruhe, Germany

- *Ulf Peschel (Ch. 15)*

  Institut für Festkörpertheorie und Theoretische Optik,
  Friedrich–Schiller–Universität Jena,
  Max–Wien–Platz 1,
  07743 Jena, Germany

- *Alexander Petrov (Ch. 15)*

  Materials in Electrical Engineering
  and Optics,
  Technische Universität Hamburg-Harburg,
  Eissendorfer Strasse 38,
  20173 Hamburg, Germany

- *Gero von Plessen (Ch. 5)*

  1. Physikalisches Institut,
  RWTH–Aachen,
  Huyskensweg,
  52074 Aachen, Germany

- *Johann–Peter Reithmaier (Ch. 9)*

  Technical Physics
  Julius-Maximilians-Universität Würzburg
  Am Hubland
  97074 Würzburg
  Germany

- *Stefan Riechel (Ch. 13)*

  Photonics and Optoelectronics Group,
  Department of Physics & Centre for NanoScience (CeNS),
  University of Munich,
  80799 Munich, Germany

- *Andrey L. Rogach (Ch. 7)*

  Photonics and Optoelectronics Group,
  Department of Physics & Centre for NanoScience (CeNS),
  University of Munich,
  80799 Munich, Germany

- *Sergei G. Romanov (Ch. 7)*

  Institute of Materials Science & Department
  of Electrical and Information Engineering,
  University of Wuppertal,
  42097 Wuppertal, Germany
  e-mail: romanov@uni-wuppertal.de

  On leave from

  A.F. Ioffe Physical Technical Institute,
  St. Petersburg, Russia

- *Vahid Sandoghdar (Ch. 11)*

  Laboratorium für Physikalische Chemie,
  Eidgenossische Technische Hochschule (ETH),
  CH-8093 Zurich, Switzerland

- *Detlef Schelle (Ch. 15)*

  Institut für Angewandte Physik,
  Friedrich–Schiller–Universität Jena,
  Max–Wien–Platz 1,
  07743 Jena, Germany

- *Ullrich Scherf (Ch. 5)*

  Photonics and Electronics Group,
  Ludwig-Maximilians–University,
  Amalienstr. 54,
  80799 München, Germany

- *Jörg Schilling (Ch. 4 and 12)*

  Max Planck Institute
  of Microstructure Physics,
  06120 Halle, Germany

  and

  California Institute of Technology,
  Pasadena, CA 91125, USA

- *Matthias Schillinger (Ch. 1)*

  Institut für Theorie
  der Kondensierten Materie,
  Universität Karlsruhe,
  76128 Karlsruhe, Germany

- *Florian Schindler (Ch. 5)*

  Photonics and Electronics Group,
  Ludwig-Maximilians–University,
  Amalienstr. 54,
  80799 München, Germany

- *Markus Schmidt (Ch. 15)*

  Materials in Electrical Engineering
  and Optics,
  Technische Universität Hamburg-Harburg,
  Eissendorfer Strasse 38,
  20173 Hamburg, Germany

- *Kai Schubert (Ch. 5)*

  Max–Planck–Institut
  für Festkörperforschung,
  Heisenbergstr. 1,
  70569 Stuttgart, Germany

- *Kay Schuster (Ch. 14)*

  Institute for Physical High Technology,
  Albert–Einstein–Straße 9,
  07745 Jena, Germany

- *Stefan L. Schweizer (Ch. 4 and 12)*

  Max Planck Institute
  of Microstructure Physics,
  Weinberg 2,
  06120 Halle, Germany

  and

  Department of Physics,
  University Paderborn,
  Warburger Str. 100,
  33098 Paderborn, Germany

- *Vladimir G. Solovyev (Ch. 7)*

  Institute of Materials Science & Department
  of Electrical and Information Engineering,
  University of Wuppertal,
  42097 Wuppertal, Germany

  On leave from

  S.M. Kirov State Pedagogical Institute,
  Pskov, Russia

- *Clivia M. Sotomayor Torres (Ch. 7)*

  Institute of Materials Science & Department
  of Electrical and Information Engineering,
  University of Wuppertal,
  42097 Wuppertal, Germany

- *Joachim Stehr (Ch. 5)*

  Photonics and Electronics Group,
  Ludwig-Maximilians-University,
  Amalienstr. 54,
  80799 München, Germany

- *Sergei G. Tikhodeev (Ch. 5)*

  General Physics Institute RAS,
  Vavilova 38,
  Moscow 119991, Russia

  and

  Max–Planck–Institut
  für Festkörperforschung,
  Heisenbergstr. 1,
  70569 Stuttgart, Germany

- *Andreas Tünnermann (Ch. 15)*

  Institut für Angewandte Physik,
  Friedrich–Schiller–Universität Jena,
  Max–Wien–Platz 1,
  07743 Jena, Germany

- *Lasha Tkeshelashvili (Ch. 1)*

  Institut für Theorie
  der Kondensierten Materie,
  Universität Karlsruhe,
  76128 Karlsruhe, Germany

- *Klaus Wandel (Ch. 16)*

  Sentech Instruments GmbH,
  Carl-Scheele-Straße 16,
  12489 Berlin, Germany

- *Martin Wegener (Ch. 8)*

  Institut für Angewandte Physik,
  Universität Karlsruhe (TH),
  Wolfgang–Gaede–Straße 1,
  76131 Karlsruhe, Germany

  and

  Institut für Nanotechnologie,
  Forschungszentrum Karlsruhe
  in der Helmholtz–Gemeinschaft,
  76021 Karlsruhe, Germany

  and

  DFG–Center for Functional Nanostructures (CFN)

- *Ralf B. Wehrspohn (Ch. 4 and 12)*

  Max Planck Institute
  of Microstructure Physics,
  Weinberg 2,
  06120 Halle, Germany
  e-mail:
  wehrspohn@physik.uni-paderborn.de

and

Department of Physics,
University Paderborn,
Warburger Str. 100,
33098 Paderborn, Germany

- *Waltraud Wischmann (Ch. 15)*

  Alcatel Research Center Stuttgart,
  Alcatel SEL AG,
  Lorenzstr. 10,
  70435 Stuttgart, Germany

- *Rudolf Zentel (Ch. 6)*

  Institute of Organic Chemistry,
  Johannes Gutenberg-University,
  Duesbergweg 10–14,
  55099 Mainz, Germany

- *Thomas Zentgraf (Ch. 5)*

  Max–Planck–Institut
  für Festkörperforschung,
  Heisenbergstr. 1,
  70569 Stuttgart, Germany

1 On the solid-state theoretical description of photonic crystals

Kurt Busch,[1]*, Marcus Diem, Meikel Frank, Antonio Garcia-Martin, Frank Hagmann, Daniel Hermann, Sergei Mingaleev, Suresh Pereira, Matthias Schillinger, and Lasha Tkeshelashvili*

1.1 Introduction

Since the invention of the laser, progress in Photonics has been intimately related to the development of optical materials which allow one to control the flow of electromagnetic radiation or to modify light–matter interaction. Photonic Crystals (PhCs) represent a novel class of optical materials which elevates this principle to a new level of sophistication. These artificial structures are characterized by two–dimensional (2D) or three–dimensional (3D) periodic arrangements of dielectric material which lead to the formation of an energy band structure for electromagnetic waves propagating in them. Recent advances in micro–structuring technology provide an enormous flexibility in the choice of material composition, lattice periodicity and symmetry of these arrangements allowing one to fabricate PhCs with embedded defect structures. As a consequence, the dispersion relation and associated mode structure of PhCs may be tailored to almost any need. This results in a potential for controlling the optical properties of PhCs that may eventually rival the flexibility in tailoring the properties of their electronic counterparts, the semiconducting materials.

One of the most striking features of PhCs is associated with the fact that suitably engineered PhCs may exhibit frequency ranges over which ordinary linear propagation is forbidden, irrespective of direction. These photonic band gaps (PBGs) [1–3] lend themselves to numerous applications in linear, nonlinear and quantum optics. For instance, in the linear regime novel optical guiding characteristics through the engineering of defects such as microcavities, waveguides and their combination into functional elements, such as wavelength add-drop filters [4, 5] may be realized. Similarly, the incorporation of nonlinear materials into PBG structures is the basis for novel solitary wave propagation for frequencies inside the PBG. In the case of lattice–periodic Kerr–nonlinearities, the threshold intensities and symmetries of these solitary waves depend on the direction of propagation [6–8], whereas in the case of nonlinear waveguiding structures embedded in a 2D PBG material, the propagation characteristics strongly depend on the nature of the waveguides [9]. Finally, the existence of complete PBGs allows one to inhibit spontaneous emission for atomic transition frequencies, deep in the PBG [1] and leads to strongly non–Markovian effects, such as fractional localization of the atomic population for atomic transition frequencies in close proximity to a complete PBG [10, 11].

---

[1] Corresponding author, e-mail: kbusch@physics.ucf.edu

Photonic Crystals. Edited by K. Busch, S. Lölkes, R. B. Wehrspohn and H. Föll
Copyright © 2004 Wiley-VCH Verlag GmbH & Co. KGaA
ISBN: 3-527-40432-5

The discovery of superrefractive phenomena such as the superprism effect [12, 13] and the resulting potential applications in telecommunication technology [14, 15] have recently attracted a lot of attention to the highly anisotropic nature of iso–frequency surfaces in the photonic band structure. Similarly, the tailoring of photonic dispersion relations and associated mode structures, group velocities, group velocity dispersions (GVDs) and effective nonlinearities through judiciously designed PhCs, allows one to explore regimes of nonlinear wave propagation in PhCs that hitherto have been virtually inaccessible. For instance, the existence of flat bands that are characteristic for 2D and 3D PhCs and the associated low group velocities may greatly enhance frequency conversion effects [16] and may lead to improved designs for distributed-feedback (DFB) laser systems [16–18]. Photonic crystals with embedded defects, such as microcavities and waveguiding structures, hold tremendous potential for the creation of photonic integrated circuits.

As in virtually any nano–photonic system, a careful theoretical analysis is of paramount importance when interpreting experimental data, and when predicting and realizing novel physical phenomena in PhCs. To date, photonic band structure calculations are used to determine and predict the dispersion relations of perfect, infinitely extended PhCs, and PhCs with simple defects such as isolated cavities and waveguides. More complex situations such as transmission and reflection from finite slabs of PhC–material or through waveguide bends are usually analyzed through direct simulations of Maxwell's equations, based on Finite–Difference Time–Domain (FDTD) or Finite Element (FE) methods. While these are perfectly legitimate approaches, which rest on some 30 years of experience, these techniques do require substantial computational resources and, as a consequence, modeling has been restricted to selected small scale PhC circuits. Moreover, certain computationally intensive aspects related to small scale PhC circuits, such as studies of the effect of fabricational tolerances and the optimization of device designs, still present serious challenges when working with FDTD or FE methods.

In this manuscript, we want to illustrate how the natural affinity of electromagnetic wave propagation in PhCs to the case of electron (wave) transport in semiconducting materials, allows us to devise a comprehensive and highly efficient theoretical framework for the qualitative, as well as quantitative determination of the optical properties of PhCs: Photonic band structure computations allow us to obtain photonic band structures and associated Bloch functions. Related physical quantities such as densities of states (DOS) and group velocities can be calculated with little additional work. Nonlinear PhCs can be studied through an appropriate multi–scale analysis that utilizes Bloch functions as carrier waves and leads to a natural generalization of the well–known slowly varying envelope approximation. Combining band structure calculations with elements from diffractive optics, enables us to determine the reflection and transmission properties of finite PhC–slabs. Finally, we show how defect structures in PhCs can be efficiently treated with the help of photonic Wannier functions. Moreover, this Wannier function approach allows us to formulate a PhC circuit theory, where a defect structure is replaced by the optical analogue of an impedance matrix.

1.2 Photonic band structure computation

The goal of photonic band structure computation is the solution of the wave equation for the perfect PhC, i.e., for an infinitely extended, strictly periodic array of dielectric material. The resulting dispersion relation and associated mode structure may then be further processed to derive related physical quantities such as DOS and group velocities. For simplicity of presentation, we consider in the remainder of the manuscript only 2D PhCs in the TM–polarized case. However, we want to emphasize that analogous considerations apply to the case of TE–polarized radiation in 2D PhCs, as well as to electromagnetic wave propagation in 3D PhCs and will give references where appropriate.

For TM–polarized radiation in 2D PhCs, the wave equation reduces to a single scalar equation for the z-component $E(\vec{r})$ of the electric field:

$$\frac{1}{\varepsilon_{\mathrm{p}}(\vec{r})}\left(\partial_x^2+\partial_y^2\right)E(\vec{r})+\frac{\omega^2}{c^2}E(\vec{r})=0. \tag{1.1}$$

Here, c denotes the vacuum speed of light and $\vec{r}=(x,y)$ denotes a 2D position vector. The dielectric constant $\varepsilon_{\mathrm{p}}(\vec{r})\equiv\varepsilon_{\mathrm{p}}(\vec{r}+\vec{R})$ contains all the structural information of the PhC and is periodic with respect to the set $\mathcal{R}=\{n_1\vec{a}_1+n_2\vec{a}_2;(n_1,n_2)\in\mathcal{Z}^2\}$ of lattice vectors $\vec{R}$, generated by the primitive translations $\vec{a}_i,\ i=1,2$ which serve as a basis for the underlying PhC lattice. Equation (1.1) represents a differential equation with periodic coefficients and, therefore, its solutions obey the Bloch–Floquet theorem: The discrete translational symmetry of the lattice allows us to label the solutions with a wave vector $\vec{k}$ that is restricted to the first Brillouin zone (BZ) of the reciprocal lattice. This back-folding of the dispersion relation $\omega(\vec{k})$ to the first BZ introduces a discrete band index n. The eigenmodes (Bloch functions) corresponding to eigenfrequency $\omega_n(\vec{k})$ exhibit the Bloch–Floquet form of modulated plane waves

$$E_{n\vec{k}}(\vec{r})=e^{i\vec{k}\vec{r}}\,u_{n\vec{k}}(\vec{r}). \tag{1.2}$$

Here, $u_{n\vec{k}}(\vec{r}+\vec{R})=u_{n\vec{k}}(\vec{r})$ is periodic with the lattice. A straightforward way of solving Eq. (1.1) and (1.2) is to expand all the periodic functions into a Fourier series over the reciprocal lattice $\mathcal{G}$

$$\frac{1}{\varepsilon_{\mathrm{p}}(\vec{r})}=\sum_{\vec{G}}\eta_{\vec{G}}\,e^{i\vec{G}\cdot\vec{r}}\,,\qquad E_{\vec{k}}(\vec{r})=\sum_{\vec{G}}a^{\vec{k}}_{\vec{G}}\,e^{i(\vec{k}+\vec{G})\cdot\vec{r}}\,. \tag{1.3}$$

The Fourier coefficients $\eta_{\vec{G}}$ are given by

$$\eta_{\vec{G}}=\frac{1}{V_{\mathrm{WSC}}}\int_{\mathrm{WSC}}d^2\vec{r}\,\frac{1}{\varepsilon_{\mathrm{p}}(\vec{r})}\,e^{-i\vec{G}\cdot\vec{r}}\,, \tag{1.4}$$

where we have designated the volume of the Wigner-Seitz cell (WSC) by V_{WSC}. Inserting this expansion into Eq. (1.1) and defining the coefficients $b^{\vec{k}}_{\vec{G}}\equiv|\vec{k}+\vec{G}|\,a^{\vec{k}}_{\vec{G}}$, transforms the differential equation into an infinite matrix eigenvalue problem

$$\sum_{\vec{G}'}|\vec{k}+\vec{G}||\vec{k}+\vec{G}'|\,\eta_{\vec{G}-\vec{G}'}\,b^{\vec{k}}_{\vec{G}'}=\frac{\omega^2_{\vec{k}}}{c^2}\,b^{\vec{k}}_{\vec{G}}\,, \tag{1.5}$$

which must be suitably truncated to become accessible to an approximate numerical solution. Further details of the plane wave method (PWM) for 2D TE and 3D isotropic systems can be found, for instance, in [19] and for anisotropic 3D systems in [20].

In Fig. 1.1(b), we show the band structure for TM–polarized radiation in a 2D PhC consisting of a square lattice (lattice constant a) of cylindrical air pores (radius $R_{\text{pore}} = 0.475a$) in a silicon matrix ($\varepsilon = 12$) (for details on the fabrication of this structure, we would like to refer the reader to Chapter 4 of this book). This structure exhibits two complete 2D bandgaps. The larger, fundamental bandgap (20% of the midgap frequency) extends between $\omega = 0.238 \times 2\pi c/a$ to $\omega = 0.291 \times 2\pi c/a$ and the smaller, higher order bandgap (8% of the midgap frequency) extends from $\omega = 0.425 \times 2\pi c/a$ to $\omega = 0.464 \times 2\pi c/a$. In the remainder of this chapter, this particular PhC will serve as the model problem for which we illustrate our solid state theoretical approach to the optical properties of PhCs.

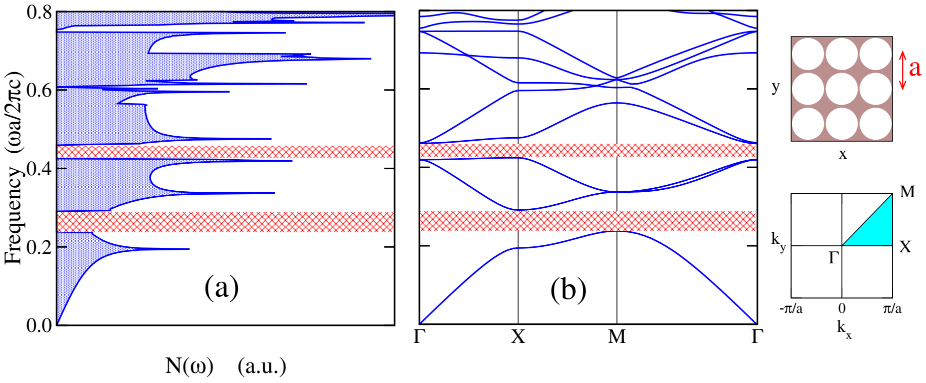

Figure 1.1: Density of states (a) and photonic band structure (b) for TM–polarized radiation in a square lattice (lattice constant a) of cylindrical air pores of radius $R_{\text{pore}} = 0.475a$ in dielectric with $\varepsilon = 12$ (silicon). This PhC exhibits a large fundamental gap extending from $\omega = 0.238 \times 2\pi c/a$ to $\omega = 0.291 \times 2\pi c/a$. A higher order band gap extends from $\omega = 0.425 \times 2\pi c/a$ to $\omega = 0.464 \times 2\pi c/a$.

1.2.1 Density of states

The photonic dispersion relation $\omega_n(\vec{k})$ gives rise to a photonic density of states (DOS), which plays a fundamental role for the understanding of the quantum optical properties of active material embedded in PhCs [11]. The photonic DOS $N(\omega)$ is defined by "counting" all allowed states with a given frequency ω

$$N(\omega) = \sum_n \int_{BZ} d^2k \; \delta(\omega - \omega_n(\vec{k})). \tag{1.6}$$

In Fig. 1.1(a) we depict the DOS for our model system, where the photonic band gaps are manifest as regions of vanishing DOS. Characteristic for 2D systems is the linear behavior for small frequencies as well as the logarithmic singularities, the so–called van Hove singularities, associated with vanishing group velocities for certain frequencies inside the bands. However, for applications to quantum optical experiments in photonic crystals, it is necessary to investigate not only the (overall) availability of modes with frequency ω, but also the local coupling strength of an emitter at a certain position $\vec{r}$ in the PhC to the electromagnetic environment provided by the PhC. Consequently, it is the overlap matrix element of the emitter's dipole moment to the eigenmodes (Bloch functions) that is determining quantum optical properties such as decay rates etc. [11]. This may be combined into the local DOS (LDOS), $N(\vec{r},\omega)$, defined as

$$N(\vec{r},\omega) = \sum_n \int_{BZ} d^2k \; |E_{n\vec{k}}(\vec{r})|^2 \, \delta(\omega - \omega_n(\vec{k})). \tag{1.7}$$

For an actual calculation, the integrals in Eq. (1.6) and Eq. (1.7) must be suitably discretized and one may again revert to the methods of electronic band structure calculations (see Ref. [19]).

1.2.2 Group velocity and group velocity dispersion

In order to understand pulse propagation in linear and nonlinear PhCs, it is necessary to obtain group velocities and the group velocity dispersion (GVD) from the photonic band structure. In principle, this can be done through a simple numerical differentiation of the band structure, but in particular for the GVD, this becomes computationally complicated and great care must be exercised in order to avoid numerical instabilities. Therefore, we want to demonstrate how to obtain group velocities and GVD through an adaptation of the so–called $\vec{k}\cdot\vec{p}$–perturbation theory (kp–PT) of electronic band structure theory. This approach has been applied to systems of arbitrary dimensions [21–23] and will be particularly useful for the investigation of nonlinear effects in PhCs.

With the help of the Bloch–Floquet theorem Eq. (1.2), we may rewrite the wave equation (1.1) as an equation of motion for the lattice-periodic functions $u_{\vec{k}}(\vec{r})$

$$\left(\Delta + 2i\,\nabla\cdot\vec{k} - \vec{k}^2\right) u_{\vec{k}}(\vec{r}) + \frac{\omega_{\vec{k}}^2}{c^2}\,\varepsilon_{\mathrm{p}}(\vec{r})\,u_{\vec{k}}(\vec{r}) = 0\;, \tag{1.8}$$

where, $\Delta = \partial_x^2 + \partial_y^2$. An inspection of Eq. (1.8) for the lattice-periodic $u_{\vec{k}+\vec{q}}(\vec{r})$

$$\left(\Delta + 2i\,\nabla\cdot\vec{k} - \vec{k}^2\right)\; u_{\vec{k}+\vec{q}}(\vec{r}) + \vec{q}\cdot\left(2\hat{\Omega} - \vec{q}\right)\; u_{\vec{k}+\vec{q}}(\vec{r}) + \frac{\omega_{\vec{k}+\vec{q}}^2}{c^2}\,\varepsilon_{\mathrm{p}}(\vec{r})\,u_{\vec{k}+\vec{q}}(\vec{r}) = 0\;, \tag{1.9}$$

at a nearby wave vector $\vec{k}+\vec{q}\,(|\vec{q}| \ll \pi/a)$ suggests that we treat the second term on the l.h.s. as a perturbation to Eq. (1.8). In writing Eq. (1.9), we have introduced $\hat{\Omega} = i(\nabla + i\vec{k})$. Comparing the perturbation series with a Taylor–expansion of frequency $\omega_{\vec{k}+\vec{q}}$ around $\vec{k}$, connects group velocities $\vec{v}_{\vec{k}} = \partial_{\vec{k}}\omega_{\vec{k}}$ and GVD tensor elements $M_{\vec{k}}^{ij} = \partial_{k_i}\partial_{k_j}\omega_{\vec{k}}$, $i = 1, 2$ to expressions familiar from second order perturbation theory [21–23]. Explicitly [22], we obtain for the group velocity

$$\vec{v}_{n\vec{k}} = \frac{c^2}{\omega_{n\vec{k}}}\langle n\vec{k}|(-i\nabla)|n\vec{k}\rangle\;, \tag{1.10}$$

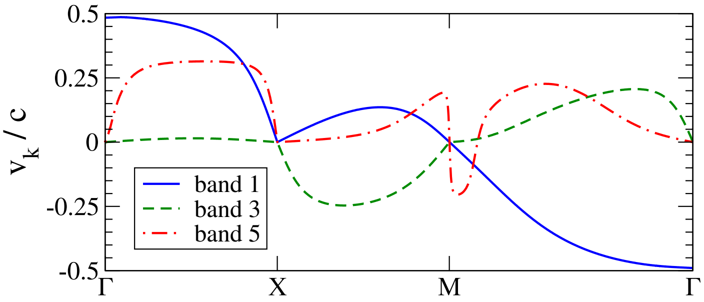

Figure 1.2: Group velocities for bands 1, 3, and 5 of our model system (see Fig. 1.1). The group velocities of these bands exhibit extreme variations which may have numerous application in superrefractive phenomena and classical nonlinear optics. This illustrates the huge parameter space of effective parameters accessible with PhCs.

and for the GVD tensor

$$\vec{q}\cdot\mathcal{M}_{n\vec{k}}\cdot\vec{q} = |\vec{q}|^2 \frac{c^2}{2\omega_{n\vec{k}}}\langle n\vec{k}|n\vec{k}\rangle - \frac{1}{2\omega_{n\vec{k}}}\left(\vec{q}\cdot\vec{v}_{n\vec{k}}\right)^2 + \frac{2c^4}{\omega_{n\vec{k}}}\sum_{m\neq n}\frac{\langle n\vec{k}|(-i\vec{q}\cdot\nabla)|m\vec{k}\rangle\langle m\vec{k}|(-i\vec{q}\cdot\nabla)|n\vec{k}\rangle}{\omega^2_{n\vec{k}}-\omega^2_{m\vec{k}}} \, . \tag{1.11}$$

Here, we have used the notation $\int_{\mathrm{WSC}} d^2r\, E^*_{n\vec{k}}(\vec{r})\,\hat{O}\,E_{m\vec{k}}(\vec{r}) = \langle n\vec{k}|\hat{O}|m\vec{k}\rangle$ for matrix elements of the operator $\hat{O}$ between Bloch functions $E_{n\vec{k}}(\vec{r})$ and $E_{m\vec{k}}(\vec{r})$.

Despite their complicated appearance, these expressions can be evaluated rather easily using standard PWM and obtain very accurate, efficient and numerically stable results. In Fig. 1.2, we display the variation of the group velocities associated with bands 1, 3, and 5 of our model system. Clearly visible, are the extreme variations ranging from $0.5c$ for band 1 in the long wavelength (effective medium) limit, all the way to the almost vanishing group velocity of band 5 along the entire Γ–X direction. This illustrates the huge parameter space of effective group velocities that can *simultaneously* be realized in PhCs.

1.3 Nonlinear photonic crystals

For large intensities of the light propagating through the photonic crystal, we should also account for the nonlinear polarization $P_{\mathrm{NL}}(\vec{r},t)$, representing the nonlinear response of the materials that comprise the PhC. In this case, Maxwell's equations for the TM-polarized light propagating in PhCs take the form

$$\left(\partial_x^2+\partial_y^2\right)E(\vec{r},t) - \frac{\varepsilon_{\mathrm{p}}(\vec{r})}{c^2}\partial_t^2 E(\vec{r},t) = \frac{4\pi}{c^2}\partial_t^2 P_{\mathrm{NL}}(\vec{r},t) \, . \tag{1.12}$$

In writing this equation we have neglected the linear dispersion of the constituent materials, which is usually negligible compared to the dispersion associated with the photonic band structure.

The existence of PBGs, the tailoring of photonic dispersion relations and mode structures through judiciously designed PhCs, represent a novel paradigm for nonlinear wave interactions. To date, only a few works have been carried out for Kerr–nonlinearities [6–8] or for $\chi^{(2)}$–nonlinearities [16, 24] in PhCs. Moreover, the approximations involved in some of these works seriously limit the applicability of these theories to real PhCs. For instance, the study of Kerr–nonlinearities in 2D PhCs [6] has been limited to weak modulations in the linear index of refraction. Similarly, the recent investigation of second harmonic generation in 2D PhCs [16, 24] failed to reproduce the well–known results for the limiting case of homogeneous materials.

In this section, we outline a systematic approach to quantitative calculations of the optical properties of nonlinear PhCs that is based on a multi–scale approach [25]. Since optical nonlinearities are generally quite weak, Eq. (1.12) should be solved in a perturbative way, taking into account that the effect of the nonlinearity accumulates only on time and spatial scales that are much slower and longer, respectively, than the natural scales of the underlying linear problem. For electromagnetic wave propagation in PhCs, these natural scales of the linear problem are determined through the inverse optical period and the associated wavelength of the light. Therefore, key simplifications to Eq. (1.12) arise from separating the fast from slow scales in space and time in the electromagnetic field [21]

$$E(\vec{r},t) = \mu e_1(\vec{r}_0, \vec{r}_1, \cdots; t_0, t_1, \cdots) + \mu^2 e_2(\vec{r}_0, \vec{r}_1, \cdots; t_0, t_1, \cdots) + \cdots \,, \qquad (1.13)$$

by formally replacing the space and time variables, $\vec{r}$ and t, with a set of independent variables $\vec{r}_n \equiv \mu^n \vec{r}$ and $t_n \equiv \mu^n t$. Here, we denote the fastest spatial scale corresponding to the wavelength of the electromagnetic waves propagating in the linear PhC by $\vec{r}_0$. Likewise, we denote the associated fastest temporal scale by t_0. Depending on the type of nonlinearity, the hierarchy is suitably truncated and a closed set of equations is obtained by collecting terms of equal order in μ. To express the results in terms of the original physical variables, one has to set $\mu = 1$ at the end of the calculation [21].

As an illustration, we consider the case of the Kerr-nonlinear material, for which the refractive index depends on the light intensity leading to the nonlinear polarization $P_{\text{NL}}(\vec{r},t) = \chi^{(3)}(\vec{r}) E^3(\vec{r},t)$. Here, we have neglected the nonlinear material dispersion. In this case, substituting Eq. (1.13) into Eq. (1.12) and assuming that third-harmonic generation effects are not phase-matched and, hence, can be neglected, we obtain in the third order in μ that

$$e_1(\vec{r}_0, \vec{r}_1, \cdots; t_0, t_1, \cdots) = a_{n\vec{k}}(\vec{z}_1; \vec{r}_2, \cdots; t_1, \cdots)\, E_{n\vec{k}}(\vec{r}_0)\, e^{i\omega_{n\vec{k}} t_0} + c.c. \,, \qquad (1.14)$$

where $\vec{z}_1 \equiv \vec{r}_1 - \vec{v}_{n\vec{k}} t_1$ with the group velocity $\vec{v}_{n\vec{k}}$ given by Eq. (1.10), the Bloch function $E_{n\vec{k}}(\vec{r}_0)$ represents a carrier wave and the envelope function $a_{n\vec{k}}(\vec{r}_1, \cdots; t_1, \cdots)$ has to be determined from the 2D nonlinear Schrödinger equation

$$\begin{aligned}
&\left[i \left(\vec{v}_{n\vec{k}} \cdot \nabla_{\vec{r}_2} + \partial_{t_2} \right) + \nabla_{\vec{z}_1} \cdot \mathcal{M}_{n\vec{k}} \cdot \nabla_{\vec{z}_1} \right] \, a_{n\vec{k}}(\vec{z}_1; \vec{r}_2 \cdots; t_2, \cdots) \\
&\quad + \alpha_{n\vec{k}} \left| a_{n\vec{k}}(\vec{z}_1; \vec{r}_2 \cdots; t_2, \cdots) \right|^2 a_{n\vec{k}}(\vec{z}_1; \vec{r}_2 \cdots; t_2, \cdots) = 0, \qquad (1.15)
\end{aligned}$$

where the GVD tensor $\mathcal{M}_{n\vec{k}}$ is given in Eq. (1.11) and the effective nonlinearity

$$\alpha_{n\vec{k}} = 6\pi\, \omega_{n\vec{k}} \int_{\text{WSC}} d^2 r\, \chi^{(3)}(\vec{r})\, |E_{n\vec{k}}(\vec{r})|^4 \qquad (1.16)$$

reflects how the carrier wave $E_{n\vec{k}}(\vec{r})$ samples the spatial distribution $\chi^{(3)}(\vec{r})$ of nonlinear material within the PhC.

The discussion of the solutions to Eq. (1.15) is outside the scope of the present work and we refer the reader to references on the inverse scattering theory and other methods [26]. However, we want to emphasize that, as a result of the foregoing analysis, we have obtained a generalization of the slowly varying envelope approximation. Within this approximation, the problem of pulse propagation in nonlinear PhCs is mapped onto the problem of an envelope function propagating in an effective homogeneous medium with group velocity $\vec{v}_{n\vec{k}}$, GVD tensor $\mathcal{M}_{n\vec{k}}$, and effective nonlinearity $\alpha_{n\vec{k}}$ that are determined by the carrier wave, which, in turn, is given by a Bloch function of the linear PhC. Therefore, the effective PhC parameters can be obtained from band structure theory via Eqs. (1.10), (1.11), and (1.16) and quantitative investigations become possible. Furthermore, we note that the above considerations are not limited to 2D TM–polarized radiation and have recently been extended to 3D systems by Bhat and Sipe [7]. Moreover, the above framework of multi–scale analysis in conjunction with $\vec{k}\cdot\vec{p}$–perturbation theory can be applied to other nonlinear PhC systems such as PhCs consisting of nonresonant $\chi^{(2)}$ [27] material and resonant distributed feedback lasing systems [18]. In the present case of Kerr–nonlinearities, other effects such as nonresonant soliton interactions can be considered and lead to interesting applications [28].

1.4 Finite structures

We now consider the problem of how a plane wave couples into a PhC of finite spatial extent. Our basic approach is to apply the Maxwell continuity conditions to the electric and magnetic fields inside and outside the crystal. However, unlike in the preceding subsections, we treat the fields inside the PhC as a linear superposition of plane waves, rather than explicitly using the Bloch functions of the crystal. We then use a scattering–matrix (S–matrix) to determine the amplitudes and phases of the fields everywhere in the system. While the S–matrix is slightly more complicated than the more familiar transfer matrix (T–matrix), it has the advantage that it deals more effectively with the highly evanescent modes that appear naturally in these types of problems.

The S–matrix approach for a fully 3D system is described in detail by Whittaker and Culshaw [29]. However, their formulation does not allow for an effective investigation of lossy PhCs. Therefore, in this section we indicate how to re–formulate the method of Whittaker and Culshaw to account for losses. We first consider the model system shown in Figure 1.3, where light in the x–z plane impinges from the left upon a metallo–dielectric grating structure. The system is finite in the z–direction, but infinite and periodic in the x–direction, with period a and fundamental lattice vector of magnitude $G = 2\pi/a$. This problem can be described in terms of a transverse-electric (TE) or a transverse–magnetic (TM) problem, where following the PhC convention, for the TE (TM) problem the electric (magnetic) field lies in the x–z plane. In the following we consider the TE problem. We divide the finite structure into a number of slices along the z–direction. Within each slice, we assume that the structure is well approximated by a grating that does not vary in the z–direction. For the model system of Fig. 1.3, this slicing process is fairly straightforward. We assume that the incident light has frequency ω, and wave vector $\vec{k} = (k_x, k_z)$. Since each slice is periodic in the x–direction,

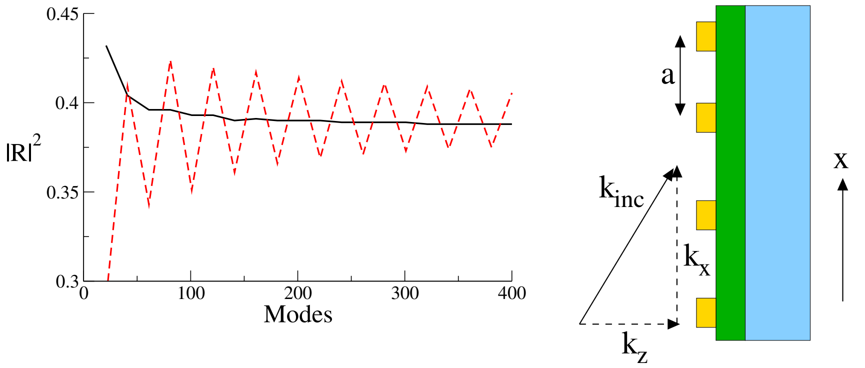

Figure 1.3: Model finite structure, in which a gold grating sits atop a buffer layer (green) and a substrate (blue). Light is incident from the left at an arbitrary angle to the normal, so that the k–vector is separated into a k_x and k_z component. Inset is the reflectivity of the structure as a function of the number of modes used in the solution for the improved choice of Töplitz matrices given in the text (black line) and for the usual choice (red dashed line, see [29]).

propagation through the system will generate a number of diffracted orders, characterized by a propagation constant q_n. Following the notation of Whittaker and Culshaw [29] , we use Fourier series to express the x–dependence of the quantities of interest, so that, for example

$$H_y^p(x,z) = \sum_{\alpha} \widetilde{H}_y^p(\alpha,z)\, e^{i(k_x+\alpha G)x}, \tag{1.17}$$

$$\widetilde{H}_y^p(\alpha,z) = \frac{1}{a}\int_0^a dx\, H_y^p(x,z)\, e^{-i\alpha G x},$$

where α is an integer, and where for the remainder of this section the p-superscript indicates the p^{th} slice. We also define the Töplitz matrices $\widehat{\varepsilon}^p_{\alpha\alpha'}$ and $\widehat{\eta}^p_{\alpha\alpha'}$, which we discuss in more detail below, and the diagonal matrix $\left(\widehat{k}_x\right)_{\alpha\alpha'} = \delta_{\alpha\alpha'}\left(k_x+\alpha G\right)$. With these definitions, we write our electric and magnetic fields in the p^{th} slice as

$$\widetilde{H}_y^p(\alpha,z) = \sum_n \left(a_n^p e^{iq_n^p(z-z_p)} + b_n^p e^{iq_n^p(z_{p+1}-z)}\right)\widetilde{\phi}_n^p, \tag{1.18}$$

$$\widetilde{E}_x^p(\alpha,z) = \sum_n \frac{1}{q_n^p}\left(a_n^p e^{iq_n^p(z-z_p)} - b_n^p e^{iq_n^p(z_{p+1}-z)}\right)\left(\mathsf{A}^p\widetilde{\phi}_n^p\right), \tag{1.19}$$

where z_p is the value of z at the *left* edge of the p^{th} layer, a_n^p and b_n^p are the amplitudes of forward and backward propagating light in the n^{th} mode, and where $\mathsf{A}^p = \omega^2 - \widehat{k}_x\widehat{\eta}^p\widehat{k}_x$. The value of $\widetilde{E}_z^p$ can be determined from Maxwell's equations. The quantity $\widetilde{\phi}_n^p(\alpha)$ is the Fourier series of the mode in the p^{th} slice associated with the propagation constant q_n^p. Using (1.18) and (1.19) in Maxwell's equations, we find an eigenvalue equation for q and $\widetilde{\phi}$:

$$\widehat{\varepsilon}\left(\omega^2 - \widehat{k}_x\widehat{\eta}\widehat{k}_x\right)\widetilde{\phi} = q^2\widetilde{\phi}, \tag{1.20}$$

where we have dropped the p–superscripts. This equation is a reduced version of Eq. (3.7) in Whittaker and Culshaw [29].

The eigenvalue problem (1.20) is solved by retaining a definite number N of plane waves in the Fourier series, so that the matrices involved in (1.20) are size $N \times N$. As $N \to \infty$, the Töplitz matrices $\widehat{\varepsilon}^p$ and $\widehat{\eta}^p$ can be generated directly from the Fourier series of $\varepsilon^p(x)$ and $\eta^p = 1/\varepsilon^p(x)$. However, for smaller values of N one must be slightly careful because these Töplitz matrices facilitate the transition from the real–space representation of Maxwell's equations to the Fourier space representation. When executing this transition, one encounters quantities such as $\varepsilon(x)\,E_x(x)$, for which the Fourier transform is most logically

$$\varepsilon(x)\,E_x(x) \to \sum_{\alpha'} \widetilde{\varepsilon}(\alpha-\alpha')\widetilde{E}_x(\alpha')\,, \tag{1.21}$$

where $\widetilde{\varepsilon}(\alpha-\alpha')$ is determined by the Fourier integral of the real-space dielectric constant $\varepsilon(x)$. This leads to the definition of the Töplitz matrix $\widehat{\varepsilon}_{\alpha\alpha'} = \widetilde{\varepsilon}(\alpha-\alpha')$. However, such a formulation ignores the fact that in many of our slices, the real–space functions $\varepsilon(x)$ and $E_x(x)$ are discontinuous. In such a situation, Li [30] has shown that the expansion (1.21) is inappropriate. Following Li's approach, the appropriate Töplitz matrices of our TE problem are given by first defining the intermediate matrices

$$\overline{\varepsilon}_{\alpha\alpha'} = \widetilde{\varepsilon}(\alpha-\alpha')\,, \qquad \overline{\eta}_{\alpha\alpha'} = \widetilde{\eta}(\alpha-\alpha')\,, \tag{1.22}$$

and then defining the final matrices

$$\widehat{\varepsilon} = (\overline{\eta})^{-1}\,, \qquad \widehat{\eta} = (\overline{\varepsilon})^{-1}\,. \tag{1.23}$$

This choice of Töplitz matrices is also appropriate for the full 3D problem.

Once the eigenvalue problem (1.20) is solved, the fields within a given slice are characterized by the values of a_n^p and b_n^p. The only remaining difficulty is the application of the Maxwell continuity conditions (that H_y and E_x must be continuous) at each interface. Typically, this is done by constructing a T–matrix that ultimately relates the set $\left(a_n^0, b_n^0\right)$ to the set $\left(a_n^P, b_n^P\right)$, where $p = P$ indexes the last layer of interest. However, it is numerically more stable to build an S–matrix that relates waves entering the structure $\left(a_n^0, b_n^P\right)$ to those leaving the structure $\left(a_n^P, b_n^0\right)$. An appropriate methodology for building this S-matrix is given in Whittaker and Culshaw [29].

In the inset of Figure 1.3, we plot the total reflection from the metallo–dielectric grating structure. For simplicity we assume that the structure has a semi–infinite substrate with index of refraction $n = 1.46$. We also include a 20 nm-thick buffer layer with $n = 1.95$, and a 20 nm–thick grating composed of gold, for which the frequency-dependent value of n is taken from ref. [31]. The elements of the grating are 32 nm wide, and have a period in the x–direction of 400 nm. We simulate normally–incident TE–polarized light with vacuum wavelength 650 nm. The solid curve uses the Töplitz matrices suggested in (1.23), while the red dashed curve uses those suggested by Whittaker and Culshaw [29]. The results with the new Töplitz matrices are displaying a significantly improved convergence behavior. We have also verified that the new Töplitz matrices are significantly better for the analysis of scattering loss in finite 3D PhCs, such as the Woodpile PhCs currently being fabricated via two–photon photopolymerization (see Chapter 9 in this book).

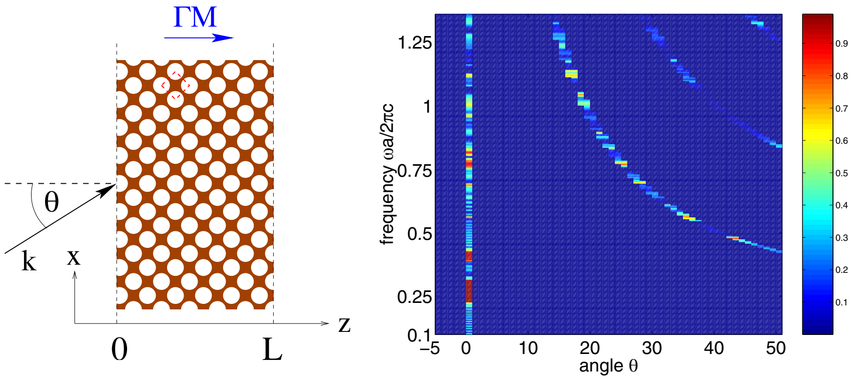

Figure 1.4: Left: Sketch of a typical setup for characterizing 2D PhC–slabs in Litrow–geometry. Right: Calculation of the reflection spectra (intensity) in Litrow–geometry for our model system when the 2D PhC is oriented along the Γ–M direction (see left panel). In this setup, only light reflected into the direct backscattering direction is collected. Clearly visible, are the different diffraction orders that are "decorated" with bulk PhC–effects. The parameters of the PhC–slab are given in the text.

We now use the S-matrix technique to consider transmission and reflection in the PhC model system, assuming that it has been cleaved along the Γ–M direction, such that it is finite in the z–direction but infinite and periodic in the x–direction (see Fig. 1.4, left panel). We further assume that the cleaving at $z = 0$ and $z = L$ cut through the center of the air pores. The cleaved structure includes 20 unit cells along the z–direction. To accurately model the circular pores, we divide the PhC into a large number of very thin layers, each of which is homogeneous along the z–direction. We find that the resulting staircase approximates the shape of the pores sufficiently well if we use about 100 layers per pore. In Fig. 1.4 right panel, we display the calculated reflection spectra (intensity) for this 2D–PhC slab in Litrow–geometry. Clearly visible, are the different diffraction orders that are "decorated" with bulk PhC–effects: The periodicity along the x–axis makes this PhC–slab an effective grating with a complicated frequency–dependent coupling to the incoming plane wave. For certain frequencies of the incoming radiation, there is no mode to which it could couple. As a result, the wave is completely reflected from the slab, albeit not entirely into the backscattering direction (incomplete blazing). For other frequencies, the light partially couples to propagating Bloch modes inside the PhC–slab, leading to a reduction in reflection. The strength of this coupling depends on the overlap of the incoming plane wave with a Bloch function at that frequency and the parallel crystal momentum, and therefore, depends both on the exact surface termination as well as on the symmetry of the Bloch function. To illustrate the latter point, we have calculated the frequency dependence of the total transmission through the PhC–slab for normal incidence. In Fig. 1.5, we compare these results with the corresponding band structure along the Γ–M direction. The wildly ranging coupling strengths are clearly visible, leading to corresponding variations in the total transmission. Also visible are the sharp Fabry-Perot resonances associated with multiple reflections at the front and end surfaces. However, while the total transmission for frequencies just above $\omega a/2\pi c = 0.5$ is almost zero due to a very weak but non-vanishing coupling constant, there exists an extended frequency band just below $\omega a/2\pi c = 0.8$ where the total transmission vanishes exactly although the photonic band structure suggests the presence of a band. This apparent discrepancy is resolved when considering the symmetry of the corresponding Bloch functions: The Bloch functions for the band in question exhibit an odd parity across the slab surface. Because the incoming plane wave by construction has an even parity across the slab surface, we have that in this case the coupling between plane wave and Bloch function vanishes exactly due to an incompatible symmetry. This is a manifestation of a profound difference between PhCs and electronic crystals: Although both types of crystals provide Bloch functions (modes), the PhC modes are generally "empty", i.e., contain no photons. In order to transmit energy through a PhC, one has to couple an external radiation source to PhC modes. As a consequence, care must be taken when interpreting transmission and reflection data from PhC–slabs. However, the existence of these so–called uncoupled bands can always be inferred through a symmetry analysis [16,32] of the photonic Bloch functions. In Fig. 1.5, we have indicated the uncoupled bands for the Γ–M direction of our model system with dashed lines.

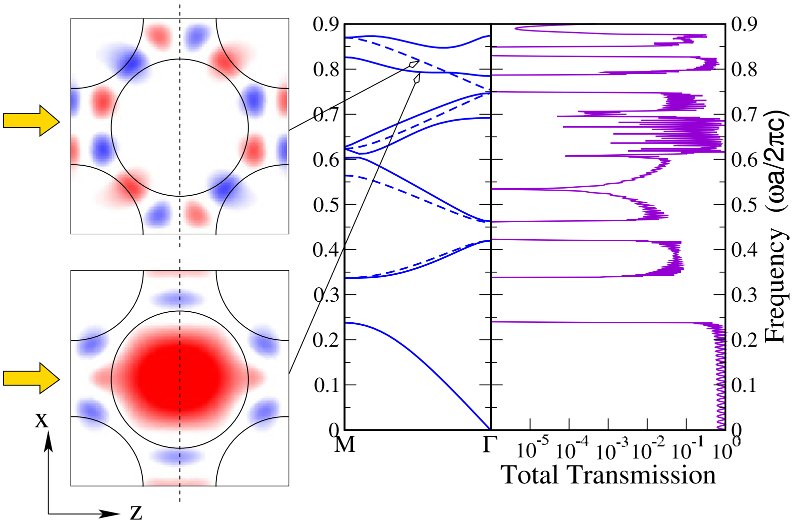

Figure 1.5: Comparison between transmission calculations (normal incidence) through a 2D PhC–slab oriented along the Γ–M direction with the corresponding photonic band structure for our model system. Uncoupled bands are marked by dashed lines. Bloch functions for a coupled and an uncoupled band are shown in the left panel, revealing the odd parity of the uncoupled bands. The direction of the incoming radiation is indicated by yellow arrows and the surface termination of the PhC is represented through the vertical dashed lines.

1.5 Defect structures in photonic crystals

In electronic micro–circuits, electrical currents are guided by thin metal wires where electrons are bound within the cross section of the wire by the so–called work function (confining potential) of the metal. As a result, electrical currents follow along the path prescribed by the wire without escaping to the background. The situation is very different for optical waves. Although optical fibers guide light over long distances, microscopic fiber–circuits for light do not exist, because empty space is already an ideal conductor of light waves. The light in an optical fiber can easily escape into the background electromagnetic modes of empty space if the fiber is bent or distorted on a microscopic scale. PBGs in the band structure of PhCs remove this problem by removing all the background electromagnetic modes over the relevant band of frequencies. As a consequence, light paths can be created inside a PBG material in the form of engineered waveguide channels. In terms of the resources required for the fabrication of these structures and the tremendous flexibility in the choice of parameters, the ability to design blueprints of PhC–based micro–optical devices and to investigate the effects of fabricational tolerances on the performance of the ideal structure, becomes both an economical and a practical must. Perhaps, even more important may be the investigation of novel operating principles of such devices.

As alluded to above, the overwhelming majority of theoretical investigations of waveguiding to date has been carried out using FDTD and/or FE techniques. However, applying general purpose methodologies such as FDTD or FE methods to defect structures in PhCs, largely disregards information about the underlying PhC structure which is readily available from photonic band structure computation. As a result, only relatively small systems can be investigated and the physical insight remains limited.

1.5.1 Maximally localized photonic Wannier functions

A more natural description of localized defect modes in PhCs consists of an expansion of the electromagnetic field into a set of localized basis functions which have encoded into them all the information of the underlying PhC. Therefore, the most natural basis functions for the description of defect structures in PhCs are the so–called photonic Wannier functions $W_{n\vec{R}}(\vec{r})$, which are formally defined through a lattice Fourier transform

$$W_{n\vec{R}}(\vec{r}) = \frac{V_{\text{WSC}}}{(2\pi)^2} \int_{\text{BZ}} d^2\vec{k}\, e^{-i\vec{k}\vec{R}}\, E_{n\vec{k}}(\vec{r}) \tag{1.24}$$

of the extended Bloch functions, $E_{n\vec{k}}(\vec{r})$. The above definition associates the photonic Wannier function $W_{n\vec{R}}(\vec{r})$ with the frequency range covered by band n, and centers it around the corresponding lattice site $\vec{R}$. In addition, the completeness and orthogonality of the Bloch functions translate directly into corresponding properties of the photonic Wannier functions. Computing the Wannier functions directly from the output of photonic band structure programs via Eq. (1.24) leads to functions with poor localization properties and erratic behavior (see, for instance, Fig. 2 in ref. [33]). These problems originate from an indeterminacy of the global phases of the Bloch functions. It is straightforward to show that for a group of several bands (we define their number as N_{W}) there exists, for every wave vector $\vec{k}$, a free unitary transformation between the bands which leaves the orthogonality relation of Wannier functions unchanged. A solution to this unfortunate situation is provided by recent advances in electronic band structure theory. Marzari and Vanderbilt [34, 35] have outlined an efficient scheme for the computation of maximally localized Wannier functions by numerically determining a unitary transformation between the bands that minimizes an appropriate spread

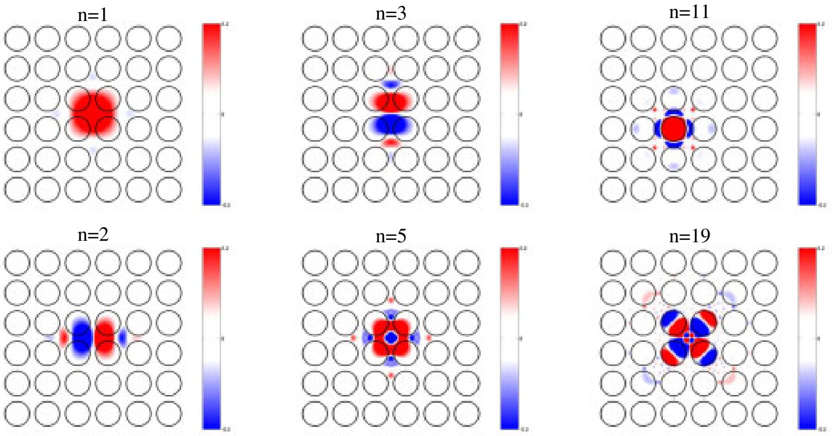

Figure 1.6: Photonic Wannier functions, $W_{n\vec{0}}(\vec{r})$, for the six bands that are most relevant for the description of the localized defect mode shown in Fig.1.7(a). These optimally localized Wannier functions have been obtained by minimizing the corresponding spread functional, Eq. (1.25). Note, that in contrast to the other bands, the Wannier center of the eleventh band is located at the air pore. The parameters of the underlying PhC are the same as those in Fig. 1.1.

functional $\mathcal{F}$

$$\mathcal{F} = \sum_{n=1}^{N_{\rm W}} \left[\langle n\vec{0}|\, r^2 \,|n\vec{0}\rangle - (\langle n\vec{0}|\, \vec{r} \,|n\vec{0}\rangle)^2 \right] = \text{Min} \; . \tag{1.25}$$

Here we have introduced a shorthand notation for matrix elements according to

$$\langle n\vec{R}|\, f(\vec{r}) \,|n'\vec{R}'\rangle = \int_{\mathbf{R}^2} d^2r \, W^*_{n\vec{R}}(\vec{r}) \, f(\vec{r}) \, \varepsilon_{\rm p}(\vec{r}) \, W_{n'\vec{R}'}(\vec{r}) \; , \tag{1.26}$$

for any function $f(\vec{r})$. For instance, the orthonormality of the Wannier functions in this notation reads as

$$\langle n\vec{R}|\,|n'\vec{R}'\rangle = \int_{\mathbf{R}^2} d^2r \, W^*_{n\vec{R}}(\vec{r}) \, \varepsilon_{\rm p}(\vec{r}) \, W_{n'\vec{R}'}(\vec{r}) = \delta_{nn'}\delta_{\vec{R}\vec{R}'} \; . \tag{1.27}$$

The field distributions of the optimized Wannier functions belonging to the six most relevant bands of our model system are depicted in Fig. 1.6 (see also the discussion in Section 1.5.3). Their localization properties as well as the symmetries of the underlying PhC structure are clearly visible. It should be noted that the Wannier centers of all calculated bands (except of the eleventh band) are located halfway between the air pores, i.e. inside the dielectric (see Refs. [34, 35] for more details on the Wannier centers). It should be pointed out that instead of working with the electric field [33,36,37], Eq. (1.1), one may equally well construct photonic Wannier functions for the magnetic field, as recently demonstrated by Whittaker and Croucher [38].

1.5.2 Wannier description of defect structures

The description of defect structures embedded in PhCs starts with the corresponding wave equation in the frequency domain

$$\nabla^2 E(\vec{r}) + \left(\frac{\omega}{c}\right)^2 \{\varepsilon_{\mathrm{p}}(\vec{r}) + \delta\varepsilon(\vec{r})\}\, E(\vec{r}) = 0 \, . \tag{1.28}$$

Here, we have decomposed the dielectric function into the periodic part $\varepsilon_{\mathrm{p}}(\vec{r})$, and the contribution $\delta\varepsilon(\vec{r})$, that describes the defect structures. Within the Wannier function approach, we expand the electromagnetic field according to

$$E(\vec{r}) = \sum_{n,\vec{R}} E_{n\vec{R}}\, W_{n\vec{R}}(\vec{r}) \, , \tag{1.29}$$

with unknown amplitudes $E_{n\vec{R}}$. Inserting this expansion into the wave equation (1.28) and employing the orthonormality relations, Eq. (1.27), leads to the basic equation for lattice models of defect structures embedded in PhCs

$$\sum_{n',\vec{R}'} \left\{\delta_{nn'}\delta_{\vec{R}\vec{R}'} + D^{nn'}_{\vec{R}\vec{R}'}\right\} E_{n'\vec{R}'} = \left(\frac{c}{\omega}\right)^2 \sum_{n',\vec{R}'} A^{nn'}_{\vec{R}\vec{R}'} E_{n'\vec{R}'} \, . \tag{1.30}$$

The matrix $A^{nn'}_{\vec{R}\vec{R}'}$ depends only on the Wannier functions of the underlying PhC and is defined by

$$A^{nn'}_{\vec{R}\vec{R}'} = -\int_{\mathbf{R}^2} d^2\vec{r}\;\, W^*_{n\vec{R}}(\vec{r})\, \nabla^2\, W_{n'\vec{R}'}(\vec{r}) \, . \tag{1.31}$$

The localization of the Wannier functions in space leads to a very rapid decay of the magnitude of matrix elements with increasing separation $|\vec{R} - \vec{R}'|$ between the lattice sites, effectively making the matrix $A^{nn'}_{\vec{R}\vec{R}'}$ sparse. Furthermore, it may be shown that the matrix $A^{nn'}_{\vec{R}\vec{R}'}$ is Hermitian and positive definite. Similarly, once the Wannier functions of the underlying PhC are determined, the matrix $D^{nn'}_{\vec{R}\vec{R}'}$ depends solely on the overlap of these functions, mediated by the defect structure:

$$D^{nn'}_{\vec{R}\vec{R}'} = \int_{\mathbf{R}^2} d^2\vec{r}\;\, W^*_{n\vec{R}}(\vec{r})\, \delta\varepsilon(\vec{r})\, W_{n'\vec{R}'}(\vec{r}) \, . \tag{1.32}$$

As a consequence of the localization properties of both the Wannier functions and the defect dielectric function, the Hermitian matrix $D^{nn'}_{\vec{R}\vec{R}'}$ is also sparse. In the case of PhCs with inversion symmetry, $\varepsilon_{\mathrm{p}}(\vec{r}) \equiv \varepsilon_{\mathrm{p}}(-\vec{r})$, the Wannier functions can be chosen to be real. Accordingly, both matrices, $A^{nn'}_{\vec{R}\vec{R}'}$ and $D^{nn'}_{\vec{R}\vec{R}'}$ become real symmetric matrices.

Depending on the nature of the defect structure, we are interested in (i) frequencies of localized cavity modes, (ii) dispersion relations for straight waveguides, or (iii) transmission and reflection through waveguide bends and other, more complex defect structures. In the following, we consider each of these cases separately.

1.5.3 Localized cavity modes

As a first illustration of the Wannier function approach, we consider the case of a simple cavity created by infiltrating a single pore at the defect site $\vec{R}_{\text{def}}$ with a material of dielectric constant ε_{def}, as shown in the inset of Fig. 1.7(a). In this case, we solve Eq. (1.30) directly as a generalized eigenvalue problem for the cavity frequencies that lie within the PBG, and reconstruct the cavity modes from the corresponding eigenvectors.

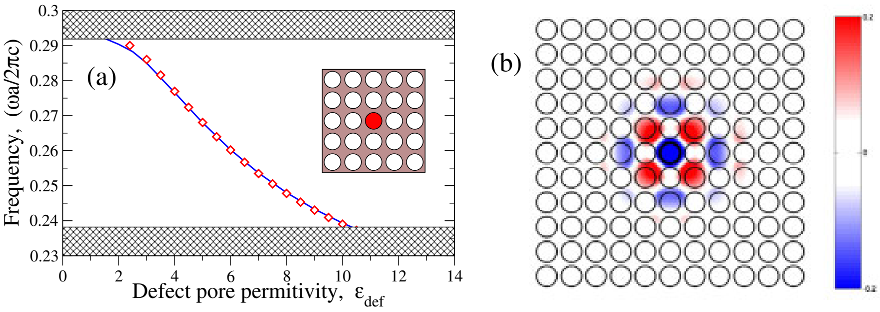

Figure 1.7: **(a)** Frequencies of localized cavity modes created by infiltrating a single defect pore with a material of dielectric constant ε_{def} (see inset). The results of the Wannier function approach (diamonds) using $N_{\text{w}} = 10$ Wannier functions per unit cell, are in complete agreement with numerically exact results of the super–cell calculations (full line). The parameters of the underlying PhC are the same as those in Fig. 1.1. **(b)** Electric field distribution for the cavity mode with frequency $\omega = 0.290 \times 2\pi c/a$, created by infiltrating the pore with a polymer of $\varepsilon_{\text{def}} = 2.4$.

In Fig. 1.7(a) we compare the frequencies of these cavity modes calculated from Eq. (1.30) with corresponding calculations using PWM–based super–cell calculations [39]. Upon increasing ε_{def}, a non–degenerate cavity mode with monopole symmetry emerges from the upper edge of the bandgap. The results of the Wannier function approach using the $N_{\text{w}} = 10$ most relevant Wannier functions *per unit cell* in Eq. (1.30), are in complete agreement with numerically exact results of the super–cell calculations. In Fig. 1.7(b), we depict the corresponding mode structure for a monopole cavity mode created by infiltration of a polymer with $\varepsilon_{\text{def}} = 2.4$ into the pore. The convergence properties of the Wannier function approach should depend on the nature and symmetry properties of the cavity modes under consideration. To discuss this issue in greater detail, it is helpful to define a measure V_n of the strength of the contributions to a cavity mode from the individual Wannier function associated with band n via $V_n = \sum_{\vec{R}} |E_{n\vec{R}}|^2$. In Fig. 1.8, we display the dependence of the parameter V_n on the band index n for the cavity modes shown in Fig. 1.7, for two values of the defect dielectric constant, $\varepsilon_{\text{def}} = 2.4$ (solid line) and $\varepsilon_{\text{def}} = 8$ (dashed line), respectively. In both cases, the most relevant contributions to the cavity modes originate from the Wannier functions belonging to bands $n = 1, 2, 3, 5, 11$ and 19, and all contributions from bands $n > 20$ are negligible. These most relevant Wannier functions for our model system are shown in Fig. 1.6. In fact, fully converged results are obtained when we work with the 10 most relevant Wannier functions per unit cell (for a comparison with numerically exact super–cell calculations see Fig. 1.7(a)).

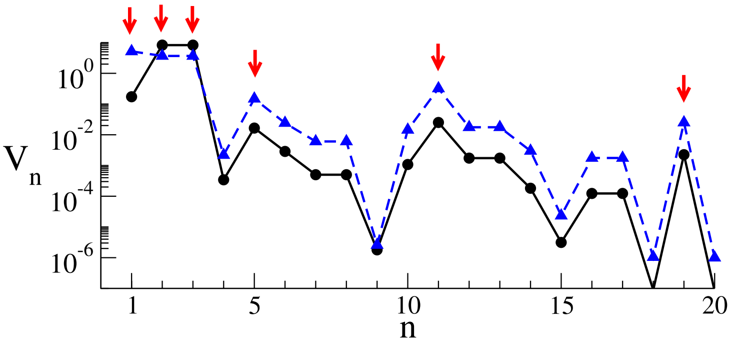

Figure 1.8: The strength V_n of the individual contributions from the Wannier functions of the lowest 20 bands (index n) to the formation of the cavity modes depicted in Fig. 1.7. The Wannier functions with $V_n \leq 10^{-3}$ may be safely left out of account. Arrows indicate the six most relevant Wannier functions depicted in Fig. 1.6. The parameters of the underlying PhC are the same as those in Fig. 1.1.

1.5.4 Dispersion relations of waveguides

The efficiency of the Wannier function approach is particularly evident when considering defect clusters consisting of several defect pores. In this case, the defect dielectric function $\delta\varepsilon(\vec{r})$, can be written as a sum over positions $\vec{R}_m$, of the individual defect pores so that Eq. (1.32) reduces to a sum

$$D^{nn'}_{\vec{R}\vec{R}'} = \sum_m D(m)^{nn'}_{\vec{R}-\vec{R}_m,\vec{R}'-\vec{R}_m} , \tag{1.33}$$

over the matrix elements $D(m)^{nn'}_{\vec{R},\vec{R}'}$ of the individual defects (see discussion in Ref. [33] for more details). Therefore, for a given underlying PhC structure, it becomes possible to build up a database of matrix elements $D(m)^{nn'}_{\vec{R},\vec{R}'}$, for different geometries (radii, shapes) of defect pores, which allows highly efficient defect computations through simple matrix assembly procedures. This is in strong contrast to *any* other computational technique known to us.

Arguably the most important types of defect clusters in PhCs are one or several adjacent straight rows of defects. Properly designed, such defect rows form a PhC waveguide which allows the efficient guiding of light for frequencies within a PBG [40, 41]. Due to the one-dimensional periodicity of such a waveguide, its guided modes $E^{(p)}(\vec{r}\,|\,\omega) = \sum_{n,\vec{R}} E^{(p)}_{n\vec{R}}(\omega)\, W_{n\vec{R}}(\vec{r})$, obey the 1D Bloch-Floquet theorem

$$E^{(p)}_{n\vec{R}+\vec{s}_{\mathrm{w}}}(\omega) = e^{i\vec{k}_p(\omega)\vec{s}_{\mathrm{w}}}\, E^{(p)}_{n\vec{R}}(\omega) , \tag{1.34}$$

and thus they can be labeled by a wave vector $\vec{k}_p(\omega)$, parallel to the waveguide director $\vec{s}_{\mathrm{w}}=w_1\vec{a}_1 + w_2\vec{a}_2$, where $\vec{a}_1 = (a, 0)$ and $\vec{a}_2 = (0, a)$ are the primitive lattice vectors of the PhC, and integers w_1 and w_2 define the direction of the waveguide (for instance, an x–axis directed W1–waveguide is described through $w_1 = 1$ and $w_2 = 0$). Commonly, investigations of PhC waveguides consist of calculations of the dispersion relations $\vec{k}_p(\omega)$, of all the guided

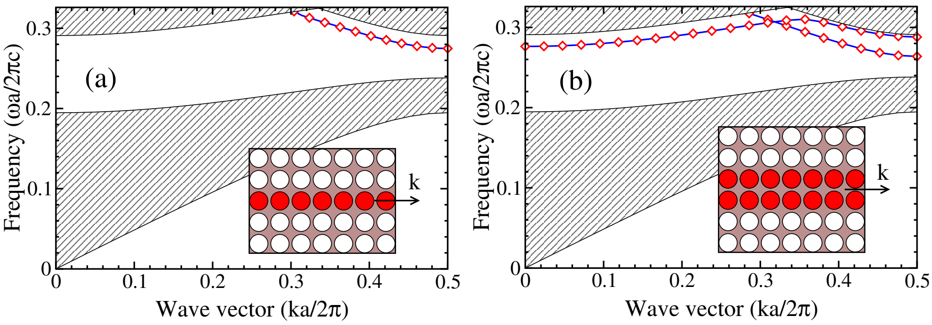

Figure 1.9: Dispersion relations of the propagating guided mode for PhC waveguides consisting of **(a)** one row (W1) and **(b)** two rows (W2) of defect pores infiltrated with a polymer with $\varepsilon_{\text{def}} = 2.4$. The calculations within the Wannier function approach (diamonds) based on Eqs. (1.30) and (1.34), in which we accounted for the interaction of 5 nearest pores along the waveguide and used 10 most relevant Wannier functions per unit cell, are in complete agreement with the results of supercell calculations (solid lines). The gray areas represent the projected band structure of the underlying model PhC (see Fig. 1.1). The red circles in the insets indicate the positions of the infiltrated pores.

modes which can be obtained by substituting Eq. (1.34) into Eq. (1.30) as we have described in detail in Ref. [33].

To date, investigations of straight PhC waveguides have concentrated on the calculation of dispersion relations for *propagating guided modes* with real wave vectors $k_{\text{p}}(\omega)$, only. Such calculations can also be carried out accurately by employing the supercell technique. In Fig. 1.9, we display the dispersion relations for the propagating guided modes of the W1– and W2–waveguides created by infiltrating a polymer into one row and two rows of pores, calculated within the Wannier function approach. The results of these calculations are fully converged and in complete agreement with the results of plane–wave based supercell computations. Similar to the calculations of complex cavity structures, the calculations of waveguide dispersion relations within the Wannier function approach require fairly minimal computational resources in comparison of the supercell technique.

We would like to emphasize that, in contrast to the supercell technique, the Wannier function approach enables us to also obtain the dispersion relations for *evanescent guided modes* with complex wave vectors $\vec{k}_{\text{p}}(\omega)$. Since such modes grow or decay along the waveguide direction, they are mainly irrelevant in perfectly periodic straight waveguides. However, they start to play an important role as soon as the perfect periodicity of the waveguide is broken either through imperfections due to fabricational tolerances, or through the deliberate creation of deviations from periodicity such as bends or coupled cavity–waveguide systems for Wavelength Division Multiplexing (WDM) applications. In such cases, these *evanescent* guided modes give rise to light localization effects and determine the non–trivial transmission and reflection properties of PhC circuits [33, 42] as we will discuss below.

1.5.5 Light propagation through photonic crystal circuits

In this section, we demonstrate that the Wannier function approach provides an efficient simulation tool for the description of light through PhC circuits which allows one to overcome most of the limitations related to FDTD or FE methods. As an illustration, we consider light propagation through two-port PhC circuits such as waveguide bends or coupled cavity–waveguide systems. The common feature of these devices is that two semi-infinite straight PhC waveguides act as leads that are connected through a finite–sized region of defects. In this case, light propagation through the device at frequency ω is governed by Eq. (1.30), which should be truncated (to obtain an equal number of equations and unknowns) by prescribing certain values to the expansion coefficients $E_{n\vec{R}}$, at some sites inside the waveguiding leads. Since these values determine the amplitudes of the incoming light, it is physically more transparent to express the expansion coefficients $E_{n\vec{R}}$ within the leads through a superposition of the guided modes $\vec{\Phi}^{(p)}(\omega)$ with wave vectors $\vec{k}_{\mathrm{p}}(\omega)$ of the corresponding infinite straight waveguide. In a numerical implementation, this is facilitated by replacing the expansion coefficients $E_{n\vec{R}}$ for all lattice sites $\vec{R}$ inside each waveguiding lead W_i, $i = 1, 2$, according to

$$E^{\mathrm{w}_i}_{n\vec{R}} = \sum_{p=1}^{N} u^{(p)}_{\mathrm{w}_i}(\omega) E^{(p)}_{n\vec{R}}(\omega) + \sum_{p=N+1}^{2N} d^{(p)}_{\mathrm{w}_i}(\omega) E^{(p)}_{n\vec{R}}(\omega) \ , \tag{1.35}$$

where $u^{(p)}_{\mathrm{w}_i}$ and $d^{(p)}_{\mathrm{w}_i}$ are amplitudes of the guided modes, and we assume that all $2N$ guided modes are ordered in the following way: $p = 1$ to N are occupied by the propagating guided modes with $\mathrm{Re}[k_{\mathrm{p}}] > 0$ and evanescent guided modes with $\mathrm{Im}[k_{\mathrm{p}}] > 0$, whereas $p = N + 1$ to $2N$ are occupied by the propagating guided modes with $\mathrm{Re}[k_{\mathrm{p}}] < 0$ and evanescent guided modes with $\mathrm{Im}[k_{\mathrm{p}}] < 0$. Assuming that the amplitudes, $u^{(p)}_{\mathrm{w}_1}$ and $d^{(p)}_{\mathrm{w}_2}$, of all the propagating (evanescent) guided modes which propagate (decay) in the direction of the device are known (they depend on the purpose of our calculation or on the experimental setup), we can now substitute Eq. (1.35) into Eq. (1.30) and, solving the resulting system of coupled equations, find the unknown expansion coefficients $E_{n\vec{R}}$ for the sites $\vec{R}$ inside the domain of the device (which can be used, e.g., for visualization of the field propagation through the device), and the amplitudes $u^{(p)}_{\mathrm{w}_2}$ and $d^{(p)}_{\mathrm{w}_1}$, of all *outgoing propagating* and *growing evanescent* guided modes.

In Ref. [33] we have demonstrated, by comparison with the FDTD calculations [40], that the results of such transmission calculations based on the Wannier function approach are indeed very accurate and agree extremely well with FDTD calculations. Now, in Fig. 1.10, we present the results of Wannier function calculations of the transmission spectra for four different bend geometries with attached single–mode waveguide leads (see Fig. 1.9) that are embedded in our model PhC.

The efficiency of the Wannier function approach for transmission calculations becomes apparent when considering that – once the Wannier functions for the underlying PhC have been obtained – the calculation of a single data point in the reflection spectra of Fig. 1.10 reduces to the solution of a single sparse system of some 800 equations, which even on a laptop computer takes only a few seconds. Therefore, the Wannier function approach outlined above will (i) enable a reverse engineering of defect structures with prescribed functionality

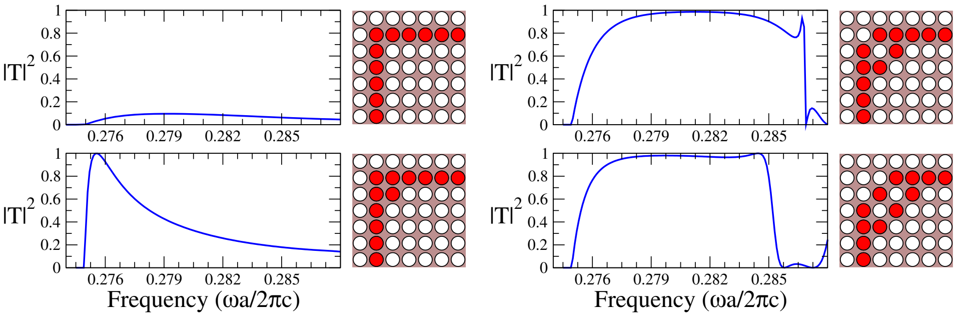

Figure 1.10: Transmission spectra $|T(\omega)|^2$, for four different bend geometries embedded in our 2D model PhC. The results of the Wannier function approach are obtained with $N_{\mathrm{R}} = 5$, $L = 5$, and the $N_{\mathrm{W}} = 10$ most relevant Wannier functions. The parameters of the underlying PhC are the same as those in Fig. 1.1.

and (ii) allow detailed studies regarding the robustness of successful designs with respect to fabricational tolerances. Moreover, the Wannier function approach can be straightforwardly applied, with comparable efficiency, to investigations of the transmission spectra through PhC circuits made from highly dispersive and/or nonlinear materials. Of paramount importance is the fact that, in contrast to the FDTD or FE methods, the Wannier function approach permits one to accurately and efficiently calculate the complete scattering matrices of PhC devices [33]. This allows us to construct a PhC circuit theory in which *individual devices are replaced by simple equivalent scattering matrices*, which are assembled by simple scattering matrix multiplication rules to form the scattering matrix of *large-scale circuits* [43]. We want to emphasize that in some sense, these scattering matrices can be regarded as the optical analogue of the impedance matrices associated with multi-port devices in microwave technology [44].

1.6 Conclusions

In summary, we have outlined a framework based on solid state theoretical methods that allows one to qualitatively and quantitatively treat wave propagation in PhCs. Photonic band structure computation of the infinitely extended PhC provides the input necessary to efficiently obtain the properties of defect structures, embedded in PhCs via expansions into localized Wannier functions. This allows us to determine effective parameters such as DOS, group velocities, GVD tensors, and effective nonlinearities. The description of nonlinear PhCs through the generalized slowly varying envelope approximation allows us to investigate such systems using a limited number of effective parameters with transparent physical meaning. Finite structures can be treated through combining techniques from diffractive optics with photonic band structure computations. In particular, the efficiency of the Wannier function approach to defect structures in PhCs allows investigations of PhC circuits which, to date, are beyond the reach of standard simulation techniques such as FDTD or FE methods.

Acknowledgements

This work was supported by the Center for Functional Nanostructures (CFN) of the Deutsche Forschungsgemeinschaft (DFG) within projects A 1.1, A 1.2, and A 1.3. The research of K.B., A.G.M., and L.T. is further supported by the DFG under grant Bu 1107/2-2 (Emmy-Noether program). M.F. acknowledges the support of the DFG Priority Program SP 1113 *Photonic Crystals*. The work of M.S. is funded in the framework of the DFG Research Training Group 786 *Mixed Fields and Nonlinear Interactions* at the University of Karlsruhe.

References

[1] E. Yablonovitch, Phys. Rev. Lett. **58**, 2059 (1987).
[2] S. John, Phys. Rev. Lett. **58**, 2486 (1987).
[3] Photonic Crystals and Light Localization in the 21st Century, C.M. Soukoulis, Ed., NATO Science Series C **563**, Kluwer Academic (Dordrecht, Boston, London), 2001.
[4] S. Fan, P.R. Villeneuve, and H.A. Haus, Phys. Rev. Lett. **80**, 960 (1998).
[5] S. Noda, A. Alongkarn, and M. Imada, Nature **407**, 608 (2000).
[6] N. Aközbek and S. John, Phys. Rev. E **57**, 2287 (1998).
[7] N. Bhat and J. Sipe, Phys. Rev. E **64**, 056604 (2001).
[8] S.F. Mingaleev and Yu.S. Kivshar, Phys. Rev. Lett. **86**, 5474 (2001).
[9] S.F. Mingaleev, Yu.S. Kivshar, and R.A. Sammut, Phys. Rev. E, **62**, 5777 (2000).
[10] S. John and T. Quang, Phys. Rev. A **50**, 1764 (1994).
[11] N. Vats, K. Busch, and S. John, Phys. Rev. A **65**, 043808 (2002).
[12] H. Kosaka, et al., Phys. Rev. B **58**, R10096 (1998).
[13] M. Notomi, Opt. Quant. Elect. **34**, 133 (2002).
[14] H. Kosaka, et al., J. Lightwave Technology **17**, 2032 (1999).
[15] T.F. Krauss, phys. stat. sol. (a) **197**, 688 (2003).
[16] Optical properties of Photonic Crystals, K. Sakoda, Springer (Berlin, Heidelberg, New York), 2001.
[17] C. Kallinger et al., Adv. Mat. **10**, 920 (1998).
[18] L. Florescu, K. Busch, and S. John, J. Opt. Soc. Am. B **19**, 2215 (2002).
[19] K. Busch and S. John, Phys. Rev. E **58**, 3896 (1998).
[20] K. Busch and S. John, Phys. Rev. Lett. **83**, 967 (1999).
[21] C. Martijn de Sterke and J.E. Sipe, Phys. Rev. A **38**, 5149 (1988).
[22] D. Hermann, M. Frank, K. Busch, and P. Wölfle, Optics Express **8**, 167 (2001).
[23] J.E. Sipe, Phys. Rev. E **62**, 5672 (2000).
[24] K. Sakoda and K. Ohtaka, Phys. Rev. B **54**, 5742 (1996).
[25] Perturbation Methods, A.H. Nayfeh, Wiley (New York), 1973.
[26] Solitons and Nonlinear Wave Equations, R.K. Dodd, J.C. Eilbeck, J.D. Gibbon, and H.C. Morris, Academic Press (London), 1982.
[27] L. Tkeshelashvili and K. Busch, Nonlinear three-wave interaction in photonic crystals, submitted.
[28] L. Tkeshelashvili, K. Busch, and S. Pereira, Giant soliton shifts in photonic band gap materials, submitted.
[29] D. M. Whittaker and I. S. Culshaw, Phys. Rev. B **60**, 2610 (1999).
[30] L. Li, J. Opt. Soc. Am. A **13**, 1024 (1996).
[31] P. B. Johnson and R. W. Christy, Phys. Rev. B **6**, 4370 (1972).
[32] W. Hergert and M. Däne, phys. stat. sol. (a) **197**, 620 (2003).
[33] K. Busch, S.F. Mingaleev, A. Garcia-Martin, M. Schillinger, and Daniel Hermann, J. Phys.: Condens. Matter. **15**, R1233 (2003).
[34] N. Marzari and D. Vanderbilt, Phys. Rev. B **56**, 12847 (1997).
[35] I. Souza, N. Marzari, and D. Vanderbilt, Phys. Rev. B **65**, 035109 (2002).

[36] A. Garcia-Martin, D. Hermann, K. Busch, and P. Wölfle, Mat. Res. Symp. Proc. **722**, L1.1 (2002).
[37] A. Garcia-Martin, D. Hermann, F. Hagmann, K. Busch, and P. Wölfle, Nanotechnology **14**, 177 (2003).
[38] D.M. Whittaker and M.P. Croucher, Phys. Rev. B **67**, 085204 (2003).
[39] S.G. Johnson and J.D. Joannopoulos, Optics Express **8**, 173 (2001).
[40] A. Mekis et al., Phys. Rev. Lett. **77**, 3787 (1996).
[41] J.D. Joannopoulos, P.R. Villeneuve, and S.H. Fan, Nature **386**, 143 (1997).
[42] S.F. Mingaleev and Yu.S. Kivshar, Opt. Lett. **27**, 231 (2002); J. Opt. Soc. Am. B **19**, 2241 (2002).
[43] S.F. Mingaleev and K. Busch, Opt. Lett. **28**, 619 (2003).
[44] Schaltungslehre linearer Mikrowellennetze, H. Brand, Hirzel (Stuttgart), 1970.

2 Spontaneous emission in photonic structures: Theory and simulation

Geesche Boedecker, Carsten Henkel[1]*, Christian Hermann, and Ortwin Hess*

2.1 Introduction

One of the first motivations for photonic band gap structures has been the control of spontaneous emission via the design of the photonic density of states (DOS) [1, 2]. Among the devices that have become possible are compact light sources and low–threshold lasers, that can readily be integrated into all–optical networks. Coherent control over spontaneous emission using optical fields may provide implementations of optical memory and even optical quantum computers [3]. Model systems of fundamental interest also become possible: 'small' quantum systems coupled to a structured 'reservoir' of photon modes with a tailored frequency spectrum. Intriguing phenomena have been predicted, like the slowdown and localization of light [4], controlled quantum electrodynamics, the strong coupling regime, and nonclassical light generation [5, 6].

In this chapter, we focus on selected quantum optical aspects of photonic crystals and provide a tutorial discussion of the basic properties of spontaneous emission. In the first section, basic concepts (Fermi's Golden Rule, local density of states) are reviewed, and possibilities of optically tuning an optical transition frequency across a band edge are discussed. We give a review of quantum electrodynamic approaches to radiative decay close to a photonic gap. In the second section, simulation techniques are described that permit the determination of the local density of photon states in arbitrary photonic structures. We conclude with a few remarks on photonic band gap microlasers.

The topics in this chapter have not been selected with the intention of completeness, but in order to provide a presentation accessible to an interdisciplinary audience. Nevertheless, we have tried to identify a few trends that may either become experimentally relevant with current photonic structures, or that have now entered the forefront of theoretical research. We apologize in advance for any omissions. The discussion is restricted, for simplicity, to the simplest case of a two–level system. Multilevel systems allow for a richer dynamics and more delicate coherent control, as discussed in the review by Woldeyohannes and John [3]. In the review of Lambropoulos, Nikolopoulos, Nielsen, and Bay [7], more details about quantum electrodynamics in a structured continuum can be found.

---

[1] Corresponding author: e-mail: carsten.henkel@quantum.physik.uni-potsdam.de, Phone: +49 331 977 1498, Fax: +49 331 977 1767

Photonic Crystals. Edited by K. Busch, S. Lölkes, R. B. Wehrspohn and H. Föll
Copyright © 2004 Wiley-VCH Verlag GmbH & Co. KGaA
ISBN: 3-527-40432-5

2.2 Basic concepts

2.2.1 Fermi's Golden Rule

Consider a two–level system with transition frequency ω_0 that interacts with the electromagnetic vacuum field. According to Fermi's Golden Rule, the radiative decay rate of the excited state $|\mathrm{e}\rangle$ to the ground state $|\mathrm{g}\rangle$ is

$$\Gamma_{\mathrm{e}\to\mathrm{g}} = \frac{2\pi}{\hbar^2} \sum_{\vec{k},n} \left| \langle \mathrm{g}, 1_{\vec{k}n} | \hat{\vec{d}} \cdot \hat{\vec{E}}(\vec{x}_0) | \mathrm{e}, \mathrm{vac} \rangle \right|^2 \delta(\omega_{\vec{k}n} - \omega_0), \tag{2.1}$$

where the sum runs over all one–photon field states $|1_{\vec{k}n}\rangle$ compatible with energy conservation. The two–level system is located at $\vec{x}_0$ and its electric dipole operator is $\hat{\vec{d}}$. In a photonic crystal, this general expression is reduced to the DOS as follows. We use the expansion of the electric field operator in Bloch modes, labelled by quasimomentum $\vec{k}$ and band index n,

$$\hat{\vec{E}}(\vec{x}) = \sum_{\vec{k},n} \sqrt{\frac{\hbar\omega_{\vec{k}n}}{2\varepsilon_0 V}} \left(\vec{E}_{\vec{k}n}(\vec{x}) \hat{a}_{\vec{k}n} + \text{h.c.} \right), \tag{2.2}$$

where $\hat{a}_{\vec{k}n}$ is the annihilation operator for a photon in mode $\vec{k}, n$, and the mode functions are normalized in the crystal volume V according to

$$\frac{1}{V} \int_V \mathrm{d}x \, \varepsilon(\vec{x}) \left| \vec{E}_{\vec{k}n}(\vec{x}) \right|^2 = 1. \tag{2.3}$$

The resulting decay rate is

$$\Gamma_{\mathrm{e}\to\mathrm{g}} = \frac{\pi\omega_0 |\vec{d}|^2}{\varepsilon_0 \hbar} \rho(\vec{x}_0, \vec{u}, \omega_0). \tag{2.4}$$

where $\rho(\vec{x}_0, \vec{u}, \omega_0)$ is the projected local density of photon states (or projected LDOS)

$$\rho(\vec{x}_0, \vec{u}, \omega) = \frac{1}{V} \sum_{\vec{k},n} \left| \vec{u} \cdot \vec{E}_{\vec{k}n}(\vec{x}_0) \right|^2 \delta(\omega_{\vec{k}n} - \omega), \tag{2.5}$$

the dipole matrix element is $\vec{d} = \langle \mathrm{g} | \hat{\vec{d}} | \mathrm{e} \rangle$, and $\vec{u}$ is the unit vector along $\vec{d}$.

The result (2.4) clearly shows that spontaneous emission is inhibited at frequencies where the LDOS is small; this occurs generically in band gaps. The decay is enhanced at band edges where the LDOS may show divergences due to the flat dispersion relation. As a function of the dipole position, the LDOS shows 'hot spots' that reveal the character of the photonic band [8, 9]. For example, 'air bands' have their field maximum in the voids of the crystal and are typically located at the upper gap edge. This situation provides a promising model system for quantum optics because an atom or nanoparticle can be trapped optically in the voids.

We note that much information about spontaneous emission can be found in a classical description without explicitly quantizing the field. Consider the emission of a Hertzian dipole with amplitude $\vec{d}$ and frequency ω_0 [1,10]. Given the time-averaged emitted power $2\,\mathrm{Re}[-\dot{\vec{d}}^* \cdot \vec{E}(\vec{x}_0)]$, we can define a decay rate by dividing by the energy quantum $\hbar\omega_0$

$$\gamma_{\mathrm{cl}} = \frac{2}{\hbar}\mathrm{Im}\big[\vec{d}^* \cdot \vec{E}(\vec{x}_0)\big] = \frac{2|\vec{d}|^2}{\hbar}\mathrm{Im}\, G(\vec{x}_0, \vec{x}_0; \omega_0). \tag{2.6}$$

In the second equality, we have expressed the electric field in terms of the Green tensor $\mathcal{G}$ or, more precisely, its projection $G = \vec{u} \cdot \mathcal{G} \cdot \vec{u}$ onto the dipole's polarization. Knowledge of the Green tensor at the transition frequency is thus sufficient to compute spontaneous emission rates. In a perfectly periodic photonic crystal, its expansion in Bloch modes reads [11]

$$\mathcal{G}(\vec{x}, \vec{x}'; \omega) = \frac{1}{\varepsilon_0 V} \sum_{\vec{k},n} \left(\frac{\omega^2 \vec{E}_{\vec{k}n}(\vec{x}) \otimes \vec{E}^*_{\vec{k}n}(\vec{x}')}{\omega^2_{\vec{k}n} - (\omega + \mathrm{i}0)^2} - \vec{F}_{\vec{k}n}(\vec{x}) \otimes \vec{F}^*_{\vec{k}n}(\vec{x}') \right), \tag{2.7}$$

where the $\vec{F}_{\vec{k}n}(\vec{x})$ are the 'longitudinal' mode functions. These modes are required [11] for the completeness of the expansion (2.7). They lead to electrostatic energy and frequency shifts that are discussed for semiconductor photonic crystals in Chapter 3 of this book. Taking the imaginary part of the expansion (2.7), we get

$$\mathrm{Im}\, G(\vec{x}_0, \vec{x}_0; \omega) = \frac{\pi\omega}{2\varepsilon_0}\rho(\vec{x}_0, \vec{u}, \omega), \tag{2.8}$$

so that the classical decay rate (2.6) agrees with the quantum result (2.4).

The coupling of the two–level system to the photon field also leads to a shift $\delta\omega_0$ of the transition frequency. This shift originates from off–resonant absorption and emission processes and requires the full frequency dependence of the LDOS. The following formula has been found in the framework of a harmonic oscillator model [12]

$$\delta\omega_0 = \frac{\Gamma_{\mathrm{vac}}}{4\pi} P\!\int_0^\infty \frac{\mathrm{d}\omega}{\omega - \omega_0} \frac{\rho(\vec{x}_0, \vec{d}, \omega) - \rho_{\mathrm{vac}}(\omega)}{\rho_{\mathrm{vac}}(\omega)} \propto \mathrm{Re}\, G_{\mathrm{sc}}(\vec{x}_0, \vec{x}_0; \omega_0), \tag{2.9}$$

where $\Gamma_{\mathrm{vac}} = |\vec{d}|^2\omega_0^3/3\pi\varepsilon_0\hbar$ is the vacuum decay rate and P denotes a principal value integral. The UV divergence has been renormalized by subtracting the vacuum LDOS. This procedure is always possible in real crystals because the material becomes transparent beyond the optical or ultraviolet absorption bands. In the second step, we have used Kramers–Kronig relations to express the frequency integral in terms of the real part of the "scattered" Green function G_{sc}, i.e., the part that is due to scattering and reflection from the photonic structure (the free space part is subtracted).

Examples. We present here two simple examples of the LDOS for illustration and further use. More details on its calculation from the band structure can be found in Chapter 1 of this volume.

In a three–dimensional photonic crystal, close to a lower band edge, a frequently used approximation is the 'effective mass' dispersion relation. The band frequency close to some point $\vec{k}_{\rm c}$ at the Brillouin zone boundary is given by

$$\omega_{\vec{k}} \approx \omega_{\rm c} + \frac{\hbar}{2m_{\rm eff}} |\vec{k} - \vec{k}_{\rm c}|^2 = \omega_{\rm c} + f_{\rm c} \frac{\omega_{\rm c}}{k_{\rm c}^2} |\vec{k} - \vec{k}_{\rm c}|^2, \tag{2.10}$$

where we have assumed an isotropic effective mass tensor for simplicity. Note that in general, the band edge occurs at more than one point $\vec{k}_{\rm c}$ on the zone boundary, say $N_{\rm c}$. The band curvature can be expressed in terms of the dimensionless number $f_{\rm c}$ which is small compared to unity for flat bands.

Let us assume that all Bloch modes at a given frequency ω have the same amplitude at the dipole position $\vec{x}_0$. This is reasonable for air bands when the dipole is located at a highly symmetric position in the Wigner–Seitz cell, but ignores polarization. By integrating over the Brillouin zone and summing over the band edge points $\vec{k}_{\rm c}$, one recovers a LDOS whose form is the same as for free electrons

$$\rho(\vec{x}_0, \vec{u}, \omega) = \begin{cases} 0 & \text{if } \omega \le \omega_{\rm c}, \\ A(\vec{x}_0, \vec{u}) \sqrt{\omega - \omega_{\rm c}} & \text{if } \omega \ge \omega_{\rm c}. \end{cases} \tag{2.11}$$

This is commonly called the ‘anisotropic’ model [7] because the dispersion relation (2.10) depends on the direction of $\vec{k}$. The prefactor can be estimated as

$$A(\vec{x}_0, \vec{u}) \sim \frac{N_{\rm c} \big| \vec{u} \cdot \vec{E}_{\rm c}(\vec{x}_0) \big|^2 k_{\rm c}^3}{(2\pi)^2 (f_{\rm c} \omega_{\rm c})^{3/2}}. \tag{2.12}$$

Below the band edge, the excited state does not decay, while the emission increases sharply when the transition frequency enters the photonic band. Close to the band edge, the decay dynamics becomes non-exponential, as discussed in detail in Section 2.2.4.

In a one–dimensional crystal, a common technique is to use transfer matrices for the computation of reflection and transmission amplitudes [13], while the LDOS is typically computed from the Green function [9]. Two of the present authors have recently shown [14] that it is possible to define a reflection coefficient $r(\omega)$ for a semi-infinite crystal. The Green function can thus be found as in a cavity, by putting a planar test source between two crystal half–spaces and taking into account the reflection of the source field. One thus finds the simple expression

$$\frac{\rho_{\rm 1D}(x, \omega)}{\rho_{\rm vac}(\omega)} = {\rm Re} \left[\frac{2r(\omega) \cos(2\omega x/c) + 1}{1 - r(\omega)^2} - 1 \right], \tag{2.13}$$

$$r(\omega) = \frac{r_1(\omega)}{{\rm e}^{-{\rm i}\omega a/c} - t_1(\omega)\, {\rm e}^{{\rm i}k(\omega)a}}, \tag{2.14}$$

where $r_1(\omega), t_1(\omega)$ are the reflection and transmission amplitudes for a primitive unit cell (length a) and $k(\omega)$ is the dispersion relation for the Bloch modes of the infinite crystal (see [14] for details). One can show that the LDOS (2.13) exhibits singularities $1/\sqrt{|\omega - \omega_{\rm c}|}$ at the band edges where $r(\omega) \to \pm 1$, as can be seen in Figure 2.1. A model DOS with such a singular behaviour has frequently been used in 3D calculations (the ‘isotropic model’), but it has been criticized as unphysical [15]. Indeed, this singularity only occurs for a spherical Brillouin zone. A finite crystal or one with absorption leads to a LDOS with smoothed singularities (see Figure 2.1), as discussed in the following Section.

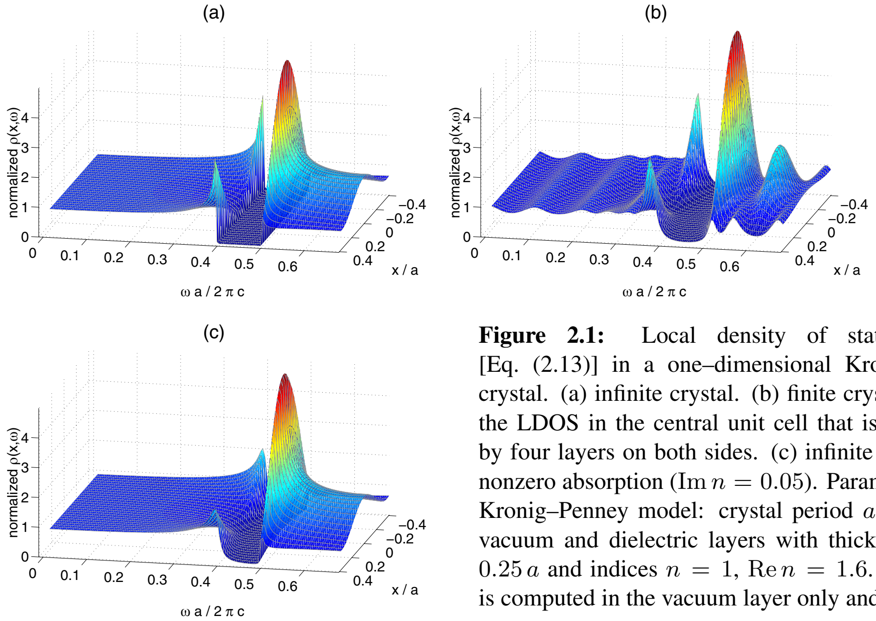

Figure 2.1: Local density of states $\rho(x, \omega)$ [Eq. (2.13)] in a one–dimensional Kronig–Penney crystal. (a) infinite crystal. (b) finite crystal; we plot the LDOS in the central unit cell that is surrounded by four layers on both sides. (c) infinite crystal with nonzero absorption ($\operatorname{Im} n = 0.05$). Parameters of the Kronig–Penney model: crystal period a, alternating vacuum and dielectric layers with thickness $0.75\,a$, $0.25\,a$ and indices $n = 1$, $\operatorname{Re} n = 1.6$. The LDOS is computed in the vacuum layer only and normalized to vacuum.

2.2.2 Beyond the simple picture

Absorption. If the dielectric backbone of the crystal shows some finite absorption, the field expansion in Bloch modes breaks down because the Bloch momentum $\vec{k}$ becomes complex (damping of the field modes). It has been shown that a consistent quantized theory is possible by including additional degrees of freedom that model the dissipative reservoir to which the field couples (see e.g., [16]). The fully quantized description leads to a spontaneous decay rate – again using perturbation theory – which is still of the form $\Gamma_{\text{tot}} \propto \operatorname{Im} G(\vec{x}_0, \vec{x}_0; \omega_0)$. The impact of absorption for the one–dimensional case can be seen in Figure 2.1: the band edge singularities are smoothed out because absorption makes the crystal effectively finite.

From early studies of fluorescence near metallic surfaces [17, 18] it is well–known that the spontaneous decay contains a significant nonradiative contribution, when the emitter approaches absorbing material walls, to distances smaller than the vacuum wavelength. This underlines the advantage of trapping the emitter in the voids. In an absorbing crystal, the LDOS can thus be separated into radiative and nonradiative parts [19]. Only the radiative decay is visible from the outside, and its rate can be found from the far field, leaving the (finite) sample

$$\Gamma_{\text{rad}} \propto \int \mathrm{d}S(\vec{r})\, \left|\mathcal{G}(\vec{r}, \vec{x}_0; \omega_0) \cdot \vec{d}\right|^2. \tag{2.15}$$

The integration points $\vec{r}$ run over a large surface in the far field. Note that this calculation also requires transmission amplitudes for Bloch modes through the crystal facets.

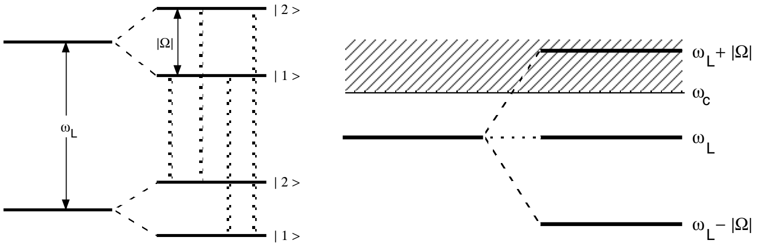

Figure 2.2: Tuning spontaneous emission with Rabi splitting. Left: transitions between Rabi-split levels. Right: Mollow triplet of emission frequencies close to a band edge.

Finite and disordered crystals. Singularities of the LDOS do not occur in finite photonic structures, and band edges are smoothed out. This is qualitatively similar to the impact of nonzero absorption, see Figure 2.1. In addition, reflection from the endfaces of the sample gives standing waves inside, that appear as additional oscillations in the LDOS [20] and also in reflection and transmission spectra (see e.g., Figure 1.5 of Chapter 1 in this book).

If the crystal is not periodic, then according to the degree of disorder, scattering between Bloch modes occurs or the modes become localized [4]. Experiments with fluorescent emitters in colloidal photonic crystals, for example, have explored the weak disorder regime [21, 22]: typically, the band gap is incomplete, and crystal defects redistribute Bloch modes between allowed directions. The emitted fluorescence photons then propagate diffusively towards the sample boundaries. The fingerprints of a photonic band gap structure originate only in a surface layer whose depth is of the order of the transport mean free path. In the strongly localized regime, one expects that light transport happens through hopping between localized modes. Model calculations predict enhanced transmission of spontaneous photons from an emitter due to destructive interference between the localized modes [23–25].

2.2.3 Coherent tuning of spontaneous decay

Once it is realized that spontaneous decay can be suppressed in a band gap, one wants to be able to control this process dynamically. A first idea is based on the optically induced Rabi splitting in a coherent laser field, as shown in Figure 2.2. When the combined atom + laser system is weakly coupled to a continuum of photon modes, spontaneous emission leads to transitions between the Autler doublet states $|1\rangle$, $|2\rangle$ because both mix with the excited state. On resonance, the fluorescence spectrum shows the famous Mollow triplet with blue (red) sidebands shifted by the Rabi frequency $|\Omega|$ relative to the laser frequency ω_{L}.

When the Mollow spectrum overlaps with a photonic band edge, the fluorescence dynamics can be tuned, as proposed in [5, 26]. Consider the case of Figure 2.2 where the band edge ω_{c} is located between the central line and the blue sideband. Transiently, the system emits on the $|2\rangle \to |1\rangle$ transition, but then stays trapped in the state $|1\rangle$ from which all transitions are inhibited. When this process is initiated by turning the laser field on, it may be used to taylor the superposition state $|1\rangle$ or to trigger single-photon emission. The authors of [5] have also considered the extreme case of a finite frequency gap covering the central line, while both sidebands are allowed. The emission then occurs in an alternating cascade $|1\rangle \to |2\rangle \to |1\rangle$, with strong photon pair correlations. These may find applications in entangled state preparation and quantum cryptography.

As a second idea, replace the laser field by a quantized defect mode [6]. (See Chapter 1 in this volume, for the calculation of defect modes and Chapter 11 for their characterization with near field microscopy.) The system then realizes the famous Jaynes–Cummings model [27], and the Rabi frequency depends on the number of photons $n_{\rm d}$ in the defect mode:

$$\Omega_{\rm d}(n_{\rm d}) = -\sqrt{\frac{2n_{\rm d}\,\omega_{\rm d}}{\varepsilon_0 \hbar V}}\vec{d}\cdot \vec{E}_{\rm d}(\vec{x}_0). \tag{2.16}$$

Here V is the mode volume and $\vec{E}_{\rm d}(\vec{x})$ is the normalized mode function. A large Rabi splitting is expected for a wavelength–sized mode and leads into the strong coupling regime. If the defect mode is located in the band gap of the crystal, the coupled system can only decay via the two–level system into a photonic band [6]. Consider again the resonant case $\omega_{\rm d} = \omega_0$. If the quantized Rabi splitting $|\Omega_{\rm d}|$ pushes the blue sideband of the Mollow triplet into the photonic continuum, a radiative decay $|2, n_{\rm d}\rangle \rightarrow |1, n_{\rm d} - 1\rangle$ is possible. Now, since the splitting of the blue sideband decreases with the photon number on the defect, there exists a critical photon number $n_{\rm crit}$ with $\omega_{\rm c} = \omega_0 + |\Omega_{\rm d}(n_{\rm crit})|$, below which all three lines are in the gap, and decay is inhibited. This stationary state realizes a highly nonclassical distribution of photon numbers for the defect mode: if the initial number distribution is broad, it is eventually nonzero only for $n_{\rm d} \le n_{\rm crit}$. The intensity correlations of the light leaking out of the defect mode (due to some finite Q) may provide a fingerprint of this nontrivial photon statistics.

2.2.4 QED in a structured continuum

Close to a photonic band edge, Fermi's Golden Rule (2.1) is no longer applicable because the density of states is singular. We give here a tutorial review of the modified radiative decay dynamics. These calculations typically suffer from divergent frequency integrals that require renormalization in the UV. Note that the corresponding nonresonant processes typically lead us beyond the validity of the two-level model, because in realistic emitters other transitions come into play. We shall focus here on a two–level model and keep only near–resonant frequencies. This is equivalent to the so–called 'rotating wave approximation' where only quantum states with approximately the same unperturbed energy are retained in the system wave function. Frequency shifts like the Lamb shift or the van der Waals interaction between emitters, that originate from nonresonant couplings ('virtual transitions'), are by construction, beyond the capabilities of this approximation For simplicity, we discuss the problem in classical terms first and comment below on additional features of a quantum description.

The basic equations for a classical dipole oscillator coupled to the electric field are

$$\ddot{\vec{d}}(t) + \omega_0^2 \vec{d}(t) = \frac{e^2}{m}\vec{E}(\vec{x}_0, t) \tag{2.17}$$

$$\vec{E}(\vec{x}_0, t) = \vec{E}_{\rm ext}(\vec{x}_0, t) + \int {\rm d}t' \int \frac{{\rm d}\omega}{2\pi} {\rm e}^{-{\rm i}\omega(t-t')} \mathcal{G}(\vec{x}_0, \vec{x}_0; \omega) \cdot \vec{d}(t'), \tag{2.18}$$

where the Green tensor has been used to express the field created by the dipole. We put the external field $\vec{E}_{\rm ext} = 0$ and focus on the decay of the dipole that is excited with some amplitude $\vec{d}(0)$ at $t = 0$. For simplicity, we use in the following a linearly polarized dipole, $\vec{d}(t) = \vec{u}\, d(t)$ and use the projected Green tensor $G = \vec{u} \cdot \mathcal{G} \cdot \vec{u}$.

As mentioned above, we shall simplify the calculations using the 'rotating wave approximation' and assume that the dipole essentially oscillates at its free resonance frequency ω_0 with a slowly varying envelope. For the dipole envelope (also denoted $d(t)$), we obtain an integro-differential equation

$$\dot{d} = \mathrm{i}g \int\limits_0^\infty \mathrm{d}\tau\, G(\tau) d(t - \tau). \tag{2.19}$$

The coupling constant g may be expressed in terms of the dipole matrix element of a quantized oscillator between the states $|0\rangle$, $|1\rangle$: $g = e^2/2m\omega_0 = |\vec{d}|^2/\hbar$. The 'memory kernel' of the convolution integral in Eq. (2.19) involves the Fourier transform of the Green function

$$G(\tau) = \int \frac{\mathrm{d}\omega}{2\pi} \mathrm{e}^{-\mathrm{i}(\omega-\omega_0)\tau} G(\vec{x}_0, \vec{x}_0; \omega). \tag{2.20}$$

The width in τ of this function determines the memory time τ_c, i.e., the range of the past dipole dynamics $d(t - \tau)$ that contributes effectively to its future via $\dot{d}(t)$ in Eq. (2.19). We observe that the memory kernel decays on a scale $\tau_\mathrm{c} \approx 1/\Delta\omega$, when the Green function varies smoothly on a frequency scale $\Delta\omega$ around ω_0. In this case the usual description leading to exponential decay is recovered when the characteristic decay time t is 'large' compared to τ_c. One can then apply the Markov approximation to the memory kernel,

$$G(\tau) \approx \delta(\tau) G(\vec{x}_0, \vec{x}_0; \omega_0). \tag{2.21}$$

In the Markov regime, the dipole's future is determined by its present only. One obtains a complex, decaying exponential with a frequency shift proportional to the real part of G (requires renormalization as in Eq. (2.9)), and a decay rate involving the imaginary part of G as in Eq. (2.6).

A richer dynamics occurs close to a band edge, where the Markov approximation breaks down. We solve Eq. (2.19) with a Laplace transformation (Laplace variable z) and get

$$d[z] = \frac{d(0)}{z - \mathrm{i}gG[z]}. \tag{2.22}$$

The singularities of this function in the complex plane determine the time dynamics: damped oscillations occur when more than one simple pole exists, a power–law decay originates from cuts starting at branch point singularities. These features generically co–exist, and details depend on the model chosen for the mode density at the band edge.

Discussion. For illustration, let us focus on a photonic crystal described by the anisotropic model (2.11) and perform an approximate Laplace transformation (see [15,28,29] for different models). Since the mode density (2.11) only applies close to the band edge frequency ω_c, its

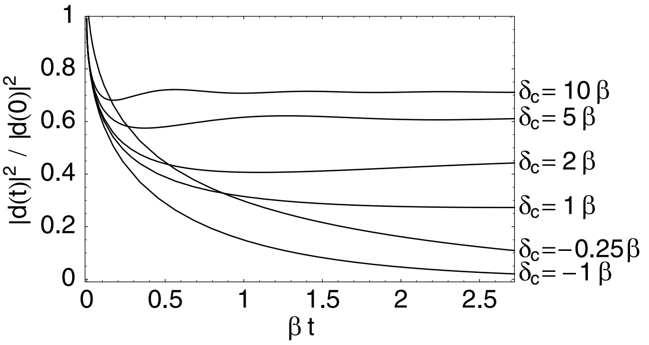

Figure 2.3: Radiative decay of a dipole close to a photonic band edge. We have numerically evaluated the Laplace transform [Eq. (2.22)] of the dipole amplitude. Time and detuning $\delta_c = \omega_c - \omega_0$ are scaled using the coupling frequency β estimated in Eq. (2.25).

UV behaviour is in any case unphysical and one has to renormalize the integral. A simple subtraction of the divergent terms yields

$$gG[z] = \frac{1}{\pi}\int\limits_0^\infty \mathrm{d}\omega\, \frac{\omega\sqrt{\beta(\omega-\omega_c)}}{\omega_0(\omega-\omega_0-\mathrm{i}z)} \approx \mathrm{i}\frac{\omega_0+\mathrm{i}z}{\omega_0}\sqrt{\beta(\omega_0-\omega_c+\mathrm{i}z)}, \tag{2.23}$$

where the coupling between dipole and photonic band is quantified in terms of the frequency $\beta = (\pi\omega_0|\vec{d}|^2/2\varepsilon_0\hbar)A(\vec{x}_0,\vec{u})$ (see Eq. (2.12)). For consistency with the rotating wave approximation, we drop the Laplace variable z in the prefactor $\omega_0 + \mathrm{i}z$. (Keeping it leads to characteristic frequencies far from resonance.) The relevant parameter is then the dimensionless detuning of the band edge $(\omega_c - \omega_0)/\beta$.

The analysis of the Laplace transform (2.22) is now quite simple: one finds a cut extending from $z = \mathrm{i}(\omega_0 - \omega_c)$ into the left half plane, and poles from a quadratic equation:

$$z^2 - \mathrm{i}\beta z + \beta(\omega_c - \omega_0) = 0. \tag{2.24}$$

At most one pole effectively contributes a nonzero residue, and by causality this pole must lie on the imaginary axis or have a negative real part. An interesting feature of this model is that the pole contributions are radiatively stable if $\omega_0 \le \omega_c + \beta/4$, i.e., even if the dipole transition slightly lies in the allowed band. Such behaviour can be understood from the mixing of the oscillator with the photonic band, leading to the formation of a ‘dressed atom + field state’ that is pushed below the band edge and thus stabilized. This does not mean, however, that the dipole does not decay at all, as is shown in Figure 2.3. In fact, the cut in the complex plane contributes an algebraic decay with an asymptotic time dependence $\sim t^{-1/2}$ close to resonance, $\omega_c \approx \omega_0$, and $\sim t^{-3/2}$ otherwise. The stable poles collect an increasing fraction of the initial energy when the dipole frequency moves into the band gap. If the transition is deep in the band ($\omega_0 - \omega_c \gg \beta$), one recovers the usual decay rate $\sim \sqrt{\omega_0 - \omega_c}$ as predicted from the anisotropic LDOS (2.11).

The coupling parameter β sets both the frequency scale around the band edge where non-exponential decay occurs, and the corresponding time scale. An estimate can be found by comparison to the LDOS (2.11, 2.12). Normalized to the vacuum decay rate, one obtains

$$\frac{\beta}{\Gamma_{\rm vac}} \sim \frac{\Gamma_{\rm vac}}{\omega_c}\frac{N_c|\vec{u}\cdot\vec{E}_c(\vec{x}_0)|^4}{|f_c|^3} \ll 1, \tag{2.25}$$

where N_c and f_c are defined in the discussion directly after Eq. (2.10). Note that the photonic band edge is extremely narrow in frequency space and appreciably slows down spontaneous decay.

Other models for the band edge DOS have been considered [15, 26, 28–31] and lead to qualitatively similar results. Quantitative differences are due to the structure of the singularities in the Laplace transform (2.22). The issue is not settled yet because calculations not involving implicitly or explicitly the rotating wave approximation are scarce (one exception is [32]). The models for the LDOS are only valid close to the band edge, while both the long– and short–term asymptotics also involve nonresonant frequencies. Only recently has it become possible to perform calculations involving the full dispersion relation [12, 33, 34].

Features of the quantum approach. Finally, how is this classical model related to the decay of a real two–level system? To begin with, we realize that the rotating wave approximation leads to a conserved quantity, the 'excitation' N_e, which is the total number of photons in the photonic band plus the number of excited atoms. Spontaneous emission is the simplest case where $N_\mathrm{e} = 1$, of a single, initially excited atom in the vacuum field. If the wave function of the total system is expanded on the resonantly coupled states, one can show that the Schrödinger equation yields an equation of motion for the amplitude $b_\mathrm{e}(t)$ of the state $|\mathrm{e}, \mathrm{vac}\rangle$ which is *identical* to the classical Eq. (2.19). The normalized dipole energy plotted in Figure 2.3 thus corresponds exactly to the excited state occupation $|b_\mathrm{e}(t)|^2$. The spectrum of the emitted fluorescence light can also be found classically; it is proportional to the Laplace transform $|d[z = -\mathrm{i}(\omega - \omega_0)]|^2$ [34]. To obtain the average number of photons emitted at frequency ω inside the crystal, one has to multiply with the LDOS. Coupling the Bloch modes out of the crystal leads to a spectrum that can, in principle, be compared to experimental data. Crystal imperfections, however, complicate a quantitative analysis, as discussed in Section 2.2.2.

The next challenge in the quantized theory, is the description of resonance fluorescence, i.e. a coherently excited two–level system, for example by a laser–driven defect mode. The excitation N_e is then no longer conserved (because energy is pumped into the system). A full analytical solution including the non–Markovian decay dynamics has not been reported to our knowledge. Numerically, one can integrate the Schrödinger equation over a suitably large set of basis vectors. One common trick is to describe the photonic band by a discrete number of modes with spacings adjusted to reproduce the LDOS [7, 34]. Off–resonant modes beyond a certain cutoff frequency can be eliminated adiabatically, incorporating the corresponding frequency shift into the bare transition frequency ω_0 [35]. However, the dimension of the Hilbert space grows rapidly when multiple excitations are taken into account, and recent calculations have been restricted to $N_\mathrm{e} \leq 3$ [35].

To avoid the blow–up of full numerical calculations, it has also been proposed to use techniques adapted from Monte Carlo simulations for the 'reduced' dynamics of a sub–system (in the simplest case only the two-level system) [36]. This approach, however, has to be used with care because in its simplest form, it seems to be inconsistent with the Markov assumption implicit in the Monte Carlo technique [37]. Advances have been possible for a smoothed LDOS, whose prominent features (band edge peaks, dips in the gap) can be lumped into a small number of 'effective photon modes'. The remaining flat background of the LDOS can be treated in the Markov approximation, while the combined two–level system plus photon modes can be treated with Monte Carlo techniques [31]. We also mention that non–Markovian reduced system dynamics has been analyzed in [38], solved with a Monte Carlo technique and applied to spontaneous emission into a band gap whose LDOS shows a Lorentzian dip.

2.3 Simulations

We have mentioned above that electromagnetic simulations are a useful tool to characterize spontaneous emission in photonic structures. The reason is that, though they treat the field classically, they give access to the local density of field modes via the imaginary part of the Green tensor or the normalized emitted power. The LDOS $\rho(\vec{x}_0, \vec{u}, \omega)$ may be obtained by solving a stationary wave equation with a monochromatic point source (simulation in the frequency domain). Alternatively, a calculation of the spatio–temporal light–field dynamics followed by Fourier transformation may be carried out. In addition, if the molecular dipole is included as a dynamical variable, one can even get access to the non–exponential decay at the band edge, as we discussed above. We recall that direct quantum simulations of a driven system or a system with multiple excitations, requires a significantly larger number of dynamical variables because the wavefunction is coupled to the high–dimensional multiphoton sector. In the following, we restrict our attention to 'classical' or 'single–excitation' simulations.

2.3.1 Frequency domain

One of our motivations has been to use the fluorescence rate of an atom or molecule as a local probe of its optical environment [17,39]. In practice, for the ease of manipulation in a scanning microscope setup, it is convenient to work with dye molecules embedded in nanocrystals [40–42]. We have addressed the impact of this sub–wavelength material on the spontaneous decay using simulations of the emitted field [43].

We assume a monochromatic dipole with frequency $\omega_0 = ck_0$. The field then solves the wave equation

$$\nabla \times \nabla \times \vec{E} - k_0^2 \varepsilon(\vec{x}) \vec{E} = \frac{k_0^2}{\varepsilon_0} \vec{d} \delta(\vec{x} - \vec{x}_0) \tag{2.26}$$

where $\vec{d}$ is the dipole matrix moment and the permittivity $\varepsilon(\vec{x})$ describes the dielectric nanocrystal. To solve this partial differential equation, we focus on a nano–object with a locally homogeneous and isotropic permittivity $\varepsilon > 1$. Inside and outside the object, the problem is reduced to propagation in a homogeneous medium, and scattering occurs due to the matching of the fields at the object boundaries. Mathematically, this property of the wave equation permits a reformulation in terms of a boundary integral equation (this result is called the 'extinction theorem', see [44,45] for details).

Let us adopt for illustrative purposes a two–dimensional model. The nanocrystal thus corresponds to a cylindrical object, and the molecule to a chain of dipoles. The polarization dependence separates into two cases, and the physically interesting one, for near field investigations, is a dipole polarized perpendicular to the cylinder axis, the z–axis say ('TE-polarization'). In that case, the problem is most conveniently formulated in terms of the magnetic field $\vec{H}(\vec{x}) = \vec{e}_z H(x,y)$ because it contains only a single nonzero component:

$$\nabla\left(\frac{1}{\varepsilon(\vec{x})}\cdot\nabla H\right) + k_0^2 H = \frac{\mathrm{i}\omega_0}{\varepsilon(\vec{x}_0)}\vec{d}\cdot(\vec{e}_z\times\nabla)\delta(\vec{x}-\vec{x}_0) \tag{2.27}$$

where we switched to $\vec{x} = (x,y)$. In a homogeneous dielectric, this equation can be solved in terms of a third kind Bessel function $H_0^{(1)}(z)$. This solution provides us with a particular solution to the wave equation inside the nano–object, the 'dipole field'

$$H_{\mathrm{dip}}(\vec{x}) = \mathrm{i}\omega_0\,\vec{d}\cdot(\vec{e}_z\times\nabla)G_\varepsilon(\vec{x}-\vec{x}_0) \tag{2.28}$$

$$G_\varepsilon(\vec{x}-\vec{x}_0) = \frac{\mathrm{i}}{4}H_0^{(1)}(k_0\sqrt{\varepsilon}|\vec{x}-\vec{x}_0|). \tag{2.29}$$

On the boundary $\mathcal{B}$ of the nano–object, the field $H(\vec{x})$ and the normal derivative $F(\vec{x}) = (1/\varepsilon)\partial H/\partial n$ (the tangential electric field) are continuous. The wave equation is then equivalent to the following pair of integral equations, where $\vec{r}\in\mathcal{B}$ is on the object boundary [45]:

$$H(\vec{r}) = 2H_{\mathrm{dip}}(\vec{r}) + 2\oint_{\mathcal{B}}\mathrm{d}a(\vec{x})\,\left[G_\varepsilon(\vec{x}-\vec{r})\varepsilon F(\vec{x}) - H(\vec{x})\frac{\partial G_\varepsilon}{\partial n}(\vec{x}-\vec{r})\right], \tag{2.30}$$

$$H(\vec{r}) = -2\oint_{\mathcal{B}}\mathrm{d}a(\vec{x})\,\left[G_1(\vec{x}-\vec{r})F(\vec{x}) - H(\vec{x})\frac{\partial G_1}{\partial n}(\vec{x}-\vec{r})\right]. \tag{2.31}$$

Here $\mathrm{d}a(\vec{x})$ is the boundary element at the point $\vec{x}$, $\partial/\partial n$ is the derivative along the outward normal, and G_1 the free space Green function. An equation similar to (2.31), but with a prefactor -1 instead of -2, gives the field outside the object in terms of its values on the boundary. The far field is computed by expanding the Green function and becomes similar to a spatial Fourier transform of the boundary field.

For numerical calculations, the object boundary is discretized into surface elements Δa and the integrals replaced by Riemann sums. More refined schemes exist, for example expansions in piecewise linear functions, and are known as 'moment methods' [46, 47]. The singularity of the derivative $\partial G/\partial n$ has already been accounted for in Eq. (2.31) and explains the factor 2 in front of the integrals. When the singularity of the Green function itself is extracted to lowest order in Δa, one gets for the integral over the boundary element containing $\vec{r}$:

$$\int_{\mathcal{B}(\vec{r})}\mathrm{d}a(\vec{x})\,\varepsilon G_\varepsilon(\vec{x}-\vec{r})F(\vec{x}) \approx -\Delta a\,\varepsilon F(\vec{r})\left[2\log(k_0\sqrt{\varepsilon}\Delta a/4) - 2 + 2\gamma - \mathrm{i}\pi\right], \tag{2.32}$$

where $\gamma \approx 0.577$ is the Euler constant. Once this term is taken care of, the other boundary elements can be treated as in a Riemann sum, leading to a linear system for the boundary field and its normal derivative.

The method has also been applied to rough surface scattering [48,49]. It has the advantage that only interfaces between objects have to be discretized and that the Sommerfeld radiation condition at infinity is automatically satisfied. The resulting linear system is not sparse, however, and in three dimensions it scales faster with system size than time–domain simulations. Iterative algorithms similar to those employed for band structure calculations [50] have been used to reduce the memory and CPU time requirements [49].

To illustrate the simulation scheme, we consider a molecular dipole inside a rectangular nano–object and study the spontaneous emission rate as a function of the object size and its

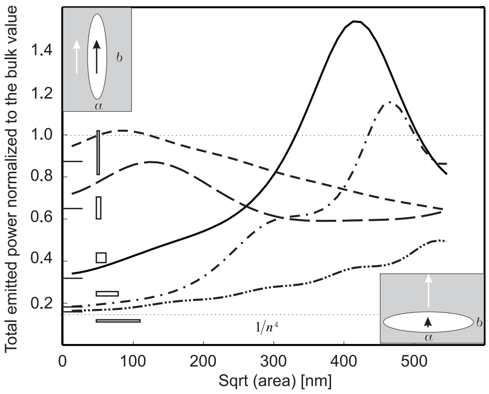

Figure 2.4: Normalized spontaneous emission rate of a dipole inside a rectangular nano–object, plotted vs. the object size. The dipole is always vertically polarized. Wavelength 620 nm, refractive index 1.59. The aspect ratios are $1:20, 1:5, 1, 5:1$, and $20:1$. Dotted lines: limits for infinitely thin objects. Horizontal lines on the left axis: electrostatic calculation for elliptic objects. The insets illustrate the jump conditions for the normal and tangential electric field components across the long edge of the object. Adapted from [43], courtesy of L. Rogobete.

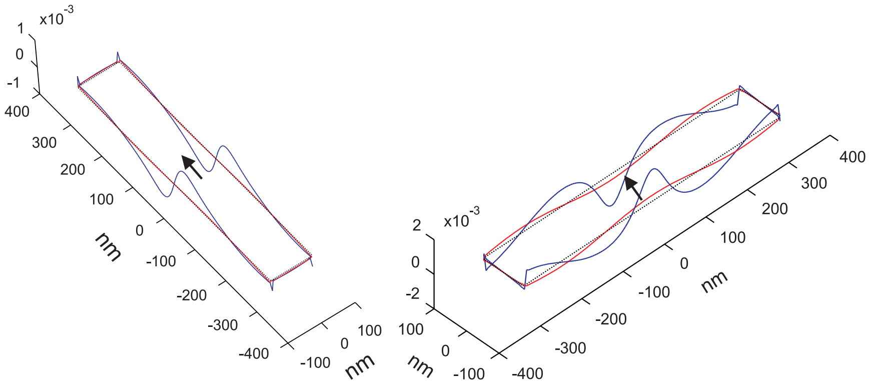

Figure 2.5: Surface charge induced on the boundary of a rectangular object for two orientations of the dipole. Parameters as in Figure 2.4, object size = $125\,\mathrm{nm} \times 625\,\mathrm{nm}$. Blue (red): surface charge in phase (in phase quadrature) with the dipole. Courtesy of L. Rogobete.

aspect ratio. Typical results are shown in Figure 2.4. For sub–wavelength objects, the decay rate is reduced if the dipole is oriented perpendicular to the long object axis. This is due to an induced surface charge that oscillates in phase opposition with the dipole and ‘screens’ it when seen in the far field, as illustrated in Figure 2.5. This near field effect becomes less pronounced when the object boundary recedes. If the object size is comparable to the wavelength, standing wave resonances (similar to waveguide modes) lead to peaks in the decay rates. They also spatially modulate the LDOS, as shown in Figure 2.6. The LDOS modulations are moderate due to the weak backreflections from the object border (the index contrast is small and the field not strongly confined).

Finally, the limit of a very small object leads us beyond the validity of the macroscopic description in terms of a permittivity. To recover the vacuum decay rate, one has to use a different model for the nano–object, for example in terms of discrete polarizable particles that are removed one by one.

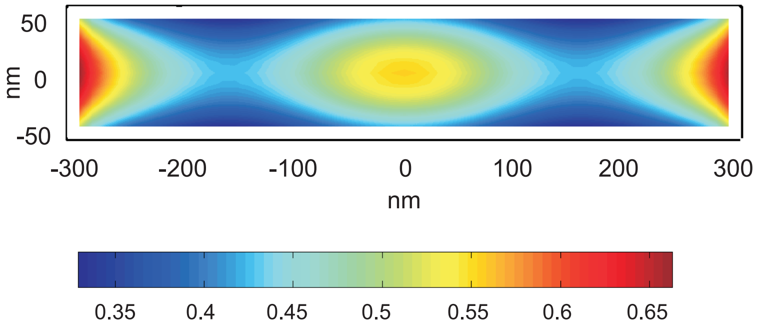

Figure 2.6: Local density of states inside the rectangular nano–object of Figure 2.5. The LDOS is normalized relative to vacuum and projected onto a vertically polarized dipole moment. Same parameters as in Figure 2.5. Courtesy of L. Rogobete.

2.3.2 Time domain

In this section, we discuss a method based on a Finite–Difference Time–Domain (FDTD) calculation of the classical electromagnetic fields, that allows one to calculate the spontaneous emission rate within the weak coupling regime for arbitrary dielectric distributions.

Before we set out to describe the method itself, we recall (c.f. Sec. (2.2.1)) that within the weak coupling regime, the ratio of the energies E radiated by a classical dipole current source within a dielectric environment and in vacuum, is equal to the ratio of the corresponding spontaneous emission rates:

$$\frac{\Gamma_{\rm diel}(\omega)}{\Gamma_{\rm vac}(\omega)} = \frac{E_{\rm diel}(\omega)}{E_{\rm vac}(\omega)}. \tag{2.33}$$

The modification of the emitted energy by the dielectric structure is due to the interaction of the current source with the back-reflected parts of the electric field. One should note that this interplay of the source with its environment depends – among various other factors – on the polarization of the dipole source.

To calculate the radiated energy of a dipole current source, we choose an FDTD–algorithm. With this method, we can directly model a particular dielectric distribution representing the photonic crystal structure in a finite space volume. The time dependent field evaluation is calculated by solving Maxwell's curl equations, using a finite differencing scheme [51, 52]. The exciting current density $\vec{j}_0(\vec{x}, t) = \dot{\vec{d}}(t)\delta(\vec{x} - \vec{r}_0)$ localized at position $\vec{r}_0$ can directly be inserted in the FDTD-$\vec{E}$–field equation. It should be noted that in many cases, it is of interest to calculate the photonics of finite structures surrounded e.g. by free space. This can be done in FDTD by surrounding the computational volume defining the photonic crystal, with an artificial absorbing medium that models the free space appropriately, by avoiding back-reflection of the fields at the interfaces. In our case, we use perfectly matched layer (PML) boundary conditions [53]. This effectively surrounds the calculation space with infinitely extended free space.

The radiated energy can now be calculated in different ways. The simplest possibility is to record the time series of $\dot{\vec{d}}(t)$ and $\vec{E}(\vec{r}_0, t)$ and to calculate E as

$$E = -\int\limits_0^{t_0} \mathrm{d}t \int \mathrm{d}^3x\, \vec{j}_0(\vec{x}, t) \cdot \vec{E}(\vec{x}, t) = -\int\limits_0^{t_0} \mathrm{d}t\, \dot{\vec{d}}(t) \cdot \vec{E}\,(\vec{r}_0, t)\,, \tag{2.34}$$

or, because we are interested in the spectral dependence of the emission rate, first Fourier-transform $\vec{d}(t)$ and $\vec{E}(\vec{r}_0, t)$ to obtain the time averaged emitted energy (c.f. Eq. (2.6))

$$E(\omega) = \mathrm{Re}\big[-\mathrm{i}\omega\, \vec{d}^*(\omega) \cdot \vec{E}(\vec{r}_0, \omega)\big]. \tag{2.35}$$

This expression gives us the over–all effect of all electromagnetic modes the dipole source can couple to. In some cases, however, it may also be interesting to estimate directional dependences. For example, in a photonic crystal slab we would like to distinguish between the confinement of the two–dimensional photonic crystal structure and the index guiding perpendicular to the crystal plane. This can be done by calculating the emitted energy via the Poynting–vector, perpendicular to a closed surface around the structure and selectively integrating the power flow over different directions (c.f. Eq. (2.15)). We want to stress, however, that the calculation of numbers like energy or Poynting–vector must correctly take into account the discrete nature of the computational mesh. A consistent discrete version of Poynting's theorem for FDTD is described in [54].

The method briefly outlined here is very general and does not have to rely a priori on any particular information on photonic crystals. It is used in the literature for example for analyzing spontaneous emission in microdisks [55], finite photonic crystal slabs [56] and finite inverse opal structures [57]. Therefore, before we focus on a photonic crystal example, we have validated the numerical method by simulating a system that is analytically solvable: the spontaneous emission rate of an emitter in the center of a dielectric sphere. Our FDTD results [57] have shown an excellent agreement with the analytical expression given in [58].

We are now on firm grounds to apply the FDTD–method to the study of three–dimensional photonic crystals. In particular, we consider an inverted opal that shows a complete photonic bandgap for frequencies between 0.795 and 0.85 $(2\pi c/a)$, where c is the vacuum speed of light and a the lattice constant of the crystal. The structure consists of close–packed air–spheres in a fcc–arrangement, connected by cylindrical holes (see Figure 2.7). These characteristic holes result from the sintering that is part of the formation process of typical inverse opal structures [59].

If we want to study the spatial dependence of the spontaneous emission rate within the unit cell, we can – due to symmetry considerations – limit our attention to a tetrahedral volume with $1/48$ of the size of the conventional unit cell. The dielectric distribution of one conventional unit cell and the reduced volume limited by the points P_1, P_2, P_3, P_4 are shown in Figure 2.7. The finite photonic crystallite that we consider, is a cube with an edge length of 5 lattice constants and consists of 500 primitive unit cells. In the simulations, the crystallite is surrounded by PML boundaries. For accurate numerical results, we used a resolution of 50 discretization points per lattice constant.

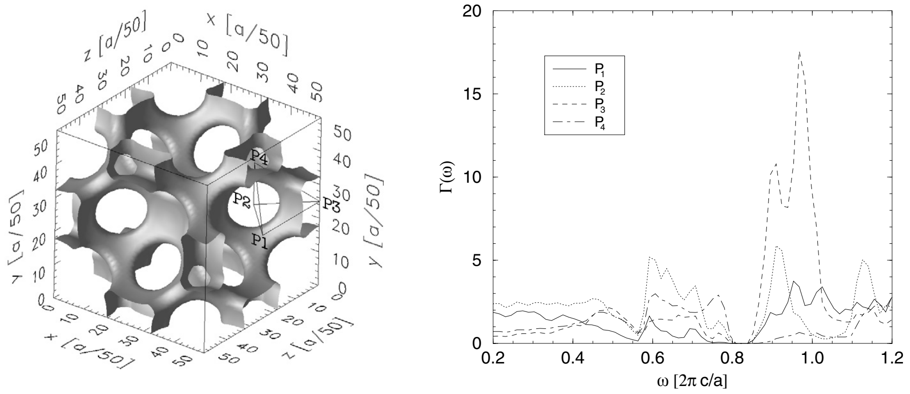

Figure 2.7: Left panel: conventional unit cell in real space of an inverted opal with a set of high symmetry points. Parameters: period a, fcc close packing of air spheres with radius $r = a/\left(2\sqrt{2}\right)$, connected by cylindrical holes of radius $0.4\,r$. The dielectric backbone has refractive index 3.6.
Right panel: normalized emission rate [Eq. (2.36)] for the four high symmetry points in the center unit cell of the crystallite. Dipole polarized along the z–direction.

Figure 2.7 shows the modification factor of the spontaneous emission rate

$$\Gamma(\omega) = \frac{\Gamma_{\mathrm{crystallite}}(\omega)}{\Gamma_{\mathrm{vac}}(\omega)} \tag{2.36}$$

for the high symmetry points P_1, P_2, P_3, P_4 in the center unit cell of the crystallite for a z–polarized dipole. For all four dipole positions, the bandgap can be clearly identified. For frequencies outside the bandgap, a very strong position dependence is observed.

To analyze this position dependence in more detail, we calculate $\Gamma(\omega)$ along a line connecting points P_1 and P_3. As this path crosses a dielectric interface, we may expect a dependence of Γ on the polarization of the dipole with respect to this interface. This is demonstrated in Figure 2.8 where the two cases of normal and parallel polarizations with respect to the dielectric surface are shown. As the dipole couples to the electric field, the continuity behaviour of the spontaneous emission factor should qualitatively be like that of the electric field. Indeed, the discontinuity for normal polarization and the continuity for parallel polarization are clearly observed in Figure 2.8. Note that the spectral properties of the emission rate also vary strongly with the dipole position and polarization. It is interesting to mention the enhancement peak for parallel polarization below the bandgap at the dielectric interface, because in experiments, infiltrated dyes may absorb at these interfaces.

2.4 Concluding remarks

The control over spontanenous emission promised by photonic crystal structures, remains a challenge both for theory and experiment. Fascinating theoretical predictions have been made in idealized, infinite structures. Current computer simulations are now able to characterize

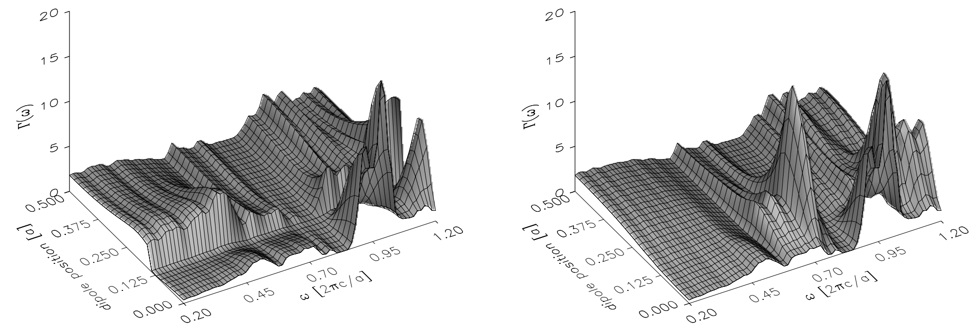

Figure 2.8: Normalized emission rates along the path $P_3 - P_1$ of Figure 2.7. Left panel: dipole polarization normal to the vacuum–dielectric interface. Right panel: dipole polarization parallel to the dielectric interface. In the position range $0 - 0.126\,a$, the dipole is located inside the dielectric backbone.

reliably realistic, albeit small samples. On the experimental side, one may in the near future achieve high–quality structures, allowing to observe the delicate quantum electrodynamical effects occurring at the photonic band edge. We have highlighted in this chapter a few of the current theoretical trends: optical control over emission or band edge frequencies, efficient quantum simulation techniques for multiple excitations and driven systems, and powerful electromagnetic computer simulations for increasingly complex structures.

A key application where quantum optics and photonic crystals meet, are compact light sources where a localized defect mode is excited by a nanoscopic gain medium (dye molecules, semiconductor quantum dots). The inhibition of spontaneous emission implies that the corresponding microlaser can operate at low threshold and pumping power, and can potentially be used for cavity quantum electrodynamics. Indeed, a photonic crystal defect laser with a single quantum dot embedded in a semiconductor, would allow us to access physical effects similar to those studied with single–atom lasers. For the semiclassical theory of the defect laser, the reader is referred to Chapter 13 in this volume, Sakoda's textbook [11] and the paper by the group of Busch and John [60]. Clearly, the simulation of the full quantum dynamics of a single quantum dot photonic crystal defect laser, represents a highly exciting and challenging topic. Computationally, it requires the solution of the time–dependent Maxwell equations in three dimensions, coupled with appropriate oscillator equations describing the carrier and dipole dynamics in the quantum dot. A theoretical framework for this kind of problem is outlined in Chapter 3 of this volume.

Acknowledgements

We thank our collaborators L. Rogobete and V. Sandoghdar (Zürich) and are indebted to A. Klaedtke and S. Scholz (Stuttgart) for support with the FDTD code. The pleasant environment of M. Wilkens's group (Potsdam) is gratefully acknowledged. This work has been supported by the *Deutsche Forschungsgemeinschaft*.

References

[1] E. M. Purcell, Spontaneous emission probabilities at radio frequencies, Phys. Rev. **69** (1946) 681.

[2] E. Yablonovitch, Inhibited spontaneous emission in solid-state physics and electronics, Phys. Rev. Lett. **58** (1987) 2059.

[3] M. Woldeyohannes and S. John, Coherent control of spontaneous emission near a photonic band edge, J. Opt. B: Quantum Semiclassical Opt. **5** (2003) R43.

[4] S. John, Strong localization of photons in certain disordered dielectric superlattices, Phys. Rev. Lett. **58** (1987) 2486.

[5] T. W. Mossberg and M. Lewenstein, Radiative properties of strongly driven atoms in the presence of photonic bands and gaps, J. Opt. Soc. Am. B **10** (1993) 340.

[6] A. G. Kofman, G. Kurizki, and B. Sherman, Spontaneous and induced atomic decay in photonic band structures, J. Mod. Optics **41** (1994) 353.

[7] P. Lambropoulos, G. M. Nikolopoulos, T. R. Nielsen, and S. Bay, Fundamental quantum optics in structured reservoirs, Rep. Prog. Phys. **63** (2000) 455.

[8] A. Asatryan, S. Fabre, K. Busch, R. McPhedran, L. Botten, M. de Sterke, and N. A. Nicorovici, Two-dimensional local density of states in two-dimensional photonic crystals, Opt. Express **8** (2001) 191.

[9] A. Moroz, Minima and maxima of the local density of states for one-dimensional periodic systems, Europhys. Lett. **46** (1999) 419.

[10] J. D. Jackson, Classical Electrodynamics, 2nd ed. (Wiley & Sons, New York, 1975).

[11] K. Sakoda, Optical Properties of Photonic Crystals (Springer, Berlin Heidelberg, 2001).

[12] K. Busch, N. Vats, S. John, and B. C. Sanders, Radiating dipoles in photonic crystals, Phys. Rev. E **62** (2000) 4251.

[13] J. B. Pendry, Photonic band structures, J. Mod. Optics **41** (1994) 209.

[14] G. Boedecker and C. Henkel, All-frequency effective medium theory for a photonic crystal, Opt. Express **11** (2003) 1590.

[15] S. Y. Zhu, Y. Yang, H. Chen, H. Zheng, and M. S. Zubairy, Spontaneous Radiation and Lamb shift in three-dimensional photonic crystals, Phys. Rev. Lett. **84** (2000) 2136.

[16] L. Knöll, S. Scheel, and D. G. Welsch, QED in dispersing and absorbing media in Coherence and Statistics of Photons and Atoms, edited by J. Perina (John Wiley & Sons, Inc., New York, 2001).

[17] W. L. Barnes, Fluorescence near interfaces: the role of photonic mode density, J. Mod. Optics **45** (1998) 661.

[18] J. M. Wylie and J. E. Sipe, Quantum electrodynamics near an interface, Phys. Rev. A **30** (1984) 1185.

[19] S. Savasta, O. D. Stefano, and R. Girlanda, Quantum theory of light scattering for arbitrary finite-size dielectric and conducting structures, J. Opt. A: Quantum Semiclassical Opt. **4** (2002) S95.

[20] J. M. Bendickson, J. P. Dowling, and M. Scalora, Analytic expressions for the electromagnetic mode density in finite, one-dimensional, photonic band-gap structures, Phys. Rev. E **53** (1996) 4107.

[21] A. F. Koenderink, L. Bechger, H. P. Schriemer, A. Lagendijk, and W. L. Vos, Broadband fivefold reduction of vacuum fluctuations probed by dyes in photonic crystals, Phys. Rev. Lett. **88** (2002) 143903.

[22] K. Totsuka, G. van Soest, T. Ito, A. Lagendijk, and M. Tomita, Amplification and diffusion of spontaneous emission in strongly scattering medium, J. Appl. Phys. **87** (2000) 7623.

[23] S. John and J. Wang, Quantum optics of localized light in a photonic band gap, Phys. Rev. B **43** (1991) 12 772.

[24] S. John and T. Quang, Photon-hopping conduction and collectively induced transparency in a photonic band gap, Phys. Rev. A **52** (1995) 4083.

[25] S. John and V. I. Rupasov, Quantum self-induced transparency in frequency gap media, Europhys. Lett. **46** (1999) 326.

[26] M. Lewenstein, J. Zakrzewski, and T. W. Mossberg, Spontaneous emission of atoms coupled to frequency-dependent reservoirs, Phys. Rev. A **38** (1988) 808.

[27] P. Meystre and M. Sargent III, Elements of Quantum Optics 3rd ed. (Springer, Berlin, 1999).

[28] S. John and J. Wang, Quantum electrodynamics near a photonic band gap: photon bound states and dressed atoms, Phys. Rev. Lett. **64** (1990) 2418.

[29] S. John and T. Quang, Spontaneous emission near the edge of a photonic band gap, Phys. Rev. A **50** (1994) 1764.

[30] S. Bay, P. Lambropoulos, and K. Mølmer, Atom–atom interaction at the edge of a photonic band gap, Opt. Commun. **132** (1996) 257.

[31] B. M. Garraway, Decay of an atom coupled strongly to a reservoir, Phys. Rev. A **55** (1997) 4636.

[32] Z. Liu, Y. Lin, L. Zeng, Q. Wu, S. Zhu, and S. Pan, The influence of virtual-photon processes on spontaneous emission from an atom in photonic band gap crystals, Phys. Lett. A **287** (2001) 39.

[33] Z. Y. Li, L. L. Lin, and Z. Q. Zhang, Spontaneous emission from photonic crystals: full vectorial calculations, Phys. Rev. Lett. **84** (2000) 4341.

[34] N. Vats, S. John, and K. Busch, Theory of fluorescence in photonic crystals, Phys. Rev. A **65** (2002) 043808.

[35] G. M. Nikolopoulous and P. Lambropoulos, Few-photon quantum electrodynamics in a structured continuum, J. Opt. B **3** (2001) 115.

[36] T. Quang and S. John, Resonance fluorescence near a photonic band edge: dressed-state Monte Carlo wave-function approach, Phys. Rev. A **56** (1997) 4273.

[37] K. Mølmer and S. Bay, Comment on "Resonance fluorescence near a photonic band edge: Dressed-state Monte Carlo wave-function approach", Phys. Rev. A **59** (1999) 904.

[38] H. P. Breuer, B. Kappler, and F. Petruccione, Stochastic wave-function method for non-Markovian quantum master equations, Phys. Rev. A **59** (1999) 1633.

[39] C. Henkel and V. Sandoghdar, Single-molecule spectroscopy near structured dielectrics, Opt. Commun. **158** (1998) 250.

[40] P. Kramper, A. Birner, M. Agio, C. M. Soukoulis, F. Müller, U. Gösele, J. Mlynek, and V. Sandoghdar, Direct spectroscopy of a deep two-dimensional photonic crystal microresonator, Phys. Rev. B **64** (2001) 233102.

[41] J. Michaelis, C. Hettich, A. Zayats, B. Eiermann, J. Mlynek, and V. Sandoghdar, Mapping an optical standing wave with a single molecule, Opt. Lett. **24** (1999) 581.

[42] J. Michaelis, C. Hettich, J. Mlynek, and V. Sandoghdar, Optical microscopy using a single-molecule light source, Nature **405** (2000) 325.

[43] L. Rogobete, H. Schniepp, V. Sandoghdar, and C. Henkel, "Spontaneous emission in nanoscopic dielectric particles", Opt. Lett. **28** (2003) 1736.

[44] M. Born and E. Wolf, Principles of Optics, 6th ed. (Pergamon Press, Oxford, 1959).

[45] M. Nieto-Vesperinas, Scattering and Diffraction in Physical Optics (Wiley & Sons, New York, 1991).

[46] R. Bancroft, Understanding electromagnetic scattering using the Moment Method: a practical approach (Artech House Inc., Norwood Mass., 1996).

[47] R. F. Harrington, Field computation by moment methods (IEEE Press, Piscataway, 1993).

[48] M. Saillard and A. Sentenac, Rigorous solutions for electromagnetic scattering from rough surfaces, Waves Random Media **11** (2001) R103.

[49] G. Soriano and M. Saillard, Scattering of electromagnetic waves from two-dimensional rough surfaces with an impedance approximation, J. Opt. Soc. Am. A **18** (2001) 124.

[50] S. G. Johnson and J. D. Joannopoulos, Block-iterative frequency-domain methods for Maxwell's equations in a planewave basis, Opt. Express **8** (2001) 173.

[51] A. Taflove and S. C. Hagness, Computational Electrodynamics: The Finite-Difference Time-Domain Method, 2nd ed. (Artech House Inc., Norwood MA, 2000).

[52] K. Yee, Numerical solution of initial boundary value problems involving Maxwell's equations in isotropic media, IEEE Trans. Antennas Propagat. **AP-14** (1966) 302.

[53] J. P. Berenger, A perfectly matched layer for the absorption of electromagnetic waves, J. Comp. Physics **114** (1994) 185.

[54] J. de Moerloose and D. de Zutter, Poynting's theorem for the finite-difference-time-domain method, Microw. and Opt. Technology Lett. **8** (1995) 257.

[55] Y. Xu, R. Lee, and A. Yariv, Finite-difference time-domain analysis of spontaneous emission in a microdisk cavity, Phys. Rev. A **61** (2000) 033808.

[56] R. Lee, Y. Xu, and A. Yariv, Modified spontaneous emission from a two-dimensional photonic bandgap crystal slab, J. Opt. B **17** (2000) 1438.

[57] C. Hermann and O. Hess, Modified spontaneous emission rate in an inverted opalstructure with complete photonic bandgap, J. Opt. B **19** (2002) 3013.

[58] F. L. Kien, N. H. Quang, and K. Hakuta, Spontaneous emission from an atom inside a dielectric sphere, Opt. Commun. **178** (2000) 151.

[59] J. E. G. J. Wijnhoven and W. L. Vos, Preparation of photonic crystals made of air spheres in titania, Science **281** (1998) 802.

[60] L. Florescu, K. Busch, and S. John, Semiclassical theory of lasing in photonic crystals, J. Opt. Soc. Am. B **19** (2002) 2215.

3 Semiconductor optics in photonic crystal structures

Torsten Meier[1] *and Stephan W. Koch*

3.1 Introduction

The light–matter interaction in atoms, molecules, and solids in the usual far–field limit, is governed by the transverse part of the electromagnetic field. The eigenmodes of this transverse field can be influenced strongly through a spatially structured dielectric environment as in a photonic crystal [1–3], see also the two preceding Chapters 1 and 2 by K. Busch, et al. and G. Boedecker, et al., respectively. In addition, as we discuss in this chapter, the longitudinal electromagnetic interaction, that is the Coulomb potential, can also be changed significantly in suitably designed arrangements of semiconductor photonic crystals. Quite generally, such combinations of semiconductor heterostructures and photonic crystals configurations allow for the possibility of studying novel light–matter coupling aspects in condensed matter.

Semiconductor heterostructures are of particular interest since they can be grown with almost molecular precision, exhibit strong excitonic resonances even at room temperature, and the quantum efficiency in well designed opto–electronic devices, approaches the fundamental radiative lifetime limit. Suitably designed hybrid semiconductor photonic–crystal structures show properties that are not only very interesting from a fundamental physics point of view but should also be useful for applications in semiconductor opto–electronics. In fact, several device applications have already been demonstrated, see for example Chapters 12–17 in this book.

Typical optically active structures that have been investigated experimentally, consist of semiconductor quantum wells which are coupled to photonic crystals [4–7]. An application of particular importance is the use of photonic crystals to optimize the characteristics of semiconductor light emitting diodes and lasers [8, 11].

The main goal of the discussion in this chapter, is to summarize important elements of a microscopic theory that is able to adequately describe the fascinating interplay between dielectric material structuring and elementary semiconductor excitations. The theoretical analysis of the optical and electronic properties of hybrid semiconductor photonic–crystal structures can be done at various levels. In the most straightforward approach, one starts from microscopic material theory [12] coupled to the modified classical light field of the photonic crystal structure. However, there are also configurations where the Coulomb interaction potential in the semiconductor material is significantly modified due to the dielectric structuring [13–15]. In this case, the material excitation properties are altered in comparison to a spatially homoge-

---

[1] Corresponding author: e-mail: torsten.meier@physik.uni-marburg.de, Phone: +49 6421 2824221, Fax: +49 6421 2827076

Photonic Crystals. Edited by K. Busch, S. Lölkes, R. B. Wehrspohn and H. Föll
Copyright © 2004 Wiley-VCH Verlag GmbH & Co. KGaA
ISBN: 3-527-40432-5

neous configuration and subsequently, the energetic position of the exciton resonance, as well as quasi–equilibrium electron and hole populations, may vary in space. These spatially inhomogeneous populations have a substantial influence on the quasi–equilibrium gain spectra of laser structures and a spatially periodic modulation of the optical properties may even result in superradiant emission properties.

In certain cases it is necessary to use a fully quantized theory, for example in order to systematically investigate spontaneous emission properties, statistical features of the emitted light, or the combined influence of optical and Coulomb correlation effects in semiconductors [16, 17]. However, quantum optical effects will not be analyzed in this chapter, which is focussed on semiclassical properties of semiconductor photonic structures.

The discussion is organized as follows: The basic analysis of the light–matter interaction is presented in Sect. 3.2. Here we show how one can obtain the generalized Coulomb potential which governs the interaction of charged particles close to structured dielectrics. Equations of motion for the material excitations coupled to a classical light field are presented. The numerical results in Sect. 3.3 demonstrate some consequences of the spatial inhomogeneity of the semiconductor excitations induced by the dielectric structuring. A summary and an outlook are given in Sect. 3.4.

3.2 Semiclassical theory

3.2.1 Light–matter coupling

In a semiclassical treatment of the optical properties, the material system is described quantum mechanically whereas the dynamics of the classical electromagnetic field is governed by Maxwell's equations. The resonant light–matter coupling is contained in the macroscopic optical polarization P of the material, which appears as a source term for the electromagnetic field. In its simplest form, the wave equation for one–dimensional propagation is given as

$$\left[\frac{\partial^2}{\partial z^2} - \frac{n^2(z)}{c^2}\frac{\partial^2}{\partial t^2}\right] E = -\mu_0 \frac{\partial^2}{\partial t^2} P \,, \tag{3.1}$$

where E is the transverse electromagnetic field, z is the space coordinate, t the time, and μ_0 is a constant prefactor depending on the system of units. Here, the response of the material has been divided into a resonant part, which is treated dynamically in terms of the optical polarization P, and a nonresonant part lumped into the frequency–independent (background) refractive index n.

For the case of a periodically structured dielectric confinement, one can calculate the photonic bandstructure and expand the electromagnetic field using Bloch function modes [3]. In order to describe the light–matter coupling, the optical polarization P has to be computed on the basis of a proper microscopic description of the material excitations.

3.2.2 Generalized Coulomb potential

A spatially structured dielectric environment introduces changes of the single–particle energies through self–energies and alters the interaction between electrons and holes [13–15]. As a consequence, the excitonic resonances and the fundamental absorption edge may vary for different positions on the sample. In the following, we briefly sketch the important steps needed to obtain the generalized Coulomb potential describing the interaction among charges close to a structured dielectric environment [13].

For spatially homogeneous systems, one can employ the standard Coulomb gauge $\nabla \cdot \vec{A}(\vec{r},t) = 0$, where $\vec{A}$ is the full vector potential. This gauge allows us to separate the longitudinal and transverse field components. However, for inhomogeneous configurations when the dielectric environment is spatially structured, the standard Coulomb gauge leads to a nonvanishing scalar potential ϕ, even in the absence of external charges. In turn, the Coulomb interaction depends not only on the scalar, but also on the vector potential, as can be seen from Maxwell's equation (in cgs units)

$$\nabla \cdot \vec{D}(\vec{r},t) = -\nabla \cdot \left[\epsilon(\vec{r}) \left(\frac{1}{c}\frac{\partial}{\partial t}\vec{A}(\vec{r},t) + \nabla\phi(\vec{r},t)\right)\right] = 4\pi\rho(\vec{r},t)\,. \tag{3.2}$$

Here, $\vec{D}(\vec{r},t)$ is the dielectric displacement field, $\epsilon(\vec{r})$ is the spatially varying dielectric function, which is assumed to depend on the material but not on frequency, and $\rho(\vec{r},t)$ is the charge density. When dealing with space dependent dielectric properties, it is therefore advantageous to use the generalized Coulomb gauge [18, 19]

$$\nabla \cdot \left[\epsilon(\vec{r})\vec{A}(\vec{r},t)\right] = 0\,. \tag{3.3}$$

Within this gauge, the vector potential obeys a wave equation

$$\left(\nabla \times \nabla \times + \epsilon(\vec{r})\frac{1}{c^2}\frac{\partial^2}{\partial t^2}\right)\vec{A}(\vec{r},t) = 4\pi\frac{1}{c}\vec{j}_T(\vec{r},t)\,, \tag{3.4}$$

with an inhomogeneity given by the transverse part of the external current $\vec{j}_T(\vec{r},t)$. Furthermore, the scalar potential is the solution of a generalized Poisson equation

$$-\nabla \cdot [\epsilon(\vec{r})\nabla\phi(\vec{r},t)] = 4\pi\rho(\vec{r},t)\,, \tag{3.5}$$

with the charge density ρ as inhomogeneity.

The generalized Coulomb potential $V_C(\vec{r},\vec{r}\,')$ describing the interaction among charged particles in an inhomogeneous dielectric environment, can be obtained as the solution of the generalized Poisson equation with a δ–function inhomogeneity:

$$-\nabla \cdot [\epsilon(\vec{r})\nabla V_C(\vec{r},\vec{r}\,')] = 4\pi\delta(\vec{r}-\vec{r}\,')\,. \tag{3.6}$$

Using V_C, the solution of Eq. (3.5) can be written as

$$\phi(\vec{r},t) = \int d\vec{r}\,'\; V_C(\vec{r},\vec{r}\,')\rho(\vec{r}\,',t)\,. \tag{3.7}$$

Except for some special geometries, for example two dielectric halfspaces separated by a plane or a single sphere embedded in a material of different dielectric constant [20], Eq. (3.6) has to be solved numerically. For the calculation of V_C, it is advantageous to start from the integral equation:

$$V_C(\vec{r},\vec{r}\,') = -\frac{1}{4\pi}\int d\vec{r}\,''\ \nabla''\frac{1}{|\vec{r}\,''-\vec{r}|}\cdot\vec{E}_l(\vec{r}\,'',\vec{r}\,')\,, \tag{3.8}$$

where $\vec{E}_l(\vec{r},\vec{r}\,') = -\nabla V_C(\vec{r},\vec{r}\,')$ is the electric field at the position $\vec{r}$ due to a unit charge at $\vec{r}\,'$.

If the dielectric function is piecewise constant, as is the typical case in a photonic crystal, one can partially evaluate the volume integral appearing in Eq. (3.8) and use the boundary conditions for the electric field $\vec{E}$ and the dielectric displacement $\vec{D}$ at the interfaces ∂D_{ij}, which separate regions D_i and D_j of different dielectric constants. As shown in Ref. [13], one obtains

$$\begin{aligned}V_C(\vec{r},\vec{r}\,') &= \frac{1}{\epsilon(\vec{r}\,')}\frac{1}{|\vec{r}-\vec{r}\,'|}\\ &\quad-\frac{1}{4\pi}\sum_{ij}\left(\frac{1}{\epsilon_i}-\frac{1}{\epsilon_j}\right)\int_{\partial D_{ij}} da''\ \frac{1}{|\vec{r}\,''-\vec{r}|}\vec{n}_i''\cdot\vec{D}_l(\vec{r}\,'',\vec{r}\,')\\ &= V_0(\vec{r},\vec{r}\,')+\delta V(\vec{r},\vec{r}\,')\,,\end{aligned} \tag{3.9}$$

where $\vec{n}_i''$ denotes the unit vector normal to the surface at $\vec{r}\,''$ pointing out of region D_i into D_j. According to Eq. (3.9), V_C is given by the sum of two contributions. V_0 has the usual $1/|\vec{r}-\vec{r}\,'|$ spatial variation but additionally, the interaction is screened with the local value of the dielectric constant $1/\epsilon(\vec{r}\,')$. The additional term δV originates from induced surface polarizations at the interfaces ∂D_{ij}, which are the surfaces separating the regions of different ϵ over which is integrated. The magnitude of δV may be large for large dielectric contrast, in particular if the charge is close to an interface. In this case. the interaction with induced surface polarizations is strong.

In contrast to the situation in spatially homogeneous media, the generalized Coulomb potential not only depends on the relative coordinate $\vec{r}_{\text{rel}} = \vec{r}-\vec{r}\,'$, but also on the center of mass coordinate $\vec{r}_{\text{COM}} = m\vec{r}+m'\vec{r}\,'$ with $m+m'=1$. This dependence of the generalized Coulomb potential on the center of mass coordinate, obeys the same symmetry properties as the dielectric function. In systems where the dielectric constant is varying periodically in space δV also exhibits this periodicity.

V_C can be calculated numerically using an integral equation for the dielectric displacement $\vec{D}_l$ at the interfaces ∂D_{ij}. This can be obtained by applying $\vec{n}_i(\vec{r})\cdot\nabla$ to Eq. (3.9), where $\vec{n}_i(\vec{r})$ denotes the unit vector normal to the surface at $\vec{r}$. Using

$$D_n(\vec{r},\vec{r}\,') = \vec{n}_i(\vec{r})\cdot\vec{D}_l(\vec{r},\vec{r}\,') \tag{3.10}$$

for the normal component of the dielectric displacement, one obtains

$$\begin{aligned}D_n(\vec{r},\vec{r}\,') &= \vec{n}_i(\vec{r})\cdot\frac{\vec{r}-\vec{r}\,'}{|\vec{r}-\vec{r}\,'|^3}\\ &\quad+\lim_{\gamma\to0_+}\frac{1}{4\pi}\left(1-\frac{\epsilon_1}{\epsilon_2}\right)\int_{\partial D_{ij}} da''\ \vec{n}_i(\vec{r})\cdot\frac{\vec{r}_\gamma-\vec{r}\,''}{|\vec{r}_\gamma-\vec{r}\,''|}D_n(\vec{r}\,'',\vec{r}\,')\,,\end{aligned} \tag{3.11}$$

with $\vec{r}_\gamma = \vec{r} - \gamma \vec{n}_i(\vec{r})$. Solving Eq. (3.11) by matrix inversion on a grid in real–space, one obtains $\vec{D}_l$, which can then be inserted into Eq. (3.9) in order to obtain the generalized Coulomb potential V_C in the regions of interest.

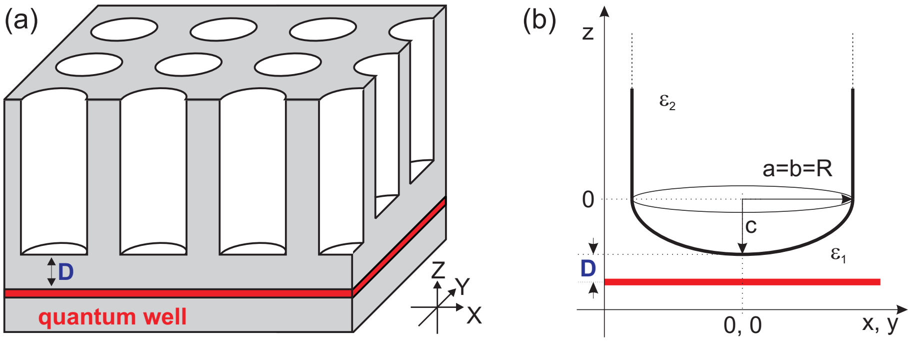

Figure 3.1: (a) Schematic drawing of the considered structure. A thin semiconductor quantum well is separated by a distance D from a two–dimensional photonic crystal, which consists of a periodic arrangement of air cylinders surrounded by a dielectric medium. (b) Detail of the model showing one cylinder with its elliptically shaped bottom. Taken from Ref. [15].

The model for which we exemplify the consequences of the spatially structured Coulomb interaction, consists of a thin GaAs quantum well separated from a two–dimensional photonic crystal by a cap layer. The photonic crystal consists of a periodic array of air cylinders with radius R in a dielectric material. For a sketch of the system see Fig. 3.1(a). Since a realistic structure consisting of etched air holes in a semiconductor medium has no sharp edges, the base of the cylinders which separates regions of different dielectric constants, is modeled to have an elliptical shape. The longer axes $a = b$ of the ellipsoid are matched to the cylinder radius R. The smaller axis c determines the curvature on the side near the quantum well such that the overall shape is characterized by the ratio R/c. D denotes the minimal distance between the air and the quantum well, see Fig. 3.1(b).

In the numerical evaluations of the generalized Coulomb potential displayed in Fig. 3.2, we assume that the quantum well is separated by $D = 0.2\,a_B$ from the two-dimensional photonic crystal, where a_B is the Bohr radius of a three-dimensional exciton. The photonic crystal is made up of air cylinders with radius $R = 10\,a_B$, surrounded by a dielectric medium with $\epsilon = 13.1$. The ratio of the axes characterizing the elliptical shape of the bottom of the cylinders is taken as $R/c = 5$.

The periodicity of the photonic crystal introduces a periodic variation with the center–of–mass coordinate for the additive contribution δV of the generalized Coulomb potential. This spatial variation is illustrated in Fig. 3.2(a)–(d) for different values of the center–of–mass coordinate. δV is largest directly underneath the cylinders, where the distance to the air is lowest and δV decreases when moving away from this position. In Fig. 3.1(c) and (d), one can see differences between the solid and dashed lines showing the anisotropy of the Coulomb potential resulting from the dielectric structuring.

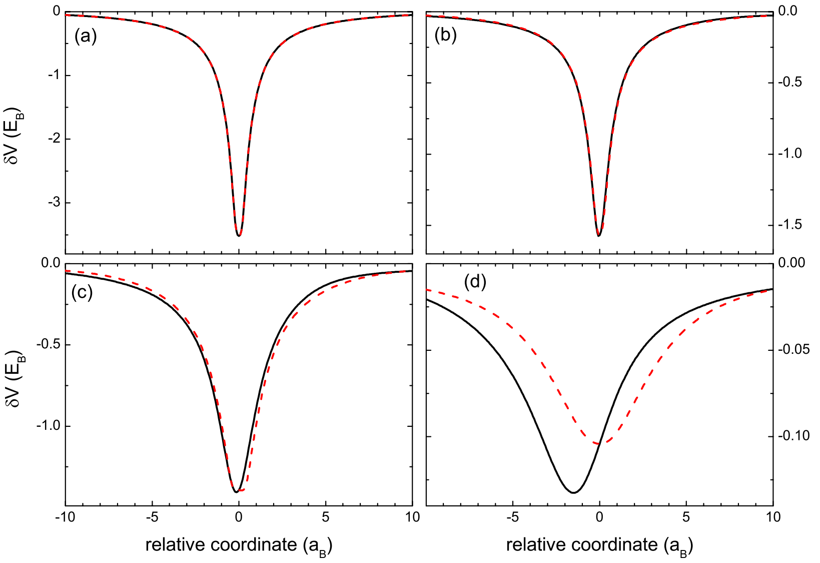

Figure 3.2: (a)–(d) Calculated variations of the Coulomb potential δV induced by the photonic crystal for fixed center-of-mass positions. (a) shows δV for $\vec{r}_{\mathrm{COM}} = 0$, i.e. underneath the center of an air cylinder. (b), (c), and (d) are for $\vec{r}_{\mathrm{COM}} = 0.2\,R\,\vec{e}_x$, $0.5\,R\,\vec{e}_x$, and $1.0\,R\,\vec{e}_x$. The solid black lines show the dependence of δV on the x–component of the relative coordinate for vanishing y–component, whereas the dashed red lines show the same for reversed x and y. E_B is the binding energy of a three–dimensional exciton (for GaAs, E_B is about $4.2\,\mathrm{meV}$ and a_B is about $13\,\mathrm{nm}$). Taken from Ref. [14].

3.2.3 Hamilton operator

The optical properties in semiconductors close to photonic crystals are described by a Hamiltonian consisting of three terms [12, 21]

$$\hat{H} = \hat{H}_{\text{bandstructure}} + \hat{H}_{\text{Coulomb}} + \hat{H}_{\text{light-matter}} \,, \tag{3.12}$$

where $\hat{H}_{\text{bandstructure}}$ contains the single-particle bandstructure, $\hat{H}_{\text{Coulomb}}$ describes the many-body Coulomb interaction among charged particles including modifications due to the dielectric structuring as introduced above, and $\hat{H}_{\text{light-matter}}$ denotes the interaction of the material with a classical electromagnetic field.

In what follows, we work in 2nd quantization using creation and annihilation operators. $\hat{c}_i^+$ ($\hat{c}_i$) creates (destroys) an electron in the conduction band at position $\vec{r}_i$, and $\hat{d}_i^+$ ($\hat{d}_i$) are the corresponding operators for holes in the valence band. For simplicity, we restrict the present treatment to a two–band situation considering only a single conduction and a single valence band, and thus describe the bandstructure part via

$$\hat{H}_{\text{bandstructure}} = \int d\vec{r}_1 \left[\hat{c}_1^+ \left(E_{\text{gap}} - \frac{\hbar^2 \nabla_1^2}{2m_e} \right) \hat{c}_1 + \hat{d}_1^+ \left(-\frac{\hbar^2 \nabla_1^2}{2m_h} \right) \hat{d}_1 \right] , \tag{3.13}$$

where E_{gap} is the band–gap energy, and m_e and m_h are the effective masses of the electrons and holes, respectively.

The Coulomb interaction contains the generalized potential $V^C(\vec{r}_1, \vec{r}_2) \equiv V_{12}^C = V_{12}^0 + \delta V_{12}$ and reads

$$\begin{aligned} \hat{H}_{\text{Coulomb}} = & \frac{1}{2} \int d\vec{r}_1 \int d\vec{r}_2 \; V_{12}^C (\hat{c}_1^+ \hat{c}_2^+ \hat{c}_2 \hat{c}_1 + \hat{d}_1^+ \hat{d}_2^+ \hat{d}_2 \hat{d}_1 - 2 \hat{c}_1^+ \hat{d}_2^+ \hat{d}_2 \hat{c}_1) \\ & + \frac{1}{2} \int d\vec{r}_1 \; \delta V_{11} (\hat{c}_1^+ \hat{c}_1 + \hat{d}_1^+ \hat{d}_1) . \end{aligned} \tag{3.14}$$

Here, the first line represents the repulsive interaction among two electrons and two holes, respectively, as well as the attractive interaction among an electron and a hole. The second line of Eq. (3.14) describes the self–interaction of the electron and hole with their respective image charges. Even though the self–interaction due to the bulk part of the Coulomb interaction is unphysical and has to be removed, the presence of a structured dielectric environment leads to interactions of the charges with their self–induced surface polarizations [22–24]. The self energy δV_{11} acts as a spatially varying single–particle potential for the electrons and holes. For a photonic crystal close to a semiconductor, one could add the single–particle potential δV_{11} to $\hat{H}_{\text{bandstructure}}$ and solve the resulting single–particle Hamiltonian by calculating Bloch–type electronic eigenfunctions, using the spatial periodicity corresponding to the period of the photonic crystal, see below.

The light–matter interaction Hamiltonian in the dipole approximation can be written as

$$\hat{H}_{\text{light-matter}} = - \int d\vec{r}_1 \; E_1(t) \cdot \mu (\hat{d}_1 \hat{c}_1 + \hat{c}_1^+ \hat{d}_1^+) . \tag{3.15}$$

Here, $E_1(t) \equiv E(\vec{r}_1, t)$ is the spatially varying electric field, μ is the interband dipole matrix element which is taken to be a real material constant, and $\hat{d}_1 \hat{c}_1$ ($\hat{c}_1^+ \hat{d}_1^+$) describes the local interband coherence which corresponds to destroying (creating) an electron-hole pair at $\vec{r}_1$. If the electric field is constant in space, Eq. (3.15) reduces to

$$\hat{H}_{\text{light-matter}} = -E(t) \cdot \int d\vec{r}_1 \; \mu \, (\hat{d}_1 \hat{c}_1 + \hat{c}_1^+ \hat{d}_1^+) = -E(t) \cdot \hat{P} . \tag{3.16}$$

The expectation value $P = \langle \hat{P} \rangle = \int d\vec{r}_1 \; \mu (\langle \hat{d}_1 \hat{c}_1 \rangle + \langle \hat{c}_1^+ \hat{d}_1^+ \rangle)$ is the total optical polarization of the system.

3.2.4 Equations of motion

We describe the dynamical properties of the photoexcited system using Heisenberg equations for the relevant material quantities. The equation of motion for the expectation value of an arbitrary two–particle operator $X_{12} = \langle \hat{X}_{12} \rangle$ is obtained from

$$i\hbar \frac{\partial}{\partial t} X_{12}(t) = \langle [\hat{X}_{12}, \hat{H}] \rangle . \tag{3.17}$$

As an example, we discuss the dynamics of the off–diagonal interband coherence $p_{12} = \langle \hat{p}_{12} \rangle = \langle \hat{d}_1 \hat{c}_2 \rangle$.

Since $\hat{H}$ is given by the sum of three contributions, we can evaluate the commutators appearing in Eq. (3.17) separately for $\hat{H}_{\text{bandstructure}}$, $\hat{H}_{\text{Coulomb}}$ and $\hat{H}_{\text{light-matter}}$, and then simply add the results. First we show how the many–body interaction is treated by considering $\hat{H}_{\text{Coulomb}}$ in the commutator and obtain

$$
\begin{aligned}
i\hbar \frac{\partial}{\partial t} p_{12}|_{\text{Coulomb}} &= \langle [\hat{p}_{12}, \hat{H}_{\text{Coulomb}}] \rangle \\
&= \int d\vec{r}_3 \, (V^C_{32} - V^C_{13})(\langle c^+_3 d_1 c_2 c_3 \rangle + \langle d^+_3 d_1 d_3 c_2 \rangle) \\
&\quad + \left(\frac{1}{2} \delta V_{11} + \frac{1}{2} \delta V_{22} - V^C_{12} \right) p_{12} \, . \qquad (3.18)
\end{aligned}
$$

As a consequence of the many–body Coulomb interactions, we find on the right hand side of Eq. (3.18), a coupling to four–operator expectation values. This is the beginning of the usual infinite hierarchy problem of many–body physics, see for example [12, 21]. A closed set of equations, which allows us to describe the spatially inhomogeneous system numerically within reasonable limits, is obtained by using the time–dependent Hartree–Fock factorization which approximates the four–operator expectation values by products of two–operator expectation values [12, 21]. For the four–operator terms contained in Eq. (3.18), this means that we use the approximation

$$
\begin{aligned}
\langle c^+_3 d_1 c_2 c_3 \rangle &\simeq \langle c^+_3 c_3 \rangle \langle d_1 c_2 \rangle - \langle c^+_3 c_2 \rangle \langle d_1 c_3 \rangle = n^e_{33} p_{12} - n^e_{32} p_{13} \, , \\
\langle d^+_3 d_1 d_3 c_2 \rangle &\simeq \langle d^+_3 d_1 \rangle \langle d_3 c_2 \rangle - \langle d^+_3 d_3 \rangle \langle d_1 c_2 \rangle = n^h_{31} p_{32} - n^h_{33} p_{12} \, , \qquad (3.19)
\end{aligned}
$$

where we have introduced the electron (hole) populations and coherences as $n^e_{12} = \langle \hat{c}^+_1 c_2 \rangle$ ($n^h_{12} = \langle \hat{d}^+_1 d_2 \rangle$).

Using similar factorizations in the equations of motion for n^e and n^h, and also evaluating the remaining commutators with $\hat{H}_{\text{bandstructure}}$ and $\hat{H}_{\text{light-matter}}$, we obtain a closed set of coupled equations of motion for the expectation values of two–operator quantities. These equations are known as the semiconductor Bloch equations (SBE) in time–dependent Hartree–Fock approximation [12]. For our inhomogeneous system, the explicit form of the SBE is

$$
\begin{aligned}
i\hbar \frac{\partial}{\partial t} p_{12} = \Bigg[& E_{\text{gap}} - \frac{\hbar^2}{2m_h} \nabla^2_1 - \frac{\hbar^2}{2m_e} \nabla^2_2 + \frac{1}{2} \delta V_{11} + \frac{1}{2} \delta V_{22} - V^C_{12} \\
& - \int d\vec{r}_3 \, (V^C_{13} - V^C_{32})(n^e_{33} - n^h_{33}) \Bigg] p_{12} \\
& + \int d\vec{r}_3 \, (V^C_{13} - V^C_{32})(n^e_{32} p_{13} - n^h_{31} p_{32}) \\
& - \mu \cdot (E_1 \delta_{12} - E_1 n^e_{12} - E_2 n^h_{21}) \; + i\hbar \frac{\partial}{\partial t} p_{12} \Big|_{\text{corr}} \, , \qquad (3.20)
\end{aligned}
$$

$$\begin{aligned}
i\hbar\frac{\partial}{\partial t}n^e_{12} = & \Bigg[\frac{\hbar^2}{2m_e}(\nabla_1^2-\nabla_2^2)-\frac{1}{2}\delta V_{11}+\frac{1}{2}\delta V_{22} \\
& -\int d\vec{r}_3\,(V^C_{13}-V^C_{32})(n^e_{33}-n^h_{33})\Bigg]\,n^e_{12} \\
& +\int d\vec{r}_3\,(V^C_{13}-V^C_{32})(n^e_{13}n^e_{32}+p^*_{31}p_{32}) \\
& +\mu\cdot(E_1p_{12}-E_2p^*_{21})\;+i\hbar\frac{\partial}{\partial t}n^e_{12}\big|_{\text{corr}}\,, \qquad (3.21)\\
i\hbar\frac{\partial}{\partial t}n^h_{12} = & \Bigg[\frac{\hbar^2}{2m_h}(\nabla_1^2-\nabla_2^2)-\frac{1}{2}\delta V_{11}+\frac{1}{2}\delta V_{22} \\
& +\int d\vec{r}_3\,(V^C_{13}-V^C_{32})(n^e_{33}-n^h_{33})\Bigg]\,n^h_{12} \\
& +\int d\vec{r}_3\,(V^C_{13}-V^C_{32})(n^h_{13}n^h_{32}+p^*_{13}p_{23}) \\
& +\mu\cdot(E_1p_{21}-E_2p^*_{12})\;+i\hbar\frac{\partial}{\partial t}n^h_{12}\big|_{\text{corr}}\,, \qquad (3.22)
\end{aligned}$$

where in Eq. (3.20) δ_{12} is a shorthand notation for the delta function $\delta(\vec{r}_1-\vec{r}_2)$ and the terms denoted by $|_{\text{corr}}$ represent all those correlations that are beyond the time–dependent Hartree–Fock limit, see Refs. [12, 21]. In the analysis presented in this chapter and in the numerical calculations, the correlations are either neglected altogether or they are treated at a phenomenological level.

In Eqs. (3.20)-(3.22) the single particle self–energies δV appear as potentials in the homogeneous part of the equations of motion, which in the equation of motion for the electron-hole interband coherence p_{12} is also influenced by the electron-hole Coulomb attraction $-V^C_{12}$. Additionally, integrals over the generalized Coulomb potential V^C and products of p's and n's appear in Eqs. (3.20)–(3.22), and all equations of motion contain inhomogeneities which represent the driving with the electric field.

3.3 Numerical results

3.3.1 Linear exciton absorption

The linear optical properties of unexcited semiconductors can be computed from the equation of motion for the electron–hole interband coherence p, Eq. (3.20). In a semiconductor, the ground state implies full valence and empty conduction bands. This means that the electron and hole populations vanish, that is $n^e = n^h = 0$ [12]. In this case, Eq. (3.20) reduces to

$$\begin{aligned}
i\hbar\frac{\partial}{\partial t}p^{(1)}_{12} = & \left(E_{\text{gap}}-\frac{1}{2m_e}\nabla_e^2-\frac{1}{2m_h}\nabla_h^2+\frac{1}{2}(\delta V_{11}+\delta V_{22})-V^C_{12}\right)p^{(1)}_{12} \\
& -\mu\cdot E_1\delta_{12}\,,
\end{aligned} \qquad (3.23)$$

where the superscript (1) indicates that the optical polarization is calculated linearly, that is to first order in the light field.

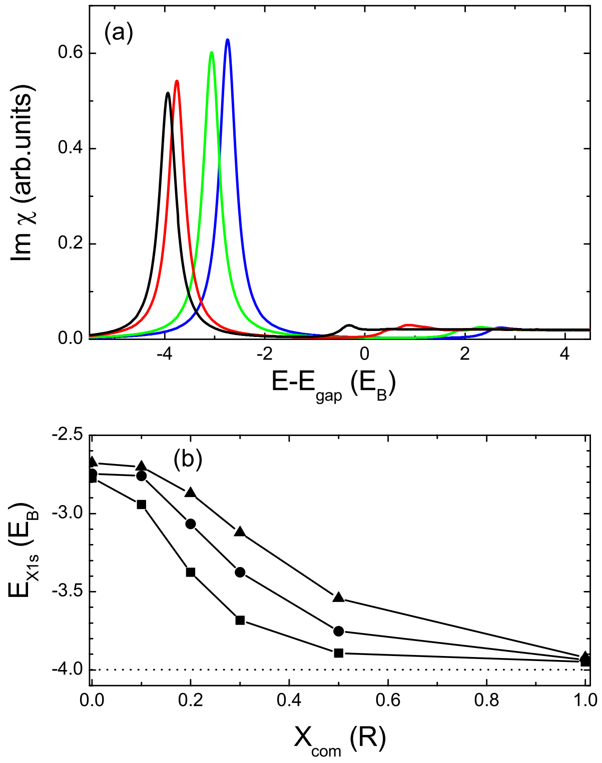

Figure 3.3: (a) Calculated excitonic linear absorption spectra for the same center–of–mass positions as considered in Fig. 3.1(b)–(e); $\vec{r}_{\mathrm{COM}} = 0$ (blue), $0.2\,R\,\vec{e}_x$ (green), $0.5\,R\,\vec{e}_x$ (red), and $1.0\,R\,\vec{e}_x$ (black). The zero of the energy scale coincides with the band gap energy of the isolated quantum well. The width of the resonances is due to a phenomenological dephasing time. (b) Dependence of the energetic position of the lowest exciton on the center–of–mass position for different ratios of the axes characterizing the elliptical shape of the bottom of the cylinders using $R/c = 10$ (triangles), 5 (circles), and 2 (squares). The symbols depict the calculated values and the lines are guides to the eye. Taken from Ref. [14].

The dependence of V_C on the center–of–mass position leads to local changes of the excitonic absorption spectra. We have solved Eq. (3.23) for the relative motion between electron and hole using fixed positions of the center of mass coordinate to highlight these spatial variations. The linear absorption is proportional to the imaginary part of the linear susceptibility, which is given by the frequency–dependent polarization divided by the incident field. Examples of the calculated spatially resolved excitonic absorption spectra are displayed in Fig. 3.3a. Underneath the dielectric medium or directly below the boundary between the dielectric and air, the excitonic spectra are essentially identical to the homogeneous case without photonic

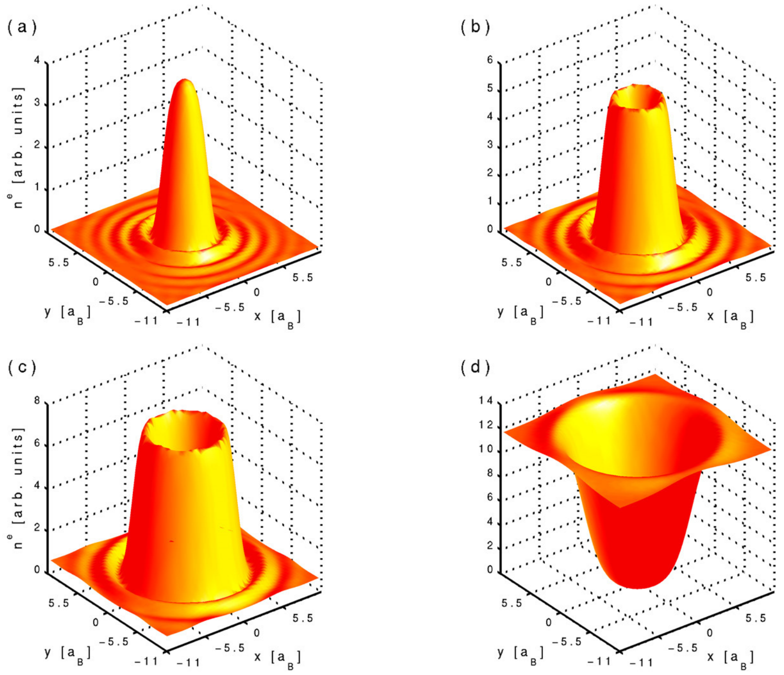

Figure 3.4: Normalized space–dependent coherent electron populations $n^e(\vec{r})$ immediately after resonant excitation with a long spatially homogeneous laser pulse. (a) exciting the highest energy exciton at $E = E_{\rm gap} - 2.6\,E_B$, (b) exciting at $E = E_{\rm gap} - 3.0\,E_B$, (c) exciting at $E = E_{\rm gap} - 3.4\,E_B$, and (d) exciting the lowest energy exciton at $E = E_{\rm gap} - 4.0\,E_B$.

crystal. Here, the two dimensional exciton has a binding energy of $4\,E_B$ and the continuum absorption starts at the band gap energy $E = E_{\rm gap}$, see black line in Fig. 3.3a. If one moves along with the excitation towards positions underneath the air cylinders, the onset of the band gap and the exciton absorption move towards higher energies. For excitation directly underneath the center of an air cylinder, the blue line in Fig. 3.3a, the continuum absorption is shifted towards higher energies ($E \approx E_{\rm gap} + 3\,E_B$), as a consequence of the single–particle self energies. In this case, the exciton resonance also appears at higher energies ($E \approx E_{\rm gap} - 2.8\,E_B$), however, its binding energy, that is its energetic distance from the continuum absorption, is increased to about $5.8\,E_B$. This increase in binding energy is also responsible for the higher absorption strength of the exciton. As shown in Fig. 3.3b, the spatial variation of the exciton energy depends on the curvature of the elliptically shaped bottom of the air cylinders.

These results verify that the excitonic absorption of a quantum well can be modified locally by the spatially varying dielectric environment. Global position–independent changes of the excitonic absorption properties already occur in semiconductor structures that are close to air, or to a material of different dielectric constant, see for example [20, 22–24]. Unlike a simple, planar semiconductor–dielectric medium interface however, a photonic crystal additionally modifies the photonic density of states. Hence, the optical semiconductor properties and the eigenmodes of the electromagnetic field can be altered simultaneously. This combined effect modifies the overall optical properties of the heterostructure.

3.3.2 Coherently excited inhomogeneous populations

As a first step beyond linear optics, one can combine Eq. (3.23) for the linear polarization with the equations for the carrier populations and coherences up to second order in the light field:

$$\begin{aligned} i\hbar\frac{\partial}{\partial t} n^{e\,(2)}_{12} &= \left[\frac{\hbar^2}{2m_e}(\nabla_1^2 - \nabla_2^2) - \frac{1}{2}\delta V_{11} + \frac{1}{2}\delta V_{22}\right] n^{e\,(2)}_{12} \\ &\quad + \int d\vec{r}_3\,(V^C_{13} - V^C_{32})(p^{(1)}_{31})^* p^{(1)}_{32} \; + \mu\cdot(E_1 p^{(1)}_{12} - E_2 (p^{(1)}_{21})^*)\,, \end{aligned} \tag{3.24}$$

$$\begin{aligned} i\hbar\frac{\partial}{\partial t} n^{h\,(2)}_{12} &= \left[\frac{\hbar^2}{2m_h}(\nabla_1^2 - \nabla_2^2) - \frac{1}{2}\delta V_{11} + \frac{1}{2}\delta V_{22}\right] n^{h\,(2)}_{12} \\ &\quad + \int d\vec{r}_3\,(V^C_{13} - V^C_{32})(p^{(1)}_{13})^* p^{(1)}_{23} \; + \mu\cdot(E_1 p^{(1)}_{21} - E_2 (p^{(1)}_{12})^*)\,. \end{aligned} \tag{3.25}$$

Working in this $\chi^{(2)}$–limit, neglecting dephasing and all other incoherent processes, it is actually not necessary to solve the combined set of Eqs. (3.23)–(3.25). Using the equations of motion, one can verify that in this limit, the carrier populations and coherences are determined by the interband coherence via the sum rules

$$n^{e\,(2)}_{12} = \int d\vec{r}_3\; (p^{(1)}_{31})^*\, p^{(1)}_{32} \;\;, \tag{3.26}$$

$$n^{h\,(2)}_{12} = \int d\vec{r}_3\; (p^{(1)}_{13})^*\, p^{(1)}_{23} \;\;. \tag{3.27}$$

The coherent spatially–resolved electron populations $n^{e\,(2)}_{11}$ are thus obtained using a numerical solution of Eq. (3.23) and then evaluating Eq. (3.26). Considering long excitation pulses with a narrow spectrum but without spatial variation, we obtain the results shown in Fig. 3.4. The computed populations strongly depend on the chosen frequency of the spatially homogeneous excitation pulse. If one excites the energetically lowest exciton at $E = E_{\text{gap}} - 4\,E_B$, see Fig. 3.4d, the population is mostly concentrated in the area outside the air cylinder which we take as centered around $(0, 0)$. If, on the other hand, the pulse is tuned to the highest exciton resonance $E = E_{\text{gap}} - 2.6\,E_B$, see Fig. 3.4a, the induced population is concentrated directly underneath the cylinder. For excitation in between these two extreme cases, at $E = E_{\text{gap}} - 3.0\,E_B$ and $E = E_{\text{gap}} - 3.4\,E_B$ as in Figs. 3.4b and c, respectively, we obtain a ring–like shape for the optically generated electron population. Since the length scale which characterizes the spatial variation of the electron populations is bigger than the exciton Bohr radius, the coherent electron and hole populations look very similar. These results demonstrate that one can use the spatial inhomogeneity induced by the dielectrically structured environment to optically create special, periodically varying inhomogeneous carrier populations.

For longer times we compute carrier redistribution originating from wave packet dynamics. Eventually, this coherent dynamics will be destroyed by incoherent scattering processes.

An analysis of the carrier populations in the other extreme, that is in the incoherent limit which describes the situation after scattering processes drive the populations into a thermal quasi-equilibrium, is presented in the following.

3.3.3 Quasi-equilibrium inhomogeneous populations and nonlinear absorption

We evaluate the quasi–equilibrium absorption spectra, that is the absorption in the presence of incoherent thermalized electron and hole populations [12]. The required quasi–equilibrium electron and hole populations are computed by diagonalizing the single–particle Hamiltonian defined by

$$\begin{aligned}\hat{H}_{\text{single-particle}} &= \hat{H}_{\text{bandstructure}} + \hat{H}_{\text{Coulomb self-energies}} \\ &= \int d\vec{r}_1 \left[\hat{c}_1^+ \left(E_{\text{gap}} - \frac{\hbar^2 \nabla_1^2}{2m_e} \right) \hat{c}_1 + \hat{d}_1^+ \left(- \frac{\hbar^2 \nabla_1^2}{2m_h} \right) \hat{d}_1 \right] \\ &\quad + \frac{1}{2} \int d\vec{r}_1 \; \delta V_{11} (\hat{c}_1^+ \hat{c}_1 + \hat{d}_1^+ \hat{d}_1) \, . \end{aligned} \tag{3.28}$$

Besides the kinetic energies, the spatially varying self–energies which act as inhomogeneous potential are also included in Eq. (3.28). By diagonalizing this Hamiltonian separately for electrons and holes using the spatial periodicity induced by the photonic crystal, we obtain the dispersions $\epsilon_{\vec{k}}^{\nu}$, where ν labels the minibands, and the corresponding Bloch–type eigenfunctions $\Psi_{\vec{k}}^{\nu}(\vec{r})$. Since the spatial period is relatively large, we have to include sufficiently many (about 100) of the energetically rather narrow minibands in our calculations. In this single-particle basis, we populate the states by quasi–equilibrium electron and hole populations. The total density n can then be expressed as

$$n = \sum_{\vec{k},\nu} n_{\vec{k}}^{\nu} = \sum_{\vec{k},\nu} F(\epsilon_{\vec{k}}^{\nu}, T, \mu) \, , \tag{3.29}$$

where $n_{\vec{k}}^{\nu}$ denotes the population of state $\vec{k}, \nu$ with energy $\epsilon_{\vec{k}}^{\nu}$. In quasi–equilibrium, $n_{\vec{k}}^{\nu}$ is given by the Fermi function F which depends on temperature T and the chemical potential μ. Since the total density n depends on the chemical potential, μ needs to be determined self-consistently. Having obtained $n_{\vec{k}}^{\nu}$, we then transform back to real space and obtain $n_{12}^{e,\,eq}$ and $n_{12}^{h,\,eq}$. This is convenient, since it is numerically much easier to perform the subsequent evaluations in real space. In order to keep the time and memory requirements of the numerical solutions within reasonable limits, we replace in all following calculations, the quantum well by a one-dimensional quantum wire.

The spatial variation of the self energy along with the quasi-equilibrium electron and hole populations are shown in Fig. 3.5. Since the self energy δV is large underneath the center of the air cylinders and the thermal energy $kT \approx 1.7\,\text{meV} = 0.4\,E_B$ is smaller than the spatial variation of δV, the carriers avoid the regions below the cylinders and accumulate predominantly in the spatial regions between them.

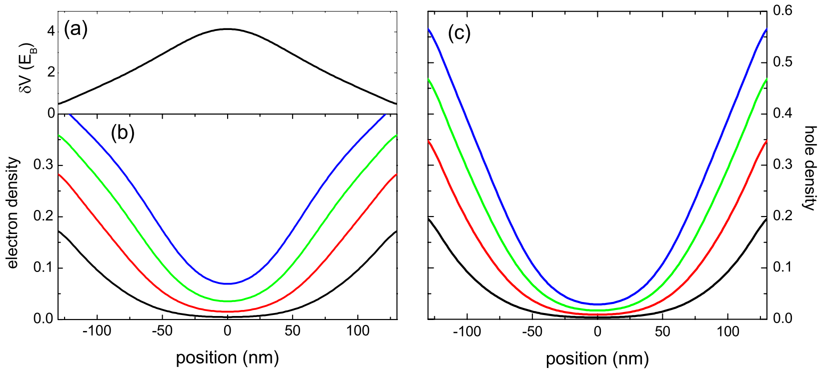

Figure 3.5: (a) The spatially varying self-energy δV in a quantum wire which extends in the x-direction and is located at $y = 0$. (b) and (c): Spatially–resolved quasi–equilibrium electron $n_{11}^{e,\,eq}$ and hole $n_{11}^{h,\,eq}$ populations at $T = 20\,\mathrm{K}$, respectively. The total densities n are $0.27\,n_0$ (black), $0.53\,n_0$ (red), $0.80\,n_0$ (green), and $1.06\,n_0$ (blue), where n_0 is the transparency density, i.e., the crossover from absorption to gain, in Fig. 3.6(b).

The quasi–equilibrium nonlinear absorption is obtained by solving the equation for p linear in the light field in the presence of quasi–equilibrium populations $n^{e,\,eq}$ and $n^{h,\,eq}$:

$$
\begin{aligned}
i\hbar\frac{\partial}{\partial t}p_{12} = {} & \Bigg[E_{\text{gap}} - \frac{\hbar^2}{2m_h}\nabla_1^2 - \frac{\hbar^2}{2m_e}\nabla_2^2 + \frac{1}{2}\delta V_{11} + \frac{1}{2}\delta V_{22} - V_{12}^C \\
& - \int d\vec{r}_3\,(V_{13}^C - V_{32}^C)(n_{33}^{e,\,eq} - n_{33}^{h,\,eq})\Bigg]\,p_{12} \\
& + \int d\vec{r}_3\,(V_{13}^C - V_{32}^C)(n_{32}^{e,\,eq}p_{13} - n_{31}^{h,\,eq}p_{32}) \\
& - \mu\cdot(E_1\delta_{12} - E_1 n_{12}^{e,\,eq} - E_2 n_{21}^{h,\,eq})\,. \qquad (3.30)
\end{aligned}
$$

The resulting density–dependent absorption spectra are displayed in Fig. 3.6. Comparing the density–dependent spatially–averaged absorption spectra of an isolated wire, Fig. 3.6a, with the one obtained for a wire close to a photonic crystal, Fig. 3.6b, we can identify distinct changes in the lineshapes which are a consequence of the spatial structuring, induced by the dielectric environment. Although in both cases the main features are a decrease (bleaching) and blue–shift of the absorption with increasing density, for example, the lineshape of the gain (negative absorption) is much narrower in Fig. 3.6b than in Fig. 3.6a, and the gain threshold is slightly reduced.

In the spatially–resolved absorption profiles, see Fig. 3.6c and d, one finds very dramatic differences which are due to the spatially inhomogeneous carrier populations, Fig. 3.5b and c. For total carrier densities which are smaller than the onset of gain in the spatially integrated spectra, the spectra are only very weakly influenced by the small carrier populations if one

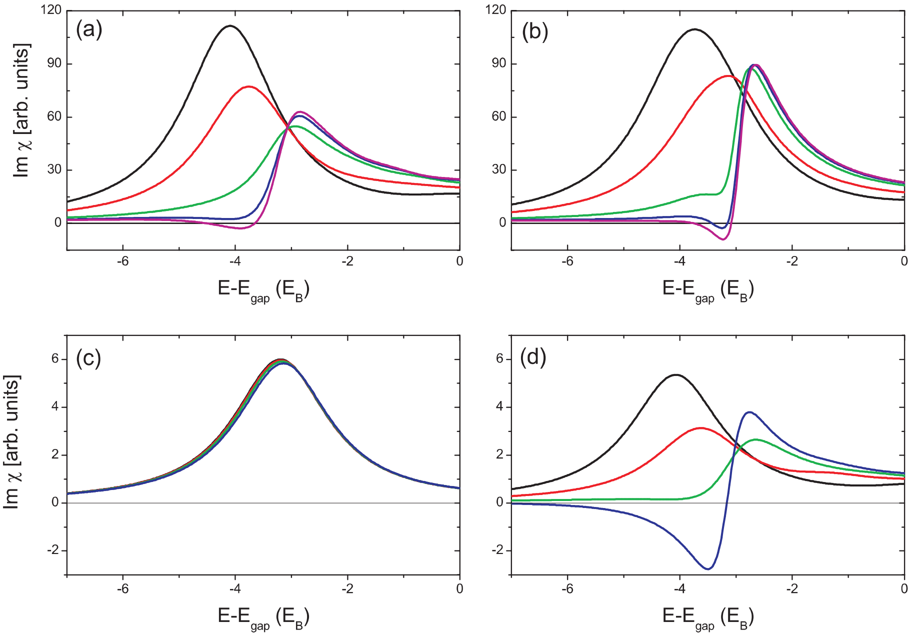

Figure 3.6: (a) and (b) quasi–equilibrium absorption spectra for a quantum wire at $T = 20\,\mathrm{K}$. In (a) a homogeneous wire has been considered, i.e. the variation of the Coulomb interaction δV has been set to zero, whereas in (b) δV has been considered. The total densities n are 0 (black), $0.44\,n_0$ (red), $0.88\,n_0$ (green), $1.02\,n_0$ (blue), and $1.08\,n_0$ (magenta), where n_0 is the density of the transparency point in (b). (c) and (d) spatially resolved quasi–equilibrium absorption spectra including δV for different total densities n as indicated in the inset of (c). In (c) the position directly underneath the air cylinder has been used, whereas in (d) the position in between the air cylinder has been considered. The total densities n in (c) and (d) are 0 (black), $0.18\,n_0$ (red), $0.35\,n_0$ (green), and $0.53\,n_0$ (blue).

looks underneath the cylinders, see Fig. 3.6c. For the same total carrier densities, however, the spectra at the positions in between the cylinders, are dramatically changed due to the large local populations in this region, see Fig. 3.6d. At this position, one has locally reached gain for carrier densities much smaller than the ones needed to obtain gain in the spatially averaged spectra [25].

These spatially inhomogeneous populations can be expected to influence the operation characteristics of laser structures. The spatially periodic modulation of the optical properties and carrier populations may even result in a superradiant increase [26] of the spontaneous emission, which will be analyzed in future work.

3.3.4 Coherent wave packet dynamics versus dephasing and thermalization

Exciting a semiconductor with a short optical laser pulse produces a coherent optical polarization in the material. With increasing time, this polarization decays due to a variety of dephasing processes. Depending on the physical mechanisms, typical dephasing times are in the ps or even sub–ps range. Radiative decay due to the finite lifetime of the excited states always contributes to the decay of the optical polarization. However, in semiconductors the dephasing is typically dominated by the interaction with phonons, by the many–body Coulomb interaction, or sometimes by disorder [27]. Concomitantly to the dephasing of the polarization, the photoexcited coherent, virtual carrier distributions change their nature and gradually become incoherent, real populations. Due to the interaction with phonons and the Coulombic scattering among the carriers, with increasing time these populations approach a thermal quasi-equilibrium distribution.

For the spatially inhomogeneous system of a semiconductor close to a photonic crystal, it is a rather substantial task to model all the discussed processes microscopically. Therefore, in order to gain some insights, we use here a simplified phenomenological approach to qualitatively model the influence of dephasing and thermalization. This is done by introducing two time constants T_2 and T_1 into Eqs. (3.20)–(3.22). The dephasing of the polarization is modeled by adding

$$-i\hbar \frac{p_{12}}{T_2}\,, \tag{3.31}$$

to the right hand side of Eq. (3.20). As a result, over the course of time, the interband polarization decays exponentially proportional to $\exp(-t/T_2)$.

Similarly, to model the thermalization of the populations, we add the terms

$$-i\hbar \frac{n_{12}^{e} - n_{12}^{e,\,eq}}{T_1}\,, \quad \text{and} \tag{3.32}$$

$$-i\hbar \frac{n_{12}^{h} - n_{12}^{h,\,eq}}{T_1}\,, \tag{3.33}$$

to the right hand sides of Eqs. (3.21) and (3.22), respectively. Thus, with increasing time, the carrier populations approach a quasi-equilibrium distribution exponentially with a time constant T_1.

The equilibrium real–space populations and coherences appearing in Eqs. (3.32) and (3.33) are obtained by transforming the Fermi–Dirac distributions back from the Bloch basis, i.e., the single–particle eigenstates, to real space. $n_{12}^{e,\,eq}$ and $n_{12}^{e,\,eq}$ thus depend on the total carrier density n and on the temperature T. In the time–dependent calculations, the carrier density is changing during the laser–pulse excitation. Therefore we use the numerically calculated time dependence of the density $n(t)$ to determine the equilibrium $n_{12}^{e,\,eq}(t)$ and $n_{12}^{e,\,eq}(t)$ real-space populations and coherences.

Fig. 3.7 shows the temporal evolution of the electron populations $n_{11}^{e}(t) \equiv n^{e}(r_1, t)$ in the coherent regime, where dephasing and thermalization are neglected by setting the time constants T_2 and T_1 to infinity. These results have been obtained by solving Eqs. (3.20)-(3.22) numerically. When exciting the lowest exciton resonance, the population is initially

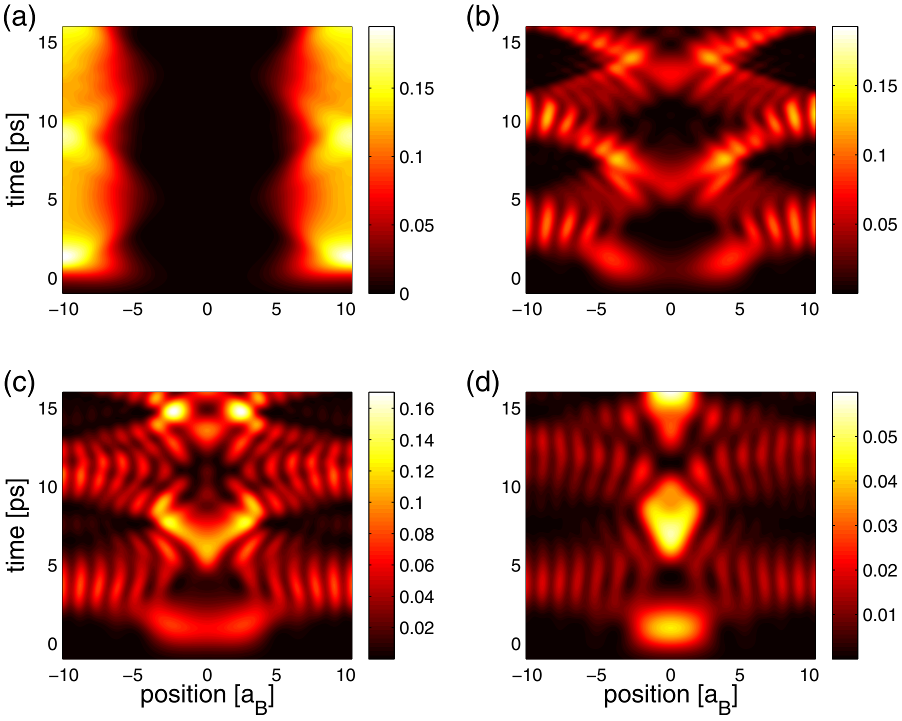

Figure 3.7: Contour plot showing the coherent temporal evolution of the electron populations $n^e_{11}(t)$ after coherent excitation with a long pulse neglecting dephasing and thermalization. (a) exciting the energetically lowest exciton with a laser frequency $\hbar\omega_L = E_{\text{gap}} - 4.0E_B$, (b) using $\hbar\omega_L = E_{\text{gap}} - 3.4E_B$, (c) using $\hbar\omega_L = E_{\text{gap}} - 3.2E_B$, and (d) exciting the close to the energetically highest exciton using $\hbar\omega_L = E_{\text{gap}} - 3.0E_B$ (for GaAs, a_B is about 13 nm and $h/E_B \approx 1$ ps, where h is Planck's constant). White corresponds to the maximum density for each case, see the respective color scales for each plot.

large in between the air cylinders and small directly underneath the cylinders, see Fig. 3.7a. As a function of time, the populations show an oscillatory behavior in space due to a kind of breathing motion of the wave packet. When exciting with higher energies, the population is initially created somewhere underneath the air cylinders, see Fig. 3.7b–d. In these cases, the wave packet dynamics is much richer, since the higher energy allows the electrons to move periodically through the entire structure. For example, in Fig. 3.7d the electrons are initially created directly underneath the center of the air cylinders. Over the course of time, they first move towards the regions in between the cylinders, then in the opposite direction, and after about 7 ps they accumulate at the position where they were created optically and this cycle repeats itself.

The transient transition from the coherent to the incoherent regime is investigated by solving Eqs. (3.20)–(3.22), supplemented by the terms of Eqs. (3.31)–(3.33), numerically [25].

As a result, we obtain the time–dependent electron populations shown in Fig. 3.8. When exciting with a long pulse energetically around the lowest exciton resonance, the photoexcited population is initially large in between the air cylinders and small directly underneath the cylinders, see Fig. 3.8a for short times. With increasing time, the populations approach an equilibrium distribution, which is also characterized by larger densities in between the air cylinders than directly underneath the cylinders, see Fig. 3.5. This is a direct consequence of the self-energies which increase the potential energy underneath the cylinders, as has been shown in the previous section.

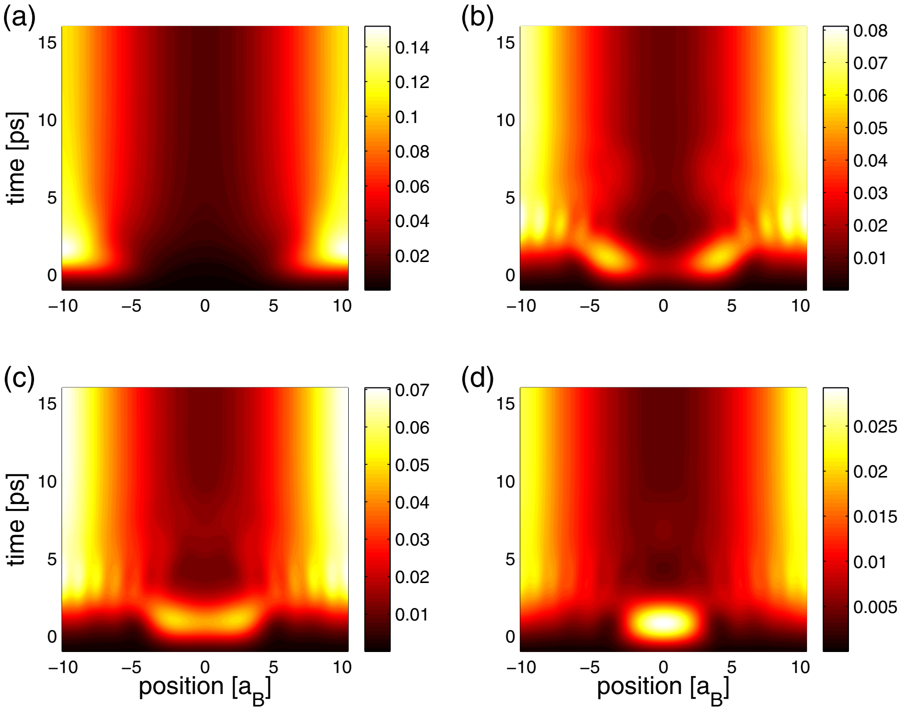

Figure 3.8: Contour plot showing the temporal evolution of the electron populations $n^e_{11}(t)$ after coherent excitation with a long pulse, including dephasing and thermalization described by time constants $T_2 = 4\,\text{ps}$ and $T_1 = 2\,\text{ps}$ and a temperature of $T = 50\,\text{K}$. (a) exciting the energetically lowest exciton with a laser frequency $\hbar\omega_L = E_{\text{gap}} - 4.0E_B$, (b) using $\hbar\omega_L = E_{\text{gap}} - 3.4E_B$, (c) using $\hbar\omega_L = E_{\text{gap}} - 3.2E_B$, and (d) exciting the close to the energetically highest exciton using $\hbar\omega_L = E_{\text{gap}} - 3.0E_B$. White corresponds to the maximum density for each case, see the respective color scales for each plot.

Immediately following the excitation, there is a time window in which one sees weakly some distorted coherent wave packet dynamics, before the incoherent limit of the quasi–equilibrium distribution is obtained. This dynamics is seen more clearly if one excites at higher energies, see Fig. 3.8b–d, where the photoexcited population is initially created somewhere underneath the air cylinders. If dephasing and thermalization are neglected, this coherent dynamics would continue indefinitely, as shown in Fig. 3.7. With finite relaxation times, however, it evolves continuously into the build-up of incoherent population distributions, which are approached in Fig. 3.8 for long times. Thus irregardless of the excitation frequency, for the structure considered here, the thermalization eventually leads to an accumulation of the carriers at the positions of low potential energy in between the cylinders [25].

3.4 Summary and outlook

The few examples discussed in this chapter have been chosen to demonstrate the significance of the locally varying Coulomb interaction potential in a semiconductor quantum well that is coupled to a photonic crystal structure. The resulting effects may offer novel ways of designing aspects of the light–matter coupling and the many–body interactions inside the semiconductor material.

The computed absorption spectra show that the modified Coulomb potential induces characteristic spatial modulations of the optical semiconductor excitations with the periodicity of the photonic crystal. This spatial structuring can be utilized to create modulated polarizations and distributions which depend on the frequency of a spectrally narrow and spatially homogeneous exciting laser pulse. In the incoherent regime, the spatial arrangement of the electron–hole–pair distributions in the material, will be characterized by accumulations in regions where the carrier pairs have the lowest energy. These spatially modulated arrangements influence the optical and electronic properties in the incoherent regime and could be utilized for improvements of optoelectronic structures, such as laser devices.

We expect, for example, a periodic spatial modulation of the carrier plasma in highly-excited structures induced by the dielectric structuring. Under appropriate conditions, this could lead to in–phase emission of the high density spots. When these are spaced on the half–wavelength scale, a coherent superposition of the partial emission and enhancement of the total emission (superradiance) is possible. Research along these lines and towards a fully self–consistent analysis of the dynamics of the coupled light–matter system is in progress.

Acknowlegements

We thank our coworkers and colleagues in Marburg, R. Eichmann, B. Pasenow, T. Stroucken, and P. Thomas, as well as L. Banyai, Frankfurt, for many discussions and ongoing collaborations. This work is supported by the Deutsche Forschungsgemeinschaft (DFG) through the Schwerpunktprogramm “Photonische Kristalle”, by the Max-Planck Research prize of the Humboldt and Max–Planck societies, by the Center for Optodynamics, Philipps University, Marburg, Germany. T.M. thanks the DFG for support via a Heisenberg fellowship. We thank the John von Neumann Institut für Computing (NIC), Forschungszentrum Jülich, Germany, for grants for extended CPU time on their supercomputer systems.

References

[1] E. Yablonovitch, Phys. Rev. Lett. **58**, 2059 (1987).

[2] S. John, Phys. Rev. Lett. **58**, 2486 (1987).

[3] J. D. Joannopoulos, R. D. Meade, and J. N. Winn, *Photonic crystals: Molding the flow of light*, Princeton University Press, Princeton, 1995.

[4] D. Labilloy, H. Benisty, C. Weisbuch, T. F. Krauss, R. M. De La Rue, V. Bardinal, R. Houdré, U. Oesterle, D. Cassagne, and C. Jouanin, Phys. Rev. Lett. **79**, 4147 (1997).

[5] M. Boroditsky, T. F. Krauss, R. Coccioli, R. Vrijen, R. Bhat, and E. Yablonovitch, Appl. Phys. Lett. **75**, 1036 (1999).

[6] A. A. Erchak, D. J. Ripin, S. Fan, P. Rakich, J. D. Joannopoulos, E.P. Ippen, G. S. Petrich, and L. A. Kolodziejski, Appl. Phys. Lett. **78**, 563 (2001).

[7] H.–Y. Ryu, J.–K. Hwang, D.–S. Song, I.–Y. Han, and Y.–H. Lee, Appl. Phys. Lett. **78**, 1174 (2001).

[8] M. Imada, S. Noda, A. Chutinan, T. Tokuda, M. Murata, and G. Sadaki, Appl. Phys. Lett. **75**, 316 (1999).

[9] J.–K. Hwang, H.–Y. Ryu, D.–S. Song, I.–Y. Han, H.–W. Song, H.–G. Park, Y.–H. Lee, and D.–H. Jang, Appl. Phys. Lett. **76**, 2982 (2000).

[10] S. Noda, M. Yokoyama, M. Imada, A. Chutinan, and M. Mochizuki, Science **293**, 1123 (2001).

[11] D.–S. Song, S.–H. Kim, H.–G. Park, C.–K. Kim, and Y.–H. Lee, Appl. Phys. Lett. **80**, 3901 (2001).

[12] H. Haug and S. W. Koch, Quantum Theory of the Optical and Electronic Properties of Semiconductors, 3rd ed., World Scientific, Singapore, 1994.

[13] T. Stroucken, R. Eichmann, L. Banyai, and S. W. Koch, Journ. Opt. Soc. Am. **B 19**, 2292 (2002).

[14] R. Eichmann, B. Pasenow, T. Meier, T. Stroucken, P. Thomas, and S. W. Koch, Appl. Phys. Lett. **82**, 355 (2003).

[15] R. Eichmann, B. Pasenow, T. Meier, P. Thomas, and S. W. Koch, phys. stat. sol. (b) **238**, 439 (2003).

[16] M. Kira, W. Hoyer, F. Jahnke, and S. W. Koch, Prog. Quantum Electron. **23**, 189 (1999).

[17] M. Kira, W. Hoyer, T. Stroucken, and S. W. Koch, Phys. Rev. Lett. **87**, 176401 (2001).

[18] W. Vogel and D. G. Welsch, Quantum Optics, Akademie Verlag, Berlin, 1994.

[19] A. Tip, Phys. Rev. A **56**, 5022 (1997).

[20] L. Banyai and S. W. Koch, Semiconductor Quantum Dots, World Scientific, Singapore, 1993.

[21] T. Meier and S. W. Koch, in Ultrafast Physical Processes in Semiconductors, special issue of Series "‘Semiconductors and Semimetals"’, Vol. 67, Academic Press, 2001, 231–313.

[22] L. V. Keldysh, Superlatt. Microstruct. **4**, 637 (1998).

[23] D. B. Tran Thoai, R. Zimmermann, M. Grundmann, and D. Bimberg, Phys. Rev. B **42**, 5906 (1990).

[24] L. V. Kulik, V. D. Kulakovskii, M. Bayer, A. Forchel, N. A. Gippius, and S. G. Tikhodeev, Phys. Rev. B **54**, 2335 (1996).

[25] B. Pasenow, et al., to be published.

[26] R. H. Dicke, Phys. Rev. **93**, 99 (1954).

[27] S. W. Koch, T. Meier, F. Jahnke, and P. Thomas, Appl. Phys. A **71**, 511 (2000).

4 Electrochemically-prepared 2D and 3D photonic crystals

Ralf B. Wehrspohn[1]*, Jörg Schilling, Jinsub Choi, Yun Luo, Sven Matthias, Stefan L. Schweizer, Frank Müller, Ulrich Gösele, Stefan Lölkes, Sergiu Langa, Jürgen Carstensen, and Helmut Föll*

4.1 Introduction

In the last ten years, photonic crystals have gained considerable interest due to their possibility to mold the flow of light [1]. Photonic crystals are physically based on Bragg reflections of electromagnetic waves. In simple terms, a 1D photonic crystal is a periodic stack of thin dielectric films with two different refractive indices n_1 and n_2. The two important geometrical parameters determining the wavelength of the photonic bandgap, are the lattice constant $a = d_1(n_1) + d_2(n_2)$ and the ratio of d_1 to a, where $d_{1,2}$ is the thickness of the layer with refractive index $n_{1,2}$. For a simple quarter-wavelength stack, the center wavelength λ of the 1D photonic stop band would be $\lambda = 2n_1d_1 + 2n_2d_2$. In the case of 2D photonic crystals, the concept is extended to either air holes in a dielectric medium or dielectric rods in air. Therefore, ordered porous dielectric materials like porous silicon or porous alumina are intrinsically 2D photonic crystals.

Electrochemically grown pores in metals and semiconductors have been studied for about 50 years [2, 3]. However, only in the last ten years intense research efforts have enabled the preparation of ordered pore arrays, with pore diameters in the range of a few nanometers to some tens of micrometers. The most studied materials are porous alumina and macroporous silicon and very recently porous III–V compounds. Porous alumina has been known for more than a century, but not before 1994 ordered arrays of porous alumina have been achieved [4]. This ordering was initially given by self–organization and the ordered domains were in the micron range. However, electron–beam lithography [5] and a new related technique of nano–indentation [6] allowed to prepare monodomain porous alumina structures with domain sizes limited only by the prepatterned area (some mm^2) and structure sizes in the nm–range.

Macroporous silicon has been pioneered in the early 1990s by V. Lehmann and H. Föll [7, 8]. Very regular pore arrays (pore size d: microns, domain size: up to wafer size) have been obtained by photolithographic prepatterning. These pores were called macropores[2] in contrast to microporous silicon, which is a sponge–like nanostructured material with photoluminescence properties that were intensively studied in the early 1990s [9]. Moreover, very

---

[1] Corresponding author: e-mail: wehrspohn@physik.uni-paderborn.de, Phone: +49 5251 602748, Fax: +49 5251 603247

[2] All pores are classified according to the IUPAC (Internat. Union for Pure and Applied Chemistry) – conventions unless otherwise indicated: microporous (equivalent to the often used term nanoporous): pore diameter $d < 5\ nm$, mesoporous: $d = 5 - 50\ nm$, macroporous: $d \geq 50\ nm$

Photonic Crystals. Edited by K. Busch, S. Lölkes, R. B. Wehrspohn and H. Föll
Copyright © 2004 Wiley-VCH Verlag GmbH & Co. KGaA
ISBN: 3-527-40432-5

recently, a few other semiconductors like InP, GaAs and GaP have been shown to exhibit micron– and nm–sized pores [10, 11]. Whereas standard nanostructuring techniques are limited to small pore aspect ratios $h/d < 40$ (ratio between pore/rod length to pore/rod diameter) and resolutions limited by the lithographic tools, electrochemically prepared pores exhibit high aspect ratios of 100 to 10000 and inherent short–range order. In the following, macroporous silicon, porous alumina, and porous III–V semiconductors will be discussed in detail. Due to the regular pore arrangements, these materials are extremely well suited as photonic crystals.

4.2 Materials

4.2.1 Porous silicon

p–type porous silicon

Porous silicon formed by anodization of p–type silicon in hydrofluoric acid has been studied by numerous groups. State–of–the–art summaries are given by Allongue [12], Lehmann [13], Zhang [14] and Föll et al. [15]. Three different pore formation regimes as a function of the dopant concentration have been observed experimentally. For degenerately doped p–type silicon, a special type of mesopores has been observed experimentally and attributed to tunneling of holes through the space–charge region [16,17]. Their size is typically in the range of 5 to 50 nm. For moderately doped p–type silicon, micropore formation is observed with pores in the range of 2 nm – 5 nm [9]. For highly resistive crystalline and amorphous p–type silicon (the resistivity is typically larger than 10 Ωcm), macropore formation (0.4 μm to 10 μm diameter) is observed below a thin layer of micropores [18]. Previously, macropore formation in low-doped Si had only been reported in anhydrous electrolyte [19, 20]. In the macropore regime, the wall thickness is about two times the space charge region, whereas the pore diameter is governed by the properties of the silicon–electrolyte interface, the resistivities of the silicon wafer and the properties of the electrolyte [21]. Depending on the current density and HF concentration, these macropores can either grow in the current–limited regime (low–currents) or in the crystallographic regime (high currents). These two regimes can easily be distinguished from the form of the pores. If the pores have a pyramidal pore tip and no micropores in the macropores, they are grown in the crystallographic regime. Electropolishing occurs at the pore bottom. If the pores are round and filled with micropores, the pores are grown in the current-limited regime. However, the exact growth mechanisms remain controversial in the literature [22, 23]. To obtain ordered arrangements of pores, being a prerequisite for photonic crystals, the crystallographic regime is typically used [24]. A p-type silicon wafer with $\langle 100\rangle$ orientation is first prepatterned by standard photo–lithography. Subsequent alkaline etching produces inverted pyramids acting as initial pores. Etching starts selectively at these etch pitches when self–ordering conditions and lithography match [21, 22, 24].

Pore growth directions are mainly governed by passivation kinetics during the etching process, i.e. surfaces which are passivated fast and effectively with hydrogen are etched less. As (100) surfaces are passivated the worst and slowest, pores on (100) wafers proceed in $\langle 100\rangle$ directions perpendicular to the wafer surface. On (111) wafers, on the other hand, $\langle 100\rangle$ pores would grow under an angle of 54° to the normal. In this configuration, the second slowest passivated direction ($\langle 113 \rangle$ with an angle of 34°) governs the pore growth [25]. At the nucleation points on the surface, tripods consisting of three equal $\langle 113 \rangle$–directions begin to grow. They form a criss–cross network of pores. If pores are grown with lithographically defined nucleation spots, a Yablonovite–like structure [26] results. However, up to now, lithographically prestructured samples have not yet reached optical quality. Application of pore etching requires homogeneous and reproducible etching of large areas, e.g. standard size Si wafers. This is not easy, but possible as demonstrated in [27–29] and by the Kiel group (cf. Fig. 4.1b).

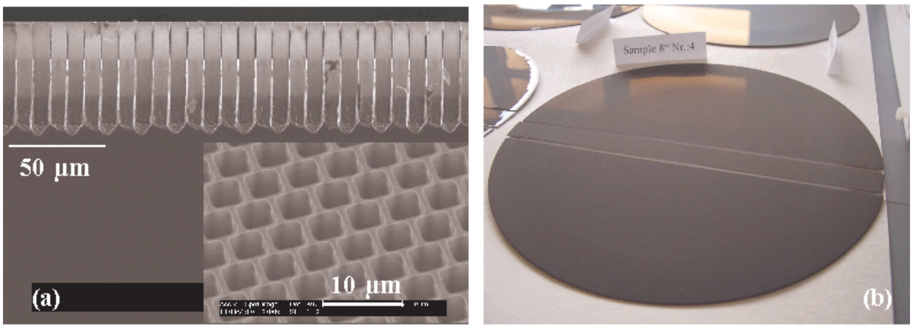

Figure 4.1: Large area etching of p–type silicon: **(a)** Scanning electron microscope (SEM) cross section of an ordered pore array with a pore diameter $d = 5$ μm and an interpore distance $a = 8$ μm. **(b)** Photograph of the first homogeneously electrochemically etched 8" wafer worldwide. (To our knowledge; previously unpublished results by the Kiel group.)

n–type porous silicon

A detailed description of macroporous silicon formation in n–type Si can be found in [7, 8]. Since holes (necessary for the dissolution reaction) are minority carriers in n-type silicon, they have to be generated by backside illumination. Then, they diffuse to the etch front through the wafer to promote dissolution of silicon, mainly at the pore tips. This technique has high requirements on the minority carrier diffusion length so that normally float-zone (FZ) wafers are used. Due to the fact that in this technique the holes move by diffusion and not by drift as in the p–type case, the strong boundary condition of a fully depleted pore wall is relaxed and thicker walls can be obtained up to 10 times the space–charge region width [8]. It is even possible to change the pore diameter during pore growth, which is hardly possible with p–type silicon in a controlled manner [30, 31]. To obtain ordered arrangements of pores, a n–type silicon wafer with (100) orientation is first prepatterned by standard photo–lithography. Subsequent alkaline etching produces inverted pyramids acting as initial pores. Under anodic bias and backside illumination, the wafer is then etched in hydrofluoric acid. As a result, pores grow straight along the (100) direction with a very high aspect ratio. The arrangement of these pores can be controlled by the lithographic mask and the pore diameter by the illumination intensity. By controlling these parameters, unintentional variations of the pore diameter with depth can be made negligible. Interpore distances in the range of a = 500 nm to a few tens of microns are possible. Figure 4.2 shows a scanning electron microscope (SEM) image of a porous Si sample, which was etched on 0.1 Ωcm n–type FZ silicon substrates, having a photo–lithographically–defined hexagonal pore arrangement. The pores have a center–to–center distance of 500 nm and a depth of 100 μm. The pore diameter after electrochemical etching is 370 nm. Initially the pores are slightly squared since etching is preferred in the (100) direction, stopping at the [110] planes of the crystal. However, by successive oxidation and etching steps, the pore diameter can be increased and the pores become rounder. It turned out recently, that for very deep pores, the dark current becomes significant. It can contribute up to 25 % to the total etching current. Carrot–shaped pores are obtained since the current contributes less to the pore growth and more to the dark current. This is very pronounced in structures exhibiting a very high surface area, thus typically structures with interpore distances smaller than 1.5 μm. By increasing the surface potential barrier at the interface HF/Si with an anionic tenside, the Halle group was able to reduce the dark current below 1 % of the etching current.

Like in p–type silicon, also in n–type silicon, $\langle 113 \rangle$–pore networks can be grown on (111)-oriented samples [32] for the production of 3D full photonic bandgap materials. Additionally, the pore diameter can be modulated during the growth which has a tremendous effect on the bandgap [33].

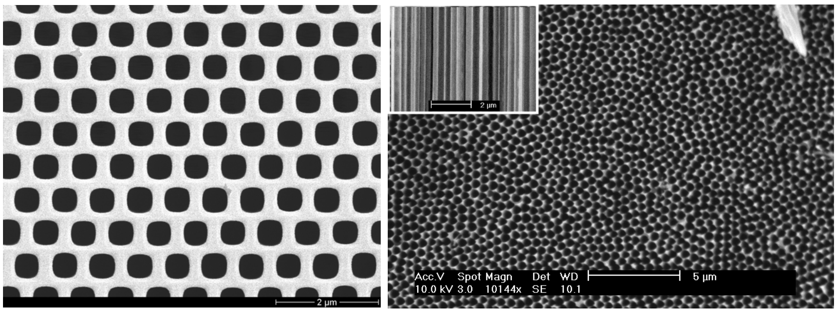

Figure 4.2: (a) Ordered porous n–type silicon ($a = 500\ nm$). (b) Self–ordered mesoporous Si. The pores ($d = 500\ nm$) self–organize in a hexagonal array (Inset: Cross section shows no significant pore wall roughness.) (Unpublished results by the Kiel group.)

Very recently, self–ordered pore arrays have been discovered in Si (Fig. 4.2b). They are something between meso- and macropores, i.e. they grow in a similar manner to mesopores but with dimensions in the macroporous regime. Conventional mesopores are normally only used for 1D – PhCs which are formed by layers of different porosity [34], while their dendritic structure with random side branches makes them unusable for 2D and 3D structures, as described above. However, in the present case, branching could be suppressed yielding extremely smooth pore walls like in InP [35]. The growth sequence is similar to InP (cf. Section 4.3.7): First a layer of crystallographically oriented pores grows which constantly increases the number of pores by branching. When the density of pores reaches a critical value, the growth switches to a current line oriented growth, i.e. follows the flow of the electrical current. This results in pore growth in the otherwise never observed $\langle 111 \rangle$–direction, e.g. on (111) Si samples. To transport the maximum electrical current through the pore tips, the system tries to close-pack the pores which results in a hexagonal self-ordering of the porous ensemble (cf. Fig. 4.2b). With this technique, it was possible to reach diameters as small as 100 nm (not possible with the conventional technique [7, 8]). The etching speed could also be increased by a factor of 6 (up to 400 μm/h compared to typically 60 μm/h for the conventional technique). Still, optical quality has yet to be demonstrated by optical measurements.

4.2.2 Porous alumina

Aluminum is electrochemically oxidized to alumina (Al_2O_3) under positive polarization. For certain electrolytes, which weakly dissolve the alumina, the growth of disordered pore arrangements has been observed and studied for a century now. A unique relationship between the anodization voltage U and interpore distance a was found: $a = d + 2\alpha U$ where d is the diameter of the pores and $\alpha \approx 1.2$ nm/V [3,36]. In 1994, Masuda and Fukuda first discovered that after long anodization times, self–ordered porous alumina films can be obtained at the growth front, which are arranged in a hexagonal close–packed pattern [4]. They have obtained ordered pore arrays with a lattice constant of 60 nm [37], 105 nm [4], and 500 nm [38] depending on the anodization conditions. The size of the pore domains increases with time [39]. The domains can reach micron size and domains touching each other have typically different orientations [39]. Mechanical stress between neighboring pores, due to the volume expansion of alumina with respect to the aluminum substrate, has been proposed as a mechanism for the self–ordering. For example, it is observed that the volume expansion for optimal pore growth is in the range of 1.2 to 1.4, i.e., there is an incorporation yield of 60 – 70 % aluminum in the alumina film. This corresponds to an initial porosity of the porous film of 10 %. We have recently shown that all ordered regimes exhibit an initial porosity of 10 % after etching (10 %-porosity rule) [39]. Since the interpore distance is determined by the potential only, the pore diameter is the key to tuning the range of selfordered pore growth. We have shown experimentally that the pH–value of the electrolyte controls the pore diameter [39]. This is in line with a recent linear stability analysis [40]. Thus, by adjusting the pH–value and the potential, other ordered regimes can also be obtained. To date, it is possible to obtain ordered pore growth with 50, 65, 105, 420 and 500 nm interpore distance.

To obtain monodomain pore arrays, three strategies are possible. First, if one starts with a single crystal seed, i.e., a single pore, one would expect that the other pores arrange themselves hexagonally around it due to repulsive forces. The second one is based on the observation of Li et al. [41]. As the anodization time increases, one should end up with a single domain since it is the total energy minimum of the system. Note that this assumes an aluminum monocrystalline substrate. However, both approaches seem to be quite impractical. Therefore, a third strategy is used. Knowing the optimum potential U and electrolyte for a certain interpore distance a, the aluminum substrate can be lithographically prepatterned. Since the feature sizes are in the range of 50 nm, electron beam or imprint lithography is applied. Figure 4.3 shows a SEM image of a hexagonally–ordered pore array in alumina, prepared from an imprint–lithography prepatterned substrate [6]. The pattern has 500 nm interpore spacing and the anodic voltage was adjusted to 195 V, based on the relationship between a and U. Very recently, Masuda et al. have shown that in addition to the hexagonal lattice, the square and honeycomb lattice can also be obtained by appropriate prepatterning, exhibiting squared or triangular pore shapes [42]. The Halle group has extended this idea and has shown that by nanoimprinting twice under different angles (Moire–pattern) even structures with a 12–fold rotational symmetry can be

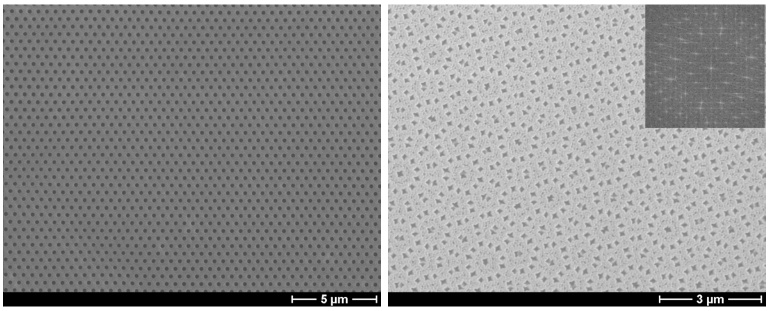

Figure 4.3: Ordered porous alumina with $a = 500$ nm obtained by imprint lithography [6]. By repeated imprint under an angle of 2.2 degrees, a 12–fold symmetry can be obtained [43].

obtained (Fig. 4.3), which have been predicted to exhibit a complete PBG for low-refractive index PhCs [43]. The inset in Fig. 4.3 shows the Fourier transform of the image.

4.2.3 Porous III–V semiconductors

As in Si, anodization of III–V single crystals can lead to uniform dissolution (electropolishing) [44] or selective dissolution, i.e. pore formation [45]. The main factors determining the actual result of anodization are the doping type of the substrate (n– or p–type), the kind of electrolyte used (acidic, basic), voltage, and the current density applied to the sample, temperature etc. It is illuminating to point out major differences to Si pore etching right away: As far as the materials are concerned, they are polar and do not easily form good (anodic) oxides; as far as pores are concerned, no pores of any kind have been found in p–type crystals, and no micropores have been found either. What has been found, are macro– and mesopores in n–type III–Vs [46].

These pores come in two totally different types: crystallographically oriented pores growing in $\langle 111 \rangle\, B$ directions ("crysto pores" for short) and current line oriented pores ("curro pores") growing in the current flow direction (or, to be more precise, perpendicular to the equipotential surfaces). Crysto pores tend to form at relatively low voltage/current density and have a special crystallographic feature because they grow only in the $\langle 111 \rangle\, B$ direction, meaning the direction from e.g. As to Ga, but not the other way around. There are thus two $\langle 111 \rangle\, B$ directions pointing into a (100)–oriented substrate with an angle of 109° between them (see Fig. 4.4a). Crysto pores tend to have a triangular shape and a high tendency for branching. Taking into account that two $\langle 111 \rangle\, B$ directions are pointing up towards the surface of the sample, branches of crysto pores may also grow upwards, an unusual behavior at first sight, never seen in Si. Moreover, crysto pores may easily intersect each other [47] which is not a common observation in pore growth. These features allow us to produce defined 3D structures of criss–crossing crysto pores. Crysto pores grow relatively slowly, about 1 μm/min similar to macropores in Si. They have been observed in GaAs, InP, GaP (and recently also in Ge [48]). Curro pores have been found in InP and GaP. Their growth rates are rather large compared to the crysto pores, can reach 30 μm/min and depend strongly on the efficiency of electrolyte flow, to the tips of the curro pores. Similar results have only recently been found in

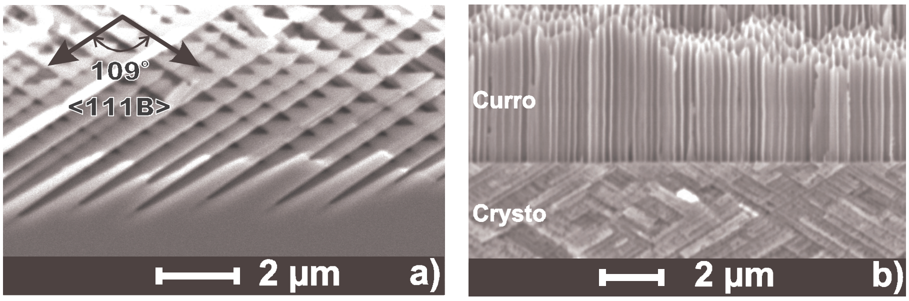

Figure 4.4: a) Crystallographically oriented pores (crysto pores) in (100)–oriented n–GaAs; b) The switch from curro to crysto pores in (100) InP by switching the current density from high to low values.

Si (cf. Sec. 4.2.1). The reason for the remarkably large growth rates are the "bad" and unstable III–V oxides (formed as a result of anodization at the tips of the pores) in acid electrolytes.

The assumption *"crysto = low"* and *"curro = high current densities"* has been verified by changing the value of the current density from high to low during the etching of a single sample. By doing so, it is possible to switch between the two morphologies (cf. Figure 4.4b): The first layer consists of curro pores (high current densities) whereas the second layer is made of crysto pores (low current densities).

4.3 Application to photonic crystals

4.3.1 Introduction

From the beginning of research on photonic crystals, a major area of investigation concerned two–dimensional (2D) photonic crystals [1]. This was mainly caused by experimental reasons as the fabrication of 3D photonic crystals appeared to be more difficult and cumbersome than that of 2D photonic crystals. Additionally, the calculation of band structures for 2D photonic crystals is less time consuming and a lot of interesting phenomena (e.g. light localization – at least in a plane) can already be studied in 2D photonic crystals. However, an ideal 2D photonic crystal consists of a periodic array of infinitely long pores or rods, so that a structure which approximates this theoretical model has to exhibit very high aspect ratios. Using conventional dry etching techniques, only structures with aspect ratios up to 10 – 30 are possible. To avoid scattering of light out of the plane of periodicity and to reduce the corresponding loss, the so-called slab structures were developed and thoroughly investigated [49,50]. In such low–aspect structures, one relies on guiding of light by total internal reflection in the third dimension and, consequently, deals with a full 3D problem. On the other hand, Lehmann and Grüning [51,52], as well as Lau and Parker [30] proposed macroporous silicon as a model system for 2D photonic crystals. Typically, high–quality photonic crystals with lattice constants of a = 500 nm to 8000 nm can be produced with this process. These structures exhibit photonic bandgaps from the near infrared to the far infrared (Fig. 4.5). Since then, new electrochemically nanostructured materials like III–V compounds or aluminum oxide with photonic properties have emerged.

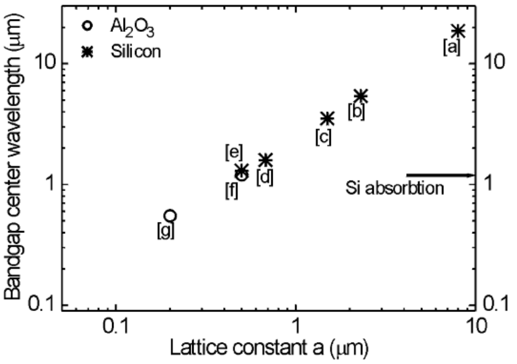

Figure 4.5: Summary of experimentally measured bandgap–center wavelengths for porous alumina (TE gap) and porous silicon (complete gap) as a function of the lattice constant (From references [a]= [51], [b] = [52], [c] = [29], [d] = [65], [e] = [31], [f] = [71], [g]= [72]). Picture taken from [68].

4.3.2 2D photonic crystals made of macroporous silicon

Bulk photonic crystals

The dispersion relation for light propagation inside a photonic crystal is calculated using the plane wave method. Due to the 2D periodicity and the uniformity along the third dimension, the light propagating in a 2D photonic crystal splits into E–polarized (E–field parallel to the pore axis) and H–polarized (H–field parallel to the pore–axis) waves. The band structures for these polarizations differ from each other and so do the bandgaps in width and spectral position. This originates in the different field distributions: Typically, the electric field of the H–polarized waves is located in the veins of the structures whereas the electric field of the E–polarized waves concentrates in the connection points of the veins. Figure 4.6 shows an example of a band structure for our system, calculated for wavevectors in the first Brillouin–zone along the path $\Gamma - M - K - \Gamma$. The assumed porosity or air filling factor is p = 0.73 which corresponds to r/a = 0.45 (r = pore radius, a = lattice constant) and the refractive index of silicon in the infrared is n = 3.4. For a triangular array of pores, a refractive index contrast exceeding 2.7 [53] and for suitable r/a ratios, the bandgaps for E– and H–polarization overlap and a complete 2D photonic bandgap exists. As the refractive index contrast for air pores in silicon amounts to $n_{\mathrm{Si}}/n_{\mathrm{Air}}$ = 3.4 in the infrared (IR), these requirements are fulfilled in our system. The band structure shown in Fig. 4.6 thus exhibits such a complete bandgap, indicated by a grey bar.

In addition to the band structure, the density of (photonic) states (DOS) is computed as well and presented in Fig. 4.6b [54]. In the spectral region of the complete photonic bandgap, the DOS is zero such that propagation of light in the plane of periodicity with these frequencies is completely forbidden in the photonic crystal. To verify these theoretical calculations, a triangular lattice was fabricated with a pitch a = 0.7 μm and r/a–ratio of 0.365. To check the spectral position of the first order bandgap, reflection measurements were performed using an IR microscope connected to a FTIR-spectrometer. The reflection for H– and E–polarized light incident in the Γ–M direction was measured separately. A gold mirror was used as a reference. Figure 4.7 shows a comparison of the measured reflection spectra with the band

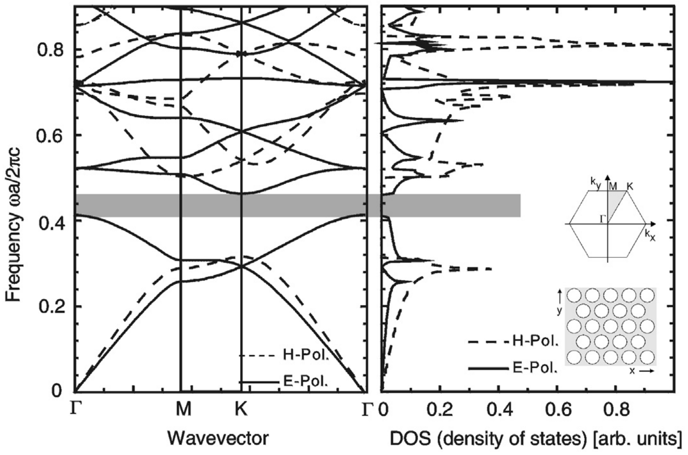

Figure 4.6: 2D band structure of a trigonal macroporous silicon photonic crystal (r/a = 0.45) and density of photonic states (DOS), inset: 2D hexagonal Brillouin–zone and appropriately oriented trigonal pore lattice in real space. The grey bar indicates the 2D complete bandgap. In this spectral range neither H–polarized nor E–polarized photonic states exist (DOS = 0). (Courtesy of K. Busch.)

structure. The shaded spectral ranges represent the theoretically expected regions of high reflectivity stemming from the bandgaps. They correspond very well to the experimental results. Although the reflected light contained contributions from beams with an incidence angle of up to 30° (due to the focusing conditions of the microscope) this off–normal incidence has only a negligible effect. The incident light is bent by refraction towards the normal, propagating with a much smaller angular deviation inside the photonic crystal. Additionally, the width and position of this first order bandgap is not very sensitive for small angular deviations [55]. Please note that the very steep band edges reflect the very high quality of these structures which were obtained by a recently developed, improved etching method. Reflectivities originating from higher order bandgaps, antisymmetric modes or modes with a low group velocity can also be observed and are in very good agreement with the theory (cf. Chapter 1 by Busch et al.).

A graphic representation of the relationship between gap frequencies and filling ratio is known as a gap map, which for our structure, has been calculated before [54]. To verify this gap map experimentally, transmission measurements for 17 different samples spanning a wide range of r/a–ratios were carried out. The band edges were determined from these measurements and are compared with the theoretical predictions in Fig. 4.7. The overall correspondence is very good. For lower r/a–ratios, only a bandgap for the H-polarization exists. A complete bandgap only appears for $r/a > 0.4$ since an E-bandgap then appears which overlaps with the H–bandgap. With increasing r/a–ratios, the E–bandgap widens while the H–bandgap shrinks for very high filling ratios. A maximum, complete bandgap of $\Delta\omega/\omega = 16\%$ for $r/a = 0.48$ can be deduced. This relatively large complete bandgap is a

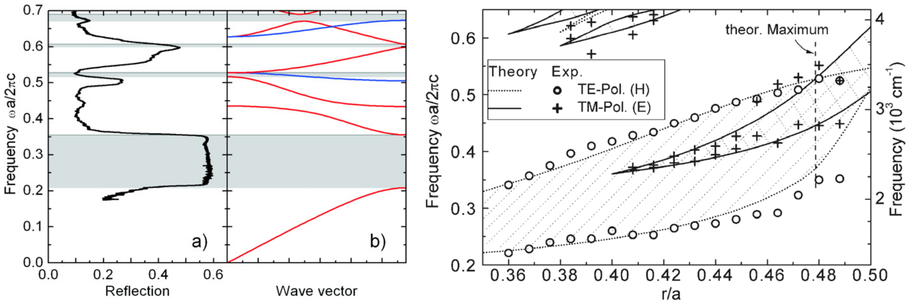

Figure 4.7: Left: Reflectivity along Γ–M for a 2D trigonal macroporous silicon photonic crystal with a lattice constant of 0.7 μm for H–polarization (TE). Left: Measured reflectivity of a semi–infinite photonic crystal. Right: Comparison with band structure. Symmetric bands contribute to transmission while for asymmetric bands, the incident plane waves cannot couple. Beside the bandgaps, they also cause total reflection. The shaded range shows the fundamental bandgap for H-Pol from 2 to 3.2 μm (courtesy from S. Richter and C. Jamois). Right: Position of the bandgaps for H–polarized light (dotted) and E–polarized light (solid) for a 2D trigonal macroporous silicon photonic crystal depending on the r/a–ratio (gap map). A complete bandgap appears as an overlap of the gaps for both polarizations and attains its maximum size for an r/a–ratio of 0.48 [54].

consequence of the strong refractive index contrast between the silicon (pore walls) and air (inside the pores) as well as the synergetic interplay of Mie resonance and Bragg scattering resonance. A summary of experimentally–measured bandgap center wavelengths for porous alumina (TE-gap) and porous silicon (complete gap) as a function of the lattice constant is shown in Fig. 4.5.

Finite photonic crystals

Strictly speaking, the band structure calculations can only be performed assuming an infinitely extended photonic crystal. Therefore, also the bandgap (zero DOS) causing perfect total reflection only appears for infinite bulk photonic crystals. For a very thin bar of the photonic crystal, the incident light of a frequency within the bulk bandgap is no longer totally reflected. A certain amount can penetrate the thin photonic crystal. To investigate this effect, 4 samples containing 1, 2, 3 and 4 crystal rows with a r/a–ratio of 0.453 were fabricated (Fig. 4.8). Transmission measurements for H-polarized light of different wavelengths along $\Gamma - K$ were performed (see Fig. 4.8) [56]. A tunable laser setup was used which covered the spectral range between $3 < \lambda < 5\ \mu$m, corresponding to the range of the H–bandgap ($3.1 < \lambda < 5.5\,\mu$m) of the corresponding bulk photonic crystal. The experimental results were compared with transmission calculations applying the already mentioned Sakoda method and showed a very good agreement (Fig. 4.8). Plotting the transmittance versus the penetrated crystal thickness, an exponential decay is observed. This corresponds to the expectation that for frequencies within the bandgap, the light penetrating into the bulk photonic crystal is exponentially damped. The slope of the line in the logarithmic plot corresponds to a decay constant of 10 dB per crystal row for light with a wavelength near the center of the bandgap. Even for a bar containing only 1 pore row, the bandgap is already perceptible. This originates in the strong scattering of the single pores due to the large refractive index contrast between air pores and silicon walls.

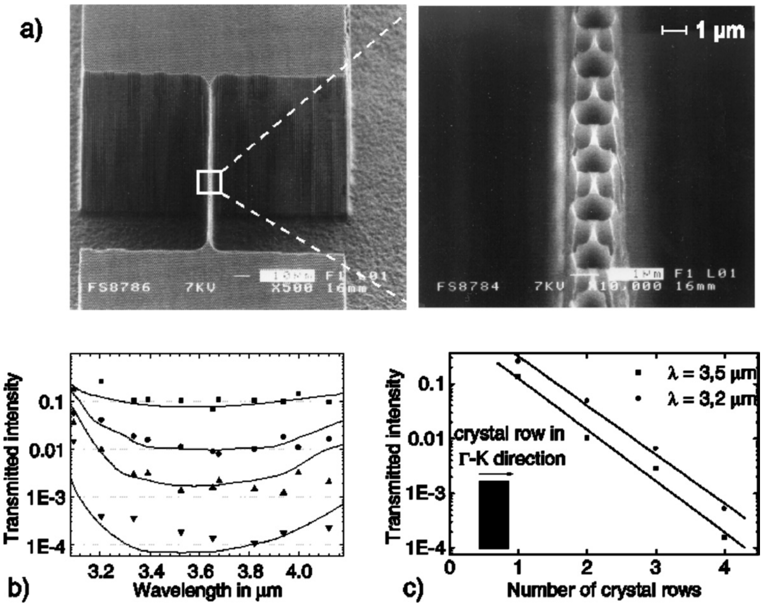

Figure 4.8: a) SEM image of the macroporous silicon bars with varying width. The inset shows an enlarged view of the center square. b) Measured and calculated transmission for wavelengths within the H-bandgap. Solid lines: calculations for transmission through 1, 2, 3 and 4 crystal rows. Points: Measurements for 0.89 ± 0.04 (■), 1.8 ± 0.1(•), 2.9 ± 0.1 (▲) and 4.2 ± 0.2 (▼) crystal rows (determined statistically). c) Measured transmission as a function of bar thickness for 2 wavelengths within the bandgap [56].

4.3.3 Photonic defects in electrochemically–prepared 2D photonic crystals

Introduction

Since the beginning of the study of photonic crystals, special attention has been paid to intentionally incorporated defects in these crystals. Point or line defects can be introduced into macroporous 2D-silicon photonic crystals by omitting the growth of a single pore or a line of pores. This can be achieved by designing a suitable mask for the lithography (the pattern defining process). Introduction of defects into porous alumina photonic crystals is more difficult, since intentionally introduced defect anneal out during electrochemical etching. However, for thin slab structures, line or point defects having a slightly smaller pore diameter, might be realizable.

Waveguides

To demonstrate waveguiding through a linear defect, a 27 μm long line defect (W1 – one missing row) was incorporated along the $\Gamma - K$ direction into a triangular 2D photonic crystal with a r/a– ratio of 0.43 (r = 0.64 μm) [60]. However, due to the photo–electrochemical fabrication process, the diameter of the pores in the rows adjacent to the waveguide is increased.

The transmission through the line defect was measured using a pulsed laser source which was tunable over the whole width of the H-stopband in the $\Gamma - K$ direction ($3.1 < \lambda < 5.5\ \mu m$). To couple light into the narrow waveguide (with a subwavelength width) with reasonable efficiency, a spatially coherent source of mid-IR light was used. A parametric source was used to produce a beam tunable from 3 to 6 μm, containing 200–fs pulses at a repetition rate of 250 kHz and a typical bandwidth of approximately 200 nm. The H-polarized beam was focused onto the sample by a 19–mm focal–length ZnSe lens, to a spot size of approximately 25 μm. Because the waveguide width was 1.1 μm, this spot size provided a theoretical coupling efficiency of approximately 4.8 %. The transmitted light was passed through a monochromator, chopped, and detected with a pyroelectric detector and a lock–in amplifier. The transmission is defined as the ratio of the transmitted power to the total power incident upon the sample and is about 2 %. The transmission deficit compared to 4.8 % is attributed to the clipping of the beam by the substrate and possible diffraction losses.

The measured spectrum (Fig. 4.9) exhibits pronounced Fabry–Perot–resonances over a large spectral range, which are caused by multiple reflections at the waveguide facets. Comparing the spectrum with an FDTD–transmission calculation, reveals very good agreement and the comparable finesse of the measured and calculated resonances indicate small losses inside the sample.

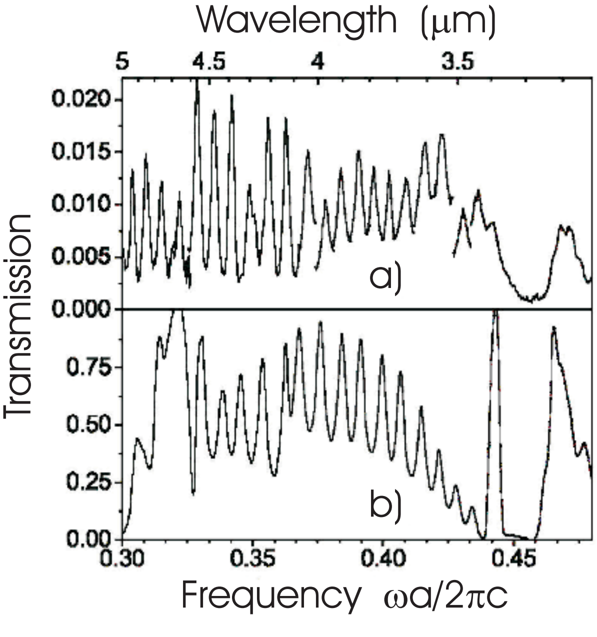

Figure 4.9: **(a)** Measured and **(b)** calculated H–polarized transmission spectrum of a 27 μm long waveguide directed along $\Gamma - K$ covering the spectral range of the H–bandgap of the surrounding perfect photonic crystal (transmission in %). Only the even waveguide modes contribute to the transmission as the incoming plane wave can not couple to the odd waveguide modes. The small stopgap at a frequency of 0.45 c/a is caused by the anticrossing of 2 even waveguide modes [60].

Microcavities

Besides line defects, point defects consisting only of one missing pore, are also of special interest. Such a micro–resonator–type defect also causes photonic states, whose spectral positions lie within the bandgap of the surrounding perfect photonic crystal. The light fields belonging to these defect states are therefore confined to the very small volume of the point defect, resulting in very high energy densities inside the defect volume. As the point defect can be considered as a microcavity surrounded by perfectly reflecting walls, resonance peaks with very high Q–values are expected in the transmission spectra. Since the symmetry is broken in both high-symmetry directions, a band structure cannot be used to describe point defects anymore. To study this experimentally, a sample was fabricated which included a point defect which was placed between two line defects, serving as waveguides for coupling light in and out [61].

Measuring transmission through a waveguide–microresonator–waveguide structure demands an optical source with a very narrow linewidth. Therefore, a continuous wave optical parametric oscillator (OPO) has been used, which is tunable between 3.6 and 4 μm and delivers a laser beam of 100 kHz line width. For spatially resolved detection, an uncoated, tapered fluoride glass fibre mounted to a SNOM–head was applied and positioned precisely to the exit facet of the outcoupling photonic crystal waveguide (for detailed information on SNOM-measurements on PhC–structures: see Chapter 11 by Sandoghdar et al.). In the transmission spectrum, two point defect resonances at 3.616 μm and 3.843 μm could be observed. Their spectral positions are in excellent agreement with the calculated values of 3.625 μm and 3.834 μm. These walls were predicted by 2D–FDTD calculations taking into account the slightly widened pores surrounding the point defect. The measured point defect resonances exhibited Q–values of 640 and 190 respectively. The differences to the theoretically predicted values of 1700 and 750 originate from the finite depth not considered in 2D–calculations and the exact pore shape near the cavity. Recent 3D–FDTD calculations show that for high Q–values, the finite depth as well as the shape of the pores near the cavity, plays an important role in the determination of the Q–value [62]. Therefore, the 2D–limits breakdown for high–Q cavities under realistic conditions. Intuitively, this can be explained as follows. Any out–of–plane component of the incoming light will result in a spreading of the mode with depth and in a reduction of the Q–value. However, the high Q–values reported for this 2D microresonator, might already be sufficient for studying the modification of radiation properties of an emitter placed in such a point defect.

4.3.4 3D photonic crystals made of macroporous silicon

Up to now, the most significant work based on macroporous silicon and photonic crystals concerned 2D photonic crystals. However, recently attempts have been undertaken to use macroporous silicon for 3D photonic crystals. One approach to introduce a refractive index variation in the third dimension is the modulation of the pore diameter with pore depth [63]. As described in the first paragraph of this review, the pore diameter of the macropores can be controlled during the fabrication process by the intensity of the back side illumination of the wafer. Strong illumination leads to high etching currents and, therefore, wide pores while the opposite is valid for low illumination.

The illumination intensity was now varied periodically during the etch process, applying a zig–zag profile. Figure 4.10 shows a SEM–image of a longitudinal section of the sample. The pore diameter modulation can be approximated well by a sinusoidal dependence on the pore depth. The modulation period amounts to 1.69 μm and the porosity varies from 81 $\%$ to 49 $\%$ between the planes of wide and narrow pore diameters. The lattice constant a of the 2D pore pattern is again 1.5 μm. The resulting 3D photonic crystal has a hexagonal lattice and the corresponding Brillouin zone has hexagonal shape, too. Note, that this is the first three–dimensional photonic crystal in the infrared region which perfectly extends over more than 10 lattice periods. To investigate the optical properties of the structure introduced by the pore diameter modulation, reflection measurements were performed along the pore axis which correspond to the $\Gamma - A$ direction. The spectrum is shown in Fig. 4.10 and compared to a 3D band structure calculation using the plane wave method. For comparison with the experiment, the leftmost part of the band structure shows the relevant dispersion relation along $\Gamma - A$. The stop gap in this direction, caused by the periodic pore diameter modulation, is indicated by a grey bar. It coincides well with the range of zero–transmission between 1350 cm^{-1} ($\lambda = 7.41$ μm) and 1680 cm^{-1} ($\lambda = 5.95$ μm) measured along the pores.

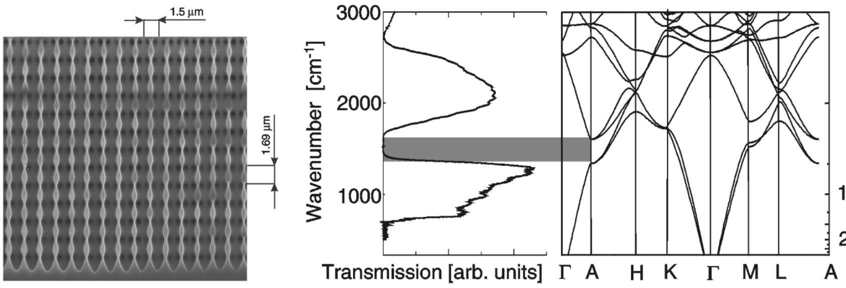

Figure 4.10: (left) SEM–image showing a longitudinal section of the modulated pore structure. The variation of the pore diameter with depth can be modelled by a sinusoidal modulation $r = r_0 + \Delta r sin(2\pi z/l_z)$ with $r_0 = 0.63\mu$ m, $\Delta r = 0.08\mu$ m and $l_z = 1.69\mu$m. [63]. **(right)** Transmission is measured in the $\Gamma - A$ direction (along the pore axis) and comparison with calculated 3D band structure. The grey bar indicates the stopgap for light propagation in this direction causing zero transmission [63].

Although the structure does not show a complete 3D bandgap, it has another distinct property: As it is not based on building blocks of a fixed shape, e.g. spheres or ellipsoids, the periodicity can be different for all directions. The modulation period along the pore axis (z–axis) can be controlled independently from the periodicity in the x–y–plane. Consequently, the dispersion relation along the pores can be adjusted nearly independently of the dispersion relation perpendicular to them. It turned out recently that the same structure but with an initial 2D cubic lattice does have a complete photonic bandgap. The resulting structure is an inverted simple cubic lattice with a complete bandgap of around 4 $\%$ for realistic etching parameters [64]. First realizations can be seen in Fig. 4.11.

Another approach to fabricate 3D photonic crystals on the basis of macroporous silicon, includes a 2–step–process [65]. In the first step, a conventional 2D array of straight pores

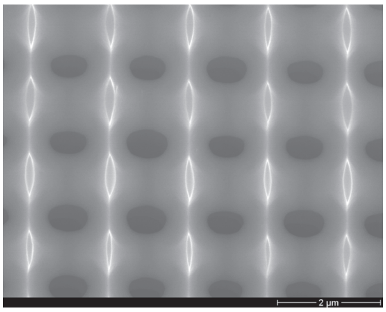

Figure 4.11: SEM cross section of one of the first modulated pore structure having an inverted simple cubic symmetry. The lattice constant a is 1.5 μm.

is photo–electrochemically etched. Afterwards, additional pores are drilled at oblique angles from the top, using a focused ion beam (FIB). In this way, a set of 3 different pore directions is established which cross each other in the depth. The fabricated structure is very similar to the well–known Yablonovite–structure for the microwave region. However, a complete 3D–bandgap could not yet be shown experimentally, as the angles between the 3 different pore sets have not been properly aligned.

A fabrication technique which should give a very similar result uses the electrochemical etching of macropores on a (111) Si surface [32], where pores grow into $\langle 113 \rangle$–directions (cf. Sec. 4.2.1). As there are three equivalent $\langle 113 \rangle$ directions available from the (111) surface, 3 pores start to grow from each nucleation point at the surface, leading to a three dimensional interconnected pore grid. The resulting structure is similar to the Yablonovite [26] but slightly distorted, as the pore angle to the normal is not 29.5° but 34°. Band structure calculations for a corresponding structure show that the pores along the three $\langle 113 \rangle$ directions grow at suitable angles, such that the structure should exhibit a complete 3D photonic bandgap of up to 16% [33] (Fig. 4.12).

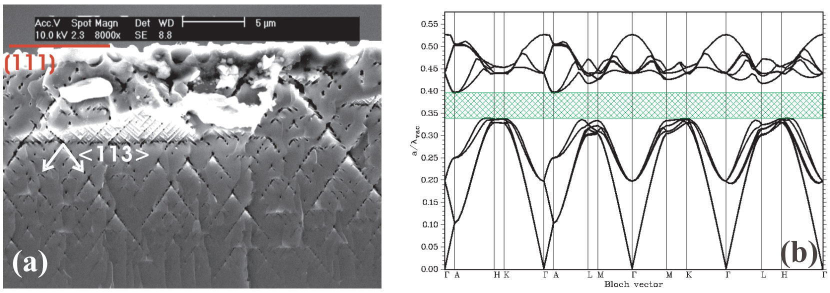

Figure 4.12: (a) SEM cross section of a $\langle 113 \rangle$-pore crystal (Kielovite). The quality has still to be improved to allow for optical experiments. (b) Calculated band structure for the Kielovite (modulated pores with $r/a = 0.26$) [33].

Very recently, different crystal structures with complete bandgaps larger than 20 %, based on macroporous silicon, have been predicted and are under current investigation [66] (Tab. 4.1).

Table 4.1: Proposed 3D silicon photonic crystals based on electrochemical pore etching.

Common name	Crystallographic structure	Complete bandgap [%]	Ref.
Kielovite	distorted fcc	8/16[a] %	[33]
Modulated hexagonal	Inv. sh	0 %	[31]
Modulated cubic	Inv. sc	4 %	[64]
Hallite or SP_2	tetragonal	25 %	[66], [67]

---

[a] for modulated pores

4.3.5 2D photonic crystals made of porous alumina

The possibility to use mono–domain porous alumina as two–dimensional photonic band gap material has been predicted theoretically. Early numerical calculations show that perfectly hexagonally-ordered porous alumina exhibits a photonic band gap for TE polarized light only due to the low refractive index ($n \approx 1.7$ for corundum). For porous alumina, the interpore spacing that can be varied between 50 nm and 500 nm, leading to theoretical photonic bandgaps centered at wavelengths in the range between 100 and 1300 nm, depending on the filling ratio. Note that the bandgap of alumina (corundum) is around 7.5 eV, while porous alumina has a lower bandgap due to its amorphous nature. Experimentally however, absorption for wavelengths above 400 nm is negligible over the size of a photonic crystal. Masuda's group has recently shown transmission measurements through porous alumina photonic crystals with 200 and 500 nm interpore distance, exhibiting photonic bandgaps around 600 nm and 1300 nm (see data point in Fig. 4.5). We have recently extended this work to also obtain the gapmap of porous alumina similar to that of porous silicon (Fig. 4.13). It turned out that porous alumina cannot simply be described by a simple refractive index of $n = 1.7$. The structure actually consists of at least three layers: An inner high-purity layer of $n \approx 1.7$, a highly anion-contaminated layer of $n \approx 1.4$ and a rather pure outer layer $n \approx 1.6$. Thus depending on the widening degree, the effective refractive index changes (Fig. 4.13).

4.3.6 1D photonic crystals made of InP

InP exhibits two growth modes: Crystallographically oriented pores ("crysto") for low current densities and current line oriented pores ("curro") for high current densities. Porous layers of crysto and curro pores have different refractive indices due to their different porosities, e.g. the porosity of the curro layer is higher therefore the refractive index is smaller. Switching the current periodically from high to low values, produces multilayers of curro/crysto pores and thus a Bragg mirror, i.e. a 1D photonic crystal. An example of such a structure is presented in Figure 4.14a. This structure could be used, e.g., as a mirror for a Vertical Cavity Surface Emitting Laser (VCSEL). The optimization of such a structure for a defined wavelength can easily be made by adjusting the periodicity of the HIGH/LOW current cycling [70].

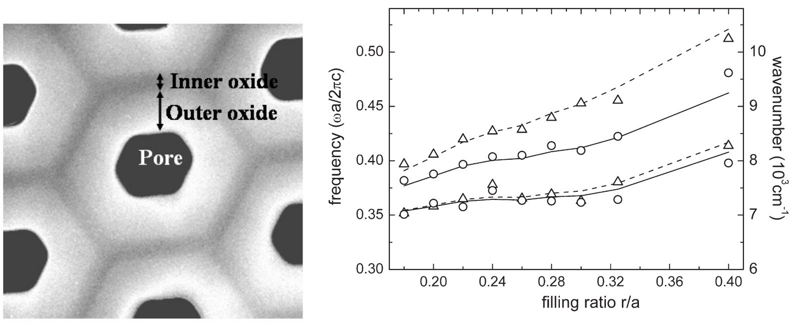

Figure 4.13: (left): Transmission electron micrograph (TEM) of porous alumina obtained by imprint lithography and subsequent anodization (195 V, 1 wt% H_3PO_4). It reveals that the two oxide layers consisting of inner oxide and outer oxide exist. Thickness of the inner oxide is 50 nm, whereas that of the outer oxide decreases with increasing the pore diameter (initial diameter: 180 nm) by the isotropic etching. **(right)**: Bandgap determined by reflectivity measurements versus theoretical band structure for different r/a–values and both polarizations (△ = TE, ○ = TM) in Γ-M direction [69].

4.3.7 2D photonic crystals made of InP

A particularly interesting feature of the curro pores is their strong tendency for self–organization into a close packed hexagonal lattice like alumina pores (see Section 4.2.2). An example of a self–arranged hexagonal curro pore lattice in n–InP is presented in Fig. 4.14b, c and d. The pores do not branch, have “high quality” pore walls (Fig. 4.14b) and diameters in the sub-μm range. The diameter of the pores as well as the pore wall thickness are mostly determined by the doping; both can be increased by choosing a lower doped sample, e.g. for $n = 10^{16}$ cm^{-3}, 5 % HCl, the pore diameters increase up to 1 μm. The 2D Fourier transform taken from Fig. 2a results in a “diffraction” ring (see the inset), which means that “single crystal” domains are arranged in a structure without long range order. The observed short range ordering is due to pore–pore interaction via space charge regions.

By optimizing the etching conditions, it is possible to obtain long range ordering of these curro pore domains, too (see Fig. 4.14d), and thus finally a single pore crystal: The Fourier transform taken from Fig. 4.14 shows a clear “diffraction pattern” of a hexagonal single crystal. Such single crystalline pore arrays are promising for 2D photonic crystal applications [57], where a highly ordered and high quality array of pores is required.

In order to understand the 2D long range ordering of the curro pores, it is necessary to discuss their nucleation in more detail: Curro pores cannot form without a nucleation layer formed by crysto pores. The thickness of this nucleation layer depends on the etching conditions; it is normally 1 – 2 μm. Its thickness decreases as the currents/voltage increases or the concentration of the HCl electrolyte decreases. As the crysto pores have much smaller diameters than the curro pores and nucleate at larger distances relative to each other; therefore the surface of an anodized sample at high current/voltages still appears mirror–like.

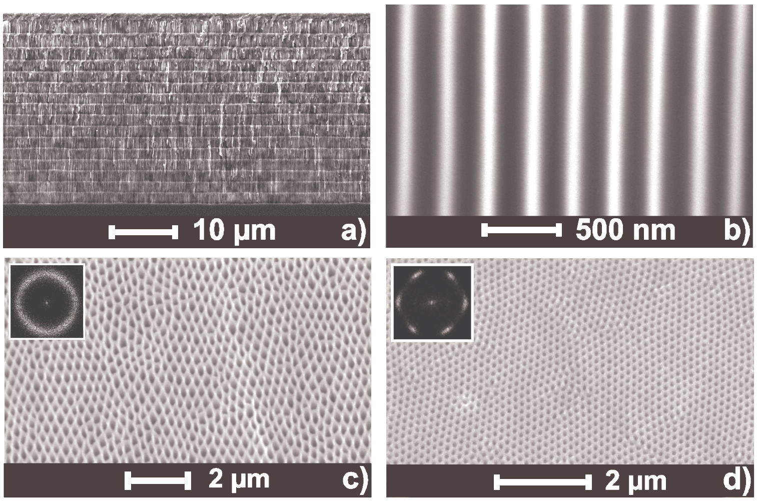

Figure 4.14: **(a)** 1D-PhC stack of crysto and curro pores. **(b)** Cross sectional view of the curro pores. **(c)** Polycrystalline hexagonal arrangement of curro pores. **(d)** The hexagonal (single crystalline) arrangement of the curro pores; plane view after the nucleation layer was removed.

The density of crysto pores increases rapidly as they grow into the substrate due to repeated upward and downward branching. Thus from one primary nucleation point at the surface, an extended set of new pores is generated, in particular for (100) oriented substrates. The set of all pore tips from one root ancestor (starting point) will form a (square) domain of nuclei for curro pores, which are to some degree aligned along $\langle 011 \rangle$ directions [58]. Consequently, the curro pores, which start from the tips of the crysto pores, will tend to align along this $\langle 011 \rangle$ direction. Thus all domains of curro pores, resulting from just one originally nucleated crysto pore, will tend to have the same global alignment. Thick nucleation layers allow for many branching events, the domains will thus be larger and the alignment tendency stronger. However, the long range order is lost at voltages deviating from some optimal conditions in either direction, because two opposing mechanisms govern the self–ordering: Close packing leads to local order while a sufficiently developed nucleation layer gives global orientation of close packed domains. If one factor is too weak, no strong ordering is possible. If the anodization voltage is lower than the optimum one, the space charge region of the pores is too small, i.e. the interaction between pores decreases and the local closed packed order disappears. This insufficient interaction between pores is also expressed by their tendency to assume triangular shapes at lower voltages. On the other hand, at voltages higher than the optimum, the thickness of the nucleation layer is too small, i.e. the domain size decreases, and as a result global order is lost. The same model can be applied to the (111) oriented samples. However, in this case the domains of crysto pores within the nucleation layer will have a triangular shape.

The quality of the self-organized pore single crystals can be rather high, but is certainly not good enough for PhC purposes. As in the case of porous Al_2O_3, lithography or nanoimprinting might be used to induce perfect ordering, but this has yet to be shown.

4.3.8 3D photonic crystals made of InP and GaAs

The results discussed above were obtained at potentiostatic conditions. At galvanostatic conditions, a new phenomenon is observed which is potentially useful for 3D PhC's: Self–induced voltage and pore diameter oscillations [59]. These (perfectly synchronized) diameter oscillations provide a certain periodicity in the third direction and a first 3D PhC self induced periodic structure was obtained in this way. [35]. A collage of such a structure is presented in Figure 4.15a. Again, the quality of the self–ordered 3D structure is not good enough to produce PhCs with optical quality, but in connection with externally defined nucleation and resonant diameter oscillations, it may be used for 3D PhCs in the future.

3D structures may also be obtained from crysto pores. An example is presented in Fig. 4.15b for GaAs. Only two $\langle 111 \rangle \, B$ pores nucleate and grow into the substrate from a (100) oriented sample (see the inset in Fig. 4.15b, randomly nucleated pores in this case). First experiments using lithography showed that externally induced order is possible in principle, but more difficult than in n–type Si, since the externally defined pore pitches and the intrinsically preferred length scales must be matched closely.

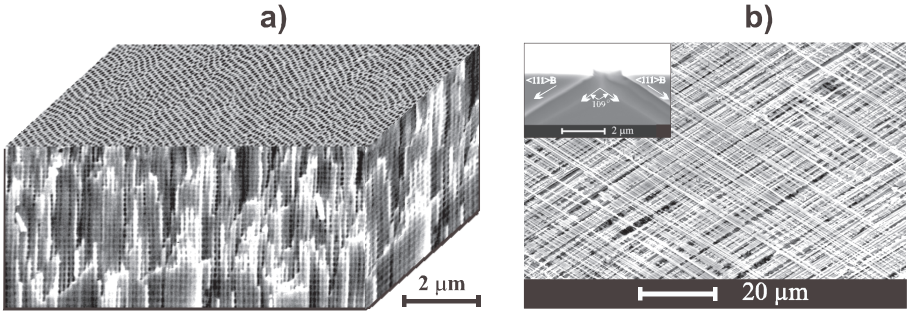

Figure 4.15: **(a)** Curro pores combined with self–induced voltage and diameter oscillations could result in a self–induced 3D structure; collage picture; **(b)** 3D structure on a (100) GaAs sample.

4.4 Summary

In the last ten years, ordered pore arrays with high aspect ratio have been studied extensively. Ordered porous dielectric materials are *intrinsic* 2D photonic crystals. Although there is a large variety of materials exhibiting pores, only silicon, alumina and InP are exhibiting the extremely high pore quality, to date, required in photonic crystal applications. Over the last 5 years, macroporous silicon as an infrared photonic crystal has been described in numerous publications. Porous alumina is a favorable candidate for photonic crystals, operating in the visible and InP for active devices as well as for non–linear optical applications.

Finally, concepts and first realizations of 3D photonic crystals based on macroporous silicon were presented.

All these experiments show that electrochemically–prepared photonic crystals are a model system to study the properties of photonic crystals in the visible and infrared regime as well as for possible technological applications operating in this spectral range.

Acknowledgements

This review article is based on the results of a very fruitful collaboration with M. Agio, A. Birner, K. Busch, M. Christophersen, K. Dichtel, H.M. van Driel, F. Genereux, R. Hillebrand, C. Jamois, S. John, P. Kramper, V. Lehmann, S.W. Leonard, J.P. Mondia, S. Richter, V. Sandoghdar, C. Soukoulis, I.M. Tiginyanu, and P. Villeneuve. We gratefully acknowledge funding within the DFG Schwerpunktprogramm "Photonische Kristalle" SPP 1113.

References

[1] J. D. Joannopoulos, R. D. Meade, J. N. Winn, *Photonic Crystals*, Princeton University Press, New Jersey (1995).
[2] A. Uhlir, Bell System Tech. J. **35**, 333 (1956).
[3] F. Keller, M. S. Hunter, D. L. Robinson, J. Electrochem. Soc. **100**, 411 (1953).
[4] H. Masuda, K. Fukuda, Science **268**, 1466 (1995).
[5] A.-P. Li, F. Müller, U. Gösele, Electrochem. Solid-State Lett. **3**, 131 (2000).
[6] J. Choi, K. Nielsch, M. Reiche, R. B. Wehrspohn, U. Gösele, J. Vac. Sci. Technol. B **21** 763 (2003).
[7] V. Lehmann and H. Föll, J. Electrochem Soc. **137**, 653 (1990).
[8] V. Lehmann, J. Electrochem. Soc. **140**, 2836 (1993).
[9] V. Lehmann, U. Gösele, Appl. Phys. Lett. **58**, 856 (1991).
[10] S. Langa, I. M. Tiginyanu, J. Carstensen, M. Christophersen, and H. Föll, Electrochem. Solid-State Lett. **3**, 514 (2000).
[11] J.-N. Chazalviel, R. B. Wehrspohn, F. Ozanam, Mat. Sci. Eng. B **69-70**, 1 (2000).
[12] P. Allongue, in INSPEC Data series, L. Canham, Editor, IEE (1997).
[13] V. Lehmann, *Electrochemistry of silicon*, WILEY-VCH, Weinheim (2002).
[14] X. G. Zhang, *Electrochemistry of silicon and its oxide*, Kluwer Academic/Plenum Publ., New York (2001).
[15] H. Föll, M. Christophersen, J. Carstensen, and G. Hasse, Mat. Sci. Eng. R 180, 1 (2002).
[16] R. L. Smith and S. D. Collins, J. Appl. Phys. **71**, R1 (1992).
[17] V. Lehmann, R. Luigart, A. Stengl, Mat. Sci. Eng. B **69-70**, 11 (2000).
[18] R. B. Wehrspohn, J.-N. Chazalviel, F. Ozanam, I. Solomon, Thin Solid Films **297**, 5 (1997).
[19] E. K. Propst, P. A. Kohl, J. Electrochem. Soc. **141**, 1006 (1994).
[20] M. M. Rieger, P. A. Kohl, J. Electrochem. Soc. **142**, 1490 (1995).
[21] H. Föll, J. Carstensen, M. Christophersen, G. Hasse, phys. stat. sol. (a) **182 (1)**, 7 (2000).
[22] J.-N. Chazalviel, F. Ozanam, R. B. Wehrspohn, J. Electrochem. Soc. **149**, C511 (2002).
[23] J. Carstensen, M. Christophersen, H. Föll, Mat. Sci. Eng. B **69-70**, 23 (2000).
[24] K. J. Chao, S. C. Kao, C. M. Yang, M. S. Hseu, and T. G. Tsai, Electrochem. Solid-State Lett., **3**, 489 (2000).
[25] S. Rönnebeck, J. Carstensen, S. Ottow, and H. Föll, Electrochem. Solid-State Lett. **2**, 126 (1999).
[26] E. Yablonovitch, T. M. Gmitter, and K. M. Leung, Phys. Rev. Lett. **67**, 2295 (1991).
[27] J. E. A. M. van den Meerakker, R. J. G. Elfrink, F. Roozeboom, and J. F. C. M. Verhoeven, J. Electrochem. Soc. **147**, 2757 (2000).
[28] V. Lehmann and S. Rönnebeck, Sensors and Actuators A **95**, 2757 (2001).
[29] A. Birner, K. Busch, and F. Müller, Phys. Bl. **55**, 27-33 (1999).
[30] H. W. Lau, G. J. Parker, R. Greef, M. Hölling, Appl. Phys. Lett. **67**, 1877 (1995).

[31] J. Schilling, A. Birner, F. Müller, R. B. Wehrspohn, R. Hillebrand, U. Gösele, K. Busch, S. John, S. W. Leonard and H. M. van Driel, Opt. Mater. **17**, 7 (2001).

[32] M. Christophersen, J. Carstensen, A. Feuerhake, H. Föll, Mater. Sci. Eng. B **69-70**, 194 (2000).

[33] T. Chan and S. John, in press Phys. Rev. E.

[34] M. G. Berger, M. Thönissen, W. Theiß, H. Münder, in: M. O. Manasreh (Ed.), *Optoelectronical Properties of Semiconductors and Superlattices*, Vol. 5, Grodon and Breach, Amsterdam (1997).

[35] H. Föll, S. Langa, J. Carstensen, M. Christophersen, I. M. Tiginyanu, Adv. Mater. **15**, 183 (2003).

[36] V. P. Parkhutik and V. I. Shershulsky, J. Phys. D: Appl. Phys. **25**, 1258 (1992).

[37] H. Masuda, F. Hasegawa, S. Ono, J. Electrochem. Soc. **144**, L127 (1997).

[38] H. Masuda, K. Yada, A. Osaka, Jpn. J. Appl. Phys. **37**, L1340 (1998).

[39] K. Nielsch, J. Choi, K. Schwirn, R. B. Wehrspohn, U. Gösele, Nano Lett. **2**, 677 (2002).

[40] S. Thamida, H. Chang, Chaos **12**, 240 (2002).

[41] F. Li, L. Zhang, R. M. Metzger, Chem. Mater. **10**, 2470 (1998).

[42] H. Masuda, H. Asoh, M. Watanabe, K. Nishio, M. Nakao, T. Tamamura, Adv. Mater. **13**, 189 (2001).

[43] J. Choi, R. B. Wehrspohn, U. Gösele, Adv. Mater. (2003), in print.

[44] P. H. L. Notten, J. E. A. M. van den Meerakker, J. J. Kelly, Elsevier Science Publishers Ltd., Oxford (1991).

[45] E. Kukino, M. Amiotti, T. Takizawa, S. Arai, Jpn. J. Appl. Phys. **34**, 177 (1995).

[46] P. Schmuki, L. Santinacci, T. Djenizian, D. J. Lockwood, phys. stat. sol. (a) **182**, 51 (2000).

[47] S. Langa, J. Carstensen, M. Christophersen, H. Föll, I. M. Tiginyanu, Appl. Phys. Lett. **78**, 1074 (2001).

[48] S. Langa, M. Christophersen, J. Carstensen, and H. Föll, Phys. Stat. Sol. (a) **195**, R4-R6 (2003).

[49] S. G. Johnson, S. Fan, P. R. Villeneuve, J. D. Joannopoulos, L. A. Kolodziejski, Phys. Rev. B **60**, 5751 (1999).

[50] D. Labilloy, H. Benisty, C. Weisbuch, T. F. Krauss, R. M. de la Rue, V. Bardinal, R. Houdré, U. Oesterle, D. Cassagne, C. Jouanin, Phys. Rev. Lett. **79**, 4147 (1997).

[51] U. Grüning, V. Lehmann and C. M. Engelhardt, Appl. Phys. Lett. **66**, 3254 (1995).

[52] U. Grüning, V. Lehmann, S. Ottow, K. Busch, Appl. Phys. Lett. **68**, 747 (1996).

[53] R. D. Meade, K. D. Brommer, A. M. Rappe, J. D. Joannopoulos, Appl. Phys. Lett. **61**, 495 (1992).

[54] A. Birner, A.-P. Li, F. Müller, U. Gösele, P. Kramper, V. Sandoghdar, J. Mlynek, K. Busch, V. Lehmann, Mater. Sci. Semicon. Process.**3**, 487 (2000).

[55] S. Rowson, A. Chelnokov, C. Cuisin, J.-M. Lourtioz, J. Opt. A: Pure Appl. Opt. **1**, 483 (1999).

[56] S. W. Leonard, H. M. van Driel, K. Busch, S. John, A. Birner, A.-P. Li, F. Müller, U. Gösele, V. Lehmann, Appl. Phys. Lett. **75**, 3063 (1999).

[57] F. Müller, A. Birner, U. Gösele, V. Lehmann, S. Ottow, H. Föll, J. Porous Mater. **7**, 201 (2000).

[58] S. Langa, I. M. Tiginyanu, J. Carstensen, M. Christophersen, H. Föll, Appl. Phys. Lett. **82 (2)**, 278 (2003).

[59] S. Langa, J. Carstensen, I. M. Tiginyanu, M. Christophersen, H. Föll, Electrochem. Sol. State Lett. **4**, 50 (2001).

[60] S. W. Leonard, H. M. van Driel, A. Birner, U. Gösele, P. R. Villeneuve, Opt. Lett. **25**, 1550 (2000).

[61] P. Kramper, A. Birner, M. Agio, C. Soukoulis, U. Gösele, J. Mlynek, V. Sandoghdar, Phys. Rev. B **64**, 233102 (2001).

[62] M. Kafesaki and V. Sandoghdar, private communication (2003).

[63] J. Schilling, F. Müller, S. Matthias, R. B. Wehrspohn, U. Gösele, Appl. Phys. Lett. **78**, 1180 (2001).

[64] S. W. Leonard, Appl. Phys. Lett. **81**, 2917 (2002).

[65] A. Chelnokov, K. Wang, S. Rowson, P. Garoche, J.-M. Lourtioz, Appl. Phys. Lett. **77**, 2943 (2000).

[66] R. Hillebrand, S. Senz, W. Hergert, U. Gösele, J. Appl. Phys. **94**, 2758 (2003).

[67] O. Toader, M. Berciu, S. John, Phys. Rev. Lett. **90**, 133901 (2003).

[68] R. B. Wehrspohn, J. Schilling, Mater. Res. Bull. **8**, 623 (2001).

[69] J. Choi, Y. Lou, R. B. Wehrspohn, R. Hillebrand, J. Schilling, U. Gösele, accepted J. Appl. Phys. (2003), issue of 15.10.2003.

[70] H. Föll, S. Langa, J. Carstensen, M. Christophersen, I. M. Tiginyanu, K. Dichtel, MRS Proceedings Spring Meeting: Materials and Devices for Optoelectronics and Microphotonics, Editors: R. B. Wehrspohn, S. Noda, C. Soukoulis, and R. März, San Francisco, **L6.4** (2002).

[71] H. Masuda, M. Ohya, K. Nishio, H. Asoh, M. Nakao, M. Notomi, A. Yokoo, T. Tamamura, Jpn. J. Appl. Phys., Part 2: Lett. **39**, L1039 (2000).

[72] H. Masuda, M. Ohya, H. Asoh, M. Nakao, M. Notomi, T. Tamamura, Jpn. J. Appl. Phys., Part 2: Lett. **38**, L1405 (1999).

5 Optical properties of planar metallo–dielectric photonic crystals

Andre Christ, Stefan Linden, Thomas Zentgraf, Kai Schubert, Dietmar Nau, Sergei G. Tikhodeev, Nikolai A. Gippius, Jürgen Kuhl, Florian Schindler, Alexander W. Holleitner, Joachim Stehr, Jana Crewett, John Lupton, Thomas Klar, Ullrich Scherf, Jochen Feldmann, Christian Dahmen, Gero von Plessen, and Harald Giessen[1]

5.1 Introduction

In most photonic crystals, the constituent materials are non–absorptive. However, a considerable amount of research has been done in recent years on photonic crystals where one of the constituents is a metal [1, 2]. Such structures may consist, e.g, of two– or three–dimensional regular arrangements of metal rods or metal spheres, surrounded by air or embedded in some transparent dielectric. Such metallo–dielectric photonic crystals have large omni–directional band gaps, with gap energies in excess of those that can be achieved with transparent dielectric materials [3–5]. This is a consequence of the large dielectric modulations $\Delta\varepsilon$ that are possible when metallic and dielectric constituents alternate. Metallo–dielectric photonic crystals have also shown to support well-defined defect modes [6, 7] and to cause negative refraction of light [8]. A potential problem for metallo–dielectric photonic crystals is the lossy character of the metal. This problem is considered to be negligible at microwave or radio frequencies, where the metal behaves as an almost perfect conductor and the fields do not penetrate substantially into the metal. Larger dissipative losses are expected at optical frequencies but may be minimized in certain situations [4, 9].

Among metallo–dielectric photonic crystals, *planar (quasi-2D)* structures have exceptional properties. Such structures are realized, e.g., in the form of metal films whose surface profile or coverage is periodically modulated, on length scales comparable to optical wavelengths [10–12]. This class of metallo–dielectric photonic crystals also includes regular arrays of holes in metal films, which have recently gained a lot of interest due to their anomalously large light transmission [13–16]. The special properties of planar metallo–dielectric photonic crystals are a consequence of the presence of *surface-plasmon polaritons* (SPPs). These mixed plasmonic–photonic excitations consist of propagating, longitudinal electron–density waves, that are accompanied by electromagnetic fields along the metal surface [17]. As a result, the photonic band structure caused by the periodic surface modulation obtains a polaritonic character which can be observed, e.g., in angle–resolved light absorption experiments [11, 13]. Besides SPPs, optical experiments on planar metallo–dielectric photonic crystals also reveal pure diffraction phenomena, such as *Rayleigh anomalies* (also known as *nonresonant Wood*

---

[1] Corresponding author: e-mail: giessen@iap.uni-bonn.de, Phone: +49 228 73 3459, Fax: +49 228 73 9827

Photonic Crystals. Edited by K. Busch, S. Lölkes, R. B. Wehrspohn and H. Föll
Copyright © 2004 Wiley-VCH Verlag GmbH & Co. KGaA
ISBN: 3-527-40432-5

anomalies), which occur when a diffracted light order becomes tangent to the photonic crystal plane, resulting in abrupt changes in optical reflection and transmission [17].

Metallo–dielectric photonic crystals usually incorporate a continuous metal film for SPP propagation. A different situation is present in planar arrays of noble–metal nanoparticles on dielectric substrates. Such nanoparticles are very strong light scatterers at the frequency of the particle plasmon resonance [18–21]. This resonance is associated with the localized dipolar oscillation of the conduction electrons in the nanoparticle. In the absence of a connecting metal film, mutual electromagnetic coupling of the nanoparticles would be required for the existence of extended, propagating plasmon modes and hence of a plasmonic–photonic band structure. While in arrays of close–lying nanoparticles with center–to–center spacings of $\sim$ 100 nm, near–field dipole–dipole coupling between particles is sufficient to give rise to extended plasmon modes [23]. It is an intriguing question to ask whether they also exist in nanoparticle arrays with wider spacings comparable to the wavelength of light, i.e., several 100 nm. Even if near–field coupling may be too weak under such conditions, far–field scattering of the light field may still provide sufficient coupling between the particles. Indeed, it has been shown recently, that under conditions where Rayleigh anomalies occur, the particle plasmons in nanoparticle arrays with wide spacings couple to light diffracted by the array. This leads to characteristic modifications of the spectral properties of the particle–plasmon resonance [24].

In this contribution, we investigate the optical properties of planar arrays of noble-metal nanoparticles on dielectric substrates. They consist of nanodisks or nanowires deposited by electron–beam lithography and have typical diameters of 100 nm, and center–to–center spacings on the order of several 100 nm. We show here that the collective interaction of the nanoparticles with the light field leads to interesting diffraction phenomena which strongly modify the optical properties of the nanoparticles with respect to the single–particle case. Our contribution has the following structure: In Section 5.2, we characterize the individual gold nanodisks using light–scattering spectroscopy. The particle plasmon is observed as a pronounced maximum of resonantly scattered light. In Section 5.3, angle–resolved reflection and transmission experiments are carried out on planar arrays of silver and gold nanostructures, deposited on glass or quartz. We find spectral features which can be explained as being associated with Rayleigh anomalies. In Section 5.4, we investigate gold nanodisk and nanowire arrays deposited on indium–tin–oxide waveguide layers. Polariton–type coupling to a waveguide mode (waveguiding anomaly), controllable transmission properties, and prolonged dephasing times of the particle–plasmon resonance are some of the new properties of these structures. Finally, in Section 5.5, we present results demonstrating that metallic nanodisk arrays can be used as substrates for organically distributed feedback lasers. Section 5.6 summarizes the results.

5.2 Optical characterization of individual gold nanodisks

The noble–metal nanodisk arrays investigated in this work were fabricated by standard electron-beam–lithography on glass substrates, covered with a very thin ($\sim$ 20 nm) indium–tin–oxide (ITO) layer [24]. The conducting ITO layer is necessary for avoiding the charging of the substrate during the electron exposure step in the fabrication process. The nanodisks studied

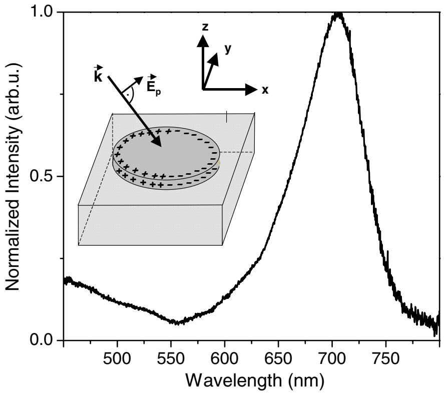

Figure 5.1: Scattered–light spectrum of a single gold nanodisk using dark–field microscopy. Inset: Sketch of the charge oscillation associated with a particle plasmon in a metal nanoparticle. The conduction electrons perform in–plane oscillations, resonantly driven by a p–polarized light field. Excitation of the perpendicular in–plane oscillation by s–polarized light is also possible (not shown here).

here have a diameter of 130 nm and a height of 30 nm. The optical properties of selected individual nanodisks are investigated using dark–field microscopy as described in Ref. [19]. For this purpose, single gold nanodisks were deposited at a large separation from the arrays, in order to resolve them in the far–field microscope. The scattered light from a single nanodisk is focused with the microscope onto the entrance slit of a spectrometer, coupled to a sensitive, cooled CCD camera [19]. Figure 5.1 shows the result of such a measurement. The intensity maximum at 700 nm is caused by light that is resonantly scattered by the long–axis particle–plasmon resonance of the nanodisk. This resonance is associated with the in–plane oscillation of the conduction electrons, as schematically shown in the inset of Figure 5.1. The particle–plasmon resonance associated with the out–of–plane oscillation is not clearly observed in the experiment, since it has a much smaller scattering cross section and radiates preferentially away from the microscope objective. The rising intensity towards shorter wavelengths is attributed to the interband absorption between the 5d and the 6sp bands of gold.

5.3 Observation of Rayleigh anomalies in metallo-dielectric nanostructures

This section summarizes the results of optical reflection and transmission experiments on planar silver and gold nanostructure arrays with spacings on the order of several 100 nm. We find evidence for Rayleigh anomalies which coexist with the particle–plasmon resonances of the individual nanoparticles.

5.3.1 Metallic nanoparticle arrays

Planar arrays of silver and gold nanodisks were fabricated by electron–beam lithography on glass substrates covered with a thin (20 nm) ITO layer [24]. Like in Section 5.2, the nanodisks have a diameter of 130 nm and a height of 30 nm. The elementary cell is quadratic and the center–to–center spacing is 350 nm. The topography of a gold nanodisk array is shown in the scanning electron microscopy (SEM) image in Fig. 5.2a. Each array covers an area of 140 × 140 μm^2. The principle of the experiment is illustrated in Figure 5.2b. The array is illuminated with polarized light from a white–light lamp under a variable angle of incidence θ, and specular reflection spectra are taken with a fiber spectrometer for each θ. The plane of incidence is parallel to one side of the quadratic elementary cell, as shown schematically in Figure 5.2b, meaning that $\mathbf{k}_{\|}$, the in–plane component of the wave vector of the incident light, is oriented along the Γ–X direction in reciprocal space. In addition, spectra are also taken on the gold array with the array rotated through an azimuthal angle of 45° around the surface normal, i.e., $\mathbf{k}_{\|}$ is in the Γ–M direction.

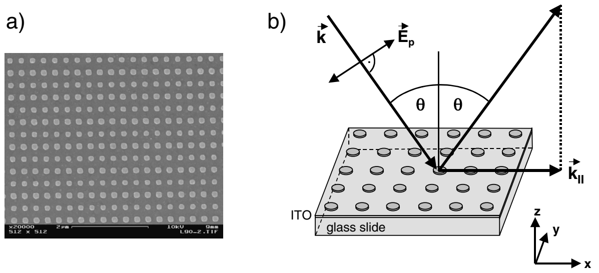

Figure 5.2: **(a)** Scanning electron microscopy (SEM) image of a gold nanodisk array. **(b)** Principle of the angle–resolved optical reflection experiment. Light with wave vector **k** (in–plane component $\mathbf{k}_{\|}$) is incident on a square array of metal nanodisks at an angle θ. The intensity of the zeroth diffraction order emitted in the specular reflection direction is measured.

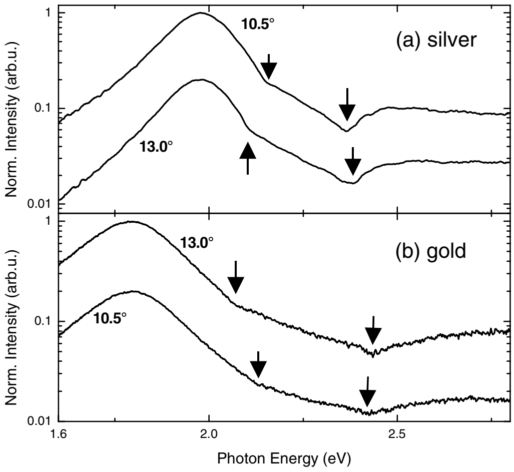

Figure 5.3: **(a)** Specular reflection spectra taken with p-polarized light on a silver nanodisk array at $\theta = 10.5°$ and $13°$, respectively. The spectra are normalized to one and offset with respect to each other for clarity. Minima are indicated by arrows. **(b)** Same measurements for a gold nanodisk array.

Figure 5.3a shows two specular reflection spectra taken with p-polarized light on a silver nanodisk array at $\theta = 10.5°$ and 13°, respectively. The pronounced maximum at approximately 2.0 eV is caused by light that is scattered by the particle-plasmon resonance, in the direction of specular reflection. The resonance is associated with the conduction electrons oscillating in the x-direction (cf. inset of Figure 5.1).

In Figure 5.3a, a reflectance continuum due to intra- and interband excitations is observed above the particle-plasmon resonance. This continuum exhibits several minima, as indicated by the arrows. Although not very pronounced, these minima are not caused by experimental noise; they are observed at all angles of incidence studied here, and their energetic positions vary systematically with θ. This systematic variation is displayed in Figure 5.4a, where the energies of the minima are shown as a function of the in-plane component of the wave vector of the incident light, $|\mathbf{k}_{\|}| = |\mathbf{k}| sin\theta$. Some minima are even found in the spectral range of the particle-plasmon resonance, where they are observed as small dips or kinks in the resonance maxima. We note that these minima are also found in spectra taken with s-polarized light.

For comparison, Figure 5.3b shows two typical specular reflection spectra from gold nanodisk arrays, taken at θ = 10.5° and 13°, respectively. As indicated by the arrows, the minima are also observed here; they are, however, less pronounced than those in the spectra from silver arrays, making identification ambiguous in some cases. Figure 5.4 (right) shows the energetic positions of all minima that can be identified clearly.

In the following, we will discuss the physical origin of the minima in the reflection spectra. Coupling to waveguide modes in the ITO layer, as described in Section 5.4 cannot explain the minima, since the ITO layer in these samples is too thin to support waveguide modes in the spectral range investigated here. The thickness of 20 nm translates into a cut–off photon energy of 5.11 eV, below which no light modes can be guided in it. Another conceivable explanation for the reflection minima observed here, could be SPPs. Pronounced minima in specular reflection spectra, with energy–wavevector dispersions somewhat similar to ours, have been observed on gratings consisting of metal films with periodic modulations of the surface profile [11]. These minima are the result of light absorption by SPPs. However, SPPs on gold surfaces are expected to be strongly damped and thus difficult to observe above 2.4 eV, due to their coupling to 5d-6sp interband transitions. The fact that the minima we observe above this energy in the spectra from the gold nanodisk arrays are not less pronounced than those below 2.4 eV, casts some doubt on an explanation of our minima in terms of SPPs.

We will now discuss the possibility that our reflection minima are caused by *Rayleigh anomalies*. This phenomenon is a diffraction effect observed on gratings when a diffraction order is tangent to the grating plane. When the incident angle, or the wavelength, is varied such that this diffraction order ceases to be tangent and disappears, its intensity will be redistributed among the remaining diffraction orders. This results in abrupt changes of the zero–order reflected intensity. Therefore, the Rayleigh anomaly usually shows up as a cusp–like change of the specularly reflected intensity, upon variation of the angle of incidence or wavelength. To check whether the energies of the minima in our spectra are consistent with Rayleigh anomalies, we compare the experimental dispersion relations in Figure 5.4 with the results of a simple empty–lattice model calculation. Following Ref. [14], the dispersion of the Rayleigh anomalies in a two–dimensional planar grating obeys the relation $|\mathbf{k}_{\|} + m\mathbf{g}_x + n\mathbf{g}_y| = \sqrt{\varepsilon_2} \cdot \omega/c_0$. Here m and n are integers denoting the diffracted order tangent to the surface, $\mathbf{g}_x$ and $\mathbf{g}_y$ are the basis vectors of the reciprocal lattice with length $2\pi/a$, ε_2 is the dielectric constant of the adjacent medium, ω is the frequency, and c_0 is the vacuum speed of light. This equation is solved for $\mathbf{k}_{\|}(\omega)$ to obtain energy–momentum pairs that can be compared with those in Figure 5.4. ε_2 is determined by fitting the calculated energy–momentum pairs to the experimental ones in Figure 5.4. The results of this procedure are shown as solid lines in Figure 5.4 for $\varepsilon_2 = 2.3$, which is consistent with the expected dielectric constant of the glass substrate. There is reasonable agreement between calculation and experiment over the whole k–space region sampled in the experiment. This agreement supports an interpretation

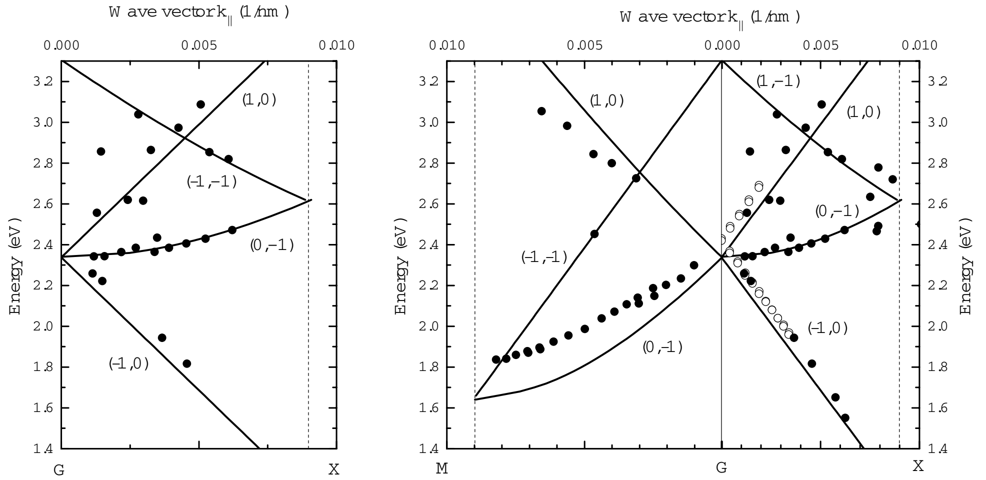

Figure 5.4: (left) Energies of the reflection minima from the silver nanodisk array as a function of the in–plane component of the wave vector of the incident light, $\mathbf{k}_{||} = |\mathbf{k}| \sin\theta$, along the Γ–X direction in reciprocal space. The solid lines show the calculated positions of the Rayleigh anomalies. The pairs of numbers refer to m and n, respectively. **(right)** Same plot for the gold nanodisk array. Here the minima obtained in the Γ–M direction are also shown. The empty circles show the results of a scattering matrix calculation for a dielectric ITO nanowire array.

of the observed reflection minima in terms of Rayleigh anomalies. Additional support for this interpretation comes from scattering matrix calculations of extinction spectra, performed for one–dimensional dielectric ITO nanowire gratings on quartz with the same spatial period as that of our gold nanodisk arrays (cf. Section 5.3.2). The spectral positions of the Rayleigh anomalies determined from these calculated spectra are shown as empty circles in Figure 5.4. They show good agreement with the two respective branches of the experimental dispersions. We conclude that the reflection minima observed in the experiment must be due to Rayleigh anomalies rather than surface-plasmon polaritons.

5.3.2 Metallic nanowire arrays

In addition to results on two–dimensional gold nanostructure arrays, one–dimensional planar structures have been investigated. The simpler one–dimensional geometry can be very advantageous for highlighting the diffraction phenomena observed in the previously discussed nanodisk case. For example, a one–dimensional metallic system gives us the possibility to turn off the particle plasmon resonance by rotating the light polarization by 90°. Gold nanowire gratings were fabricated by electron-beam lithography on top of 15–nm–thick ITO layers, deposited on a quartz substrate. Figure 5.5 shows the schematic arrangement of our sample structure and the measurement geometry. For all measured transmission spectra, the ITO thickness of L_z = 15 nm, the grating height of 20 nm, and the wire width of 100 nm were kept fixed, whereas the grating period a_x was varied between 250 nm and 650 nm. Each measured nanograting covers an area of 100 × 100 μm^2.

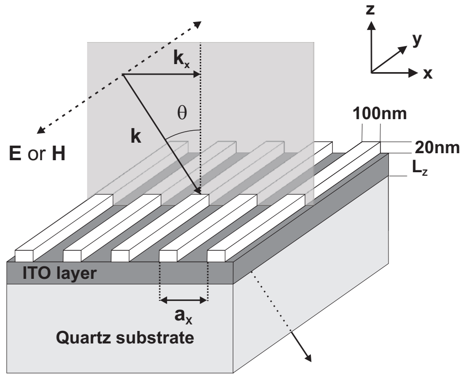

Figure 5.5: Schematic view of the gold nanowire array on top of a thin ITO layer. Measurements with electric (s–polarization) or magnetic (p–polarization) field parallel to the nanowires are possible.

For the theoretical description of the optical properties of the one–dimensional system, we used the scattering matrix based method presented in [25, 26]. Within this method, the electromagnetic field is decomposed into plane waves on a subset of Bragg vectors in reciprocal space, with momenta $k_{g,x} = k_x + g_x,\ g_x = 2\pi g/a_x,\ g = 0, \pm1, \pm2, ... \pm G$ (the decomposition is truncated at $N_G = 2G+1 = 301$ for p and $N_G = 49$ for s–polarization). The in–plane component of the wave vector of the incident light is given by $k_x = \omega \sin\theta / c_0$, where ω and θ are the incoming photon frequency and the angle of incidence, respectively. There were no fitting parameters used in the theory, and the dielectric function of gold was taken from Ref. [27]. The ITO dispersion was taken into account as well.

Figure 5.6a shows a series of measured and calculated extinction spectra ($-ln(\mathrm{I}_t/\mathrm{I}_0)$) for different grating periods at normal incidence. Spectra for s– (electric field parallel to the nanowires) and p–polarization (magnetic field parallel to the nanowires) are depicted for each period. From top to bottom, the nanowire period is increased from 350 nm to 500 nm in steps of 50 nm. Uncertainties in the exact experimental determination of the nanowire geometry and of the grating period, lead to minor deviations between experimental and theoretical results. Thus, instead of the assumed 20 nm (experiment), all calculations shown in Section 5.3.2 were performed for gold nanowires with a height of 15 nm. While the wire width of 100 nm has been found to remain unchanged, this minor modification leads to an excellent qualitative agreement between experiment and theory. In contrast to the nanodisk case, no particle plasmon resonance can be found for s–polarized light (E–vector parallel to the nanowires), due to the lack of surface modulation in the y–direction. For p–polarization, a broad resonance centered at approximately 1.85 eV, is observed; it is attributed to an oscillation of the conduction band electrons of the metallic nanowires. This oscillation is perpendicular to the nanowire direction and corresponds to the localized particle–plasmon of the nanodisk case. Furthermore, an additional spectral feature appears, indicated by an arrow. This feature shifts to lower energy with increasing a_x. Although differently pronounced in s– and p–polarization, the extracted resonance positions do not depend on polarization. However, the spectral shape of this grating anomaly seems to be very sensitive with respect to the spatial distribution of the electromagnetic field in the vicinity of the particle plasmon resonance. Due to the highly dispersive behavior of these grating anomalies, a strong modification of the plasmon resonance can be observed in case of p–polarization and spectral overlap between particle plasmon and the grating anomaly.

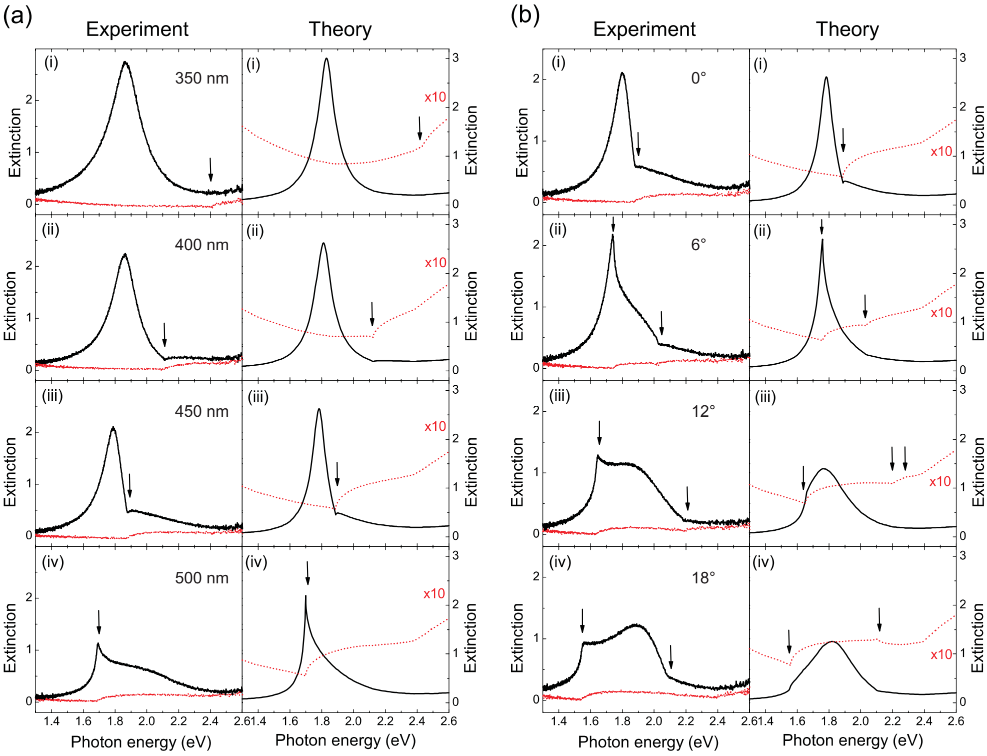

Figure 5.6: **(a)**: Measured (first column) and calculated (second column) extinction spectra for different nanowire gratings at normal incidence. Spectra for s (dotted line) and p (solid line) polarization are shown. From top to bottom, the nanowire period a_x is increased from 350 nm to 500 nm in steps of 50 nm (**(i)**–**(iv)**). **(b)**: Measured (first column) and calculated (second column) extinction spectra for different angles of incidence and a fixed nanowire period of 450 nm. Spectra for s (dotted line) and p (solid line) polarization are shown. From top to bottom, the angle θ is increased from 0° to 18° in steps of 6° (**(i)**–**(iv)**). In **(a)** and **(b)** calculated spectra for s–polarization are drawn to a larger scale. Diffraction anomalies are indicated by the arrows.

Figure 5.6b shows the angle-resolved extinction spectra for different angles of incidence and a fixed nanowire period of 450 nm. The incidence angle θ is increased from 0° to 18° in steps of 6°. Again, measured and calculated spectra are included for comparison. The oblique incidence leads to a splitting of the spectral feature which was unsplit at normal incidence. Then the angle–resolved dispersion of the observed anomalies can be extracted. Considering the spectra for p–polarization only, a strong angle dependent modulation of the plasmon shape and width becomes visible again, similar to the earlier case of normal incidence and various grating constants.

The physical origin of all spectral modifications, as depicted in Figure 5.6, can be explained by the well known Rayleigh anomalies [24]. As discussed in Section 5.3.1, these anomalies are based on diffractive effects when a diffraction order becomes tangent to the

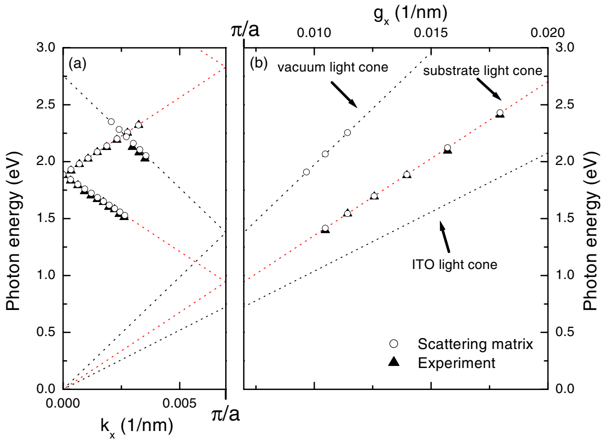

Figure 5.7: Positions of all spectral anomalies extracted from Figure 5.6. The dependence on k_x **(a)** and g_x **(b)** is shown. The dotted lines mark the dispersion of the light cones expected for vacuum, quartz and ITO. For substrate and air light cones, the folded branches are depicted also. For the angle resolved measurements, a period of a = 450 nm was chosen.

grating plane. To verify the interpretation of our results, measured and calculated dispersion relations are depicted in Figure 5.7. The dependencies on k_x (panel a) and g_x (panel b) are included in this figure. The exact positions of all spectral anomalies have been extracted from measured and calculated extinction spectra. The dispersions of angle– and period–dependent spectral anomalies show an excellent agreement with a simple calculation using a one–dimensional empty–lattice approximation. Within this approximation, the dispersion of the Rayleigh anomalies can be traced by the different light cones, assuming $n = 1.9$ for ITO and $n = 1.46$ for the quartz substrate. The depicted light cones specify the exact positions where the light fields change from evanescent to radiative character. Based on the excellent agreement of this fit, the interpretation as Rayleigh anomalies seems to be reasonable. Another important fact that indicates the correctness of our interpretation as a diffractive phenomenon, is the absence of any polarization dependence. Although the particle plasmon resonance exists for p–polarization only, all other spectral features can be found at identical spectral positions for s– and p–polarization. This means that the particle plasmons of the metal wires play no role in the observation of this effect.

In principle, parts of our measurements on periodic metallic nanostructures show spectral effects somewhat similar to the results already shown in Ref. [24]. In this publication, diffractive effects leading to modified widths and energy positions of the particle–plasmon resonance in extinction spectra, were discussed in terms of dipolar particle interaction. Surprisingly, this former contribution exhibits none of the sharp spectral features observed in our work, although comparable measurement techniques were used. The reason is most likely our use of a narrow pinhole for a high angular selectivity.

5.4 Waveguide–plasmon polaritons: Strong coupling in a metallic photonic crystal

In contrast to Section 5.3, where modifications of the particle plasmon resonance are discussed in terms of diffractive Rayleigh anomalies, this section will give an extensive survey of strong coupling effects, leading to the formation of a waveguide–plasmon polariton. In particular, we show that the interaction of electronic and photonic resonances of metallic photonic crystals can lead to impressive modifications of their optical response. In addition to potential technical applications of such active photonic structures, the observed photonic effects are very important from a fundamental point of view: a controlled tailoring of the light–matter interaction becomes possible.

5.4.1 Metallic nanoparticle arrays on dielectric waveguide substrates

One important realization of an active photonic nanostructure is the metallic photonic crystal slab structure (PCS), which offers insight into a new class of light–matter interaction phenomena. In order to observe coupling phenomena of photonic and electronic resonances, optical modes have to be supported within the metallic nanostructure. We achieve this requirement by a suitable dielectric waveguide underneath regular arrays of gold nanodisks. This new metallic slab structure can be considered as a planar optical microcavity, providing plasmon and waveguide resonances simultaneously. If the period of the nanodisk array is appropriately chosen and if the slab waveguide is able to support waveguide modes, strong coupling between the waveguide mode and gold nanodisks will occur [21]. For a particular choice of parameters, the optical waveguide resonance will energetically coincide with the localized particle plasmon resonance of the gold disks. This will lead to the formation of a new quasiparticle, a waveguide-plasmon polariton.

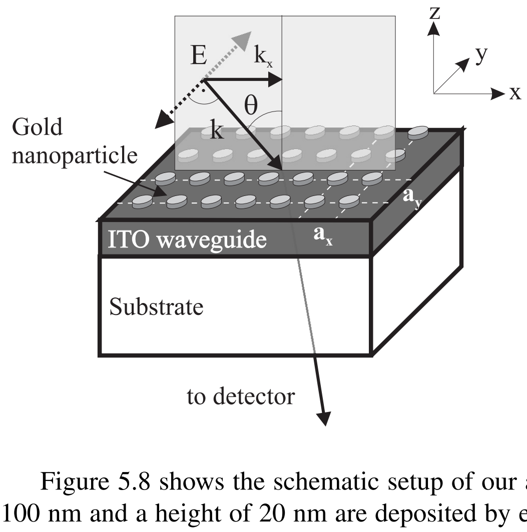

Figure 5.8: Experimental setup and measurement geometry. Samples with different grating period a_x and waveguide thickness are investigated.

Figure 5.8 shows the schematic setup of our arrangement: gold disks with a diameter of 100 nm and a height of 20 nm are deposited by electron-beam lithography and a subsequent lift-off process, on a 140–nm–thick indium tin oxide (ITO) slab waveguide. The whole assembly is fabricated on a quartz substrate. The gold dot arrays have a size of 100×100 μm^2. The spectroscopic setup consists of a white–light halogen lamp, a beam collimation system, a polarizer, a pinhole, two microscope objectives, and a spectrometer with a cooled CCD–camera. The pinhole is essential for limiting the numerical aperture of the probing beam, to a very small value to restrict the angular dispersion of the beam to a minimum. The sample was mounted on a rotation stage to measure the angular dispersion of the transmission properties.

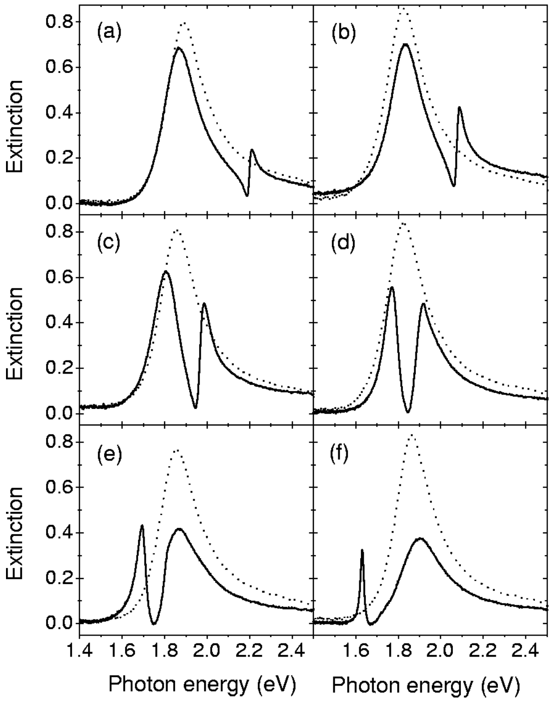

Figure 5.9: Extinction spectra of regular gold nanoparticle arrays (diameter: 100 nm, thickness: 20 nm) for normal incidence and s–polarized light. The quartz substrate is covered with a 140–nm–thick ITO waveguide. Solid lines: Arrays with fixed period a_y=300 nm and periods ranging from a_x = 350 nm to 475 nm in 25 nm steps ((**a**)–(**f**)). Dotted lines: reference array with $a_x = a_y = 300$ nm.

Figure 5.9 (solid line) shows extinction spectra of a series of samples with the wavevector of the light normal to the slab surface. The polarization of the light is parallel to the y–axis of the sample, and the periodicity of the gold nanodisks is 300 nm in y–direction. The period in the x–direction is varied from 350 to 475 nm in steps of 25 nm. The dotted line gives the absorption of a reference spectrum corresponding to an isolated particle plasmon resonance, taken on a reference array with 300 nm × 300 nm periodicity. For a better visibility of the coupling phenomena, the maxima extracted from all measured extinction spectra are plotted in Figure 5.10 in dependence on the grating period. The dashed line marks the positions of the extinction maxima from the reference array. The solid line represents the calculated dispersion of the TE$_0$ mode of an unmodulated ITO slab waveguide.

The reference array with $a_x = a_y = 300$ nm in Figure 5.9 shows the uncoupled particle plasmon resonance. Increasing the distance between the particles allows light to be coupled into a first waveguide mode. The regular array of gold nanodisks acts as waveguide coupler and pronounced maxima arise due to coupling to the first Bragg resonance ($k_x = \pm 2\pi / a_x$) of the TE waveguide modes. Due to the mirror symmetry of our structure, only the upper symmetric quasiguided mode is visible for measurements at normal incidence. For a period

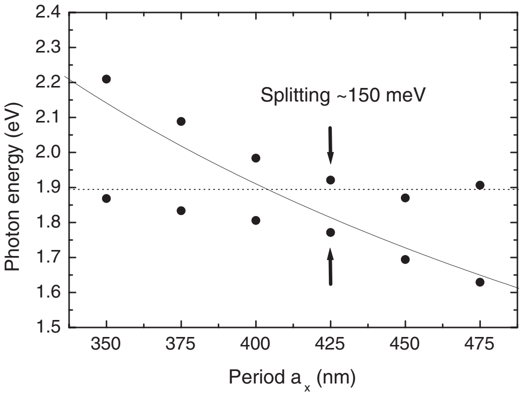

Figure 5.10: Position of the extinction maxima (circles) as a function of the grating period for s-polarized light. All data points are extracted from the measured spectra shown in Figure 5.9. A Rabi splitting of $\sim$150 meV is visible. Solid line: calculated dispersion of the lowest TE_0 waveguide mode for a 140–nm–thick ITO layer. Dotted line: position of the uncoupled particle plasmon resonance.

of 475 nm, the waveguide resonance can be found around 1.62 eV. The position of this waveguide resonance can be shifted by changing the nanodisk period a_x. In our measurements, the waveguide mode energy is close to the particle plasmon energy, and the strong coupling leads to drastic changes of the isolated particle plasmon spectrum. For perfect overlap of the waveguide mode with the particle plasmon mode, a splitting of the extinction spectrum into two branches occurs. This phenomenon is known as normal mode splitting or polariton splitting and can be interpreted as the formation of a new polariton state, comparable to the normal mode splitting in semiconductor microcavities [28]. Considering Fig. 5.10, a splitting of nearly 150 meV between the upper and lower polariton branches is visible. The strongly asymmetric spectral shape of this polariton resonance (see for example Figure 5.9 b) can be attributed to the Fano–type nature of the excited waveguide resonance. Strictly speaking, all of the considered waveguide modes are quasiguided. Thus, their leaky character enables the coupling to the photon continuum.

The waveguide–plasmon splitting and hence the resulting dip in the extinction leads to some remarkable spectral effects: the extinction value drops down to zero, which means in turn that the transmission through the sample (neglecting surface reflections) is nearly 100%. This is remarkable for a metallic (and hence lossy) resonance which is nearly homogeneously broadened. The key for understanding this feature is to realize that we no longer investigate a single metallic particle phenomenon, but rather the extinction of a new compound system, namely a strongly coupled waveguide–plasmon polariton.

The dip in the spectrum can also be understood in a simple electromagnetic model: the light that is re–emitted from the particles into the waveguide, is 180 degrees out of phase with the incident light [21]. This leads to destructive interference and therefore the interaction of the light with the disks is reduced or even turned off for specific wavelengths.

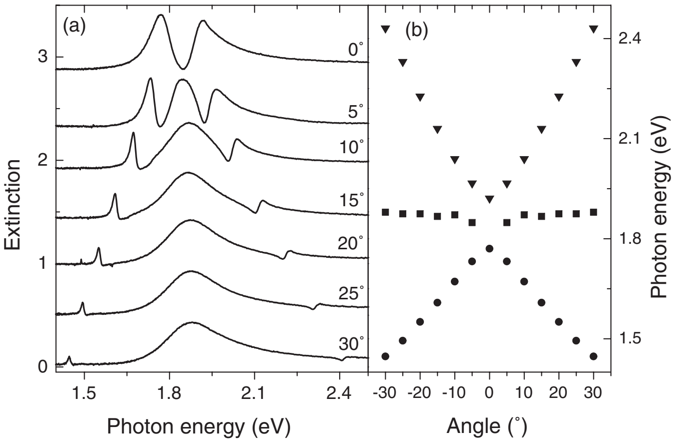

Figure 5.11: **(a)** Measured extinction spectra for light incidence with angles θ from 0° to 20° (grating period: $a_x = 425$ nm and $a_y = 300$ nm). **(b)** Extinction maxima for s-polarized light extracted out of the measurements in **(a)**.

Using Figure 5.11a, we can nicely study the influence of angular dispersion on the extinction properties of our samples. The gold nanodisk sample is rotated about the y–axis in steps of 5 degrees for these measurements. All plotted extinction spectra are recorded with light polarized along the y–axis. In Figure 5.11b, the angular dispersion of the extinction maxima, extracted out of Figure 5.11a, is shown for completeness. Instead of the two extinction maxima at normal incidence (normal modes of the strongly coupled system) a third maximum becomes visible between them for inclined incidence. With increasing angle, the upper and lower polariton modes also shift to higher and lower energies, respectively. The reason for these effects is the lifted degeneracy between the waveguide modes that travel in opposite directions in the waveguide: in a simple picture, we have to add and subtract the grating vector g_x to the wavevector component k_x, yielding two different waveguide propagation vectors $\beta = k_x \pm g_x$ (symmetric and antisymmetric quasiguided modes). Therefore, the particle plasmon resonance interacts with two waveguide resonances at inclined incidence, leading to the observed spectral modifications [29].

5.4.2 Metallic nanowire arrays on dielectric waveguide substrates

So far, we have shown that strong coupling leads to a waveguide–plasmon polariton whose dispersion and polarization properties we can understand. How is it possible to increase the strong coupling even further? Again the answer is to use a nanowire system with localized particle plasmons, that can be excited with light polarized perpendicularly (TM mode) to the wires (see Figure 5.5). Due to the larger spatial overlap between the localized plasmon modes and the waveguide modes, a stronger coupling and therefore a larger polariton splitting compared with the nanodisk case, can be achieved [30, 31]. Another advantage of these nanowire samples is the possibility to turn off the localized particle plasmon resonance. Again, this is easily achieved if the light polarization is directed along the metal nanowires (TE mode). Thus, due to the lack of surface modulation in the y–direction, only the unperturbed TE waveguide mode remains visible and no particle plasmon resonances can be excited.

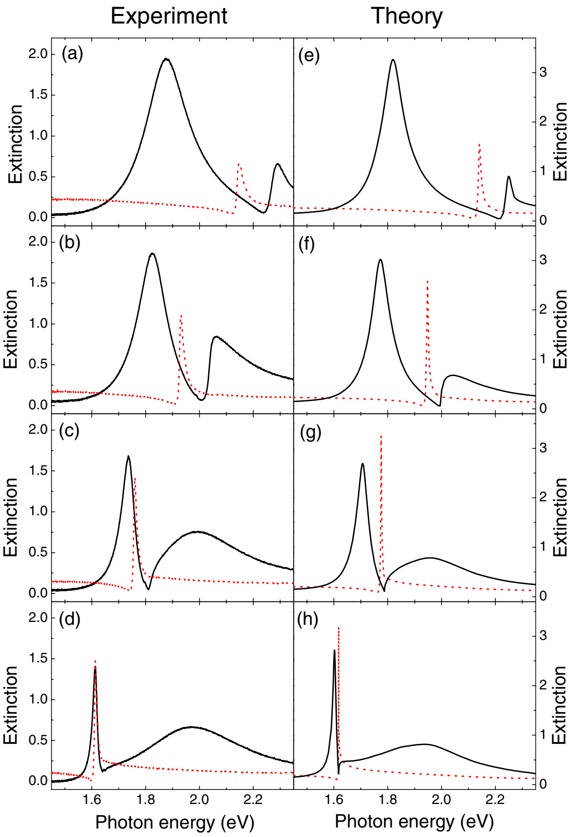

Figure 5.12: Measured (first column) and calculated (second column) extinction spectra for different nanowire gratings at normal incidence. Spectra for TE (dotted line) and TM (solid line) polarization are shown. From top to bottom, the nanowire period a_x is increased from 375 nm to 525 nm in steps of 50 nm (**(a)**–**(d)** and **(e)**–**(h)**, respectively).

Figure 5.12 (first column) shows the experimental results when changing the wire period from 375 nm to 525 nm, in steps of 50 nm. For these measurements, the same setup as in section 5.4.1 was used. Here the one–dimensional gold gratings were prepared on top of 140–nm–thick ITO layers on a quartz substrate. For all measurements, the grating height of 20 nm and the wire width of 100 nm were kept fixed (see Figure 5.5 for a schematic view of the sample structure, now L_z = 140 nm). As mentioned earlier, the particle plasmon resonances of the nanowire arrays can only be excited in TM polarization. Like in the case of metallic nanodisk arrays, the coupling to quasiguided modes gives rise to a strong modulation of the particle plasmon signature. Here the origin of this strong spectral modification can be related to simultaneous excitation of the lowest quasiguided TM mode and the localized particle plasmons of the wires. On the other hand, the sharp spectral feature visible in TE polarization is unambiguously attributed to the excitation of the lowest quasiguided TE mode. With changing periods and for both polarizations, the dispersion of the different modes becomes visible. The second column of Figure 5.12 shows theoretical calculations using the scattering matrix based method [26] as presented in Section 5.3.2. For the calculations presented, a wire width of 100 nm, a grating height of 20 nm, and an ITO thickness of 140 nm have been assumed. The agreement between theory and experiment is excellent. Again it is worth mentioning that no fitting parameters (besides independently measured dispersions of the refractive indices) were used in the theory.

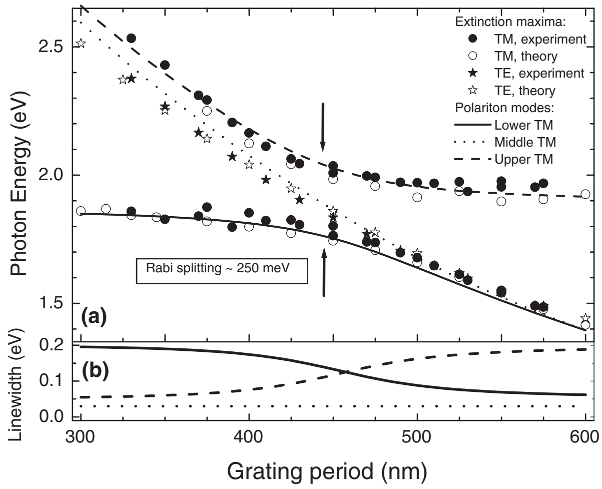

Figure 5.13: Measured and calculated positions of the extinction spectra maxima in TE (stars) and TM (circles) polarization. A Rabi splitting of ∼250 meV is visible. Thick lines are the calculated dispersions of the three TM waveguide–plasmon polariton modes near the center of the 1st Brillouin zone. Real **(a)** and imaginary **(b)** parts of the eigenenergies are shown.

Figure 5.13a demonstrates nicely the large normal mode coupling which can be achieved in such a system depicting the positions of the extinction spectra maxima. The Rabi splitting of the waveguide dispersion and the particle–plasmon dispersion reaches about 250 meV. Due to an increased coupling between the gold nanowires and the waveguide resonance, the measured Rabi splitting exceeds the two–dimensional value by 100 meV (see Section 5.4.1). The solid lines in the plot have been obtained by a theory similar to that describing the behavior of exciton polaritons in semiconductors [31]. Within this model, an effective Hamiltonian (Eq. (5.1)) can be used to calculate the new waveguide-plasmon polariton dispersion from the bare modes.

$$H_{\text{eff}} = \begin{pmatrix} E(K_+ + k_x) & V_1 & V_2 \\ V_1 & E(K_- + k_x) & V_2 \\ V_2 & V_2 & E_{\text{pl}} \end{pmatrix} \tag{5.1}$$

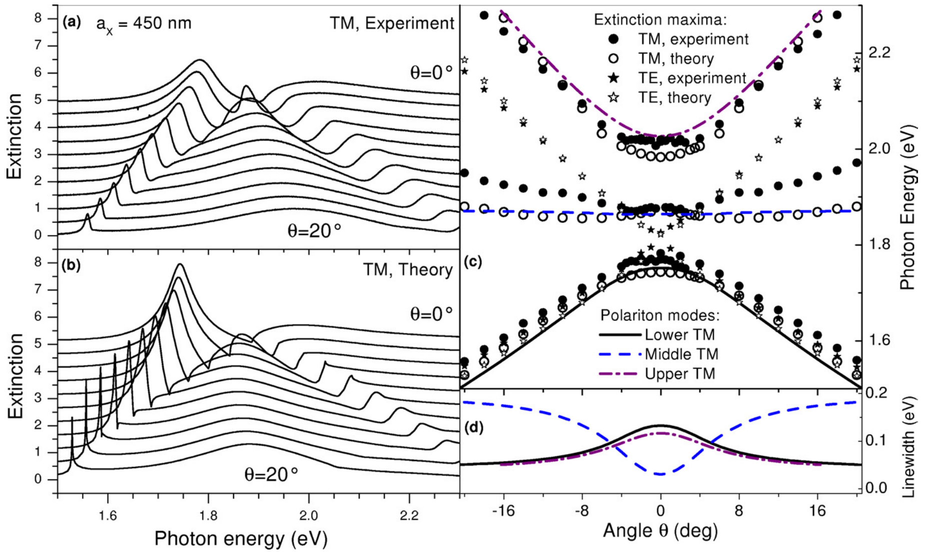

Figure 5.14: Measured **(a)** and calculated **(b)** extinction spectra for a nanowire period of 450 nm. Spectra for different angles of incidence are depicted (θ varies from 0° to 20°). The extracted extinction maxima can be found in panel **(c)**. Thick lines are the calculated dispersions of the three TM waveguide-plasmon polariton modes near the center of the 1st Brillouin zone. Real **(c)** and imaginary **(d)** parts of the eigenenergies are shown.

The diagonal elements are the bare energies of the TM_0 guided modes with momenta $K_\pm + k_x$ ($K_\pm = \pm 2\pi/a_x$) and the individual wire plasmon energy E_{pl}. Although they can in principle be calculated within a microscopic theory, the photonic bandgap halfwidth V_1 of the one–dimensional photonic crystal and the waveguide–plasmon coupling strength V_2 were used as simple fitting parameters. With a slightly modified version of this Hamiltonian (see Ref. [31]), the linewidths of the different polariton branches can also be calculated. In accordance with the experimental results, the calculated linewidths of the different branches (Figure 5.13b) are strongly varying, depending on whether a branch is more plasmon– or more photon–like.

Figure 5.14 shows the angular dependence of the considered resonances. The angle of incidence θ is therefore varied between 0° and 20°. Extinction measurements (a) and scattering matrix results (b) are depicted. When plotting the TE and TM angular extinction maxima (c), one can recognize the dispersion relation with the photonic valence and conduction bands nicely. It should be noted that at normal incidence, a full photonic bandgap (both in TE and TM polarization) independent of polarization, appears. The angular dependence can also be modelled within our simple effective Hamiltonian model [31] with an excellent qualitative agreement. The dispersions and the linewidths of the different polariton branches are shown in Figure 5.14c and d.

5.4.3 Ultrafast dynamics of waveguide-plasmon polaritons

The strong interaction between an optical and an electronic resonance also leads to altered dynamics of the conduction band electrons in the metal nanoparticle. The narrow-band absorption and the near-field enhancement close to the particle is now connected to a long living photonic mode. This coupling enables the controlled modification of optical and electronic phenomena on a femtosecond time scale. The investigation of these features is motivated by their potential application in future sub-wavelength light technology.

The homogeneous linewidth $\Delta\nu_{hom}$ (in cm^{-1}) of a particle-plasmon resonance is determined by the damping γ of the electron plasma oscillation, through the relation $\gamma = \pi c \Delta\nu_{hom}$. This damping can be described by the dephasing time of the collective electron oscillation $T_2 = 1/\gamma$. Typically, dephasing times of single noble metal nanoparticles lie in the sub–10 fs range [19, 20, 32]. In our case, the strong coupling between the waveguide–mode and the particle plasmon leads to two different polariton branches (one which is more photon/waveguide–like and one that is more plasmon–like), and intuitively, these branches should have different dephasing times. Also, polarization modulations should be observable as a time–domain manifestation of the normal–mode coupling.

The experimental setup for the observation of the time–domain behavior is a modified interferometric autocorrelator as it is used for measurements of ultrashort laser pulse durations [33]. We replace the thin BBO crystal for the second-harmonic generation (SHG) by the waveguide–nanodisk sample (see Fig. 5.15a). The electromagnetic field of the laser pulse now interacts with the particle plasmon and leads, together with the electron–plasma oscillation, to a strong field enhancement of the local field E_{loc} at the surface of the particle. Due to these strong fields, a nonlinear material polarization originating from an optical second–order nonlinearity $\chi^{(2)}$ will evolve. One signature of this nonlinear polarization is the generation of photons with twice the frequency (SH). Measuring the SH intensity $I^{2\omega}(\tau)$ as a function of the delay time τ of the two laser pulses, gives the autocorrelation function caused by the transient plasma oscillation of the electrons in the particle:

$$I^{2\omega}(\tau) \propto \int_{-t_d}^{t_d} \left| |E_{loc}(t) + E_{loc}(t-\tau)|^2 \right|^2 dt. \tag{5.2}$$

t_d is the integration time of the detector. Experiments show that the SH intensity for resonant excitation of the particle plasmon is much larger than for off–resonant excitation. This indicates that the obtained SH intensity originates from the plasma oscillation only and not from the lack of inversion symmetry at the surface of the sample substrate. Compared to the nanodisks in Section 5.4.1, the particles on the sample are heart–shaped (Fig. 5.15b), thus breaking centrosymmetry and leading to an enhanced SHG efficiency, without fundamentally changing the parameters of the plasmon polariton.

For simulating the autocorrelation function obtained by the nanoparticle–arrays, a simple oscillator model can be used. The electron-plasma oscillation will be described as a damped harmonic oscillator with the plasmon frequency ω_{pl} and the sum of the two interfering laser pulse fields as a driving force $K(t, \tau)$. Then the plasmon field is defined by:

$$E_{loc}(t, \tau) \propto \int_{-\infty}^{t} K(t', \tau) e^{-\gamma(t-t')} \sin(\omega_{pl}(t-t'))dt'. \tag{5.3}$$

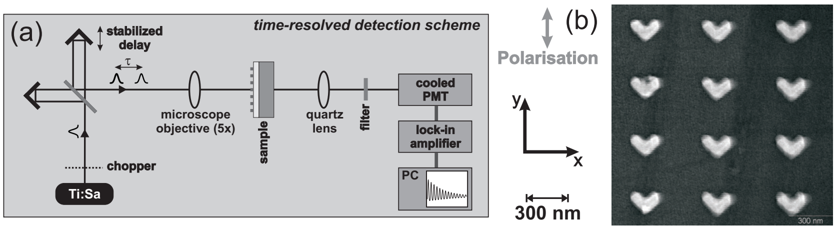

Figure 5.15: **(a)** Experimental setup used to study the polarization decay of waveguide–particle–plasmon polaritons. **(b)** SEM picture showing the noncentrosymmetric shape and arrangement of the nanoparticles.

With this electric field and Equation 5.2, one can calculate the autocorrelation function and compare with the measured one. Here $\gamma = 1/T_2$ is used as a fit parameter.

Figure 5.16 shows first results of the autocorrelation measurements: For reference, the second–order autocorrelation of our 14.5 fs laser pulse in a thin BBO crystal is plotted in Figure 5.16a. Setting the period of our nanodisk array to 300 nm, only the particle plasmon is resonant with the spectral position of the laser pulse (Fig. 5.17a). The slightly broadened autocorrelation function (Fig. 5.16b) can be fitted with a dephasing time T_2 for the particle plasmon that is as short as 6 fs. This is in good agreement with previous measurements [34]. Tuning the period to 400 and 510 nm (Fig. 5.17b) leads to an increased coupling strength between the waveguide mode and the particle plasmon and therefore tunes the lower polariton mode towards the laser wavelength. Examination of the broadened autocorrelation trace in Figure 5.16c leads to an increased dephasing time of 20 fs [35]. For a period of 510 nm, not only the upper polariton mode (plasmon–like) is covered by the laser spectra but also the lower polariton mode (waveguide–like) (Fig. 5.17b). The simple damped oscillator model [32] is, however, not able to fit the decay spectra very well (Fig. 5.16d). Certainly, the more complex dynamics including both branches of the polariton and their different dephasing times, have to be taken into account. Here a more complex model for description is needed. When adjusting the particle period so that the two polariton branches are perfectly resonant with the laser pulse, polariton beats with a period of approximately 20 – 30 fs appear (see Figure 5.16d). This is in nice agreement with the energetic difference between the two polariton branches for this period of approximately 150 – 200 meV.

The coupling of the waveguide mode and the particle plasmon results in a slower dephasing of the collective electron oscillation, if compared with the uncoupled case. The prolonged dephasing time of the polariton can be understood in terms of an increased coupling of the waveguide mode light field to the particle plasmon: due to destructive interference exactly at resonance, the field distribution is expelled out of the nanodisks. Therefore, the main dephasing mechanism of the particle plasmons, namely radiative decay, is reduced. In principle, it should be possible with an appropriate laser linewidth and with suitable tunability of the spectrum, to distinguish the different contributions to the dephasing mechanisms [19].

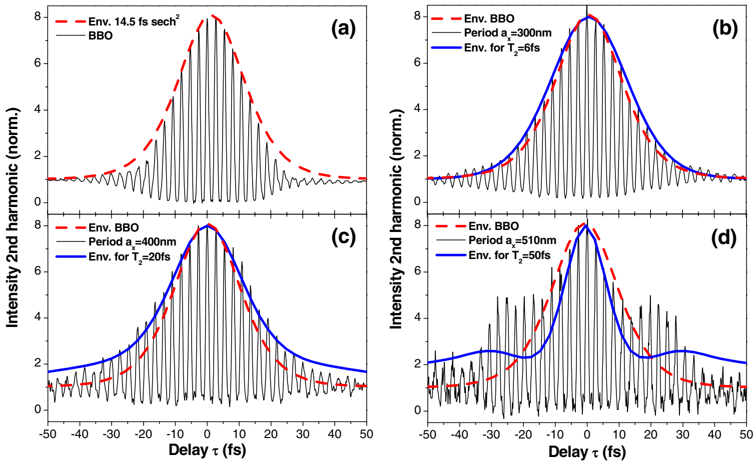

Figure 5.16: Experimental results for the determination of the dephasing time T_2 of the particle plasmon. (**a**) Second order autocorrelation of the driving laser pulse in a 45–μm–thick BBO crystal and (**b**)–(**d**) of the pulses interacting with the nanoparticle arrays with increased coupling to the waveguide modes. Dashed lines denote the envelope of the autocorrelation at the BBO crystal with a pulse length of 14.5 fs. Solid lines mark the fits for the envelope of the nanoparticle field autocorrelations. The fit parameter was the dephasing time T_2 shown in the diagram.

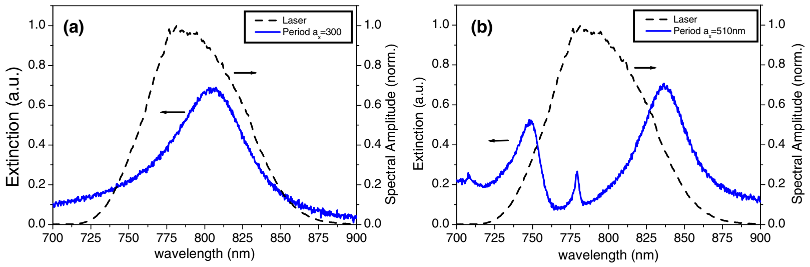

Figure 5.17: Measured extinction spectra for a period of the particles of 300 nm and 510 nm (solid line) and the laser spectra for the 14.5 fs laser pulses (dashed line).

5.5 A polymer DFB laser based on a metal nanoparticle array

This section summarizes experiments that demonstrate optically pumped lasing in a device consisting of a conjugated polymer on top of a gold nanodisk array [36]. The nanodisk array couples to the lasing modes in the polymer, giving rise to distributed feedback (DFB). Although the nanodisks are dissipative energy absorbers, we only find a marginal increase in lasing threshold when compared to conventional dielectric DFB resonators.

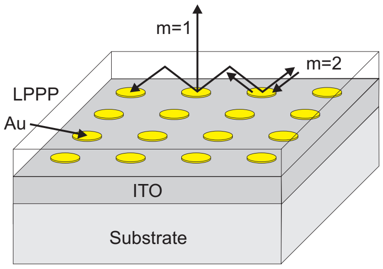

Figure 5.18: Sketch of a polymer (LPPP) film on top of a gold nanodisk array template. Feedback is achieved by second-order ($m = 2$) Bragg scattering while the first order ($m = 1$) scattering couples the lasing mode out in the vertical direction.

Our device consists of a glass substrate coated with a 110-nm-thick ITO layer which is covered by a square array of gold nanodisks (Figure 5.18). The array has a total area of 96×96 μm^2 and is produced by electron beam lithography. The nanodisks have a diameter of 110 nm and a height of 30 nm. Their center–to–center spacing is a = 300 nm. A film of the polymer methyl–substituted ladder–type poly–(para)–phenylene (LPPP) is spin coated onto the sample from toluene solution. Besides offering excellent photophysical properties, this material also has high charge carrier mobilities [37], which make it a suitable candidate for electrically pumped laser devices. The average film thickness, as determined from optical density measurements, is $456{\pm}10$ nm. Figure 5.18 shows a sketch of the sample and illustrates the DFB mechanism, which uses the second order diffraction for feedback and the first order for coupling the light out perpendicularly to the film surface.

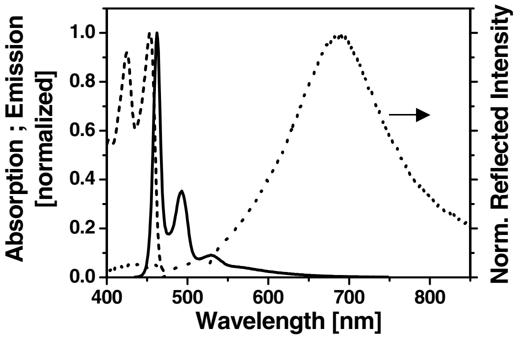

Figure 5.19: Absorption (dashed line) and emission (solid line) spectra of LPPP. Dotted line: Intensity of light reflected by a gold nanoparticle array not covered by LPPP. The pronounced maximum at approximately 690 nm corresponds to light scattered by the particle–plasmon resonance.

The spectral properties of the organic film and the metallic 2D grating can be seen in Figure 5.19, where the absorption (dashed line) and emission (solid line) spectra of LPPP are displayed. The light reflected by a similar gold nanoparticle grating without a LPPP film is shown by the dotted line. The pronounced maximum at approx. 690 nm corresponds to light scattered by the particle plasmon resonance. Note that this particle plasmon resonance and the LPPP fluorescence do not overlap.

For optical pumping of the laser structure, the output of a regeneratively amplified femtosecond Ti:Sapphire laser is frequency doubled, resulting in pulses of 130 fs duration and 400 nm wavelength. The excitation beam is focused onto a spot with a diameter of $470\ \pm\ 5\ \mu$m. The sample is kept under vacuum and the emission is collected in reflection geometry, and spectrally analyzed with a grating spectrometer and a CCD array.

Figure 5.20a shows the first vibronic sideband of the photoluminescence spectrum for three different excitation pulse energies between 1.5 nJ and 2.7 nJ. While an excitation pulse

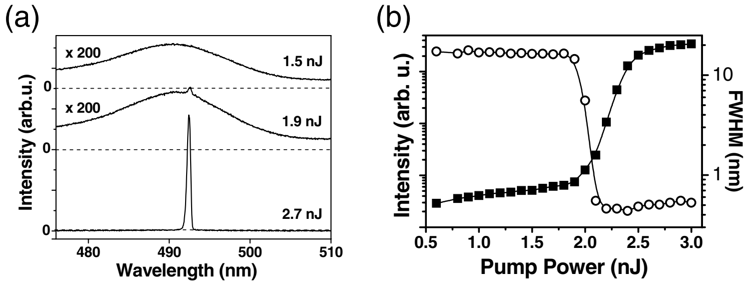

Figure 5.20: **(a)** Emission spectra in the spectral region of the first vibronic sideband of LPPP below, at and above lasing threshold. The pump pulse energies are indicated. **(b)** Plot of the intensity at the laser wavelength (full squares) and full width at half maximum (FWHM) of the emission band (empty circles) versus pump-pulse energy.

energy of 1.5 nJ is well below the lasing threshold, at an excitation energy of 1.9 nJ a small peak emerges at 492 nm. At a pump pulse energy of 2.7 nJ, a clear lasing mode is observed.

Figure 5.20b shows the output power at the laser wavelength versus the pump energy (full squares). A clear laser threshold behavior is observed with a threshold energy of approximately 2 nJ. The surprising result is that this lasing threshold is only a factor of two larger than the lasing threshold for a metal-free LPPP–DFB laser [38]. This is unexpected as the gold nanodisks are prone to quench molecular excitations via energy transfer to the metal and should therefore increase the laser threshold. One possible reason for this result is that the LPPP emission does not spectrally overlap with the nanoparticle plasmon. Moreover, in comparison to metal films, the quenching effect of the gold intraband absorption will strongly be reduced since a large part of this kind of absorption in gold nanoparticles is concentrated at the particle plasmon frequency [18], and since the metal fill factor of the nanoparticle array is smaller than that of metal films. Finally, the gold interband absorption at the LPPP emission energy, which is essentially the same in metal nanoparticles and films, is relatively weak and not expected to contribute significantly to the quenching. Figure 5.20b also shows the full width at half maximum (FWHM) of the emission as a function of pump energy. The figure displays a clear laser threshold behavior with the FWHM shrinking down to 0.44 nm at 2.4 nJ pump pulse energy. A subsequent increase in pulse energy results in a slight line broadening to 0.55 nm at 2.9 nJ, which may be due to excitation of further lateral laser modes. This is also manifested in the saturation behavior of the peak count rate [39].

Next, we address the question of the feedback mechanism in our device. Feedback by DFB structures can, in principle, be established by index–coupling, by gain coupling or a superposition of both resulting in complex coupling. The absence of a stop band in the sub–threshold luminescence spectrum suggests that index coupling plays only a marginal role [39]. This is understandable, as the gold nanodisks are only 30 nm in height, so their volume fill factor is small. We therefore have to consider the imaginary part of the coupling constant as the source of the feedback. At this stage of the research, it is hard to tell whether gain or loss coupling dominates. Usually, in second order feedback DFB devices, the loss is facilitated by first order Bragg scattering into radiation modes. In the case of the gold nanodisk template used in this study, another important loss mechanism has to be taken into account, namely absorption by the gold nanodisks. Gold nanoparticles have been shown to be extremely effective fluorescence quenchers [40], and therefore the quenching processes due to the presence of the gold nanodisks, which should extend well into the LPPP layer, may contribute substantially to the feedback mechanism [41]. Therefore, it is possible that our laser operates on a combination of gain and loss coupling, which would have the same periodicity, whereas conventional lasers usually rely on index coupling. Further research is needed to distinguish between these different coupling mechanisms.

Finally, we should note that it has previously been demonstrated that fabrication of an organic laser on an ITO substrate only slightly increases the laser threshold [42, 43]. By nanostructuring the metal cathode on top of the organic semiconductor and using an ITO bottom contact, it should therefore be possible to achieve a fully contacted laser structure with only a minimal reduction in optical gain.

5.6 Summary

In summary, we have investigated the optical properties of planar arrays of noble–metal nanoparticles on dielectric substrates. They consist of nanodisks or nanowires with center–to–center spacings on the order of several 100 nm.

Angle–resolved reflectivity measurements on arrays deposited on glass, show reflection minima with characteristic energy–momentum dispersions, which are explained as being associated with Rayleigh anomalies.

By enhancing the coupling through a slab waveguide underneath the nanodisks, strongly coupled waveguide–particle–plasmon–polaritons can be created. This coupling leads to a strong modulation of the extinction spectra of the isolated gold disks and can be regarded as normal mode splitting between two polariton modes.

Using nanowires instead of nanodisks yields an even stronger coupling, leading to a normal mode splitting of more than 200 meV. Scattering matrix theory gives an excellent agreement between the experimentally measured and theoretically modelled extinction spectra.

Ultrafast measurements show that the dephasing times of the strongly coupled polariton system can be increased from 6 fs (uncoupled particles) to 20 fs, in the case of coupling between the particle plasmon in the disks and long-living waveguide modes. Polariton beats as clear signature for temporal normal-mode coupling between the two polariton branches, are also observed.

Furthermore, we have shown that a planar photonic crystal of gold nanodisks on ITO can be used as a DFB substrate for organic lasers. Contrary to expectation, the metal does not increase the threshold for lasing significantly compared to purely dielectric gratings. This suggests a method for contacting thin films of organic semiconductors for lasers.

Acknowledgements

This work was supported financially by the German Bundesminister für Bildung und Forschung (FKZ 13N8340/1), the Deutsche Forschungsgemeinschaft (DFG, Priority Program SP 1113) and in partially by the Russian Foundation for Basic Research and the Russian Ministry of Science. The authors are grateful to K. von Klitzing for continuous support.

References

[1] A. R. McGurn and A. A. Maradudin, Phys. Rev. B **48**, 17576 (1993).

[2] E. R. Brown and O. B. McMahon, Appl. Phys. Lett. **67**, 2138 (1995).

[3] D. F. Sievenpiper, E. Yablonovitch, J. N. Winn, S. Fan, P. R. Villeneuve, and J. D. Joannopoulos, Phys. Rev. Lett. **80**, 2829 (1998).

[4] A. Moroz, Phys. Rev. Lett. **83**, 5274 (1999).

[5] J. G. Fleming, S. Y. Lin, I. El-Kady, R. Biswas, and K. M. Ho, Nature **417**, 52 (2002).

[6] E. Özbay, B. Temelkuran, M. Sigalas, G. Tuttle, C. M. Soukoulis, and K. M. Ho, Appl. Phys. Lett. **69**, 3797 (1996).

[7] F. Gadot, A. De Lustrac, J. M. Lourtioz, T. Brillat, A. Ammouche, and E. Akmansoy, J. App. Phys. **85**, 8499 (1999).

[8] E. Cubukcu, K. Aydin, E. Özbay, S. Foteinopoulou, and C. M. Soukoulis, Nature **423**, 604 (2003).

[9] M. J. Bloemer and M. Scalora, Appl. Phys. Lett. **72**, 1676 (1998).

[10] S. C. Kitson, W. L. Barnes, and J. R. Sambles, Phys. Rev. Lett. **77**, 2670 (1996).

[11] U. Schröter and D. Heitmann, Phys. Rev. B **60**, 4992 (1999).

[12] S. I. Bozhevolnyi, J. Erland, K. Leosson, P. M. W. Skovgaard, and J. M. Hvam, Phys. Rev. Lett. **86**, 3008 (2001).

[13] T. W. Ebbesen, H. J. Lezec, H. F. Ghaemi, T. Thio, and P. A. Wolff, Nature **391**, 667 (1998).

[14] H. F. Ghaemi, T. Thio, D. E. Grupp, T. W. Ebbesen, and H. J. Lezec, Phys. Rev. B **58**, 6779 (1998).

[15] J. A. Porto, F. J. Garcia Vidal, and J. B. Pendry, Phys. Rev. Lett. **83**, 2845 (1999).

[16] L. Martin Moreno, F. J. Garcia Vidal, H. J. Lezec, K. M. Pellerin, T. Thio, J. B. Pendry, and T. W. Ebbesen, Phys. Rev. Lett. **86** 1114 (2001).

[17] H. Raether, Surface Plasmons on Smooth and Rough Surfaces and on Gratings, Springer, Berlin, (1988).

[18] U. Kreibig and M. Vollmer, Optical Properties of Metal Clusters, Springer, Berlin, (1995).

[19] C. Sönnichsen, T. Franzl, T. Wilk, G. von Plessen, J. Feldmann, O. Wilson, and P. Mulvaney, Phys. Rev. Lett. **88**, 077402/1 (2002).

[20] T. Klar, M. Perner, S. Grosse, G. Von Plessen, W. Spirkl, and J. Feldmann, Phys. Rev. Lett. **80**, 4249 (1998).

[21] S. Linden, J. Kuhl, and H. Giessen, Phys. Rev. Lett. **86**, 4688 (2001).

[22] K. T. Carron, W. Fluhr, M. Meier, A. Wokaun, and H. W. Lehmann, J. Opt. Soc. Am. B **3**, 430 (1986).

[23] S. A. Maier, M. L. Brongersma, P. G. Kik, and H. A. Atwater, Phys. Rev. B **65**, 193408 (2002).

[24] B. Lamprecht, G. Schider, R. T. Lechner, H. Ditlbacher, J. R. Krenn, A. Leitner, and F. R. Aussenegg, Phys. Rev. Lett. **84**, 4721 (2000).

[25] D.M. Whittaker and I.S. Culshaw, Rhys. Rev. B **60**, 2610 (1999).

[26] S.G. Tikhodeev et al., Phys. Rev. B **66**, 045102 (2002).

[27] P.B. Johnson and R.W. Christy, Phys. Rev. B **6**, 4370 (1972).

[28] C. Weisbuch, M. Nishioka, A. Ishikawa, and Y. Arakawa, Phys. Rev. Lett. **69**, 3314 (1992).

[29] S. Linden, A. Christ, J. Kuhl, and H. Giessen, Appl. Phys. B **73**, 311 (2001).

[30] A. Christ, S.G. Tikhodeev, N.A. Gippius, J. Kuhl, and H. Giessen, phys. stat. sol. (c) **0**, 1393 (2003).

[31] A. Christ, S.G. Tikhodeev, N.A. Gippius, J. Kuhl, and H. Giessen, Phys. Rev. Lett. 91, 183901 (2003).

[32] B. Lamprecht, J.R. Krenn, A. Leitner, and F.R. Aussenegg, Phys. Rev. Lett. **83**, 4421 (1999).

[33] C.-J. Diels, W. Rudolph, Ultrashort Laser Pulse Phenomena (Harlekijn 1996).

[34] B. Lamprecht, J. R. Krenn, A. Leitner, F. R. Aussenegg, Appl. Phys. B **69**, 223 (1999).

[35] K. Schubert, J. Kuhl, and H. Giessen, phys. stat. sol. (c) **0**, 1412 (2003).

[36] J. Stehr, J. Crewett, F.Schindler, R. Sperling, G. von Plessen, U.Lemmer, J. M. Lupton, T. A. Klar, J. Feldmann, A. W. Holleitner, M. Forster, and U. Scherf, Adv. Mat. (in press).

[37] D. Hertel, U. Scherf, and H. Bässler, Advanced Materials **10**, 1119 (1998).

[38] S. Riechel, C. Kallinger, U. Lemmer, J. Feldmann, A. Gombert, V. Wittwer, and U. Scherf, Appl. Phys. Lett. **77**, 2310 (2000).

[39] S. Riechel, U. Lemmer, J. Feldmann, T. Benstem, W. Kowalsky, U. Scherf, A. Gombert, and V. Wittwer, Appl. Phys. B **71**, 897 (2000).

[40] E. Dulkeith, A. C. Morteani, T. Niedereichholz, T. A. Klar, J. Feldmann, S. A. Levi, F. C. J. M. Van Veggel, D. N. Reinhoudt, M. Möller, and D. I. Gittins, Phys. Rev. Lett. **89**, 203002 (2002).

[41] M. Kamp, J. Hofmann, A. Forchel, F. P. Schäfer, and J. P. Reithmaier, Appl. Phys. Lett. **74**, 483 (1999).

[42] V. G. Kozlov, V. Bulovic, P. E. Burrows, M. Baldo, V. B. Khalfin, G. Parthasarathy, and S. R. Forrest, J. Appl. Phys. **84**, 4096 (1998).

[43] M. C. Netti, S. Coyle, J. J. Baumberg, M. A. Ghanem, P. R. Birkin, P. N. Bartlett, and M. Whittaker, Advanced Materials **13**, 1368 (2001).

6 Preparation of 3D photonic crystals from opals

Marc Egen, Rudolf Zentel[1]*, Patrick Ferrand, Stefanie Eiden, Georg Maret, and Frank Caruso*

6.1 Introduction

Three-dimensional Photonic Chrystals (3D PhCs) are materials with a three dimensional periodic variation of the refractive indices. The wavelength of the photons, to be manipulated, is determined by the periodicity of the refractive index modulation: for visible light, it is some hundreds nm and about one μm for IR–radiation. 3D PhC offer a significant advantage over 2D PhC: they allow the full control of light propagation in all three dimensions (see Chapter 1 and 2). In a 3D PhC a "full band gap" may evolve if the magnitude of the refractive index modulation is high enough. In this case, light propagation is prohibited in all directions of the Brillouin zone. This immobilizes photons, changes the density of states inside the photonic material and allows e.g. a modification of light emission by the environment, including a change of the lifetime of excited states. In addition, properties like lasing at a very low threshold [1] are predicted for such materials.

3D photonic structures are, however, more difficult to prepare than 2D PhCs, since they need a patterning in all three dimensions. 2D PhCs are – usually – made by processes known from silicon technology, which include either (i) lithography and deep etching or alternatively, (ii) electrochemical processes (see Chapter 4). However with these techniques, it becomes very difficult to control a periodic structure in the depth. Therefore, the preparation of 3D photonic crystals is dominated by techniques like the self–assembly of preformed objects. Alternatively, a 3D photo processing of polymers by holography (see Chapter 9) or confocal microscopy [2, 3] can be used.

In this article, we will describe artificial opals [2–17], which are made by a crystallization (self–assembly) of preformed colloids or beads, into a face centered cubic packing (FCC). Since the diameter of the constituent colloids or beads lies in the range of several hundred nm, these three dimensional periodic structures are able to reflect visible light, which matches their lattice constants. The constituent beads are thereby composed of SiO_2 (artificial opals) or, more recently, of polymer beads (polymer opals). Since the refractive index of these building blocks is always below 1.6, no full band gap is possible. In addition, the high filling factor of the high refractive index component (74% for a FCC packing), makes the necessary refractive index contrast unrealistically high. A full band gap may, however, become possible for replica of these materials [8–11, 13, 18–29] (filling factor 26%) with high refractive index inorganics. The primary opals will then serve as an intermediate step, which gives the desired periodicity and which allows patterning[2].

---

[1] Corresponding author: e-mail: zentel@mail.uni-mainz.de. http://staudinger.chemie.uni-mainz.de/akzentel.

[2] Natural and artificial opals are basically the same. Natural opals, however, are locally heterogenous, as they are

Photonic Crystals. Edited by K. Busch, S. Lölkes, R. B. Wehrspohn and H. Föll
Copyright © 2004 Wiley-VCH Verlag GmbH & Co. KGaA
ISBN: 3-527-40432-5

In the following chapter, we will describe the preparation of the constituent building blocks, Section 6.2, which are monodisperse colloids or beads, their "crystallization" into an FCC lattice, Section 6.3, their further structuring, Section 6.4, and their conversion into replica from high refractive index inorganics, Section 6.5. The optical properties of the resulting opals will be described in Chapter 7.

6.2 Preparation of monodisperse colloids

The precondition for the preparation of artificial opals is the preparation of monodisperse beads or colloids, which may be composed of inorganic or polymeric materials. They are made by chemical methods nucleating from micellar systems.

6.2.1 General methods

Inorganic colloids

The use of different inorganic materials offers – in a very general sense – a very broad variability of photonic materials. For most materials, except for SiO_2, the monodispersity and size range of the prepared colloids, does however not yet allow the fabrication of high quality artificial opals. Therefore a lot of synthetic work is still necessary to optimize these materials.

Inorganic colloids are usually prepared via precipitation reactions. Early papers explained the formation of monodisperse colloidal particles by the LaMer´s model [30], according to which precipitation involves two steps; nucleation and growth of the nuclei. To achieve monodisperse particles, these two steps should be separated strictly and nucleation should be avoided during the period of growth. However, this is not always the case, and since the pioneering work on α–FeOOH [31], which describes that rod–shaped particles of 100 nm formed by aggregation of nanoparticles, several other colloidal particles have been shown to form by aggregation of smaller subunits [32, 33]. It is obvious that in order to produce monodisperse particles such an aggregation process has to be controlled. Den Ouden has shown theoretically that separating the nucleation and growth step is not an essential feature in the preparation of monodisperse particles. The final particle size uniformity could be achieved by a self–sharpening growth process, where small particles grow faster than the larger ones [34].

Silica colloidal particles represent one of the best characterized inorganic systems that have been manufactured as monodisperse samples (Fig. 6.1). They are usually prepared by the Stöber method [18]. The surface properties of these particles can easily be tuned by using siloxane chemistry. Furthermore, other materials such as semiconductors, rare–earths [35], or organic chromophores [36] can also be incorporated into silica particles during the synthesis. The production of other inorganic particles is also possible [37–44]. As the size distribution of these particles is larger than 10%, they cannot be used for crystallization processes. So, in the last years, efforts have been made to improve the monodispersity of high–index particles. Recently, Velikov reported the synthesis of highly monodisperse ZnS particles [45]. For the

---

composed of various crystallites, differing in the size of the beads. This makes them more precious gemstones due to the variety in diffracted colors. However, this excludes all of their photonic applications. In addition, the interstices between the silica beads are usually filled with other minerals. This prohibits replica formation.

crystallization of binary crystals, tailored particles are desirable since, for instance, a similar density of both species is required for the growth of binary colloidal alloys: as the density of silica particles is higher than the density of latex particles, the silica particles sediment faster so that the crystallization of mixtures of these particles is suppressed. A solution to this problem is the use of mesoporous particles [46] since their density is much lower and tunable as opposed of normal Stöber silica particles. Other very interesting particles are rutile [47] colloidal beads because of their high refractive index and a low absorption in the visible frequency range.

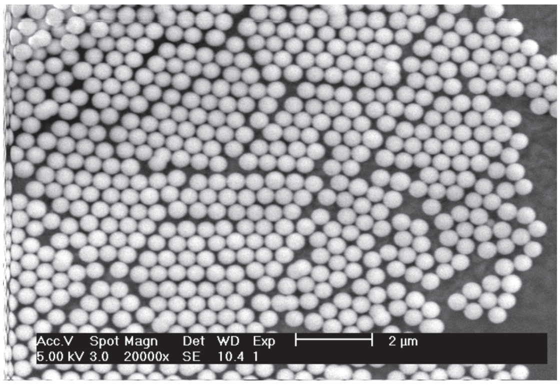

Figure 6.1: Monodisperse silica particles synthesized by a seeded growth process.

Polymers colloids

Polymer colloids offer the advantage over inorganic colloids that (i) highly monodisperse particles can easily be obtained, that (ii) they can be functionalized easily, e.g. with fluorescent dyes and that (iii) properties like thermal stability or refractive indices can easily be changed. In addition, they offer the potential for post–crystallization processing like E–beam lithography (EBL) and – generally – complete removal after replica formation. Many methods to synthesize polymer beads or colloids, like dispersion and emulsion polymerizations, are technically applied and run in large quantities [48]. However to cover the size range, monodispersity and crystallizability required, only some are useful.

Generally, to prepare an artificial opal, it is desirable that the colloids crystallize in solution at a volume ratio, which is already rather high (in the FCC packing it is finally 74%). This minimizes a destruction of the packing during the shrinkage accompanying the final drying. Of equal importance is the fact that the colloids do not stick to each other, if brought in close contact. They have to be free to slide and roll over each other to find the equilibrium position. That means, it is desirable for the colloids to interact as hard objects. On the other hand, some stabilization is necessary to keep the colloids in solution.

An important property to determine this, is the charge density on the surface. If the charge density is high, the colloids start to interact already at large distances. This happens for most colloids prepared by classical emulsion polymerization with the help of charged detergents. In addition, the detergents migrate from colloids to colloids, as soon as the colloids are close to each other. This leads to gluing of the colloids. The surfactant free emulsion polymerization (SFEP) provides a possibility to circumvent this problem [49–51].

Polymers colloids by "surfactant free emulsion polymerization": The surfactant free emulsion polymerization (see Fig. 6.2) is the most frequently used method to prepare monodisperse colloids for the preparation of polymer opals [4, 14, 17]. For this process, the water–insoluble monomer is dispersed in water and polymerized with the help of a charged water soluble radical initiator (mostly peroxodisulfate). The charged sulfate radicals initiate the polymerization of traces of monomer, which are dissolved in equilibrium in water. The oligomers formed thereby posses one charge resulting from the initiator, but are otherwise hydrophobic. They act as detergents and form micelles as soon as their concentration grows above the critical micelle concentration. As soon as micelles are formed, the further polymerization proceeds inside these micelles, as described in textbooks for the classical emulsion polymerization [48]. It is the advantage of this method (SFEP) that the micelle concentration is low and all micelles grow for a long time (during polymerization) at equal rate. This leads to large and very monodisperse polymer colloids. In addition, the micelles are charged, but the charge density is rather low and the charges are chemically linked to the polymer chains. This means they cannot migrate between colloids as for low molar mass detergents.

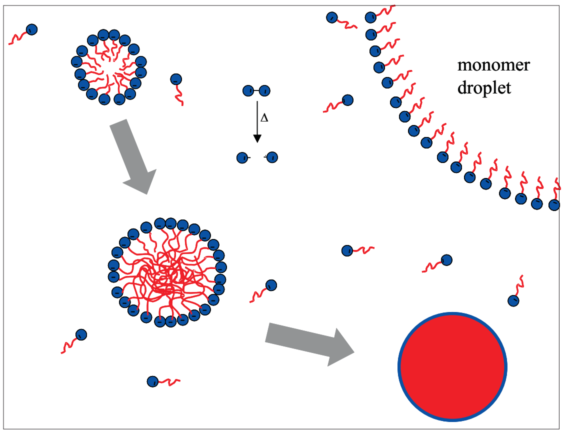

Figure 6.2: Schematic representation of the preparation of monodisperse polymer spheres [48].

By modification of the polymerization conditions, many methacrylate monomers can be polymerized successfully, resulting in monodisperse polymer colloids (see Fig. 6.3).In this context, the potential of polymer opals is related to their processibility and the ease of internal pattern formation (see Chapter 6.4). Thereafter, the complex structure with an internal pattern can be transformed into inorganic replica. This is an advantage of polymers over inorganics, because the use of different monomers allows it to tailor many properties [17], like the glass transition temperature, which determines the thermal stability of the resulting polymer opals or the refractive index. The glass transition temperature can be varied between 80°C and 160°C, but additional crosslinking allows it to prepare polymer opals with long time stability above 200°C [56]. The refractive index of the polymers can be varied between 1.35 (fluorinated monomers) and a value slightly above 1.6 (bromine containing monomers). The use of chemically labile monomers allows a chemical modification of the beads after crystallization, while crosslinking leads to an increase of the thermal stability. This will be described in more detail later in this section.

It is important that the size of the individual polymer colloids can be tailored by varying the ratio of monomer to water [49, 52] (see Fig. 6.4). This is possible since the number of

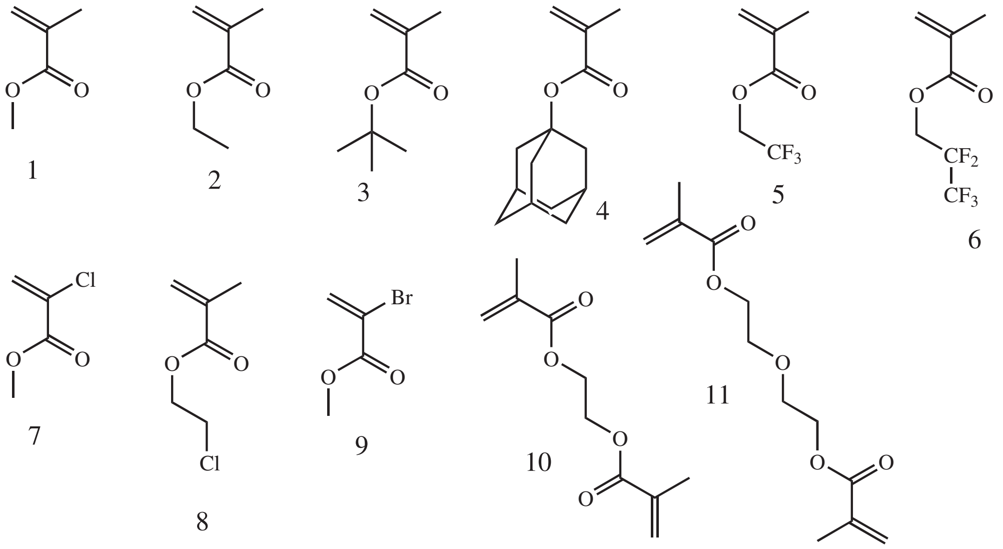

Figure 6.3: 1. methyl methacrylate; 2. ethyl methacrylate; 3. *tert.*-butyl methacrylate; 4. 1–adamantyl methacrylate; 5. 2,2,2,–trifluoroethyl methacrylate; 6. 1*H*,1*H*–perfluoropropyl methacrylate; 7. methyl α–chloro acrylate; 8. 2–chloro–ethyl methacrylate; 9. methyl α–bromo acrylate; 10. ethylene–glycol–bis–methacrylate; 11. diethyleneglycol–bis–methacrylate.

growing micelles (to become the colloids later on) is determined at an very early stage of polymerization, by the solubility of the monomer in water and by the critical micelle concentration. They grow until all monomers are polymerized inside the micelles. Therefore, the amount of monomers available determines how long the micelles grow and how large they can get. Thereby, it becomes possible to pre–set the photonic band gap, which scales with the diameter of the beads (see Fig. 6.4). Differences in the hydrophobicity of the different monomers determines the steepness of the curve, as more hydrophobic oligomers have a lower solubility in water.

Polymers colloids by dispersion polymerization: An alternative approach to monodisperse colloids for the preparation of polymer opals, uses sterically stabilized colloids obtained by a dispersion polymerization [53–55]. For this process, the monomer (mostly styrene) and the stabilizer (mostly cellulose derivatives) are dissolved in a solvent which is a non-solvent for the resulting polymer. The polymer formed, phase separates into seed particles, which are sterically stabilized, because some stabilizer is chemically linked to the polymer by radical transfer reactions. That means, the polymerization starts as one phase and nucleates – at an early stage – a “polymer micelle phase”, which transforms during further polymerization into polymer colloids. With this method, larger colloids (size over 1 μm) can be prepared. The colloids formed thereby are in addition rather hydrophobic since they are polymerized in an organic solvent. They can e.g. be used especially well for the generation of colloids monolayers on water and they can be transfered – as monolayer – to various substrates (see Chapter 6.4.2).

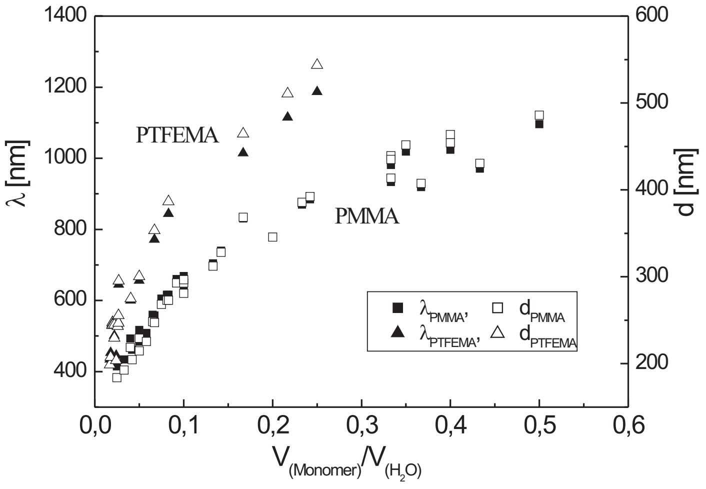

Figure 6.4: Variation of the diameter (d) of the colloids and the maximum wavelength (λ) by the monomer/water ratio [52]. Values given for poly(methyl methacrylate) (PMMA) and poly(2,2,2,–trifluoroethyl methacrylate) (PTFEMA).

Synthesis of functional colloids

It is one of the advantages of polymer colloids that they can easily be functionalized [14, 17]. This is e.g. possible by:

1. the incorporation of fluorescent dyes [14] (see Fig. 6.5 for a table of dyes under investigation). They can be incorporated into the colloids by addition to the polymerization mixture. If they are chemically incompatible with radical polymerization conditions, partially crosslinked polymer colloids can be swollen in a solution of the dye. Interest in the thus accessible dye containing polymer opals are the question of the influence of the photonic structure on the dye emission, and lasing [1, 25, 29].

2. the incorporation of bifunctional monomers [17] (see Fig. 6.3), which results in crosslinked colloids. Crosslinking increases the thermal stability of the resulting polymer opals to values well above 200°C, as the colloids soften at higher temperatures, but cannot fuse since they are rubber–like. In addition, crosslinking increases the solvent and mechanical stability of the resulting polymer opals [56].

3. the use of monomers with chemically labile groups like *t*–butyl–methacrylate [17] (see Fig. 6.3). Splitting off the t–butyl groups as isobutene leads to polymethacrylic acid. This conversion allows it to modify the polarity of polymer opals after their crystallization or to shrink their lattice constants during partial thermal decomposition.

4. the preparation of colloids from fluorinated monomers [52, 56] (see Fig. 6.3). The use of fluorinated monomers leads to colloids with an especially low refractive index and increases the solvent stability of the polymer opals, due to the low solubility of fluorinated compounds. Fluorinated monomers allow it, in addition, to obtain extra large colloids because of the high hydrophobicity (low critical micelle concentration) of the fluorinated compounds (see Fig. 6.4).

5. the preparation of colloids with different surface charges. This can be achieved by the use of radical initiators, which lead to negatively or positively charged colloids (see Fig. 6.6). The positively or negatively charged colloids can be used e.g. for a selective deposition of monolayers on charged surfaces.

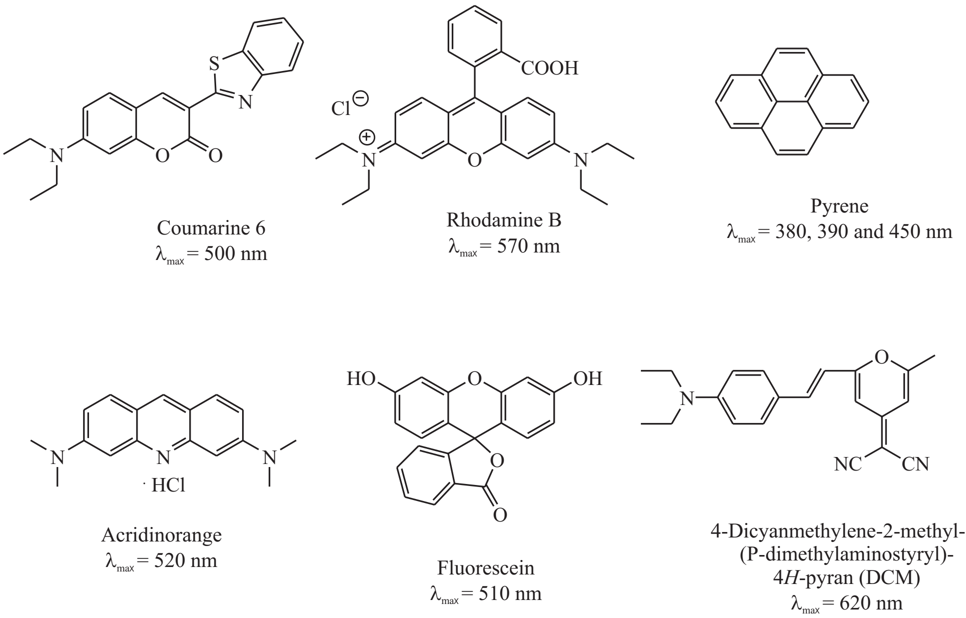

Coumarine 6
λ_{max}= 500 nm

Rhodamine B
λ_{max}= 570 nm

Pyrene
λ_{max}= 380, 390 and 450 nm

Acridinorange
λ_{max}= 520 nm

Fluorescein
λ_{max}= 510 nm

4-Dicyanmethylene-2-methyl-6-(P-dimethylaminostyryl)-4*H*-pyran (DCM)
λ_{max}= 620 nm

Figure 6.5: Fluorescencent dyes used for the preparation of dye containing polymer opals with emission wavelength [14, 52].

6.2.2 Preparation of functional core shell structures

Since the build-up of colloids or beads starts from micellar systems, various core-shell structures become possible by an sequential build-up.

Incorporation of inorganic materials into the colloids

The properties of colloidal particles can be modified by coating them with shells of varying chemical composition and thickness. For the fabrication of photonic crystals, particles with

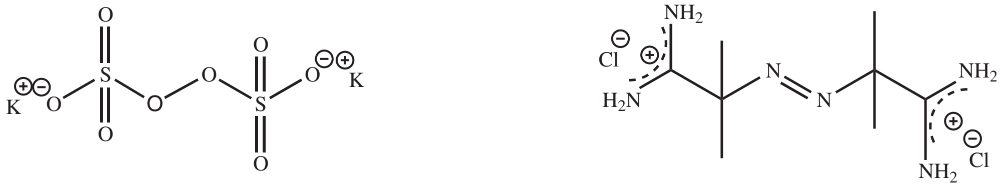

potassium peroxodisulfate

α,α'-azodiisobutyramidin dihydrochloride

Figure 6.6: Different surface charges of the colloids can be obtained by the use of initiators with negative or positive charge.

a high–index shell or hollow high–index particles are very interesting. Previous investigations [57–61] have demonstrated that polymeric and inorganic particles dispersed in water or ethanol, can be coated with layers of inorganic high–index material. This can be achieved by either precipitation of the coating material or by controlled deposition of preformed inorganic nanoparticles. High-index coatings that have been prepared by precipitation include titania (TiO_2) [62–66], tin oxide [64], zinc sulfide [45, 67] and gold [68]. Alternatively, core–shell particles can be obtained by a layer–by–layer technique [57]. Submicrometer sized composite particles with multilayers of TiO_2, gold [69] and luminescent semiconductors [70] have been synthesized with this approach. All these materials except for gold have a high refractive index combined with low absorption in the visible, which make them interesting for photonic applications, if they can be crystallized properly. Zhang et al. [71] described that metal–coated colloidal particles as buildings blocks for photonic crystals should result in PBGs for any periodic structure. As PhCs containing metal can be strongly absorbing at optical frequencies, the choice of the coating materials is important. As demonstrated, it is desirable to choose a metal such that the real part of the dielectric function is large and negative, while the imaginary part is relatively small at optical and IR frequencies. Silver, for instance, satisfies these conditions.

Furthermore, to generate hollow beads of the coating material, the cores can also be removed in a subsequent step using procedures such as solvent extraction or calcination at elevated temperatures. In many cases, these hollow beads may exhibit optical properties that are substantially different from those of solid ones.

Rutile hollow beads are of special interest because of their very high refractive index combined with low absorption in the visible [63].

Magnetic colloid particles: Since magnetic particles can be influenced by an external magnetic field, they are predestined for the production of self–assembled ordered structures. 3D suspensions of magnetic particles in a liquid have been known as ferrofluids for several decades. They are magnetically tunable. However, particles in ferrofluids tend to arrange in long chains rather than crystalline structure. In contrast to the very small ferrofluid particles (1–20 nm), magnetic colloidal particles (500–5000 nm) that are trapped on the surface of a liquid, form 2D crystalline structures if the magnetization is perpendicular to the liquid surface. In this case, each particle is trapped by magnetic forces from the neighbors (in–plane) and by gravity forces (out–of–plane). Superparamagnetic colloidal particles on the surface of water droplets and in the presence of a uniform magnetic field, have been studied in the context of

2D melting [72–74] of planar magnetic colloidal crystals [75] and pattern formation [76, 77]. While floating ferromagnetic particles have been used as a model system for magnetic interactions and vortices in superconductors [78]. Recently, the self–assembly of magnetic particles into ordered 2D and 3D structures whose symmetry and lattice parameter may be controlled by an external magnetic field [79, 80] has been reported. Most of the present results have been obtained with macroscopic magnetic particles and are therefore appropriate for PhCs in the microwave range. For a PhC in the visible, smaller magnetic particles are required. These particles need to be monodisperse in the size as well as in the magnetization. Particles that meet these requirements are not commercially available. Therefore, many efforts have been made in order to obtain superparamagnetic particles of good quality. Monodisperse spherical beads of tunable size from 1 to 100 μm in diameter, can be prepared by activated swelling of polymer particles [81, 82]. These porous beads form the basis for magnetizable monodisperse polymer particles, which contain small grains of magnetic iron oxides distributed throughout the volume of the beads. Caruso et al. obtained smaller magnetic particles by the layer–by–layer technique [83]. As only the shell consists of magnetic particles, the magnetization is not very high. Monodisperse, highly charged superparamagnetic colloidal particles of size 134 nm were synthesized by emulsion polymerization of styrene in the presence of 10 nm iron oxide particles [84]. A similar method uses [85] inverse emulsion polymerization in the presence of magnetic iron oxide. This gives particles with a diameter of roughly 200 nm, but the polydispersity is too high for crystal growth. The synthesis of highly charged monodisperse polymer particles with a diameter of 400 and 800 nm were reported later [86]. The size and the properties of these particles were tuned in such a way, that they can be used as buildings block for photonic crystals.

Polymer core-shell nanoparticles

Polymer core–shell lattices are a general topic in emulsion polymerization [87–89]. For the aspect of photonic crystals, they offer the possibility to make e.g. pore–free elastomeric opaline films [90, 91]. The monodispersity of the core-shell structure necessary for crystallization requires, however, a lot of fine tuning of the synthesis. A major problem is the preparation of an outer shell of constant thickness, which requires a proper chemical linking of the polymers of the core and shell [90, 91]. (The problem to overcome is the fact that different polymers are immiscible. Therefore they want to minimize their interface. As a result, the outer polymer film, the shell, tends to concentrate at one side of the core.) If these problems are overcome and the shell has a lower Tg–value as the core, film formation of the outer shell becomes possible, while keeping the periodic structure of the cores [90, 91] (see Fig. 6.7). TEM measurement through a thin cut of such a film, which show the periodic structure are shown in Fig. 6.8 [91]. Possible application of such films involve the preparation of non–porous rubber like polymer films with angle dependent reflection colors.

Polyelectrolyte multilayers on colloids

Generally polyelectrolytes tend to adsorb to an oppositely charged surface and form a thin layer. If this adsorption is done under the right conditions, it is possible to convert the surface charge. Thus, it becomes possible to adsorb another layer of an polyelectrolyte, now of the

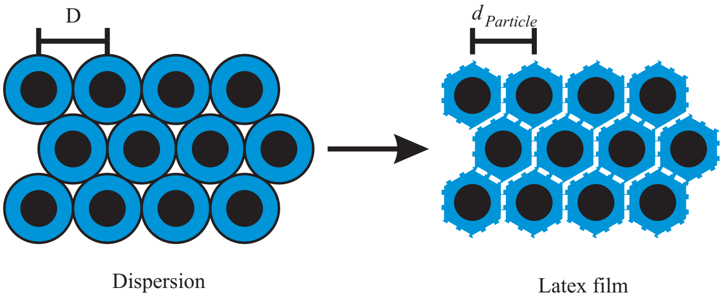

Figure 6.7: Film formation from core-shell lattices with a hard core.

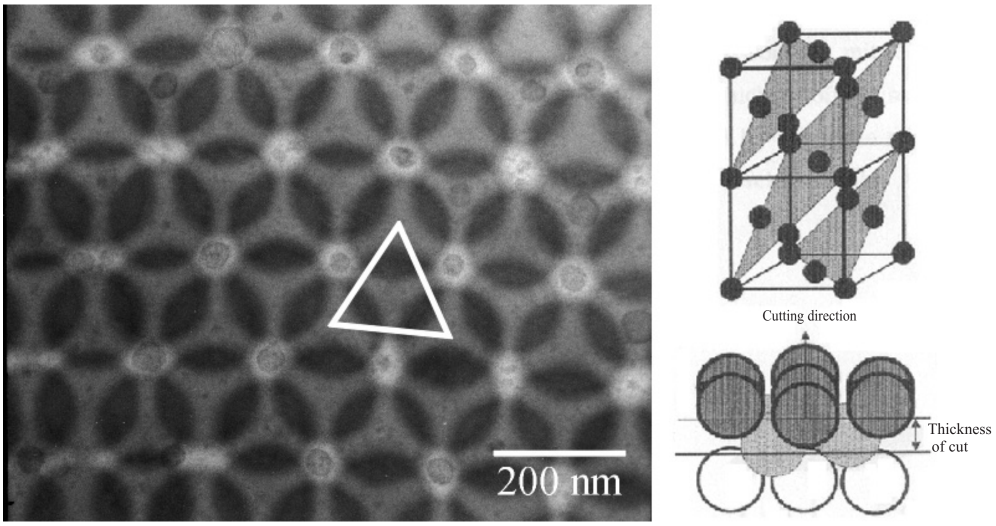

Figure 6.8: Structure of films from core-shell lattices with a hard core [91].

opposite charge and so on. This process is known as multilayer build–up by electrostatic interaction [92, 93] and it allows the build–up of multilayer structures from various charged objects, while controlling the thickness of the sublayers in the nm range. This process is not limited to flat surfaces, but can also be applied for the coating of colloids [57, 69, 70, 83, 94–96]. For monodisperse colloids it offers the potential to create a thin functional surface layer, into which fluorescent materials and especially inorganic quantum dots like CdSe, HgTe (see Fig. 6.10) and so on can be incorporated in a very flexible way. In addition, the formation of hollow spheres becomes possible after dissolution of the polymer core [97].

These colloids with polyelectrolyte outer shells can be crystallized into opaline materials (Fig. 6.10), however the result is sometimes not perfect, presumably due to two reasons. On one hand, the charge density at the surface is often rather high; on the other hand the very thin polyelectrolyte multilayers (thickness about one nm) may not cover the surface perfectly. Thus patches of the underlying polyelectrolyte layer (now of opposite charge) may reach the surface. If the colloids get close to each other during crystallization, this can lead to attractive forces and induce “sticking” of the colloids (see Fig. 6.9a). The problem can, however, be solved by adsorption of an outer PEO layer with amino end–groups [94] (see Fig. 6.9b). In this case the charge density gets reduced and the colloids become – in addition – sterically stabilized. The resulting colloids crystallize very well.

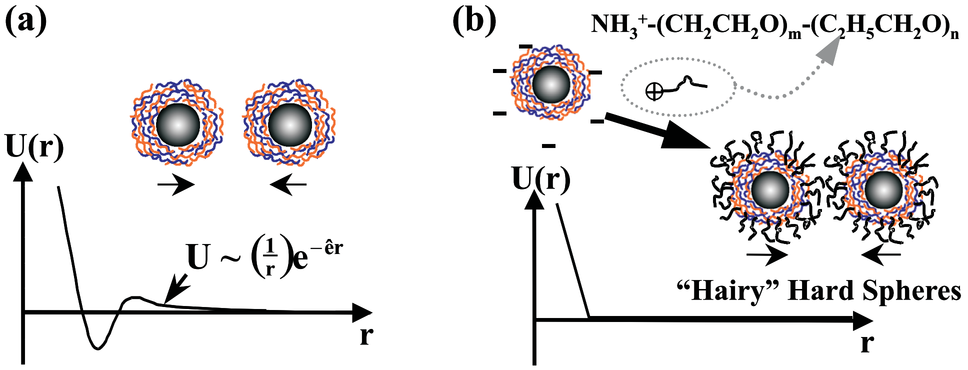
(a)
U(r)
$U \sim \left(\frac{1}{r}\right)e^{-\hat{e}r}$
r
(b)
NH_3^+-$(CH_2CH_2O)_m$-$(C_2H_5CH_2O)_n$
U(r)
“Hairy” Hard Spheres
r

Figure 6.9: Potential between latices with multilayers at their surface. (a). An attractive potential can result from an inhomogeneous layer formation; (b). Adsorption of amino–terminated poly ethylenoxide leads to sterically stabilized colloids [94] with no attractive potential.

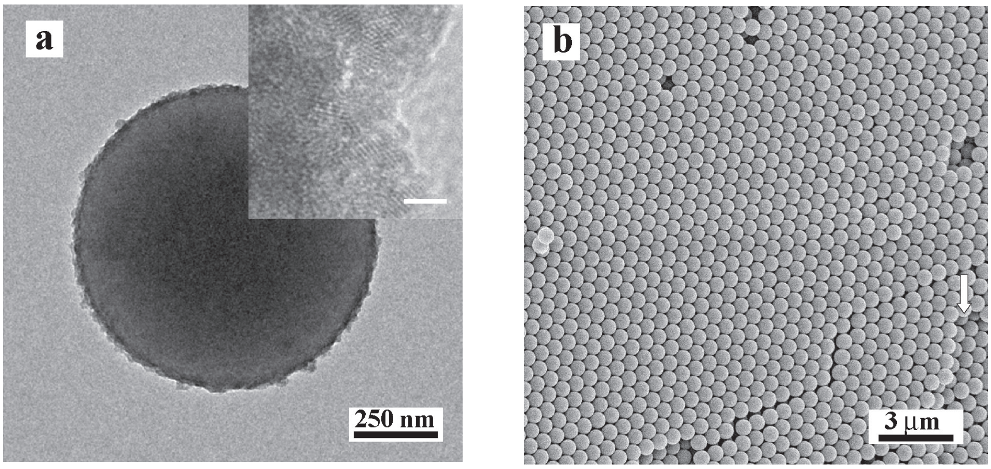

Figure 6.10: a) Colloids coated with HgTe by the multilayer technique (TEM); b) Crystallized array of such colloids. Pictures taken from ref. [96] by permission.

6.3 Crystallization into opaline structures

6.3.1 Sedimentation

The density of colloids from inorganic materials like SiO_2 is significantly larger than that of water. As a consequence, crystallization by sedimentation dominates in this case. It usually leads to thick bulk samples (bulk opals), which are called artificial opals after the sintering necessary for mechanical stabilization [5–7, 98]. The time needed for sedimentation thereby depends on the size of the spheres (see Fig. 6.11).

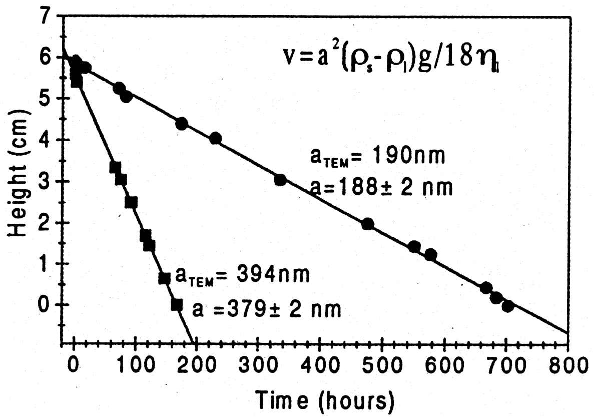

Figure 6.11: Sedimentation of SiO_2 spheres into artificial opals [98].

6.3.2 Crystallization mediated by the magnetic field

For the preparation of bulk opals from inorganic materials, it is attractive to control the crystallization by external fields. In general, the interactions between the colloidal particles are important for the crystallization process. There are three terms: the short–range steric repulsive interaction, the long–range attractive interaction (with a range of around 100 nm) that is usually referred to as the van der Waals force, and the long-range Coulomb repulsion shielded by electrolytes (Yukawa potential (see Fig. 6.9)). The magnitude of the Yukawa potential strongly decreases strongly with increasing concentration of electrolytes due to the screening effect caused by counterions present in the double layers. Therefore it is possible to tune the interactions between the colloidal particles by varying salt concentration in the solvent. Highly long range–interactions can be observed in a magnetic or electric field [99]. Zahn and co–worker [72, 73] reported large defect-free 2D crystals obtained with magnetic colloidal particles with absolutely calibrated dipole-dipole interactions that can be tuned with an external magnetic field. Recently, van Blaaderen et al. [100] used an applied electric field to induce strong dipole-dipole interactions. Using a magnetic or electric field, a fourth potential, resulting in an orientation-dependent dipole force (with magnitude proportional to the electric or magnetic field strength) is superposed on the other three interactions. In the case of the electric field the range of the force is comparable to the particle radius. The result is a three–dimensional phase diagram (Fig. 6.12) defined by the volume fraction and the strength of the electric field. In the case of the magnetic field, the range of the force is much larger but investigations in the 3D are not published yet out because magnetic fluorescent particles with well-defined sizes are not available so far. We therefore expect that the magnetic field will also become very useful in the fabrication of highly long ranged ordered 3D crystals, since the interactions are stronger and more long ranged than in the electric field.

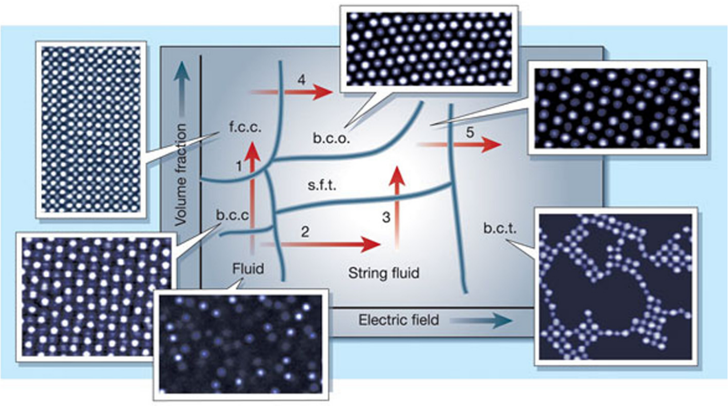

Figure 6.12: At low field values, increasing the volume fraction causes the random, fluid arrangement of colloidal particles to take a body–centered cubic phase (b.c.c), then face–centered cubic (f.c.c) crystal structures (shown in the insets). Increasing the electric field at fixed volume fraction (2), however, transforms the colloids into a string fluid structure. If the volume fraction is then increased (3), a space filling tetragonal structure (s.f.t.) results. Alternatively, starting from high volume fraction with f.c.c structure and increasing the electric field (4) produced the body–centered orthorhombic (b.c.o) state. From the s.f.t state, if the electric field is pushed up still further (5), the colloidal crystal takes another, more open structure, known as body–centered tetragonal (b.c.t.). Reproduced with permission [101].

6.3.3 Two dimensional crystallization to photonic crystal films

The density of polymer colloids is close to that of water. As a consequence, sedimentation becomes rather slow and the crystallization is dominated by the evaporation of water. Preferably it is done in thin films of the colloidal dispersion on hydrophilic substrates and leads to thin opaline films. In some ways they present a 3D PhC in it's two dimensional limit. The process of crystallization is, thereby, very close to the so–called "two dimensional crystallization" [102–104]. Drying and crystallization starts at the edges of the film (in the meniscus). This leads to an increased evaporation of water at the drying front. As a result, a water current sets in, which "pushes" the colloids into the growing colloidal crystal and supports further crystallization.

Crystallization on horizontal substrates

In the simplest version the crystallization of polymer opals is done by spreading the colloidal dispersion on horizontal substrates [14, 17]. Thereafter, the dispersion is dried slowly (time varying from over night to one week). In this way large substrates (many cm^2) can be covered by an opaline film (thickness some μm) with an optically homogeneous appearance. A picture of such a film is shown in Fig. 6.13. The large opaline film may consist of many different crystallites, but all have their {111} plane nicely parallel to the substrate.

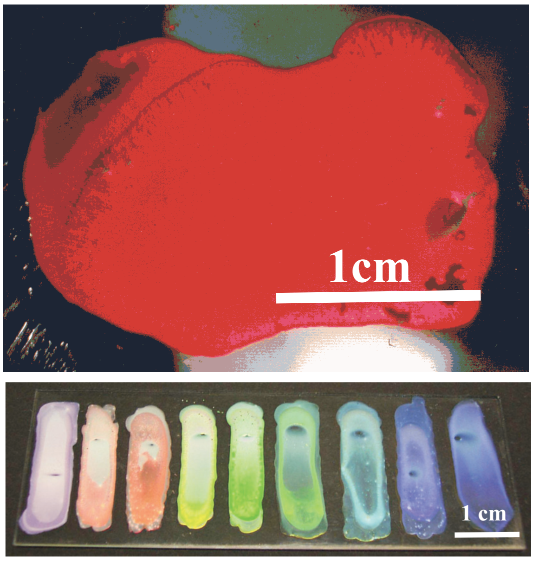

Figure 6.13: Crystallization of polymer spheres into thin photonic crystal film. Different colored films result from spheres of different size.

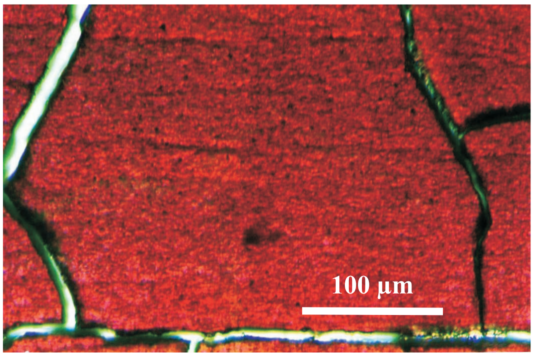

Figure 6.14: Large cracks in an opaline film determined by optical microscopy. The film had been carefully dried. (picture taken with permission from Ref. [17])

Optical microscopy shows the cracks, which separate the crystallites and which appear due to volume shrinkage during drying of the colloidal crystal. However, large crystallites can be obtained, if the film is dried carefully [17] (see Fig. 6.14). In addition, the orientation of the hexagonal order in different crystallites is almost the same. This corresponds to a situation in which a larger crystal is formed at first, which breaks into pieces at the end of drying (volume shrinkage). Inspection by scanning electron microscopy (SEM) shows that the crystalline order extends into the depth of the opaline films (see Fig. 6.15 left). At crack edges, all facets of the FCC packing are visible (see Fig. 6.15 right).

The problem of the formation of cracks can be solved, if the crystallization is done on a fluid matrix, e.g. liquid mercury or liquid gallium [104, 105] (see Fig. 6.16). Crystallization on gallium leads to crack free opaline films of cm^2 size. They have a very low defect density, which consists mostly of missing beads in the outer layer (see Fig. 6.16b).

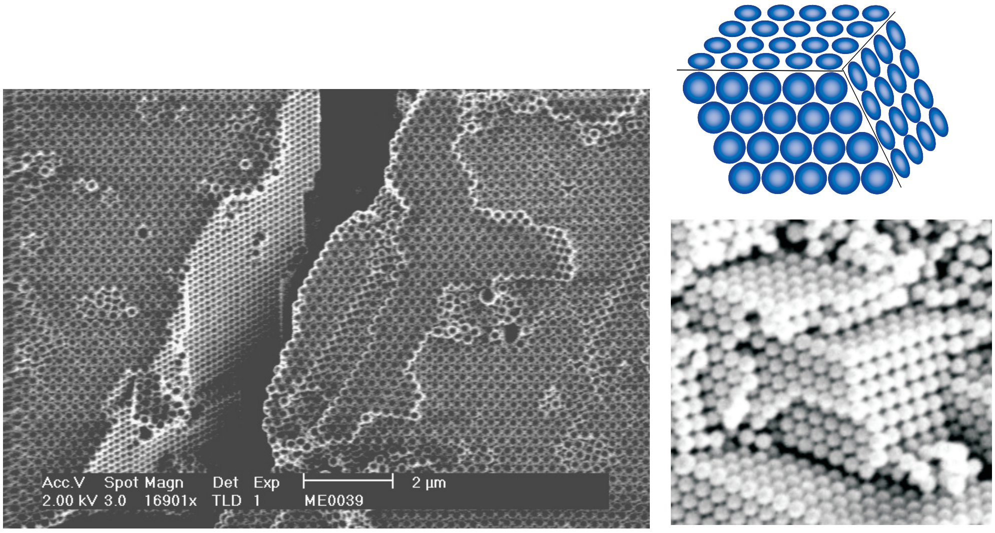
Acc.V Spot Magn Det Exp 2 µm
2.00 kV 3.0 16901x TLD 1 ME0039

Figure 6.15: SEM picture of the crack edge of a polymer opal film. Left side: The order extends into the depth of the film; right side: All facets of an FCC packing can be seen on the fracture edge; top inset: Schematic representation of the $\{111\}$ plane (hexagonal, front) and the $\{100\}$ plane (rectangular, right side) in correspondence to the SEM image below.

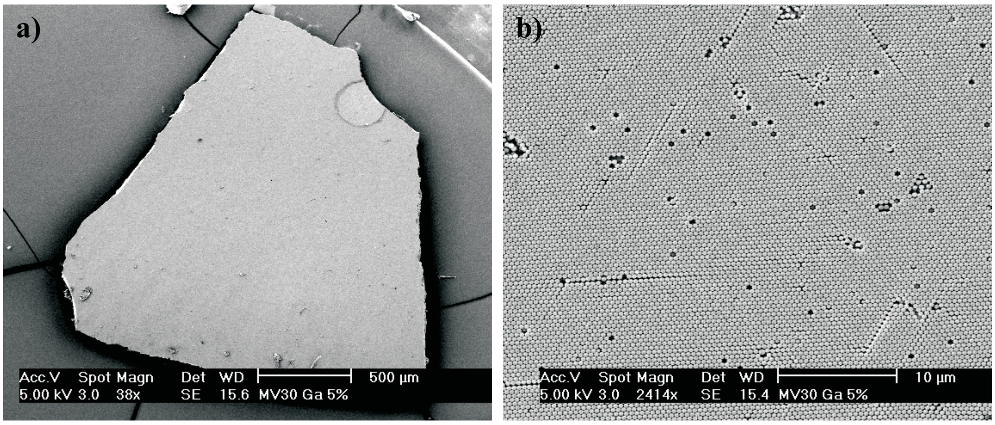
a)
Acc.V Spot Magn Det WD 500 µm
5.00 kV 3.0 38x SE 15.6 MV30 Ga 5%
b)
Acc.V Spot Magn Det WD 10 µm
5.00 kV 3.0 2414x SE 15.4 MV30 Ga 5%

Figure 6.16: Large nearly defect-free photonic crystal film obtained by crystallization on liquid substrates (picture taken with permission from Ref. [105]). b): Inner part of a) with larger magnification.

Crystallization on vertical substrates with a controlled moving meniscus

Crystallization on a horizontal substrate (described above) leads to opaline films, whose thickness usually varies from the edge (the drying front) to the center (late crystallization). The preparation of opaline films of a homogeneous thickness and a control of the thickness of the opaline films is possible by crystallizing in a meniscus moving with a controlled speed [52, 106–111]. For this purpose, the substrate has to be moved vertically with respect to the surface of the colloidal suspension (see Fig. 6.17 for a schematic presentation). Experimentally this is either achieved by lowering the liquid level by slow evaporation of the solvent [109, 110, 112, 113] (mostly used for SiO_2 beads suspended in ethanol) or by slowly lifting the substrate [106, 114] with a speed of some 100 nm/sec. This last process is commonly applied for polymers, which are dispersed in water (slow evaporation rate). Opaline films of a very homogeneous thickness result. They show excellent optical properties, even if the measurement is integrated over areas of many mm^2, with a virtual absorption due to reflection of more than 99% (see Fig. 6.18) [106].

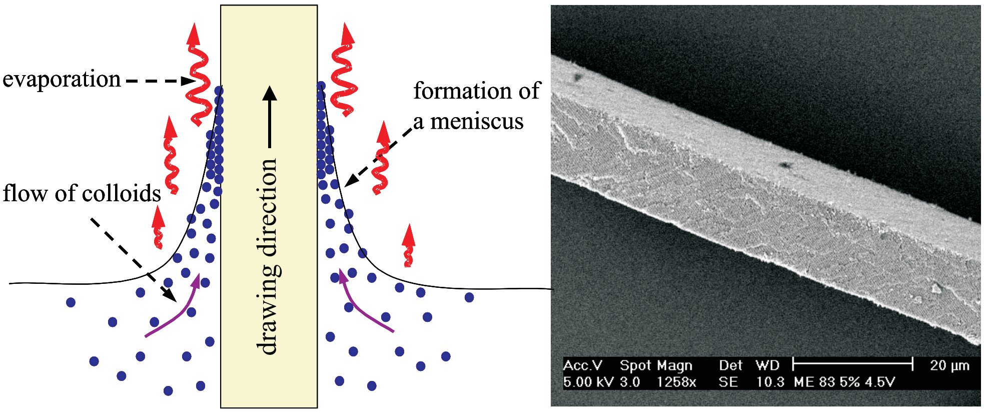
evaporation
formation of a meniscus
flow of colloids
drawing direction
Acc.V Spot Magn Det WD 20 µm
5.00 kV 3.0 1258x SE 10.3 ME 83 5% 4.5V

Figure 6.17: Schematic representation of the process of crystallization in a moving meniscus (left) and a piece of an opaline film thus obtained (right) [106].

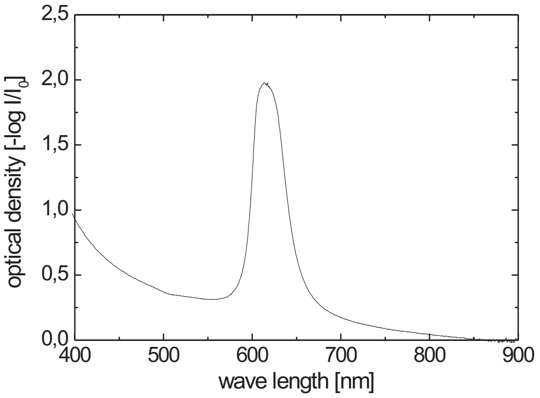

Figure 6.18: Optical measurement of an opaline film crystallized in a moving menisus.

6.4 Structured photonic crystals

Beyond the fabrication of highly ordered crystals, it is very important to develop structuring methods, in order to provide conceptual tools to construct complex circuit architectures. We present here two complementary approaches for this purpose.

6.4.1 Lateral patterning

Crystallization on patterned substrates

Patterned substrates offer the possibility to control the growth stage, and thus to fabricate crystals of predefined size, shape, orientation at predefined locations with a sufficient number of periods to provide an effective Bragg reflection. We have demonstrated the validity of this approach using deeply etched trenches in silicon wafers [115]. More recently, the use of silicon–on–insulator substrates allowed fabrication of substrates with a better control of the etching geometry, and thus to obtain defect–free crystals, as it can be seen in the left panel in Fig. 6.19.

Post–crystallization structuring by electron–beam lithography

In order to incorporate advanced functions such as optical resonators, intentional microscopic defects need to be introduced in the photonic crystal. We have recently developed a versatile and accurate post–crystallization structuring approach based on electron–beam lithography (EBL), by using an opaline film made of PMMA as an EBL resistance [14, 116]. The fabrication process involves two steps: i) Direct exposure of selected areas on the opaline film, ii) developing in order to dissolve the exposed spheres. Since the voltage which accelerates the electrons influences the penetration of electrons in the material, the writing depth can be tuned from one layer up to several microns. Thus, microscopic defect structures such as waveguides or cavities can be fabricated with a resolution below the sphere diameter, without affecting the surrounding crystal, as illustrated in the right panel of Fig. 6.19.

6.4.2 Preparation of heterostructures from different colloids

The process of crystallization in a moving meniscus allows it to crystallize different photonic crystal films on top of each other [52, 106, 110] (see Fig. 6.20). Such structures composed of different photonic crystal films are called heterostructures. They can have different band gaps due to differences in the lattice constant and/or the refractive index. Inspection by scanning electron microscopy shows that the interface between both films is usually very sharp [52,106, 110] (see Fig. 6.20), even if the lattice constant is incommensurable. Optically this leads to a superposition of stop bands as shown in Fig. 6.21.

The use of functional polymers allows the making of switchable heterostructures [52,106]. As an example, Figure 6.20 shows a heterostructure composed of a rather thermo–labile opaline film (low Tg–value) and a more thermo–stable one. Heating of the heterostructure to the low Tg–value leads to a partial melting. The results on structure and resulting optical properties are shown in Figs. 6.20 and 6.21.

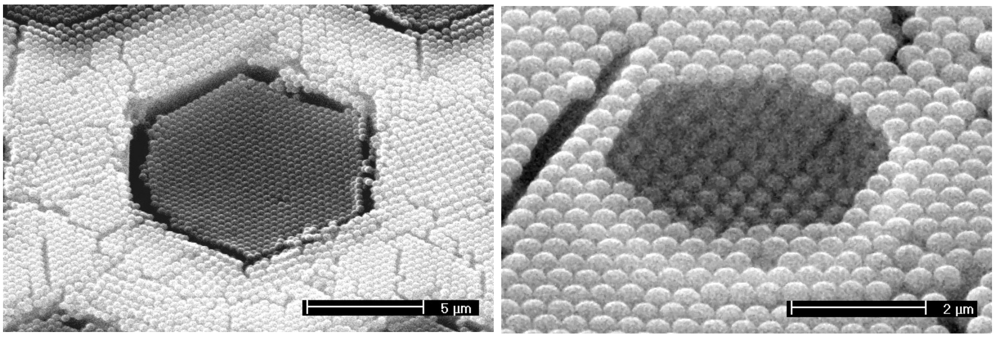

Figure 6.19: SEM micro-graphs of structured opaline films. Left: Hexagonal crystal grown on a patterned silicon substrate. The 7–μm thick crystal fills the etched (dark) areas completely, whereas a few residual layers of spheres cover non–etched (light) areas. Right: 1–μm deep hexagonal defect directly written on an opaline film using electron–beam lithography.

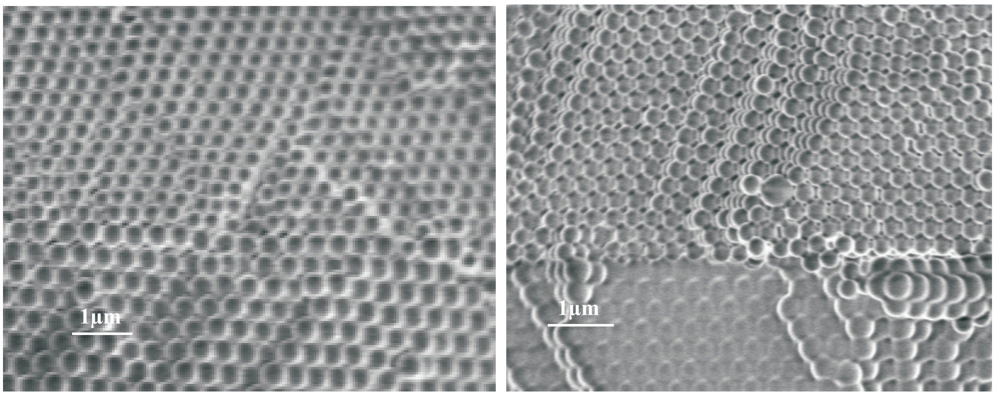

Figure 6.20: SEM picture of heterostructures of polymer beads with a different thermal stability, left: before heating; right: after heating. The colloids on the bottom had a size of 392 nm, the ones on top of 309 nm [106].

With regard to the incorporation of defect planes it is interesting that monolayers of the hydrophobic beads prepared by dispersion polymerization (6.2.1) can be spread on the water surface and transferred to a photonic crystal film. Figure 6.22 shows an EM picture of a system prepared in that way, from a monolayer of larger beads between two opaline films.

Combined with the EBL structuring method described above and the porous nature of the opal film, it is possible to use this process for the fabrication of buried defects, using a three-step process: i) EBL writing, ii) subsequent growth, iii) developing.

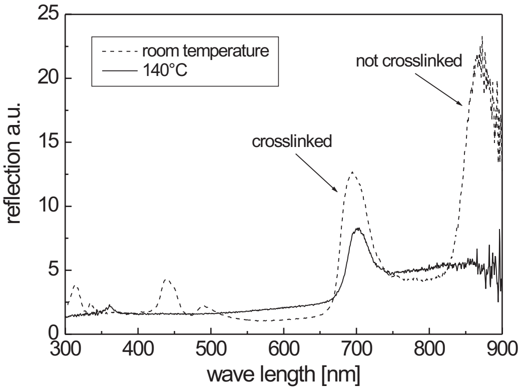

Figure 6.21: Change of reflection due to partial melting of the heterostructure in Fig. 6.20, picture taken with permission from Ref. [106]

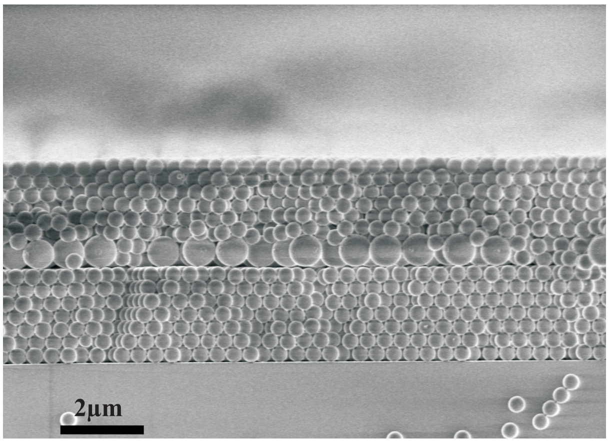

Figure 6.22: Monolayer of beads in an ABA heterostructure, picture taken with permission from Ref. [106]

6.5 Replica from opaline structure

The refractive index (between 1.4 and 1.6) of the colloids or beads -polymer or inorganic- accessible for the preparation of opals, is too low to open a full band gap for an FCC packing. To open the full band gap it is necessary to increase the refractive index contrast (refractive index of the high index material at least 2.8 for air in the voids) and to lower the filling fraction [19, 26]. This is generally possible by the preparation of replica with inorganic materials.

If a full band gap in the IR–region is desired, silicon or germanium with their very high refractive index in the IR–region, are the materials of choice [5, 13, 20]. With these materials the full band gap has already been realized for this wavelength region [13]. For the visible range no full band gap could be obtained so far, because of the lack of transparent, very high refractive index materials in this wavelength region. Here mostly TiO_2 ($n \approx 2.8$ in the rutile form) and sometimes SnS_2 ($n = 3.2$ at 600 nm) are used [22, 27, 28, 117–119]. Typical structures of such inorganic replica are shown in Fig. 6.23. For TiO_2 they are mostly

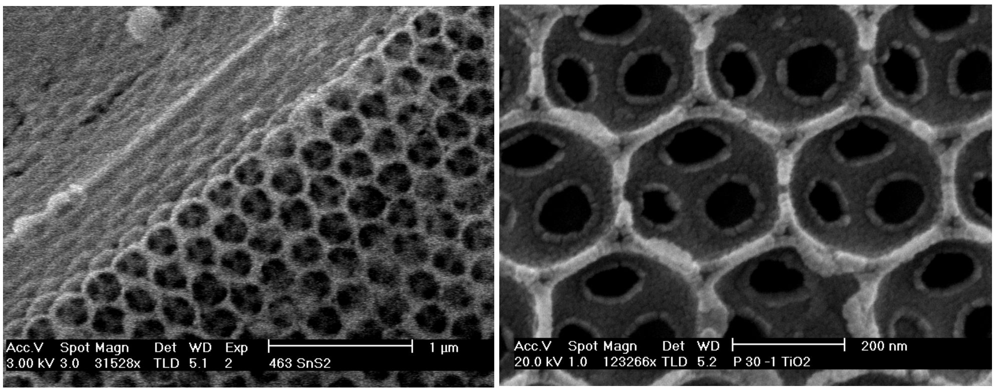
Acc.V Spot Magn Det WD Exp 1 µm
3.00 kV 3.0 31528x TLD 5.1 2 463 SnS2
Acc.V Spot Magn Det WD 200 nm
20.0 kV 1.0 123266x TLD 5.2 P 30 -1 TiO2

Figure 6.23: SEM-images of a SnS_2–replica (left) and a TiO_2–replica (right)

formed by a sol-gel process inside the interstices of the opaline material. For a filling with semiconductors or SnS_2, vapor deposition processes are mostly used. Thereafter, the original opaline material has to be removed. This is done with diluted HF solution for silica and with organic solvents for the polymer opals. Alternatively, the polymers in polymer opals can be burned away at high temperatures.

In this context, the potential of polymer opals is related to their processibility and the ease of internal pattern formation (see Chapter 6.4). Thereafter, the complex structure with an internal pattern can be transformed into inorganic replica.

Acknowledgements

The authors are grateful to Dr. S. G. Romanov and Prof. C. M. Sotomayor Torres for useful discussion and to Prof. C. K. Ober for his advice in making colloids by dispersion polymerization. Rudolf Zentel thanks Jianhui Ye for the help in preparing this manuscript. Last, but not least, the DFG (SPP 1113) and the EU is thanked for funding this research.

References

[1] S. John and T. Quang, Phys. Rev. Lett.**74**, 3419,(1995).
[2] M. Campbell, D.N. Sharp, M.T. Harrision, R.G. Denning, and A.J. Turberfield, Nature **404**, 53, (2000).
[3] J. Serbin, A. Egbert, A. Ostendorf, B. N. Chichkov, R. Houbertz, G. Domann, J. Schulz, C. Cronauer, L. Fröhlich, and M. Popall, Opt. Lett. **28**, 301, (2003).
[4] W. Luck, M. Klier, and H. Wesslau, Ber. Bunsenges. Physik. Chem. **67**, 75, (1962).
[5] C. López, L. V. Vásquez, F. Meseguer, R. Mayoral, M. Oscaña, and H. Miguez, Superlattices Microstruct **22**, 399, (1997).
[6] Y.A. Vlasov, V.N. Astratov, O.Z.Kaplianski, A.A. Karimov, V.N. Bogomolov,and A.V. Prokofiev, Phys. Rev. B **55**, R13357, (1997).
[7] A. von Blaadren, R. Ruel, and P. Wiltzius, Nature **385**, 321, (1997).
[8] S. H. Parck, D. Qin, and Y. Xia, Adv. Mater. **10**, 1028, (1998).

[9] J. S. Yin and Z. L. Wang, Adv. Mater. **11**, 469, (1999).

[10] G. Subramanian, K. Constant, R. Biswas, M. M. Sigalas, and K.–M. Ho, Appl. Phys. Lett. **74**, 3933, (1999).

[11] G. Subramanian, V. N. Manoharan, J. D. Thorne, and D. J. Pine, Adv. Mater. **11**, 1261, (1999).

[12] Y. Xia, B. Gates, Y. Yin, and Y. Lu, Adv. Mater. **12**, 693, (2000).

[13] A. Blanco, E. Chomski, S. Grabtchak, M. Ibisate, S. John, S. W. Leonard, C. López, F. Meseguer, H. Miguez, J. P. Mondia, G. A. Ozin, O. Toader, and H. M. van Driel, Nature **405**,437, (2000).

[14] M. Müller, R. Zentel, T. Maka, S. G. Romanov, and C. M. Sotomayer–Torres, Chem. Mater. **12**, 2508-2512, (2000).

[15] Special issue: on Photonic Crystals, Adv. Mater. **13**, 369, (2001).

[16] Y. Xia, B. Gates, and Z.–Y. Li, Adv. Mater. **13**, 409, (2001).

[17] M. Egen and R. Zentel, Chem. Mater. **14**, 2176, (2002).

[18] W. Stöber, A. Fink, and E. Bohn, J. Colloid Interface Sci. **26**, 62, (1968).

[19] H. S. Sözüer and J. W. Haus, Phys. Rev. B **45**, 13962, (1992).

[20] U. Grüning, V. Lehmann, S. Ottow, and K. Busch, Appl. Phys. Lett. **68**, 747, (1996).

[21] S. G. Romanov, N. P. Johonson, H. M. Yates, M. E. Pemble, V. Y. Butko, and C. M. Sotomayor-Torres, Appl. Phys. Lett. **70**, 2091, (1997).

[22] J. E. G. J. Wijnhoven and W. L. Voss, Science **281**, 802, (1998).

[23] B. T. Holland, C. F. Blanford, and A. Stein, Science **281**, 538, (1998).

[24] Y. A. Vlasov, K. Luterova, I. Pelant, B. Hönerlage, and V. N. Astratov, Appl. Phys. Lett. **71**, 1616, (1998).

[25] A. Blanco, C. López, R. Mayoral, H. Miguez, F. Meseguer, A. Mifsud, and J. Herrero, Appl. Phys. Lett. **73**, 1781, (1998).

[26] K. Busch and S. John, Phys. Rev. E **58**, 3896, (1998).

[27] M. Müller, R. Zentel, T. Maka, S. G. Romanov, and C. M. Sotomayer–Torres, Adv. Mater. **12** (2000), 1499-1503.

[28] S. G. Romanov, T. Maka, C. M. Sotomayor–Torres, M. Müller, and R. Zentel, Appl. Phys. Lett. **79**, 731, (2001).

[29] S. G. Romanov, T. Maka, C. M. Sotomayor-Torres, M. Müller, and R. Zentel, J. Appl. Phys. **91**, 9426, (2002).

[30] V. K. LaMer and R. H. Dinegar, J. Am. Chem. Soc. **72**, 4847, (1950)

[31] P. J. Murphy, A. M. Posner, J. P. Quirk, J. Colloid Interface Sci. **56**, 284, (1976).

[32] G. H. Bogush, M. A. Tracy, C. F. Zukoski, J. Non–Cryst. Solids **104**, 95, (1988).

[33] C. F. Zukoski, M. K. Chow, G. H. Bogush, J.–L. Look, Mater. Res. Soc. Symp. 131, (1990).

[34] C. J. d. Ouden, R. W. Thompson, J. Colloid Interface Sci. **143**, 77, (1991).

[35] M. J. A. d. Dood, B. Berkhout, C. M. v. Kats, A. Polman, A. v. Blaaderen, Chem. Mater. **14**, 2849, (2002).

[36] A. v. Blaaderen, A. Vrij, Langmuir **8**, 2921, (1992).

[37] N. Amin, S. Arajs, E. Matijevic, phys. stat. sol. **104**, K65, (1987).

[38] J. Gobet, E. Matijevic, J. Colloid Interface Sci. **100**, 555, (1984).

[39] Y.–S. Her, E. Matijevic, M. C. Chon, J. Mater. Res.**10**, 1, (1995).

[40] W. P. Hsu, L. Rönnquist, E. Matijevic, Langmuir **4**, 31, (1988).

[41] E. Matijevic, M. Budnik, L. Meites, J. Colloid Interface Sci. **61**,302, (1977).

[42] E. Matijevic, P. Scheiner, J, Colloid Interface Sci. **63**, 509, (1978).

[43] E. Matijevic, Acc. Chem Res. **14**, 22, (1981).

[44] D. M. Wilhelmy, E. Matijevic, J. Chem. Soc., Faraday Trans. 1 **80**, 563, (1984).

[45] K. P. Velikov, A. v. Blaaderen, Langmuir (2001).

[46] S. Eiden-Aßmann, B. Lindlar, G. Maret, J. Colloid Interface Sci., submitted.

[47] S. Eiden-Aßmann, J. Widoniak and G. Maret, Adv. Mater, submitted.

[48] D. Distler (editor), Wäßrige Polymerdispersionen, WILEY–VCH, Weinheim (1999).

[49] J. W. Goodwin, J. Heosu, C. C. Ho, and R. H. Ottewill, Colloid Polymer Sci. **252**, 464, (1974).

[50] J. W. Goodwin, R. N. Ottewill, R. Pelton, G. Vianello, and D. E. Yates, Br, Polym. J. **10**, 173, (1978).

[51] H. Ni, Y. Du, G. Ma, M. Nagai, and S. Omi, Macromolecules **34**, 6577, (2001).

[52] Marc Egen, Funktionale dreidimensionale Photonische Kristalle aus Polymerlatizes, Ph. D. Thesis, Uni–Mainz, Germany (2003).

[53] K. P. Lok and C.K. Ober, Can. J. Chem. **63**, 209, (1985).

[54] C. K. Ober and K. P, Lok, Macromolecules **20**, 268, (1987).

[55] K. E. J. Barrett, Br. Polym. J. **5**, 259, (1973).

[56] M. Egen, L. Braun, R. Zentel, K. Tännert, P. Frese, O. Reis, and M. Wulf, Macromol. Mat. Eng. submitted.

[57] F. Caruso, Adv. Mater.**13**, 11, (2001).

[58] A. Garg, E. Matijevic, J. Colloid Interface Sci. **126**, 243, (1988).

[59] N. Kawahashi, E. Matijevic, J. Colloid Interface Sci. **138**, 534, (1990).

[60] M. Ohmori, E. Matijevic, J. Colloid Interface Sci. **150**, 594, (1992).

[61] W. P. Hsu, R. Yu, E. Matijevic, J. Colloid Interface Sci. **156**, 56, (1993).

[62] A. Imhof, Langmuir **17**, 3579, (2001).

[63] S. Eiden, G. Maret, J. Colloid Interface Sci. **250**, 281, (2002).

[64] Z. Zhong, Y. Yin, B. Gates, Y. Xia, Adv. Mater. **12**, 206, (2000).

[65] H. Shiho, N. Kawahashi, Colloid Polym. Sci. **278**, 270, (2000).

[66] F. Caruso, X. Shi, R. A. Caruso, and A. S. Susha, Adv. Mater. **13**, 740, (2001).

[67] M. L. Breen, A. D. Dinsmore, R. H. Pink, S. B. Qadri, B. R. Ratna, Langmuir **17**, 903, (2001).

[68] C. Graf, A. v. Blaaderen, Langmuir **18**, 524, (2002).

[69] F. Caruso, M. Spasova, V. Salgueirino–Maceira, L. M. Liz–Marzan, Adv. Mater. **13**, 1090, (2001).

[70] A. Rogach, A. Susha, F. Caruso, G. Sukhorukov, A. Kornowski, S. Kershaw, H. Möhwald, A. Eychmüller, H. Weller, Adv. Mater. **12**, 333, (2000).

[71] W. Y. Zhang, X. Y. Lei, Z. L. Wang, D. G. Zheng, W. Y. Tam, C. T. Chan, P. Sheng, Phys. Rev. Lett. **84**, 2853, (2000).

[72] K. Zahn, G. Maret, Current Opinion Colloid Interface Sci. **4**, 60, (1999).

[73] K. Zahn, R. Lenke, G. Maret, Phys. Rev. Lett. **82**, 2721, (1999).

[74] R. Bubeck, C. Bechinger, S. Neser, P. Leiderer, Phys. Rev. Lett. **82**, 3364, (1999).

[75] W. Wen, L. Zhang, P. Sheng, Phys. Rev. Lett. **85**, 5464, (2000).

[76] A. S. Dimitrov, T. Takahashi, K. Furusawa, K. Nagayama, J. Phys. Chem. **100**, 3163, (1996).

[77] T. Takahashi, A. S. Dimitrov, K. Nagayama, J. Phys. Chem. **100**, 3157, (1996).

[78] P. J. Flanders, Am. J. Phys. **33**, 346, (1965).

[79] Y. Saado, T. Ji, M. Golosovsky, D. Davidov, Y. Avni, A. Frenkel, Opt. Mater. **17**, 1, (2001).

[80] M. Golosovsky, Y. Saado, D. Davidov, Appl. Phys. Lett. **75**, 4168, (1999).

[81] J. Ughelstad, T. Ellingsen, A. Berge, B. Helge, US Patent, PCT/NO83/00014, (1983).

[82] J. Ugelstad, P. Stenstad, L. Kilaas, W. S. Prestvik, R. Herje, A. Berge, E. Hornes, Blood Purif. **11**, 349, (1993).

[83] F. Caruso, A. S. Susha, M. Giersig, H. Möhwald, Adv. Mater. **11**, 950, (1999).

[84] X. Xu, G. Friedman, K. D. Humfeld, S. A. Majetich, S. A. Asher, Adv. Mater. **13**, 1681, (2001).

[85] K. Wormuth, J. Colloid Interface Sci. **241**, 366, (2001).

[86] B. Lindlar, M. Boldt, S. Eiden–Assmann, G. Maret, Adv. Mater. **14**, 1656, (2002).

[87] M. Okubo, M. Seike, and T. Matsumoto, J. Appl. Polym. Sci. **28**, 383, (1983).

[88] T. I.Min, A. Klein, and M. S. El–Ausser, and J. W. Vanderhoff, J. Polym. Sci., Polym. Chem. Ed. **21**, 2845, (1983).

[89] D. I. Lee and T. Jshihuma, J. Polym. Sci., Polym. Chem. Ed. **21**, 147, (1983).

[90] T. Ruhl and G. P. Hellmann, Macromol. Chem. Phys. **202**, 3502, (2001).

[91] T. Ruhl, Elastomere Kolloidale Kristalle aus hart-weichen Kern-Mantel-Latices, Ph.D. Thesis, Uni-Darmstadt, Germany, (2003).

[92] G. Decher, Science **277**, 1232, (1997).

[93] P. Bertrand, A. Jonas, A. Laschewsky, and R. Legras, Macromol. Rapid. Commum. **21**, 319-348, (2000), 319.

[94] G. Kumaraswamy, A. M. Dibaj, F. Caruso, Langmuir **18**, 4150, (2002).

[95] Z. Liang, A. S. Susha, and F. Caruso, Adv. Mater. **14**, No. 16, 1160, (2002).

[96] D. Wang, A. L. Rogach, and F. Caruso, Chem. Mater. **15**, 2724, (2003).

[97] F. Caruso, R. A. Caruso, and H. Möhwald, Science **282**, 1111, (1998).

[98] R. Mayoral, J. Requena, J. S. Moya, C. López, A. Cintas, H. Míguez, F. Meseguer, L. Vázquez, M. Holgado, and A. Blanco, Adv. Mater. **9**, 257, (1997).

[99] R. Tao, Q. Jiang, Phys. Rev. **57**, 5761, (1998).

[100] A. Yethiraj, A. v. Blaaderen, Nature **421**, 513, (2003).

[101] W. R. Russel, Nature **421**, 490, (2003).

[102] H. Yoshimura, M. Matsumoto, S. Endo, and K.Nagayama, Ultramicroscopy **32**, 265, (1990).

[103] A. S. Dimitrov, C. D. Dushkin, H. Yoshimura, and K.Nagayama, Langmuir **10**, 432, (1994).

[104] G. S. Lazarov, N. D. Denkov, O. D. Velev, P. A. Kralchevsky, and K. Nagayama, J. Chem. Soc. Faraday Trans. **90** No. 14, 2077, (1994).

[105] B. Griesebock, M. Egen, R. Zentel, Chem. Mater. **14**, 4023, (2002).

[106] M. Egen, R. Voß, B. Griesebock, and R. Zentel, Chem. Mater., in press (2003).

[107] N. D. Denkov, O. D. Velev, P. A. Kralchevsky, I. B. Ivanov, H. Yoshimura, and K. Nagayama, Langmuir **8**, 3183, (1992).

[108] Y. A. Vlasov, M. Deutsch, D: J. Norris, Appl. Phys. Rev. **76**, 1627, (2000).

[109] Y. A. Vlasov, X.–Z. Bo, J. C. Sturm, and D. J. Norris, Nature **414**, 289, (2001).

[110] R. Rengarajan, P. Jiang, D. C. Larrabee, V. L. Colvin, and D. M. Mittleman, Phys. Rev. B **64**, 205103, (2001).

[111] A. S. Dimitrov and K. Nagayama, Langmuir **12**, 1303, (1996).

[112] P. Jiang, J. F. Bertone, K. S. Hwang, and V. L. Colvin, Chem. Mater. **11**, 2132, (1999).

[113] P. Jiang, G. N. Ostojic, D. M. Mittleman, and V. L. Colvin, Adv. Mater. **13**, 389, (2001).

[114] Z. Z. Gu, A. Fujishima and O. Sato, Chem. Mater. **14**, 760, (2002).

[115] P. Ferrand, M. Egen, B. Griesebock, J. Ahopelto, M. Müller, R. Zentel, S. G. Romanov, and C. M. Sotomayor Torres, Appl. Phys. Lett. **81**, 2689, (2002).

[116] P. Ferrand, M. Egen, R. Zentel, J. Seekamp, S. G. Romanov, and C. M. Sotomayor Torres, Appl. Phys. Lett., in press.

[117] B. T. Holland, C. F. Blanford, T. Do, and A. Stein, Chem. Mater. **11**, 795, (1999).

[118] J. E. G. J. Wijnhoven, L. Bechger, and W. L. Vos, Chem. Mater. **13**, 4486, (2001).

[119] H. Míguez, E. Chomski, F. García–Santamaría, M. Ibisate, S. John, C. López, F. Meseguer, J. P. Mondia, G. A. Ozin, O. Toader, and H. M. van Driel, Adv. Mater. **13**, No. 21, 1634, (2001).

7 Light emitting opal–based photonic crystal heterojunctions

Sergei G. Romanov[1], *Nikolai Gaponik, Alexander Eychmüller, Andrey L. Rogach, Vladimir G. Solovyev, Dmitri N. Chigrin, and Clivia M. Sotomayor Torres*

Abstract

We introduce a three–dimensional photonic crystal heterojunction, synthesized by successive self–assembly of one opal film on top of another using monodisperse polystyrene beads of dissimilar sizes. This structure possesses two minima in the transmission spectrum due to the Bragg photonic gaps in the individual films and gives rise to anisotropy of the reflectance spectrum as well as to appearance of an interface photonic gap. Light sources were selectively embedded in the bottom opal film by alternate impregnation with oppositely charged layers of polyelectrolyte and luminescent CdTe nanocrystals. The emission of CdTe nanocrystals was chosen to match the Bragg resonances of both opal films. Following the band gap anisotropy, the emission experiences a strong spectral and spatial modification. An acceleration of the emission rate at frequencies of the interface gap has been deduced from changes of the emission saturation threshold. It has tentatively been explained as the result of the low group velocity of light at frequencies of the interface gap.

7.1 Introduction

The development of photonic crystals (PhC) approached a phase, where their functionality became a measure of progress. The incorporation of artificial defects in periodic structures for waveguiding, filtering, and lasing is a current engineering target for 2D PhCs [1]. This aim appears substantially more complicated for 3D PhCs and so far has been realized in the case of successive assembling of scatterer lattices, for example, using a wafer bonding approach [2]. Being about a quarter– to a few–wavelengths in size, such defects pose enormous technological challenge in the optical frequency range. On the other hand, most experiments with 3D PhCs in the visible have been done with opals [3] and inverted opals [4], so that a substantial body of knowledge is available to begin with their functionalization.

Artificial opals are ensembles of monodisperse latex or silica beads, which tend to crystallize in the face centered cubic lattice (FCC). This “bottom–up” approach is well documented and reproducible [5]. With respect to application of opals as PhCs [6], two major research directions are currently under consideration. The first one is the impregnation of opals with

---

[1] Corresponding author: e-mail: romanov@uni-wuppertal.de, Phone: +49 202 4392232, Fax: +49 202 4393037

Photonic Crystals. Edited by K. Busch, S. Lölkes, R. B. Wehrspohn and H. Föll
Copyright © 2004 Wiley-VCH Verlag GmbH & Co. KGaA
ISBN: 3-527-40432-5

efficient light sources without deterioration of the photonic band gap (PBG), which targets PBG–based light emitters for the visible and near–IR spectral range [7]. The second one is the fabrication of opals with intentionally introduced defects [8] aiming to achieve resonant conditions for the emission enhancement. It is especially desirable to accomplish the second target within a self-assembly approach used for opal preparation itself. Otherwise, the manufacture of opal-based functional materials will be dependent upon increasingly complicated nanolithography [9].

Due to the statistical nature of self–assembly, approximately 1/100 of opal unit cells are distorted [10]. In this case, a distance between defects is comparable to the Bragg attenuation length. This factor renders *a priori* any attempt of using artificial wavelength-scale defects as senseless, because in currently available research grade opals it is technically impossible to control the location of a defect mode. Since the realization of thin film opals [11], the concentration of defects was reduced by at least one order of magnitude with respect to the best bulk opals. Another advantage is that thin opal films are always oriented along the [111] growth direction of their FCC lattice. Thus, this conventional approach can be used to create localized modes in the PBG by disturbing the lattice periodicity, when a sort of cavity is inserted in an opal body [9]. However, it would be more attractive to localize optical modes in a larger volume of the PhC by modifying the propagation of the Bloch waves across a PhC using, for example, a plane defect. Of course, one should take into account that the plane defect is a 2D defect. In this case, the localization applies to the transverse dimension only and the propagation is allowed along the defect plane. As the result, the achievable engineered localization is not a 3D one, which is the consequence of the insufficient ordering of self–organized PhCs.

As far as the propagation of PhC eigenmodes is concerned, a planar defect can be considered either as a distortion of the eigenmode structure of an otherwise homogeneous PhC or as an impenetrable barrier in the case of a complete PBG. The former approach can be applied if the defect thickness remains comparable to the wavelength of interest and, consequently, the defect does not possess its own PBG structure. By carefully choosing the size of the defect, it becomes possible to form a defect band inside the omnidirectional PBG of the host PhC [12]. Similar results were obtained for a planar defect in an opal with a directional PBG [13] (Fig. 7.1), but the transmission spectrum in this case becomes a strong function of the direction of the light propagation. In the latter case, a thick planar defect can be characterized by its own PBG structure. This leads to the necessity to couple the light flow from one PhC to another at each interface. A simplified version of a heterogeneous PhC, which allows to retain the essential physics, but makes the preparatory work easier, would be a single interface formed by two different PBGs.

So far, theoretically considered heterostructured PhCs were quantum well structures, heterostructures and superlattices, the aim of which is to tailor the transmission spectrum. Most studies are limited to heterostructures based on 1D PhCs with partly overlapping PBGs of their constituents [14,15]. Efforts to simulate heterogeneous 3D PBGs are limited [12,16,17]. Either tunneling of electromagnetic (EM) waves across PhC barriers and PhC superlattices composed of two different PBG structures (perpendicular transport) or propagating EM waves along PhC barriers (parallel transport) were addressed. The formation of photonic minibands in a PhC superlattice has been studied in more details [16]. So far, the driving force behind the majority of theoretical constructions in the area of hetero–PhCs, is the analogy with the

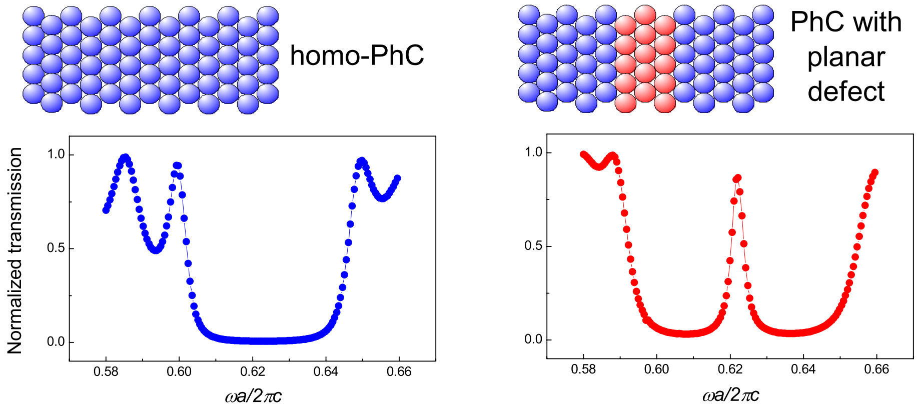

Figure 7.1: Transfer matrix simulation of the transmission spectrum along [111] axis of the opal with the wavelength–thick "defect" film. *Left* – homogeneous opal. *Right* – opal with a planar defect. The refractive index of spheres in the opal and in the defect film is 1.5 and 1.2, respectively.

electronic transport in heterostructured semiconductors. However, the limits of such analogy in the case of photonic hetero–crystals have not been explored yet.

From a general point of view, both the perpendicular and parallel transport of EM waves takes place if the radiation flow impinges at some angle on the interface between different PhCs. The perpendicular transport is the coupling of the radiation flow from one PhC to the other, which neglects tunneling. If the light frequency is far away from PBGs of both PhCs, the requirement of EM field continuity at the interface leads to well-known boundary conditions. By contrast, when the light frequency matches the PBG on either side of a PhC interface, the perpendicular transport is blocked. In the vicinity of the PBG, the field coupling at the interface is a complicated process, because the characteristic pattern of EM field cannot terminate exactly at a geometrical boundary of a PhC. Coupling conditions in this case depends on the mismatch of dispersion characteristics in depth of constituting PhCs and on the structure of the interface itself. Thus, any description in terms of PhC eigenmodes cannot be applied within the volume along the interface, the transversal size of which is comparable to the decay length of non–propagating modes. The consequence is a possibility of interference of EM waves originating from different PhC reservoirs, if they have the same frequency and wavevector but possess an arbitrary phase shift. This is a precondition for appearance of a resonance at the PhC interface. Apparently, this phenomenon is a unique property of PhC interfaces and has no analogy in electronic properties of semiconductor heterojunctions.

The simplest case of an opal–based hetero–PhC is a composition of two opals in tight contact. For example, it can be assembled from two different opal films, grown successively on top of each other. If both opals are made from beads of the same material, but of different diameters, the photonic band structures of both opal films will be similar, although scaled along both the energy and the wavevector axes, in proportion to the lattice constants. The Bragg gaps along the same direction do not overlap, if the difference in bead diameters is large enough. Figure 7.2 shows the energy band model of such PhC heterojunction along

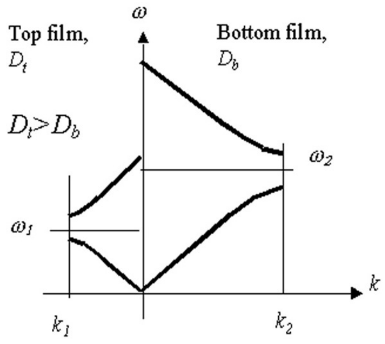

Figure 7.2: PBG diagram of a heterojunction consisting of two opals from beads of different sizes ($D_b < D_t$) along the Γ-L direction, which corresponds to the [111] axis in real space. Scaling is applied to both the frequency and the wavevector axis following the difference of the lattice constant of both opal types.

the Γ-L direction in the Brillouin zone of the opal, which corresponds to the [111] growth direction of the opal lattice.

Early experimental studies of opals with a step–like variation of the index of refraction (RI) demonstrated that two independent PBGs can co–exist in one opal slab [18]. Preparation of a wide variety of heterogeneous opals becomes possible with thin opal films, which allow interfacing of opal films with different PBG characteristics [19]. Recently, we developed a technique to make a sharp interface between two opal films of different lattice parameters, introduced light emitting hetero–opals, and demonstrated some structure–dependent aspects of their optical properties [13,20,21]. CdTe nanocrystals (NCs) were used in light–emitting hetero–opals as a light source. Overlap of the NC band-to-band emission with the band gaps of hetero-opals was achieved by purposive selection of the NC size using the quantum size effect [22]. The strong anisotropy of optical reflectance and emission with respect to the interface plane is the most pronounced optical effect in these hetero–opals. The range of possible hetero–opals may include, for example, (i) the above–mentioned hetero–opals made as sandwiches of similar opals films, whose PBGs scale linearly with the lattice parameter, (ii) hetero–opals made from materials of different dielectric constants that combine band gaps of different width and dispersion and (iii) hetero–opals combining direct and inverted opals, which possess an abrupt change of the EM field pattern. In this chapter, we review the preparation of hetero–opals, which are composed from opal films with different lattice parameters, and selective impregnation of one of the films with luminescent CdTe NCs. We also discuss the anisotropy of optical reflectance and emission and report the observation of an interface-related minimum in the transmission spectra. We support these observations using numerical modeling of transmission spectra of hetero-PhC and considering the combined PBG diagram in the vicinity of the interface.

7.2 Experimental techniques and material preparation

7.2.1 Measurement techniques

Scanning electron microscopy (SEM) was used to visualize the heterojunction between two opal films. Transmission/reflectance spectra were measured under white light illumination from a tungsten lamp: a well–collimated beam of 1 mm diameter was directed on the opal

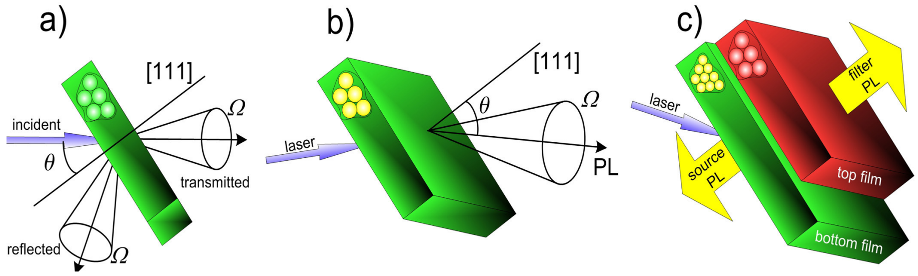

Figure 7.3: Layout of experiments. (a) The reflectance/transmission in the Bragg configuration where the angle of incidence is equal to the angle of reflectance/transmission. (b) and (c) The photoluminescence, where θ denotes the angle of detection, and Ω is the light collection solid angle. The film of the hetero–opal, which is impregnated with light emitting NCs is called a source and the other film – a filter (Fig. 7.3c). The photoluminescence, which is observed from a source film, is called "source PL". Correspondingly, "filter PL" denotes emission collected from the filter film.

surface under a certain angle of incidence θ and either reflected or transmitted light was collected within a solid angle of approximately 2°. The layout of the experiments is shown in Fig. 7.3a. Both faces of a hetero–opal were illuminated successively to catch the anisotropy. The photoluminescence (PL) was excited by the 351 and 457.9 nm lines of a continuous wave (cw) Ar–ion laser with an excitation power of up to 30 mW in a 0.1 mm diameter spot and collected within a $\Omega = 5^\circ$ fraction of the solid angle from the opal face opposite to that exposed to the laser beam, thus allowing the emission to traverse the PhC (Fig. 7.3b). The excitation power was kept sufficiently low to avoid degradation of CdTe NCs. PL spectra were recorded after stabilization of the PL intensity with respect to the excitation power. In order to trace the emission anisotropy, PL spectra were measured at several angles θ with respect to the [111] axis of the FCC opal lattice.

7.2.2 Preparation of hetero–opals

Self-assembly of monodisperse latex or silica beads is a widely used technique to produce 3D artificial opals in the bulk and thin film forms [5,11,23]. When opals are used as PhCs, tuning of the PBG position from the visible to the near–IR can be achieved by changing bead diameters.

Opal films were grown on transparent substrates (glass or quartz slides) using commercially available polystyrene (PS) beads with diameters D = 210, 240, 269, 300, 404 and 503 nm supplied by Duke Scientific Corporation, USA. Aqueous colloidal suspensions of PS beads were carefully washed by two subsequent centrifugations and placed in a Teflon cylindrical cell (7 mm inner diameter). The solvent was allowed to evaporate under a moderate flow of warm air from a hot gun. A gentle vibration of the suspension induced by airflow was found to improve the opal quality with respect to samples grown by drying at ambient conditions. An added advantage was the shorter time needed for the solvent evaporation and the formation of colloidal crystals. The quality of these opals was also found to depend on the concentration of PS beads in aqueous colloidal suspensions with an optimum range of 1–5 vol.%. The thick-

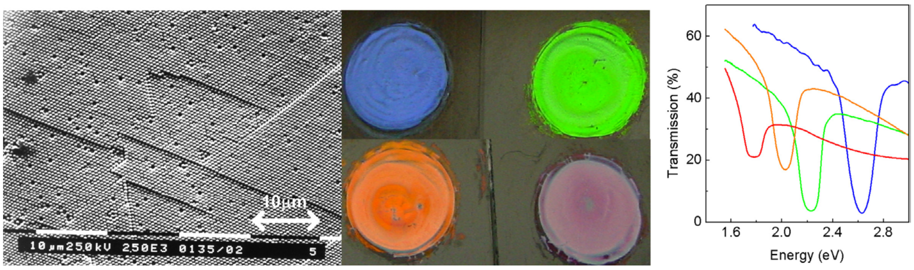

Figure 7.4: *Left*: SEM image of the surface of an opal film crystallized from 503 nm PS beads. *Middle*: True–color images demonstrating the light reflection from opal films crystallized from 210 (blue), 240 (green), 269 (orange) or 300 nm (red) diameter beads. *Right*: Transmission spectra of the same samples.

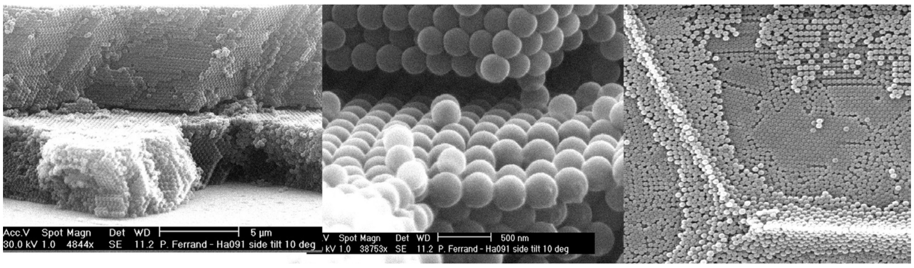
Acc.V Spot Magn Det WD 5 µm
30.0 kV 1.0 4844x SE 11.2 P. Ferrand - Ha091 side tilt 10 deg
V Spot Magn Det WD 500 nm
kV 1.0 38763x SE 11.2 P. Ferrand - Ha091 side tilt 10 deg

Figure 7.5: *Left and middle*: SEM images of a cleaved 300/240 nm hetero–opal. *Right*: SEM micrograph showing the disordered phase of 269 nm PS beads in the initial phase of the film formation on top of a 240 nm diameter bead film.

ness of the films was varied from 15 to 200 monolayers of beads, which was controlled by the amount of suspension in a cell. The formation of a stable opal film suitable for further processing, was accomplished by sintering at 90° for 1 h. Figure 7.4 shows a representative SEM image of the surface of a single-film opal made from 503 nm PS beads. The high quality of these opal films is highlighted by the bright Bragg coloration. The Bragg resonance was tuned over the visible spectral range using PS beads of diameters from 200 to 300 nm (Fig. 7.4).

Hetero–opals were prepared by growing one opal film on top of the other using PS beads of different diameters. Each film, in turn, consists of 15–200 monolayers of PS beads. In what follows, we refer to the opal film crystallized first on the substrate as the *bottom film* while the film grown on top using beads with a different diameter is called *top film*.

Figure 7.5 shows SEM images of a hetero-opal, where the bottom film consists of larger (300 nm) and the top film of smaller (240 nm) PS beads (notations in the following: e.g. 300/240 nm opal). A high degree of lattice ordering is present in both opal films. The abrupt boundary between them indicates that the formation of the top film proceeds independently on the geometrical profile provided by the bottom one. This occurs due to the weaker adhesion of PS beads in the colloidal suspension to the bottom film after sintering. Indeed, if the bottom film was not sintered, a disordered intermediate structure with a thickness of 3–5 monolayers precedes the crystallization of the top film (Fig. 7.5, right).

7.2.3 Selective impregnation of hetero–opals with luminescent nanocrystals

The next step in the formation of hetero–PhCs with engineered optical properties is the incorporation of light emitters in one of the opal films. Infiltration of organic dyes [24] or luminescent semiconductor NCs [25] into the pores of colloidal crystals, results in inhomogeneous impregnation over the opal volume or the non–uniform coating within the cages. In particular, selective impregnation of one of the hetero–opal films is not a trivial process since there is high probability of redistribution of embedded species over the whole structure.

CdTe NCs are used in our work to impregnate opal films. The choice of CdTe NCs obeys to the tunability of the NC emission, the high emission efficiency and small NC size. By changing the particle size from 2 to 6 nm, the PL band of these NCs can be centered everywhere in the visible spectral range starting from 500 nm for 2nm NCs. The NCs are capped with thioglycolic acid carrying a negative charge at appropriate pH. They were synthesized in aqueous colloidal solutions as described elsewhere [22]. The PL quantum efficiency of CdTe NCs is about 25–30% at room temperature [22].

In this work, NCs were embedded into the bottom film of the hetero–opals using the layer–by–layer (LbL) deposition technique. This technique is based on alternating adsorption of oppositely charged species. It was originally developed for positively and negatively charged polyelectrolyte pairs [26] and was later extended to the assembly of polymer–linked NCs [27,28]. Following this method, it is feasible to produce large-area homogeneous films almost irrespectively to the substrate or NC materials. Due to the exceptional versatility of the LbL deposition, this method can be equally effective in coating both planar and highly curved surfaces [29].

Alternating layers of oppositely charged polyelectrolyte and NCs were deposited on the internal surface of the opal voids resulting in a controlled–thickness coating and providing a uniform environment for NCs. In particular, opal films on supporting glass slides were immersed in a 5 mg/ml aqueous solution of poly(diallyldimethylammonium) chloride (positively charge polyelectrolyte) for 30 minutes, thoroughly washed with water and then immersed in a 10^{-3} M aqueous suspension of CdTe NCs for 30 minutes. Both solutions contained 0.2 M NaCl for efficient film formation [30]. Moderate stirring was used to accelerate the mass transfer. This procedure was repeated several times to increase the NC fraction in the opal composites (Fig. 7.6). The opal contains voids of $0.41D$ and $0.23D$ size, which are connected via $0.15D$ channels [31]. These porosities are sufficiently large for the penetration of both polyelectrolyte molecules and NCs. The incorporation of NCs in opals using this technique does not lead to deterioration of the opal structural quality as confirmed by SEM. Figure 7.6 shows true color photos of thin film opals, which are LbL–loaded with luminescent CdTe NCs.

In the case of hetero–opals, the opal film crystallized on a substrate was loaded with NCs as described above and, subsequently, the second opal film was grown on top. No migration of NCs from the LbL–modified bottom film into the top film was observed. The CdTe NC/polymer film formed on the backside of the glass substrate was finally removed by washing in acetone and ethanol.

The PL spectrum of the 240 nm bead opal infiltrated with CdTe NCs and recorded at $\theta = 70°$ is represented by curve 1 in Fig. 7.7. At this angle, no (111) PBG-related minimum has been detected in the transmission spectrum, i.e. the 70°-PL spectrum can be considered as the reference spectrum of CdTe NCs in the opal environment. Curve 2 is the spectrum of

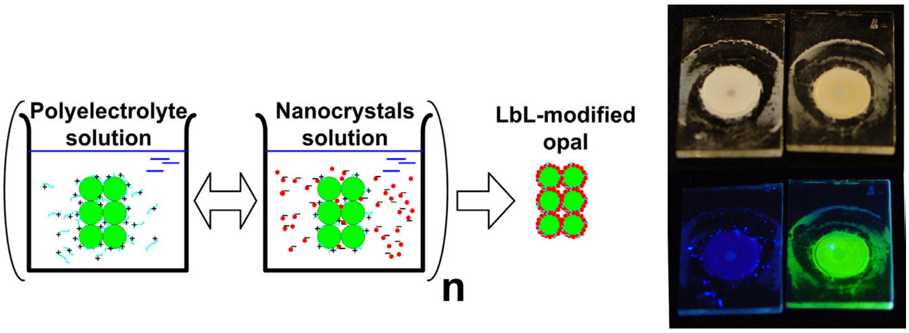

Figure 7.6: *Left*: Schematics of the LbL coating of the inner opal surface with CdTe NCs. Positively (negatively) charged species are polyelectrolyte molecules (NCs). Infilling is made by soaking an opal film first in polyelectrolyte and then in NC solution. This cycle was applied n times (n = 1–12) to increase the CdTe content. *Right*: Photo images of opal films crystallized from 503 nm PS beads as prepared (left column) and infilled with 2.5 nm size CdTe NCs (right column). The images were taken under daylight (top row) and under UV illumination (bottom row). The green coloration of the UV illuminated sample is the luminescence of CdTe NCs.

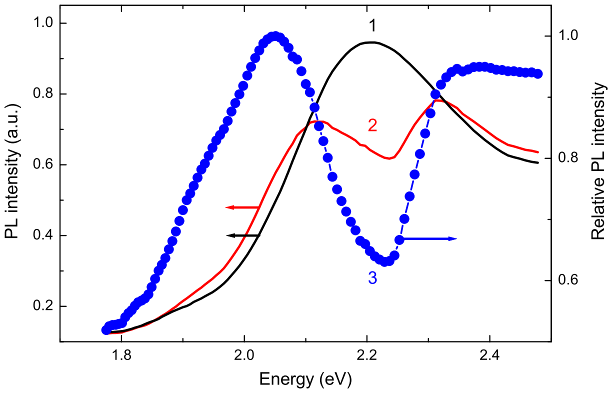

Figure 7.7: PL spectra of an opal film (beads of $D = 240$ nm) loaded with CdTe NCs: the minimum of the PL intensity at 2.23 eV (curve 2) is due to the overlap of the opal PBG with the emission band of CdTe NCs (curve 1). Curves 1 and 2 are normalized to have the same intensity at 1.8 eV, which is far below the PBG. Curve 3 (circles) shows the relative suppression of the PL emission of CdTe NCs in the region of the PBG.

the same sample at $\theta = 0°$. The latter shows a well–defined dip due to the overlap of the PL band with the Bragg band gap of the opal along its [111] axis. The relative PL spectrum (curve 3) given by the ratio of spectrum 2 to spectrum 1, estimates a PBG-induced emission suppression as $\sim 40\%$ in the middle of the gap. This value agrees with the light attenuation obtained in transmission (Fig. 7.4). The discrepancy in the light attenuation obtained from the transmission and luminescence experiments is due to the distribution of the light emitting NCs along the optical path in the latter case.

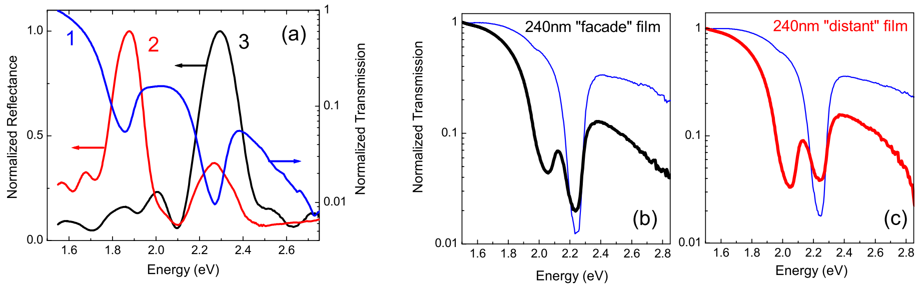

Figure 7.8: (a) The transmission spectrum of 240/300 nm hetero–opal (1) at $\theta = 10°$and reflectance spectra at $\theta = 15°$, if either the 240 nm bead film (2) or the 300 nm bead film (3) is the “facade” film. (b) and (c) Transmission spectra of a 240/269 nm hetero–opal (thick black and red lines) in comparison with the spectrum of an opal film from 240 nm beads (thin blue lines). Panels (b) and (c) compare the transmission in the case of either the 269 or 240 nm bead film positioned as the “facade” film, respectively.

7.3 Reflectance and transmission spectra of hetero–opals

7.3.1 Observation of two Bragg band gaps

Transmission and reflectance spectra of hetero–opals clearly exhibit two minima and maxima (Fig. 7.8). The most obvious evidence of the optical anisotropy of hetero–opals is their different coloration seen from the top and bottom sides, which results from the difference in the mid–frequencies of the Bragg resonance in each film (Fig. 7.8a). In general, the reflectance spectrum of the hetero–opal is a linear composition of two individual filmspectra. Therefore, the Bragg resonances from both opal films can be observed (Fig. 7.9). However, the reflectance from the film, which faces the detector, dominates the spectrum. In what follows, we will denote this film as the “facade” to distinguish it from the “distant” one, whose optical signal has to cross the “facade” film to reach the detector. Under these conditions, the diffraction resonance of the “distant” film can be observed if the “facade” film is relatively thin and the defect concentration in it allows quasi–ballistic propagation of photons. This consideration agrees well with the reflectance spectra shown in Fig. 7.8a, where the dominating Bragg resonance corresponds to the “facade” film.

Assembling two films in one sample does not change the mid–frequency of the Bragg resonances with respect to that in individual films (Fig. 7.8 and 7.9), because the opal lattices retain their periods. The mid–frequencies of transmission minima and reflectance maxima coincide for one and the same sample, thus confirming their diffraction origin (Fig. 7.8a). Fabry–Perot oscillations, which are superimposed on the reflectance spectrum (Fig. 7.8a), prevent the more detailed analysis of weak features in the reflectance.

The resonances in the reflectance spectrum of the 240/300 nm hetero-opal follow the Bragg law $\lambda^2 = (2 \times 0.816D)^2(n^2 - \sin^2\theta)$ for diffraction on the set of (111) planes (Fig. 7.9), where λ is the mid-wavelength of the reflectance band, n is the average RI. And $n^2 = n^2_{\text{bead}} f_{\text{bead}} + n^2_{\text{air}} f_{\text{air}}$ is the sum of RIs of beads ($n_{\text{bead}} = 1.5$) and interstitials ($n_{\text{air}} = 1$) weighted with their volume fractions in the opal lattice. Because the full width at the half max-

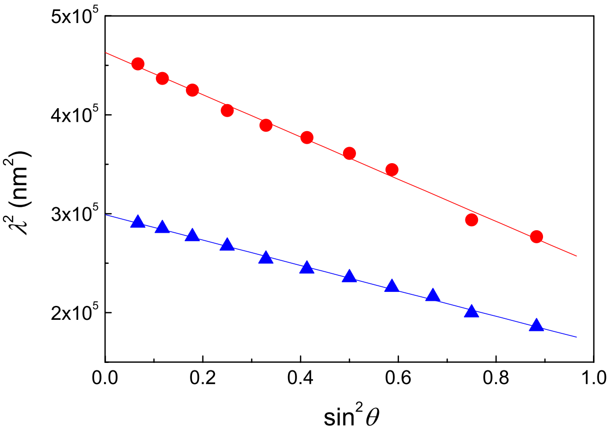

Figure 7.9: Experimental angular dispersions of the Bragg band gap in the 240 nm bead film (triangles) and the 300 nm bead film (circles) of the 240/300 nm hetero–opal. Lines represent the corresponding dispersions of the Bragg diffraction resonances.

imum of these resonances is about 6% of their mid–wavelength, they do not overlap at any angle of observation. The fact that we are able to trace the Bragg minimum in the transmission spectrum down to $\theta = 60^\circ$, is an argument in favor of a good crystallinity of these opal films comparable to the structural quality of single–film opals.

It is instructive to have an idea about the correlation between opal crystallinity and the visibility of the Bragg gap of the "distant" film in the transmission spectrum of the hetero-opal. Comparing the transmission spectra shown in Fig. 7.8b and c, a change in the relative attenuation in the gaps can be seen, namely, the light suppression in the band gap of the opal films appears less pronounced if this film turns out to be the "distant" film. We suggest that the deterioration of the transmission dip of the "distant" film is the result of diffuse light scattering at the interface and in the "facade" film.

7.3.2 The interface gap

Transmission and reflectance spectra of 240/300 nm hetero–opals are shown in Fig. 7.10. The two minima in the transmission spectrum at 2.24 and 1.84 eV are due to the Bragg diffraction resonances in each film of the 20 μm–thick hetero–opal. The 7 μm–thick hetero–opal exhibits a less pronounced attenuation in the Bragg gap, but corresponding peaks in reflectance are well shaped. Simultaneously, an additional transmission minimum at 1.99 eV becomes observable. This additional minimum, which we denote as the interface minimum, appears between the two Bragg minima of the films composing the hetero–opal.

The evolution of the transmission spectra of a 7 μm thick 240/300 nm hetero-opal with the angle of light incidence is shown in Fig. 7.11a. Bragg resonances of the constituent films shift to shorter wavelengths following the Bragg law, but the interface minimum obeys a different dispersion (Fig. 7.11b). The latter can be seen in the angular range, where it is not overshadowed by the Bragg gap of the top film. At angles larger than $\theta \geqslant 50^\circ$, the dominating

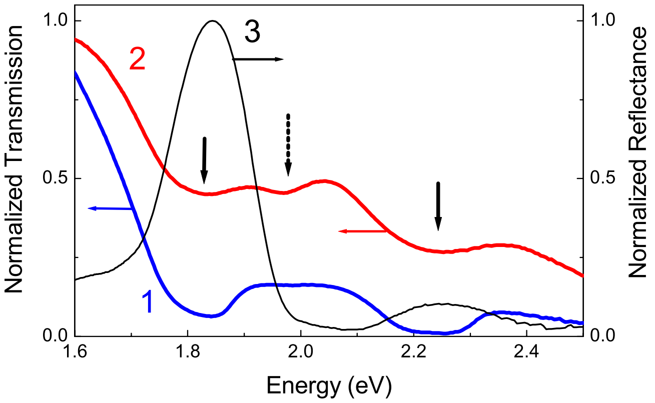

Figure 7.10: Transmission and reflectance spectra of 240/300 nm hetero–opals. Curve 1 is the transmission spectrum of the 20 μm thick hetero–opal along the [111] axis ($\theta = 0°$) of the opal lattice. Curve 2 is the spectrum of the 7 μm thick sample. Curve 3 is the reflectance spectrum of the last sample measured from the 240 nm bead film side at $\theta = 15°$. Arrows indicate transmission minima.

minimum is due to the light attenuation by the (200) directional gap of the top film, whereas the (111) gap of this film is shifted to frequencies above 2.2eV and becomes hardly visible. Moreover, in this spectral range the (111) gap of the top film overlaps with the (200) gap of the bottom film. Note, that the reflectance peak, which corresponds to the (200) gap, cannot be detected in the Bragg configuration used in the present experiment. To perform thorough examination of (200) resonance in transmission, hetero-opals of improved crystallinity (see Chapter 6 of Zentel et al.) are required. Similar angular behavior of the transmission minima was observed in the case of a 300/400 nm hetero–opal, which confirms the general character of the interface minimum formation.

Numerical modeling of the transmission of 3D PhCs is a time consuming process. In order to simplify this task, the finite difference time domain (FDTD) method was applied to simulate the transmission spectrum in the 2D PhC heterojunction of two triangular lattices with different lattice constants and rod diameters (Fig. 7.12a). This model picks up some important features of the studied hetero–opal, like the RI contrast, the lattice constant ratio and the number of scatterer rows on either side of the junction, but does not exactly reproduce the lattice symmetry of the hetero–opal cross–section. The latter depends on the orientation of the cross–section plane with respect to the opal lattice, as it is illustrated in Fig. 7.13, left. The simulated transmission spectra of individual 2D PhCs are compared to spectra of the PhC heterojunction composed from those PhCs in Fig. 7.12b. The interface minimum emerges between two Bragg minima of individual PhCs with increasing number of rows and saturates after approaching 9 row–thick heterojunction. This numerical experiment reveals that evolving the interface minimum requires PhCs on both sides of the junction, but the transverse dimension of the hetero–PhC where the interface minimum is formed, is limited to 4–5 μm for optical frequencies. Further increase of the hetero–PhC thickness leads to intense Fabry-Perot oscillations, which overshadow the interface minimum. Taking the arbitrary choice of

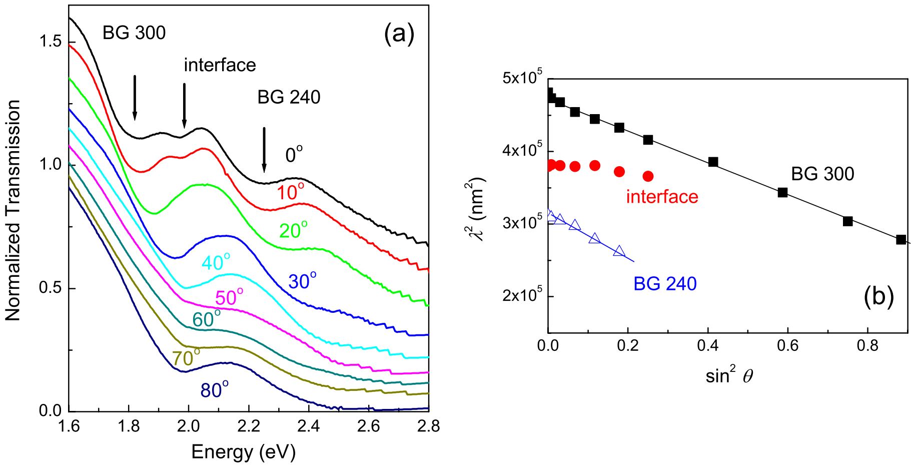

Figure 7.11: (a) Transmission spectra of a 7 μm thick 240/300 nm hetero–opal at different angles of light incidence. Numbers indicate the angle θ, arrows show the Bragg related minima. (b) Dispersions of the transmission minima. Triangles and squares denote central wavelengths of the (111) Bragg resonances of hetero–opal films. Lines show the Bragg law. Red circles represent the angular dispersion of the interface minimum.

the 2D PhC lattice into account, the correspondence between the numerically simulated and the observed interface minimum has an important consequence, namely, the optical transmission of the hetero–PhC differs from the linear sum of transmission spectra of its constituents.

The obvious question is the interrelation of the interface minimum and the PBG diagram of the hetero-PhC: do directional and interface minima have the same physical origin? In this context, it is instructive to consider the PBG diagram of two PhCs in contact. Each part of the heterojunction is a periodic structure with a well–defined PBG (Fig. 7.12c). Their band gap frequencies coincide in the plane wave and the FDTD calculations. To have an idea about possible interactions in the volume near the interface, the transverse dimension of which is determined by the continuity requirements applied to the EM field on both sides of the interface, this diagram can be folded onto the ΓM–axis of a triangular lattice. In the folded diagram the intersection of two bands occurs at the relative energy of about 0.58, which fits the central frequency of the interface minimum in the FDTD simulation well. This consideration emphasizes the role of PhCs in the interface interactions: the PhC determines the dispersion of EM modes on both sides of the junction and defines the limits of EM wave modification in the interface volume. In particular, co–existing of modes of hetero–opal counterparts in the same interface volume, could lead to anti-crossing of two dispersions thereby opening the interface gap (IG). The intrinsic drawback of using the PBG diagram obtained by the plane wave expansion method in the interface volume, is the voluntary extension of results obtained for the infinite lattice to the system with a boundary. Correspondingly, the PBG diagram (Fig. 7.12c) is relevant only as the indicator of the energy range of the probable interference. It is noteworthy that to obtain band intersection, the band diagrams were scaled along the energy axis following the difference in the lattice parameter, the wavevector axis was kept

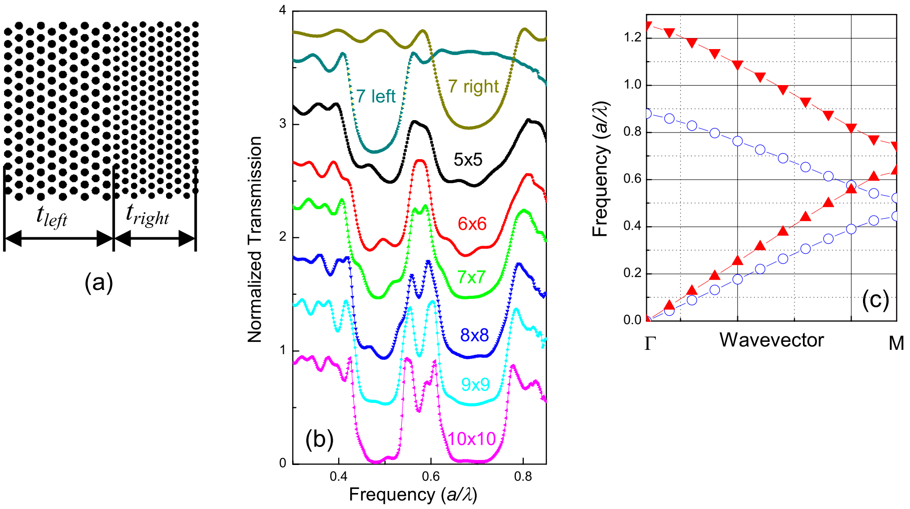

Figure 7.12: Model of the interface minimum in a 2D PhC heterojunction. (a) Model triangular lattice, t_{left} (t_{right}) is the number of pillar rows on the left (right) side of the interface. (b) FDTD simulations of transmission spectra of this hetero–PhC. The development of the interface minimum between two Bragg gaps with increasing thickness is shown. Numbers at curves denote the number of scatterer rows. (c) The band diagram of the PhC heterojunction folded along the interface. Red solid (blue open) symbols denote the dispersion of bands in the PhC with smaller (larger) scatterers.

common to both. This reflects our main assumption concerning the interface volume, where a mixed state of PhC–shaped EM field is formed and the EM field continuity allows to disregard the underlying lattice.

In the folded PBG diagram of the hetero–opal, which is constructed assuming the common wavevector axis, two bands intersect at about 1.99 eV (Fig. 7.13). This frequency is in good agreement with the central frequency of the interface minimum, as it is seen in Fig. 7.11. Thus, 2D and 3D band gap arguments similarly suggest the opening of the IG in the frequency range between the two Bragg band gaps in the near-interface volume of the PhC heterojunction.

Modelling of transmission spectra of a 2D hetero–PhC as a function of the angle of incidence, shows the shift of the interface minimum along the Bragg band gaps of individual films. Extending the analogy between the IG in 2D and 3D PhCs, the interface minimum in a hetero-opal is expected to be angle–dependent as well. The explanation of the apparent difference of angle dispersions of the Bragg and interface minima (Fig. 7.11) in hetero–opals requires separate studies. It seems reasonable to link the peculiar angular dispersion of the IG to the higher dimensionality of the hetero–opal as compared to 2D PhC heterojunction. This suggestion is based on the complexity of the Bloch waves at frequencies above the Bragg band gap, which should be represented as the superposition of several plane waves, in contrast to the relatively simple structure of the Bloch waves below the Bragg band gap. Moreover, the higher the PhC dimensionality, the more the wave front differs from a sphere. For example,

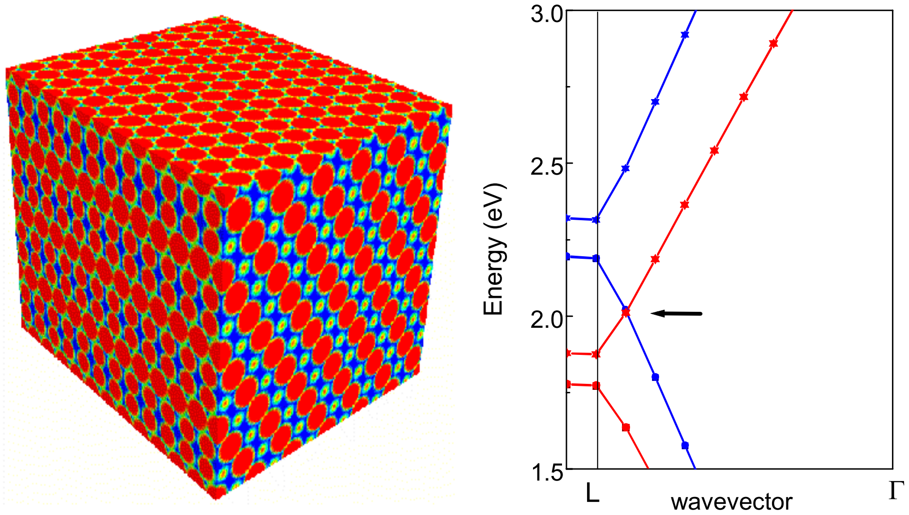

Figure 7.13: *Left*: Two cross–sections of the opal showing different symmetries of the lattice in planes, which are both perpendicular to the interface [111] plane. *Right*: Photonic band structure of the hetero–opal folded onto the Γ-L–axis in the vicinity of the L point. Blue (red) curves denote the photonic band structure of the 240 (300) nm opal. The energy axis is scaled to take into account the frequency of the Bragg gaps of opal films. The arrow indicates the frequency of the dispersion curve crossing.

the dispersion of the Bragg band gap can be well described by the interaction of two spherical waves. However, the dispersion of the IG should obey another law, because this is the interaction of Bloch waves of more complex topology. It follows that the directionality of the IG can be nearly flat over the explored angle range. Flattening of the IG dispersion is also supported by the necessity to average different dispersions over many particular 2D lattice symmetries existing in the case of interfacing 3D PhCs, due to intermixing of spectral responses from a variety of opal cross-sections in experimental spectra.

7.4 Light emission in hetero–opals

7.4.1 Anisotropy of photoluminescence in hetero–opals

The most straightforward consequence of the PBG anisotropy in hetero-opals, whose source film is selectively impregnated with light emitters, is the corresponding spectral and spatial anisotropy of the luminescence. Figure 7.14 shows how the spectral separation of the PBGs in a hetero–opal leads to an anisotropy of the PL from the filter and the source films. As expected, the source PL (for definition see Fig. 7.3c) is suppressed in the PBG range of this film and shows a minimum induced by the filter film (Fig. 7.14b). Surprisingly, in the filter PL spectrum only the intensity suppression due to its own band-pass filtering is observed (Fig. 7.14c). The absence of the source PL minimum in the filter PL spectrum suggests that trajectories of

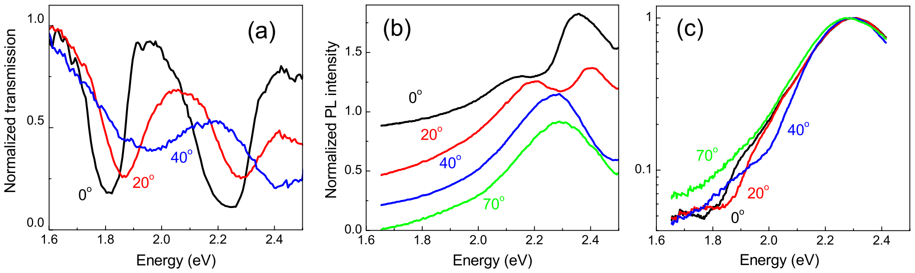

Figure 7.14: Transmission (a), source PL (b) and filter PL (c) spectra of a 240/300 nm CdTe hetero–opal along different directions identified by angles θ, which are indicated by numbers at curves. Curves in the panel (b) are shifted vertically for clarity.

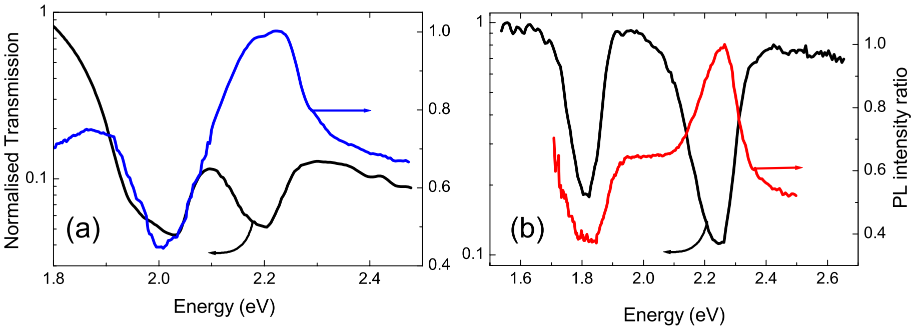

Figure 7.15: Transmission and PL intensity ratio spectra $I_{\mathrm{filter}}/I_{\mathrm{source}}$ of the 240/269 nm (a) and 240/300 nm (b) CdTe hetero–opals. Both transmission and PL refer to the [111] direction.

emitted photons are scrambled, when the radiation traverses the filter film. While this result is at odds with the observation of two gaps in the transmission spectrum, it can be understood by taking into account the number of boundaries, which are crossed by light in the transmission and emission experiments. In the former, the collimated incident beam experiences a total intensity reduction in the “distant” source PBG frequency range due to the backward reflection at the air-source boundary and, additionally, at the internal interface for PBG frequencies of the “facade” filter film. In contrast, the intensity of the light radiated inside the source film experiences only the Bragg reflection at the internal interface, where photons of the filter PBG range are subtracted from the emission spectrum. At the same time, the intrinsic deficit of a source PL intensity with Bragg gap frequencies along the [111] axis becomes compensated by the strong diffuse scattering of the same frequency emission, which impinges the filter film along other directions and, therefore, does not suffer suppression in this frequency range. It is worth mentioning that the diffuse scattering (e.g. the Rayleigh scattering) for source PBG frequencies is strong in a filter film because the ratio of wavelength to scatterer size is less than two in this range.

An estimate of the difference in the emission anisotropy in the hetero-opal is given by the source–to– filter PL intensity ratio, which compares the spectra of emission outgoing in oppo-

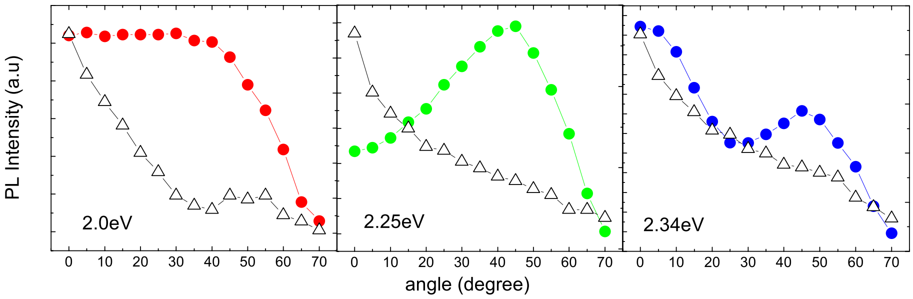

Figure 7.16: Directionality diagrams of the source (circles) and filter (triangles) emission at different frequencies (indicated in the panels) for a 240/300 nm CdTe hetero-opal.

site directions (Fig. 7.15). The PL ratio clearly displays a minimum and a maximum, which correlate remarkably well with the transmission minima, thus confirming the PBG origin on the emission anisotropy.

In addition to the spectral anisotropy, two PBGs of a hetero–opal give rise to different radiation patterns, observed at the same emission frequency from opposite sides of a sample (Fig. 7.16). In order to understand this phenomenon, a realistic model of the light source is needed. We consider the spatial location of light emitting NCs first. The thin film of CdTe NCs overlays the internal surface of opal voids. Due to the random orientation of NCs there is no domination of any particular radiation direction, that allows us to consider a point source after averaging all individual NC radiation diagrams. Consequently, the radiation pattern of a point source embedded in an opal follows the spatial structure of the opal optical eigenmodes at a given frequency. If this frequency falls in the PBG range, the corresponding wavefront acquires the spatial anisotropy due to forbidden propagation along directions of the diffraction resonance. An example of such a wavefront in a homogeneous opal is discussed in [32] and more details will be given elsewhere [33]. The radiation diagram of the source PL evolves rapidly along changing the emission frequency across the source PBG centered at 2.25 eV. In contrast, the angular diagram of the filter PL remains nearly unchanged in the same frequency range because this range is set above the 1.85 eV mid–frequency of the filter PBG. Remarkably, the filter film concentrates the emission flow towards the surface normal ($\theta = 0°$).

As can be seen, the filter film modifies the radiation diagram of the emission intensity with respect to that of the original source PL. This observation opens a possibility to control the directionality of the emission flux, as it was observed after passing the filter film, by changing the mismatch of the PBG mid–frequencies in hetero–opals, the band gap dispersion, or the symmetry of the filter film.

7.4.2 Emission modification at the interface

Emission studies of homogeneous opal films have demonstrated the decrease of the spontaneous emission rate [32,34] and the development of the emission stimulation [32,35] at PBG frequencies. The non–linearity of the emission was visualized by examination of the PL saturation threshold, which was revealed by increasing the excitation power P. When the emitter possesses a multi-level electronic energy band structure and there is a competition between radiative and non–radiative relaxation of optically excited emitters, the saturation threshold becomes a function of the emission rate. The functional dependence of emission intensity upon the power $I(P)$, can be satisfactorily described by the expression $I = I_0(1 - \exp(-P/P_0))$, where I_0 and P_0 are fitting parameters describing the radiation power of the saturated emitter and the saturation threshold, respectively. Applying this fitting procedure to data obtained at different frequencies, the spectra of the saturated emission intensity $I_0(\omega)$ and the saturating threshold $P_0(\omega)$ were constructed. The spectrum $I_0(\omega)$ can be associated with the spectrum of the spontaneous emission rate. The $P_0(\omega)$ value depends on the backreaction of the emitted radiation upon the emitter. In analogy with microresonators, the increase of the saturation threshold is an indication of acceleration of the radiative recombination by the large EM field accumulated in the resonator. Similar resonator conditions are fulfilled for the slow propagating opal optical modes of the PBG frequency range as discussed in [32,36]. It is noteworthy that emission stimulation becomes observable if (i) the light source is spatially distributed in accord with the profile of the opal eigenmode EM field and (ii) there is a sufficiently large number of photons, which complete ballistically their path from emitter to detector in the detected emission flux.

The $I_0(\omega)$ spectrum of the source film retains the shape of the source PL spectrum $I(\omega)$, including the PBG–induced minimum (Fig. 7.17a). This correlation suggests the domination of spontaneously emitted photons over the total radiation flux. The $P_0(\omega)$ spectrum shows the global minimum in the frequency range of the emission band maximum and the peak at PBG frequencies. The rapid increase of the threshold towards the “red” edge of the emission band is the result of the ineffective energy transfer from the optically pumped states to the states radiating at these frequencies. The $I_0(\omega)$ spectrum of the filter film (Fig. 7.17b) does not show a detectable minimum in accord with the PL spectra of Fig. 7.14. The filter $P_0(\omega)$ spectrum shows only a weak modulation compared to that of the source film. This is a consequence of the absence of emitters in the filter film and the scrambling of photon trajectories in it.

With the present level of understanding of the emission modification in an opal–based PhC, we cannot interpret the absolute values of saturation parameters. Therefore, aiming to extrapolate the above–described method to the emission in hetero–opals, we will address the spectral variation of these parameters with the angle of emission detection only.

A comparison of saturated emission spectra for different detection angles (Fig. 7.18a) shows that the direction–sensitive parts of these spectra falls in the PBG frequency range. The radiated power approaches its maximum at the PL band maximum independently of the angle of detection, whereas the minimum of the radiated power is shifted following the angular dispersion of the Bragg resonance. Similarly, the angle dependence of the saturation threshold spectra (Fig. 7.18b) can be referred to the dispersion of the PBG. The saturation threshold approaches its minimum at the PL band maximum and peaks in the PBG. Moreover, the threshold minimum is an angle–independent feature in contrast to the threshold maximum which is in agreement with the behavior of homogeneous opal films of similar composition. Therefore, no influence of the interface was detected in the source emission.

A similar analysis in the case of the filter emission demonstrates opposite tendencies. The filter $I_0(\omega)$ spectra (Fig. 7.19a) acquire the maximum, which develops at 1.94 eV during the angle increase, but does not experience a shift. The central frequency of this maximum

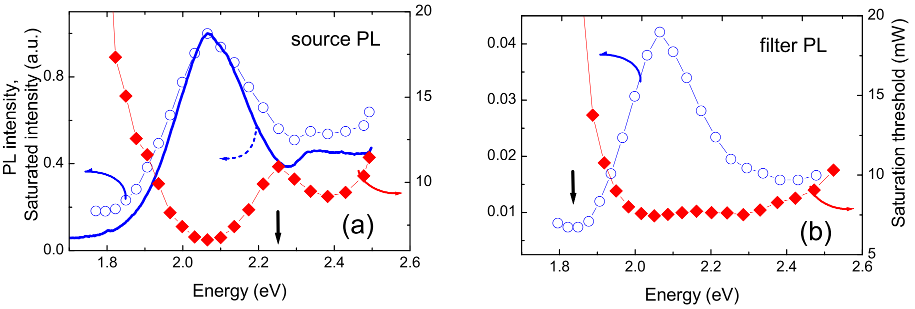

Figure 7.17: (a) PL spectrum $I(\omega)$ (blue line), saturated PL intensity $I_0(\omega)$ (circles) and saturation threshold $P_0(\omega)$ (red squares) spectra of the source film emission of a 240/300 nm CdTe hetero–opal along the [111] axis of the opal lattice. Black arrows indicate the central frequency of the corresponding PBG. (b) Saturated PL intensity (circles) and the saturation threshold (red squares) spectra along [111] axis of the filter film.

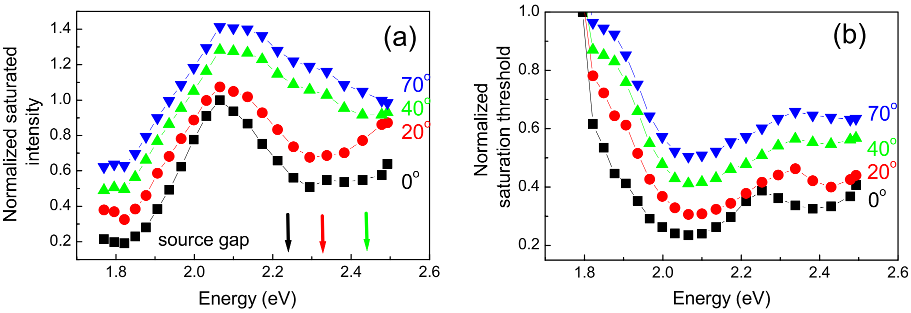

Figure 7.18: (a) Normalized $I_0(\omega)$ spectra of the source film of a 240/300 nm CdTe hetero–opal at different angles of detection. Arrows indicate the position of the PBG at corresponding angles in accord with the curve color coding. (b) Normalized $P_0(\omega)$ spectra of the same sample. Curves are shifted vertically for clarity and labeled with detection angles.

corresponds to the position of the IG (Fig. 7.11). In parallel, the $P_0(\omega)$ spectra show the growing peak of the saturation threshold centered at 1.91 eV at $\theta = 70°$(Fig. 7.19b). This observation suggests the acceleration of emission in the frequency range of the IG. Similarly to the emission stimulation in the source Bragg PBG, this effect is reasonably related to the low group velocity of EM waves at frequencies of the IG. The (200) filter gap, which appears in the same frequency range at large angles, cannot affect the emission rate in accord with the same reasons as the (111) filter gap. The fact that the emission enhancement is observed at high angles of detection only, can be taken as a consequence of the emission coupling to interface modes propagating along the heterojunction.

Spectra of the PL intensity ratio obtained as described above (Fig. 7.16) also show the development of the emission non–linearity at frequencies around the IG (Fig. 7.20a). On the one hand, the spectral anisotropy associated with the mismatch of source and filter PBGs is preserved along the excitation power increase. On the other hand, with increased pumping

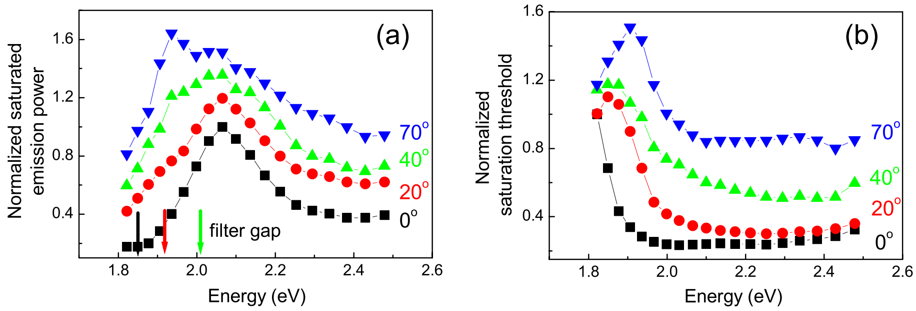

Figure 7.19: (a) Normalized $I_0(\omega)$ spectra of the filter film of a 240/300 nm CdTe hetero-opal at different angles of detection. Arrows indicate the position of the PBG at corresponding angles according to the curve color. (b) Normalized $P_0(\omega)$ spectra of the same sample. Curves are shifted vertically for clarity. Numbers indicate detection angles.

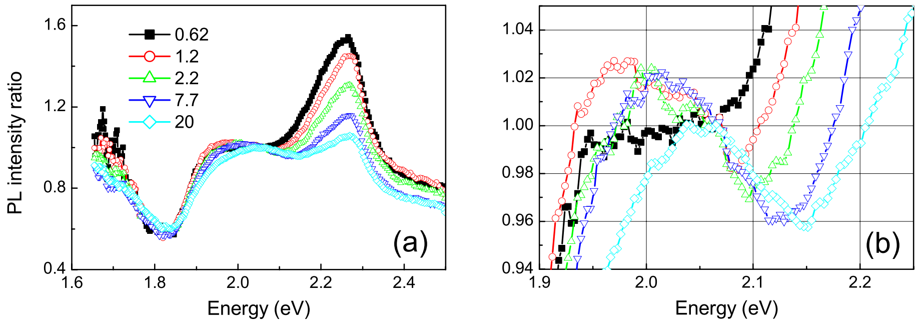

Figure 7.20: (a) The ratio of filter and source PL intensities of a 240/300 nm CdTe hetero–opal at different pumping intensities. The emission was detected along the interface normal. The pumping power is shown for each curve in mW. (b) The same ratios in the vicinity of the IG.

the attenuation of the source PL becomes less pronounced due to the stimulation of emission at source PBG frequencies, whereas the filter PBG attenuation remains unchanged. The filter and source PL intensities are nearly the same in the IG range from 1.92 to 2.05 eV at the lowest pumping power. With increasing pumping power a maximum arises in this range, moreover, it shifts gradually to higher frequencies (Fig. 7.20b). The focal point, where filter and source intensities are the same, appears at 2.06 eV. The noteworthy fact is that this frequency corresponds to the maximum transmission observed between the two Bragg gaps of the hetero–opal. This focal point respects the balance of two tendencies, namely, the emission enhancement in the source PBG, which pushes the ratio down, and emission enhancement in the IG, which pulls the ratio up. At the highest pumping power, the PBG enhancement overcomes the IG one and the IG–related peak disappears. The non–linearity of the emission in the IG frequency range suggests that the near–interface volume is a functionalized part of the hetero–opal with special properties. This finding opens a way to control the emission properties of opal–embedded light sources by tuning the IG in purpose.

Conclusions

Hetero–opals were synthesized by successive growth of one opal film on top of the other using self-assembly of monodisperse latex beads of different sizes. Heterostructuring gives rise to a strong anisotropy of the reflectance spectrum due to the presence of different PBGs in the same sample. The bottom film of hetero–opals was selectively impregnated with luminescent CdTe NCs, using a layer–by–layer deposition technique. The emission of CdTe NCs, which was chosen to match the Bragg PBG of opal films, experiences a strong spectral and spatial anisotropy following the mismatch of PBGs.

Coupling of EM waves at the heterojunction leads to an interference in the volume near the interface between the opal films of different PBGs and to the opening of an IG. The experimentally observed dispersion of the latter gap differs from that of the Bragg gaps in opal films. Numerical simulations indicate the possibility of interface phenomena in PhC heterojunctions. Studies of the emission suppression/enhancement in hetero-opals revealed a non–linearity of the emission in the frequency range of the IG, if the radiation flow crosses the interface. This effect can be a consequence of the emission in resonator conditions, which are imposed effectively on radiating dipoles by the heterojunction.

Summarizing, interfacing the PhCs of different PBGs is a prospective way to functionalize and control the PhC optical properties in a more flexible manner than it is possible with homogeneous PhCs.

Acknowledgements

This work was supported by the DFG priority program “Photonic Crystals” SPP 1113 and EU research grants. We thank Thomas Franzl for his help with LaTeX.

References

[1] Special issues: Optical and Quantum Electronics **34**, issues 1-3 (2002); IEEE J. Quantum Electronics **38**, issue 7 (2002).

[2] S. Noda, K. Tomoda, N. Yamamoto, A. Chutinan, Science **289**, 604 (2000).

[3] S. G. Romanov, A. V. Fokin, V. I. Alperovich, N. P. Johnson, R. M. De La Rue, phys. stat. sol. (a) **164**, 169 (1997).

[4] J. E. G. J. Wijnhoven, W. L. Vos, Science **281**, 802 (1998).

[5] N. D. Deniskina, D. V. Kalinin, L. K. Kazantseva, Gem quality opals, their synthesis and natural genesis (in Russian), Nauka, Novosibirsk (1980).

[6] S. G. Romanov, C. M. Sotomayor Torres, in Handbook of Nanostructured Materials and Technology, v.4, ch.4, ed. H.S. Nalwa, Academic Press, New-York, pp.231-323 (2000).

[7] V. N. Astratov, V. N. Bogomolov, A. A. Kaplyanskii, A. V. Prokofiev, L. A. Samoilovich, S. M. Samoilovich, Yu. A. Vlasov, Il Nuovo Cimento, **17D**, 1349 (1995).

[8] Yu. A. Vlasov, Xiang Zheng Bo, J. C. Sturm, D. J. Norris, Nature **414**, 289 (2001).

[9] S. G. Romanov, P. Ferrand, M. Egen, R. Zentel, J. Ahopelto, N. Gaponik, A. Eychmüller, A. L. Rogach, C. M. Sotomayor Torres, Synthetic Metals **139**, 701 (2003).

[10] Yu. A. Vlasov, V. N. Astratov, A. V. Baryshev, A. A. Kaplyanskii, O. Z. Karimov, M. F. Limonov, Phys. Rev. E **61**, 5784 (2000).

[11] Y. Xia, B. Gates, Y. Yin, Y. Lu, Adv. Mater. **12**, 693 (2000).

[12] V. Karathanos, A. Modinos, N. Stefanou, J. Phys.: Condens. Matter **6**, 6257 (1994).

[13] S. G. Romanov, T. Maka, V. G. Solovyev, P. Ferrand, C. M. Sotomayor Torres, B. Griesebock, M. Egen, M. Müller, R. Zentel, N. Gaponik, A. Eychmüller, A.L. Rogach, J. Manzanares-Martinez, D. Cassagne, MRS Symp. Proc. **722**, L7.7 (2002).
[14] C. Zhang, F. Qiao, J. Wan, Jian Zi, J. Appl. Phys. **87**, 3174 (2000).
[15] F. Qiao, C. Zhang, J. Wan, J. Zi, Appl. Phys. Let. **77**, 3698 (2000).
[16] E. Istrate, M. Charbonneau-Lefort, E. H. Sargent, Phys. Rev. B **66**, 075121 (2002).
[17] E. Istrate, E. H. Sargent, J. Opt. A: Pure Appl. Opt. **4**, S242 (2002).
[18] S. G. Romanov, H. M. Yates, M. E. Pemble, R. M De La Rue, J. Phys.: Cond. Matter, **12** 8221 (2000).
[19] P. Jiang, G. N. Ostojic, R. Narat, D. M. Mittleman, V. L. Colvin, Adv. Mater. **13**, 389 (2001); S. M.Yang, H. Migues, G. A. Ozin, Adv. Funct. Mat., **12**, 425 (2002); M. Egen, R. Voss, B. Griesebock, R. Zentel, S. G. Romanov, C. M. Sotomayor Torres, Chem. Materials, **15**, 3786 (2003).
[20] V. G. Solovyev, S. G. Romanov, C. M. Sotomayor Torres, N. Gaponik, A. Eychmüller, A. L. Rogach, MRS Symp. Proc., **708**, K7.8.1 (2002).
[21] N. Gaponik, A. Eychmüller, A. L. Rogach, V. G. Solovyev, C. M. Sotomayor Torres, S. G. Romanov, accepted J. Appl. Phys.
[22] N. Gaponik, D. V. Talapin, A. L. Rogach, K. Hoppe, E. V. Shevchenko, A. Kornowski, A. Eychmüller, H. Weller, J. Phys. Chem. B **106**, 7177 (2002).
[23] R. Mayoral, J. Requena, J. S. Moya, C. Lopez, A. Cintas, H. Miguez, F. Meseguer, L. Vazkuez, M. Holgado, A. Blanco, Adv. Mater. **9**, 257 (1997); P. Jiang, J. F. Bertone, K. S. Hwang, V. L. Colvin, Chem. Mater. **11**, 2132 (1999); A. L. Rogach, N. A. Kotov, D. S. Koktysh, J. W. Ostrander, G. A. Ragoisha, Chem. Mater. **12**, 2721 (2000); O. Vickreva, O. Kalinina, E. Kumacheva, Adv. Mater. **12**, 110 (2000); M. Müller, R. Zentel, T. Maka, S. G. Romanov , C. M. Sotomayor Torres, Chem. Mater. **12**, 2508 (2000).
[24] K. Yoshino, K. Tada, M. Ozaki, A. A. Zakhidov, R. H. Baughman, *Jpn. J. Appl. Phys.* **36**, L714 (1997).
[25] S. V. Gaponenko, A. M. Kapitonov, V. N. Bogomolov, A. V. Prokofiev, A. Eychmüller, A. L. Rogach, JETP Lett. **68**, 142 (1998).
[26] G. Decher, Science **277**, 1232 (1997).
[27] N. A. Kotov, I. Dekany, J. H. Fendler, J. Phys. Chem. **99**, 13065 (1995).
[28] A. L. Rogach, D. S. Koktysh, M. Harrison, N. A. Kotov, Chem. Mater. **12**, 1526 (2000).
[29] F. Caruso, Adv. Mater. **13**, 11 (2001).
[30] S. T. Dubas, J. B. Schlenoff, Macromolecules **32**, 8153 (1999).
[31] V. G. Balakirev, V. N. Bogomolov, V. V. Zhuravlev, Y. A. Kumzerov, V. P. Petranovskii, S. G. Romanov, L. A. Samoilovich, Crystallography Reports **38**, 348 (1993).
[32] S. G. Romanov, D. N. Chigrin, V. G. Solovyev, T. Maka, N. Gaponik, Eychmüller, A. L. Rogach, C. M. Sotomayor Torres, phys. stat. sol. (a) **197**, 662 (2003).
[33] D. N. Chigrin, T. Maka, S. G. Romanov, C. M. Sotomayor Torres, in preparation.
[34] A. F. Koenderink, L. Bechger, H. P. Schriemer, A. Lagendijk, W. L. Vos, Phys. Rev. Lett. **88**, 143903 (2002).
[35] V. G. Solovyev, S. G. Romanov, C. M. Sotomayor Torres, M. Müller, R. Zentel, N. Gaponik, A. Eychmüller, A. L. Rogach, J. Appl. Phys. **94**, 1205 (2003).
[36] S. G. Romanov, D. N. Chigrin, C. M. Sotomayor Torres, N. Gaponik, A. Eychmüller, A. L. Rogach, To be published in Physical Review E, **69**, 01 February (2004).

8 Three–dimensional lithography of Photonic Crystals

Alvaro Blanco, Kurt Busch, Markus Deubel, Christian Enkrich, Georg von Freymann, Martin Hermatschweiler, Wolf–Peter Koch, Stefan Linden, Daniel C. Meisel, and Martin Wegener[1]

8.1 Introduction

The publications of Yablonovitch [1] and John [2] in 1987 on the optical properties of three–dimensional (3D) periodic structures have triggered an enormous interest in the scientific community. They predicted that the electromagnetic modes in Photonic Crystals (PhCs) are strongly influenced by the periodic variation of the dielectric constant. For certain symmetries and material compositions, Bragg scattering leads to the formation of a complete photonic band gap (PBG). This is a frequency range in which the propagation of electromagnetic waves in the 3D PhC is forbidden for any wave vector and polarization. Accordingly, Bragg scattering opens a PBG in the direction or plane of periodicity for appropriate one–dimensional (1D) or two–dimensional (2D) structures.

The excitement about PhCs is based partially on the prospect of "molding the flow of light" by intentionally introducing defects in the crystal structure [3]. These defects give rise to localized photonic states inside the PBG and can be used as functional elements for photonic devices. For example, a microcavity can be implemented by a point defect and a line defect constitutes a waveguide. Compared to their conventional counterparts, these elements can be realized on a much smaller scale based on PhCs. Ultimately, the goal is to make use of the interplay between PBGs and defect modes to create integrated photonic circuits.

So far, this field of research is mainly driven by progress in the theoretical description of light in PhCs and by the development of more efficient numerical methods. On the experimental side, insufficient quality of the PhCs is still a mayor issue. The problems of sample fabrication are associated with the fact that the lattice constant of a PhC has to be on the order of half the wavelength of light in the material. While this does not represent a big challenge in the microwave regime — in this case, one can literally drill holes in a slab of material [4] — things are much harder in the telecommunications window and the visible spectral region.

Electron beam lithography and selective etching processes have been used for the fabrication of 2D PhCs. The most common designs consist of periodically structured slab waveguides [5]. Another successful approach is to fabricate 2D PhCs with a large aspect ratio based on macroporous silicon [6]. On account of their exceptional quality, 2D PhCs have been used for many experiments in the near–infrared. Nevertheless, there is a principal drawback. 2D PhCs do not possess a complete PBG and therefore are only suited for a limited set of applications. For example, it is not possible to suppress the spontaneous emission in all directions

---

[1] Corresponding author, e-mail: martin.wegener@physik.uni-karlsruhe.de

Photonic Crystals. Edited by K. Busch, S. Lölkes, R. B. Wehrspohn and H. Föll
Copyright © 2004 Wiley-VCH Verlag GmbH & Co. KGaA
ISBN: 3-527-40432-5

within a 2D PhC. For the same reason, these structures are also prone to scattering losses in the third dimension which ultimately restricts their performance.

Since electron beam lithography is a planar technique, it is not straightforward to transfer this method to the fabrication of 3D PhCs. A possible way to overcome this problem is to fabricate samples based on a layer–by–layer design [7,8]. In a first step, the surface of a wafer is processed with the above mentioned techniques. The next layer is then added either by deposition and subsequent patterning of a dielectric film or by bonding two pieces of the wafer followed by removal of one of the substrates. This procedure is repeated several times until the desired number of layers is reached. In practice, PhCs made by the layer–by–layer method are limited by the complexity of the fabrication process to only a few periods. Additionally, a high degree of mechanical precision is required to avoid offsets between the different layers.

So far, the most common method to produce 3D PhCs is based on self–assembly of sub–micrometer spheres. Here one takes advantage of the natural tendency of monodisperse spheres to form a face–centered cubic (fcc) lattice during segregation [9]. In nature, this process leads to the formation of opals. This gemstone is also the eponym for artificial crystals assembled by self–organization. Unfortunately, a fcc lattice of dielectric spheres does not have a complete PBG. The inverted structure, a fcc lattice of air spheres in a dielectric medium, on the other hand has a complete PBG, provided the refractive index of the medium is larger than 2.8 [10]. This inversion process can be accomplished, for example, by chemical vapour deposition (CVD) and subsequent selective etching of the opal template. Silicon inverted opals with a complete PBG centered at $1.46\ \mu\mathrm{m}$ have been demonstrated [11]. However, inverted opals are extremely sensitive to disorder. It has been predicted [12], that deviations in sphere size as small as 2% will result in a destruction of the complete PBG. The fragility of the PBG can be attributed to the fact that the PBG is rather small and is located between the eighth and ninth band in the high–frequency range of the band structure. This poses severe demands on the synthesis of the colloidal spheres and on the uniformity of the inversion process.

Our approach to 3D PhC fabrication comprises two different lithographic methods: Holographic lithography and direct laser writing. These optical methods, which are highly qualified for the production of top–quality polymeric 3D PhCs, are described in detail in Section 8.2 and 8.3. Scanning electron microscope (SEM) micrographs and optical spectra of samples made by our group are presented in either case. Since the refractive index of the used polymer is only 1.6, a supplementary inversion process of the polymeric PhCs with a high refractive index material is necessary to open up a complete PBG. Our roadmap to accomplish this task is outlined in Section 8.4.

8.2 Holographic lithography

Light fields resulting from multiple beam interference have been studied in detail for the purpose of trapping and cooling of atoms [13]. Such fields are also of great interest for the fabrication of PhCs since the light distribution can be spatially periodic or quasi–periodic with a period on the order of half the wavelength. The interference pattern can be recorded as a volume hologram and converted into a correspondingly structured matter distribution. The resulting material, in principle, can serve as a PhC because its refractive index varies accordingly [14–17].

Photoresists are used as recording medium. In the following, we describe how to fabricate materials periodically structured in 3D on a wavelength scale by holographic lithography. These structures can also serve as templates for PhCs.

8.2.1 The photoresist

Essentially two kinds of photoresists are in use with cationic or radical polymerization. In radical-curing systems, absorption of light generates free radicals that initiate polymerization processes. Radical systems are sensitive to oxygen which must be excluded, otherwise the polymerization can be affected severely. Therefore the material must be processed in an inert atmosphere or protected by some other means. For a detailed comparison with cationic systems cf. [18].

This problem is absent in cationic systems. An often used representative of this group is the commercially available thick film photoresist SU-8 (sold by MicroChem Corporation). It consists of an octafunctional epoxy resin (EPON® SU–8), a photoinitiator (mixed Triarylsulfonium/Hexafluoroantimonate salt in propylene carbonate solvent), both dissolved in gamma–butyrolactone (GBL) [19, 20]. The photoinitiator generates an acid upon irradiation by near UV light ($350 - 400$ nm). The spatial acid concentration is an image of the irradiation dose. In a post–exposure bake, the latent picture is converted into a cross–linking density by a chain reaction during thermal treatment at $65°$ to $93°$ C for several minutes.

The cross–linking degree determines the solubility in the "developing" solvent. GBL or another appropriate solvent are used in this step. Thus, sufficiently illuminated resin remains ("negative" photoresist) whereas underexposed resin is washed away. The remaining material therefore has a shape that follows the surface for the threshold irradiation, which is the boundary between over– and under–exposed regions. Effectively, the interference pattern is stored in a digitized form: It is a porous air–polymer–structure showing the isodose surface for the threshold dose value.

A "positive" photoresist requires a resin that upon irradiation undergoes chemical changes that make it soluble [19]. When a positive photoresist is illuminated with the same interference pattern the inverted structure is obtained as compared to a negative photoresist.

8.2.2 The crystallography of multiple-beam interference patterns

It is of importance to predict the structure that is obtained for a given beam configuration. The respective calculations allow one to systematically study the influence of the experimental parameters like beam directions, intensities and polarizations on the resulting structure. Because of the threshold dose feature of the photoresist process, the quantities of interest are the isodose surfaces. The mathematics for the intensities suggests to make use of the laws developed for crystallographic purposes.

The interfering light beams are treated as plane waves with the electric field vector as the real part of a complex quantity:

$$\vec{E}_n(\vec{r},t) = \mathrm{Re}\{\vec{E}_n^0 e^{i(\vec{k}_n\cdot\vec{r}-\omega t)}\} \qquad \text{with integer } n = 1,\dots,N \tag{8.1}$$

In what follows it is assumed that the N beams are obtained by splitting one beam, i. e. all $|\vec{k}_n|$ are the same. The exposure dose $\mathcal{D}(\vec{r})$ is proportional to the light intensity (meant as time–averaged Poynting vector) of the superposition of the N waves. It can be expressed as a Fourier sum [14, 15, 21] according to

$$\mathcal{D}(\vec{r}) \propto \left| \sum_{n=1}^{N} \vec{E}_n^0 \, \mathrm{e}^{\mathrm{i}(\vec{k}_n \cdot \vec{r} - \omega t)} \right|^2 = \sum_{n,m=1}^{N} a_{nm} \, \mathrm{e}^{\mathrm{i}\vec{G}_{nm} \cdot \vec{r}} \tag{8.2}$$

The (generally complex) "form factors" $a_{nm} := \vec{E}_n^0 \cdot \vec{E}_m^{0^*}$ result from the relative amplitudes, polarizations and phases of the light beams. It has to be noted that the Fourier sum results in a real quantity. The differences $\vec{G}_{nm} := \vec{k}_n - \vec{k}_m$ of the wave vectors in essence result from the relative directions of the beams.

Translational symmetry

The representation of $\mathcal{D}(\vec{r})$ as a Fourier sum (8.2) is the same as that one describing the periodicity of a crystal [22]; it relates the spatial behavior of $\mathcal{D}(\vec{r})$ in real space $\vec{r}$ to vectors $\vec{G}_{nm}$ in reciprocal space. As usual in crystallography, the existence of a set of primitive basis vectors $\{\vec{b}_i\}$ for the set $\{\vec{G}_{nm}\}$ allows one to conclude that the interference pattern has lattice properties.

The number of basis elements $\{\vec{b}_i\}$ gives the dimensionality d of the reciprocal lattice. For $d = 2$, the five 2D Bravais lattices are at choice. If d turns out to be 3, one of the 14 3D Bravais lattices applies. All 14 Bravais lattices can be generated by four noncoplanar beams [23]. Four beams constitute the minimal set allowing for the fabrication of 3D periodic structures. Adding further beams in general destroys the lattice property unless they fit to the lattice already present [13].

The corresponding real space lattice with basis $\{\vec{a}_i\}$ follows from the condition:

$$\vec{b}_i \cdot \vec{a}_j = 2\pi\delta_{ij} \tag{8.3}$$

with δ_{ij} as the Kronecker delta. In 3D periodic systems the solution is:

$$\vec{a}_1 = 2\pi \frac{\vec{b}_2 \times \vec{b}_3}{\vec{b}_1 \cdot (\vec{b}_2 \times \vec{b}_3\,)} \qquad \text{and cyclic permutations of the indices.} \tag{8.4}$$

Under special circumstances the lattice can degenerate to lower dimensionality through the form factors. Pathological cases have to be considered separately.

A phase shift of one beam with respect to the others, in general, leads to another pattern. Under special conditions the topology of the interference pattern is phase independent and the interference pattern is shifted in space only [13].

At present, the favorite lattice type for a full PBG is a fcc lattice [1, 10]. The respective reciprocal lattice is body–centered cubic (bcc). For this reason all $\vec{G}_{mn}$ occurring in sum (8.2) have to lie on a bcc lattice. One choice for a realization is the so–called "umbrella–like" beam configuration with 4 beams as described below (Section 8.2.3).

The basis element of the structure

Given a lattice, the structure repeated at every lattice point in real space is called "basis element"; it is the structure inside a Wigner–Seitz cell (WSC). In solid state crystallography, this

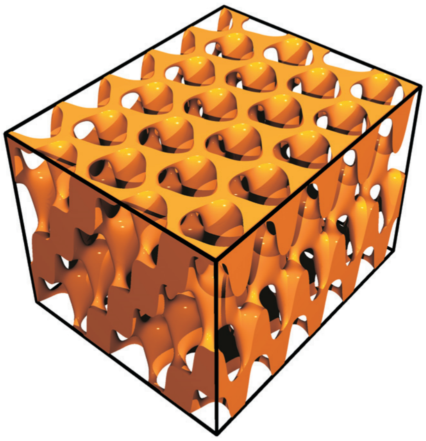

Figure 8.1: Simulation of a fcc structure with a filling factor $f = 0.29$ [21]. Four beams are arranged in a so–called "umbrella–like" configuration. A detailed description with parameter values is given in Section 8.2.3.

corresponds to the electron density at a lattice point. For a given lattice type (i. e. for fixed directions of the $\vec{k}_n$) the shape and volume of the basis element is determined by the form factors a_{nm} and thus by both, the intensities and the polarizations of the beams. The filling factor f is the volume of the basis element divided by the volume of the WSC.

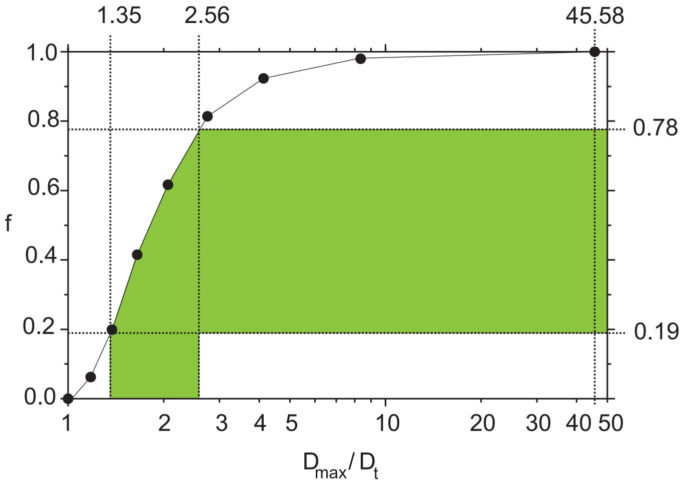

Figure 8.2: Computed filling factor f of our fcc structures (see Fig. 8.1) as a function of the exposure dose $\mathcal{D}_{\max}/\mathcal{D}_{\mathrm{t}}$. $\mathcal{D}_{\max}$ is the maximum dose occurring in the interference pattern and $\mathcal{D}_{\mathrm{t}}$ is the threshold dose of the photoresist [21]. Useful material requires $\mathcal{D}_{\max}/\mathcal{D}_{\mathrm{t}}$ to be between 1.35 and 2.56 or f between 0.19 and 0.78 (shaded green). More details are given in the text.

All features of the resulting structure can be calculated using (8.2) to find the isosurface for a certain threshold dose value (see Fig. 8.1). As an example, a question of practical importance is studied numerically: To obtain a structure that is of practical use, it must be mechanically stable, i. e., the basis elements have to be interconnected, otherwise the structure falls apart. On the other hand, the underexposed regions have to be interconnected, too. This is required to make sure that the pores are washed out by the developer. For this purpose the structure was calculated for different exposure doses, i. e. for different filling factors. Figure 8.2 shows the result of this calculation for the fcc structures described in Section 8.2.3. It gives the filling factor f as a function of the peak dose $\mathcal{D}_{\max}$ occurring in the interference pattern. $\mathcal{D}_{\max}$ in turn is given in units of the threshold dose $\mathcal{D}_{\mathrm{t}}$. Below $\mathcal{D}_{\max}/\mathcal{D}_{\mathrm{t}} = 1$ no regions are sufficiently illuminated, resulting in $f = 0$. If the minimum dose $\mathcal{D}_{\min}$ reaches $\mathcal{D}_{\mathrm{t}}$ all material is fully exposed, i. e. $f = 1$. This is the case for $\mathcal{D}_{\max}/\mathcal{D}_{\mathrm{t}} \geq 45.58$. Only in the range $\mathcal{D}_{\max}/\mathcal{D}_{\mathrm{t}} = 1.35 \ldots 2.56$ are both interconnectivity conditions simultaneously fulfilled. From $\mathcal{D}_{\max}/\mathcal{D}_{\mathrm{t}} = 1.35$ on, the basis elements are interconnected and above $\mathcal{D}_{\max}/\mathcal{D}_{\mathrm{t}} = 2.56$ the pores are closed. The corresponding filling factors are 0.19 and 0.78. It is to be noted that in the useful range ($\mathcal{D}_{\max}/\mathcal{D}_{\mathrm{t}} = 1.35 \ldots 2.56$) the dose varies by less than a factor of two [21].

8.2.3 Experimental realization

The SU-8 photoresist solution is spun on a glass substrate and heated to 95° C for several minutes for drying ("soft bake"). A hard photoresist layer of about 10 $\mu\mathrm{m}$ thickness is obtained.

A frequency-tripled Nd:YAG laser at 355 nm wavelength is used as light source (model GCR 170–10 by Spectra-Physics). This Q-switched laser emits pulses of 6 ns duration so that any problems due to mechanical vibrations during exposure are avoided. In order to make the laser oscillant on a single longitudinal mode only it is seeded. The beam diameter is about 8 mm.

The output of the laser is split into four beams, the polarization and intensities of which can be adjusted independently. A 3D periodic interference pattern is produced by the so–called “umbrella–like” configuration [24]: One beam (central beam $\#1$) is made perpendicular to the photoresist layer. The three other beams are equally distributed on a cone with beam $\#1$ on the cone axis (cf. Fig. 8.3a). The apex angle γ of the cone determines the lattice type which in general is trigonal.

The central beam is circularly polarized while the others are linearly p–polarized. The energy ratios of beam $\#1 : \#2 : \#3 : \#4$ are $1.5 : 1 : 1 : 1$. After a single laser shot exposure the sample is heated (“post–exposure bake”) to fully cure the overexposed regions.

Thereafter the underexposed regions are dissolved in the developer liquid. Figure 8.3 shows a SEM image of a sample with an internal angle $\gamma_{\mathrm{tri}} = 22.82°$ which results in a trigonal structure.

A fcc lattice requires an internal apex angle of $\gamma_{\mathrm{fcc}} = \arccos(7/9) = 38.94°$ [24]. This angle is not directly accessible since the refraction of the beams at the air photoresist interface has to be taken into account. The index of refraction limits the angles γ inside the photoresist layer to values below the critical angle of total internal reflection which is $36.78°$ for SU–8.

In order to solve this problem, the light is coupled through a fused silica prism into the photoresist layer. We use a corner cube prism with a chopped–off tip for this purpose. The coupling from the prism into the photoresist is through a water immersion film. To get $\gamma_{\mathrm{fcc}} = 38.94°$ inside the photoresist layer, γ_{air} in air has to be $40.36°$ taking into account the corner cube geometry [21].

Figure 8.4 shows a SEM picture of a true fcc sample [17]. Due to the shrinkage of the structure during polymerization by about $7.5\,\%$ [25] the lattice constant a_{fcc} (length of the cubic cell) of the fcc structure including the shrinkage is calculated to be 509 nm.

Due to shrinkage the samples tend to crack and to peel off the substrate. Both effects can be reduced considerably by surrounding the porous samples with narrow frames of fully polymerized bulk material. The frames are prepared by illuminating the SU–8 film with a UV lamp while the area inside the frames is protected by an appropriately patterned mask [21]. Thereafter the film is exposed to the interfering laser beams. After heat treatment and

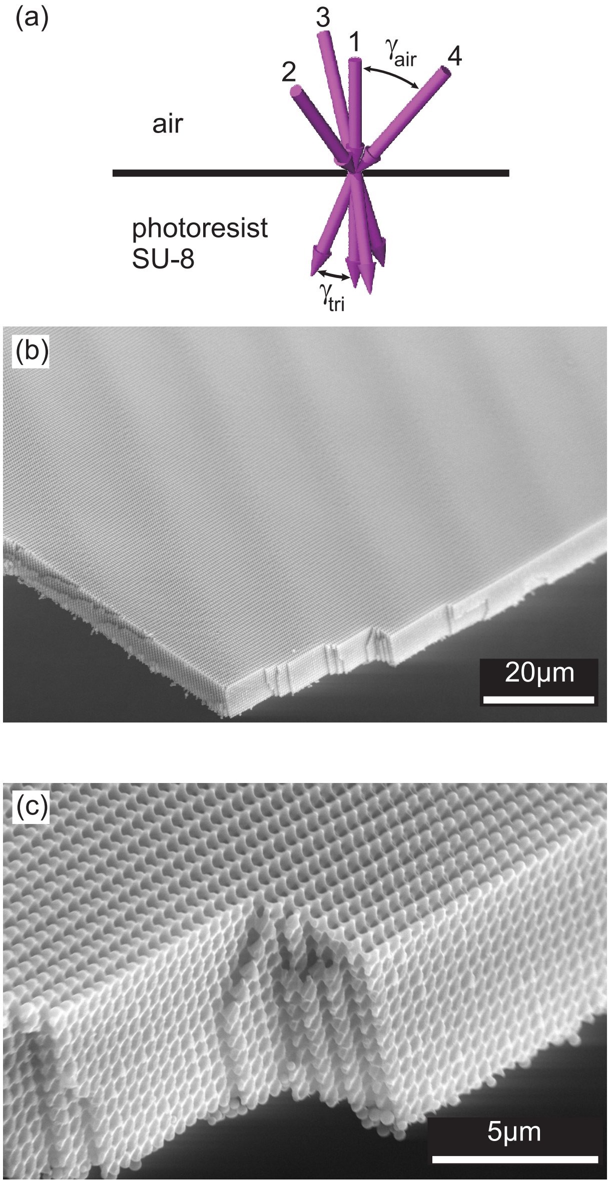

Figure 8.3: (a) The “umbrella–like” configuration with beam #1 perpendicular to the photoresist surface and the remaining beams equally distributed on the surface of a cone with an apex angle $\gamma_{\mathrm{air}} = 40.36°$ in air. Due to refraction at the air–photoresist interface, the angle inside the photoresist layer is smaller ($\gamma_{\mathrm{tri}} = 22.83°$) resulting in a trigonal structure. (b) and (c) are SEM images of an edge of the trigonal structure obtained for the values as of (a) for two magnifications.

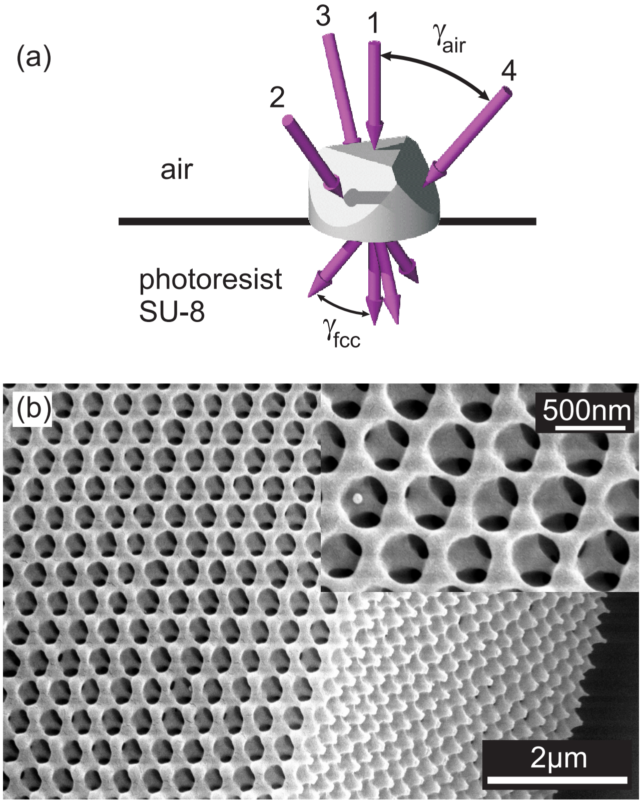

Figure 8.4: (a) The "umbrella–like" configuration including the coupling prism. An angle $\gamma_{\rm air} = 40.36°$ in air leads to the necessary angle of $\gamma_{\rm fcc} = 38.94°$ inside the photoresist required for a fcc structure. The beams are coupled through a water film into the photoresist. (b) SEM images of the fcc structure. The inset is a closeup showing the hexagonal pattern of a (111) net plane of the fcc structure. The filling factor is estimated to be 0.29 (cf. Fig. 8.1).

development, the porous regions are held by the surrounding frames which adhere well to the substrate. Mesh widths of 50 μm to 500 μm have been used successfully so far.

8.2.4 Optical properties of the photoresist structures

In order to enable band structure calculations and to interpret measured data, the index of refraction for polymerized bulk SU–8 for 633 nm is determined by measuring Brewster's angle. The index is found to be $n = 1.61$. By comparing the SEM images visually with computer simulations (see Fig. 8.1) the filling factor is estimated to be 0.29 [21].

The optical properties of fcc structures fabricated by holography were studied by means of both transmission and reflection experiments. The experimental setup allows focusing of the incident beam in a region smaller than 100 μm (typically 50 μm). This is very important due to the actual geometry of the samples and also to check their homogeneity in short range.

Figure 8.5 is a combination of measured transmission data along the (111) direction with a corresponding band structure calculation. It shows a reasonable agreement between the measured transmission dip and the calculated stop band position and width in Γ-L direction [17].

In the reflection experiments, white light is sent onto the sample at normal incidence with respect to the (111) face and the specular reflectance is collected, using a beam splitter, in the detector. The transmission experiment allows us as well to explore the dependence of

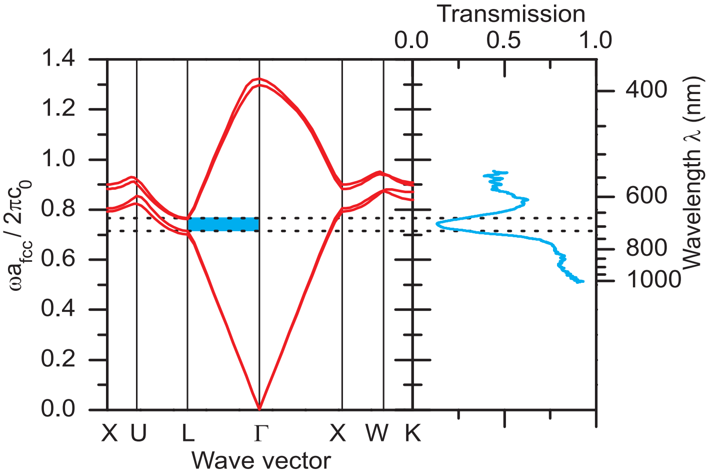

Figure 8.5: Calculated band structure (left) and transmission spectrum in the (111) direction (Γ-L) (right) for the structure shown in Fig. 8.4. The measured position and width of the dip is in fair agreement with the calculations. At 680 nm the transmission drops to 15 %.

the optical properties with respect to the incidence angle θ, which is a must to fully characterize any PhC structure. In Fig. 8.6a the transmission for different angles of incidence ($\theta = 0° \ldots \theta = 55°$) is shown. At normal incidence, the wave vector is parallel to the Γ–L direction. As θ increases we move away from Γ–L to other crystal directions following either L–U, L–W or L–K. The spectral evolution of the Bragg peak, here a dip, can easily be followed as θ increases (see 8.6a and b).

The value of transmission measurements is that every single photon missing is taken into account as a dip in the transmitted intensity. Reflection measurements, on the other hand, are only sensitive for specularly reflected light while photons scattered in other directions are not recorded. This allows the observation of higher energy features which can be related with other crystal directions [26] or higher photonic bands.

8.3 Direct laser writing

Holographic lithography of PhC structures can easily produce samples with defect–free areas of several square millimeters and offers a high flexibility in tailoring the unit cell. Due to the fabrication principle, these structures are strictly periodic, i.e., defect structures cannot be included in a controlled fashion. However, the controlled fabrication of defect structures, such as microcavities or waveguides, in otherwise defect–free PhCs is essential for many technological applications. Therefore, an additional method to introduce defect structures into the holographic PhC templates has to be applied.

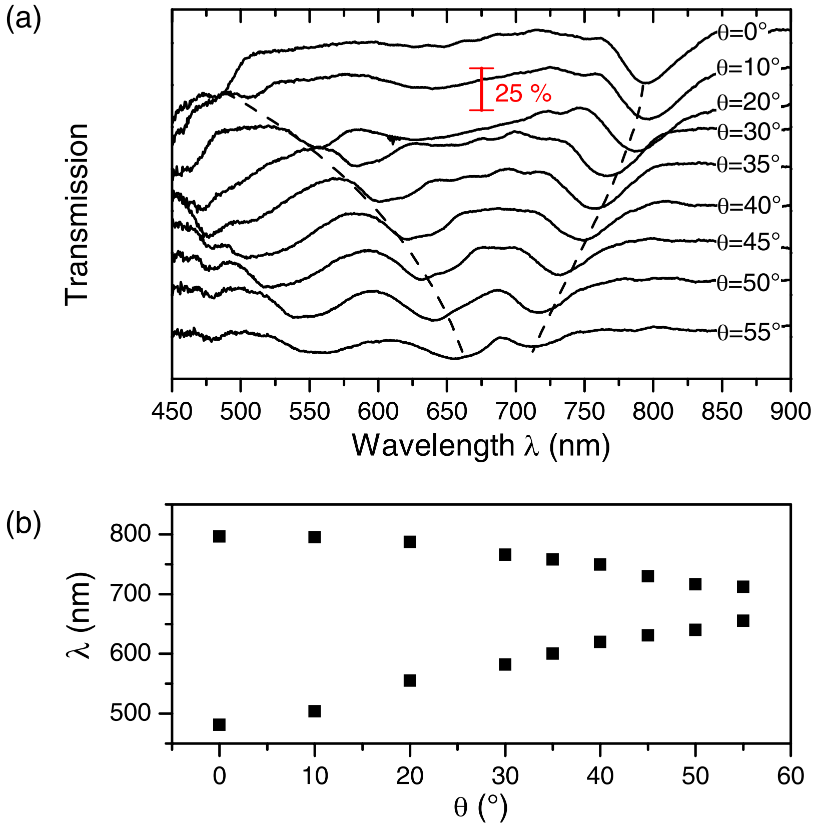

Figure 8.6: (a) Transmission spectra of a fcc structure fabricated by holographic lithography for different angles of incidence θ. At normal incidence, the wave vector is parallel to the Γ-L direction. The individual curves are vertically displaced for clarity. The dashed lines are guides to the eye in order to follow the spectral evolution of the transmission minima. (b) Spectral position of the transmission minima for different angles of incidence θ.

8.3.1 Multi–photon polymerization

Conventional photolithographical microstructuring of photosensitive materials is a well established technique to convert patterns of light into physical structures. However, structures fabricated by this method are mostly 2D as the absorption of light in the photosensitive media proceeds from the illuminated surface to the substrate. 3D arrangements may be formed by layer–by–layer techniques, where after exposure and structuring of one layer, this layer is lowered in a bath of liquid photoresist, and a second layer is exposed on top of the first. By sequentially repeating this process, 3D multilayer structures can be fabricated. Besides the limitations of structure size, this concept is not applicable to the problem considered here,

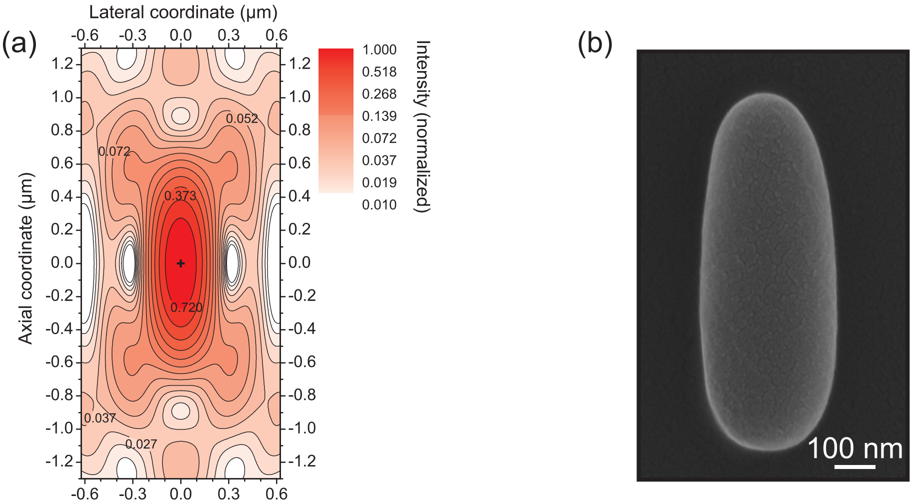

Figure 8.7: (a) Calculated isophotes of the microscope objective used in our experiments (for calculational model see [39]; $NA = 1.4$, $\lambda = 800\ \mathrm{nm}$, polarization perpendicular to lateral coordinate). The intensity is normalized to the value in the origin (geometrical focus). (b) Voxel exposed by a single laser pulse.

where defect structures need to be fabricated *inside* PhC templates: A writing method is required which itself provides 3D resolution.

A technique that is able to accomplish this task and which is especially suitable for polymeric PhCs is 3D direct laser writing (DLW) by multi–photon polymerization [27–29].

For colloidal PhCs, where the integration of defect structures is a similar problem, two–photon absorption DLW has already been demonstrated successfully for the writing of waveguide structures inside self–assembled opal templates [30].

Multi–photon absorption (MPA) DLW may also be used for the fabrication of complete 3D PhC lattices. Several groups have reported the fabrication of such structures in photoresists [28, 31–35] and silica glass [36], [37].

In MPA DLW, photosensitive threshold systems, mostly photoresists exhibiting an intensity threshold for exposure, are illuminated by laser light that has insufficient photon energy to expose the photosensitive medium by a one–photon absorption process. When the laser light is sharply focused into the medium, however, the light intensity near the focus may become sufficiently high to exceed the exposure threshold by multi–photon processes. As the probability of these processes scales with I^n where I is the light intensity and n the number of photons involved in the absorption process, the exposed region is confined to a small volume element ("voxel") inclosing the focus, whereas the rest of the medium remains unexposed. By scanning the focus relative to the medium, in principle, any 3D structure may be written directly into the photosensitive medium.

The size and shape of the exposed voxels depend on the isodose surfaces, the isophotes, of the microscope objective and the multi–photon exposure threshold of the photosensitive medium. The calculated isophotes of the microscope objective that is used in our experiments are shown in Fig. 8.7a. The isophotes in the vicinity of the geometrical focus exhibit a typical near–elliptical shape. The aspect ratio, i.e. the ratio between the axial and the lateral diameter of a voxel, strongly depends on the numerical aperture NA of the microscope objective. Since the ellipticity decreases for larger NA, mostly oil–immersion objectives with the highest numerical apertures currently available are used for DLW.

Figure 8.7a seems to suggest that the size of a voxel may be chosen arbitrarily small: Given a particular exposure threshold by the photosensitive medium, the whole volume inside the corresponding isophote will be exposed upon illumination. If one simply reduces the light intensity, this value will move to isophotes closer and closer to the geometrical focus, resulting in smaller and smaller voxels. Ultimately, the smallest feature size would be limited by the physical and chemical resolution of the photosensitive medium. In practice, it is the stability of the laser light intensity that determines the smallest reproduceably writable structures, as the susceptibility to fluctuations of the isophote–distribution increases strong, close to the geometrical focus.

Nevertheless, MPA DLW offers the possibility of sub–diffraction limited resolution for the 3D structuring of photosensitive media. A spatial resolution of $120\ \mathrm{nm}$ at a fabrication wavelength of $780\ \mathrm{nm}$ has been reported (lateral structure size), which corresponds to $\lambda/6.5$ [29].

8.3.2 Experimental realization

Photoresist

We use SU–8 negative photoresist in the DLW fabrication process (see Section 8.2.1), as the compatibility of the photoresist systems for holography and DLW is crucial. When utilizing the same resist, DLW may simply be added as a second exposure step to the holographic fabrication process prior to development of the PhC. Additionally, the cationic polymerization mechanism of SU–8 is of great advantage, since the monomers do not polymerize directly after exposure. Therefore, the difference in the refractive indices of exposed and unexposed photoresist is negligible and structures that have already been exposed will not affect further exposure steps. Another advantage is that SU–8 is solid during the writing process. This does not only make the sample handling much more comfortable, but also offers a higher degree of freedom in the scanning pattern, since successively written structures do not have to be interconnected immediately.

Like many other commercially available photoresists, SU–8 has a rather low sensitivity for multi–photon absorption (MPA). Therefore, sharp focusing of laser light alone is insufficient to surpass the MPA threshold. To supply sufficiently high intensities, pulsed laser sources are necessary. For femtosecond (fs) laser pulses, it has been reported that even single shot exposure of SU–8 is possible [38]. This can be a great advantage in terms of writing time, as the polymerization in most resist systems currently in use for DLW relies on multishot exposure of single voxels.

Experimental setup

Prior to exposure, a $20\ \mu\mathrm{m}$ thick SU–8 photoresist film is spin coated on a coverslide and solidified by a soft–bake process. The laser, a regeneratively amplified Ti:sapphire laser system

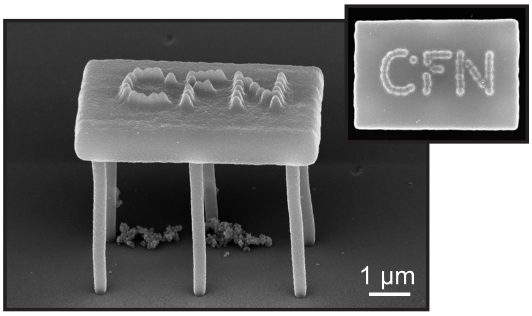

Figure 8.8: 3D structure fabricated by DLW: Logo of the DFG–Center for Functional Nanostructures.

(Spectra Physics Hurricane, pulse duration 120 fs, repetition rate adjustable from single shot mode to 1 kHz) is tuned to a central wavelength of 800 nm, where the one–photon absorption of SU–8 is negligible [38]. The beam is attenuated by a halfwave–plate/polarizer combination and after beam expansion coupled into a custom designed inverted microscope (Leica). The beam is then focused into the photoresist by a $100\times$ oil–immersion microscope objective ($NA = 1.4$). The inverted microscope allows a prepositioning of the substrate relative to the spatially fixed focal spot of the laser beam. This substrate is held in a three–axis piezoelectric scanning stage (Physik Instrumente) that is operated in closed loop and reaches a resolution of 5 nm at a full scanning range of $200\ \mu\text{m} \times 200\ \mu\text{m} \times 20\ \mu\text{m}$. A personal computer controls the scanning operation of the piezo stage and synchronizes its movement with the pulsing of the laser system via a laser controlling interface. After DLW of a preprogrammed pattern, the exposed sample is postbaked and developed as described in Section 8.2.3 for the holographic PhC templates.

Figure 8.7b shows a single voxel that has been polymerized by a single laser pulse. Its near-elliptical shape corresponds quite nicely to the calculated intensity distribution for our optical system and shows the typical aspect ratio of about 2.7 for the microscope objective employed here. This shape now forms the basic building block for all fabricated structures shown in this article. The diameter of the single voxels can be adjusted by changing the laser pulse energy from about $2\ \mu\text{m}$ (higher pulse energies lead to evaporation of the unpolymerized SU–8) to less than 200 nm. In structures consisting of connected voxels, the single voxel distance can be used as an additional degree of freedom to adjust the structural details. In Fig. 8.8, the logo of the DFG–Center for Functional Nanostructures written on a table of only $6\ \mu\text{m}$ side length, shows the high flexibility and accuracy of our 3D writing.

8.3.3 Direct laser writing of three–dimensional photonic crystals

Because of their simple geometrical structure, the so–called layer–by–layer [40] or woodpile [41] PhCs are ideal structures for DLW.

Figure 8.9 shows a schematical drawing of the design of this group of PhCs: Layers consisting of straight parallel rods with a center–to–center distance a are stacked to a 3D lattice. Adjacent layers have the orientation of the rods rotated by 90° and second nearest neighbouring layers are shifted by a distance of $a/2$ perpendicular to the rod axes. This stacking sequence repeats itself after every four layers with a lattice constant c. For $c/a = \sqrt{2}$, this 3D lattice has a fcc primitive unit cell with a basis of two rods, and face centered tetragonal

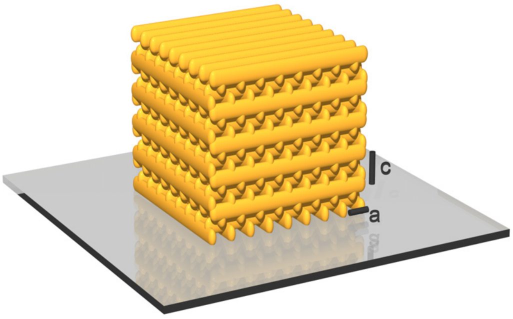

Figure 8.9: The layer–by–layer or woodpile structure: Straight parallel rods with an axis–distance a form layers that are stapled into a 3D lattice. The stacking sequence repeats itself after every four layers.

(fct) symmetry otherwise. Its structure can be derived from the diamond lattice by replacing the (110)–chains by the straight rods [40]. Theoretical calculations by Ho et al. [40] have shown, that such PhCs can have a complete PBG for an index contrast as small as 1.9. It is located between the second and third band, and has a gap/midgap ratio of up to 28 % for air rods in silicon. In addition to that, various rod cross sections, filling fractions and overlapping of adjacent layers show sizeable PBGs. Further calculations by Chutinan et al. [42] predict that these structures are also relatively insensitive to structural imperfections.

Layer–by–layer structures have already been fabricated by DLW in photosensitive polymers that exhibit PBGs at mid– and near–infrared wavelengths [28, 31–35]. As the refractive index of the employed polymers is approximately 1.5, these structures have no complete PBG.

Figure 8.10 shows two 20–layer structures that have been fabricated with our setup. The cross–section of the individual rods is elliptical which is a direct consequence of the single voxel shape. For means of stability, adjacent layers need to overlap to a certain extent. The single voxel distance here was chosen, still large enough, to keep the single voxels distinguishable. In the inset, the nanometer–scale roughness on the surface of the single voxels shows the physical resolution of the resist itself.

In order to do optical experiments on such samples, the area of the structures needs to be increased. Figure 8.11a shows a sample consisting of 32 layers with an area of $70\,\mu\text{m} \times 70\,\mu\text{m}$. The in–plane rod distance a is $0.8\ \mu\text{m}$ and c/a is adjusted to $\sqrt{2}$ for fcc symmetry. To reduce lattice distortions and sample bending due to polymer shrinkage, a massive wall has been polymerized around the PhC structure by the same technique. Although this is quite a large structure for DLW with that resolution, the writing time of the PhC lattice is just 25 minutes with a scanning algorithm optimized for the layer–by–layer structures.

To check that the sample quality is not just restricted to the surface, and to make sure that the development process also leads to a porous structure inside the PhC, a sample with 12 layers was broken through the middle of the structure. Fig. 8.11 (b) shows SEM images of the top and an edge view of the sample that indicate that also the interior of the layer–by–layer PhC matches the designed structure.

With the highly flexible DLW technique, it is now possible to write a wide variety of lattice constants and filling fractions by changing the scanning pattern and the laser pulse energy

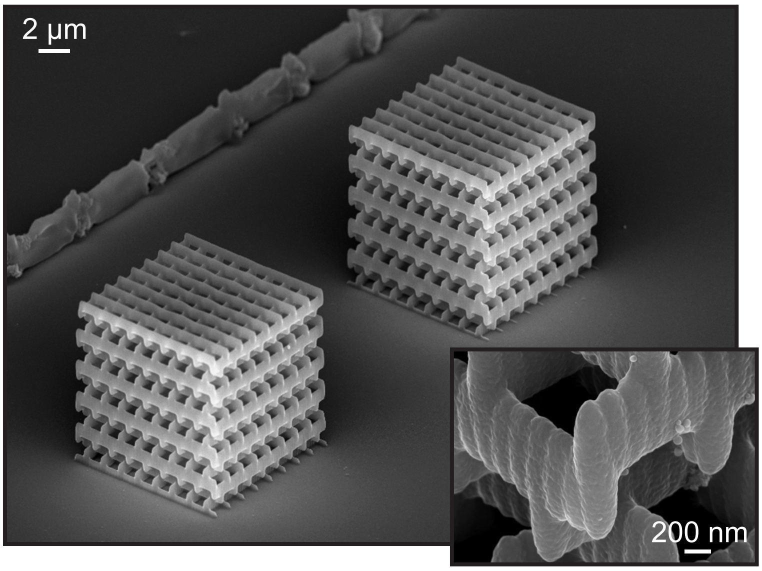

Figure 8.10: SEM image of two layer–by–layer structures with $a = 1.5\ \mu\mathrm{m}$; total size is $12\ \mu\mathrm{m} \times 12\ \mu\mathrm{m} \times 11\ \mu\mathrm{m}$. In the inset, the single voxels that build the rods can be distinguished. The surface roughness of the voxels is determined by the resolution of the resist itself.

respectively. Figure 8.12 shows an overview over several structures that we have fabricated. All lattices were designed with $c/a = \sqrt{2}$ for fcc symmetry. The in–plane rod distance a here ranges from a rather large $1.5\ \mu\mathrm{m}$ down to $650\ \mathrm{nm}$. The images reveal the precise large–scale periodicity as well as the high fabrication accuracy even for small lattice constants.

8.3.4 Optical characterization

We have performed optical transmission and reflection measurements on layer–by–layer samples consisting of six lattice constants and an effective area of $100\ \mu\mathrm{m} \times 100\ \mu\mathrm{m}$. The transmission and reflection spectra are measured in a Fourier Transform Infrared Spectrometer (Hartmann–Braun Bomen) combined with an infrared microscope (SpectraTech, $15\times$ Cassegrain objectives, $NA = 0.56$, aperture size $50\ \mu\mathrm{m} \times 50\ \mu\mathrm{m}$). The samples are aligned with their surfaces perpendicular to the optical axis, which corresponds to Γ-X direction for fcc symmetry. The spectra are normalized to the glass substrate in the case of transmission and to a gold mirror in the case of reflection. Figure 8.13 shows the dataset of a sample with an in–plane rod distance of $a = 1.0\ \mu\mathrm{m}$. The fundamental stop band at about $1.9\ \mu\mathrm{m}$ is clearly visible, both in reflection and transmission, as well as a higher order stop band at $1.1\ \mu\mathrm{m}$. The presence of this higher order stop band displays the high optical quality of the sample.

Figure 8.14 compares the reflection spectra of three other samples with different in–plane rod distances. As expected, a pronounced shift of the stop band towards higher energies with decreasing rod distance can be observed. The maximum of the reflection shifts from $1.9\ \mu\mathrm{m}$

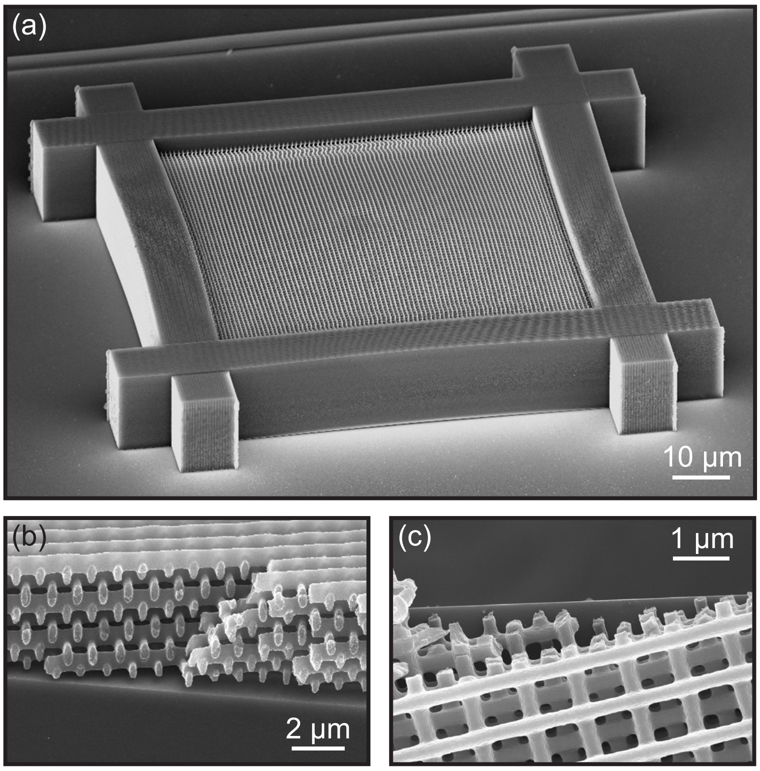

Figure 8.11: (a) Larger layer–by–layer structure with a massive wall that prevents bending and reduces lattice distortions due to polymer shrinkage during polymerization. (b) Side and (c) top view of a broken sample with 12 layers that exhibit the sample quality inside the structures.

for the $a = 1.0\ \mu\text{m}$–sample to $1.4\ \mu\text{m}$ for $a = 0.8\ \mu\text{m}$. For the sample with $a = 1.0\ \mu\text{m}$, again the reflection peak of the higher–order stop band is visible and even more pronounced than the respective one of the fundamental stop band. For the $a = 0.9\ \mu\text{m}$–sample, a rise in the reflection also hints at the existence of a higher–order stop band, but due to the spectral shift, it does not fall into the measured spectral window.

8.4 Templates infiltration

SU–8 fcc periodic structures do not possess a full PBG. However, a number of very interesting applications are just related to their photonic properties and not to the full gap itself: anomalous propagation is caused by the unique features coming from the shape of the photonic bands (equienergy surfaces) and leads to interesting phenomena such as superprism effects [43], or negative refraction [44]; in nonlinear optics, a full PBG is not required to efficiently produce second harmonic generation [45]. Nevertheless, the “Holy Grail”, the so–called complete PBG is a must to mold the flow of light. Waveguides, microcavities, engineered defects,

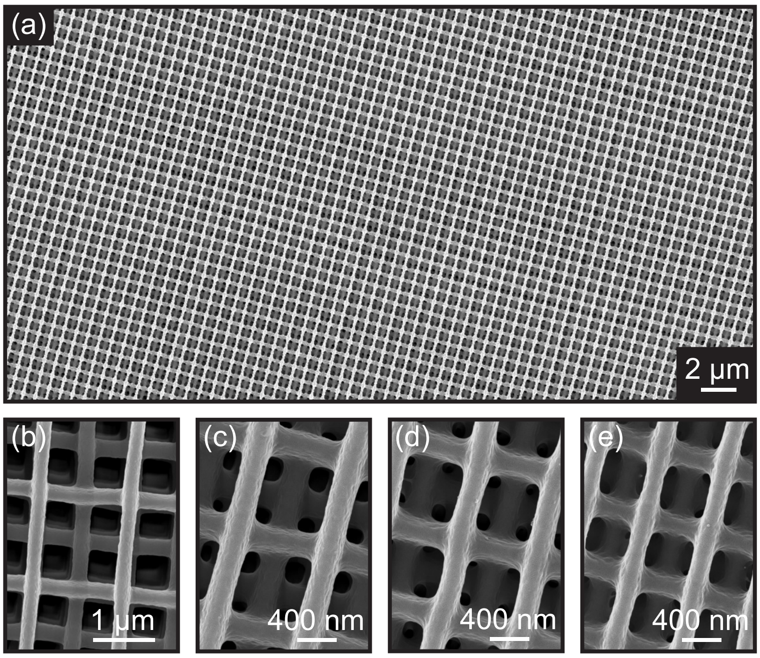

Figure 8.12: (a) The overview of a sample with $a = 0.65$ μm reveals the large scale periodicity of our samples, whereas closeups for samples with different a exhibit the small scale fabrication accuracy: (b) $a = 1.5$ μm, (c) $a = 1.0$ μm, (d) $a = 0.8$ μm, (e) $a = 0.65$ μm.

spontaneous emission inhibition and other fundamental quantum optical effects are related, or linked to the existence of a full PBG.

In this way, the SU–8 fcc structures can be seen as templates where other compounds with higher dielectric constant can be grown into, in order to achieve the dielectric contrast that is theoretically predicted. In the holographic structures, materials such as silicon, germanium, III–V semiconductors, etc., with refractive indices higher than 2.8 are good candidates to overcome this problem. In the layer-by-layer structures, this threshold is lower due to their diamond symmetry. Therefore, the list of appropriate materials is larger. The different techniques that can be used depend on the material to grow: chemical vapor deposition (CVD) for silicon [11] and germanium [46], electrodeposition, which has been used for II–VI [47] and III–V [48] semiconductors, chemical bath deposition [49], etc.

8.4.1 Silicon CVD

Infiltration by silicon CVD is a standard technique, which is commonly used for the fabrication of inverted opals. In contrast to the artificial opal templates that consist of silica spheres and can be inverted with silicon directly, the temperature stability of SU–8 raises a major problem: Experiments on our structures have shown that for temperatures above 250° C, the SU–8 structures lose their mechanical integrity. As the silicon CVD works at temperatures above

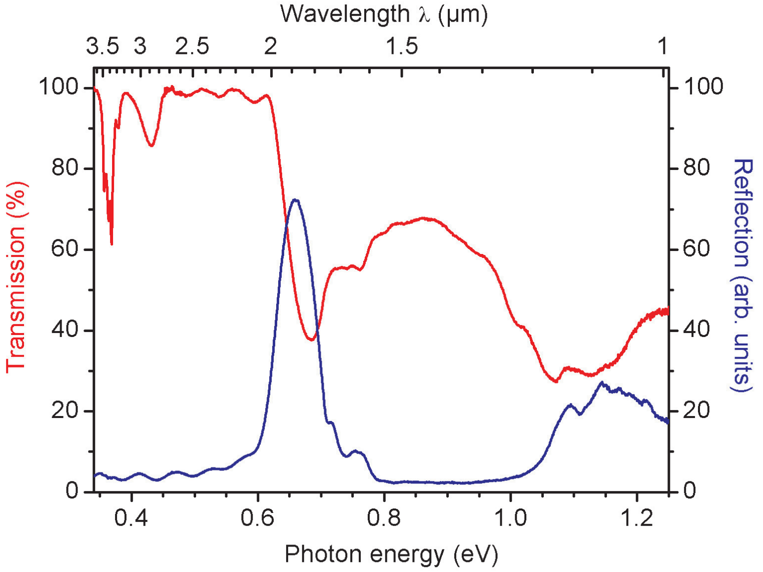

Figure 8.13: Transmission and reflection spectra of our $a = 1.0\ \mu\mathrm{m}$ layer–by–layer structures. The transmission dips around $3\ \mu\mathrm{m}$ and $3.5\ \mu\mathrm{m}$ stem from polymer absorption bands.

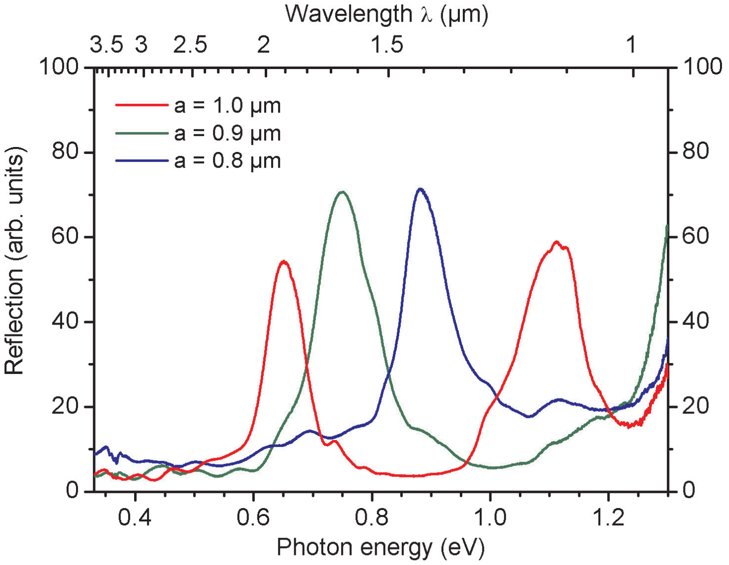

Figure 8.14: Reflection spectra of samples with different in–plane rod distance a.

350° C, the method has to be adapted for our templates. This procedure will be sketched for the case of the layer–by–layer templates next.

In an initial step, the layer–by–layer templates and their substrate are covered with a thin polymer layer. The structural changes caused by this layer are negligible since the deposited layer is less than $5\ \mathrm{nm}$ thick. Next, the templates are completely inverted with silica (SiO_2) in a process which can be accomplished at room temperature and thus leaves the structure unaffected [50]. For this purpose, the templates are first dried in a stream of nitrogen gas and followed by the addition of a defined amount of water which is physiosorbated. The water reacts in the next step with $SiCl_4$ and forms a $30 - 40\ \mathrm{nm}$ thick layer of SiO_2. By repeating these steps several times, the templates are completely infiltrated with SiO_2.

After the infiltration, the template as well as the substrate are completely covered with SiO_2. In order to remove the SU–8 a new substrate is placed on top of the layer–by–layer structure. Since the old substrate was covered with a polymer film before the SiO_2 CVD, it can be removed easily. A direct burn–up of the SU–8 could destroy the moulded SiO_2 structure if the flue gases are not dissipated fast enough. Therefore, drains in the residual polymer film and in the SU–8 are opened beforehand by exposing the sample to an oxygen–plasma. After that, the sample is heated up to 500° C for 4 hours which removes the remaining resist.

The resulting SiO_2-inverted template is compatible with the silicon CVD process. Here, the sample is heated up to 375° C at an ambient pressure of $10^{-6}\ \mathrm{mbar}$. Disilane (Si_2H_6) gas is added to the reaction chamber which decomposes on the surface of the inverted template due to the high temperature. This leads to the formation of a silicon layer whose thickness is monitored by a sensing crystal. After the silicon CVD process, the SiO_2 is removed with an aqueous solution of hydrofluoric acid.

8.4.2 Electrochemical deposition

So far, transparent materials with low intrinsic losses in the spectral region of interest are prefered for the fabrication of PhCs. However, compound structures of dielectric materials and metals have been proposed [51] as an interesting alternative to all-dielectric PhCs for some applications. These systems can be useful to study the interaction between light and surface plasmons in nanostructured metals, a topic which has gained much attention in the last few years [52]. Even all-metallic photonic structures with very interesting properties in the infrared region [53] have been demonstrated.

Electrodeposition is a versatile technique suitable for the infiltration of our SU–8 PhC templates with metals or other materials. For this purpose, we are currently developing a computer controlled electrodeposition setup which comprises a standard three–electrode configuration. By exchanging the counter electrode and the electrolyte, different materials can be utilized. The applied potential can either be held constant or can be varied with time in a controlled manner. In order to check the deposition conditions, a voltammogram can be measured before the real electrochemical deposition process.

Clearly, a conductive substrate is required for the electrodeposition process. Unfortunately, coating the substrate with a thin metal film is not compatible with the holographic fabrication process of the SU–8 templates since the metal coating gives rise to unwanted reflections. A good alternative is the use of indium–tin–oxide (ITO). We have deposited ITO layers which are at the same time almost transparent and exhibit a sufficient conductance for the electrodeposition process.

The deposition of silver in the voids of the SU–8 templates is currently under way. The first results are very promissing.

8.5 Conclusions

We have shown that the combination of two complementary and compatible techniques, namely holographic lithography and Laser Direct Writing, allows the rapid, flexible and cheap fabrication of 3D PhC templates as well as the controlled incorporation of defects and waveguides. The optical transmission and reflection spectra of these structures in the visible and near–infrared respectively agree well with theory, which is evidence of the high quality of the fabricated structures. The next logical step and challenge is the infiltration of these structures with dielectrics with large refractive indices and/or with metals. Our corresponding first results along the lines of electrochemistry and, alternatively, CVD are very encouraging. It should be noted that the combination of such 3D nanolithography with e.g. CVD, is compatible with possible future mass production of 3D PhCs.

References

[1] E. Yablonovitch, Phys. Rev. Lett. **1987**, 58, 2059.

[2] S. John, Phys. Rev. Lett. **1987**, 58, 2486.

[3] J.D. Joannopoulos, R.D. Meade, and J.N. Winn, Photonic Crystals – Molding the Flow of Light, Princeton University Press, USA, 1995.

[4] E. Yablonovith, T.J. Gmitter, and K.M. Leung, Phys. Rev. Lett. **1991**, 67, 2295.

[5] T.F. Krauss, R.M. De La Rue, and S. Brand, Nature **1996**, 383, 699.

[6] A. Birner, R.B. Wehrspohn, U.M. Gösele, and K. Busch, Adv. Mater. **2001**, 13, 377.

[7] S.Y. Lin, J.G. Fleming, D.L. Hetherington, B.K. Smith, R. Biswas, K.M. Ho, M.M. Sigalas, W. Zubrzycki, S.R. Kurtz, and J. Bur, Nature **1998**, 394, 251.

[8] S. Noda, K. Tomoda, N. Yamamoto, and A. Chutinan, Science **2000**, 289, 604.

[9] Y. Xia, B. Gates, and Z.H. Li, Adv. Mater. **2001**, 13, 409.

[10] K. Busch and S. John, Phys. Rev. E **1998**, 58, 3896-3908.

[11] A. Blanco, E. Chomski, S. Grabtchak, M. Ibisate, S. John, S.W. Leonard, C. Lopez, F. Meseguer, H. Miguez, J.P. Mondia, G.A. Ozin, O. Toader, and H.M. van Driel, Nature **2000**, 405, 437.

[12] Z.Y. Li and Z.Q. Zhang, Phys. Rev. B **2000**, 62, 1516.

[13] G. Grynberg and C. Robilliard, Phys. Rep. **2001**, 355, 335.

[14] V. Berger, O. Gauthier-Lafaye, and E. Costard, J. Appl. Phys. **1997**, 82, 60.

[15] M. Campbell, D.M. Sharp, M.T. Harrison, R.G. Denning, and A. J. Turberfield, Nature **2000**, 404, 53.

[16] S. Shoji and S. Kawata, Appl. Phys. Lett. **2000**, 76, 2668.

[17] Yu. V. Miklyaev, D.C. Meisel, A. Blanco, G. v. Freymann, K. Busch, W. Koch, C. Enkrich, M. Deubel, and M. Wegener, Appl. Phys. Lett. **2003**, 82, 1284.

[18] F. Sitek, M. Rembold, SME technical papers **1987**, FC870274.

[19] J.M. Shaw, J.D. Gelorme, N.C. LaBianca, W.E. Conley, and S. Holmes, IBM J. Res. Dev. **1997**, 41, 81.

[20] J.D. Gelorme, R.J. Cox, S.A.R. Gutierrez, U.S. Patent **1987**, No. 4, 882, 245.

[21] D.C. Meisel, Diploma Thesis, Universität Karlsruhe **2002**.

[22] C. Kittel, Introduction to solid state physics, John Wiley & Sons, 6th edition **1996**.
[23] L.Z. Cai, X.L. Yang, and Y.R. Wang, J. Opt. Soc. Am. A **2002**, 19, 2238.
[24] K.I. Petsas, A.B. Coates, and G. Grynberg, Phys. Rev. A **1994**, 50, 5173-5189.
[25] L.J. Guérin, M. Bossel, M. Demierre, S. Calmes, and P. Renaud, Proceedings of the International Solid State Sensors and Actuators Conference (Transducers '97) **1997**, 2, 1419.
[26] H. Miguez, C. Lopez, F. Meseguer, A. Blanco, L. Vazquez, R. Mayoral, M. Ocana, V. Fornes, and A. Mifsud, Appl. Phys. Lett. **1997**, 71, 1148.
[27] S. Maruo, O. Nakamura, and S. Kawata, Opt. Lett. **1997**, 22, 132.
[28] B.H. Cumpston, S.P. Ananthavel, S. Barlow, D.L. Dyer, J.E. Ehrlich, L.L. Erskine, A.A. Heikal, S.M. Kuebler, I.-Y.S. Lee, D. McCord-Maughon, J. Qin, H. Röckel, M. Rumi, X.-L. Wu, S.R. Marder, and J.W. Perry, Nature **1999**, 398, 51.
[29] S. Kawata, H.-B. Sun, T. Tanaka, and K. Takada, Nature **2001**, 412, 697.
[30] W. Lee, S.A. Pruzinsky, and P.V. Braun, Adv. Mater. **2002**, 14, 271.
[31] J. Serbin, A. Egbert, A. Ostendorf, B.N. Chichkov, R. Houbertz, G. Domann, J. Schulz, C. Cronauer, L. Fröhlich, and M. Popall, Opt. Lett. **2003**, 28, 301.
[32] M. Straub and M. Gu, Opt. Lett. **2003**, 27, 1824.
[33] H.-B. Sun, S. Matsuo, and H. Misawa, Appl. Phys. Lett. **1999**, 74, 786.
[34] H.-B. Sun, V. Mizeikis, Y. Xu, S. Juodkazis, J.-Y. Ye, S. Matsuo, and H. Misawa, Appl. Phys. Lett. **2001**, 79, 1.
[35] M.J. Ventura, M. Straub, and M. Gu, Appl. Phys. Lett. **2003**, 82, 1649-1651.
[36] H.-B. Sun, Y. Xu, S. Juodkazis, K. Sun, M. Watanabe, S. Matsuo, H. Misawa, and J. Nishii, Opt. Lett. **2001**, 26, 325.
[37] S. Juodkazis, S. Matsuo, H. Misawa, V. Mizeikis, A. Marcinkevicius, H.–B. Sun, Y. Tokuda, M. Takahashi, T. Yoko, and J. Nishii, Appl. Surf. Sci. **2002**, 197, 705.
[38] G. Witzgall, R. Vrijen, E. Yablonovitch, V. Doan, and B.J. Schwartz, Opt. Lett. **1998**, 23, 1745.
[39] A. Yoshida and T. Asakura, Optik **1974**, 41, 281-292.
[40] K.M. Ho, C.T. Chan, C.M. Soukoulis, R. Biswas, and M. Sigalas, Solid State Commun. **1994**, 89, 413.
[41] H.S. Sözüer and J.P. Dowling, J. Mod. Optic. **1994**, 41, 231.
[42] A. Chutinan and S. Noda, J. Opt. Soc. Am. B **1999**, 16, 240.
[43] H. Kosaka, T. Kawashima, A. Tomita, M. Notomi, T. Tamamura, T. Sato, and S. Kawakami, Phys. Rev. B **1998**, 58, R10096.
[44] C.Y. Luo, S.G. Johnson, J.D. Joannopoulos, and J.B. Pendry, Opt. Express **2003**, 11, 746.
[45] J. Martorell, R. Vilaseca, and R. Corbalan, Appl. Phys. Lett **1997**, 70, 702.
[46] H. Miguez, E. Chomski, F. Garcia-Santamaria, M. Ibisate, S. John, C. Lopez, F. Meseguer, J.P. Mondia, G.A. Ozin, O. Toader, and H.M. van Driel, Adv. Mater. **2001**, 13, 1634.
[47] P.V. Braun and P. Wiltzius, Nature **1999**, 402, 603.
[48] Y.C. Lee, T.J. Kuo, C.J. Hsu, Y.W. Su, and C.C Chen, Langmuir **2002**, 18, 9942.
[49] A. Blanco, C. Lopez, R. Mayoral, H. Miguez, F. Meseguer, A. Mifsud, and J. Herrero, Appl. Phys. Lett. **1998**, 73, 1781.
[50] H. Miguez, N. Tétreault, B. Hatton, S.M. Yang, D. Perovic, and G.A. Ozin, Chem. Commun. **2002**, 22, 2736.
[51] E.R. Brown and O.B. McMahon, Appl. Phys. Lett. **1995**, 67, 2138-2140.
[52] H.J. Lezec, A. Degiron, E. Devaux, R.A. Linke, L. Martin–Moreno, F.J. Garcia–Vidal, and T.W. Ebbesen, Science **2002**, 297, 820.
[53] J.G. Fleming, S.Y. Lin, I. El–Kady, R. Biswas, and K.M. Ho, Nature **2002**, 417, 52.

9 Tunable photonic crystals using liquid crystals

Heinz–Siegfried Kitzerow[1] *and Johann Peter Reithmaier*

An essential requirement for the practical use of photonic crystals is the ability to tune the frequency of the stop bands or the band edges. Different strategies for tuning have been developed. This chapter is focused on the utility of liquid crystals. After a short review of alternative examples of variable band gaps (Section 9.1), we shortly summarize the basic properties of liquid crystals (Section 9.2). Periodic liquid crystals and systems based on colloidal crystals (Section 9.3) are easily available but exhibit a rather low dielectric contrast. Structured semiconductors (Section 9.4) are more difficult to fabricate but show a higher dielectric contrast, so far. The possibilities, drawbacks and challenges of applications are summarized in Section 9.5 of this chapter.

9.1 Introduction: Concepts of tunable photonic crystals

The large variety of promising applications of photonic crystals (PhC) [18] depends on many adjustable parameters. A spatially periodic modulation of the dielectric constant alone may lead to the existence of a photonic stop band with low density of states, low transmission, and high reflectivity. However, unique PhC effects, like inhibited spontaneous emission [8], or the localization of photons [7] require a complete photonic band gap and thus high dielectric contrast and a suitable shape of the Brillouin zone. For some effects, like DFB–type lasing [14] or second harmonic generation [74], the small group velocity $v_g = d\omega/dk$ at photonic band **edges**, or – for the shape and delay of short pulses in PhC waveguides (soliton propagation and optical coding or decoding) – the anomalous dispersion of the inverse group velocity ($d^2k/d\omega^2$) are essential [25]. Other effects like microresonator properties and the associated localization of light are related to single **defect states** within the band gap. A dislocation line, a line of defects or a periodic array of defects can give rise to wave–guiding. The array of defects can correspond to an **impurity band** within the band gap. If this array contains two alternating, slightly different types of defects, detuning (for example due to optical nonlinearity) can open a gap within the impurity band [89]. Making use of the benefits of these complex structures is not possible without fine–tuning of the structure, thereby controlling the optical properties.

Due to the demanding fabrication processes of nanostructures, even passive PhC elements depend on the possibility to adjust the band gap in order to tune the final properties, thereby compensating fabrication tolerances. Consequently, a considerable part of the current literature describes methods of tuning **passive** systems or "tuning by design" (Table 9.1). On the other hand, a spectral shift of the photonic band gap can be used for **active** elements, like

---

[1] Corresponding author: e-mail: kitzerow@chemie.upb.de, tel: 05251 60 2156, fax: 05251 60 4208

Photonic Crystals. Edited by K. Busch, S. Lölkes, R. B. Wehrspohn and H. Föll
Copyright © 2004 Wiley-VCH Verlag GmbH & Co. KGaA
ISBN: 3-527-40432-5

adjustable wavelength filters, tunable laser structures, sensors or detectors [29], integrated optical switches, interconnects and logical gates. An important special case is the use of nonlinear optical materials where the local dielectric constant and its dispersion are not adjusted by an external parameter but controlled by the intensity of the transmitted light pulse. This principle is a prerequisite for all–optical switches and for realizing the fiction of optically integrated circuits [90].

Since PhCs are systems with a spatially periodic variation of the refractive index $n = (\varepsilon \cdot \mu)^{1/2}$, tuning can generally be achieved by changing

- the dielectric constant of at least one component [9, 21, 44, 58, 70, 73, 80, 84, 89, 92, 115]
- the magnetic permeability [24],
- the filling fraction [95],
- the lattice constant(s) [38, 43, 46, 51, 60, 79, 85, 101, 107, 113, 116],
- the symmetry (space group) [52, 83, 106],
- the orientation of the crystal lattice (or the polarization of light) [9, 35, 84, 103]
- the size (number of unit cells) of the PhC [117], or
- the size [23, 49, 63], dielectric constant [96], shape and orientation [68], or position [46, 63, 100] **of a defect**.

Very large photonic structures – for centimeter– and millimeter–wave applications – may even be field– or light–controlled by incorporating active elements like p–i–n diodes, varactor diodes or varistors [28]. In integrated optics, the use of distributed Bragg reflectors (DBR) is well established [11]. More recently, a wealth of tuning schemes for periodic structures with small spacings has been developed, or at least predicted [31, 38, 47, 58, 70, 73, 80, 85, 89, 92, 95, 101, 107, 113, 116]. Representative examples are listed in Table 9.1. In addition to the methods indicated in this table, the photonic properties can be tuned by changing the plasma frequency of semiconductors [42, 82], or making use of photochemical reactions [78], mechanical strain [30] or surface acoustic waves [66]. A very promising approach is the change of the periodicity by varying the dielectric constant of one component in a PhC consisting of three components. If, for example, rods or spheres of two of these components form alternating layers, the period of the lattice can be changed by a factor of 2, due to suitable index matching [83, 106]. In coupled cavity waveguides, nonlinear effects using the same principle, may be suitable for effective all–optical switching [89]. LCs (see Section 9.3, Table 9.2) are particularly suitable in order to control the optical properties by temperature, external electric or magnetic fields, light intensity (due to optical nonlinearities) and the state of light polarization (due to optical anisotropy).

Table 9.1: Some recent reports on tunable photonic properties in periodic structures (for effects using LCs, see Table 9.2). The symbols in brackets indicate the **dimension** (1D, 2D, 3D); the **frequency range**; the **essential photonic property** ($\Delta\omega = (\omega_{hi} - \omega_{lo})$ band gap width, $\omega_0 = {}^1\!/_2\,(\omega_{hi} + \omega_{lo})$ midgap frequency, ω_d frequency of a defect mode, β_2 dispersion of the inverse group velocity, τ transmission); the **tuned structural property** (a lattice constant or spacing, s space group, ε dielectric constant ($\underline{\varepsilon}$: tensor), μ magnetic permeability, ξ filling fraction, o orientation, d defect size, –position or –orientation); the **control parameter** (T working temperature, θ temperature during preparation, E electric field, H magnetic field, j current, I light intensity, c concentration, h cavity gap, L size (number of unit cells), $\vec{q}$ reciprocal lattice vector, ϑ angle of light incidence,φ polarization of light, r radius of a defect).

System, Effect	Shift	Ref.
Erbium doped porous silicon microcavity [1D; IR; ω_0; ε; θ; exp.]	$\delta\lambda/\lambda \approx 185$ nm/1550 nm	[44]
Inverted opal made of a semiconductor with variable free–carrier density [3D; IR; ω_d; ε; T, j, I; theory]	$\delta\omega_d/\omega_d \approx 7\%$	[80]
Soliton generation and soliton self–frequency shift in PhC fibers [2D; IR; β_2; ε; I; exp. + theory]	$\delta\lambda/\lambda \approx 90$ nm/900 nm 850–1050 nm 1.3–1.65 μm	[92] [93] [94]
All–optical switching in coupled cavity waveguides [1D, 2D; IR; ω_g; ε; I; theory]	$\tau = -130$ dB @ $\delta\varepsilon = 0.01$	[89]
Thermochromism of synthetic opal infiltrated with conducting polymer [3D; vis; ω_0; ε; T; exp.]	δn/n $\approx 5\%$	[70]
Optical shutter made of superconductor PhC [2D; $\Delta\omega$; ε, λ_L; T; theory]	$\Delta\omega/\omega_0 \leq 0.15$ for $T < 0.86\, T_c$	[73]
Electromagnetic crystal (EMXT) waveguide band–stop filter [2D; microwave; ω_0; V_{bias} ; exp.]	$\delta\omega_0/\omega_0 \approx 9$ GHz/36 GHz	[115]
Waveguide cavity switched by photoionization of deep donor levels (DX centers) [1D; vis, IR; ω_0; ε; I; theory]	$\delta n/n = 0.003$: $\delta\omega_0/\omega_0 \approx 0.0024$	[21]
Pockels effect in bi–oriented crystals [1D; IR; τ; ε; E; theory]	(-3 dB)–(-27 dB)	[58]
Liquid phase deposition on inverted colloidal crystals [3D; vis; ω_0; (ξ; deposition parameters), (ε; $n_{liq.}$); exp.]	$\delta\lambda_0(\xi)/\lambda_0 \approx 96$ nm/532 nm $\delta\lambda_0(n_{liq.})/\lambda_0 \approx 30$ nm/494 nm	[95]
Narrow-band (black body) MIR emitter [2D; MIR; λ_{em}; d; d; exp. + theory]	$\lambda_{em} = 3.7 - 4.5\ \mu$m	[98]
Lamellar block copolymer / homo–polymer blends [1D; vis; ω_0; d; c; exp.]	$\lambda_0 \approx 330 - 630$ nm	[51]

System, Effect	Shift	Ref.
Emission of a defect cavity in a quantum well PhC structure [$(2+1)$D; IR; ω_d; d; lithography; exp.]	$\lambda_d \approx 1.58$–$1.46\ \mu$m	[46]
Thermo– and pH–responsive hydrogel nanoparticles [3D ; vis ; ω_0; d; (T, pH); exp.]	λ_0(T) $\approx$ 150–400 nm λ_0(pH) $\approx$ 150–250 nm	[107]
Electrostatic actuation of an air–gap between DBR mirrors, GaInAsP VCSEL [1D; IR; ω_d; d; V; exp. + theory]	$\delta\lambda_0/\lambda_0 \approx$ 120 nm/1600 nm	[79]
PhC on a piezoelectric substrate [2D; IR; $\Delta\omega$; (d, s); (E, H); theory]	$\delta\omega/\Delta\omega$ = 52–73% at 2–3% shear strain	[60]
Coupled PhC slabs with mechanically tunable distance [$(2+1)$D; τ; d; h; theory]	20 dB @ $\delta h \approx 0.02\lambda_0$	[113]
Microstructured optical fibers (MOF) with microfluidic plugs, long period grating and tunable birefringence [$(2+1)$D; IR; ω_0; $d(T)$, p(φ), $\varepsilon_C(T)$; exp.]	$\delta\lambda_0\{d(T)\}/\lambda_0 \approx$ 19 nm/1520 nm $\delta\lambda_0\{\mathrm{p}(\varphi)\}/\lambda_0 \approx$ 3 nm/1520 nm $\delta\lambda\{\varepsilon_C(T)\}/\lambda \approx$ 17 nm/1560 nm	[85] [86] [87]
Floating magnetic NdFeB particles [3D; microwave; τ; d; B; exp. + theory]	(-15 dB)–(-40 dB)	[101]
Magnetic $\mathrm{MnFe_2O_4}$ nanoparticles [2D; IR; ω_0; (d, s); H; exp.]	0.7–1 μm, 1.1–3.8 μm	[116]
Structure of electrorheological fluids [3D ; (vis-IR); –; (d, s); E ; exp.]	transition FCC–BCT	[38]
Tunable three–component PhC [2D, ω_0; (d, s); ε_c ; theory]	$\omega_0 \rightarrow \sqrt{2}\omega_0$	[83]
Tunable three–component structures with double periodicity [(2D, 3D); (vis, IR); ($\Delta\omega$, ω_0); ε; T; theory]	$\Delta\omega/\omega_0 = 0$–$2.5\%$	[106]
Gap state lasing: dye–infiltrated opal [3D; vis; ω_d; $\vec{q}(\vartheta)$, ε(C), ϑ; exp.]	$\delta\lambda\{\vec{q}(\vartheta)\}/\lambda \approx$ 230 nm/690 nm; $\delta\lambda\{\varepsilon(\mathrm{C})\}/\lambda \approx$ 70 nm/730 nm; $\delta\lambda\{\vartheta\}/\lambda \approx$ 6 nm/694 nm.	[103]
SHG in birefringent layers made of porous silicon with alternating porosity [1D; IR→vis; v_g; $\underline{\varepsilon}$; φ; exp. + theory]	I_{SHG} enhancement by factor 5	[84]
PhC–fiber, light perp. to guiding direction [2D; IR; ω_0; ϑ; ϑ; exp.+ theory]	$\delta\lambda_0/\lambda_0 \approx 930 - 1030$ nm	[35]
Reduced pulse width due to β_2 in a 2D PhC [2D; IR; β_2; –; L; theory]	$(\mathrm{t}_{out}/\mathrm{t}_{in})^2 \geq 0.65$	[117]
Trapping and emission by a single defect [2D; IR; ω_0; r; r; exp. + theory]	$\delta\omega_0/\omega_0 \approx 0.0024$	[49]

9.2 Properties of liquid crystals

Liquid crystals (LC) combine fluid behavior and anisotropic properties in a unique way [10, 12, 54, 59]. Thermotropic, calamitic LCs consist of rod–like organic molecules which form mesophases (Fig. 9.1) in the temperature range between the solid state and the isotropic fluid phase. The nematic mesophase (N) is characterized by uniaxial orientational order. Smectic mesophases (Sm) show an additional layer structure. Chiral liquid crystals typically show a twisted director field $\vec{n}(\vec{r})$, where $\vec{n}$ is a unit vector locally describing the preferred orientation of the molecules.

The most striking anisotropic property is *birefringence*. The effective refractive index for linear polarized light with the electric field direction perpendicular to the director (ordinary refrative index n_o) is different from the effective value for polarized light with the electric field direction parallel to the director (extraordinary refractive index n_e). The birefringence $\Delta n := n_e - n_o$ decreases with increasing temperature (decreasing orientational order) and vanishes above the nematic – isotropic transition temperature T_{NI} (clearing temperature). A typical value for a biphenyl compound a few degrees below T_{NI} is $\Delta n \approx 0.2$. Similarly, the static dielectric constant $\varepsilon_{\|}$ for a field applied parallel to the director, is different from the effective value $\varepsilon_{\perp}$ observed for a field perpendicular to the director. If the *dielectric anisotropy* $\Delta\varepsilon := \varepsilon_{\|} - \varepsilon_{\perp}$ is positive, the electric polarization for $\vec{n} \| \vec{E}$ is larger than for $\vec{n} \perp \vec{E}$, and the director tends to align along the field. For $\Delta\varepsilon < 0$, a director orientation in the plane perpendicular to the field is favorable. Typical values of $\Delta\varepsilon$ range from -5 to $+12$. Also, magnetic fields can lead to a reorientation of liquid crystals due to the *anisotropy of the magnetic susceptibility*. Typically, LCs are diamagnetic, and the anisotropy of the volume susceptibility $\Delta\chi_m = \chi_{\|} - \chi_{\perp}$ is of the order $|\Delta\chi_m| \approx 10^{-7}$ – 10^{-6}. [12, 54]. In conclusion, LCs are predestined for photonic applications for several reasons:

- Birefringence makes them suitable for optical retarders and for non–linear optical applications under phase matching conditions.

- The birefringence is sensitive to the temperature and to external electric and magnetic fields. This dependence gives rise to many thermo–, electro– or magneto–optical effects, and to larger optical nonlinearity.

- Several mesophases spontaneously show a periodic structure with characteristic spacings in the μm and sub–μm range, thereby showing diffraction and Bragg–like reflection in the visible and infrared wavelength range.

The electro–optic switching behavior of nematic LCs is governed by the competing influences of the director anchoring at interfaces, the alignment of the director field in the bulk due to external fields, and the elastic behavior of the director field. For a uniformly oriented nematic LC in a planar cell with cell gap L and strong anchoring at the walls, the field–induced reorientation of the director (Frederiks transition) requires a field strength higher than the critical electric or magnetic field $E_c = \pi/L\ [K_{\text{eff}}/(\varepsilon_0 \Delta\varepsilon_{\text{static}})]^{1/2}$ or $H_c = \pi/L\ [K_{\text{eff}}/(\mu_0\ \Delta\chi_m)]^{1/2}$, respectively. For typical values ($\Delta\varepsilon_{\text{static}} \approx 12$, $\Delta\chi_m \approx 1.2 \cdot 10^{-7}$, effective elastic constant $K_{\text{eff}} \approx 5 \cdot 10^{-12}$ N), the critical fields are $E_c \approx 0.7$ V/μm and – for a cell gap of 2 μm – $H_c \approx 9 \cdot 10^6$ A/m ($B_c \approx 11$ T), respectively. Generally, the increase of the critical field with decreasing cell gap L limits the use of magnetic fields in the case of small cavities.

However, it is also important to consider that the director fields in non–planar cavities are defect structures, where the topology is governed by the anchoring conditions.

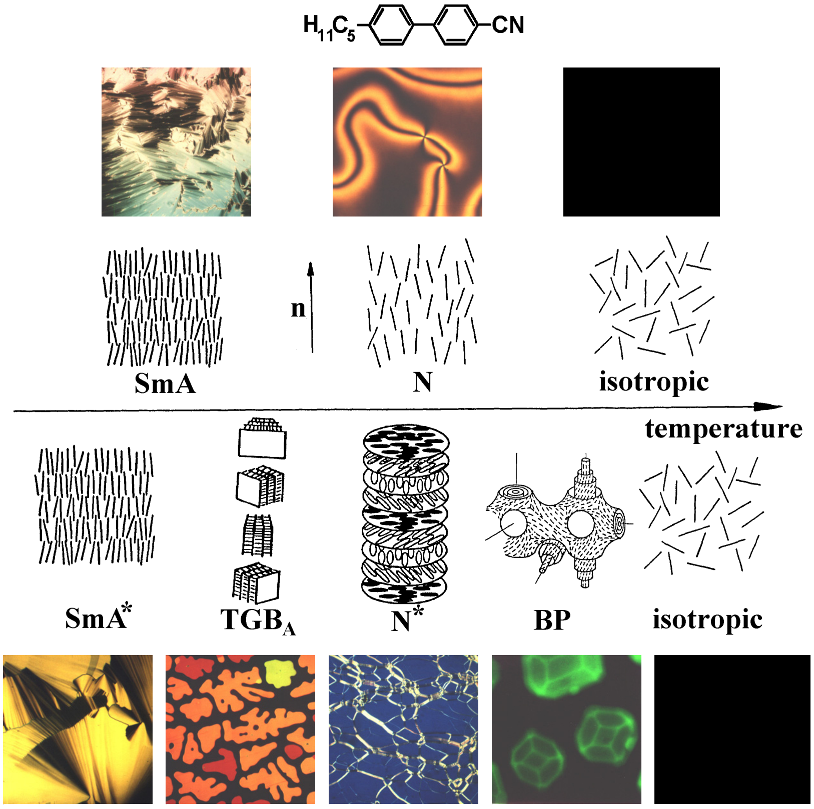

Figure 9.1: The structure of some calamitic LCs. Above: non-chiral smectic (SmX), nematic (N) and isotropic (I) phase. Below: chiral LCs: Chiral smectic (SmX*), twist grain boundary (TGB), and cholesteric (= chiral nematic, N*) phase. Blue phase (BP). The colored photographs show characteristic textures of the respective mesophase in a polarizing microscope. The molecular structure shown corresponds to a typical non–chiral liquid crystal, 5CB.

Using field–induced changes of the effective refractive index, a PhC consisting of a dielectric material and air can be made tunable if the air is replaced by a LC [27]. A stack of alternating dielectric layers ABABAB…may serve as a simple model system to discuss the possible band gap changes achievable in such structures. Let one of the two dielectric materials have a constant refractive index n_A (dielectric constant ε_A), and the second be a LC with variable refractive index n_B (dielectric constant ε_B). Assuming that the edges of the band gap correspond to two eigenmodes where the intensity maxima are located in materials 1 and 2, respectively, [18] the frequencies limiting the band gap are given by $\omega_x = |\vec{k}|$ $(c_0/\sqrt{\varepsilon_x}) = {}^1\!/\!_2|\vec{G}|$ $(c_0/\sqrt{\varepsilon_x}) = \pi$ c_0 / (d n_x) with x =A or B, where $\vec{k}$ (with $|\vec{k}| = 2\pi/\lambda$) is the wavevector of light and $\vec{G}$ (with $|\vec{G}| = 2\pi$ / d) is the fundamental reciprocal lattice vector of the dielectric structure. In analogy to the "dielectric band" and "air band" of a porous dielectric material in air [18], we may call the frequency range of propagating modes close to ω_A and ω_B, the "matrix band" and the "liquid crystal band", respectively. In this simple example, a field-induced variation of the effective refractive index n_B of the LC would leave the matrix band edge ω_A unchanged and lead to a relative frequency shift of the LC band edge $\delta\omega_B/\omega_B(0) = n_B(0)/n_B(E) - 1 = -[n_B(E) - n_B(0)]/n_B(E) \approx -\delta n_B/n_B(0)$. If a uniform director field is reoriented by $\pi/2$, the effective refractive index for linearly polarized light can change between the ordinary and the extraordinary refractive index, and $|\delta\omega_B/\omega_B(0)| \approx |\delta n_B/n_B(0)| \approx 0.2/1.5 = 13.3\%$ can be expected from typical values. Alternatively, the shift of the midgap frequency can be estimated from the average value ε_{av} of the dielectric constant which can be obtained approximately from the Maxwell–Garnet relation [1]. Detailed calculations [57] based on the Berreman method [4] show that the change of the birefringence in a stack of alternating ZnS ($n = 2.35$) and planar oriented 5CB ($n_o = 1.54$, $n_e = 1.75$) layers is sufficient to induce an omnidirectional reflection band at voltages of $V > 1.22V_c$. In the planar field–off state, the reflection band of p–polarized light ($n_{\text{eff}}(p) = n_e$) is narrower and depends more on the angle of light incidence than the s–polarized reflection band ($n_{\text{eff}}(s) = n_o$). However, the birefringence decreases and the dielectric contrast increases with increasing voltage due to reorientation of the director towards the layer normal. Thus, reflectivity for any polarization and any angle of light incidence occurs in a limited frequency range if the voltage is sufficiently high.

9.3 Spatially periodic LCs and colloidal crystals

Photonic liquid crystals with low dielectric contrast are readily available: Chiral LCs, where only the anisotropic part of the dielectric tensor is spatially modulated, and PhCs made of two components with slightly different dielectric constants. Most of these systems show brilliant Bragg reflection, but no complete photonic band gap. Nevertheless, they are interesting model systems which demonstrate new degrees of freedom in PhC design. Moreover, they can be used as possible templates, leading to new materials with high dielectric contrast.

9.3.1 Periodic liquid crystals

The cholesteric phase (Fig. 9.2) and tilted chiral smectic phases (like SmC*) are characterized by a one–dimensional helical structure. These phases and the blue phases show a conspicuous selective reflection of circularly polarized light if the helical pitch p is sufficiently short. A right–handed structure selectively reflects right circularly polarized light at the Bragg wavelength and is transparent for left circularly polarized light (vice versa for a left–handed structure). This striking optical effect was probably the reason for the discovery of LCs, and the use of the temperature dependence p(T) for thermometers was one of the first commercial applications of LCs. The dispersion relation of cholesteric LCs (Fig. 9.2a) [12] shows a band gap for circularly polarized light of the same handedness as the director helix between the two frequencies $\omega_\perp$ and $\omega_{||}$, where $\omega_\xi = c\, q_0 / \varepsilon_\xi^{1/2}$ and $\xi = ||, \perp$. The frequency gap between $\omega_\perp$ and $\omega_{||}$ is limited by two guided modes where the helical sense is the same as that of the helix. The direction of the electric field is always perpendicular ($\varepsilon_{\text{eff}} = \varepsilon_\perp$) or always parallel to the director ($\varepsilon_{\text{eff}} = \varepsilon_{\|}$), respectively. Pieranski [65] gives an illustrative analysis of the modes appearing in different regimes of the dispersion relation. The group velocity diminishes close to the band gap, giving rise to distributed feedback (DFB) lasing [3] and enhanced second harmonic generation.

The stability of the DFB lasing in cholesteric LCs, doped with a laser dye [5], was recently improved using reactive LC monomers which can be cross–linked to give thermally, extremely stable polymers [55, 102]. In addition to the well–known lasing at the band edge, also a defect mode emission appears if [112] two cholesteric polymer films are stacked so that a phase jump of the helical structure appears at the interface (Fig. 9.2b). Low contents of the cross–linking compound result in cholesteric elastomers [55] where the pitch and thus the laser wavelength can be tuned by mechanical strain (Fig. 9.2c). Electric field–induced changes of the laser wavelength are possible due to helical unwinding which appears in the cholesteric phase due to the local dielectric anisotropy (if $\varepsilon_{\|} > \varepsilon_{\perp}$) and in ferroelectric smectic phases with short pitch due to the spontaneous polarization $\vec{P}_s$ [108] (Fig. 9.2d).

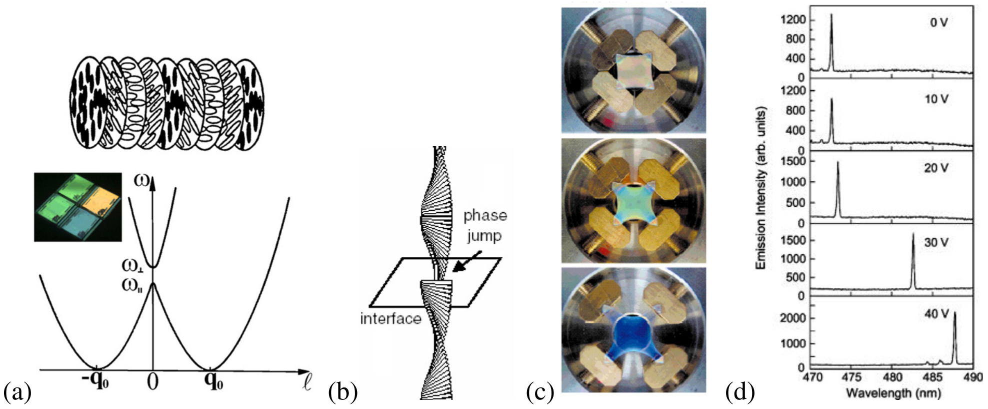

Figure 9.2: (a) Structure and dispersion relation of the cholesteric phase [12]. (Inset: selective reflection of cholesteric samples with a different helical pitch.) (b) Defect between two adjacent cholesteric layers [112]. (c) Cholesteric rubber changes the wavelength of selective reflection due to mechanical strain; mechanical tuning of the band edge lasing wavelength in a dye–doped cholesteric elastomer is possible [55]. (d) Stimulated emission from a dye–doped ferroelectric SmC* phase and its electric field–induced shift due to helical unwinding [108]. Figures (c) and (d) are reproduced with kind permission by Finkelmann et al. [55] and Kasano et al. [108], respectively.

Chiral LCs with a very short pitch show blue phases (BP) close to the clearing temperature. These mesophases show double twist, and a three–dimensional superstructure with lattice constants of a few hundred nanometers. The director field is composed of double twist tubes where the director angle changes continuously with increasing distance from the central tube axis along any radial direction (Fig. 9.3). These double twist cylinders form a body centered cubic O^8 structure for blue phase 1 (BP1), a simple cubic O^2 structure for BP2 and a structure with very short range order for BP3. Blue phases show a variety of transformations in external fields. The lattice constants of BP1 and BP2 are affected by ac electric fields [6]. The electrostriction coefficients can be positive or negative. Their absolute value is in the range of 10^{-15} – 10^{-14} m^2/V^2. Thus, a field strength of about 1 – 10 V$_{rms}$/μm is necessary in order to induce a change of the lattice constant by a few per cent. In addition, sufficiently high fields can induce discontinuous changes, leading to tetragonal or hexagonal phases.

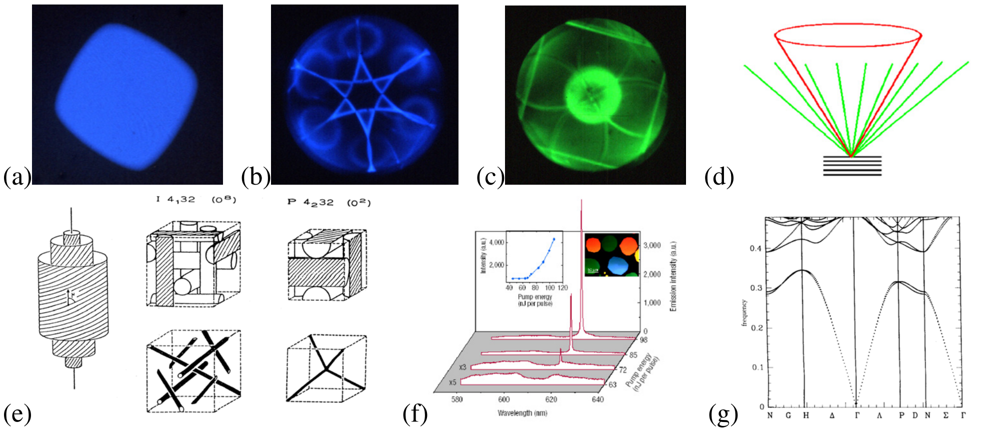

Figure 9.3: (a) Liquid single crystal of BP2. (b-c) Kossel diagrams of BP1 which appear if single crystals are illuminated with monochromatic, convergent light (d) and observed along the [111] (b) and [100] direction (c), respectively. (e) Double twist cylinder and (top:) arrangement of double twist cylinders in the O^8 structure of BP1 and the O^2 structure of BP2. Below: disclination lines in the respective structures. (f) Lasing of dye doped blue phase (with kind permission from Cao et al. [71]). (g) Dispersion relation for a cubic O^8 structure composed of cylinders with a high dielectric constant in a matrix with low dielectric constant [15].

Recently, dye–doped blue phases have been studied [39,71], and lasing along several crystallographic directions has been found [71] (Fig. 9.3f). The importance of BP–like structures for photonic band gap materials was recognized in 1994 already by Hornreich, Shtrikman and Sommers [15] who calculated the band structure for materials with the space group O^8 (the symmetry of BP1) if the double twist cylinders are replaced or decorated by either dielectric or conducting rods (Fig. 9.3g). The problem of limited thermal stability of blue phases can, in principle, be solved by in–situ photopolymerization [13]. A recent work about polymer–stabilized blue phases [88] shows that the temperature range of blue phases can be increased to more than 60 K including room temperature (260 K – 326 K). Kikuchi et al. [88] assume that the polymer network within a polymer–stabilized blue phase, is localized along the regular lattice of disclination lines. If so, decoration with materials of higher dielectric constant might be possible, as well.

9.3.2 Colloidal crystals containing LCs

Three–dimensional self–assembled tunable PhCs can be obtained by preparing monodisperse colloidal particles [2,48,76,91], allowing the particles to form a colloidal crystal [22,56,69], and filling the voids of this artificial opal with nematic or ferroelectric smectic LCs [27,31,32,62,67]. More details are given in Chapter 6 of this book.

Replacing the air ($n \approx 1$) by a LC [$\tilde{n} = (\frac{1}{3}n_e^2 + \frac{2}{3}\ n_o^2)^{1/2} \approx 1.5$] results in a large red–shift and narrowing of the stop band due to the increase of the average dielectric constant and the decrease of the dielectric contrast, respectively. Increasing temperature leads to a blue shift of the stop band, typically by a few nm (Table 9.2, Fig. 9.4b). Phase transitions between different mesophases can cause a discontinuous change. However, it should be emphasized that orientational order of the LC has little influence on the change of the refractive index. The anchoring of the director at the surface of the spheres is likely to cause a complicated director field with an isotropic distribution of the director orientation. Thus, attempts were made to address the LC by external electric fields [62, 64, 67]. Again, shifts of the stop band of a few nm can be observed (Table 9.2, Fig. 9.4c).

While a normal fcc colloidal crystal, consisting of spheres with a high dielectric constant and air (or voids with a low dielectric constant) shows no complete photonic band gap, an inverted fcc structure of weakly polarizable spheres and highly polarizable sticks can have a band gap between bands 8 and 9. Consequently, Busch and John [27] suggested inverted colloidal crystals made of silicon where the spherical cavities are filled with air and their surface is wetted with a LC. For this case, it is expected [27] that an initial 8.6% band gap disappears due to the filling with LC, but can be re–induced by external fields. If the director rotates continuously from the [001] through the [111] to the [110] direction, the band gap $\Delta\omega$ appears, increases gradually, reaching a maximum at the [111] direction, and becomes smaller again. Inverted structures can be made by using a normal colloidal crystal as a template [26, 69]. For example, the gaps between PMMA spheres can be filled with SnS_2 by exposing the crystal to $SnCl_4$ and H_2S vapors [48]. Subsequent removal of the PMMA spheres in an organic solvent, leaves the inverted SnS_2 structure filled with air. We have filled such a structure with 5CB and investigated the temperature dependence of the reflection bands. This experiment does not precisely correspond to the suggestion of ref. [27], but we expected a larger relative shift than in normal opals because the filling fraction of the LC in the inverted opal (75.5%) is much larger than in a normal opal (24.5%). Indeed, the temperature–induced shift of the (111) stop band by 14 nm (Fig. 9.4d) [91] is relatively large ($\approx 2\%$) compared to the typical shift ($< 1\%$) in normal opals (Table 9.2). Yoshino's group [97] has even found a discontinuous shift in polymer inverted opals under the influence of electric fields, leading to a shift by more than 4%. For LCs with very high birefringence, they expect a shift of up to 11%. Calculation of the band diagram [105] indicates the appearance of additional weak reflection peaks (for only one polarization) in the case of anisotropic materials. The peak corresponding to a gap between the third and fourth band is expected to be shifted even by more than 20% [105]. Large thermal tunability is also predicted for metallic PhCs infiltrated with LCs [61].

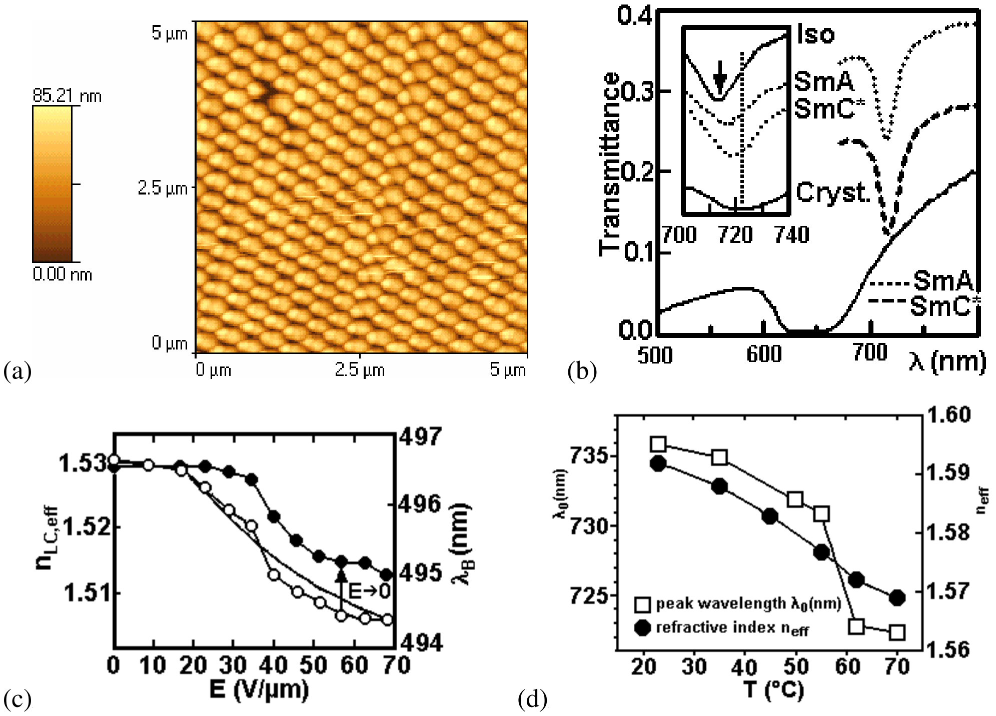

Figure 9.4: (a) AFM image of a {111} plane of a fcc colloidal structure. (b – d) Variation of the Bragg wavelength of face centered cubic (fcc) colloidal crystals containing LCs. (b) Temperature dependence for an artificial opal (consisting of SiO_2-spheres) filled with a chiral smectic LC [31]. (c) Electric field–induced shift for an artificial opal filled with the LC PCH5 [62]. (d) Variation of $\lambda_{1,1,1}$ with temperature in an inverted fcc structure filled with the LC 5CB [91].

Table 9.2: Tunable LC structures. In brackets: **dimension** [1D, 2D, 3D]; **frequency range**; **essential photonic property** ($\Delta\omega$ band gap width, ω_0 midgap frequency, ω_d frequency of a defect mode, ω_{co} cut-off frequency of a waveguide); **tuned structural property** (ε dielectric constant, $\vec{n}$ director, p helical pitch); **control parameter** (T working temperature, E electric field, σ mechanic strain, φ polarization of light).

System, Effect	Shift	Ref.
Inverse opal made of Si, wetted with LC [3D; vis; $\Delta\omega$; ε; $\vec{n}$; theory]	$\Delta\omega$(n ∥ [001]) = 0, $\Delta\omega$(n ∥ [111])/ω = 1.6%	[27]
Opal infiltrated with a nematic (ZLI 1132) or chiral smectic LCs [3D; vis; ω_0; ε; T; exp.]	λ(30–75°C) $=$ 730–723 nm, $\delta\lambda/\lambda \approx 0.96$ % $\lambda_{iso} = 718$ nm, $\lambda_{SmC^*} = 715$ nm, $\delta\lambda/\lambda \approx 0.4\%$	[32] [33]
Synthetic **opal** filled with 5CB [3D; vis; ω_0; ε; E; exp.]	$\lambda_0(0–60\text{ V}) = 726.5–724.5$ nm, $\delta\lambda/\lambda \approx 0.3\%$	[64]

System, Effect	Shift	Ref.
Colloidal crystal filled with PCH5 [3D; vis; ω_0; ε; E; exp. + theory]	λ_0(0–70 V/μm) $=$ 496.6–495 nm, $\delta\lambda/\lambda \approx 0.3\%$	[62]
SnS_2 **inverse opal** filled with E7 [3D; vis; ω_0; ε; T; exp.]	λ(23–70°C) $= 736 - 722$ nm, $\delta\lambda/\lambda \approx 2\%$	[91]
Inverse opal filled with LC [3D; vis; ω_0; ε; E; theory]	$\delta\lambda_0(\mathrm{n}_{LC} = 1.5\text{–}2.1)/\lambda_0$ $\approx$ 100 nm/870 nm $\approx 11\%$	[105]
	$\delta\lambda_2(\mathrm{n}_{LC} = 1.5\text{–}2.1)/\lambda_2$ $\approx$ 220 nm/1000 nm $\approx 22\%$	
Polymer **inverted opal** filled with 5CB [3D; vis; ω_0; ε; E; exp.]	λ_0(0–170 V/50 μm) $=$ 730–695 nm, $\delta\lambda/\lambda \approx 4.8\%$	[97]
Colloidal PhC (fcc)with **double periodicity** [3D; –; ω_0; ε; –; theory]	$\nu_0(n = 1.46) = 0.64$ c/a, $\nu_0(n = 1.7) = 0.3$ c/a	[106]
Mechanically tunable laser using a **cholesteric elastomer** [1D; vis; ω_0; ε; σ; exp.]	$\lambda_0 \approx 230 - 360$ nm $\delta\lambda/\lambda \approx 36\%$	[55]
Electrically tunable laser using a **ferroelectric LC** [1D; vis; ω_{lo}; p; E; exp.]	472 nm(0 V)–488 nm(40 V/150 μm)	[108]
Alternating **ZnS/LC** layers [1D; –; $\Delta\omega$; ε; E; theory]	$\Delta\omega/\omega =$ 0–6.5% (V $>$ 1.2 V_c)	[57]
2D hexagonal macroporous silicon [2D; IR; ω_{hi}; ε; T; exp.]	$\delta\lambda/\lambda \approx$ 70 nm/4.3 μm $\approx 1.6\%$	[45]
3D hexagonal macroporous silicon [3D; IR; ω_{hi}; ε; T, φ; exp.]	$\delta\lambda(T)/\lambda \approx$ 144 nm/11.3 μm $\approx 1.3\%$ $\delta\lambda(\varphi)/\lambda \approx$ 152 nm/11.3 μm $\approx 1.3\%$	[109]
III-V Semiconductor waveguide with LC [2D; IR; ω_d; ε; T; exp. + theory]	$\delta\lambda$(20–70°C)$/\lambda \approx$ 9.5 nm/1 μm $\approx 1\%$	[111]
Y-shaped waveguide switch with LC [2D; IR; ω_{co}; ε; E; theory]	$\delta\omega_{co}(\phi =$ 0–90°$)/\omega_{in}$ $\approx 0.02/0.376 \approx 5\%$	[114]
LC as a **defect layer** between periodic SiO_2-TiO_2 layers [1D; vis; ω_d; ε; E; exp. + theory]	$\delta\lambda_d$(0–8 V/μm)$/\lambda_d$ $\approx$ 50 nm/615 nm $\approx 8\%$	[96]
Channel drop filter: 2D macroporous Si filled with LC [2D; IR; ω_d; ε; E; theory]	$\delta\lambda_d(\mathrm{n}_{LC} = 1.5\text{–}1.7)/\lambda_d$ $=$ 18 nm/1436 nm $\approx 1.2\%$	[99]

9.3.3 Polymer–dispersed liquid crystals

A novel and interesting approach towards PhCs is the holographic formation of polymer–dispersed LCs (PDLC) [36, 104]. PDLC are heterogeneous structures composed of a low molar mass LC and a polymer [16]. They can be produced either by an emulsion technique or by phase separation. In the latter case, a homogeneous mixture of the polymer and the LC is made either by heating to high temperatures or by dissolving the components in a common solvent. Then, the separation into two phases is induced by cooling (thermally induced phase separation, TIPS) or by controlled solvent evaporation (solvent evaporation-induced phase separation, SIPS). Alternatively, the LC can be mixed with a reactive monomer and then polymerized (polymerization-induced phase separation, PIPS). In the PIPS [17] and TIPS process [20], the final spatial distribution of the separated components can be controlled by exposing the sample to a holographic pattern of modulated radiation intensity during the phase separation process (Fig. 9.5). This leads to electrically switchable holograms. Recently, Tondiglia et al. [104] and Escuti et al. [75] adopted the method of holographic lithography by Campbell et al. [37], where interference of three or four non–coplanar beams is used to obtain two– or three–dimensional structures, respectively (Fig. 9.5). In principle, all 14 Bravais lattices can be obtained, depending on the direction and intensity of four interfering plane waves [72]. So far, electric field–induced switching of the diffraction efficiency on an orthorhombic P crystal, made of a PDLC, has been demonstrated [104]. However, systems with higher dielectric contrast are necessary in order to obtain a photonic band gap. Additive nanolithography using electron–beam induced deposition can provide at least two–dimensional structures with dielectric constants of 2.2 to 8 [19].

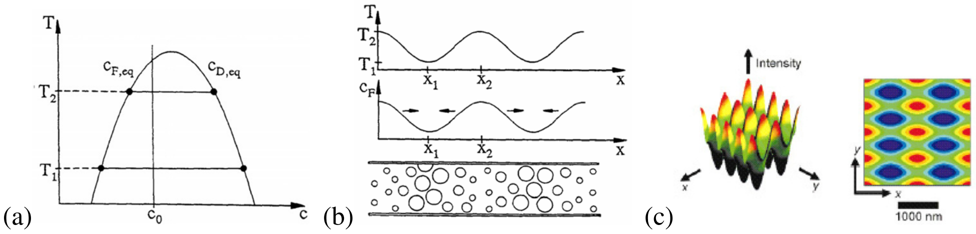

Figure 9.5: (a), (b) Schematic representation of the phase separation in polymer–dispersed LCs in the case of thermally induced phase separation [20]. (c) Intensity distribution for a hologram formed of four beams (with kind permission by Tondiglia et al. [104]).

9.4 Microstructured semiconductors

The realization of tunable PhCs in semiconductors is motivated by the aim to monolithically integrate tunable properties with other optoelectronic components, like lasers, waveguides and detectors. In this section, fundamental investigations on LC / silicon PhCs and the fabrication, infiltration and basic optical properties of planar III–V semiconductor PhCs are described.

9.4.1 Macroporous silicon

Macroporous structures in n–doped silicon can be prepared using an electrochemical etching process (see Chapter 4 of this book). Leonard et al. [45] have filled a two–dimensional hexagonal array of pores with a LC, and found that the band gap can be shifted by changing the temperature. For pores with a diameter of about 1 μm and a lattice constant of 1.58 μm, the photonic stop band is in the IR range (3.3–5.5 μm) where silicon is transparent. After filling with the nematic LC mixture E7 (Merck), the band gap is shifted to 4.4–6.0 μm. The transmission of a 100 μm wide bridge of the PhC was measured with a beam propagating parallel to the plane of the Si wafer, i. e. perpendicular to the pores. By changing the temperature from

35 °C to 65 °C, a shift of the high frequency band edge by 70 nm was observed (Fig. 9.6a). In order to explain this result, Leonard et al. assumed an escaped radial (ER) structure. In this case, the effective refractive index of the LC is an average value of the ordinary and extraordinary refractive index, which explains why the observed shift (70 nm) was smaller than the shift expected for a uniform orientation of the LC (113 nm).

More recently, three dimensional structures were fabricated in which the diameter of the pores varies along the pore axis (Fig. 9.6c). In this case, it was also possible to observe a stop band for light propagation along the pore axes (Fig. 9.6b). As expected, the stop band was centered at about 10.5 μm. The pores were filled with the nematic LC 4–cyano-4'–pentylbiphenyl (5CB) which shows a clearing temperature of $T_{NI} = 34°$C. Filling the pores with 5CB resulted in a shift of the stop band to $\lambda \approx 12$ μm. The band edge at lower wavelengths (corresponding to the "liquid crystal band") can be tuned by more than 140 nm while heating the LC from the nematic phase (24°C) to the isotropic state (40°C). The shift of the photonic band edge towards larger wavelengths indicates an increase of the effective refractive index with increasing temperature. Figure 9.6d shows some possible director configurations in cylindrical cavities, obtained by computer simulation using the relaxation equation of the alignment tensor [9]. In order to understand the optical behavior, it is necessary to identify which of these structures exists in the investigated samples. For this purpose, pores were filled with deuterated 5CB and the intensity distribution of the ^{2}H–NMR signal was analyzed. Due to the quadrupolar splitting [59], the intensity distribution of the ^{2}H–NMR signal indicates the orientational distribution f(ϑ), averaged over the sample volume.

The result (Fig. 9.6e) indicates a uniform parallel alignment of the director along the pore axis and explains the observed increase of the edge wavelength, which in turn is due to an increase of the effective refractive index from $n_{\text{eff}} \approx n_o$ to $n_{\text{eff}} = n_{iso} = (1/3\ n_e^2 + 2/3\ n_o^2)^{1/2}$. It is interesting to note that the band gap was also found to depend on the polarization of the incident light: Rotation of the sample with respect to the plane of polarization caused a shift of the LC band edge by $\Delta\lambda \approx 152$ nm. This behavior can be attributed to the non-circular (partial quadratical) shape of the pores (Fig. 9.6c) which breaks the three–dimensional symmetry of the hexagonal lattice [40]. Due to this symmetry breaking, the polarization dependence also appears in the isotropic phase of the LC. Due to recent calculations for the behavior of waveguides [99, 114], very interesting applications are predicted for macroporous silicon structures filled with a LC. These perspectives are discussed in Section 9.5.

9.4.2 Group III–V semiconductors

Fabrication of planar III–V semiconductor photonic crystals

The fabrication technology for planar PhCs in III–V semiconductors is based on electron beam lithography to achieve lattice constants in the range of 200 – 400 nm, suitable for optical frequencies. To obtain a high interaction between the electromagnetic optical field and the PhC, a vertical waveguide layer structure is used with high optical confinement. In Fig. 9.7a, an example of such a layer structure is shown grown by molecular beam epitaxy. With this design, more than 95 % of the vertical field distribution of the guided light mode can be influenced by about 1.2 μm deeply etched PhCs.

In order to fabricate the lateral structure (Fig. 9.7b), the sample is coated by an SiO_2–layer, which serves later as etch mask. The pattern of the PhC is defined by high resolution

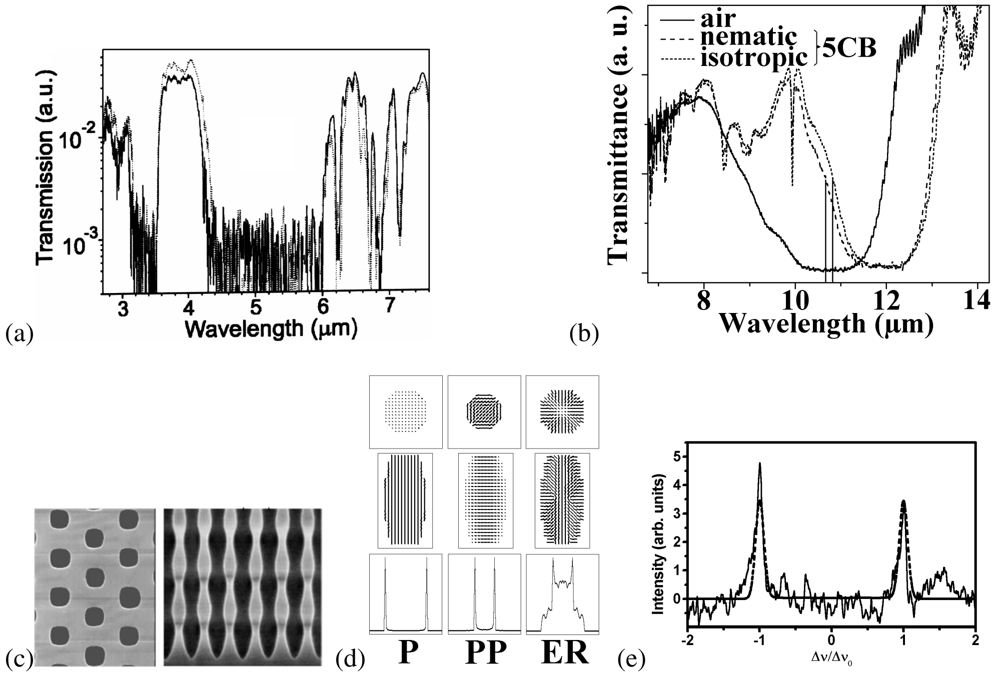

Figure 9.6: (a) Stop band in a two–dimensional hexagonal macroporous silicon structure filled with a LC at two different temperatures. Reproduced with kind permission from Leonard et al. [45]. (b) Transmission spectrum at two different temperatures for a 3D hexagonal structure with a pore spacing of a = 1.5 μm, and variation of the pore radius between R_{min} $\approx$ 0.38 $\pm$ 0.05 μm and R_{max} $\approx$ 0.63 $\pm$ 0.05 μm with a period of b = 2.6 μm along the pore axes. (c) Side– and top–view of a hexagonal array of modulated pores in silicon. (d) Calculated director configurations in cylindrical pores and their ^{2}H–NMR–spectra. (P) Parallel, (PP) planar polar, (ER) escaped radial configuration (e) Experimental ^{2}H–NMR spectrum of α-deuterated 5CB in macroporous silicon (pore radius R = 1.0 μm = const.). Dashed line: Calculated spectrum for a uniform parallel (type **P**) director field.

electron beam lithography. For that purpose, an electron beam resist [in this case PMMA = poly(methylmetacrylate)] is spinned on top of the SiO_2–layer and exposed by electron beams. PMMA is a negative–tone resist, so only the holes are exposed to radiation. After resist development, the pattern is transferred by a plasma etching process (e.g. RIE = reactive ion etching) with a gas mixture of CHF_3/Ar. The fluoro component is necessary to get a chemical reaction with silicon dioxide. The argon component removes residual solid etching products by physical sputtering during the etch process. The etching is stopped by time control but could also be monitored by mass–spectrometry to detect the transition in material composition. For the etch process into the semiconductor, a different technology is used which is specific for III/V–semiconductors. For GaAs/AlGaAs compounds an Cl_2/Ar process gas is used in a more advanced plasma–etching system. Either electron cyclotron resonance (ECR-RIE) or (chemically assisted ion beam etching) (CAIBE) systems are used to achieve very high aspect ratios and vertical side–walls [53]. With these techniques, aspect ratios of up to

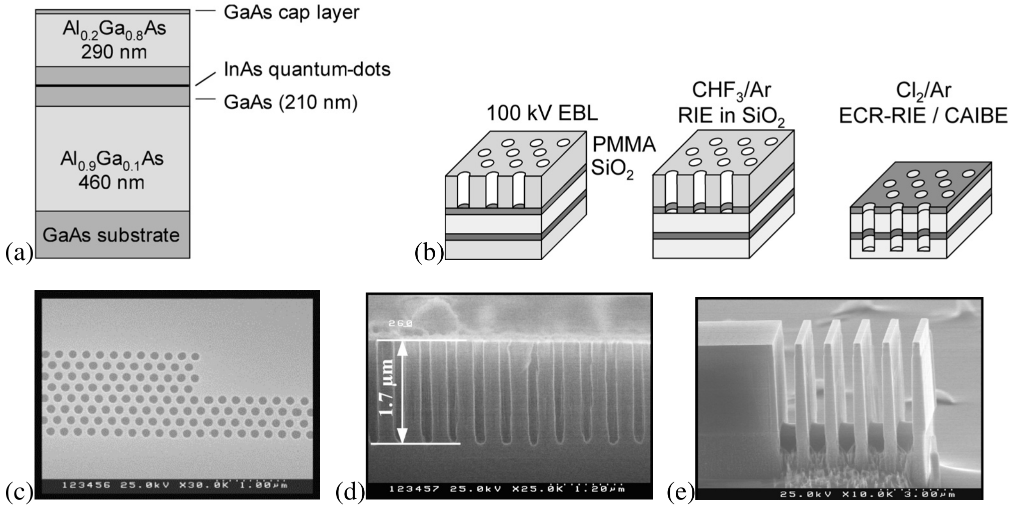

Figure 9.7: (a) Layer structure of a compact waveguide. (b) Fabrication process of planar PhCs. From left to right: Pattern definition by electron–beam lithography into resist (PMMA), transfer of pattern into SiO_2 etch mask by reactive ion etching (RIE) and transfer into semiconductor by electron cyclotron resonance (ECR) –RIE or chemically assisted ion beam etching (CAIBE). (c–d) SEM images of a PhC in top view (c) and cross section (d). Crystal period: 260 nm; Hole diameter: 85 nm; Etching depth: 1.7 μm. (e) One–dimensional PhC (deeply etched Bragg mirror) with a 3^{rd} order crystal period and an etch depth of about 3.5 μm in the center, 5 μm at the ridge waveguide edge, respectively.

20 were demonstrated in III–V materials. Further improvement in etching speed and possible aspect ratios is expected with newly developed inductive coupled plasma (ICP)–systems [77]. In Figures 9.7c–e, examples for two– (9.7c,d) and one–dimensional photonic crystals (9.7e) are shown. Further details about the fabrication of photonic crystals in III–V–semiconductors are discussed in “PhC based active optoelectronic devices”.

Based on these etch processes, one– and two–dimensional PhC structures were produced in III–V semiconductors which are suitable for the realization monolithically integrated laser mirrors [50], compact waveguides [41] and high quality planar microcavities [81]. For all these photonic band gap structures, the crystal period and the band structure of the PhC are fixed by the geometry defined by the fabrication process. The properties can be modified by infiltrating another material into the voids, for example a LC, thereby changing the refractive index contrast between the holes and the semiconductor. This change strongly affects the band structure. In addition, tuning of the PhC properties after the whole fabrication process becomes possible.

The infiltration of LC into one–dimensional structures is quite simple, because the air can escape easily and the voids are completely filled by LCs due to capillary forces. To localize the LC to some specific structures and to realize a full coverage, trenches perpendicular to the waveguide were defined by optical lithography. The trenches are 150 μm wide and 2–3 μm deep. The LC is transferred by dipping a glass fiber into the LC and dropping one droplet on the sample. The LC then spreads throughout the trench. However, filling the narrow pores of a planar two–dimensional PhC requires a two–step procedure [45]. In the first step, the air has to be removed from the voids by evacuating the sample to less than 0.1 mbar. For tests, we used a mechanical roughing pump with an end pressure of about 10^{-2} mbar. After evacuation, the LC is transferred into the vacuum by sticking the needle of a syringe through the sealing plug of the container. After deposition of a LC droplet, the container is flooded by air and the residual LC is blown away by a nitrogen gas jet.

Tunable two–dimensional photonic crystals

The investigated two–dimensional structure [111] consists of a one–dimensional microcavity where the two mirrors are formed by 2D PhCs (Fig.9.8). To allow transmission experiments, a quantum dot layer with a broad band emission is integrated into the waveguide structure. The quantum dots are excited by a focused Argon ion laser (λ = 514.5 nm) at about 50 μm away from the microcavity structure. The vertically guided light is transmitted through the microcavity and detected by a CCD camera from the cleaved facet. In this configuration, only transverse (TE) polarized light can be excited. This means, the $\vec{E}$–vector is parallel to the layer structure. Because the internal light source is limited in bandwidth (about 120 nm), several microcavity structures are defined on the same sample with slightly different grating periods to allow a scan over a wider range of the normalized wave number or $\vec{k}$–vector.

The transmission spectrum (Fig. 9.8c) shows a stop band which covers the range of normalized wave number a/λ between a/λ = 0.18 and 0.3. Within this stop band, two additional resonances exist which are the eigenmodes of the microcavity. The resonance at higher wave numbers corresponds to a mode where most of the field intensity is localized in the air voids. The mode at lower wave numbers has the maximum field intensity within the semiconductor. Therefore, the resonance near the so–called air band at the high–frequency side of the stop band is the mode which should be most sensitive on index changes in the voids. For the microcavity without LC, a quality (Q) –factor of 90 is achieved which is only slightly lower than theoretically predicted for an ideal two dimensional microcavity structure with 40 % air–filling factor and 5 rows of holes on each side. This good agreement confirms a high optical quality of the real structure.

For temperature–controlled tuning, the sample was mounted on a heat sink with a Peltier temperature controller. On increasing the temperature, the peak position is continuously shifting to lower wave numbers which corresponds to an increase of the refractive index (Fig. 9.8 d,e). A jump in the spectral peak position at about 60 °C coincides with the clearing temperature of the E7 LC. By further increasing the temperature the peak position remains fixed. The total resonance shift between 20 °C and 70 °C corresponds to a wavelength shift of 9.5 nm. Finite difference time domain (FDTD) calculations show good agreement with the experimental spectrum of the empty microcavity, if an air–filling factor of 39 % is used. This, in turn, is in very good agreement with the value determined by SEM. The shift in wavelength after the infiltration of LCs into the voids, can be fitted by assuming an effective refractive index of the filled holes of 1.41, which is only slightly lower than expected from bulk LC. The differences can be explained partially by the compact vertical waveguide design where already nearly 5 % of the propagating wave is penetrating into the vacuum. The remaining 10 % difference may be attributed to insufficient filling of the holes with LCs. By fitting the spectrum for the microcavity with LC above the clearing temperature, an effective refractive

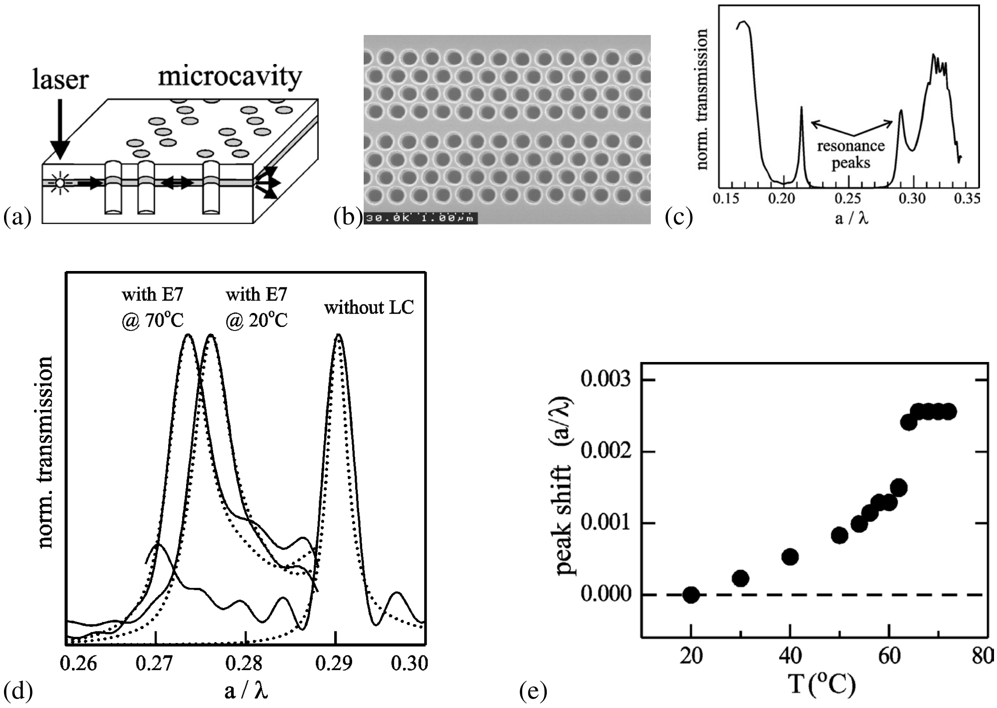

Figure 9.8: (a) Microcavity formed by two 2D photonic crystal mirrors. For transmission experiments, an internal light source is excited by an external laser and the vertically guided wave is detected from the cleaved facet. (b) SEM image of a microcavity structure. The crystal period is 300 nm and the spacing of the two PhC mirrors is 0.6 lattice constants. The air-filling factor is about 40 %; the etch depth 1.2 μm. (c) Calculated transmission spectrum. (d) Measured (solid lines) and simulated (dotted lines) transmission spectra for a microcavity with and without LC at different temperatures. (e) Shift of the microcavity resonance peak near the air–band in normalized wave numbers as function of the sample temperature.

index of 1.45 can be determined. This change in the refractive index of $\delta n = 0.04$ is in agreement with bulk properties of the ordinary refractive index branch of the E7 LC. The simulated spectra describe not only the peak position but also the line width and symmetry, without any further fitting parameter. The line width broadening and the increasing asymmetry are due to the reduction of the refractive index contrast between semiconductor and LC, which reduces the photonic band gap and the distance of the resonance peak position to the air band–edge. Apart from the spectral distribution, an increase of the refractive index of the LC corresponds to a higher transmission of the structure, because a larger index step between the LC and the vacuum leads to better vertical wave guiding.

In conclusion, first experiments on tunable planar PhCs in the optical wavelength regime confirm the predicted properties and allow a temperature tuning of a cavity resonance by 9.5 nm. The corresponding refractive index change of $\delta n = 0.04$ is about one order of magnitude larger than the refractive index change of semiconductors for the same temperature range. The results on planar PhCs show that the effective refractive index of the LC for TE polarization corresponds to the ordinary component. This indicates that the director of the LC is parallel to the cavity walls and perpendicular to the layer structure. Further improvement of the change in the refractive index of the liquid crystal from $\delta n = 0.04$ to $\delta n \approx \Delta n = n_e - n_o \approx 0.2$ might be possible by utilizing the birefringence more effectively. In general, very compact tunable, switchable or reconfigurable photonic devices based on PhCs may be feasible by using LCs, but further basic investigations, e.g. electric tuning and birefringent properties, are necessary to optimize the tuning behavior. A brief outlook for possible applications is given in Section 9.5.

9.5 Summary and perspectives

Liquid crystals have been demonstrated to be suitable for tunable PhCs in various ways. However, most of the experimental work performed so far shows mere "proofs of principle". The sensitivity of the birefringence to temperature and external fields is suitable to shift the LC band edge by several per cent. It has been demonstrated that inverted structures with a high filling fraction of LC show larger tunability than normal colloidal crystals filled with LCs. Unfortunately, the dielectric contrast of the systems where electric field–induced switching was shown is rather low. On the other hand, systems with high dielectric contrast (like the semiconductor structures shown in Section 9.4 of this chapter) exhibit high conductivity, thereby short–circuiting electric fields. Maybe inverted structures (like isolated semiconductor rods in a LC matrix) can here lead to better solutions, too. Decoration of the spontaneous periodic structures of LCs – as suggested by Hornreich and Shtrikman – is possibly a way towards new photonic materials with higher dielectric contrast. Recent material developments indicate that it is worthwhile trying this challenge. The nonlinear optical properties of LCs also offer many perspectives which are still waiting to be connected with PhCs. In the current literature, theoretical predictions about LCs are ahead of experiments (Table 9.2). So, within the next few years we will certainly see some progress in the development of "photonic liquid crystals". The following sections briefly present some concepts for application in silicon and III–V semiconductors.

9.5.1 Possible applications of macroporous silicon

Very interesting applications are predicted for macroporous silicon structures filled with a LC due to recent calculations for the behavior of waveguides [99, 114]. It is predicted that a switchable Y–shaped waveguide can be made by selectively filling a Y–shaped row of pores with LC, the other pores remaining filled with air [114]. The cut–off frequency of the waveguides can be tuned by the azimuthal angle of the director so that a waveguide is blocked if the director is parallel to the respective waveguide axis ($n_{core} = n_o$, $\phi = 0$). This allows one to block the beam completely, to deflect the beam into one arm of the switch, or to use the Y–shaped waveguide as a beam splitter (Fig. 9.9).

Pustai et al. [99] suggest a channel drop filter where edge dislocations serve as waveguides in the hexagonal silicon structure. A single pore filled with LC is used to tune the wavelength which is selectively coupled through a defect mode, from one waveguide equipped with white incident light, to a neighboring drop waveguide (Fig. 9.10).

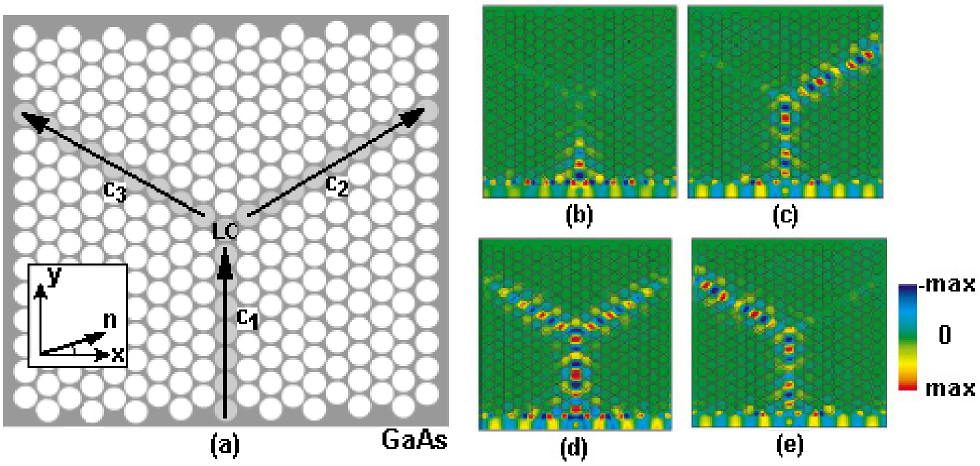

Figure 9.9: Y–shaped waveguide infiltrated with a LC. (a) Schematic setup and definition of the azimuthal angle ϕ of the director $\vec{n}$. Right: Calculated magnetic field patterns for (b) $|\phi| = 90°$, (c) $\phi = -30°$, (d) $\phi = 0$, (e) $\phi = +30°$. With kind permission from Takeda Yoshino [114].

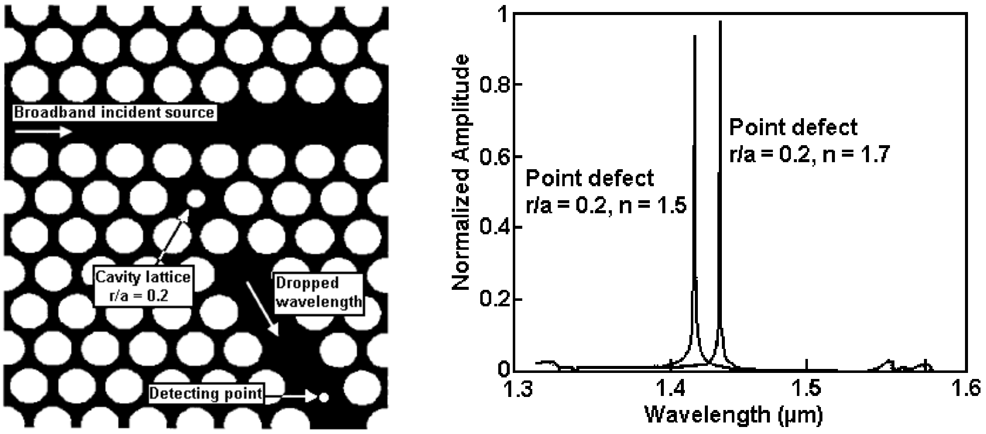

Figure 9.10: Channel drop filter design and wavelength shift in the channel drop filter due to point defect index modulation. With kind permission from ref. [99].

9.5.2 Possible applications for tunable planar III/V–semiconductor photonic crystals

Planar PhCs in III/V–compounds filled with LCs can be addressed either directly by an external electric field or by local heating. In the first case, a possible design makes use of a PhC structure, e.g. in microcavity geometry, which is integrated in a ridge waveguide structure. The electric field is applied by lateral contacts to allow an in–plane electric field orientation. For a standard nematic LC, an electric field in the range of $5 \times 10^4 - 1 \times 10^5$ V/cm is sufficient to change the orientation of the director significantly. In this waveguide geometry with a typical ridge width of 2 μm, an external voltage of $10 - 20$ V has to be applied. With specifically designed LCs, lower voltages might also be feasible. However, electrical switching within semiconductor holes of diameter 100 nm has still to be confirmed. In addition to the necessity of higher field strengths, we expect complications due to the non–uniform defect structures induced by anchoring. Nevertheless, this approach is most promising due to the expected high refractive index contrast change of up to 0.2.

An easier approach is local heating, thereby making use of the temperature dependence of the effective refractive index (see Section 9.4.2). The heating of the PhC structure may be obtained by lateral resist structures. If high–Q microcavities are formed by the PhC, this approach could be used as variable filter or switching device, e.g. in a Mach–Zehnder configuration which would allow routing applications.

A limiting condition for all these approaches is the large switching time ($\approx$ 50–100 ms) of conventional LCs. Ferroelectric LCs show switching times down to the μs range, but their alignment is much more difficult. Therefore, LC devices would be mainly dedicated to network reconfiguration, switching between different functionalities or adjustment of interference and filter devices. For fast switching, other physical effects have to be used, for example optical nonlinearity. The fabrication of more dense tunable devices is also an issue which has to be addressed. One solution could be the application of ink–jet technology to control the transferred volume and the localization of LCs. This technique would also be compatible with mass–production techniques.

Acknowledgements

The authors would like to thank Guido Mertens, Thorsten Röder and Heinrich Matthias for their enthusiastic work in the "tunable photonic crystal" project, Isabella Koralewicz for her assistance typing the manuscript and the Deutsche Forschungsgemeinschaft (Schwerpunktprogramm 1113 "Photonic Crystals") for financial support.

References

[1] J. C. Maxwell Garnett, Philos. Trans. R. Soc. London, Ser. A, **203** (1904), 385.
[2] W. Stöber, A. Fink, and E. Bohn, Journal of Colloid and Interface Science **26** (1968), 62.
[3] H. Kogelnik and C.V. Shank, Phys. Rev. Lett. **18** (1971), 152.
[4] D. W. Berreman, J. Opt. Soc. Am. **63** (1973), 1374.
[5] L. S. Goldberg and J.M. Schnur, (1973), US Patent 3,771,065.
[6] G. Heppke, M. Krummrey and F. Oestreicher, Mol. Cryst. Liq. Cryst. **99** (1983), 99.
H.–S. Kitzerow, Mol. Cryst. Liq. Cryst., **202** (1991), 51.
[7] S. John, Phys. Rev. Lett. **58** (1987), 2486.
[8] E. Yablonovitch, Phys. Rev. Lett. **58** (1987), 2059.
[9] A. Kilian and S. Hess, Z. Naturforsch. **44a** (1989), 693.
[10] S. Chandrasekhar, Liquid crystals (second edition), Cambridge University Press (1992).
D. Demus, J. Goodby, G. W. Gray et al., Handbook of Liquid Crystals, Wiley-VCH Vol. **1** (1998).
H.–S. Kitzerow and Ch. Bahr (Editors), *Chirality in Liquid Crystals*, Springer-Verlag, New York, 2001.
V. Vill, LiqCryst Data Base of Liquid Crystals, Version 4.2 (2002).
[11] T. Sasaki, Y. Sakata, T. Kato et al.; NEC Research and Development, Japan **33** (1992), no.3, 372.
T. Sasaki, M. Yamaguchi, T. Kato et al., Electronics and Communications in Japan, Part 2 (Electronics), **76** (1993), no. 4, 1.

[12] P. G. Gennes and J. Prost, 1993, The physics of liquid crystals, Clarendon Press, Oxford, GB.

[13] H.–S. Kitzerow, H. Schmid, G. Heppke et al., Liquid Crystals **14** (1993), 911.

[14] J. P. Dowling, M. Scalora, M.J. Bloemer et al., J. Appl. Phys. **75** (1994), 1896.
V.I. Kopp, B. Fan, H.K.M. Vithana et al., Opt. Lett. **21** (1998), 1707.

[15] R. M. Hornreich, S. Shtrikman, and C. Sommers, Phys. Rev. B **49**, (1994), 10914.

[16] H.–S. Kitzerow, Liquid Crystals **16** (1994), 1.
H.–S. Kitzerow, Polymer Dispersed and Polymer Stabilized Chiral Liquid Crystals, in: "Liquid Crystals in Complex Geometries Formed by Polymer and Porous Networks", edited by G. P. Crawford and S. Zumer, Taylor & Francis, London (1996), 187.

[17] T.J. Bunning, L.V. Natarajan, V. Tondiglia et al., Polymer, **36** (1995), 2699.
H.–S. Kitzerow, Mol. Cryst. Liq. Cryst., **321** (1998), 457.

[18] J.D. Joannopoulos, R.D. Meade and J.N. Winn, Photonic crystals: molding the flow of light, Princeton Univ. Press, Princeton, NJ, 1995

[19] H.W.P. Koops, Proc. SPIE **2849** (1996), 248.

[20] H.-S. Kitzerow, J. Strauß, and S.C. Jain, Proc. SPIE, **2651**(1996), 80.

[21] P.R. Villeneuve, D.S. Abrams, S. Fan et al., Optics Letters **21** (1996), no. 24, 2017.

[22] A. van Blaaderen, R. Ruel, P. Wiltzius, Nature **385/23** (1997), 321.

[23] J.S. Foresi, P.R. Villeneuve, J. Ferrera et al., Nature **390 (**1997), 143.
Y. Yi, P. Bermel, K. Wada et al., Low voltage tunable one dimensional photonic crystal with large air defects, in: Materials and Devices for Optoelectronics and Microphotonics. Symposia, edited by R.B. Wehrspohn, R. Marz; S. Noda; and C. Soukoulis, MRS Symp. Proc. **722** (2002), xv+493, 391.

[24] A. Figotin; Y.A. Godin and I. Vitebsky, Phys. Rev. B, **57** (1998), no. 5, 2841.
C.S. Kee, J.E. Kim, J.-Y. Park et al., Phys. Rev. **61** (2000), no. 23, 15523.

[25] S. Wang, H. Erlig, H. Fetterman et al., Proc. SPIE. **3228** (1998), 408.
S. Wang, H. Erlig, H.R. Fetterman et al., Microwave and Optical Technology Letters **20** (1999), no.1, 17.

[26] J.E.G.J. Wijnhoven and L.W. Vos, Science **281** (1998), 802.
P.V. Braun and P. Wiltzius, Nature **402** (1999), 603.
A. Blanco, E. Chomski, S. Grabtchak et al., Nature **405** (2000), 437.
I. Soten, H. Miguez, S. M. Yang et al., Advanced Functional Materials **12** (2002), no. 1, 71.

[27] K. Busch and S. John, Phys. Rev. Lett. **83** (1999), no. 5, 967-970.
S. John and K. Busch, J. Lightwave Technology **17** (1999), no. 11, 1931.

[28] J.M. Lourtioz, A. de Lustrac, F. Gadot et al., J. Lightwave Technology **17** (1999), no. 11, 2025.
O. Vanbesian, J. Danglot and D. Lippens, Annales des Telecommunications **57** (2002), 22.

[29] M.Takeda and T. Kurokawa, Proc. SPIE **3729** (1999), 415.
B. Temelkuran and E. Ozbay, Proc. SPIE **3620** (1999), 388.

[30] K. Yoshino, Y. Kawagishi, M. Ozaki et al., Jpn. J. Appl. Phys. **38**, (1999), no. 7A, L786.

[31] K. Yoshino, S. Satoh, Y. Shimoda et al., Jpn. J. Appl. Phys. **38** (1999), L 961.

[32] K. Yoshino, Y. Shimoda, Y. Kawagishi et al., Appl. Phys. Lett. **75** (1999), 932.

[33] K. Yoshino, Y. Shimoda, K. Nakayama et al., Mol. Cryst. Liq. Cryst. **364**, (2001), 501.

[34] K. Yoshino, K. Nakayama, Y. Kawagiishi et al., Mol. Cryst. Liq. Cryst. **329** (1999), [1045]/433.

[35] M.V. Alfimov, A.M. Zheltikov, A.A. Ivanov et al., JETP Lett. (Russia), **71** (2000), 489.

[36] C.C. Bowley, A. Fontecchio, J.J. Lin et al., Appl. Phys. Lett., **76** (2000), 523.

[37] M. Campbell, D.N. Sharp, M.T. Harrison et al., Nature, **404**, (2000), 53.

[38] U. Dassanayake, S. Fraden and A. van Blaaderen, J. Chem. Phys. **112** (2000), no. 18, 3851.

[39] P. Etchegoin, Phys. Rev. E **62**, (2000), 1435.

[40] R. Hillebrand and W. Hergert, Solid State Commun. **115** (2000), 227.

[41] T.D. Happ, M. Kamp, F. Klopf et al., Electron. Lett., **36** (2000), 324.
J. Zimmermann, M. Kamp, R. Schwertberger et al., Electron. Lett., **38** (2002), 178.

[42] P. Halevi and F. Ramos-Mendieta, Phys. Rev. Lett. **85** (2000), no. 9, 1875.
C. S. Kee and H. Lim, Phys. Rev. B **64** (2001), no. 12, 121103/1-4.
[43] G. Kiriakidis and N. Katsarakis, Mater. Phys. Mech. (Russia), **1** (2000), 20.
[44] H. A. Lopez and P. M. Fauchet, Appl. Phys. Lett. **77**, (2000) 3704.
[45] S. W. Leonard, J. P. Mondia, H. M. van Driel, O. Toader, S. John; K. Busch; A. Birner, U. Gösele and V. Lehmann, Phys. Rev. B **61** (2000), no. 4, 2389.
[46] R. K. Lee, O. Painter, B. Kitzke-B et al., Opt. Soc. America **17** (2000), no. 4, 629.
[47] A. Moroz, Europhysics Letters **50** (2000), no. 4, 466.
A.B. Fedotov, M.V. Alfimov, A.A. Ivanov et al., Laser Physics (Russia) **11** (2001), no.1, 138.
[48] M. Müller, R. Zentel, T. Maka et al., Adv. Mater. **12** (2000), 1499.
[49] S. Noda, A. Chutinan, and M. Imada, Nature, **407** (2000), 608.
[50] S. Rennon, K. Avary, F. Klopf et al., Electron. Lett., **36** (2000), no. (16), 1548.
S. Rennon, F. Klopf, J. P. Reithmaier et al., Electron. Lett., **37** (2001), issue (11), 690.
T. D. Happ, M. Kamp, F. Klopf et al., Semicond. Sci. Technol. **16** (2001), 227.
[51] A. Urbas, R. Sharp, Y. Fink et al., Advanced Materials, **12** (2000), no. 11, 812.
[52] Z.L. Wang and J.S. Yin, Mater. Sci. Eng. A, **A 286** (2000), no. 1, 39.
[53] K. Avary, S. Rennon, F. Klopf et al., Microelectronic Engineering, **57-58** (2001), 593.
K. Avary, J.P. Reithmaier, F. Klopf et al., Microelectron. Eng., **61-62** (2002), 875.
[54] D.A. Dunmur, A. Fukuda and G.R. Luckhurst, Physical properties of liquid crystals: nematics, emis Datareviews series no 25, (2001).
[55] H. Finkelmann, S.T. Kim, A. Munoz et al., Adv. Mater. **13 (**2001), 1069.
[56] Z. Z. Gu, Q. B. Meng, S. Hayami et al., J. Appl. Phys., **90** (2001), no. 4, 2042.
[57] Y.-K. Ha, Y.-C. Yang, J.-E. Kim et al., Appl. Phys. Lett. **79** (2001), 15.
[58] P. Kopperschmidt, Applied Physics B **73** (2001), no. 7, 717.
[59] S. Kumar, Liquid Crystals Experimental study of physical properties and phase transitions, Cambridge University Press (2001).
[60] S. Kim and V. Gopalan, Appl. Phys. Lett., **78** (2001), 3015.
[61] C. S. Kee, H. Lim, Y.-K. Ha et al., Phys. Rev. B **64** (2001), 085114/1-7.
[62] D. Kang, J.E. Maclennan, N.A. Clark et al., Phys. Rev. Lett. **86** (2001), 4052.
[63] M. Loncar, J. Vuckovic and A. Scherer, J. Opt. Soc. Am. B **18** (2001), no 9, 1362.
[64] Q.B. Meng, C.H. Fu, S. Hayami et al., J. Appl. Phys., **89** (2001), 5794.
[65] P. Pieranski, Classroom experiments with chiral liquid crystals, in: Chirality in Liquid Crystals, edited by H.-S. Kitzerow and Ch. Bahr, Springer, New York, 2002.
[66] P. V. Santos, J. Appl. Phys. **89** (2001), 5060.
[67] Y. Shimoda, M. Ozaki and K. Yoshino, Appl. Phys. Lett. **79** (2001), 3627.
[68] K. Takano, T. Sugano and K. Nakagawa, Lasers and Electro-Optics Society 14^{th} Annual Meeting (Piscataway, NJ, USA), IEEE product-No. CH37242-TBR, IEEE (2001), vol. **1**, 206.
[69] Y.A. Vlasov, X.–Z. Bo, J.C. Sturm et al., Nature, **414** (2001), 289.
[70] K. Yoshino, S. Satoh, Y. Shimoda et al., Synth. Met., **121** (2001), 1459.
S. Satoh, Y. Kawagishi, A. Fujii et al., Jpn. J. Appl. Phys. **38** (1999), no.12, L1475.
S. Satoh, H. Kajii, Y. Kawagishi et al., Synth. Met. **121** (2001), 1503.
[71] W. Cao, A. Munoz, P. Palffy-Muhoray et al., Nature Materials **1** (2002), 111.
[72] L.Z. Cai, X.L. Yang and Y.R. Wang, Opt. Lett. **27** (2002), 900.
[73] Y.-B. Chen, C. Zhang, Y.-Y. Zhu et al., Materials Letters **55** (2002), 12.
[74] Y. Dumeige, I. Sagnes, P. Monnier et al., J. Opt. Soc. Am. B **19** (2002), 2094.
D. Pezzetta, C. Sibilia, M. Bertolotti et al., J. Opt. Soc. Am. B, **18** (2001), 1326.
[75] M.J. Escuti and G.P. Crawford, Polymer dispersed liquid crystals as mesoscale 2D and 3D lattices, in: Advances in Liquid Crystalline Materials and Technologies. Symposium, edited by P.T. Mather, D.J. Broer, T.J. Bunning, D.M. Walba, and R. Zentel, Mater. Res. Soc., **709** (2002), 293.
[76] M. Eden and R. Zentel, Chem. Mater. **14**, (2002), 2176.
[77] R. Ferrini, B. Lombardet, B. Wild et al., Electron. Lett. **38**, (2002) 962.

[78] Z.Z. Gu and O. Sato, Japan Soc. Appl. Phys. **71** (2002), 336. See also the chapter by Eich et al. in this book.

[79] H. Hillmer, J. Daleiden, C. Prott et al., Applied Physics B, **75** (2002), 3.

[80] Y.-K. Ha, J.-E. Kim, H. Y. Park et al., Phys. Rev. B **66** (2002), no. 7, 075109/1.

[81] T. D. Happ, I. I. Tartakovskii, V. D. Kulakovskii et al., Phys. Rev. B **66** (2002), 041303/1.

[82] P. M. Johnson, A. F. Koenderink, and W. L. Vos, Phys. Rev. B **66** (2002), 081102/1.
S.W. Leonard and H.M. van Driel, J. Schilling et al., Phys. Rev. B **66**, (2002), 161102/1.

[83] J. Kim and S. Lee, J. Appl. Phys. **92** (2002), 1185.

[84] P-K. Kashkarov, L-A. Golovan, A-B. Fedotov et al., Optical Physics **19** (2002), no. 9, 2273.

[85] C. Kerbage, P. Steinvurzel, A. Hale et al., Electronics Letters **38 (**2002), 310.

[86] C. Kerbage and B. J. Eggleton, Appl. Phys. Lett., **82** (2003), 1338.

[87] C. Kerbage, R. S. Windeler, B. J. Eggleton et al., Optics Communications **204** (2002), 179.

[88] H. Kikuchi, M. Yokota, Y. Hisakado et al., Nature Materials **1** (2002), 64.

[89] S. Lan, S. Nishikawa, H. Ishikawa et al., IEICE Transactions on Electronics, **E85-C** (2002), no. 1, 181.

[90] S. Mingaleev and Y. Kivshar, Optics & Photonics News **(July 2002)**, 49.

[91] G. Mertens, T. Röder, R. Schweins et al., Appl. Phys. Lett. **80** (2002), 1885.

[92] N. Nishizawa, Y. Ito and T. Goto, IEEE Photonics Technology Letters **14** (2002), no. 7, 86.

[93] B.R. Washburn, S.E. Ralph, P.A. Lacourt et al., Electronics Lett. **37** (2001), 1510.

[94] X. Liu, C. Xu and W. H. Knox, J. K. Chandalia, B.J. Eggleton, S.G. Kosinski and R.S. Windeler, Opt. Lett. **26**, (2001) 358.

[95] S. Nishimura, A. Shishido, N. Abrams et al., Appl. Phys. Lett. **81** (2002) 4532.

[96] R. Ozaki, T. Matsui, M. Ozaki et al., Jpn. J. Appl. Phys., Part 2 (Letters), **41** (2002), no. 12B, L1482.

[97] M. Ozaki, Y. Shimoda, M. Kasano et al., Advanced Materials **14**, (2002), no 7, 514.

[98] M. U. Pralle, N. Moelders, M. P. McNeal et al., Appl. Phys. Lett. **81** (2002), no. 25, 4685.

[99] D. M. Pustai, A. Sharkawy, S. Shi et al., Applied Optics **41** (2002), 5574.

[100] T. Stroucken and R. Eichmann, L. Banyai et al., J. Opt. Soc. Am. **19**, (2002) no 9, 2292.

[101] Y. Saado, M. Golosovsky, D. Davidov et al., Phys. Rev. B **66** (2002), 195108/1.
Y. Saado, M. Golosovsky, D. Davidov et al., Synth. Met. **116** (2001), 427.
Y. Saado, T. Ji, M. Golosovsky, D. Davidov et al., Opt. Mater., **17** (2001), 1.

[102] J. Schmidtke, W. Stille, H. Finkelmann et al., Adv. Mater. **14** (2002), 746.

[103] M.N. Shkunov, Z.V. Vardeny, M.C. DeLong et al., Advanced Functional Materials **12** (2002), 21.

[104] V.P. Tondiglia, L.V. Natarajan, R.L. Sutherland et al., Adv. Mater. **14** (2002), 187.

[105] H. Takeda and K. Yoshino, J. Appl. Phys. **92** (2002), 5658.

[106] H. Takeda and K. Yoshino, Jpn. J Appl. Phys., Part 2 (Letters), **41** (2002), L773.

[107] S. B. Debord and L. A. Lyon, J. Phys. Chem. B **107** (2003), 2927.
J.D. Debord and L.A. Lyon, Journal of Physical Chemistry B **104** (2000), no. 27, 6327.

[108] M. Kasano, M. Ozaki, K. Yoshino et al., Appl. Phys. Lett., **82** (2003), 4026.

[109] G. Mertens, T. Röder, H. Matthias et al., Two– and three–dimensional photonic crystals made of macroporous silicon and liquid crystals, Appl. Phys. Lett. (2003), in press.

[110] T. Röder, T. Kramer, K. Huber et al., Preparation of positively and negatively charged organic colloids from a single precursor, to be published.

[111] Ch. Schuller, F. Klopf, J.P. Reithmaier et al., Appl. Phys. Lett. **82** (2003), 2767.

[112] J. Schmidtke, W. Stille and H. Finkelmann, Phys. Rev. Lett., **90** (2003), 083902/1.

[113] W. Suh, M.F. Yanik, O. Solgaard et al., Appl. Phys. Lett. **82** (2003), 1999.

[114] H. Takeda and K. Yoshino, Phys. Rev. B **67** (2003), 73106/1.

[115] H. Xin, A. Higgins, J. Hacker et al., IEEE Microwave and Wireless Components Letters **13** (2003), no. 3, 108.

[116] S.Y. Yang, H.E. Horng, C.-Y. Hong et al., J. Appl. Phys. **93** (2003), no 6, 3457

[117] S. Yamada, Y. Watanabe, Y. Katayama et al., J. Appl. Phys., **93** (2003), no. 4, 1859.

10 Microwave modelling of photonic crystals

Wolfgang Freude[1]*, Guy–Aymar Chakam, Jan–Michael Brosi, and Christian Koos*

Integratable waveguiding photonic bandgap (PBG) structures and photonic crystals (PhC) are of special interest in the optical communication range near a vacuum wavelength of $\lambda_o = 1.5\,\mu\mathrm{m}$ (frequency $f_o = 200$ THz). The typical scale-size of the PhC is much smaller than λ_o, while the total structure usually extends over regions significantly larger than λ_o. Numerical simulations quickly run into limitations of computing time and memory size, because the problems are numerically large. To verify and optimize any design process, the expensive fabrication and measurement of optical PBG test structures as well as trial–and–error steps are unavoidable.

To simplify the experiments, we scale up the geometry of our test structures to an operating frequency near $f_m = 10$ GHz ($\lambda_m = 30$ mm), where PTFE-based, low-loss materials with refractive indices $n = 3.03, 2.45, 2.12, 1.81, 1.71, 1.48$ and $n \approx 1$ (dielectric foam) are readily available. This allows the investigation of high and moderate–index devices. The geometrical scaling factor is of the order $\sigma = 200$ THz/10 GHz $= 30\ \mathrm{mm}/1.5\ \mu\mathrm{m} = 20\,000$.

Microwave equipment in this frequency range is usually based on coaxial metallic transmission lines, while our up–scaled model waveguides are dielectric strips. To connect these components, we developed an appropriate low–loss coaxial–to–dielectric strip waveguide transition, which represents a key component for the present investigations.

Understanding loss in PBG waveguides will be crucial for any communication application. However, the various loss mechanisms are not easily separated in the optical region, and are difficult to access. We discuss microwave techniques suitable for this task.

10.1 Fundamentals

Electromagnetic waves (magnetic and electric field vectors $\vec{H}$ and $\vec{E}$, respectively) are solutions of Maxwell's equations as functions of time t and position in space $\vec{r}$. The medium at the frequencies of interest is assumed to be isotropic, linear and non–magnetic (medium properties given by scalar, amplitude–independent quantities, relative magnetic permeability $\mu_r = 1$). Currents and electric space charges are assumed not to exist. In vacuum, the dielectric constant (permittivity) and the magnetic permeability as well as the velocity of light and the wavelength at frequency f (angular frequency $\omega = 2\pi f$) are ϵ_0, μ_0, $c = 1/\sqrt{\epsilon_0\mu_0}$, and $\lambda = c/f$. The vacuum propagation constant is denoted as $k_0 = \omega/c$. Further, we concentrate on low-loss dielectric media, characterized by a complex and virtually frequency-independent

---

[1] Corresponding author, e-mail: W.Freude@etec.uni-karlsruhe.de, fax: 0431 880 6178

Photonic Crystals. Edited by K. Busch, S. Lölkes, R. B. Wehrspohn and H. Föll
Copyright © 2004 Wiley-VCH Verlag GmbH & Co. KGaA
ISBN: 3-527-40432-5

relative dielectric permittivity $\bar{\epsilon}_r$, which for most purposes may be approximated by its real part ϵ_r.

10.1.1 Maxwell's equations and scaling laws

Reshaping Maxwell's equations, we find the wave equations for the magnetic and electric fields,

$$\left(\operatorname{curl}\frac{1}{\epsilon_r}\operatorname{curl}\right)\vec{H} = \left(-\frac{1}{c^2}\frac{\partial^2}{\partial t^2}\right)\vec{H}, \quad \left(\frac{1}{\epsilon_r}\operatorname{curl}\operatorname{curl}\right)\vec{E} = \left(-\frac{1}{c^2}\frac{\partial^2}{\partial t^2}\right)\vec{E}. \tag{10.1}$$

We seek harmonic solutions of the form

$$\vec{H}(t,\vec{r}) = \vec{H}(\vec{r})\,\mathrm{e}^{\mathrm{j}\,\omega t}, \quad \vec{E}(t,\vec{r}) = \vec{E}(\vec{r})\,\mathrm{e}^{\mathrm{j}\,\omega t}, \tag{10.2}$$

where ω is the angular eigenfrequency, and $\vec{H}(\vec{r})$ and $\vec{E}(\vec{r})$ are the eigenfunctions of the wave equations.

The fields of Eq. (10.1) are macroscopic quantities, which result from space–averaging their microscopic, atomic counterparts [11, Sect. 1.1], [16, Sect. I.4]. All vector fields are functions of time t and position vector $\vec{r} = x\,\vec{e}_x + y\,\vec{e}_y + z\,\vec{e}_z$, choosing Cartesian coordinates with unit vectors $\vec{e}_{x,y,z}$. The medium permittivity $\epsilon(\vec{r}) = \epsilon_0\epsilon_r(\vec{r})$ at any given frequency may depend on the spatial coordinate. The refractive index is defined by Maxwell's formula $n = \sqrt{\epsilon_r\mu_r} = \sqrt{\epsilon_r}$.

When discussing the properties of real media we need to define the complex permittivity $\bar{\epsilon}_r$ with real part ϵ_r and imaginary part $-\epsilon_{ri}$, the complex refractive index $\bar{n}$ with real part n and imaginary part $-n_i$ (extinction coefficient n_i), and the complex propagation constant $\bar{k} = \bar{n}k_0$. For passive microwave materials, the loss factor $\tan\delta = \epsilon_r/\epsilon_{ri}$ is usually specified. Maxwell's formula for a complex dielectric constant (permittivity) results in

$$\begin{aligned} \bar{n} &= n - \mathrm{j}\,n_i = \sqrt{\bar{\epsilon}_r}\,, & \bar{\epsilon}_r &= \epsilon_r - \mathrm{j}\,\epsilon_{ri} = \bar{n}^2, \\ \epsilon_r &= n^2 - n_i^2, & \epsilon_{ri} &= 2nn_i = \epsilon_r\tan\delta\,, \\ n &\approx \sqrt{\epsilon_r} \quad \text{for } |\epsilon_{ri}| \ll \epsilon_r\,, & n_i &\approx \epsilon_{ri}/\big(2\sqrt{\epsilon_r}\big) = \tfrac{\sqrt{\epsilon_r}}{2}\tan\delta \quad \text{for } |\epsilon_{ri}| \ll \epsilon_r\,. \end{aligned} \tag{10.3}$$

Assuming a weakly lossy medium, we propagate a (virtually) homogeneous plane wave in the z–direction. Its initial power P_0 decays exponentially with the power attenuation constant α (measured in m^{-1}); a logarithmic quantity is the attenuation a (measured in dB),

$$\begin{gathered} P(z) = P_0\big|\mathrm{e}^{-\mathrm{j}\,\bar{k}z}\big|^2 = P_0\big|\mathrm{e}^{-n_ik_0z}\,\mathrm{e}^{-\mathrm{j}\,nk_0z}\big|^2 = P_0\,\mathrm{e}^{-2n_ik_0z} = P_0\,\mathrm{e}^{-\alpha z}, \\ \alpha = 2n_ik_0\,, \qquad \frac{a}{\mathrm{dB}} = 10\lg\frac{P_0}{P(z)} = \alpha z \times 10\lg\mathrm{e} = 4.34 \times \alpha z\,. \end{gathered} \tag{10.4}$$

For comparing various materials in possibly vastly differing frequency ranges, we define an attenuation a_{λ_n} per medium wavelength $\lambda_n = \lambda/n$ for a propagation distance $z = \lambda_n$. From Eq. (10.4), and with the approximations for n and n_i given in Eq. (10.3), we find the relation

$$\frac{a_{\lambda_n}}{\mathrm{dB}} = \alpha\frac{\lambda}{n} \times 10\lg\mathrm{e} = \underbrace{2\pi \times 10\lg\mathrm{e}}_{\approx 27.3} \times \frac{2n_i}{n} \approx 27.3 \times \frac{\epsilon_{ri}}{\epsilon_r} \approx 27.3 \times \tan\delta\,. \tag{10.5}$$

Scaling the structural dimensions Instead of investigating a (possibly tiny) dielectric structure $\epsilon_r(\vec{r})$, we are interested in a version $\epsilon'_r(\vec{r})$, which is enlarged by a real scaling factor $\sigma \geq 1$. This scaling is expressed by the relation $\epsilon'_r(\vec{r}) = \epsilon_r(\vec{r}/\sigma)$. We transform Eq. (10.1) according to $\vec{r}\,' = \sigma\,\vec{r}$ and $\mathrm{curl}' = \frac{1}{\sigma}\,\mathrm{curl}$. Because $\epsilon_r(\vec{r}\,'/\sigma) = \epsilon'_r(\vec{r}\,')$ holds by definition, Eq. (10.1) and (10.2) reduces to

$$\left(\mathrm{curl}'\,\frac{1}{\epsilon'_r(\vec{r}\,')}\,\mathrm{curl}'\right)\vec{H}(\vec{r}\,'/\sigma) = \frac{\omega'^{\,2}}{c^2}\,\vec{H}(\vec{r}\,'/\sigma)\,, \qquad \omega' = \omega/\sigma\,. \tag{10.6}$$

For the enlarged structure $\epsilon'_r(\vec{r}\,')$ we find the same eigenfunctions $\vec{H}(\vec{r}\,'/\sigma)$ as in Eq. (10.1) and (10.2); we only have to scale the argument $\vec{r} = \vec{r}\,'/\sigma$ together with the associated angular eigenfrequency $\omega' = \omega/\sigma$. There is no fundamental length scale other than implied by the basic assumption of a macroscopic, non–atomistic treatment of matter as noted on Page 199.

Scaling the dielectric constant If we know the solutions for a dielectric structure $\epsilon_r(\vec{r}) = n^2(\vec{r})$, and we look for the results of a structure $\epsilon''_r(\vec{r}) = n''^{\,2}(\vec{r})$, where the refractive index is scaled *everywhere* with a real constant σ_n according to $n''(\vec{r}) = n(\vec{r})/\sigma_n$ and $\epsilon''_r(\vec{r}) = \epsilon(\vec{r})/\sigma_n^2$, we find

$$\left(\mathrm{curl}\,\frac{1}{\epsilon''_r(\vec{r})}\,\mathrm{curl}\right)\vec{H}(\vec{r}) = \frac{\omega''^{\,2}}{c^2}\,\vec{H}(\vec{r})\,, \qquad \omega'' = \sigma_n\omega\,. \tag{10.7}$$

The eigenfunctions $\vec{H}(\vec{r})$ remain unchanged, but the associated eigenfrequencies are scaled to $\omega'' = \sigma_n\omega$.

Optics and microwaves Making use of the scaling law Eq. (10.6), we see that the dimensions of optical structures operating at f_o may be scaled up by a factor of, e. g., $\sigma = 20\,000$ for a convenient microwave operating frequency near $f_m = f_o/\sigma = 10$ GHz ($\lambda_m = 30$ mm). Here, the structures are large enough to allow a virtually perfect fabrication, and the necessary high–precision microwave equipment is readily available. Provided that low–loss microwave dielectrics with similar dielectric properties are available, the microwave results can be carried over directly to structures made of silicon–on–silica, SiGe/Si, InGaAsP/InP or GaAs/GaAlAs.

Dielectric materials Table 10.1 displays some properties of common optical materials being transparent near $\lambda_o = 1.55\ \mu$m. The refractive indices range from $n = 1.444$ (fused silica glass) to $n = 4.275$ (Ge). Material losses are negligible on the scale of an optical medium wavelength λ_n. For fused silica ($a = 0.15$ dB/km) we calculate from Eq. (10.4) and (10.5) a per–wavelength attenuation of $a_{\lambda_n} = 1.6 \times 10^{-10}$ dB.

The properties of common PTFE–based microwave dielectrics are listed in Table 10.2. Refractive indices range from $n = 1.48$ (micro glass fibre–reenforced PTFE, RT/duroid 5880 or RT5880 for short) to $n = 3.13$ (ceramic–filled PTFE, TMM10i) and match well with fused silica and many semiconductors. Material losses are not negligible and range from $a_{\lambda_n} = 0.025$ dB (RT5880) up to $a_{\lambda_n} = 0.049$ dB (TMM6). Loss studies using microwave models have to take care of this fact. In [4, 22], measurement techniques for losses at microwave and terahertz frequencies are described.

There are other microwave dielectrics which could be considered, notably Al_2O_3 ceramic. With a refractive index comparable to the refractive index of TMM10, the loss for Al_2O_3 is an order of magnitude smaller than for TMM10 (see caption of Table 10.2). However, the structuring of PTFE–based organic materials can be done simply with ordinary milling machines, while machining Al_2O_3 ceramics is time consuming, and needs special tools. A low–loss material also suitable for mass production is Low Temperature Cofired Ceramic (LTCC) [24, e. g.]. Multilayer structures are fabricated by laminating single greensheets (unfired tapes; Green TapeO, DuPont), possibly with conductor lines printed on the surfaces, on top of each other. The stack is fired at a temperature of $850\ldots875°\mathrm{C}$. However, substrate sizes are limited to $89\ \mathrm{mm} \times 89\ \mathrm{mm}$ [24, http://www.ltcc.de/prototyping/protototyping.htm]. Suppliers' addresses may be found at [23]. Permittivities are $\epsilon_r = 3.9\ldots10$ for frequencies ≤ 40 GHz. To simplify fabrication, we chose PTFE-based materials.

Table 10.1: Refractive index n and extinction coefficient n_i for various optical materials transparent near an operating wavelength $\lambda_o = 1.55\ \mu\mathrm{m}$ ($f_o = 193$ THz, $hf_o = 0.801$ eV). Fused silica [7, 42]; Si [27, Vol. I, p. 566], [42]; SiGe stands for $\mathrm{Si_{0.75}Ge_{0.25}}$ [28]; InP [27, Vol. I, p. 512], [42]; InGaAsP for $\mathrm{In_{0.68}Ga_{0.32}As_{0.69}P_{0.31}}$ with bandgap energy (wavelength) $hf_G = 0.953$ eV ($\lambda_G = 1.3\ \mu\mathrm{m}$) [13], lattice–matched [1] to InP; GaAlAs for $\mathrm{Ga_{0.5}Al_{0.5}As}$ [12, estimated]; GaAs [27, Vol. I p. 439], [42]; Ge [27, Vol. I, p. 474].

	silica	Si	SiGe	InP	InGaAsP	GaAlAs	GaAs	Ge
n	1.444	3.4764	3.53	3.221	3.57	3.26	3.3737	4.275
n_i	0.000	0.000		0.000			0.000	0.00567

Table 10.2: Refractive index n, relative permittivity ϵ_r, permittivity tolerance $\pm\Delta\epsilon_r$, and material loss (complex permittivity $\bar{\epsilon}_r = \epsilon_r - \mathrm{j}\,\epsilon_{ri}$, loss factor $\tan\delta = \epsilon_{ri}/\epsilon_r$, extinction coefficient n_i, loss a_{λ_n} in dB per medium wavelength $\lambda_n = \lambda_m/n$) for various microwave sheet materials transparent near an operating frequency $f_m = 10$ GHz ($\lambda_m = 30$ mm). The data displayed are for micro glass fibre-reenforced PTFE (polytetrafluoroethylene or Teflon, RT/duroid 5880 or RT5880 for short), and for PTFE filled with ceramic powder (TMMx and RT6002) [25]. As a reference, Al_2O_3 (99 %) ceramic is specified with $n = 3.15$, $\epsilon_r = 9.90$, $\tan\delta = 0.0002$, $n_i = 0.0003$, and $a_{\lambda_n} = 0.0055$ dB.

	RT5880	TMM10	RT6002	TMM3	TMM4	TMM6	TMM10i
n	1.48	3.03	1.71	1.81	2.12	2.45	3.13
ϵ_r	2.20	9.20	2.94	3.27	4.50	6.00	9.80
$\pm\Delta\epsilon_r$	0.02	0.23	0.04	0.02	0.05	0.08	0.25
$\tan\delta$	0.0009	0.0017	0.0012	0.0016	0.0017	0.0018	0.0015
n_i	0.0001	0.0026	0.0010	0.0014	0.0018	0.0022	0.0023
$\frac{a_{\lambda_n}}{\mathrm{dB}}$	0.025	0.046	0.033	0.044	0.046	0.049	0.041

10.1.2 Numerical tools

Whenever the problem size allowed, we compared our measured results with the outcome of numerical simulators operating either in the time domain or in the frequency domain.

Time domain: Finite differences The method of Finite Differences in the Time Domain (FDTD) [35, 38] directly integrates Maxwell's first–order differential equations $\mathrm{curl}\,\vec{H} = \epsilon_0\epsilon_r\,\mathrm{d}\vec{E}/\,\mathrm{d}t$ and $\mathrm{curl}\,\vec{E} = -\mu_0\,\mathrm{d}\vec{H}/\,\mathrm{d}t$ via central differences in time and space. A computationally efficient implementation of this principle dates back to the publication of Yee's algorithm [41], where a new grid staggered in time and space was introduced. Practically, a three–dimensional (3D) FDTD solver for real–world problems requires both large storage (e. g., ≥ 1.5 GB because of the fixed grid size) and long computation time (e. g., ≥ 48 h). We use a commercially available 3D FDTD package [32, FullWAVE] with a computer–aided design interface. Further, we run a 3D Interpolet Collocation Time Domain (ICTD) code [8–10], for which field details can be resolved better by choosing an appropriate spatial wavelet basis. This code has been ported to a massively–parallel computer available at the Computing Centre of the University of Karlsruhe. The system has 256 CPU and 1 GB RAM per CPU. There are 112 nodes having 2 CPU each, and 4 main nodes with 8 CPU each.

FDTD can be used to calculate band diagrams of PBG structures by searching for resonances in the Fourier–transformed impulse response of the system. However, for many problems, a plane–wave eigenmode solver is numerically more efficient [6, 19] [32, BandSOLVE].

Frequency domain: Finite elements The Finite Elements (FE) method solves Maxwell's equations most commonly in the frequency domain [17, 36]. The structure and its surrounding space is discretized by a number of contiguous tetrahedra elements, and the field equations in and on the surface of each elementary tetrahedron are found in terms of unknown coefficients, defined on the nodes using either simple linear or also higher order functions. We employ a commercially available 3D FE High Frequency Structure Simulator (HFSS) in the frequency domain [3]. It provides a graphical interface for the structural design, a field solving engine with adaptive solution facilities, and a powerful post–processor for evaluating results and displaying fields. Again, the solution process is time consuming, but — because of the adaptive choice of the element size — less demanding in computer memory than the FDTD method. Frequency-domain FE techniques are not optimally suited for simulating large nonlinear problems.

With the HFSS package [3], eigenmodes may be computed and scattering parameters (Eq. (10.9) on Page 203) determined, and it analyses PBG structures [31].

10.2 Microwave measurements

10.2.1 Scattering matrix

Any linear single–mode waveguide can be described equivalently by a general linear 2–port network; m–mode propagation would require a $(2m)$–port equivalent network. Incoming and outgoing monochromatic electromagnetic waves with frequency f are represented by

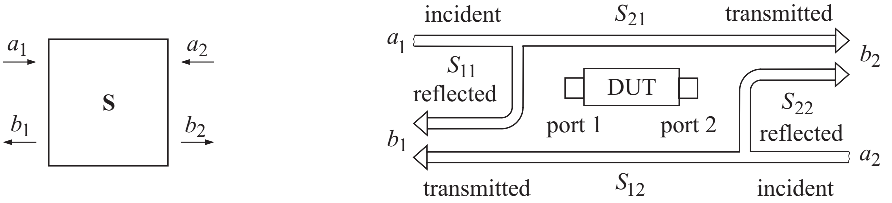

(a) Incoming and outgoing wave amplitudes $\vec{a} = (a_1, a_2)^T$ and $\vec{b} = (b_1, b_2)^T$

(b) Signal path representation of scattering matrix $\mathcal{S}$ and physical meaning of its scattering parameters S_{ij} for a device under test (DUT)

Figure 10.1: Scattering matrix $\mathcal{S}$ and wave amplitudes. (a) general scattering matrix (b) signal paths.

scalar complex wave amplitudes, which in the reference plane of port i are denoted by a_i for the incoming and by b_i for the outgoing waves, see Fig. 10.1(a). These quantities are defined with respect to the impedance Z_i of the transmission line, which connects port i to the measurement equipment. The powers associated with the wave amplitudes are $P_{a_i} = \frac{1}{2}|a_i|^2$ and $P_{b_i} = \frac{1}{2}|b_i|^2$. The incoming and outgoing wave amplitudes at both ports are elements of column matrices $\vec{a} = (a_1, a_2)^T$ and $\vec{b} = (b_1, b_2)^T$, which are related via the so–called scattering matrix $\mathcal{S}$ [5, 26]. This matrix has complex elements S_{ij} $(i, j = 1, 2)$ and refers to a given configuration of reference wave impedances Z_i,

$$\begin{pmatrix} b_1 \\ b_2 \end{pmatrix} = \begin{pmatrix} S_{11} & S_{12} \\ S_{21} & S_{22} \end{pmatrix} \begin{pmatrix} a_1 \\ a_2 \end{pmatrix}, \quad \vec{b} = (b_1, b_2)^T, \quad \vec{a} = (a_1, a_2)^T, \quad \vec{b} = \mathcal{S}\,\vec{a}. \tag{10.8}$$

10.2.2 Microwave equipment

Scattering parameters S_{ij} of a Device Under Test (DUT) are measured with a Vector Network Analyser (VNA [40, Chapter 8], [2]). In principle, this instrument performs a microwave interference experiment to register amplitudes and phases of the relevant complex phasors ("vectors") $a_{1,2}$ and $b_{1,2}$ in Fig. 10.1(b). At any given microwave frequency f, the complex forward and reverse reflection and transmission coefficients S_{11} (input match), S_{22} (output match) and S_{21} (transmission), S_{12} (isolation), respectively, are measured according to the definitions

$$S_{11} = \left.\frac{b_1}{a_1}\right|_{a_2=0}, \quad S_{22} = \left.\frac{b_2}{a_2}\right|_{a_1=0}, \quad S_{21} = \left.\frac{b_2}{a_1}\right|_{a_2=0}, \quad S_{12} = \left.\frac{b_1}{a_2}\right|_{a_1=0}. \tag{10.9}$$

The notion "forward" and "reverse" refers to a source connected to input port 1 or to output port 2, respectively. It is common to specify the modulus of S_{ij} on a decibel scale, where $|S_{ij}|_{\mathrm{dB}} := 20\lg|S_{ij}|\mathrm{dB}$. For a simplified notation we drop the subscript dB. Then, whenever $|S_{ij}| = x$ dB is specified, it has to be read as $x\ \mathrm{dB} = 20\lg|S_{ij}|\mathrm{dB}$, i. e., $|S_{ij}| = 10^{x/20}$.

Experimentally, incoming and outgoing waves a_i and b_i at both ports are separated with directional couplers. Directional couplers and loads ("absorbers") are VNA–inbuilt standard components matched to a real line impedance of usually $Z_{1,2} = Z_L = 50\ \Omega$. However, to establish, e. g., a zero–input condition $a_2 = 0$ at port 2 with the source connected to port 1 of the DUT, port 2 should be impedance–matched with an appropriate complex load. Generally, this is not possible. Load/source mismatches as well as any other systematic VNA errors like reflection/transmission frequency response, coupler directivity, and crosstalk are represented by 12 complex error terms [40, Sect. 8.2.3.3, Fig. 8.28], [2], which may be measured by connecting a known (i. e., factory–calibrated) short, open, load and "thru" (direct through-connection of VNA ports at output and input of DUT) to the VNA reference planes. This is known as SOLT calibration. A calibrated transmission line and other calibrated reflection standards may be employed instead of short, open and load. This thru–reflect–line (TRL) calibration is used for non–coaxial equipment. With this data, a full "vectorial" error correction can be performed numerically.

10.2.3 Coupling of coaxial metallic to dielectric strip waveguide

Our dielectric strip waveguides are made of ceramic–filled PTFE sheets (TMM10), and fixed on inexpensive bulk PTFE as a substrate (see Table 10.2 on Page 201). The strip has a rectangular cross–section with a width of $w = 11$ mm in the plane of the substrate along the x–direction, and a height of $h = 8.1$ mm perpendicular to the substrate along the y–direction, Fig. 10.2(a). For an angular frequency ω, the waveguide eigenmodes propagate with a propagation constant $\beta(\omega)$ (effective index n_{eff}) according to

$$\exp\left[\mathrm{j}\left(\omega t - \beta(\omega) z\right)\right], \qquad n_{\text{eff}} = \beta / k_0\,, \qquad k_0 = \omega / c\,. \tag{10.10}$$

The intensity schematic for the mode classification is illustrated in Fig. 10.2(b). All modes are hybrid having longitudinal components along the propagation direction $\vec{e}_z$ for both the electric and the magnetic fields, so that the naming of modes is somewhat arbitrary.

However, for a symmetric two–dimensional (2D) slab waveguide with $w \to \infty$, the fundamental mode with $\vec{E}$ parallel to the slab interfaces is a truly transverse–electric TE or H_0–

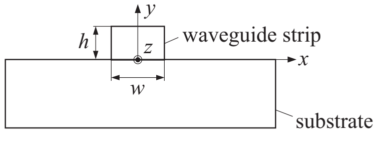

(a) Dielectric strip and coordinate system

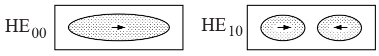

(b) Schematic strip mode contour plots

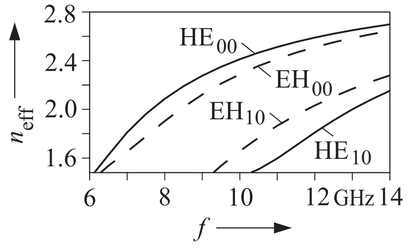

(c) Dispersion of effective index n_{eff}

Figure 10.2: High–index dielectric strip waveguide (made of a TMM10 sheet, $n = 3.03$, $w = 11\,\text{mm}$, $h = 8.1\,\text{mm}$) on a low–index substrate (PTFE, $n = 1.48$) (a) layout and coordinate system (b) schematic contour plots of transverse electric fields in xy–plane: HE_{00} (quasi–TE, fundamental mode), orthogonally polarized EH_{00}–mode (quasi–TM, not drawn, intensity schematic as HE_{00}), and higher–order EH_{10} and HE_{10}–modes (c) dispersion diagram of waveguide mode $\sim \exp\left[\mathrm{j}\left(\omega t - \beta z\right)\right]$ with propagation constant β and effective modal refractive index $n_{\text{eff}} = \beta / k_0$, $k_0 = \omega / c$ (computed with [3, HFSS]).

mode, having a longitudinal z–component for the magnetic field only. Therefore, we also keep to this notation for the case of our three–dimensional (3D) strip waveguide, the fundamental mode of which also has its dominant $\vec{E}$–component parallel to the substrate along the x–axis. So the fundamental strip field is named a HE_{00}–mode, and also referred to as a quasi–TE mode. For the sake of simplicity, we drop the specification “quasi–” in the following text.

The EH_{00}–mode is mainly orthogonally polarised with an electric field pointing along the y–axis; in our notation, this is called a (quasi–)TM mode. Both modes have a similar intensity schematic. The dispersion diagram for various modes has been calculated semi–analytically with an effective refractive index method [37], and it agrees well with a mode calculation using a semi–vectorial beam–propagation [32, BeamPROP] or a finite–element method [3, HFSS]; FE has actually been employed for the graphs shown in Fig. 10.2(c) . The modal cutoff frequency is defined at a frequency where the wave essentially propagates in the substrate so that $n_{\text{eff}} = 1.48$. Provided that the feeding arrangement does excite the TE mode HE_{00} only, the single–mode regime extends from about $6.2\ \mathrm{GHz}$ to $10.5\ \mathrm{GHz}$. For TM excitation, the waveguide is single–moded in a frequency range of about $6.3\ \mathrm{GHz}$ to $9.3\ \mathrm{GHz}$.

The arrangement for coupling to a coaxial metallic waveguide is shown as an exploded view in Figure 10.3(a). It consists of a microstrip slot antenna (Fig. 10.3(b) top left), a dielectric waveguide taper (Fig. 10.3(b) bottom left), and the dielectric waveguide itself. The slot antenna has high polarisation purity. The dominant electric field component is oriented alongside the smaller edges of the slot, so that the configuration Fig. 10.3 excites the fundamental TE–mode HE_{00}. The cross–polarised TM–mode EH_{00} is attenuated by more than $20\ \mathrm{dB}$.

From left to right in Fig. 10.3(a), the antenna consists of a metallic reflector plate preventing backward radiation, a spacer made of dielectric foam material with a thickness of $7.5\ \mathrm{mm}$, the standard microstrip substrate TMM 4 with a thickness of $0.79\ \mathrm{mm}$ carrying the $50\ \Omega$ metallic microstrip on its left–hand side, and the metallic ground plane on the right–hand

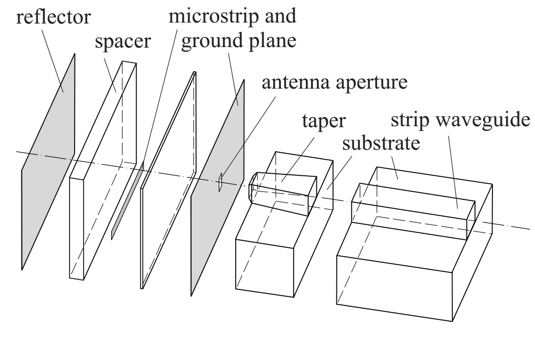

(a) Coaxial–to–dielectric waveguide connector, exploded view

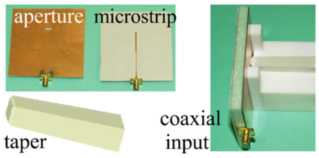

(b) Antenna, taper, mounted device

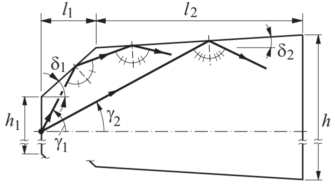

(c) Taper in plane $x = 0$

Figure 10.3: Coaxial feeder for dielectric strip waveguide with microstrip feeder, slot antenna and two–section waveguide taper (a) exploded view of TE feeder; metallic sheets shaded in grey (b) microstrip slot antenna, two–section taper, and mounted connector in TE configuration (conter–clockwise, from top left) (c) schematic of two–section taper.

side with the etched slot, Fig. 10.3(b) (top left). The whole structure has been developed with Ansoft HFFS [3] following state–of–the–art design rules [6, 30].

In all practical respects, the slot antenna realizes a point source radiating in a large aperture, which exceeds the numerical aperture of the waveguide Fig. 10.2(a). For a better coupling efficiency, we designed a two–section strip waveguide taper made of TMM10 ($n = 3.03$). The taper cross–section in the plane $x = 0$ is depicted in Fig. 10.3(c) with taper angles $\delta_{1,2}$ and section lengths $l_{1,2}$. The front height and width of the taper is $h_1 = 4.1$ mm and $w_1 = 5.5$ mm, respectively, and it ends with the standard waveguide dimensions $h = 8.1$ mm, $w = 11$ mm as in Fig. 10.2.

In a first approximation, we assume that homogeneous plane waves emerge from the center of the aperture slot into all directions, but regard only the associated rays parallel to the planes $x = 0$ and $y = h/2$. For $\delta_{1,2} = 0$, the largest limiting angle of total internal reflection (TIR) as measured from the z–axis is denoted as γ_T. The largest (smallest) refractive index ratio $1/3.03$ for an air/strip interface ($1.48/3.03$ for a substrate/strip interface) is $\gamma_T = \arccos(1/3.03) = 71^\circ$ ($\gamma_T = \arccos(1.48/3.03) = 61^\circ$).

In the plane $x = 0$ we choose a primary section angle $\delta_1 = 45^\circ$, so that inside this section $\gamma_1 < \gamma_T + \delta_1$ holds. For maintaining TIR throughout both taper sections, the primary–section length l_1 should be related to the maximum possible radiation angle $\gamma_{2\,\max}$ in the second-section taper by $(h - h_1)/2 \geq l_1|_{\delta_1 = 45^\circ} = (h_1/2)/(\tan\gamma_{2\,\max} - 1)$, where $\gamma_{2\,\max} \leq \gamma_T + \delta_2$ is necessary for TIR. With the substitutions $h, h_1 \rightarrow w, w_1$, an analogous expression holds for the plane $y = h/2$.

For a smooth taper transition, we require $l_2 = 56 \text{ mm} \approx 4\lambda_n$ to be of the order of four medium wavelengths, and we fix $l_1 = 1$ mm, $\delta_2 = 1^\circ$. For this design, we end up with $\gamma_{2\,\max} = \arctan[1 + h_1/(2l_1)] = 71.8^\circ$. Therefore, at the air/strip interface with $\gamma_T + \delta_2 = 72^\circ \geq \gamma_{2\,\max}$, TIR is maintained throughout the taper sections, while for the substrate/strip interface with $\gamma_T + \delta_2 = 62^\circ$, waves in the angle range $62^\circ < \gamma_2 < 72^\circ$ give rise to some radiation loss into the substrate. For the cross–section $y = h/2$, we have $\gamma_{2\,\max} = \arctan[1 + w_1/(2l_1)] = 75^\circ$, and radiation losses at the air/strip interface result for a narrow angle range $72^\circ < \gamma_2 < 75^\circ$.

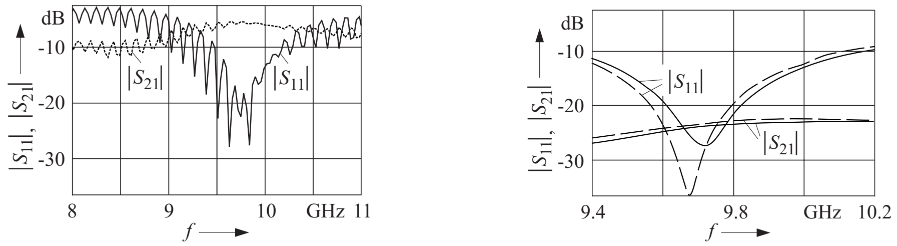

(a) Input match $|S_{11}|$ and transmission $|S_{21}|$. Well-matched $|S_{11}| \leq -14$ dB for $f = 9.6 \ldots 10$ GHz

(b) $|S_{11}|$ and $|S_{21}|$ for strip waveguides with lengths $L_R = 191$ mm (——) and $L'_R = 91$ mm (– – –)

Figure 10.4: TE excitation of an arrangement with two identical coaxial-to-strip waveguide transitions (see Fig. 10.3(a)) connected through TMM10 strip waveguides (see Fig. 10.2(a)) with differing lengths L_R, L'_R (a) $L_R = 191$ mm. Ripple structure due to Fabry–Perot resonances (b) $L'_R = 91$ mm. Fabry–Perot resonances suppressed by damping material attached to the tops of both tapers.

For an arrangement of coaxial connector, slot antenna and waveguide taper on each side of an intermediate $L_R = 191$ mm–long TMM10 strip waveguide (Fig. 10.2(a)) we measured the quantities input match $|S_{11}|$ and forward transmission $|S_{21}|$, both of which exhibit a frequency ripple typical for a Fabry–Perot waveguide transmission line resonator. For the design frequency range $f = 9.6 \ldots 10$ GHz, a well–matched input reflection factor of $|S_{11}| \leq -14$ dB is to be seen, Fig. 10.4(a).

The Fabry–Perot ripple can be suppressed by attaching damping material on the tops of both tapers, see Fig. 10.4(b) (——). For such a setup, we compared the transmission to that of a shorter intermediate strip waveguide having a length of $L'_R = 91$ mm. A waveguide loss of $a = (0.43 \pm 0.08)$ dB/100 mm resulted at a frequency of $f_m = 9.7$ GHz ($\lambda_m = 31$ mm). Because the guide wavelength is $\lambda_n = \lambda_m / n_{\text{eff}} = 12.9$ mm for $n_{\text{eff}} = 2.4$ from Fig. 10.2(c), the attenuation per wavelength amounts to $a_{\lambda_n} = (0.055 \pm 0.01)$ dB. This measured loss agrees well with the bulk material loss $a_{\lambda_n} = 0.046$ dB specified for TMM10 in Table 10.2.

By directly evaluating the ripple contrast, i. e., the ratio of minima and neigbouring maxima in Fig. 10.4(a), the propagation loss may be inferred for a single waveguide section.

10.3 Loss measurement of waveguide resonator

Loss measurements in PhC are complicated, because usually the couplings to and from the PhC waveguides are difficult to determine. In the following, we describe a technique which overcomes this deficiency. The basic assumption must be emphasized, namely that the waveguides are single–moded (described by 2–port networks only). Usually, this is not considered in reports on measurements [39, 43]. The implicit assumption is that the possibly multimoded guiding PhC structure is connected to single–mode waveguides, and that all inevitable mode conversion losses add to the intrinsic PhC guide loss. However, it should also be possible to extend the method to multimoded waveguides ($2n$–port networks). The main problem to be solved is to formulate the unavoidable mode couplings [15].

From the power transmission characteristics of a Fabry–Perot (FP) resonator, its optical properties may be determined. This classical technique, named the Hakki–Paoli method (HKM) [14] after its inventors, has been used widely to investigate not only semiconductor lasers, but also simple straight photonic crystal waveguides.

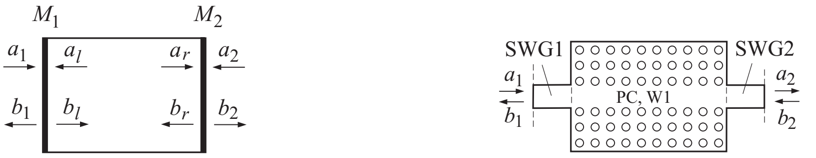

(a) FP resonator. Length L_R, mirrors $M_{1,2}$. Internal wave amplitudes a_l, b_l and a_r, b_r at left and right mirror. External wave amplitudes as in Fig. 10.1(a)

(b) $W1$ waveguide in a photonic crystal of length L_P with two connected single-mode strip waveguides SWG1, 2

Figure 10.5: Fabry–Perot resonance method [14] (a) wave amplitudes of Fabry–Perot resonator (b) wave amplitudes of PhC with single–row ($W1$) line–defect connected to single–mode strip waveguides.

In the following, the HKM principle is explained. An extension of this technique can also be applied to a sequence of mismatched single–moded transmission lines, which are treated as equivalent coupled FP resonators. These transmission lines may represent single–moded photonic crystal waveguides, conventional strip waveguides, bends, and crossings.

Transmission line resonator The model waveguide resonator under investigation consists of a lossy single–moded waveguide medium with length L_R having a power loss coefficient $\alpha(\omega)$, an effective propagation constant $\beta(\omega)$, a wave impedance Z_L and a scattering matrix $\mathcal{S}_R$. This resonator medium is sandwiched between two identical, partially transmitting, possibly lossy mirrors M_i $(i = 1, 2)$ as shown in Fig. 10.5(a). These mirrors could represent, e. g., the coaxial–to–strip waveguide transitions of Fig. 10.3. In this case, the wave amplitudes $a_{1,2}$, $b_{1,2}$ are measured in a coaxial transmission line system with a wave impedance of $Z_L = 50\,\Omega$, while the wave amplitudes $a_{r,l}$, $b_{r,l}$ are measured with reference to the fundamental-mode wave impedance of the strip waveguide taper end. The non–unitary mirror scattering matrices $\mathcal{S}^{(i)}$ and the resonator matrix $\mathcal{S}_R$ read

$$\mathcal{S}^{(1)} = \begin{pmatrix} M_{11} & M_{12} \\ M_{21} & M_{22} \end{pmatrix}, \quad \mathcal{S}_R = \mathrm{e}^{-(\alpha/2+\mathrm{j}\beta)L_R} \begin{pmatrix} 0 & 1 \\ 1 & 0 \end{pmatrix}, \quad \mathcal{S}^{(2)} = \begin{pmatrix} M_{22} & M_{21} \\ M_{12} & M_{11} \end{pmatrix}. \tag{10.11}$$

Using these relations, we can eliminate [21, 21, Sect. 3.4 C6 pp. 393 ff.] the wave amplitudes a_l, b_l and a_r, b_r to the left and the right–hand side of the resonator medium, Fig. 10.5(a). By doing so, we obtain for the Fabry–Perot resonator Fig. 10.5(a), a scattering matrix $\mathcal{S}$ with elements S_{ij}, which connect the input and output wave amplitudes a_1, b_1 and a_2, b_2 at the reference planes located to the left of M_1 and to the right of M_2, respectively. The relative power transmitted through the Fabry–Perot resonator in Fig. 10.5(a) for $a_1 \neq 0$, $a_2 = 0$ is $T = |S_{21}|^2$,

$$\begin{aligned} T = |S_{21}|^2 &= \left.\frac{|b_2|^2}{|a_1|^2}\right|_{a_2=0} \\ &= \frac{|M_{12}M_{21}|^2\,\mathrm{e}^{-\alpha L_R}}{1 + |M_{22}^2|^2\,\mathrm{e}^{-2\alpha L_R} - 2\,\mathrm{e}^{-\alpha L_R}\,\mathrm{Re}\left\{M_{22}^2\,\mathrm{e}^{-\mathrm{j}\,2\beta L_R}\right\}}\,. \end{aligned} \tag{10.12}$$

As an example, we choose the reflection $M_{11} = M_{22} = -|r|$ and transmission factors $M_{12} = M_{21} = \mathrm{j}\,|t|$ of an ideal lossless mirror, where the power conservation law $|r|^2 + |t|^2 = 1$ holds. Then, the matrices $\mathcal{S}^{(i)}$ are unitary, $(\mathcal{S}^{(i)})^{\dagger}\,\mathcal{S}^{(i)} = \mathbf{I}$, meaning $|M_{11}|^2 + |M_{21}|^2 = 1$, $|M_{12}|^2 + |M_{22}|^2 = 1$, $M_{11}M_{12}^* + M_{22}^*M_{21} = 0$, and Eq. (10.12) reduces to

$$T = |S_{21}|^2 = \left.\frac{|b_2|^2}{|a_1|^2}\right|_{a_2=0} = \frac{|t|^4\,\mathrm{e}^{-\alpha L_R}}{1 + |r|^4\,\mathrm{e}^{-2\alpha L_R} - 2|r|^2\,\mathrm{e}^{-\alpha L_R}\cos(2\beta L_R)}\,. \tag{10.13}$$

When plotting the power transmission $T = T(\omega)$, we obtain a fringe pattern due to the cosine-expression in the denominator of Eq. (10.13), where $\beta = \beta(\omega) = n_{\text{eff}}k_0$, see Fig. 10.2(a). A maximum occurs for $\cos(2\beta L_R) = 1$, whereas T becomes minimum for $\cos(2\beta L_R) = -1$. The envelopes of the maxima and minima, and their ratio u are

$$T_{\text{max, min}} = \frac{|t|^4\,\mathrm{e}^{-\alpha L_R}}{(1 \mp |r|^2\,\mathrm{e}^{-\alpha L_R})^2}\,, \qquad u = \frac{T_{\text{max}}}{T_{\text{min}}} = \left(\frac{1 + |r|^2\,\mathrm{e}^{-\alpha L_R}}{1 - |r|^2\,\mathrm{e}^{-\alpha L_R}}\right)^2\,. \tag{10.14}$$

From the measured ratio $u(\omega)$ of neigbouring $T_{\text{max, min}}(\omega)$ at various angular frequencies ω, we find the power loss coefficient $\alpha(\omega)$ via the relation

$$\alpha(\omega)L_R = \ln\left(\frac{\sqrt{u(\omega)}+1}{\sqrt{u(\omega)}-1}\right) + \ln|r|^2. \tag{10.15}$$

The parameters M_{22} and $M_{12}M_{21}$ required in Eq. (10.12) ($M_{12}M_{21}$ needed only in product form) may be measured using a single transition $\mathcal{S}^{(1)}$ (Eq. (10.11)) together with a back–to–back connection of two identical coaxial-to-strip waveguide transitions having a total scattering matrix

$$\mathcal{S}^{(12)} = \frac{1}{1-M_{22}^2}\begin{pmatrix} M_{11}-M_{22}\Delta & M_{12}M_{21} \\ M_{12}M_{21} & M_{11}-M_{22}\Delta \end{pmatrix}, \quad \Delta = M_{11}M_{22} - M_{12}M_{21}. \tag{10.16}$$

We refer to the notation of Fig. 10.1 and Eq. (10.8). When connecting a matched load ($a_2 = 0$) at the coaxial output port 2 of the back–to–back connection, we measure the transmission $S_{21}^{(12)} = b_2/a_1|_{a_2=0}^{(12)} = M_{12}M_{21}/(1-M_{22}^2)$ between the coaxial ports 1 and 2. In addition, we measure for a single transition $\mathcal{S}^{(1)}$ (Eq. (10.11)) the coaxial input reflection factors when connecting a *s*hort ($S_s^{(1)} = b_1/a_1|_{a_2=-b_2}^{(1)} = M_{11} - M_{12}M_{21}/(1+M_{22})$) and a matched load ($S_l^{(1)} = b_1/a_1|_{a_2=0}^{(1)} = M_{11}$) to the strip waveguide. A short may be established by putting an electric wall (i. e., a metallic sheet) flush against the open waveguide end, thereby also defining a strip–waveguide reference plane. The matched load can be realized by placing absorptive pads on the top of the strip waveguide. Thus, from the resulting three complex equations, we can compute the unknown complex parameters $M_{22} = 1 - (S_l^{(1)} - S_s^{(1)})/S_{21}^{(12)}$ and $M_{12}M_{21} = (1-M_{22}^2)S_{21}^{(12)}$ for each ω. With additional, but redundant measurements we can check the consistency of the data.

PhC resonator with lossy interface When measuring loss in PhC waveguides, the waveguide resonator model described above has to be modified. Usually, a PhC waveguide is accessed via single–moded sections of strip waveguides (SWG) as illustrated in Fig. 10.5(b). Even if it could be arranged that the transitions between the strips and the PhC waveguides are virtually free of reflections into the SWG fundamental mode, the fundamental mode in the strips does not match the fundamental $W1$ waveguide mode, which scatters the field into radiation modes at the SWG–PhC transitions. Thus, an additional real amplitude transmission factor $s < 1$ is introduced to describe each strip–PhC waveguide transition in a first approximation [39]. The quantity s may be measured along with α by observing the transmission loss when varying the PhC length L_P.

10.4 Experimental results

A few experimental results serve to illustrate our measurement technique. First, we report on transmission measurements for 2D–periodic bulk photonic crystals, second, we give results on transmission loss measurements for a $W2$ line–defect PhC slab waveguide.

10.4.1 2D infinite–height PhC

Figure 10.6(a) shows the 2D structure under investigation. Ideally, it is infinitely extended. Technically, it consists of a dielectric block with dimensions $100\ \mathrm{mm} \times 100\ \mathrm{mm} \times 100\ \mathrm{mm}$ made of TMM10 ($\epsilon_r = 9.2$), see Table 10.2 on Page 201. The PhC was formed by drilling cylindrical air holes ($\epsilon_{r,h} = 1$, radius $r = 2.1\ \mathrm{mm}$) arranged in a triangular lattice with a lattice constant $a = 7.1\ \mathrm{mm}$ ($r/a = 0.30$). This leads to an air filling factor of $f_\triangle = (2\pi/\sqrt{3}\,)(r/a)^2 = 0.32$ and to an estimate of the average refractive index $n_{\text{av}} = [f_\triangle \epsilon_{r,h} + (1 - f_\triangle)\,\epsilon_r]^{1/2} = 2.56$. For a more accurate average index determination, the polarisation of the wave and the depolarisation of the cylinders has to be taken care of [20, Maxwell-Garnet result Eq. (10)]. With $n_{\text{av}} = 2.56$, the equivalent medium wavelength is $\lambda_{\text{av}} = 11.7\ \mathrm{mm}$ for $f_m = 10$ GHz.

We computed the photonic bandgap structure with tools based on the plane wave expansion method [29], [18, pp. 261–264] [32, BandSOLVE] [19], see Sect. 10.1.2 on Page 202. The result is seen in Fig. 10.7(a) for TE polarisation, and in Fig. 10.7(b) for TM polarisation. If a TE wave is launched in either of the Γ–M directions indicated in Fig. 10.6(a), we expect a low transmission inside the stopband $8.95 < f_{G\,\text{TE}} < 13.2$ GHz. A TM wave sees a stopband for $8.72 < f_{G\,\text{TM}} < 10.1$ GHz.

The transmission was measured with the setup depicted in Fig. 10.6(b). Sending and receiving antennas are broadband horns with a usable frequency range 1.5 . . . 20 GHz. The PhC and the receiving antenna were covered with absorption material such that the resulting tube narrowed the receiving aperture angle to about 4°. The result is seen in Fig. 10.8(a) for TE polarisation, and in Fig. 10.8(b) for TM polarisation. For TE excitation in any of the equivalent Γ–M(1,2) directions of Fig. 10.6(a), the measured stopbands agree reasonably well with the numerical calculations. However, for TM polarisation, we observe differences, which we attribute to the different "termination" of the PhC at its various surfaces. If we launch a wave into the Γ–M(2) direction, the transmission is low for 8.72 GHz $\leq f \leq 10.1$ GHz as predicted by the band diagram Fig. 10.7(b). In the Γ–M(1) direction, the transmission is also reduced beyond 10.4 GHz, and this cannot be understood from the band diagram Fig. 10.7(b), which was calculated for an infinitely extended structure excluding surface effects.

10.4.2 2D finite–height PhC with line–defect waveguide

Figure 10.9(a) displays a 2D slab with a triangular arrangement of cylindrical air holes as in Fig. 10.6(a). The structure is similar to the schematic Fig. 10.5(b) on Page 207. Two missing rows of holes form a $W2$ line–defect (LD) waveguide. The PBG concentrates the field laterally in the plane of the slab, while total internal reflection provides guiding in the vertical direction, parallel to the axes of the air cylinders. By a proper arrangement of the coaxial–to–strip waveguide transitions, we excite the two lowest-order TE modes (HE_{00} and HE_{10}). The taper endfaces were directly connected to the $W2$ LD waveguide (length L_P). The external single–mode strip waveguides were dimensioned such that the strip–LD waveguide transition loss was only 0.8 dB. We compared the transmission $|S_{21}|$ of two $W2$ LD waveguides with a length of $L_P = 191\ \mathrm{mm}$ and $L'_P = 91\ \mathrm{mm}$.

According to Fig. 10.9(b), the resulting mean transmission loss between 10.3 GHz and 12.7 GHz amounts to $2.5\ \mathrm{dB}/100\ \mathrm{mm}$. With an estimated effective modal index of $n_{\text{eff}} = 2.7$

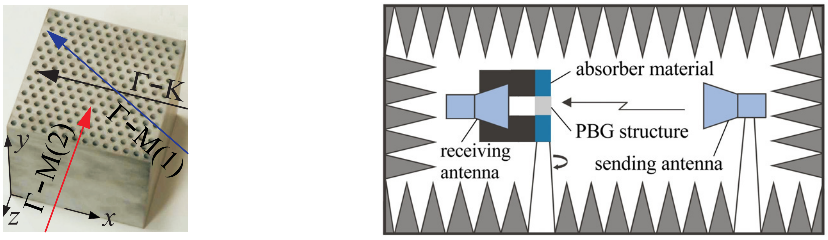

(a) 2D–periodic PC and irradiation directions

(b) Anechoic chamber with sending antenna and turntable mounted receiving antenna

Figure 10.6: Technical realization and measurement setup for a 2D PhC (a) TMM10 material with $\epsilon_r = 9.2$ and dimensions $100 \text{ mm} \times 100 \text{ mm} \times 100 \text{ mm}$, triangular lattice of cylindrical air holes drilled along the y-axis ($\epsilon_{r,h} = 1$, radius $r = 2.1$ mm), lattice constant $a = 7.1$ mm ($r/a = 0.30$), air filling factor $f_\triangle = 0.32$ (b) measurement set–up with absorber material forming a tube for narrowing the receiving aperture angle to 4°.

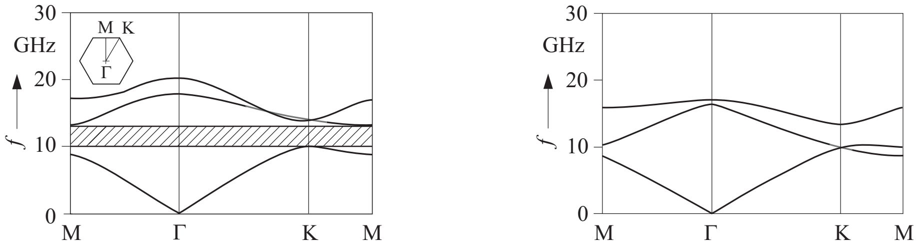

(a) Computed TE band diagram

(b) Computed TM band diagram

Figure 10.7: Computed band diagrams of a 2D PhC for (a) TE polarisation and (b) TM polarisation. Triangular lattice of cylindrical air holes as in Fig. 10.6(a) ($\epsilon_{r,h} = 1$, radius $r = 2.1$ mm), lattice constant $a = 7.1$ mm ($r/a = 0.30$), air filling factor $f_\triangle = 0.32$. Inset (a) shows arrangement of reciprocal lattice and directions.

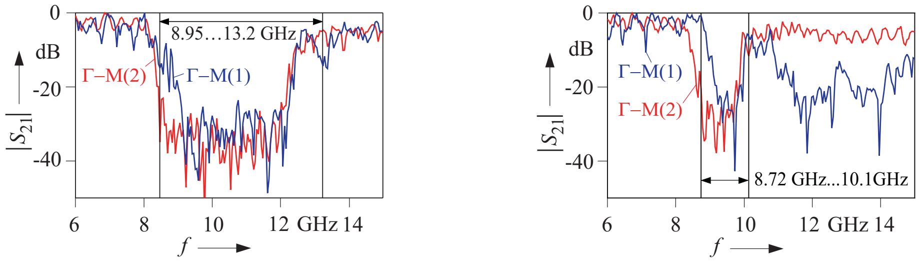

(a) TE excitation in Γ–M(1,2)–directions

(b) TM excitation in Γ–M(1,2)–directions

Figure 10.8: Transmission $|S_{21}|$ in Γ–M directions as indicated in Fig. 10.6(a), measured with setup Fig. 10.6(b) and normalized to transmission when PhC is replaced by air (a) TE excitation, Γ–M(1,2) data essentially identical (b) TM excitation, Γ–M(1,2) data significantly different.

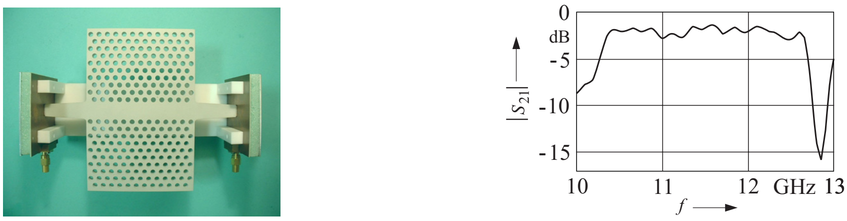

(a) TE–excited 2D–PC slab with short $W2$ LD (b) TE transmission of 100 mm long $W2$ LD PC slab

Figure 10.9: 2D suspended PhC slab with a height of $h = 8.1$ mm and a lattice as described in Fig. 10.6. Two missing rows of air holes form a $W2$ line defect (LD) waveguide (a) arrangement with single–mode strip waveguides, TE excitation and TE detection (b) TE transmission $|S_{21}|$ for a PhC LD waveguide length of $L_P - L'_P = 100$ mm by comparing the transmission of a long and a short PhC LD guide with lengths $L_P = 191$ mm and $L'_P = 91$ mm.

at 11 GHz, the LD guide wavelength is about $\lambda_n = 27 \text{ mm}/2.7 = 10 \text{ mm}$, so that an attenuation per wavelength of $a_{\lambda_n} = 0.25$ dB is measured. The material loss per wavelength amounts to $a_{\lambda_n} = 0.046$ dB according to Table 10.1 on Page 201, a specification which was confirmed by measurements described on Page 207.

For a similarly structured InGaAlAs PhC layer with a $W3$ LD waveguide on an InP substrate, a loss of $21\,\text{dB/mm}$ was measured [43]. An estimated effective modal index of $n_{\text{eff}} = 3.2$ and a vacuum wavelength $\lambda_o = 1.55\ \mu\text{m}$ lead to a LD guide wavelength of about $\lambda_n = 1.55\ \mu\text{m}/3.2 = 0.5\ \mu\text{m}$, and the attenuation per wavelength becomes $a_{\lambda_n} = 0.01$ dB.

It was observed that the loss decreases sharply when the lateral waveguiding region becomes wider [43]; attenuations of $21, 4, 1.6$ dB/mm were measured for $W3, 5, 7$ LD optical waveguides. Further, the symmetry of a $W2$ LD guided field differs from a $W3$ LD waveguide mode, and this could also contribute to the observed differences. Outside the about 3 GHz wide full–bandgap range $10 \text{ GHz} \leq f \leq 13.2 \text{ GHz}$ (hatched region in Fig. 10.7(a)), the PhC allows wave propagation for TE polarisation, so that the wave confinement decreases and the transmission loss increases, Fig. 10.9(b).

References

[1] Adachi, S., Phys. Rev. B 39 (1989) 12612–12621
[2] Agilent Technologies (2001): Network analyzer basics. http://www.agilent.com/find/backtobasics
[3] Ansoft (2003): 3D electromagnetic simulation software for RF, wireless, packaging, and optoelectronic design — HFSS 8.5. http://www.ansoft.com/products/hf/hfss
[4] Bolivar, P. Haring; Brucherseifer, M.; Rivas, J. G.; Gonzalo, R.; Ederra, I.; Reynolds, A. L.; Holker, M.; de Maagt, P., IEEE Trans. Microw. Theory Tech. 51 (2003) 1062–1066
[5] Brand, H., Schaltungslehre linearer Mikrowellennetze. Stuttgart: S. Hirzel 1970
[6] Chakam, G.–A., Periodische Strukturen im Mikrowellenbereich für planare Antennen und zur Modellierung integriert-optischer Komponenten. PhD Thesis, University of Karlsruhe, Febr. 2003
[7] Fleming, J. W., Electron. Lett. 14 (1978) 326–328
[8] Fujii, M.; Hoefer, W. J. R., IEEE J. Quantum Electron. 37 (2001) 1015
[9] Fujii, M.; Freude, W.; Russer, P., Efficient high–spatial–order FDTD analysis of 3D optical ring resonator filters. 19th Annual Symposium of the Applied Computational Electromagnetic Society

(ACES'03), Monterey (CA), USA, 24.–28.03.2003. Time Domain Numerical Modeling Beyond FDTD, Session 2

[10] Fujii, M.; Freude, W.; Russer, P., Wavelet–collocation finite-difference analysis of 3D optical ring resonator. Technical Digest Conference on Lasers and Electro–Optics Europe (CLEO/Europe-EQEC 2003), Laser 2003 World of Photonics, International Congress Centre Munich, Germany, 23.–27.06.2003. Topic: CJ – Optical Technologies for Communication, Switching and Interconnects. Session: Filters and Gratings

[11] Grau, G. K., Quantenelektronik. Braunschweig: Vieweg 1978

[12] Grau, G.; Freude, W., Optische Nachrichtentechnik. Berlin: Springer 1991. (Since 1997 out of print; corrected University reprint available 1998, 1999, 2003. mailto:W.Freude@etec.uni-karlsruhe.de)

[13] Guden, M.; Piprek, J., Material parameters of quarternary III–V semiconductors for multilayer mirrors at 1.55 um wavelength. Modelling and Simulation in Materials Science and Engineering 4 (1996) 349

[14] Hakki, B.W.; Paoli, T. L., J. Appl. Phys. 46 (1975) 1299

[15] Hammer, M.; Groesen, E. van, J. Lightwave Technol. 20 (2002) 1549

[16] Jackson, J. D., Classical electrodynamics, 2. Ed. New York: John Wiley & Sons 1962

[17] Jin, J., The finite element method in electromagnetics, 2. Ed. New York: John Wiley & Sons 2002

[18] Joannopoulos, J. D.; Meade, R. D.; Winn, J. N., Photonic crystals. Princeton: Princeton University Press1995

[19] Johnson, S. G.; Joannopoulos, J. D., The MIT photonics-bands package home page (http://ab-initio.mit.ed/mpb)

[20] Kirchner, A.; Busch, K.; Soukoulis, C. M., Phys. Rev. B 57 (1998) 277

[21] Jin Au Kong, Electromagnetic wave theory. Cambridge (MA): EMW Publishing 2000

[22] Li, Daiqing; Free, C. E.; Pitt, K. E. G.; Barnwell, P. G., IEEE Microw. Wireless Components Lett. 11 (2001) 118

[23] LTCC: Addresses of various suppliers [24] are to be found at http://www.ltcc.de/what-is-ltcc/material-supplier/material-supplier.htm. We thank P. Mayer, Lucent Technologies, Nürnberg, for providing this information.

[24] LTCC: IMST GmbH, Carl–Friedrich–Gauß–Str. 2, D–47475 Kamp–Lintfort, Germany. Tel: +49 2842 981-100; fax: +49 2842 981-199; mailto:contact@imst.de; mailto://ltcc@imst.de; http://www.ltcc.de/service/service.htm

[25] Mauritz GmbH+Co: Datasheets for PTFE–based microwave substrates (Rogers Corp., USA 2002, http://www.rogers-corp.com). P. O. Box 10 43 06, D–20030 Hamburg, Germany. Phone: +49 40 24 165-4; fax: +49 40 24165-7; mailto:MauritzHH@aol.com

[26] Montgomery, C. G.; Dicke, R. H.; Purcell, E. M., Principles of microwave circuits. McGraw–Hill: New York 1948

[27] Palik, E. D., Handbook of optical constants of solids. San Diego: Academic Press; 1998

[28] Pearson, M. R. T.; Jessop, P. E.; Bruce, D. M.; Wallace, S.; Mascher, P.; Ojha, J., J. Lightwave Technol. 19 (2001) 363

[29] Plihal, M.; Maradudin, A. A., Phys. Rev. B 44 (1991) 8565

[30] Pozar, D. M., IEEE Trans. Antennas Propag. 34 (1986) 1439

[31] Remski, R., Analysis of photonic bandgap surfaces using Ansoft HFSS. Microw. J. Sept. (2000) 190–198

[32] RSoft (2003): Component design products — BeamPROP, FullWAVE, BandSOLVE. http://www.rsoftinc.com/products/component_design

[33] Russell, P. St. J.; Birks, T. A., J. Lightwave Technol. 17 (1999) 1982

[34] Sakoda, K., Optical properties of photonic crystals. Berlin: Springer-Verlag 2001

[35] Scarmozzino, R.; Gopinath, A.; Pregla, R.; Helfert, S., IEEE J. Sel. Topics Quantum Electron. 6 (2000) 150

[36] Silvester, P.; Ferrari, R., Finite elements for electrical engineers, 2. Ed. Cambridge: Cambridge University Press 1990

[37] Stöckel, B., Dielektrische Wellenleiter für integrierte Terahertzschaltungen. Fortschritt-Berichte / VDI: Reihe 10, Informatik, Kommunikationstechnik, 387. Düsseldorf: VDI-Verlag 1995

[38] Taflove, A., Computational electrodynamics: The finite–difference time–domain method. Norwood: Artech House 1995

[39] Talneau, A.; Le Gouezigou, L.; Bouadma, N., Opt. Lett. 26 (2001) 1259

[40] Thumm, M.; Wiesbeck, W.; Kern, S., Hochfrequenzmeßtechnik. Verfahren und Meßsysteme. Stuttgart: B. G. Teubner 1997

[41] Yee, K. S., IEEE Trans. Antennas Propag. AP-14 (1966) 302

[42] Voges, E.; Petermann, K. (Eds.), Optische Kommunikationstechnik. Handbuch für Wissenschaft und Industrie. Berlin: Springer 2002; pp. 6–9

[43] Zimmermann, J.; Kamp, M.; Schwertberger, R.; Reithmaier, J. P.; Forchel, A.; März, R., Electron. Lett. 38 (2002) 178

11 Scanning near-field optical studies of photonic devices

Vahid Sandoghdar[1], *Ben Buchler, Peter Kramper, Stephan Götzinger, Oliver Benson, and Maria Kafesaki*

11.1 Introduction

Visualization and manipulation of optical processes at the sub–wavelength scale has important applications in a wide range of science and technology. High resolution optical lithography has, for instance, been the key to the rapid progress of the chip industry, while modern techniques in fluorescence microscopy have opened new doors in biological and medical research. The photonics community has both benefited from, and contributed to, the advance of sub-wavelength optics. From the conceptual point of view, photonics researchers are interested in manipulating optical phenomena in confined geometries to realize more efficient and versatile miniaturized optical devices. From the application side, once a structure has been fabricated, it has to be characterized and tested using high resolution optical microscopy and spectroscopy.

Among various photonic devices, photonic crystals (PhCs) are perhaps the prime candidates for high resolution studies. By definition, light inside a PhC undergoes substantial changes both in phase and amplitude, over distances much smaller than a wavelength. Imaging the flow of light through the crystal structure would be highly advantageous for characterization of devices and comparison with numerical models. Application of conventional optical microscopy to photonic crystal devices is only of limited use since the resolution is limited by diffraction to about half the wavelength of light. To overcome the diffraction limit, scanning near–field optical microscopy (SNOM) can be applied. As we will see, SNOM techniques let us study the behavior of light at sharp bends in a PhC waveguide, allow us to make absolute measurements of transmission losses and reflection coefficients at junctions, make it possible to visualize the subwavelength spatial extent of the mode in a point defect microcavity and thereby identify tiny imperfections in the fabrication of PhCs.

11.2 Scanning near-field optical microscopy (SNOM)

11.2.1 Brief historical background

During the 1980s, microscopy witnessed a big revolution when scanning probe microscopes (SPM) were invented. The scanning tunnelling microscope (STM) and the atomic force microscope (AFM) offered atomic resolution in surface studies, and although they are not suitable for optical experiments, their technological development has had important consequences for

---

[1] Corresponding author: e-mail: `vahid.sandoghdar@ethz.ch`

Photonic Crystals. Edited by K. Busch, S. Lölkes, R. B. Wehrspohn and H. Föll
Copyright © 2004 Wiley-VCH Verlag GmbH & Co. KGaA
ISBN: 3-527-40432-5

the realization of the third member of the SPM family, the scanning near-field optical microscope (SNOM).

After the pioneering works of two independent groups around Pohl [1] at IBM Zurich and Lewis [2] at Cornell University in the years 1983–1984, it took several more years of technical development before the advantages of SNOM could be exploited in different applications in the 1990s. The most valuable contribution towards a reliable device was the discovery of a convenient tip–sample distance stabilization in 1992 by Toledo–Crow et al. [3] and Betzig et al. [4]. Perhaps the most spectacular scientific goal achieved with SNOM was the detection of single fluorescent molecules at room temperature in 1993 [5]. Over two decades, many different configurations of illumination and detection as well as several concepts of probe design have been examined [6]. In the next section, we will give a brief review of these with a particular emphasis placed upon the applications of SNOM for photonics. More detailed and thorough treatments of SNOM can be found in the literature [6–10].

11.2.2 The operation principle of SNOM

Let us consider the situation in Figure 11.1. A sample is illuminated with light of wavelength λ (we are not interested in the details of the illumination process at this point) and part of the incident light is reflected or transmitted. We can consider the sample to be a Fourier sum of many periodic gratings. Those gratings with periods greater than $\lambda/2$ will give rise to a diffraction pattern. Gratings with periods less than $\lambda/2$ will, on the other hand, only give rise to zeroth order diffraction which carries no spatial information about the grating. As a result, one cannot learn about a sample's sharp corners and rapid changes of the optical contrast, if one collects the light that *propagates* away from the sample. This was pointed out by Abbé [11] in the 1870s, who formulated a rigorous limit of $\lambda/(2n\sin\theta)$ to the resolution of an optical microscope with a full collection angle of 2θ in a medium of refraction index n.

Although Abbé's limit is quite robust, it only holds for the propagating waves. The interaction of high spatial frequency gratings with light, also results in a surface dwelling evanescent field [12], the strength of which is directly related to the optical contrast of the sample. The essence of near–field microscopy is to measure these non–propagating fields with subwavelength resolution by scanning a very small local detector close to the sample surface (see Fig. 11.1). Two parameters decide on the performance of a SNOM in a fundamental manner. First, the size of the detector determines the resolution. A finer probe is usually desirable because it can scatter the evanescent field more locally and yield a higher resolution. One must, however, bear in mind that the strength of scattering processes typically scales as a power law, so that better resolution is accompanied by a weaker signal. The second important factor is

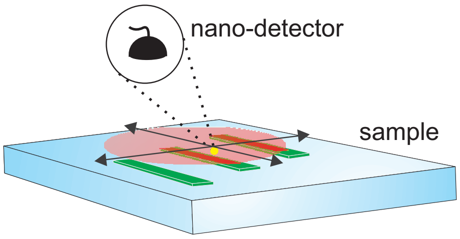

Figure 11.1: A nano–detector can be scanned to measure the intensity of the nonpropagating evanescent fields on the surface of a sample. The red region displays the illuminated area.

the distance between the probe and the sample. The evanescent field associated with a certain spatial frequency, κ, loses strength rapidly over distances of order $1/\kappa$. It is, therefore, important that the probe explores the sample surface as closely as possible. Scanning the sample at larger distances means not detecting the higher spatial frequency components and therefore lower resolution.

Aside from the probe size and its distance to the sample, several issues such as the polarization of light as well as illumination and detection configurations, strongly influence SNOM images. A thorough and quantitative treatment of the imaging process in SNOM remains a challenge for both experimentalists and theorists alike. From the experimental point of view, it is difficult to characterize each individual probe and sample to the extent that the measurement results can be interpreted in a fully quantitative manner. The theory on the other hand, is confronted by the challenge of performing three–dimensional numerical calculations, taking into account all geometric and material properties of realistic samples. In the following we provide a minimum working knowledge of near–field microscopy to set the ground for discussing its applications to photonics.

11.2.3 Instrumentation

Figure 11.2a shows the schematics of the main components of a SNOM setup. As in any SPM, the heart of the setup is the tip. Depending on the mode of operation, SNOM tips can be made of glass, metal or semiconductors, each either naked or coated. We focus our attention on glass fibre tips which can be made by either chemical etching or by heat pulling of optical fibres [6]. In most applications, the tip is coated with a metallic layer from all sides except at the very end, leaving a subwavelength aperture. It is important that the coating is thick enough to prevent leakage through the metal. Leakage is also minimized by choosing a metal with a small skin depth such as aluminium.

As argued above, the tip has to be positioned at a separation much smaller than a wavelength. This is a nontrivial task because a sharp tip is very fragile and any accidental contact with the surface could ruin it. To control the tip–sample distance, a servo–loop based on the ‘shear–force’ interaction [3, 4] can be used. Shear force control relies on the not fully understood fact that the amplitude of a fibre tip, oscillating parallel to a surface, is damped when the tip approaches within 10–20 nm of the surface. There are various techniques for exciting and detecting the fibre oscillation [6], but the most common method is to glue the fibre to a prong of a tuning fork with an oscillation frequency of about 32kHz (see Figure 11.2a) [13].

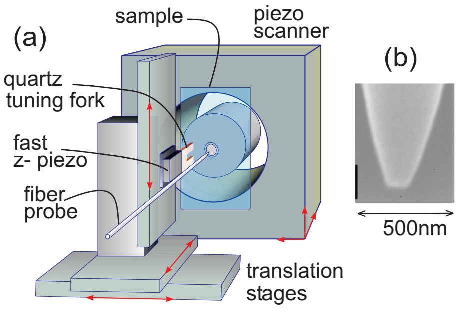

Figure 11.2: a) Schematic drawing of the SNOM machinery. A tip is mounted on a quartz tuning fork. The probe can be positioned against the sample using coarse translation stages and a piezoelectric scanner unit. b) Electron microscope image of glass fibre tip.

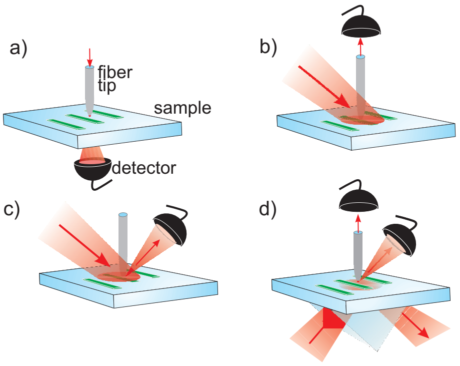

Figure 11.3: a) Illumination SNOM: the fibre is used to illuminate the sample. b) Collection SNOM: the sample is illuminated globally and evanescent fields are scattered by a sharp tip and collected through the fibre. c) Apertureless SNOM: the sample is illuminated globally. An “apertureless" tip is used to scatter the light into the far field. d) The sample is illuminated via total internal reflection. A tip is used to scatter the evanescent field into the fibre (collection mode) or the far–field (apertureless mode).

The shear–force interaction of the fibre tip with the surface modifies the amplitude and phase of the fork oscillation. Lock-in detection of the phase and amplitude can be used to keep the distance separation between the tip and the sample constant. A bonus of this procedure is that one also obtains a topographic map of the sample surface via the piezo voltage, which is regulated to keep the shear–force signal constant. Piezoelectric elements are used to scan the sample relative to the probe or vice versa. In general, great care should be paid to the stability of the mechanical components against vibrations and drifts.

11.2.4 Various modes of SNOM operation

In photonics applications, we are mostly interested in investigating the propagation of light in a device or its confinement to various regions. The majority of SNOM experiments reported in the literature, however, aim at optical microscopy in the conventional sense of characterizing sample features such as size, form, color and index of refraction. To put the configurations discussed in later sections in the broader context, we now briefly mention some of the other SNOM arrangements that are often encountered in the literature. Depending on how the sample is illuminated and the signal is detected, different modes of operation can be identified. These are not hard and fast categories, combinations can be, and are, used.

In the most common mode, a tapered optical fibre is aluminum coated at an angle so that a very small subwavelength opening is left at the front. This is an ‘apertured’ mode of SNOM. When light is coupled into the fibre, it is mostly back reflected but some light reaches the small aperture where it induces electronic oscillations in the metallic layer. This oscillation results in the production of nonpropagating fields at the aperture exit, as well as the emission of propagating radiation. When the tip is brought close to a sample, the evanescent components are scattered into the far field and then detected either in transmission (Figure 11.3a) or reflection. We refer to this configuration as the ‘illumination mode’. In the reverse mode known as the ‘collection mode’ one illuminates the sample globally and detects through the apertured fibre tip (Figure 11.3b).

In so–called ‘apertureless SNOM’ [14], one illuminates the sample globally and uses a solid metallic or dielectric tip to scatter the evanescent waves into the far field where they are detected (Figure 11.3c). Some samples are suited to a third type of illumination via total internal reflection [15, 16] as shown in Figure 11.3d. In this case, light is introduced into a transparent sample in such a way that it undergoes total internal reflection. On the surface, a SNOM tip is introduced to scatter the evanescent waves present due to the internally reflected light. The scattered light can be detected using apertured or non–apertured techniques. This arrangement is sometimes thought of as the optical equivalent of the STM, in the sense that the photons that would have been otherwise evanescent can tunnel through the gap between the glass fibre and the sample. For this reason it has also been referred to as the photon scanning tunnelling microscopy (PSTM). It is, perhaps, more appropriate to talk about scattering instead of tunnelling when one of the bodies, in this case the tip, has subwavelength dimensions. For this reason we prefer to keep the terminology general and refer to all the different modes simply as SNOM.

11.3 Imaging photonic devices with SNOM

One of the early experiments that demonstrated how the high spatial resolution of SNOM could be useful for investigating photonic devices was reported by Choo et al. [17]. They mapped the intensity distribution in a channel waveguide and directional coupler using SNOM. At about the same time, a fibre tip was used to perform spatial mode mapping of the whispering–gallery modes (WGMs) in a high–finesse microresonator [18,19]. Since the mid 1990s, several groups have applied this technique to investigate light propagation and confinement in waveguides [20–23], laser diodes [24], VCSELs [25], microdisks [26], microrings [27], fibres [28] and photonic crystal structures [29–43].

Although our discussion will mostly focus on the work performed in our own laboratories, in the rest of the chapter we will endeavour to present an overview of SNOM and its application to photonic devices and photonic crystals. There are various SNOM techniques that have yet to be applied to photonic crystal structures. These will be discussed in order to highlight the potential that SNOM has for future experiments. We start, in the following section, with a simple introduction to SNOM experiments by presenting a measurement of the evanescent field formed by total internal reflection. In Section 11.3.2, we discuss SNOM experiments on silica microspheres. As we will see, the complexity of this system makes it a very good example for elaborating on various issues of interest. Section 11.3.3 deals with phase sensitive interferometric SNOM measurement. This system is a powerful extension to the regular intensity measurement made with SNOM probes. In Section 11.3.4, the applications to PhC structures will be presented with particular emphasis on a point defect microcavity.

11.3.1 The evanescent field on a prism

To begin our discussion of SNOM experiments, we will consider the measurement of the evanescent field at the surface of a prism. This is a useful illustration of the ability of SNOM in a simple system. As shown in Figure 11.4a, a laser beam illuminates a prism at a supercritical angle and a sharp uncoated optical fibre tip is inserted in the evanescent field at the prism surface to spy on the optical intensity. The tip used in this experiment was an uncoated glass fibre and the optical detection is performed at the output of the fibre. In terms of the previously defined SNOM modes, this example shows apertureless collection mode SNOM using total internal reflection for illumination.

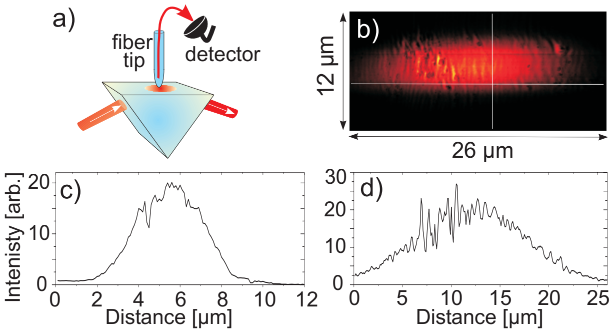

Figure 11.4: a) Experimental arrangement for the detection of evanescent waves on the surface of a prism using SNOM in the collection mode. b) The SNOM image of the laser beam focus. c) A cross section along the vertical axis. d) A cross section along the hoizontal axis.

Figure 11.4b displays the image obtained from the prism surface, whereas Figures 11.4c and d show two cross sections of it. The rapid modulations in parts of these figures reveal the high spatial resolution in this image and give direct evidence of subwavelength roughness on the prism surface. This provides a simple first example in our discussion where SNOM offers information that far–field imaging could not have acquired.

11.3.2 SNOM on whispering–gallery resonators

A challenging goal in quantum optical experiments of the past two decades has been to achieve a strong coupling between a single emitter and a high–Q mode of a resonator [44, 45]. Conventional resonators can offer very high quality factors with large mode volumes while the microscopic systems provide very low mode volume with a moderate Q. Ideally, one seeks a system with both low volume and high Q. In our laboratory, we have investigated two microresonator systems that have the potential to achieve this goal, namely silica microspheres and photonic crystal point defects. In this section, we discuss the properties of silica microspheres and how SNOM can be used to characterize them.

Whispering–gallery modes (WGMs) belong to the larger class of Mie modes in dielectric objects of circular cross section [46]. The characteristic property of a WGM is that light undergoes a large number of total internal reflections before it closes on itself in phase. The losses at each total reflection are negligible compared to those from metallic or even Bragg mirrors. As a result, WGMs in silica can reach very high quality factors, up to 10^{10}, limited by absorption [47]. In the 1990s, silica microspheres were studied by several groups [48–50]. As shown in Figure 11.5a, in order to couple to these modes in an efficient manner, one can use prism coupling and frustrated total internal reflection. As the frequency of the laser is scanned, dips in the transmitted light or peaks in the light scattered from the sphere can be used to detect the resonances.

Three characteristic numbers n, l and m and two polarizations specify in a unique manner, each WGM associated with a resonance frequency and spatial mode. The spatial mode is governed by spherical Bessel functions and Legendre polynomials. In general, a given mode could have a large number of nodes and antinodes in the $\vec{r}$ and $\vec{\theta}$ directions. The simplest WGMs circulate in the equatorial plane of the sphere and have one intensity maximum in these directions. The parameter m is degenerate for a perfect sphere. The degeneracy is lifted by the introduction of ellipticity. For a typical microsphere of diameter 100 μm fabricated in

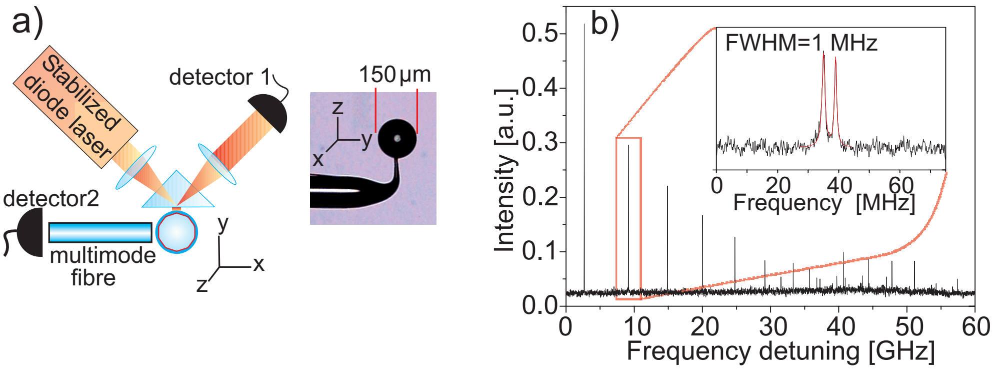

Figure 11.5: a) Top view of the setup for performing spectroscopy on WGMs of a microsphere. An optical microscope image shows a microsphere melted at the end of a pure silica fibre. b) A typical spectrum of WGMs recorded by detector 2 over a frequency range of 60 GHz.

the laboratory, the resonance frequencies of the modes with identical n and l but different m are spaced by a few GHz. Figure 11.5b shows a spectrum obtained by scanning a narrow–band diode laser and recording the tiny amount of the light that is scattered out of the sphere when a resonance is met. The inset in this figure displays a zoom into one of the resonances, showing two lines as narrow as 1 MHz, implying a quality factor of about 10^8. The doublet structure is due to the coupling between clockwise and counter–clockwise propagating modes [51].

Given the rich and complex composition of the WGM spectrum, identifying a mode based on the frequency information alone would require scanning the laser frequency at at least one free spectral range (about 600 GHz) with a high resolution. Alternatively, because the WGMs rely on total internal reflection, an evanescent field exists on the surface of the sphere, and SNOM can be used to interrogate the spatial features of a given WGM along $\vec{\theta}$ and $\vec{\phi}$ [18, 19, 52]. Figure 11.6a shows the schematics of the setup. The sphere–prism distance is set at a few tens to a few hundreds of nanometers. The laser frequency is scanned through the sphere resonance, and the tip is approached to the sphere surface using the shear–force signal. Figure 11.6b plots a spatio–spectral map of several WGM modes with increasing number of maxima along $\vec{\theta}$. In particular, the fundamental WGM corresponding to $l = m$ is clearly identified. These modes are of special interest because they offer the lowest mode volume, leading to largest effects in quantum optical studies.

By recording the 2D intensity modulations of the WGMs, SNOM can discover subwavelength deviations from their predicted behavior. Figure 11.7a shows a two–dimensional spatial

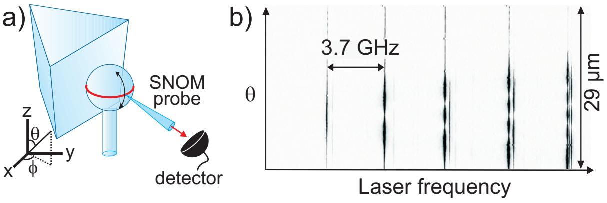

Figure 11.6: a) Schematic view of near-field imaging of WGMs using a tip. b) A spatio–spectral map of WGMs. The fundamental mode with only one intensity maximum in the $\vec{\theta}$ direction is clearly identified. From [52].

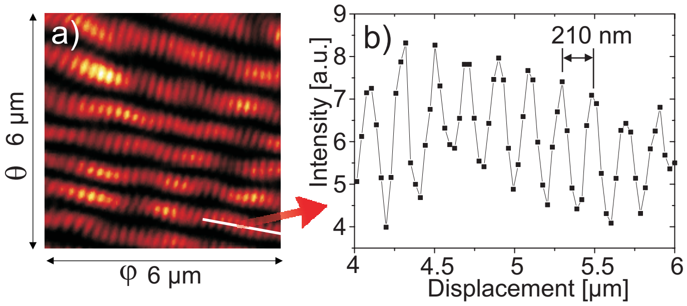

Figure 11.7: A two–dimensional spatial map of a WGM with $l-|m| \gg 1$. The tilt of the microsphere in the xz plane is put into evidence. b) A cross section from a) shows the periodic modulations of the intensity along $\vec{\phi}$.

map of a given WGM with $l - |m| \gg 1$. In addition to the expected nodes and antinodes in the $\vec{\theta}$ direction, one finds subwavelength intensity modulations along the perimeter of the sphere (Figure 11.7b) [53]. These fast modulations indicate the existence of residual counter propagating waves that lead to standing waves. The periodicity of this pattern allows one to determine the parameter $|m|$ so that together with our knowledge of $l - |m|$ one can also identify l [19].

The combination of high resolution microscopy and spectroscopy allows detailed mapping and characterizing of the mode patterns and frequencies in silica microspheres. Experiments with microspheres are mechanically complex. This work shows that even under such conditions, SNOM is a practical addition to the experimental setup. This work also demonstrates that SNOM can make measurements of optically sensitive high–Q devices, although as will be discussed in Section 11.4, caution is still required in some circumstances.

11.3.3 Interferometric SNOM measurements

The great majority of SNOM experiments detect field intensities. It has, however, been shown by several groups that by interfering the SNOM signal with a reference laser beam, one can obtain valuable information about the field amplitude and phase [21, 54–56]. Here we briefly discuss this technique through two examples of recent work done at the University of Twente.

A schematic of the experiment is shown in Figure 11.8. Light collected by the SNOM tip is mixed with a frequency shifted reference beam that has been generated using acousto–optic modulation. The resulting signal is detected using a lock–in amplifier. The X and Y quadratures of the lock–in signal then provide the cosine and sine of the phase difference

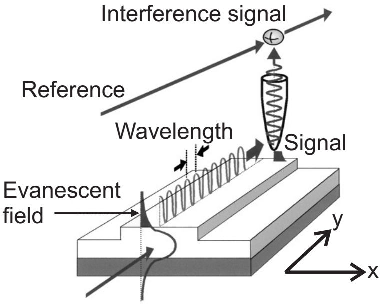

Figure 11.8: Schematic illustration of a heterodyne SNOM setup. The light collected by the SNOM tip is mixed with a frequency shifted reference beam. From [21].

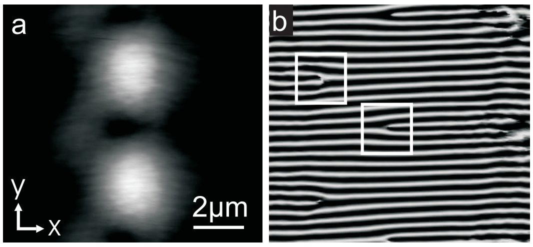

Figure 11.9: a) amplitude of the light inside the waveguide; b) cosine of optical phase of the light inside the waveguide. From [21].

between the SNOM light and the reference beam. As with all interferometric devices, care is required to eliminate signal drift due to thermal and acoustic changes in the interferometer arm lengths, lest the phase signal be swamped by spurious noise.

Figure 11.9 shows the results obtained by Balistreri et al. on a waveguide that supports modes with TE and TM polarizations [21]. Figure 11.9a shows the amplitude of the field in a lateral scan (see axes in Figure 11.8 for reference.). Figure 11.9b shows the cosine of the phase for the same area. The amplitude of the field inside the waveguide is strongly modulated. There are two distinct lobes along the y direction due to the interference of various TM and TE modes excited in the waveguide. Ideally, these should not interfere since they are orthogonal. The detection via the SNOM tip and coupling of polarization modes in the fibre leads, however, to substantial interference. The overall optical phase, shown in Figure 11.9b, is seen to correspond to that of a plane wave. There are some points in the phase map, such as those highlighted in the white squares, where the phase fronts appear to meet at a point to form a phase singularity. Taking into account the TE_{00}, TE_{01} and TM_{00} modes, Balistreri et al. were able to reconstruct the observed amplitude and phase.

Using the setup depicted in Figure 11.8, the propagation of femtosecond pulses in a waveguide has also become accessible to SNOM measurement [22,23]. Once again, acousto–optic modulation has been used to generate the reference beam that is mixed with the signal from the SNOM tip. The important differences are that the cw beams have been replaced with a pulsed laser source and the path length of the reference beam can be accurately tuned. The interference of the reference beam and the SNOM signal will now only occur when their photons arrive at the detector simultaneously. Tuning the path length of the reference beam therefore allows one to choose what part of the waveguide will be imaged. The results are shown in Figure 11.10. As the path length of the reference beam is varied in Fig 11.10a–e, the pulse is seen to move from left to right. This measurement allowed direct determination of the group and phase velocities in the waveguide.

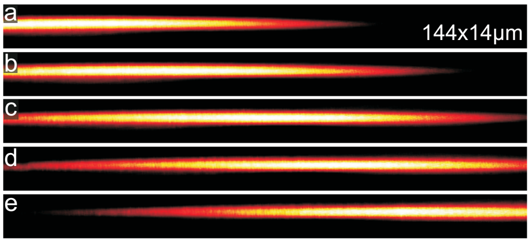

Figure 11.10: The optical field amplitude as measured by the instrument for different positions of the optical delay line. From (a) through (e), the optical path length of the reference branch is increased by 40.0 ± 0.6 μm. This results in steps of the reference time of 133±2fs. From [22].

11.3.4 Photonic crystals

The optical properties of PhCs stem from collective interference between fields scattered by many, many subwavelength dielectric features of the structure. Probing a PhC by transmission and reflection measurements provides valuable information about the propagation of the light through the crystal, however such measurements remain only indirect signatures of how light interacts with the complex geometry of a photonic crystal. To get a visual picture of light propagation in coordinate space, numerical simulations such as finite–difference time–domain (FDTD) can be performed, but to really 'see' what happens when light goes through a defect or around a sharp bend in a waveguide, we require an imaging scheme. One might imagine using a microscope based on some lenses and a camera [57], but this is not satisfactory for two reasons. First, if the quality of the PhC structure is high, only very little light leaks out into the microscope. More importantly, however, we know from Abbés limit (defined in Section 11.2.2) that a far–field microscope cannot resolve features separated by distances below $\lambda/(2n\sin\theta) = \lambda/(2\,NA)$, where $NA = n\sin\theta$ denotes the numerical aperture of the imaging instrument [58]. Near–field microscopy is, therefore, a particularly attractive and valuable tool for studying PhCs. Indeed, this has been recognized by several groups in the past few years. Limited access to high quality PhC fabrication and to sophisticated three–dimensional numerical simulations has, however, seriously hampered the application of SNOM to ultra–high resolution imaging of light confinement in complex PhC structures. In particular, measurements that allow quantitative characterization of PhCs and a robust comparison with theory are just beginning to appear.

One of the early attempts to perform optical near–field measurements on photonic crystal structures was done in the illumination mode and is due to McDaniel et al. [29, 30]. As depicted in Figure 11.11, in this configuration, the evanescent near field of the probe is scattered by the subwavelength features of the PhC surface into many of its modes. As the probe is positioned laterally, the strength of this coupling is varied and the overall transmission is modulated, yielding interesting information about the PhC. In the work done by McDaniel et al. the PhC consisted of a deep glass sample with a two–dimensional lattice of pores, without a strong photonic band gap effect. Light was sent through a coated tip along the pores and was detected with a large area detector at the other side of the sample. The researchers examined the transmission of the sample as a function of the probe position and wavelength. The illumination mode was also used by Flück et al. very recently to investigate a three–dimensional artificial opal photonic crystal [31].

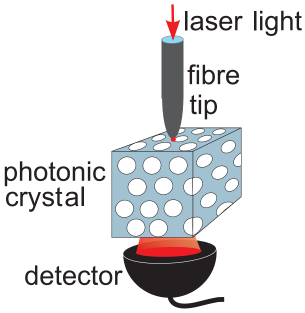

Figure 11.11: Illumination mode SNOM. Light from the fibre is incident on the sample and then detected behind the sample.

Earlier reports in the literature include collection mode SNOM on grating–type waveguide structures [32], two–dimensional PhC slabs [33] and deep channel glass structures [34]. In particular, the results obtained by Phillips et al. [33] nicely show how SNOM can be used to investigate scattering and interference phenomena at the subwavelength scale. An important observation made by these authors, and many other groups, is the difficulty of distinguishing the evanescent fields from propagating components caused by scattering processes that take place away from the tip. A prudent and useful experimental check that helps to discriminate the contribution of the evanescent waves at the surface from those of propagating ones, is to record the signal with the tip scanned at different heights above the sample surface. Even so, one has to keep in mind that scattering from a periodic structure yields periodic intensity modulations even at larger tip-sample separations, making it difficult to distinguish the far and the near fields [59]. To minimize the effect of stray light, coated tips have often been used. Furthermore, the sample design and fabrication quality also play important roles in minimizing unwanted scattering at the sample surface.

Theoretical treatments of near–field studies on photonic crystals have been even rarer than the experimental works. The reason lies in the fact that numerical solutions of the Maxwell equations are very demanding for systems that impose many boundary conditions at the nanometer scale. To reach a good level of accuracy, the system has to be discretized into very small elements so that the computation time quickly tends to days. When dealing with shallow slab type PhCs, three–dimensional calculations become manageable. Fan et al. [60] have considered such a system that even includes the effect of the SNOM tip. They show that high resolution SNOM images of the intensity modulations could not only portray the path that light takes in the crystal, but also determine frequency/wave–vector dispersion information of the PhC. In order to do this, they suggest exciting modes at different frequencies and propagation directions, and analyzing the resulting modulation patterns.

Some of the most exciting applications of PhCs are based on the introduction of functionalities through the incorporation of defects in the otherwise periodic lattice. Defects influence the photonic band structure of the PhC and can result in the flow or confinement of light along particular pathways in the crystal. A point defect yields a region surrounded by high reflecting mirrors, thereby establishing a microresonator. A line defect could act as waveguide, while combinations of these building blocks could achieve complex units such as interferometers, filters, etc. As was the case for the silica microspheres (see Section 11.3.2), the spectral information from PhCs alone cannot determine the spatial extent of the light in them. Here too, SNOM proves to be a very valuable tool.

The first near–field imaging experiment on photonic crystals containing defects was reported by Smith et al. in 1993 [35]. The sample was an array of dielectric rods placed in a microwave waveguide structure with one rod missing. A local microwave probe was positioned at different locations at the top of the structure to map the intensity distribution about the point defect. The small length scales required for PhCs in the optical domain make similar experiments more challenging. Aside from the difficulties in the fabrication of high quality PhCs, researchers are also confronted by other technical barriers in the process of characterization. Firstly, the appropriate light source is not always available. In order to couple the light into subwavelength defects, a focusable source like a laser is desirable. Commercially available lasers often lack the required degree of wavelength tunability or have linewidths that are too broad. Secondly, handling and alignment of tiny samples consisting of subwavelength features is not trivial and calls for many motional degrees of freedom in the setup.

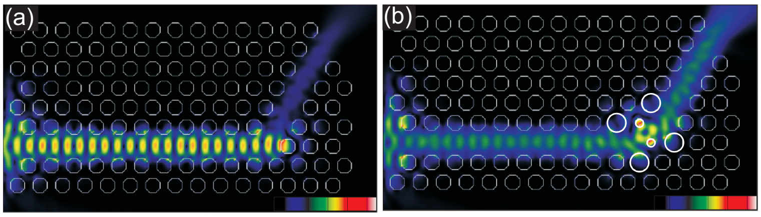

Figure 11.12: 2D FDTD models showing field amplitude. a) A sixty degree bend in a waveguide with poor transmission. b) Modified bend with 96% transmission over a broad frequency range. Parameters: $r/a = 0.34$, $n = 3.43$, $a = 500\,\text{nm}$, $a/\lambda = 0.2844$. The larger holes in (b) have $r/a = 0.41$ and the smaller holes have $r/a = 0.17$. Polarization mode is TE.

A landmark in the unique properties of PhC devices has been the efficient transmission of light around sharp bends. Early simulations and experiments showed that transmission at as high as 98% could be achieved around $90°$ bends in PhCs with a quadratic lattice [61, 62]. But similar results on PhCs with other designs proved to be less trivial to accomplish, especially if broadband transmission is required [63–65]. Figure 11.12a shows the results of two–dimensional FDTD simulations for the intensity distribution along a waveguide with a $60°$ bend. Most of the light is reflected from the bend, giving rise to standing waves in the incident arm. Figure 11.12b shows that more than 96% of light, at the identical frequency, can be guided around the bend, if the diameters of a few holes are modified.

Given the intricacies of the fabrication process and the sensitivity of the PhC performance to fine geometric details, SNOM is almost indispensable for characterization and testing of such devices. Figure 11.13a shows the topography image of a test sample based on InP technology in the preliminary phase of the fabrication [66]. The lattice constant was chosen to be 500 nm and the holes had a diameter of 300 nm, but their depth profile was not optimized and no capping layer was integrated. As a result, the sample is not expected to possess a photonic band gap. Figure 11.13b shows a SNOM image taken with an uncoated fibre tip in collection mode, while the beam from a diode laser at $\lambda = 1550$ nm was coupled into the waveguide using a lens with a $NA = 0.68$. The image reveals that there exists some guiding in the input waveguide which is expected to be due to index guiding. Moreover, the near–field image is good evidence that most of the light is reflected at the bend, resulting in the standing waves observed in the entrance arm of the structure. This study gives a good example of the advantage of SNOM in characterizing photonic devices even when numerical results are not available to guide one's intuition.

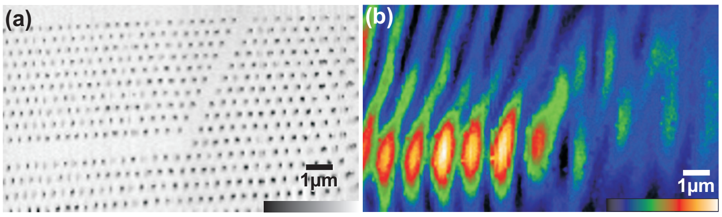

Figure 11.13: a) Topography image of waveguide b) Optical image of the waveguide. Polarization mode is TM.

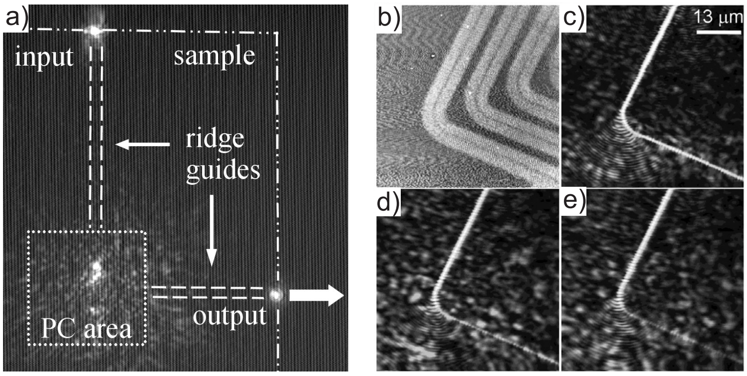

Figure 11.14: a) Far field image. b) Topographical image taken with SNOM tip. Near field images taken at wavelengths of c) 1520 nm, d) 1550 nm and e) 1570 nm. Weak optical signals have been enhanced to highlight the concentric fringes originating at the waveguide bend. Taken from [37].

Bozhevolnyi et al. have reported on SNOM investigations of PhC waveguides containing 90° bends [36, 37]. Light from a tunable laser at $\lambda = 1500$ nm was externally coupled into PhC waveguides and a coated fibre tip was used to image the propagation of light at the top surface. Figure 11.14a shows the far–field image of the sample. Three major scattering locations are identified at the end junctions of the waveguides and around the bend of the PhC waveguide. Figure 11.14b displays the topography image from parts of three PhC waveguides investigated by SNOM. The images in Figures 11.14 c, d and e show propagation at three different wavelengths of $\lambda = 1520, 1550$ and 1570 nm, respectively. The increase in losses for longer wavelengths is evident. The concentric rings observed in the SNOM images give more insight into the scattering process at the bend. The authors attribute these to the interference between the contributions from the waveguide mode and a quasi–homogeneous coherent background. Figure 11.15a shows a topography zoom of the region around the bend for one waveguide whereas Figures 11.15b–f display corresponding SNOM images recorded at different heights above the sample. These images clearly demonstrate that the resolution deteriorates as the tip is removed. The image in Figure 11.15b also shows standing waves that have resulted from back reflections in the system.

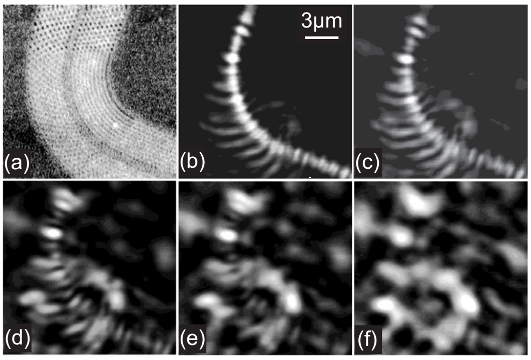

Figure 11.15: a) Topographical image taken with SNOM tip. Images b) to f) show SNOM images at λ=1520 nm with different tip–surface separation: b) 10 nm (with shear force control); c) 100 nm; d) 300 nm; e) 500 nm and f) 700 nm. From [37].

Another important question that Bozhevolnyi et al. addressed was that of the quantitative measurement of the transmission around the waveguide bend. Measurements of absolute transmission through PhC structures are nontrivial because it is difficult to correctly take into account the losses related to the in–coupling process. A working solution has been to use internal light sources and to compare the power out of the waveguide with that out of the unstructured part of the sample [67]. It has also proved to be possible to use internal cavities formed by residual reflections to measure the loss of a single device [68]. Although such solutions are valuable, they do not provide practical answers to the characterization of a sophisticated device after fabrication. In particular, they do not provide any information about the point–to–point loss, only the sum total. By comparing the SNOM signal before and after a given location, one can directly obtain a quantitative estimate of transmission efficiency through any part of the system.

The last example we treat, is that of a microresonator studied in our own laboratory. The seemingly simple but most interesting and challenging configuration of defects in PhCs is the so–called point defect where a single site, for example a pore, is missing. The fundamentally small nature of this microresonator is of great interest for quantum optical effects because a photon confined to such a tiny region, carries very large electric fields. Needless to say, applications in integrated optics and analytics also welcome very small building blocks. The challenge in the design and realization of PhC microresonators is to maintain the lowest volume and achieve the highest quality factor Q possible. Quality factors as high as a few thousand for point-defect microcavities [69], 13,000 for a two-point defect [71] and 45,000 for a three point defect [70] have so far been demonstrated.

Figure 11.16a shows a scanning electron microscope image of a two–dimensional microresonator made of silicon. The structure has a lattice constant of $a = 1.5\ \mu$m with a depth of 100 μm and was fabricated by electrochemical preparation of macroporous silicon [72–74]. A point defect is surrounded by two pores and two waveguides that help couple light in and out of the cavity. FDTD calculations predict two sharp resonances at nominal wavelengths of $3.732\ \mu$m and $3.957\ \mu$m within the fundamental band gap between $3.4\ \mu$m and $5.8\ \mu$m.

We could put these resonances into evidence by coupling in laser light from a continuous-wave optical parametric oscillator and by using a SNOM probe to detect the transmission through [38] and propagation along [39] the structure. Figure 11.16 shows the experimental setup. The laser beam is focused onto the entrance facet of the first waveguide. The sample's position and tilt can be adjusted to optimize the coupling. Some of the light scatters around the sample, leading to unwanted background at the output facet. This prompted us to scan

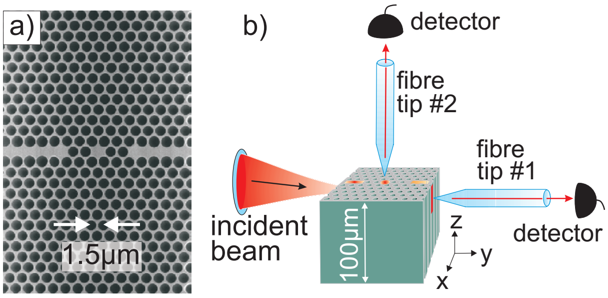

Figure 11.16: a) Top view of a photonic crystal microcavity in macroporous silicon. b)Schematic of the microcavity SNOM setup. Tip 1 is used to detect the output of the cavity while tip 2 is used to scan the surface of the crystal.

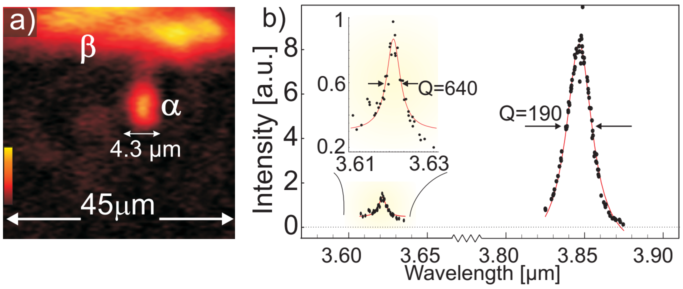

Figure 11.17: a) The light emitted form the photonic crystal as measured using SNOM tip 1. b) The transmission spectrum of the point defect cavity measured using the SNOM tip 1. (b) taken from [38].

the uncoated fibre tip #1 in a head–on configuration to image the output facet. Figure 11.17a shows an example of the image recorded by this tip. The signal detected cannot be attributed to evanescent fields only. Nevertheless, it is intriguing that the full width at half–maximum (FWHM) of the spot α at the exit facet is about 4 μm, corresponding to only a bit more than λ. The great advantage of this detection scheme can be appreciated when considering the bright spot β, which is due to the stray scattered light travelling above the sample. Without a local detector it would have been extremely difficult to discriminate against this signal. By repeating measurements such as Fig. 11.17a at different laser frequencies, the experimental resonance wavelengths could be determined to be 3621 nm and 3843 nm, as shown in Figure 11.17b.

Figures 11.18a and b display the intensity distribution expected for the two modes as calculated by two–dimensional FDTD simulations. The very rapid and strong intensity modulations at length scales well below a wavelength, are the features that one would like to capture with SNOM, but one has to keep in mind that a finite resolution would inevitably cause washing out some details. Figures 11.18c and d show image b after a convolution process with Gaussian filter functions of FWHM 500 nm and 1400 nm, corresponding to $\lambda/7$ and $\lambda/3$ respectively. We emphasize that, strictly speaking, the choice of this filter is not rigorous. The problem is that the interaction mechanism of a SNOM tip with the sample is neither theoretically nor experimentally known in a quantitative manner. We therefore simply convolve the intensity with a Gaussian filter function. Clearly, any coherent effects or complex polarization–dependent processes are neglected in this coarse treatment. Nevertheless, this procedure is very helpful in acquiring intuitive and qualitative understanding of the problem at hand. A comparison of images c and d emphasizes the important role of resolution in optical microscopy.

In order to monitor the propagation of light through the structure and to identify the resonator modes spatially, we use the second SNOM device to probe the crystal's upper surface

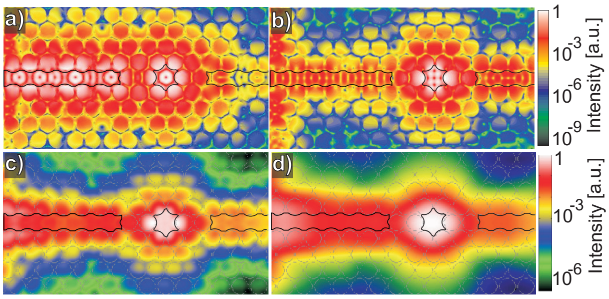

Figure 11.18: a) FDTD model of the intensity of the short wavelength mode in Figure 11.17b. b) FDTD model of the intensity of the long wavelength mode in Figure 11.17b. c) Convolution of the model in b) with a 500 nm detection window. d) Convolution of the model in b) with a 1400 nm detection window. a) and b) taken from [38].

(see Figure 11.16) [39]. Figure 11.19b displays the topography signal of that part of the sample that is examined. This image was recorded using an AFM tip that we mounted at the end of an optical fibre (see probe #2 in Figure 11.19a). Another topography image taken by an etched fibre tip, is shown in Figure 11.19c. The tips used in these experiments were made of fragile fluoride glass and were prone to breakage. For this reason, the probe in this run was not very sharp, leading to a very low lateral topography resolution. We point out that although it is necessary to use very sharp tips for SNOM studies in the visible range, a less pointed fibre tip could still serve as a subwavelength probe for the middle infrared regime. In any case, although the individual pores are not easy to recognize in Figure 11.19c, the topography image suffices to identify the two waveguides and the point defect. One can, therefore, correlate the optical signal with the PhC structure. Figure 11.19d shows the raw data of the optical intensity signal recorded by near–field probe #2 while the laser wavelength was tuned to the resonance at $\lambda = 3.84\ \mu$m. This data was taken simultaneously with the topography signal of Figure 11.19c that we have used, together with our knowledge of the scan range, to overlap the PhC geometry as a guide to the eye. The propagation of light in the first waveguide and its confinement about the point defect are clearly seen.

The SNOM image in Figure 11.19d reveals several properties that are not predicted by the FDTD simulations of Figure 11.18b, c or d, i.e. regardless of any resolution considerations. Firstly, the microresonator mode is tilted whereas the image in Fig. 11.18b suggests symmetry along the x and y axes. Secondly, the light is pushed to one side by a fraction of a wavelength in the last part of the input waveguide. Thirdly, the measurements reveal subwavelength details of the intensity modulations along this waveguide, which again seem to be different from that of Figure 11.18. It turns out that these observations indicate small deviations of the PhC structure from its nominal geometry. In fact, electron microscopy studies of macroporous silicon PhCs have shown that one might typically obtain up to 10% fluctuations in the diameters of the pores neighboring the missing pores [75].

Although, as we will see shortly, a quantitative description of the light propagation in a deep PhC requires three–dimensional FDTD calculations, we first consider two–dimensional FDTD simulations for a qualitative understanding of the central phenomena. Figures 11.20a, c and e show three examples of the microresonator mode from Figure 11.18b, when slight changes are made to the pores surrounding the point defect. The percentage change in pore

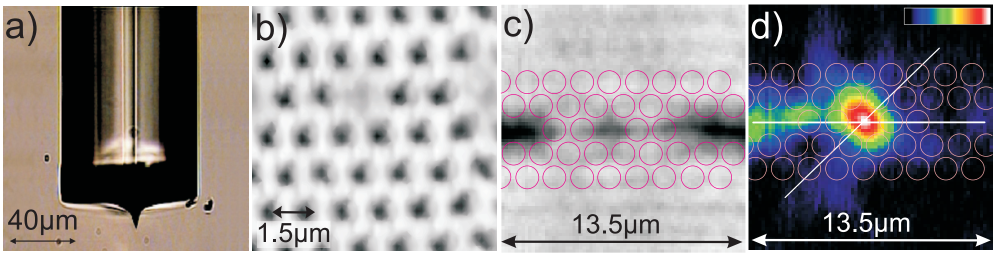

Figure 11.19: a) A SNOM probe with silicon AFM tip mounted on the end. b) Topography signal from combined SNOM/AFM tip showing micro–cavity. c)Topography image taken using etched SNOM tip. d) SNOM image taken simultaneous with c). c) and d) taken from [39].

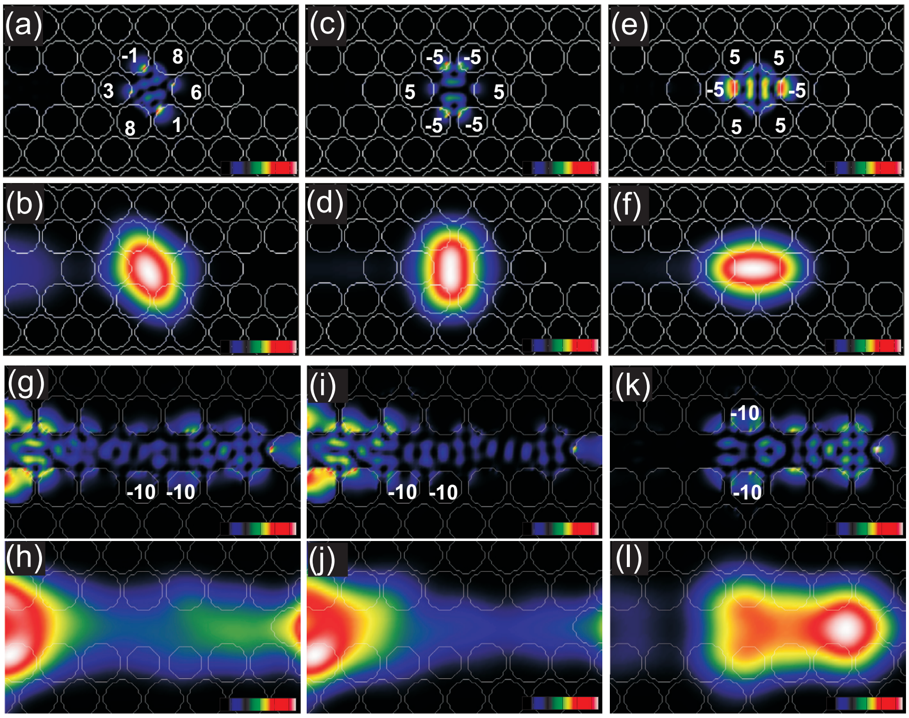

Figure 11.20: (a)–(f): Top pictures show the 2D FDTD model of field intensity and the percentage change in the hole size near the cavity. Bottom pictures show the simulated measurement with a tip aperture of 1.4 μm. (g)–(l): Top pictures show the 2D FDTD model of field intensity and the percentage change in the hole size near the waveguide. Bottom pictures show the simulated measurement with a tip aperture of 1.4 μm. Parameters used in this model are $r/a = 0.437$, n=3.43 and $a = 1.5$ μm. Dimensionless frequencies are (a,b) 0.3939, (c,d) 0.3746, (e,f) 0.3765, (g,h) 0.3886, (i,j) 0.3886, and (k,l) 0.3931

diameter is indicated in the figures. Figures 11.20b, d and f display the intensity distribution after the consideration of a finite SNOM resolution. In the same manner, the properties of light in the waveguide can also be affected by deviations of pore diameters surrounding the waveguide. Figure 11.20g–l show three examples of light propagation in structures with only two pores being 10% smaller than other holes along the waveguide. The substantial tilt angles of the resonator mode and the sensitive response of the intensity distribution inside the waveguide, due to very small modifications of the geometry, are impressive. Considering that none of the existing fabrication methods are capable of achieving 100% uniformity of pore geometry, these numerical studies show that the details of light propagation may vary from device to device in a substantial manner. SNOM measurements could reveal the subtle differences.

Another interesting aspect of the SNOM image in Figure 11.19d, is that the light intensity drops dramatically at the surface of the second waveguide. To recover this behavior, we performed three–dimensional FDTD calculations. Figure 11.21a shows the intensity distribution at the PhC–air interface for a structure where two holes surrounding the microcavity and two holes along the input waveguide, are taken to be 10% smaller than the nominal value. The in-depth intensity distribution in the yz–plane along the middle of the waveguides and the point defect is displayed in Figure 11.21b. After interacting with the point defect, the light is pushed downward in the second waveguide so that there is much less light at the surface of the PhC, in agreement with our experimental observation.

Figure 11.21c plots the intensity distribution on the upper surface after convolution with a Gaussian profile of FWHM 1.4 μm corresponding to about $\lambda/3$. The outcome has a striking resemblance to Figure 11.19d. The mode is clearly tilted. There are intensity modulations in the waveguide and there is no significant amount of light in the second waveguide. The very good quantitative agreement between the two becomes clear in Figures 11.21d and 11.21e, where we plot two cross–sections corresponding to those shown in Figures 11.21c and 11.19d. Nevertheless, not all aspects of the experimental observations could be recovered. For example, the deflection of light to one side by a few hundred nanometers is not reproduced, the tilt angle of the mode is not identical to the SNOM image, and a very small intensity asymmetry within the microcavity spot remains unexplained. The lack of a full quantitative match between experiment and theory lies in the practical difficulties of three–dimensional calculations that are very time consuming for deep samples.

The PbSe detectors used in this work are not very sensitive. The measurement noise is, however, so low that a signal–to–noise ratio greater than 100 is obtained. Furthermore, background scattering is insignificant in our experiments. The cross–sections shown in Figures 11.21c and d allow us to put a lower limit of 20 to the signal–to–background ratio. This low background is a convincing indication that the field on the upper surface of the PC is evanescent and that although our deep photonic crystal does not confine light in the third dimension, we do not detect propagating fields along the z–axis at the PC–air interface. To this end, we believe that even at a moderate resolution of $\lambda/3$, the SNOM image of Figure 11.19d

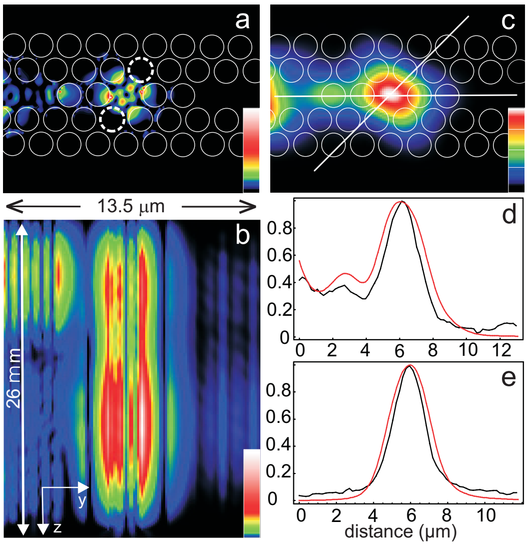

Figure 11.21: a) 3D FDTD model of the field intensity at the crystal surface with the indicated holes being 10%, smaller than nominal value and the waveguide configured as shown in Figure 11.20i. b) 3D FDTD model of the field intensity as a function of depth through the crystal. Cross section is taken along the centre of the structure. c) Modelled intensity after convolution with 1.4 μm detection window. Images d) and e) show a comparison of theoretical and experimental cross–sections along the waveguide and diagonal to the waveguide respectively. Black is experimental data, red is theoretical. From [39].

provides features that could reveal small variations of the PhC structure from its nominal parameters.

Other recent experiments have also studied PhC microcavities with SNOM in the collection mode. Gerard et al. [40] examined a hexagonal ring cavity of fairly large area using uncoated fibre tips. Shin et al. [41] probed a large area PhC laser also with uncoated tips, while Okamoto et al. [42] have imaged the light distribution around a point defect using apertured tips. These experiments took advantage of the near infrared luminescence of internal light sources such as quantum wells. The active region is optically pumped and the luminescence light is sent to a detector via the SNOM tip and spectral filters. Okamoto et al. could examine the polarization dependence of nondegenerate modes of their microcavity and also used the SNOM tip for the near–field excitation of the luminescence. When working with internal light sources, one should bear in mind, that although the high index of refraction of semiconductor material keeps most of the luminescence within the structure, a considerable amount of light can escape perpendicular to the PhC face. This introduces a certain level of propagating background light that adds to the signal obtained from evanescent fields, deteriorating the signal–to–noise ratio in this configuration. This issue is of much less concern when the active medium undergoes lasing action. Indeed, Shin et al. have performed extensive far–field and near–field studies of the laser modes in a large area PhC microcavity. These authors used uncoated fibre tips in order to minimize the influence of the tip (see Section 11.4) and investigated the intensity distribution in different modes at different emission wavelengths.

11.4 Manipulating photonic devices with SNOM

The last issue that we address, is concerned with the question of whether the tip perturbs the device operation. The short answer is that it certainly could, but mostly it does not. The volume of the SNOM probe inserted in the evanescent field is of the order of $(100\ \mathrm{nm})^3$. If the scattering caused by this nano–object is comparable or larger than the other types of loss in the system, we can expect a considerable change in the performance of the device during the measurement. In order to minimize the perturbation, it is helpful to use finer tips which are of course also desirable due to the higher spatial resolution they offer. This in turn requires a sensitive detection since the signal strength drops rapidly as the tip size is reduced.

A concrete example of device perturbation due to SNOM can be given in the case of silica microspheres. In Figure 11.22a, we see how a 2 micron–sized tip can degrade the quality factor of a fundamental mode ($l = m$). Figure 11.22b shows how the insertion of a fine tip into the evanescent fields at the sphere surface, could do no harm for a Q of 10^8 [76]. In the same spirit, a certain tip perturbs a mode with a larger volume less than another mode with the same quality factor, but a smaller volume.

In addition to introducing losses, the insertion of a small object changes the local index of refraction and therefore the optical path which could in turn modify the frequency spectrum. Figures 11.22c and d display examples of such an effect when a 1 μm tip is positioned at different regions of two high–Q WGM modes with $l = m$ and $l - m = 1$ [52]. The horizontal axis denotes the WGM resonance frequency, the vertical axis shows the scan distance in the $\vec{\theta}$ direction. The gray–scale indicates the intensity detected through the tip. The resonance frequency is clearly shifted when the tip is placed at the antinode.

In the case of photonic crystals, there are no concrete experimental studies of the tip influence to this date. For imaging purposes, it is certainly advantageous to use fine tips. The tip influence will be noticable especially when light is confined to a very small region because then the local light intensity increases, and the ratio of the tip scattering rate to other losses becomes more important. This could be the case for single point defect microcavities of very high Q in slab photonic crystals. Measurements on extended structures such as waveguides, on the other hand, should not pose serious problems.

The influence of a dielectric tip could also be used in an advantageous configuration. Here it might be possible to fine–tune the PhC spectra, by introducing a tip. Figure 11.23a depicts the schematic arrangement of a thought experiment where a silicon tip is used to introduce a local defect. The depth and the size of the tip could then control the extent of the perturbation. The combination of such configurations involving scanning probe techniques such as AFM, could offer attractive opto–mechanical devices.

11.5 Conclusion

The results presented here show that SNOM has a vital role to play when it comes to characterizing photonic crystal devices. The light inside a photonic crystal is modulated at the subwavelength scale and SNOM is the only technique that can actually image these behaviours. The key advantage of being able to resolve such fine detail, is being able to compare experimental results with numerical models directly. Another important feature is the ability to measure from the surface of the crystal, thereby allowing measurement of point–to–point loss. We believe, furthermore, that SNOM is sensitive enough to demonstrate optical effects due to the tiny, but inevitable, imperfections in device fabrication. Direct measurement of these effects will allow refinement and optimization of device design. Finally, experiments carried out so far on silica microspheres and ridge waveguide structures, point the way for future applications to photonic crystal structures involving phase sensitive measurements and combinations of spectroscopy and microscopy.

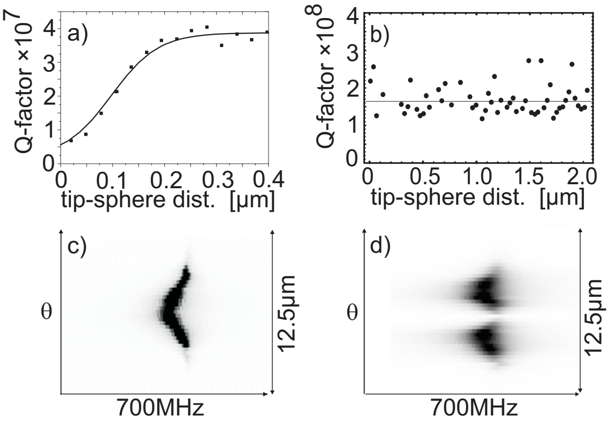

Figure 11.22: a) An uncoated fibre of diameter 2 micrometer affects the quality factor of a fundamental WGM when it is placed within the evanescent range of the sphere surface. b) A fine fibre tip with a radius of curvature of about 100 nm leaves the Q unchanged. c–d) The introduction of a 1 μm fibre tip in the intensity maxima of WGMs results in tuning their resonance frequencies. From [52, 76].

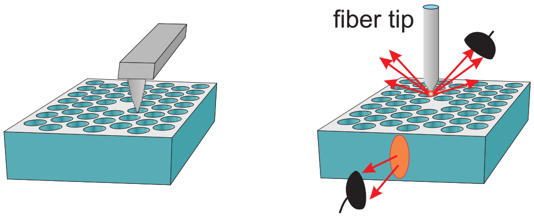

Figure 11.23: a) Arrangement for manipulating the photonic crystal with an AFM tip. b) Arrangement for coupling a nano–emitter mounted at the end of a tip to a photonic crystal microcavity.

The applications of scanning probe techniques to photonic crystals is still in its infancy. Aside from imaging the flow of light, there are many modes of operation yet to be explored. One such possibility is the direct manipulation of photonic crystal devices using a local probe. This could lead to active control of devices by creating or removing defects on demand (see Figure 11.23a). A second path to follow would be the application of SNOM techniques to control the coupling of atoms and light. Figure 11.23b sketches a possible arrangement where the a tip is used to position a nano–emitter [77,78] with respect to a photonic crystal microcavity, where cavity QED effects may be observable. Similar experiments on silica microspheres have already begun to bear fruit in our laboratories [79].

Acknowledgements

We are grateful to Albert Birner, Ralf Wehrspohn and Ulrich Gösele for collaborating on PhCs made of macroporous silicon. We also thank Robert Wüest, Robert Franck and Daniel Erni at ETH for providing us with InP-based slab PhCs. We acknowledge many fruitful discussions with Mario Agio and Costas M. Soukoulis and thank Wolfgang Stumpf for help with some of the recent measurements. We thank Niek van Hulst and Sergei Bozhevolnyi for kindly providing us with the artwork of their results. Finally, we are grateful to the Deutsche Forschungsgemeinschaft (DFG) for the generous support of our research.

References

[1] D. W. Pohl, W. Denk and M. Lanz, Appl. Phys. Lett., 44, 651 (1984).
[2] A. Lewis, M. Isaacson, A. Harootunian and A. Muray, Ultramicroscopy, 13, 227 (1984).
[3] R. Toledo-Crow, P. C. Yang, Y. Chen and M. Vaez-Iravani, Appl. Phys. Lett, 60, 2957 (1992).
[4] E. Betzig, P. L. Finn and J. S. Weiner, Appl. Phys. Lett, 60, 2484 (1992).
[5] E. Betzig and R. J. Chichester, Science, 262, 1422 (1993).
[6] M. A. Paesler and M. P. J, Near-Field Optics: Theory, Instrumentation, and Applications, Wiley-Interscience (1997).
[7] V. Sandoghdar, Proc. of the International School of Physics, IOS Press Amsterdam, pages 65–119 (2001).
[8] J. W. P. Hsu, Mat. Sci. Eng. R, 33, 1 (2001).
[9] J. J. Greffet and R. Carminati, Prog. Surf. Sci., 56, 133 (1997).
[10] D. W. Pohl, in C. J. R. Sheppard and T. Mulvey, eds., Advances in Optical and Electron Microscopy, pages 243–312, Academic Press, London (1991).
[11] E. Abbe, Archiv. f. Mikroskopische Anat., 9, 413 (1873).
[12] K. Iizuka, Elements of photonics, volume 1, Wiley-Interscience (2002).
[13] K. Karrai and R. D. Grober, Appl. Phys. Lett., 66, 1842 (1995).
[14] F. Zenhausern, M. P. O'Boyle and H. K. Wickramasinghe, Appl. Phys. Lett., 65, 1623 (1994).

[15] R. C. Reddick, R. J. Warmack and T. L. Ferrell, Phys. Rev. B, 39, 767 (1989).
[16] D. Courjon, K. Sarayeddine and M. Spajer, Opt. Comm., 71, 23 (1989).
[17] A. G. Choo, H. E. Jackson, U. Thiel, G. N. D. Brabander and J. T. Boyd, *Appl. Phys. Lett.*, 65, 947 (1994).
[18] J. C. Knight, N. Dubreuil, V. Sandoghdar et al., Opt. Lett., 20, 1515 (1995).
[19] J. C. Knight, N. Dubreuil, V. Sandoghdar et al., Opt. Lett., 21, 698 (1996).
[20] S. Bourzeix, J. M. Moison, F. Mignard et al., Appl. Phys. Lett., 73, 1035 (1998).
[21] M. L. M. Balistreri, J. P. Korterik, L. Kuipers, and N. F. van Hulst, Phys. Rev. Lett, 85, 294 (2000).
[22] M. L. M. Balistreri, H. Gersen, J. P. Korterik et al., Science, 294, 1080 (2000).
[23] H. Gersen, J. P. Korterik, N. F. van Hulst and L. Kuipers, Phys. Rev. E, 68, 026604 (2003).
[24] C. Lienau, A. Richter, A. Klehr and T. Elsaesser, Appl. Phys. Lett., 69, 2471 (1996).
[25] I. Hörsch, R. Kusche, O. Marti, B. Weigl and K. J. Ebeling, J. Appl. Phys., 79, 3831 (1996).
[26] M. L. M. Balistreri, D. J. W. Klunder, F. C. Blom et al., Opt. Lett., 24, 1829 (1999).
[27] G. H. Vander-Rhodes, B. B. Goldberg, M. S. Ünlü, S.-T. Chu and B. E. Little, IEEE J. Selec. Top. Quant. Elect., 6, 46 (2000).
[28] J. D. Mills, C. W. J. Hillman, W. S. Brocklesby and B. H. Blott, Appl. Phys. Lett., 75, 4058 (1999).
[29] E. B. McDaniel, J. W. P. Hsu, L. S. Goldner et al., Phys. Rev. B, 55, 10878 (1997).
[30] G. W. Bryant, E. L. Shirley, L. S. Goldner et al., Phys. Rev. B, 58, 2131 (1998).
[31] E. Flück, N. F. van Hulst, W. L. Vos and L. Kuipers, Phys. Rev. E, 68, 15601 (2003).
[32] G. H. Vander-Rhodes, M. S. Unlu, B. B. Goldberg, J. M. Pomeroy and T. F. Krauss, IEE Proc. Optoelectr., 145, 379 (1998).
[33] P. L. Phillips, J. C. Knight, B. J. Mangan et al., J. Appl. Phys., 85, 6337 (1999).
[34] A. L. Campillo, J. W. P. Hsu, C. A. White and and A. Rosenberg, J. Appl. Phys., 89, 2801 (2000).
[35] D. R. Smith, R. Dalichaouch, N. Kroll et al., J. Opt. Soc. Am. B, 10, 314 (1993).
[36] S. I. Bozhevolnyi, V. S. Volkov, J. Arentoft et al., Opt. Commun., 212, 51 (2002).
[37] S. I. Bozhevolnyi, V. S. Volkov, T. Søndergaard et al., Phys. Rev. B, 66, 235204 (2002).
[38] P. Kramper, A. Birner, M. Agio et al., Phys. Rev. B, 64, 233102 (2001).
[39] P. Kramper, M. Kafesaki, C. M. Soukoulis et al., To appear in Opt. Lett. (2003).
[40] D. Gerard, L. Berguiga, F. de Fornel et al., Opt. Lett., 27, 173 (2002).
[41] Dong-Jae-Shin, Se-Heon-Kim, Jeong-Ki-Hwang et al., IEEE J. Quantum Elect., 38, 857 (2002).
[42] K. Okamoto, M. Lončar, T. Yoshie et al., Appl. Phys. Lett., 82, 1676 (2003).
[43] B. Buchler, P. Kramper, M. Kafesaki, C. M. Soukoulis and V. Sandoghdar, To be published in IEICE Trans. Elect. (2004).
[44] H. Kimble, Physica Scripta, T76, 127 (1998).
[45] A. Kiraz, C. Reese, B. Gayral et al., J. Opt. B, 5, 129 (2003).
[46] C. F. Bohren and D. R. Huffman, Absorption and Scattering of Light by Small Particles, John Wiley and Sons (1983).
[47] M. L. Gorodetsky, A. A. Savchenkov and V. S. Ilchenko, Opt. Lett., 21, 453 (1996).
[48] V. B. Braginsky, M. L. Gorodetsky and V. S. Ilchenko, Phys. Lett. A, 137, 393 (1989).
[49] L. Collot, V. Lefevre-Seguin, M. Brune, J. M. Raimond and S. Haroche, Eur. Phys. Lett., 23, 327 (1993).
[50] D. W. Vernooy, A. Furusawa, N. P. Georgiades, V. S. Ilchenko and H. J. Kimble, Phys. Rev. A, 57, R2293 (1998).
[51] D. S. Weiss, V. Sandoghdar, J. Hare et al., Opt. Lett., 20, 1835 (1995).
[52] S. Götzinger, O. Benson and V. Sandoghdar, Appl. Phys. B, 73, 825 (2001).
[53] S. Götzinger, S. Demmerer, O. Benson and V. Sandoghdar, J. Microsc., 202, 117 (2001).
[54] M. Vaez-Iravani and R. Toledo-Crow, Appl. Phys. Lett., 62, 1044 (1993).
[55] J. Walford, K. Nugent, A. Roberts and R. Scholten, Appl. Opt, 38, 3508 (1999).
[56] P. L. Phillips, J. C. Knight, J. M. Pottage, G. Kakarantzas and J. St. P. Russell, Appl. Phys. Lett., 76, 541 (2000).
[57] M. Lončar, D. Nedeljković, T. P. Pearsall et al., Appl. Phys. Lett., 80, 1689 (2002).

[58] M. Born and E. Wolf, Principles of Optics: Electromagnetic Theory of Propagation, Interference and Diffraction of Light, 7th edition (1999).
[59] M. Mansuripur, Classical Optics and its Applications, Cambridge University Press (2002).
[60] S. Fan, I. Appelbaum and J. D. Joannopoulos, Appl. Phys. Lett., 75, 3461 (1999).
[61] A. Mekis, J. C. Chen, I. Kurland et al., Phys. Rev. Lett., 77, 3787 (1996).
[62] S.-Y. Lin, E. Chow, V. Hietala, P. R. Villeneuve and J. D. Joannopoulos, Science, 282, 274 (1998).
[63] E. Chow, S. Y. Lin, J. R. Wendt, S. G. Johnson and J. D. Joannopoulos, Opt. Lett., 26, 286 (2001).
[64] A. Chutinan, M. Okano and S. Noda, Appl. Phys. Lett., 80, 1698 (2002).
[65] H. Benisty, S. Olivier, C. Weisbuch et al., IEEE J. Quant. Electon., 38, 770 (2002).
[66] R. Wüest, P. Strasser, M. Jungo et al., Microelectron. Eng., 67-68, 182 (2003).
[67] H. Benisty, C. Weisbuch, D. Labilloy et al., J. Lightwave. Technol., 17, 2063 (1999).
[68] A. Talneaua, M. Mulot, S. Anand and Ph. Lalanne, Appl. Phys. Lett., 82, 2577 (2003).
[69] T. Yoshie, J. Vučković, A. Scherer, H. Chen and D. Deppe, Appl. Phys. Lett., 79, 4289 (2001).
[70] Y. Akahane and T. Asano and B.-S. Song and S. Noda, Nature, 425, 6961 (2003).
[71] K. Srinivasan, P. E. Barclay, O. Painter et al., Appl. Phys. Lett., 83, 1915 (2003).
[72] V. Lehmann, J. Electrochem. Soc., 140, 2836 (1993).
[73] A. Birner, U. Grüning, S. Ottow et al., Phys. Stat. Sol. A, 165, 111 (1998).
[74] J. Schilling, R. B. Wehrspohn, A. Birner et al., J. Opt. A: Pure Appl. Opt., 3, S121 (2001).
[75] A. Birner, Ph.D. thesis, Martin-Luther University at Halle-Wittenberg (2000).
[76] S. Götzinger, O. Benson and V. Sandoghdar, Opt. Lett., 27, 80 (2002).
[77] J. Michaelis, C. Hettich, J. Mlynek and V. Sandoghdar, Nature, 405, 325 (2000).
[78] S. Kühn, C. Hettich, C. Schmitt, J.-P. Poizat and V. Sandoghdar, J. of Microscopy, 202, 2 (2001).
[79] S. Götzinger, L. de S. Menezes, A. Mazzei et al. (Submitted 2003).

12 Application of photonic crystals for gas detection and sensing

Ralf B. Wehrspohn[1]*, Stefan L. Schweizer, Jörg Schilling, Torsten Geppert, Cecile Jamois, Regine Glatthaar, Peter Hahn, Arno Feisst, and Armin Lambrecht*

Abstract

Gas sensors are widely used in technical, medical and environmental applications: for the control of exhaust gases (NO_x), the monitoring of respiratory gases (CO_2), and the surveillance of air quality (O_3), respectively. Optical gas sensors make use of the characteristic absorption lines in the mid infrared wavelength region (3–20 μm).

Spectroscopy–based sensor techniques play a key role in this market but with the major drawback of high costs for such systems. In this chapter, we present the scheme of an optical gas sensor based on photonic crystals for the spectroscopic detection of gases [1]. The advantage of such systems over conventional ones could be the possibility of miniaturization, integration, batch processing and thus cost reduction. Macroporous silicon is intended to be used as photonic crystal material, from which structures for optical detection in the mid infrared region can be fabricated with great reproducibility.

12.1 Principle

An optical sensor consists of three basic parts: the radiation source, the absorption section, and the detector. For typical gas sensors, the length of the absorption section is in the range of 10 to 50 cm to obtain a reasonable signal–to–noise–ratio. This results in a relatively large volume with several practical limitations: first it is sometimes difficult to fill the detection volume (e.g. when monitoring breathing of babies), second, the energy consumption for keeping the temperature of an isolated system stable is very high (e.g. random breath testing), third, the dynamics of the measurements is poor (for high repetition control).

To reduce the dimensions of the absorption section, the effective light path between the light source and the detector has to be increased. This can be done with mirrors, i.e., using White or Herriott–type multipass cells or by exploitation of the multiple internal reflection in a photonic crystal (Fig. 12.1). This may, however, result in mechanical instabilities of the system and thus alignment problems of the light path.

---

[1] Corresponding author: e-mail: wehrspohn@physik.uni-paderborn.de, Phone: +49 5251 602748, Fax: +49 5251 603247

Photonic Crystals. Edited by K. Busch, S. Lölkes, R. B. Wehrspohn and H. Föll
Copyright © 2004 Wiley-VCH Verlag GmbH & Co. KGaA
ISBN: 3-527-40432-5

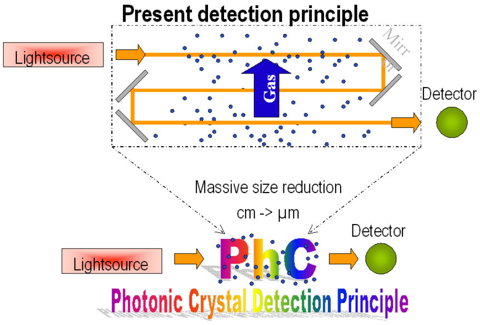

Figure 12.1: Schematic setup of a conventional optical gas sensor with internal mirrors (top) and a photonic crystal gas sensor (bottom). By using photonic crystals, the length of the gas absorption cell can be reduced dramatically.

At the band edges of a photonic crystal, there is the strong spectral dependence of the group velocity. Near the band edges of 1D, 2D and 3D PhCs the bands are extremely flat. Therefore, the group velocity v_g of the light, which is defined as the slope of the dispersion relation, vanishes as the frequency ω approaches the band edge.

$$v_g = \frac{\partial \omega}{\partial k} \tag{12.1}$$

This strong dispersion of the group velocity can be exploited for components like prisms or even super–prisms [2]. A beam with a small frequency spread $\Delta\omega$ is split into its frequency components which are distributed in a fan with a wide angle spread Δdeg. The physical origin for this small group velocity is easily understood considering a 1D PhC. The multiple reflections at the interfaces of the different materials extend the path length the photon travels through the structure. Thus, the effective path for a photon with a mean frequency close to the band edge is much longer than in a homogeneous structure. This causes a smaller mean velocity of the photon which corresponds to the observed small group velocity. Note, that only at the band edge, do the multiple reflections interfere coherently, resulting in a standing wave.

This concept has recently been verified by Notomi et al. who showed experimentally that $c/v_g \approx 50$, i.e, 2% of the vacuum velocity of light in a photonic crystal waveguide with a low group velocity [3]. The small group velocity extends the time the photons need to travel through the structure. Thus, the probability of interactions between the light field and the atoms is enhanced. This effect is the basis for a proposed band edge laser [4]. The enhanced interaction time results in an increased gain. Additionally, the low group velocity causes a high effective refractive index which increases the reflection at the interface PhC/surrounding air considerably. Both effects support amplified spontaneous emission and lasing which was experimentally verified for a 3D PhC [5] and for a flat–band region in a 2D PhC [6]. The increased interaction time at the band edges due to the small group velocity is also responsible for enhanced absorption. This is also connected with the field distribution above and below the gap. The field energy of the bands below the gap (low ω) is concentrated in the high index region while the light field above the gap (high ω) peaks in the low index region. Absorption is enhanced if the field is mainly concentrated in the absorbing material. This was theoretically calculated for 1D and 2D PhCs [7]. The appearance of small group velocities is not limited to the band edges. In 2D and 3D PhCs, flat bands can exist. The group velocity attached to them can be small over a wide range of the Brillouin zone.

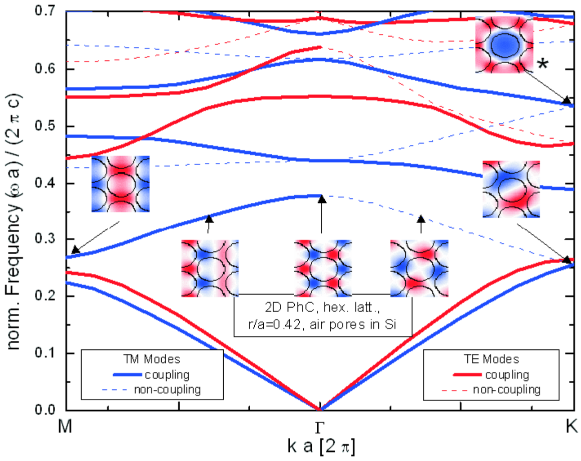

Figure 12.2: Band structure of a 2D silicon photonic crystal (hexagonal lattice of air holes, r/a = 0.42, $\epsilon = 11.6$). The field distribution of some bands are shown. Dashed lines correspond to bands with odd symmetry, solid lines correspond to bands with even symmetry. Only bands with even symmetry can couple to plane waves excitations. The highlighted field distribution (*) corresponds to an air band with a low group velocity and even symmetry.

Figure 12.2 shows the band structure of a 2D silicon photonic crystal, where specific low–v_g air bands with different symmetries are highlighted. Note, that there are hardly any configurations where for both polarizations, low–v_g air bands with even symmetry occur at the same frequency, so that the device has to work with one polarization only. This could be advantageous for a future device, since the other polarization might then be used as reference signal.

A drawback of this non–coherent reduction of the group velocity in contrast to cavity structures [8], is that low–v_g bands also have a high insertion reflectivity. In the linear regime, the effective refractive index can be expressed as

$$n \approx c\frac{\partial k}{\partial \omega} = \frac{c}{v_g} \tag{12.2}$$

Thus, the lower v_g, the lower the efficiency to couple light into the structure. Therefore, an effective taper is mandatory for this device. The straight–forward approach would be an adiabatic taper, where the lattice constant is increased towards the interfaces. In the band structure of Fig. 12.2, this could be understood as coupling to the device in a region where the effective refractive index is close to that of the effective medium. Adiabatically reducing the lattice constant for constant porosity, then tapers into the low–v_g modes.

12.2 Realizations with 3D photonic crystals

As proof of principle, we tested all these ideas with our 3D macroporous silicon samples [12]. These have the advantage that the modulation period along the Γ–A direction can be adjusted after lithography by the electrochemical etching (as described in Chapter 4 of Wehrspohn et al.).

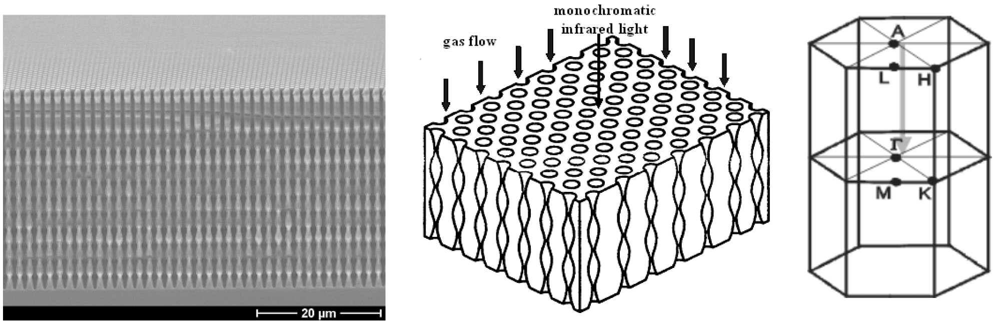

Figure 12.3: Left: Scanning electron micrograph of the 3D photonic crystal with 10 modulation periods (parameters: 2D hexagonal lattice with $a = 1.5$ μm, modulation period of sinusoidal modulation of 3.2 μm, and modulation amplitude from $r/a = 0.27$ to $r/a = 0.42$). Center: Schematic setup of the measurement. The interference effect along the pore axis is used. This is the same direction as of that of the gas flow. Right: Brillouin-zone of the 3D simple hexagonal photonic crystal.

Figure 12.3 shows an SEM image of the 3D photonic crystal, the corresponding schematic measurement setup and Brillouin zone including the high–symmetry points of a simple hexagonal crystal [9]. We have designed 3D–photonic crystals based on the structure in Fig. 12.3 where the first upper band edge in the Γ–A direction coincides with an absorption line of the gas intended to be used for the test measurements (NH_3: 972 cm^{-1} and SF_6: 948 cm^{-1}, respectively). The calculations have been done by the 3D plane wave expansion method taking into account the slightly quadratic pore shape (Fig. 12.4). A squared pore shape in a hexagonal lattice leads to a reduced overall symmetry [2] and results in a small birefringence when light propagates along the modulated pore axis ($\Gamma - A$) (see Fig. 12.4) [10].

Fixing the lattice constant of the lithographically defined 2D lattice at $a = 1.5\mu$m, we varied the modulation period and amplitude of the macropores with depth. For a modulation period of 3.2 μm and a modulation amplitude from $r/a = 0.27$ to $r/a = 0.42$, the upper band edge for the Γ–A direction coincides with the NH_3 absorption line. These structures were then optically characterized by IR measurements. From the Fabry–Perot resonances in the air band, we determined the group velocity of light propagating in the air holes. Since the

---

[2] The symmetry can be described by a base-centered orthorhombic symmetry. The Brillouin zone can still be represented by a 3D hexagon (see Fig. 12.3). However, due to the lower symmetry, the degeneracy of the L and H points is removed. There are now L_1 and L_2 as well as H_1 and H_2 symmetry points [10].

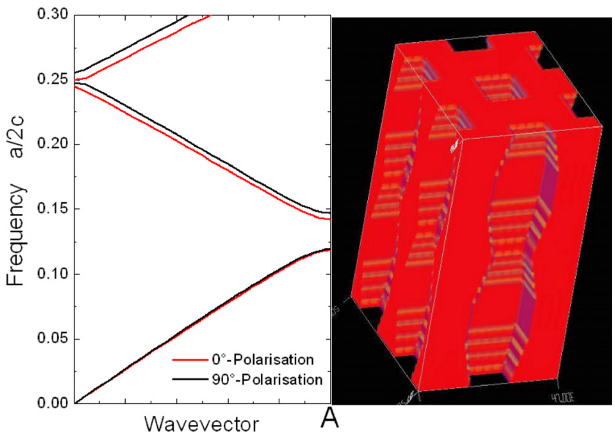

Figure 12.4: Left: band structure in Γ–A direction of the 3D photonic crystal consisting of modulated air pores in silicon. Due to the squared pore shape, the symmetry of the crystal is reduced and the two polarizations are not degenerate anymore. Parameters: $a = 1.5$ μm, modulation in Γ–A direction is 3.2 μm, modulation amplitude of pore radius from $r/a = 0.27$ to $r/a = 0.42$. Right: computer generated profile of the dielectric constant of the 3D photonic crystal used in the calculation.

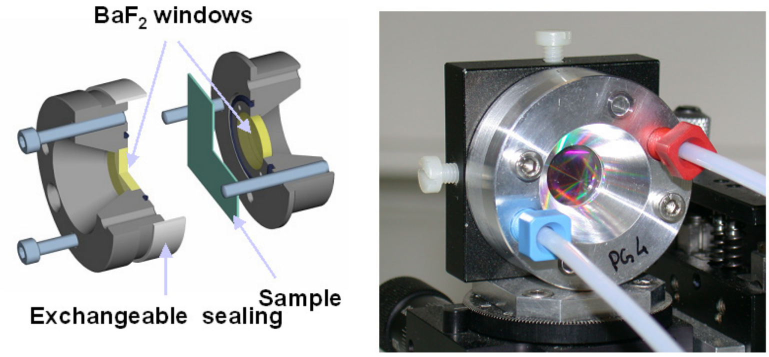

Figure 12.5: Left: Design of our gas cell containing of exchangeable sealing and BaF_2 windows. Right: Photograph of the cell containing a 3D photonic crystal.

structure had only 10 modulation periods, we were able to extract group velocities down to 0.3c [10].

For absorption measurements, a gas cell (Fig. 12.5) was constructed and fabricated which allowed an easy adaptation to different sample geometries with minimum space between the sample and the front and rear BaF_2–window respectively (a minimum free space is important, otherwise the effects due to the PhC would probably be obscured by the absorption effects of the gas in the free space). The cell can easily be adapted to an FT–IR spectrometer (Bruker IFS 66v/S) for spectral characterization and the cell with the sample can be rotated as well as tilted.

For optical testing, a 3D photonic crystal with 10 modulation periods was prepared and fixed in the gas cell (Fig. 12.5). We optimized the modulation period in the Γ–A direction in such a way that the airband spectrally overlaps with the absorption line of SF_6 (948 cm^{-1}). Figure 12.6a shows the transmission of the optimized structure. 3D simulation of the final refractive index modulation of our structure, as well as the corresponding band structure are shown in Fig. 12.4. The numerical calculations agree very well with the measured transmission. In the next step, SF_6 was infiltrated into the pores and the transmission was measured and normalized to the transmission of N_2 in the pores, which has no absorption line in this spectral range. The spectrum obtained (black) is rather noisy which results from the low coupling efficiency due to the high effective refractive index. In the next step, we prepared straight pores with no modulation along the pore axis but with the same effective porosity and measured, as reference, again the transmission with SF_6 and N_2 (green curve in Fig. 12.6). At the wavelength of 948 cm^{-1}, there is no difference in absorption in contrast to what is expected from the lowering of the group velocity.

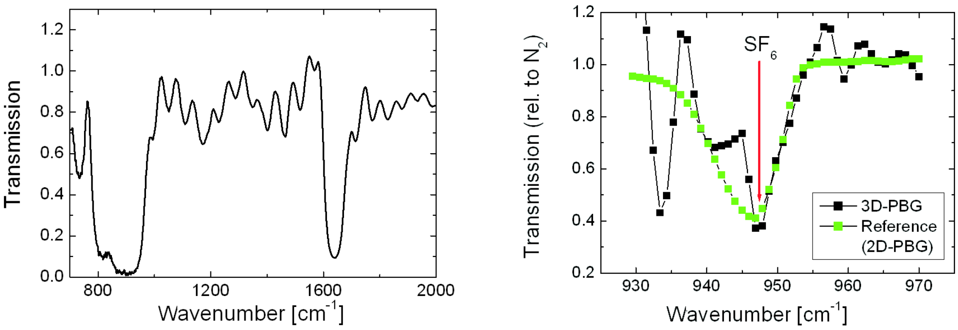

Figure 12.6: Left: Transmission through the 3D photonic crystal under vacuum. Right: Transmission of the 3D photonic crystal filled with SF_6, normalized to that filled with N_2 and compared to a 2D photonic crystals with the same porosity in the direction of the pores.

The non-occurrence of the expected effect can be understood by analyzing Eqs. (12.1) and (12.2). Since in the linear approximation, the group velocity is reduced in the same way as the refractive index increases, and the same is true for the intensity enhancements E^2 ($E^2 \propto v_g^{-2}$) and transmission T ($T \propto n^{-1}$ for $n \gg 1$), we do not expect any significant difference between the two spectra.

Therefore, for a possible device, a taper is necessary to adiabatically decrease the effective refractive index. This could be done in the simplest way by continuously changing the modulation period at the interfaces. Figure 12.7 shows a first realization and the corresponding points in the band structure. By starting at the interface with an initial 10% increase in the modulation period, the effective refractive index is close to the effective medium index of this structure ($n \approx 2$). By continuously reducing the modulation period to the optimum one for

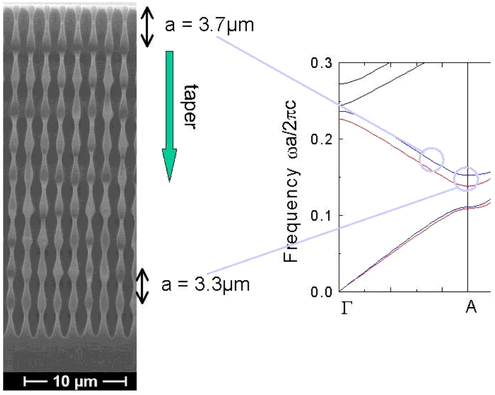

Figure 12.7: 3D photonic crystal with adiabatic taper by reduction of the modulation period. The corresponding points in the band structure are shown on the right. For a modulation period of 3.7 μm, the effective refractive index is that of the effective medium. By continuously reducing the modulation period, light is coupled to the low v_g region.

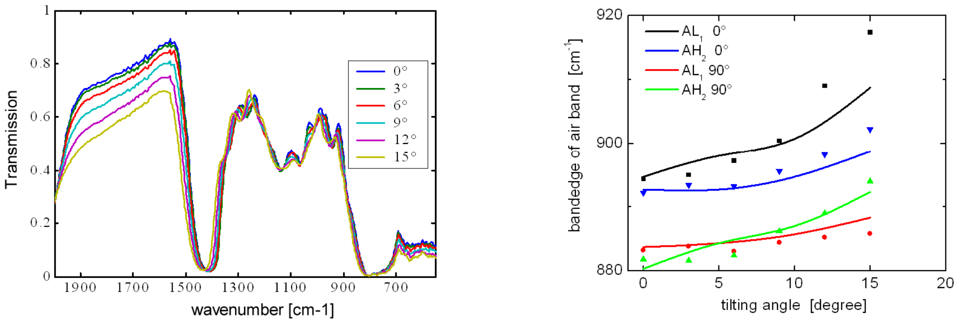

Figure 12.8: Left: Angle-dependent transmission measurements through the 3D macroporous silicon photonic crystal. Right: The change of air band edge at around 890 cm^{-1} (for both tilting directions and both polarizations) as a function of the tilt angle (points) and comparison to theory (lines).

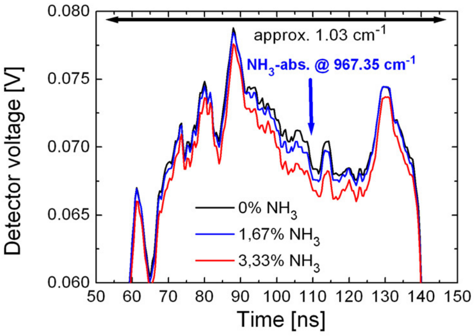

Figure 12.9: Transmission signals of a QCL though a 3D photonic crystals (band edge around 890 cm^{-1}) filled with three different NH_3 concentrations. Because of the adiabatic heating of the active region during short pulses, the emitted wavelength of the QCL is proportional to the time (typical tuning rates are -0.01 cm^{-1}/ns).

enhanced absorption (here within 5 modulation periods), the refractive index is adiabatically reduced and high reflectivities can, in principle, be avoided.

Even though macroporous silicon can be prepared in a very controlled manner, a way to tune the bands after fabrication to exactly the point of the lowest group velocity, is required. Probably the simplest method is to use the effect of a blue-shift of the bands when tilting the device. First angle–resolved transmission measurements with a 3D crystal (one sided closed pores, 10 periods) using NH_3 (10% in N_2) as test gas, showed that the upper band edge can be shifted to higher wavenumbers by 35 cm^{-1} for a tilt angle of 15° (Fig. 12.8) . This corresponds to a relative shift of about 4% of the upper band edge and corresponds roughly to the fabrication tolerances of the macroporous etching process. Thus, the uncertainty of the wavelength of the upper band edge due to fabrication uncertainties, can be compensated by this technique. Comparison with numerical calculations shows that the trend for both high-symmetry tilting directions and both polarizations, respectively, is in good agreement with theory .

Quantum cascade lasers (QCL) are new semiconductor laser sources which are well suited for the investigation of photonic crystals in the mid to far infrared spectral region . They offer average powers in the mW range, well defined polarization states and narrow line width. QCL are successfully applied for high resolution and fast gas spectroscopy [11]. Recently, QCL emission at 3.5 THz has been reported [13]. In Fig. 12.9, a first transmission experiment using a pulsed QCL at 967.35 cm^{-1} is shown. However, because the wavelength is far from the photonic band edge in this case, no enhancement of the NH_3 absorption was observed.

12.3 Conclusion

We have presented a new concept of the photonic crystal–based compact gas absorption cell. By the overlap of an absorption line of a gas with a low group velocity air band of a photonic crystal, an increased absorption of light is possible. This effect can be understood as an incoherent field enhancement in the air pores near the air band edge of a photonic crystal. As proof of principle, we have shown our results on 3D photonic crystals. Even though we were not able to show a significant enhancement, we were able to detect the absorption of SF_6 at the air band edge of a photonic crystal. The enhancement due the low group velocity was compensated by the increased reflectivity of the structure. In future, tapers are mandatory for coupling to low group velocity modes. In addition, we presented a very simple technique to spectrally tune the air band edge. By tilting the structure up to 15° off–axis, a spectral shift of the air band edge of about 4% is possible. This is on the order of the fabrication tolerances of macroporous silicon being typically in the range of a few percent.

References

[1] F. Müller, A. Feisst, A. Lambrecht, J. Schilling, and R. B. Wehrspohn, Device and method for analysing the qualitative and/or quantitative composition of liquids, World Patent pending WO 0250514 (2002).
[2] H. Kosaka et al., J. Lightwave Technol. **17**, 2032 (1999).
[3] M. Notomi, K. Yamada, A. Shinya, J. Takahashi, C.Takahashi, and I. Yokohama, Phys. Rev. Lett. **87**, 3902 (2001).
[4] J. P. Dowling, M. Scalora, M. J. Bloemer, and C. M. Bowden, J. Appl. Phys. **75**, 1896 (1994)

[5] Yu. A. Vlasov, K. Luterova, I. Pelant, B. Hönerlage, and V. N. Astratov, J. Cryst. Growth **184/185**, 650 (1998)

[6] K. Inoue, M. Sasada, J. Kawamata, K. Sakoda, and J. W. Haus, Jpn. J. Appl. Phys. **38**, L157 (1999)

[7] V. Kuzmiak and A. A. Maradudin, Phys. Rev. B **55**, 7427 (1997)

[8] P. Kramper, A. Birner, M. Agio, C.M. Soukoulis, F. Müller, U. Gösele, J. Mlynek, and V. Sandoghdar, Phys. Rev. B **64**, 233102 (2001).

[9] J. Schilling, F. Müller, S. Matthias, R.B. Wehrspohn, U. Gösele, and K. Busch, Appl. Phys. Lett. **78**, 1180 (2001)

[10] J. Schilling, F. Müller, R.B. Wehrspohn, U. Gösele, and K. Busch, MRS Symp. Proc. **722**, L6.8 (2002)

[11] T. Beyer, M. Braun, and A. Lambrecht, J. Appl. Phys. **93**, 3158 (2003).

[12] R.B. Wehrspohn et al., Chapter 4, this volume.

[13] G. Scalari, L. Ajili, J. Faist, H. Beere, E. Linfield, D. Ritchie, and G. Davies, Appl. Phys. Lett. **82**, 3165 (2003).

13 Polymeric photonic crystal lasers

Karen Forberich, Stefan Riechel, Suresh Pereira, Andreas Gombert, Kurt Busch, Jochen Feldmann, and Uli Lemmer[1]

13.1 Introduction

The enormous progress in the field of electroluminescent conjugated polymers has led to performances of organic light–emitting devices (OLEDs) that are comparable and in some aspects superior to their inorganic counterparts [1]. Besides being a promising material for electroluminescence display applications, conjugated polymers are also well suited for being combined with photonic nanostructures. These organic semiconductors can be deposited from a liquid solution onto nanostructured substrates. In comparison to inorganic light emitting semiconductors, the use of these materials in the field of photonic crystals is much more straightforward. This is due to the fact that organic semiconductors are formed by van–der–Waals interactions rather than by covalent bonds. Thus, large internal interfaces between materials with different refractive indices (the typical situation in a photonic crystal) do not give rise to a high density of nonradiative defects that quench the emission. A particularly interesting approach towards 2D photonic crystals relies on the combination of organic semiconductors with organic surface relief gratings, fabricated by micoreplication. Two technologies that are suited for large–area, low–cost production scenarios are thus combined. In this contribution we describe the fabrication, characterization and detailed theoretical analysis of such all organic two–dimensional photonic crystal lasers (2D PhC–lasers). We start with the description of the different steps during the fabrication of the microreplicated nanopatterns in Sect. 13.2. After briefly introducing the active materials in Sect. 13.3, the lasing properties of our 2D PhC–lasers are presented in Sect. 13.4. A detailed analysis of the underlying 2D laser operation is then given in Sect. 13.5.

13.2 Fabrication of microstructured surfaces by interference lithography

The structured plastic substrates used for the polymer laser were fabricated by interference lithography and subsequent replication. Interference lithography provides the possibility to structure large areas homogeneously on a sub–micron scale, in contrast to other techniques like e–beam lithography or gray–tone lithography which only allow the fabrication of small

---

[1] Corresponding author, e-mail: uli.lemmer@lti.uni-karlsruhe.de, Phone: +49-721-608-2530, Fax: +49-721-358149

Photonic Crystals. Edited by K. Busch, S. Lölkes, R. B. Wehrspohn and H. Föll
Copyright © 2004 Wiley-VCH Verlag GmbH & Co. KGaA
ISBN: 3-527-40432-5

areas at reasonable effort. Together with the possibility to replicate a large number of plastic substrates using a master structure made of photoresist, this gives the opportunity to produce large area nanostructures at low cost.

13.2.1 Interference lithography

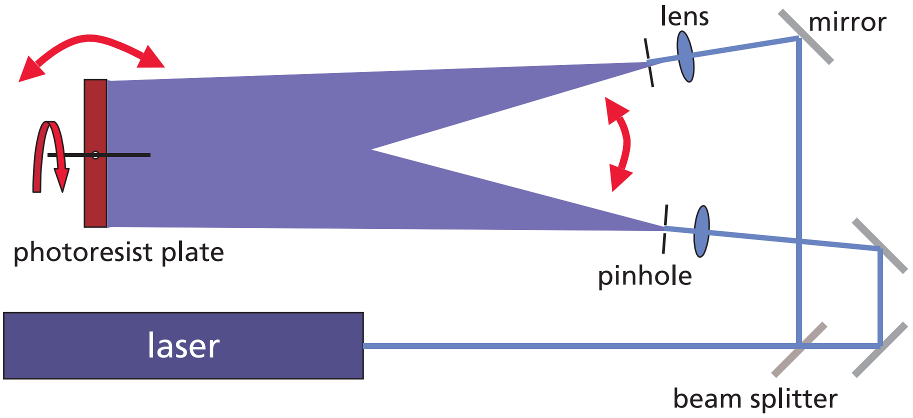

Figure 13.1: Schematic of a holographic setup with two laser beams. The beams are expanded, spatially filtered and superposed. The periodicity and the resulting pattern in photoresist can be adjusted by varying the angle between the laser beams. Patterns which are periodic in two directions can be made by two subsequent exposures and an intermediate rotation of the photoresist plate.

Interference lithography makes use of the interference pattern which is formed when two or more coherent light waves are superposed [2]. In a typical optical set–up which is shown schematically in Fig. 13.1, a laser is used as a source for ultra–violet (UV) radiation for which the photoresist is sensitive. The laser beam is split into two or more beams. Each of the beams is directed towards a substrate coated with photoresist, where the beams are superposed after being expanded and spatially filtered. After the filtering, no collimation of the laser beams was used in order to prevent parasitic interference patterns due to dust particles on additional optical components. If the position of the photoplate is sufficiently far away from the expanding lens, the expanded beams can nevertheless be approximated as plane waves. Two interfering beams produce a one–dimensional pattern with a sinusoidal intensity distribution to which the photoresist is exposed. The main challenge is to achieve stable conditions such that neither the interference pattern nor the photoresist plate moves during an exposure time of up to 10 minutes necessary to expose a 150 mm × 150 mm photoresist plate homogeneously.

After exposure, the photoresist plate is developed. During development, the exposure dose distribution according to the intensity distribution of the interference pattern is transferred into a surface relief structure. The solubility of the photoresist in the developer is changed during exposure, areas of different exposure doses resulting in areas of different removal rates. Either exposed or unexposed photoresist is removed depending on its type. This process is nonlin-

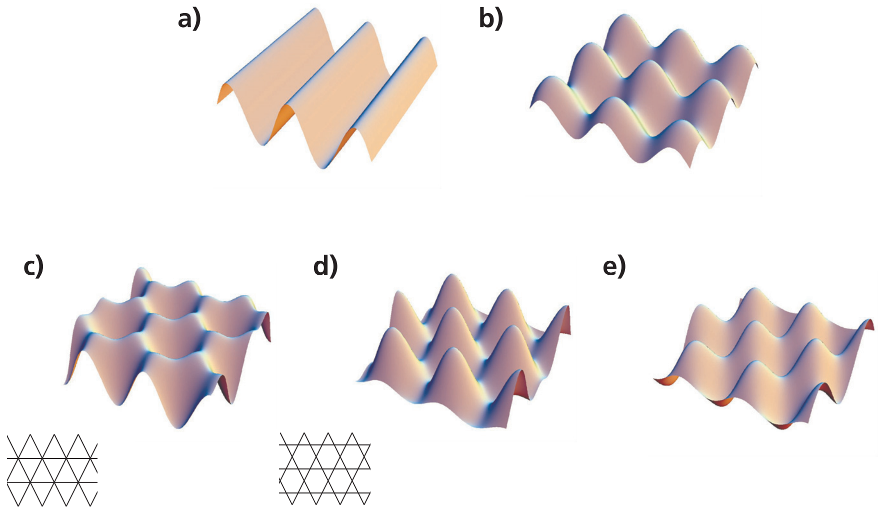

Figure 13.2: Exposure dose patterns resulting from different configurations. The insets in c) and d) show the interference maxima of the respective exposures as black lines. a) Linear pattern resulting from a single exposure, b) square pattern resulting from two consecutive exposures with a rotation of 90 degrees, c) hexagonal pattern resulting from three consecutive exposures with a rotation of 60 degrees where the interference maxima lines intersect in one point, d) hexagonal pattern resulting from three consecutive exposures where the interference minima lines intersect in one point, e) hexagonal pattern resulting from two exposures.

ear, which results in a profile that deviates from the sinusoidal intensity distribution of the interference pattern. Depending on several parameters like exposure dose, development time etc. gratings of different aspect ratios (the ratio of structure depth to structure period) can be produced [4]. The maximum aspect ratio in photoresist depends mainly on the period, for sub-micrometer structures it is about 2:1. However, the maximum aspect ratio of structures that can be replicated into polymers by the methods described below is about 1:1. The minimum aspect ratio which can be fabricated reproducibly is in the range of 0.1. For a symmetric setup in air, the periodicity Λ of the pattern depends on the laser wavelength λ_{Laser} and the angle θ between the laser beams only:

$$\Lambda = \frac{\lambda_{\text{Laser}}}{\sin\theta}$$

The theoretical lower limit for the periodicity is half the laser wavelength when the set-up shown in Fig. 13.1 is used. This theoretical limit cannot be reached in practice because at very high angles of incidence, most of the laser radiation is reflected. This would result in extremely long exposure times. We use an argon ion laser at a laser wavelength of 364 nm which is suitable to fabricate gratings with periods larger than 200 nm.

To produce two–dimensional gratings with different geometries, the substrate with the photoresist can be rotated and exposed again after the first exposure. The resulting interference patterns for different configurations are illustrated in Fig. 13.2. In addition to linear gratings,

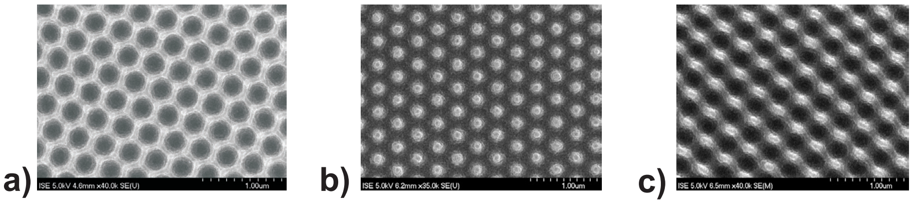

Figure 13.3: a) Photoresist pattern resulting from three consecutive exposures with a rotation of 60 degrees each time in between, resulting from the configuration in Fig. 13.2 c). b) Photoresist pattern resulting from three consecutive exposures with a rotation of 60 degrees each time in between, resulting from the configuration in Fig. 13.2 d). c) Photoresist pattern resulting from two consecutive exposures with a rotation of 60 degrees. The hexagonal symmetry is broken because of the missing third exposure.

square gratings were fabricated by a rotation of 90 degrees between two consecutive exposures and hexagonal gratings by two or three consecutive exposures with a rotation of 60 degrees at each case in between. The resulting period of the hexagonal grating is not the same as the period of the linear gratings that it consists of, but is larger by a factor of $1/\cos(30°)$.

In the case of the hexagonal gratings made by three consecutive exposures, the form of the elementary cell depends on the phase of the third exposure relative to the first two. In Figs. 13.2 c and d, two extreme cases are illustrated. The insets show the interference maxima of the three exposures as black lines. In c the respective interference maxima lines of all three exposures intersect in one point, in d all interference minima intersect in one point. The resulting interference pattern consists of holes in c and pillars in d. Examples of the pattern in photoresist corresponding to the situation in Figs. 13.2 c, d and e are pictured in Fig. 13.3. However, in the setup described above, the periodicity of the interference pattern varies over the sample because of the exposure with divergent waves. For a distance between the expanding lens and the photoresist plate of about 1 m and for a grating period of 300 nm, this results in a period variation of about 2 nm over a sample size of 10 cm $\times$ 10 cm. This leads to a situation where all possible phase differences between the three exposures – the two extreme cases shown in Figs. 13.2 c and d and everything in between – are present on the same sample. For a hexagonal grating resulting from two consecutive exposures, the pattern is constant over the whole sample, but there is no complete hexagonal symmetry due to the missing third exposure (Figs. 13.2 e and 13.3 c).

13.2.2 Replication and subsequent substrate processing

The master structures in photoresist are normally not used as embossing tools directly [3,5,6]. The standard process chain includes the replication of the master structures by electroforming into nickel. As the first step, a thin conducting layer is deposited by evaporation, sputtering or by wet chemical reduction of silver. Then, a nickel layer with a thickness in the range of 50 μm to 3 mm is grown on top of the master structures using nickel sulphamate solutions. This first nickel replica is then separated from the original. After passivation, the first replica is copied by electroforming again. By repeating this process, several generations of so–called nickel shims can be produced without too much loss in the structural details.

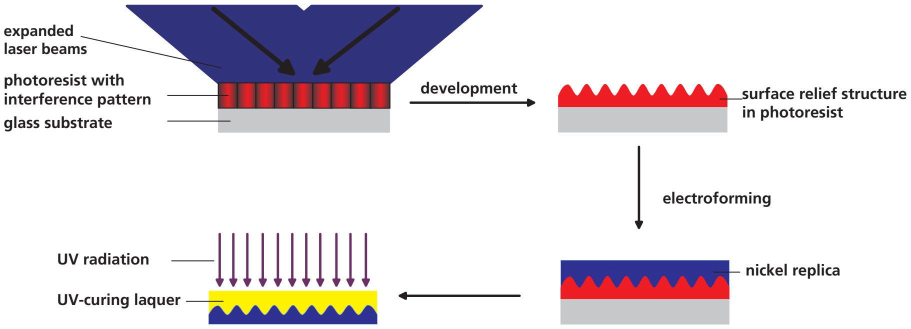

Figure 13.4: Fabrication of microstructured surfaces by interference lithography and subsequent replication: A UV–sensitive photoresist is exposed to the interference pattern of two laser beams. During development, this is transferred into a surface relief structure. Next, a nickel replica is fabricated from the photoresist via electroforming. The nickel replica is then used as an embossing tool, typically by applying a UV–curing lacquer.

The daughter generations of the nickel shims are used for replicating the microstructures in polymer materials. For polymers, a large variety of replication techniques exists, e.g., hot compression molding, injection molding, and reactive processes including radiation curing. The latter provides large flexible substrates with a highly cross–linked hard coating in which the microstructures are formed. This coating is rather resistant to organic solvents and such substrates are therefore preferably used to manufacture polymer PhC–lasers for which the active polymer, e.g. MeLPPP, is spin–coated onto the substrate. For a continuous production of radiation cured grating substrates, the nickel shims are mounted onto a roller. A polymer film substrate is continuously coated with a lacquer containing a photo–active compound and pressed against the roller with the microstructured nickel shims. The lacquer is hardened while in contact with the nickel shim by UV irradiation. The whole process, starting from the exposure of photoresist, is shown schematically in Fig. 13.4. As a fast alternative for experimental purposes, the lacquer can be applied to the structured photoresist directly, without the manufacture of a nickel shim. However, only one replica per structured photoresist plate can be made this way as the separation of the cross–linked film from the photoresist is not possible without damaging the latter.

Hot–embossed grating substrates are better suited for solvent–free coatings e.g. for organic semiconductors which are coated onto the substrates by evaporation. For this technique, a polymer substrate like PMMA is heated to about 200°C. Then, the nickel shim is pressed into the substrate at 20–60 bar. The substrate and the shim are cooled down together before separation. The surface relief structure in PMMA is not resistant to most organic solvents and can therefore not be used when the laser active polymer is spin–coated onto the substrates.

Evaporation of high refractive index materials onto the substrates is a measure to modify the refractive index contrast of the photonic crystal before coating it with the laser active polymer. Dielectrics like titanium dioxide can be vaporized by an electron beam and evaporated onto the substrate at an oblique angle (Fig. 13.5a). This results in a porous, amorphous structure on top of the substrate as shown in an SEM micrograph (Fig. 13.5b). The density

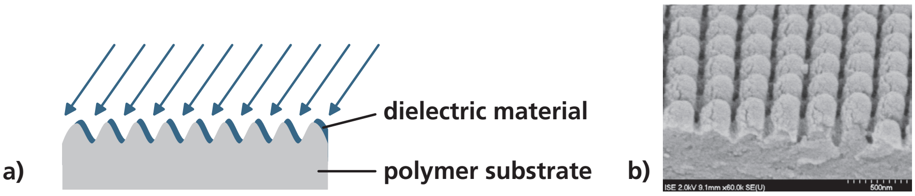

Figure 13.5: a) Schematics of the polymer substrate that can additionally be coated with a high index dielectric material by evaporation at oblique incidence. b) SEM micrograph of a substrate evaporated with titanium dioxide. In the case of two–dimensional substrates, one has to take care not to break the symmetry by the evaporation process.

and therefore the refractive index of the dielectric depend strongly on the parameters during evaporation and are generally lower than in the crystalline state.

13.3 Active materials for organic photonic crystal lasers

An important ingredient for any laser is the optically amplifying material. We have explored the use of conjugated polymers for photonic crystal lasers. The relevant electronic structure of such polymers is shown schematically in Fig. 13.6b and compared with the structure in related organic dye molecules. As a lasing medium, conjugated polymers possess many similarities with organic dye molecules dissolved in liquid solution. The most important optical transition connects the S_0 electronic ground state and the first excited singlet state S_1. Due to the strong coupling of the electronic system to the nuclear motion, vibronic sublevels of the two involved electronic levels have to be considered. Additional spectral broadening of the transitions is caused by the rotational degrees of freedom and inhomogeneous broadening mechanisms. Thus a quasi–continuum of states is formed. After relaxation into the lowest lying vibronic level of the S_1–manifold, the excitations can undergo a radiative transition into higher lying vibronic levels of the electronic ground state. In terms of laser physics, the situation described here corresponds to a four–level–system where the lasing transition connects two levels that are not directly involved in the optical pumping process.

In most of our experiments we have used a methyl substituted ladder-type poly(para-phenylene)(MeLPPP) as the emitter material. MeLPPP is a very attractive π-conjugated polymer for blue-light emitting diodes [7] and lasers [8] due to its high luminescence quantum yield in the solid state ($\approx 30\%$) and a strong stimulated emission band [9]. In addition MeLPPP exhibits relatively high carrier mobilities [10] thus rendering the material attractive for future organic diode lasers. The photoluminescence spectrum is more or less symmetrical to the absorption and exhibits only a very small Stokes shift. Many of the valuable properties of MeLPPP are caused by the high intra–chain order. It is reached by a stabilization of the PPP backbone against torsional displacement of the phenyl rings through covalent bridging of neighboring phenyl rings (see Fig. 13.8 for the chemical structure). The stiff backbone explains why the Stokes shift, due to structural relaxation, is negligible. The side chains lead to a good solubility of the polymer in unpolar solvents such as toluene.

Figure 13.7a shows emission spectra of a 300 nm thick film of MeLPPP on a glass substrate for various excitation densities. All the spectra are normalized at a wavelength of

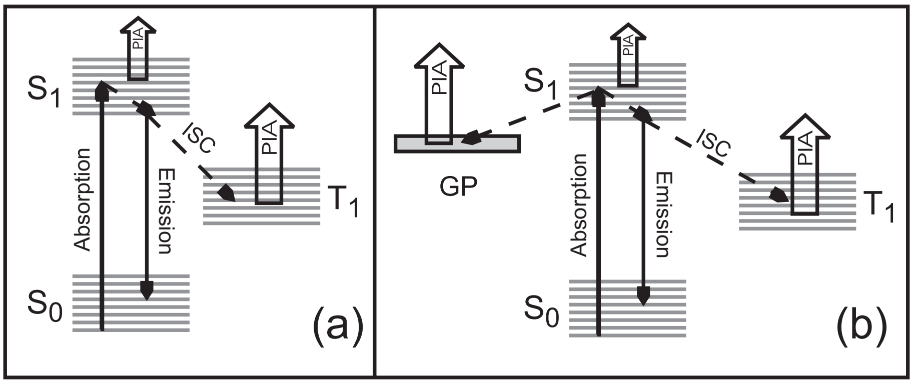

Figure 13.6: Energy scheme of the relevant electronic levels that are affecting stimulated emission in an isolated dye molecule in solution (a) and in a conjugated polymer (b). In both systems, absorption of a photon induces a transition from the singlet ground state S_0 to a vibronically excited state within the S_1–manifold. After vibronic relaxation, a red–shifted emission can be observed. This transition can occur in a spontaneous as well as in a stimulated manner. As competing processes in both systems, a photoinduced absorption (PIA) due to the population of the triplet state T_1 may occur. In the conjugated polymer a pair of oppositely charged carriers (GP) can be generated due to dissociation of the S_1–state. This can lead to additional photoinduced absorption bands that compete with the stimulated emission.

459 nm, the spectral position of the maximum photoluminescence intensity. At the lowest shown excitation density, the typical photoluminescence spectrum of MeLPPP is recorded. When the excitation density is gradually increased, a qualitative change of the emission spectrum is observed, dominated by an increasing relative intensity in the spectral range of the $S_{0,\nu=1} \leftarrow S_{1,\nu'=0}$ transition. The spectral narrowing is caused by amplified spontaneous emission. Photons emitted from photoexcited chromophores in MeLPPP are coupled into the waveguide formed by the film of polymer on the glass substrate. As these photons propagate through the photoexcited region, they can be scattered out of the waveguide, be reabsorbed or cause stimulated emission. If the pump intensity is high enough for the gain to exceed the scattering losses then spontaneously emitted photons are exponentially amplified as they travel through the waveguide. Since predominantly those photons are amplified whose energy coincides with the spectral position of maximum gain, the overall emission spectrum changes. The magnitude of stimulated emission can be quantified in a differential transmission experiment. The sample is excited by an intense femtosecond pump pulse and the resulting transmission changes are monitored with a spectrally broad, time–delayed probe pulse. The gain spectrum is extracted from the differential transmission spectrum by correction for the absorption. Fig. 13.7b shows the spectral dependence of the gain coefficient of an MeLPPP film immediately after photoexcitation. Strong stimulated emission is observed between 485 nm and 500 nm coincident with the $(S_0, \nu = 1) \leftarrow (S_1, \nu' = 0)$ transition. The maximum stimulated emission cross section ($\sigma_{SE,Max} \approx 1.5 \cdot 10^{-16}\text{cm}^2$) is observed at a wavelength of 490 nm.

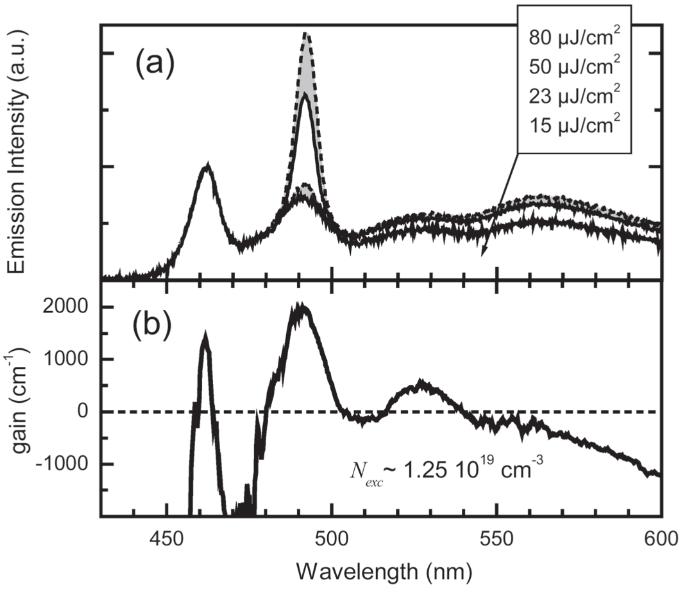

Figure 13.7: (a) Emission spectra of a film of MeLPPP for increasing excitation density. All spectra are normalized at the wavelength where the peak of the emission spectrum occurs at low excitation density. The excitation beam is focused to a circular spot of $\sim 200\ \mu$m diameter. (b) Gain spectrum of MeLPPP measured after pulsed optical excitation at $\lambda = 400$ nm.

13.4 Lasing in two dimensional polymeric photonic crystals

Prior to this work, one-dimensional distributed feedback resonators based on nanopatterned substrates have shown to be a promising method to fabricate organic semiconductor thin film lasers [11–13]. One of their major drawbacks, however, is the presence of lateral modes leading to multimode laser operation [15]. A very elegant method for mode selection and threshold reduction is the use of two-dimensionally (2D) nanopatterned substrates, giving rise to a 2D distributed feedback (2D–DFB) or in other words a 2D photonic crystal [14, 16].

The fabrication of the 2D–PhC relies on the combination of conjugated polymers and surface relief structures. As the active laser material, the conjugated polymer MeLPPP is used which is spincast onto the mechanically flexible surface relief grating, fabricated by the processes described in Sect. 13.2. In our case two perpendicular sinusoidal corrugations with a periodicity of $\Lambda_z = \Lambda_x = 300$ nm and a depth of $h_z = h_x = 160$ nm form the grating for the 2D photonic crystal laser. An AFM image of the resulting corrugation is displayed in the scheme of the laser depicted in Fig. 13.8.

Figure 13.9 presents emission spectra for two different excitation conditions corresponding to excitation densities below and well above the laser threshold, respectively. The dashed line shows the photoluminescence observed when the sample is excited below threshold. The

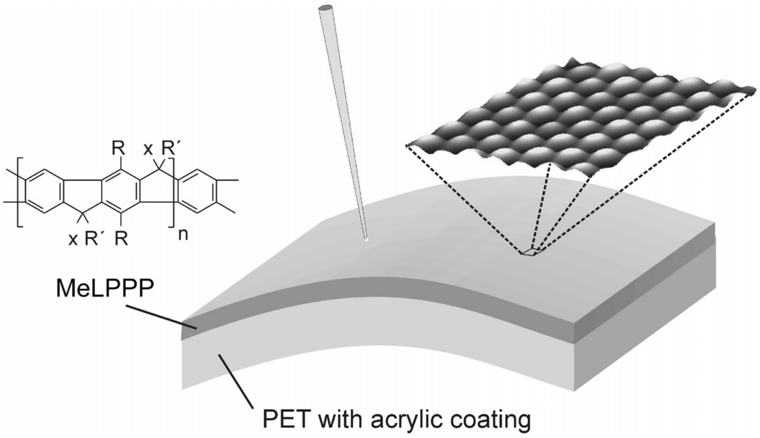

Figure 13.8: Schematic setup of the 2D photonic crystal laser. A film of MeLPPP is spincast onto a flexible, nanopatterned substrate. The surface of the substrate has a two-dimensional periodic corrugation shown by the AFM image. Laser emission is observed perpendicular to the substrate.

first vibronic transition has a slightly higher intensity than in the photoluminescence spectrum of an MeLPPP–film on a planar glass substrate. This difference is due to the effect of the periodic modulation, which acts as a grating coupler and scatters waveguided light with a wavelength around 490 nm into the direction of the detector. The emission behavior changes drastically at a fluence of $5.6\ \mu\text{Jcm}^{-2}$. At a wavelength of 491 nm, a sharp laser peak evolves. Upon further increase of the pump pulse energy, the spectrum is completely dominated by the laser peak. The solid line in Fig. 13.9 shows the emission spectrum at a fluence of $8.4\ \mu\text{Jcm}^{-2}$. The measured halfwidth is 0.25 nm, limited by the spectral resolution of the setup. It is interesting to compare these results with the findings for a laser utilizing an MeLPPP–film of the same thickness but a substrate with a purely one–dimensional periodic height modulation of the same maximum amplitude as in the 2D–case [11]. In the inset of Fig. 13.9, the emission intensity at the laser wavelength collected perpendicular to the substrate with a numerical aperture of 0.26, is plotted as a function of the pump fluence for a 1D DFB–laser and a 2D PhC–laser. For the 2D PhC–laser, the threshold is reduced by 30% and the differential efficiency is substantially increased.

As the most intriguing feature, the divergence of the emission is drastically reduced in the 2D laser. While a strongly polarized emission with rather high divergence parallel to the grating lines is observed in the case of 1D distributed feedback lasers without any lateral waveguiding, highly directed unpolarized emission is achieved with the 2D structure. The inset in Fig. 13.10 shows an image of the circularly shaped far–field emission pattern of the photonic crystal laser. The corresponding transverse irradiance profile, depicted as solid squares in Fig. 13.10, can be fitted with a Lorentzian curve (solid line). The value of 2.4 mrad for the angular radius of the far–field emission indicates diffraction limited emission from the entire area of the excited spot (excitation diameter $\approx 150\ \mu$m). This clearly shows that the laser oscillates in phase over the entire excited area, i.e. the laser operates in a single, spatially

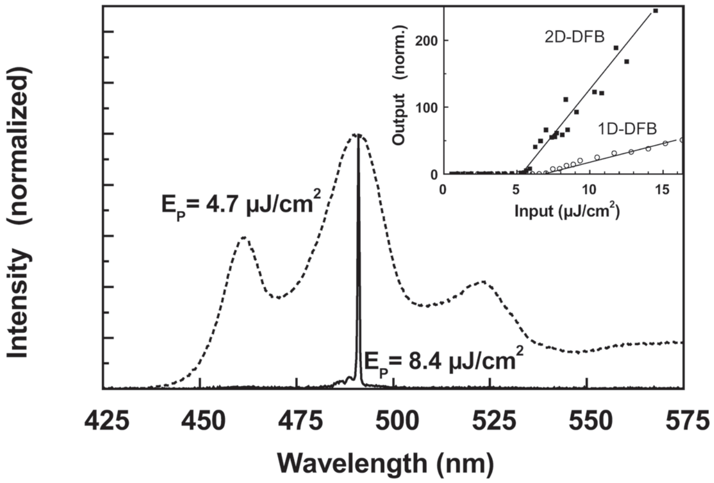

Figure 13.9: Emission spectra of a 2D PhC–laser below (dashed line) and above the laser threshold (solid line). The spectral half–width (FWHM) of the laser line is 0.25 nm. The inset shows the radiated power at the laser wavelength normalized to the threshold value as a function of excitation fluence. Direct comparison with a 1D–DFB laser shows an increase of efficiency and a reduction of the laser threshold.

extended, mode. In contrast to the inherent multimode operation of a 1D–DFB laser without lateral confinement, one single lateral mode is selected in the 2D PhC–laser.

13.5 Semiclassical theory of lasing in surface relief structures

Over the past years, several theoretical models relevant to laser action in periodic structures have been developed [17–21]. These studies unveiled valuable information on lasing action in periodic structures. However, most of them are either confined to 1D [17] or linear systems (modeling an active medium with a complex refractive index) [18] or rely heavily on numerical simulations [19, 20] which permit only limited insight into the underlying physical processes. Therefore, we apply the recently developed semiclassical theory of lasing action in photonic crystals [21] to the present situation of lasing in 2D surface relief structures. This approach utilizes the linear eigenmodes of the structures as carrier waves and, in conjunction with a multiscale analysis, allows one to derive the generalized Maxwell–Bloch equations for an incoherently pumped active medium, interacting with the electromagnetic modes of the surface relief structure. As a result, expressions for gain– and saturation–enhancement factors as well as the cavity losses of finite–sized systems can readily be evaluated and/or estimated from realistic mode calculations. These effective parameters are of paramount importance for identifying the relevant lasing modes and determining their laser thresholds.

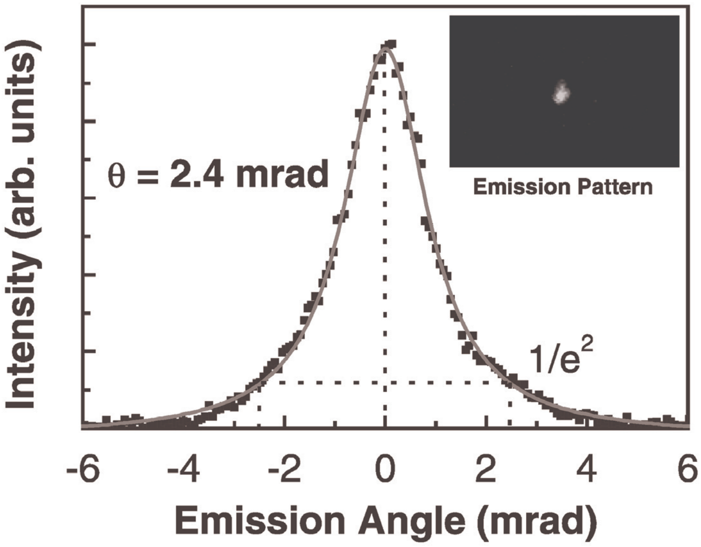

Figure 13.10: Inset: Image of the circularly shaped far-field emission of the 2D laser in monomode operation (Fluence = 8 μJcm^{-2}). The solid squares show the angular dependence of the corresponding transverse irradiance profile.

13.5.1 Semiclassical laser theory in structured media

The propagation of electromagnetic radiation through a nonlinear optical medium is described by the wave equation (in cgs-units)

$$-\nabla \times \nabla \times \vec{E}(\mathbf{x},t) - \frac{\epsilon(\mathbf{x})}{c^2}\frac{\partial^2 \vec{E}(\mathbf{x},t)}{\partial t^2} - \frac{4\pi\tilde{\sigma}(\mathbf{x})}{c^2}\frac{\partial \vec{E}(\mathbf{x},t)}{\partial t} = \frac{4\pi}{c^2}\frac{\partial^2 \vec{P}_{nl}(\mathbf{x},t)}{\partial t^2} \ , \quad (13.1)$$

where $\epsilon(\mathbf{x})$ is the spatially varying dielectric function, describing the linear polarization effects of the photonic structure and $\vec{P}_{nl}(\mathbf{x},t)$ is the nonlinear macroscopic polarization of the active medium. The losses caused by the background absorption are described by the conductivity $\tilde{\sigma}(\mathbf{x})$, which can also be adjusted to include damping due to diffraction (out of plane losses due to the coupling of the waveguide modes to radiation modes) and cavity losses (in plane losses due to a finite sample size or pumping region) as will be discussed below.

The polarization $\vec{P}_{nl}$ induced by the electromagnetic field in the active medium is determined through individual atoms or molecules at positions $\vec{x}_a$ with a dipole transition (dipole moment $\vec{d}_{12}$) at frequency ω_a

$$\vec{P}_{nl}(\mathbf{x},t) = \sum_a \delta(\vec{x}-\vec{x}_a)\vec{P}_a(t) = n(\vec{x})\vec{\tilde{P}}(\vec{x},t) \ , \quad (13.2)$$

where $\vec{\tilde{P}}(\vec{x},t)$ denotes the polarization density at position $\vec{x}$ and $n(\vec{x})$ is a dimensionless weight function that characterizes the distribution of active material within the photonic structure. For instance, $n(\vec{x}) = 1$ for a uniform distribution of emitters in the active material. The time evolution of single–atom or single–molecule polarization $\vec{P}_a(t)$ is described by

$$\frac{d^2\vec{P}_a(t)}{dt^2} + 2\gamma_\perp \frac{d\vec{P}(t)_a}{dt} + \omega_a^2 \vec{P}_a(t) = -2\omega_a \tilde{\Omega}\, \vec{d}_{12}\, \Delta N_a(t) \ . \tag{13.3}$$

Here, $\gamma_\perp$ is the dephasing rate of the dipole moment and $\tilde{\Omega}$ represents the instantaneous Rabi frequency

$$\tilde{\Omega} = \frac{\vec{d}_{12} \cdot \vec{E}(\mathbf{x}_a, t)}{\hbar} \ , \tag{13.4}$$

measuring the strength of the interaction between the driving field and the dipole transition. For simplicity, we assume here a sufficiently weak dependence of the dipole moment $\vec{d}_{12}$ on the transition frequency ω_a, so that we can regard the Rabi frequency and the dipole dephasing rate $\gamma_\perp$ as a constant for all relevant transitions. Finally, the saturable nonlinearity responsible for lasing action appears in the driving term that contains the population inversion $\Delta N_a(t) = N_{2,a}(t) - N_{1,a}(t)$ between the energetically upper and lower lying states of the dipole transition, $N_{2,a}(t)$ and $N_{1,a}(t)$, respectively. This population inversion is, in turn, driven (on a time scale much longer than the optical period $2\pi/\omega$) through radiative emission and relaxation processes, as well as through incoherent pumping of the active medium

$$\frac{d\Delta N_a(t)}{dt} = R - \tilde{\gamma}_{||} \Delta N_a(t) + 2\frac{\tilde{\Omega}}{\omega_a} \frac{1}{|\vec{d}_{12}|^2} \left(\vec{d}_{12} \cdot \frac{d\vec{P}_a(t)}{dt} \right) \ , \tag{13.5}$$

where $R = \tilde{\gamma}_{||} \Delta N_{eq}$ is the rate at which the atoms or molecules are incoherently pumped from the lower to the upper state (ΔN_{eq} is the equilibrium population inversion density) and $\tilde{\gamma}_{||}$ is the decay rate of the upper state. In accordance with the sufficiently weak dependence of the Rabi frequency on the transition frequency ω_a, we have neglected the corresponding frequency dependence of the upper state decay rate $\tilde{\gamma}_{||}$ and the pump rate R.

Before proceeding further, we analyze the various quantities that enter Eqs. (13.1), (13.3), and (13.5) to facilitate their subsequent approximate solution. For any realistic laser system, the loss term in Eq. (13.1) is significantly smaller than the first two terms on the left–hand side (l.h.s.) of Eq. (13.1) that describe the free evolution of the electromagnetic field at optical frequencies ω, i.e. $\omega\epsilon(\vec{x}) \ll \tilde{\sigma}(\vec{x})$. Similarly, for realistic parameters of any active medium (concentration of resonant atoms or molecules etc.) we have that in the linear regime, the effective susceptibility χ describing the polarization density $\tilde{\vec{P}}(\vec{x}, t) = \chi \vec{E}(\vec{x}, t)$, which is coherently induced by the cavity mode field $\vec{E}(\vec{x}, t)$, is a small parameter $\chi \ll 1$. In addition, for typical dipole moments $\vec{d}_{12}$ of optical transition and typical field amplitudes, we obtain Rabi frequencies $\tilde{\Omega}/\omega \ll 1$ that are small compared to optical frequencies ω. The same considerations apply to the rates $\tilde{\gamma}_\perp/\omega \ll 1$ and $\tilde{\gamma}_{||}/\omega \ll 1$, describing dephasing and relaxation processes, respectively. The analysis presented above, suggests a perturbative treatment of Eqs. (13.1), (13.3) and (13.5) by introducing a small dimensionless parameter $\mu \ll 1$ that allows us to rewrite all the small quantities according to

$$\tilde{\sigma}(\vec{x}) \to \mu\sigma(\vec{x}), \quad \tilde{\vec{P}}(\vec{x}, t) \to \mu\vec{P}(\vec{x}, t), \quad \tilde{\Omega} \to \Omega, \quad \tilde{\gamma}_\perp \to \gamma_\perp, \quad \tilde{\gamma}_{||} \to \gamma_{||} \ . \tag{13.6}$$

Here, $\sigma(\vec{x})$ and $\vec{P}(\vec{x},t)$ are quantities comparable with $\omega\epsilon(\vec{x})$ and $\vec{E}(\vec{x},t)$, respectively. Similarly, Ω, $\gamma_\perp$ and $\gamma_\|$ represent quantities comparable to the optical frequency ω.

The presence of the small parameter μ facilitates the separation of the different time and length scales inherent in Eqs. (13.1), (13.3), and (13.5) through an appropriate multi-scale analysis [21]. This multi-scale analysis represents a generalization of the slowly varying envelope approximation to the case of microstructured photonic systems and allows us to take advantage of the fact that the effects of the nonlinearity, build up on time and length scales much larger than the optical period $2\pi/\omega$ and associated wavelength λ. Assuming one mode is dominant, we employ the ansatz

$$\vec{E}(\vec{x}_0,\vec{x}_1,\ldots;t_0,t_1,\ldots) = \mathcal{E}(\vec{x}_1,\vec{x}_2,\ldots;t_1,t_2,\ldots)\vec{\Phi}_m(\vec{x}_0)\,e^{-i\omega_m t_0} + \text{c.c.} \qquad (13.7)$$

Here, the linear eigenmode of the structure $\vec{\Phi}_m(\vec{x}_0)$ with eigenfrequency ω_m acts as a carrier wave for the slowly varying envelope function $\mathcal{E}(\vec{x}_1,\vec{x}_2,\ldots;t_1,t_2,\ldots)$. The variables $\vec{x}_i = \mu^i\vec{x}$ and $t_i = \mu^i t$ $(i = 1,2,\ldots)$ represent the different time and length scales of the problem. For instance, the fastest spatial scale $\vec{x}_0$ corresponds to the wavelength of electromagnetic radiation and the fastest temporal scale t_0 is associated with the optical period $2\pi/\omega$. The dielectric function $\epsilon(\vec{x}) = \epsilon(\vec{x}_0)$, the conductivity $\sigma(\vec{x}) = \sigma(\vec{x}_0)$, and the distribution function $n(\vec{x}) = n(\vec{x}_0)$ exclusively vary on the smallest length scale $\vec{x}_0$. To generate the hierarchy of equations that reflect the different scales involved in the problem, we insert expansion (13.7) and analogous expansions for the polarization $\vec{P}(\vec{x},t)$ and the population inversion $\Delta N_a(\vec{x},t)$ into the equation of motion Eqs. (13.1), (13.3) and (13.5), respectively, expand the time and space derivatives in the new variables and collect terms with equal powers of μ. For the situation of most physical relevance, optical pulses that are longer than the polarization–relaxation time, it is well justified to assume a quasi–equilibrium situation and to eliminate adiabatically, the polarization from the Maxwell–Bloch equations derived from Eqs. (13.1) and (13.5), in second order multi–scale analysis in μ. In the steady–state limit, we obtain for the resulting field-envelope equation [21]

$$\vec{v}_m \cdot \nabla\mathcal{E}(\vec{x}) = \frac{1}{2}\left(-\gamma_m + \frac{\mathcal{G}_m}{1+\beta_m I(\vec{x})}\right)\mathcal{E}(\vec{x}) \ . \qquad (13.8)$$

Here, we have returned to the physical coordinate $\vec{x}$ and have introduced the dimensionless intensity $I(\vec{x}) = |\mathcal{E}(\vec{x})|^2/I_{sat}$ in units of the line-center saturation intensity $I_{sat} = \hbar^2\gamma_\perp\gamma_\|/4|\vec{d}_{12}|^2$.

In Eq. (13.8), the effect of the photonic structure is manifested in the occurence of a number of effective parameters. $\vec{v}_m$ represents the group velocity associated with the carrier wave $\vec{\Phi}_m$. $\mathcal{G}_m$ denotes the unsaturated gain coefficient

$$\mathcal{G}_m = \alpha_m \frac{4\pi|\vec{d}_{12}|^2\omega_m R}{\hbar\gamma_\perp\gamma_\|} \ , \qquad (13.9)$$

where the gain enhancement factor α_m describes how the carrier wave $\vec{\Phi}_m$ samples the distribution of active material

$$\alpha_m = \int |\vec{\Phi}_m(\vec{x})|^2 n(\vec{x})\,d\vec{x} \ . \qquad (13.10)$$

Likewise, the saturable nonlinear response is expressed through the effective nonlinear coupling enhancement factor β_m

$$\beta_m = \frac{\int |\vec{\Phi}_m(\vec{x})|^4 n(\vec{x})\, d\vec{x}}{\int |\vec{\Phi}_m(\vec{x})|^2 n(\vec{x})\, d\vec{x}} \;, \tag{13.11}$$

and the effective cavity-loss rate γ_m is determined through

$$\gamma_m = 4\pi \int |\vec{\Phi}_m(\vec{x})|^2 \sigma(\vec{x})\, d\vec{x} + 2\kappa_m \;, \tag{13.12}$$

where additional losses for mode $\vec{\Phi}_m$ other than the background absorption were incorporated phenomenologically through the cavity leakage term κ_m.

It follows directly from Eq. (13.8) that there are two distinct regimes of pulse growth. For small values of the field envelope $\mathcal{E}(\vec{x})$, $\beta_m I(\vec{x})$ can be neglected. As a conseqeunce, the envelope grows exponentially with a rate $(\mathcal{G}_m - \gamma_m)/|\vec{v}_m|$. For sufficiently large values of the field envelope, a saturation regime develops such that the saturation term $\beta_m I(\vec{x})$ gradually reduces the effective growth rate to zero . The limiting steady-state value I_{ss} of the intensity, corresponding to the spatial-saturation regime, is given by

$$I_{ss} = \frac{1}{\beta_m}\left(\frac{\mathcal{G}_m}{\gamma_m} - 1\right) \;. \tag{13.13}$$

Equation (13.13) suggests that amplification is possible only if $\mathcal{G}_m/\gamma_m > 1$, and therefore the laser threshold condition is identified as $\mathcal{G}_m = \gamma_m$.

As a result of the foregoing analysis, we have obtained a number of effective parameters which determine the behavior of an active medium in a photonic structure. For a given photonic system with certain material properties, these effective parameters can be evaluated from its linear eigenmodes. Consequently, in the subsequent section we derive an effective 2D model for surface relief structures which allows us to determine the photonic band– and modestructures for these systems.

13.5.2 Effective 2D model for surface relief structures

We start our analysis of the surface relief structures by reducing the problem of propagation of the quasi–guided waveguiding modes in the plane of corrugation to an effective 2D model. Within this model, coupling to radiation modes into the third dimension will be considered as additional cavity–losses associated with these modes. This mapping onto an effective 2D model is achieved through translating the actual surface relief profile into a corresponding profile of the index of refraction experienced by the quasi–guided TE–like or TM–like modes.

From the SEM and AFM–pictures of the actual structures with square symmetry, we have deduced a spatially varying thickness $d_{\text{var}}(x, y)$ of the waveguiding layer at the two–dimensional position $\vec{r} = (x, y)$ according to

$$d_{\text{var}}(x, y) = d_{\min} + \frac{1}{4}(d_{\max} - d_{\min})\Big(1 - \sqrt{\frac{1}{4}\big(2 - \cos(2\pi x/a) - \cos(2\pi y/a)\big)}\Big) \tag{13.14}$$

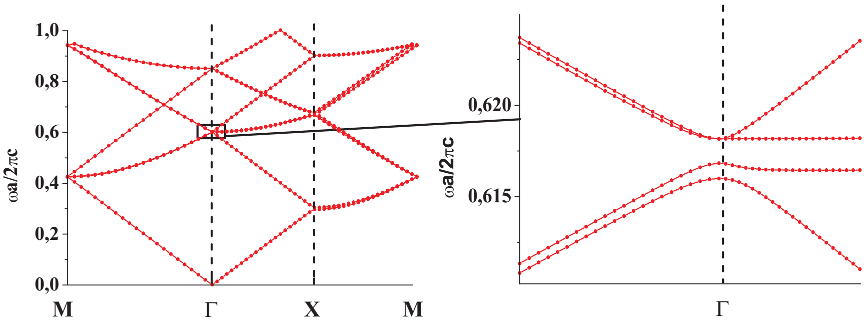

Figure 13.11: Photonic bandstructure of TE–like modes of a 2D surface relief structure with square lattice symmetry within the effective 2D model. The right diagram represents a magnification of frequency and k–vector space relevant for lasing action in this system. The parameters of the surface relief structures are given in the text.

where $a \approx 300$ nm is the in-plane lattice constant, and the minimal and maximal thickness of the waveguiding layer are $d_{\mathrm{min}} \approx 100$ nm and $d_{\mathrm{max}} \approx 300$ nm, respectively. Depending on whether we consider TE–like or TM–like modes, we can now determine the dispersion relation for a corresponding asymmetric waveguiding structure with a thickness $d_{\mathrm{var}}(x, y)$ of the waveguiding layer [22] sandwiched between air and the substrate. The group index at the relevant laser frequency associated with this dispersion relation then defines the effective index $n_{\mathrm{eff}}(x, y)$ at the location $\vec{r} = (x, y)$. As a result, we obtain a spatially varying dielectric constant $\epsilon(x, y) = n^2_{\mathrm{eff}}(x, y)$ which allows us to determine the photonic bandstructure (linear eigenmodes) associated with TE–like and TM–like guided modes. However, for the experimentally determined minimal thickness $d_{\mathrm{min}} \approx 100$ nm, the waveguiding layer supports a single TE–mode only. Therefore, we subsequently concentrate on the discussion of TE–like modes.

In Fig. 13.11, we display the photonic bandstructure of TE–like modes for the surface relief structure with square symmetry within the effective 2D model based on Eq. (13.14) that has been obtained through a plane wave approach [23]. The right diagram in Fig. 13.11 displays that part of the dispersion relation that is of relevance to the lasing action in this system. It should be noted that the center frequency and spectral width of the gap near the Γ–point agree well with the experimentally observed luminescence data for TE–polarized radiation. In addition, we would like to note that the lower frequency band edge at the Γ–point is non-degenerate.

13.5.3 Discussion of lasing behavior in surface relief structures

To understand the threshold behavior of our surface relief structures, it is necessary to evaluate the effective gain enhancement factors α_m and total cavity losses γ_m for the modes m in Fig. 13.11, that lie within the relevant frequency range. Assuming that the distribution function $n(x, y) \propto d_{\mathrm{var}}(x, y)$ of the active material varies proportional to the width of the

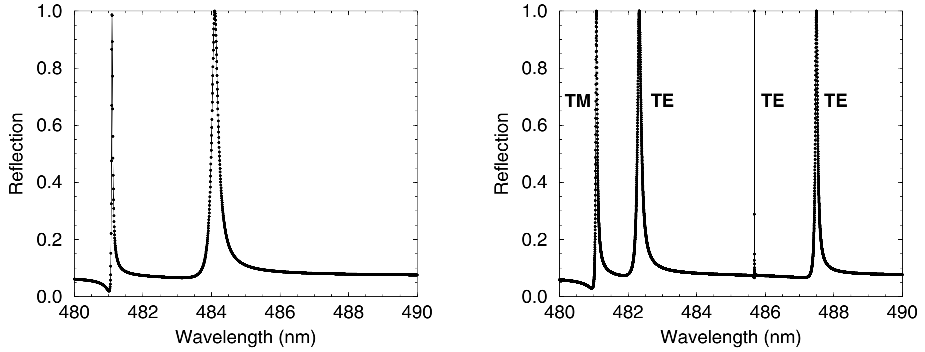

Figure 13.12: Reflection spectrum from a 2D surface relief structure with square lattice symmetry for different illumination conditions. Left panel: Reflection spectrum for light incident normal to the surface (0 degree to the normal, polarized along the $\hat{y}$–axis). Right panel: Reflection spectrum for light incident from a direction 0.5 degrees away from the normal along the Γ–X direction (0.5 degree to the normal, polarized along the $\hat{y}$–axis). Upon moving 0.5 degrees away from the normal, the reflection peaks (corresponding to waveguiding modes) of the initial peaks shift to smaller wavelengths and the long wavelength peak splits into a wide peak and a narrow peak 485.68 nm. At 0 degree–incident light, this narrow peak has been obscured by the dominant wide peak. The peak at 488 nm is a down–shifted peak belonging to a peak outside the displayed range in the 0 degree plot. The peaks are classified into TE– and TM–like modes according to the symmetries of the corresponding waveguiding modes. The parameters of the surface relief structures are given in the text.

waveguiding layer, we find that all the relevant modes exhibit a comparable gain enhancement factor. Therefore, the lasing characteristics of our surface relief grating is determined by the total cavity–losses of the individual modes. If we neglect the background absorption, these losses are determined by in–plane losses due to a finite sample size or a finite pumping region and out–of–plane losses, associated with the coupling of the waveguide modes to the radiation modes of substrate and air. In fact, it has been shown [19, 21] that the in–plane losses are proportional to the group velocity $|\vec{v}_m|$ for both finite sample size and finite pumping region. This suggests that the modes at the Γ–point have a potentially reduced lasing threshold as compared to the modes away from the Γ–point. This observation is consistent with our emission measured perpendicular to the surface.

In order to determine the out–of–plane losses of these modes, we have computed in Fig. 13.12 (left panel), the reflection spectrum for light incident normally onto the surface relief grating using a scattering matrix technique [24]. The incident light is polarized parallel to the $\hat{y}$–axis because only this polarization allows us to couple to the modes in question. Two peaks corresponding to the resonant coupling into and out of the waveguiding modes lie in the relevant frequency range; unfortunately, because of the degeneracy at the Γ–point, the field patterns associated with these two peaks are a complicated combination of TE– and TM–like modes, and therefore cannot be compared directly to the effective 2D model presented in Sect. 13.5.2.

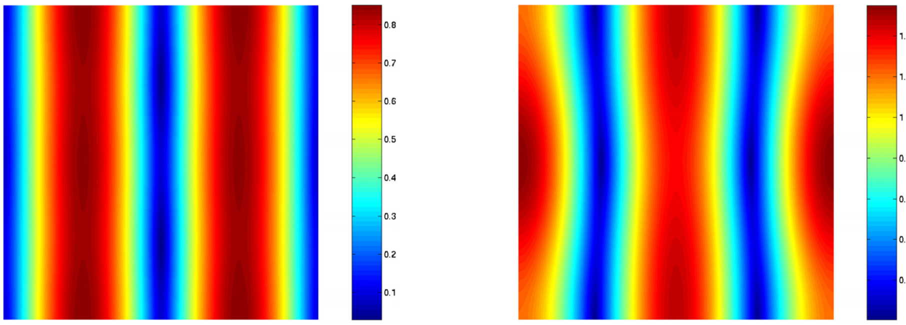

Figure 13.13: Field distributions inside the surface relief structure associated with the narrow reflection peak in Fig. 13.12, right panel. Left panel: The absolute value of the in–plane electric field. The out–of–plane electric field is an order of magnitude smaller, confirming the TE–like nature of the mode. Right panel: The absolute value of the out–of–plane magnetic field. The in–plane magnetic field is an order of magnitude smaller, confirming the TE-like nature of the mode. The parameters of the surface relief structures are given in the text.

However, this problem is resolved when we calculate the reflection spectrum for light incident 0.5 degrees away from the normal along the Γ–X direction, keeping the polarization fixed along the $\hat{y}$–axis (see Fig. 13.12 (right panel)). The four peaks in the right panel of Fig. 13.12 can each be associated with a definite TE– or TM–like field pattern. Moreover, one of these peaks at 485.68 nm exhibits a spectral width which is about two orders of magnitude smaller than all the other peaks, making it *the* candidate for our lasing mode. The field pattern associated with this mode is displayed in Fig. 13.13, which confirms its TE–like symmetry. The above considerations clearly suggest that we have identified the lasing mode as one of the degenerate TE–like modes at the Γ–point of our effective 2D model. While the in–plane losses can be neglected for all modes and their gain enhancement factors are similar, it is this mode's out–of–plane loss that is about 100 times smaller than that of the competing modes.

13.6 Conclusions

A brief overview of the fabrication, experimental characterization and theoretical analysis of the two–dimensional polymeric photonic crystal laser has been given. Organic photonic crystal lasers based on plastic surface relief structures, coated with conjugated polymers, were fabricated. Monomode and diffraction limited surface emission from a Bloch–mode at the Γ–point was observed. In comparison to conventional one-dimensional distributed feedback lasers, the emission properties and the laser threshold were significantly improved. The 2D lasing mode has been identified using an effective 2D model. These findings open novel approaches towards low threshold nanolasers as well as coherent large area emitters in the visible part of the electromagnetic spectrum.

Acknowledgements

We thank Ulli Scherf for providing the polymer material. We gratefully acknowledge financial support by the DFG within the German priority program on photonic crystals (SPP 1113). S. P. thanks the NSERC for financial support. K.B. further acknowledges the support by the DFG under grant Bu 1107/2–3 (Emmy-Noether program).

References

[1] R. H. Friend, R. W. Gymer, A. B. Holmes et al., Electroluminescence in conjugated polymers, Nature **397**,121(1999)

[2] M.C. Hutley, Diffraction gratings, Academic Press, London (1982)

[3] M.T. Gale, Replication technology for holograms and diffractive optical elements, J. Imaging Science and Technol. **41**, 211 - 220 (1997)

[4] Ch. Zanke, A. Gombert, A. Erdmann, and M. Weiss, Fine-tuned profile simulation of holographically exposed photoresist gratings, Optics Communications **154**, 109 - 118 (1998).

[5] A. Gombert, Surface patterns to serve a purpose, Materials World **8**, Nr. 9, 25 - 27 (2000).

[6] A. Gombert, Mikrooptik im großen Stil, Physik-Journal **1**, Nr. 9, 37 - 41 (2002).

[7] S. Tasch, A. Niko, G. Leising, and U. Scherf, Highly efficient electroluminescence of new wide band gap ladder-type poly(para-phenylenes), Appl. Phys. Lett. **68**, 1090 (1996)

[8] U. Scherf, S. Riechel, U. Lemmer, and R. F. Mahrt, Conjugated polymers: lasing and stimulated emission, Current Opinion in Solid State and Materials Science **5**, 143 (2001)

[9] A. Haugeneder, M. Neges, C. Kallinger, et al., Nonlinear emission and recombination in conjugated polymer waveguides, J. Appl. Phys. **85**, 1124 (1999)

[10] D. Hertel, U. Scherf, and H. Bässler, Charge carrier mobility in a ladder-type conjugated polymer, Adv. Mater. **10**, 1119 (1998)

[11] C. Kallinger, M. Hilmer, A. Haugeneder, et al., A flexible conjugated polymer laser, Adv. Mater. **10**, 920 (1998)

[12] A. Dodabalapur, M. Berggren, R. E. Slusher et al., Resonators and materials for organic lasers based on energy transfer, IEEE J. Quantum Electron. **4**, 67 (1998)

[13] M. D. McGehee, M. A. Diaz-Garcia, F. Hide, R. Gupta, E. K. Miller, D. Moses, and A. J. Heeger, Semiconducting polymer distributed feedback lasers, Appl. Phys. Lett, **72**, 1536 (1998)

[14] M. Meier, A. Mekis, A. Dodabalapur, A. A. Timko, R. E. Slusher, J. D. Joannopoulos, and O. Nalamasu, Laser action from two-dimensional distributed feedback in photonic crystals, Appl. Phys. Lett. **74**, 7 (1999)

[15] S. Riechel, U. Lemmer, J. Feldmann, T. Benstem, W. Kowalsky, A. Gombert, and V. Wittwer, Laser modes in organic solid state distributed feedback lasers, Appl. Phys. B **71**, 897 (2000)

[16] S. Riechel, C. Kallinger, U. Lemmer, J. Feldmann, A. Gombert, V. Wittwer, and U. Scherf, A nearly diffraction limited surface emitting conjugated polymer laser utilizing a two-dimensional photonic band structure, Appl. Phys. Lett. **77**, 2310 (2000)

[17] J.P. Dowling, M. Scalora, M.J. Bloemer, and C.M. Bowden, The photonic band edge laser: a new approach to gain enhancement, J. Appl. Phys. **75**, 1896–1899 (1994)

[18] S. Nojima, Enhancement of optical gain in two-dimensional photonic crystals with active lattice, Jpn. J. Appl. Phys. Lett. **37**, L565–L567 (1998)

[19] K. Sakoda, K. Ohtaka and T. Ueta, Low-threshold laser oscillation due to group-velocity anomaly pelicular to two- and three-dimensional photonic crystals, Optics Express **4**, 481–489 (1999)

[20] N. Susa, Threshold gain and gain-enhancement due to distributed-feedback in two-dimensional photonic-crystal lasers, J. Appl. Phys. **89**, 815–823 (2001)

[21] L. Florescu, K. Busch, and S. John, Semiclassical theory of lasing in photonic crystals, J. Opt. Soc. Am. B **19**, 2215–2223 (2002)

[22] B.E.A. Saleh and M.C. Teich, Fundamentals of Photonics, Wiley-Interscience, New York, NY, USA (1991)

[23] K. Busch and S. John, Photonic band gap formation in certain self-organizing systems, Phys. Rev. E **58**, 3896–3908 (1998)

[24] D.M. Whittaker and I.S. Culshaw, Scattering-matrix treatment of patterned multilayer photonic structures, Phys. Rev. B **60**, 2610–2618 (1999)

14 Photonic crystal fibers

Johannes Kirchhof, Jens Kobelke, Kay Schuster, Hartmut Bartelt[1]*, Rumen Iliew, Christoph Etrich, and Falk Lederer*

14.1 Introduction

Optical fibers are the backbone of modern optoelectronics and telecommunication systems and are widely used for guiding and distributing light in optical systems. The standard fiber consists of a fiber core surrounded by a lower index cladding, thus light is confined by total internal reflection. A novel type of optical fibers, developed mainly during the last decade and pioneered by P. Russell and coworkers [1, 2], is the microstructured fiber, frequently called photonic crystal fiber (PCF) (Figure 14.1). A PCF typically has a cross section incorporating numerous air holes (usually in a periodic arrangement) within a silica host surrounding either a solid silica (holey fiber, high-delta or cobweb fiber) or a hollow core (photonic band gap fiber – PBGF). The guiding mechanism is provided either by means of modified total internal reflection (holey and cobweb fiber) or a photonic band gap effect. These fibers may exhibit various peculiarities attractive for applications.

The simplest type of PCF, the holey fiber, comprises a regular hexagonal lattice of small air holes with a defect in the center (missing hole) with the guiding provided by modified total internal reflection [1]. Although the same material is used for core and cladding, the incorporation of air holes in the cladding area results in an effective lowering of the average refractive index. This allows for much more variability in the index step and for peculiar dispersion properties. Holey fibers with a large air filling fraction of the cladding resulting in a high effective Δ–parameter (see e.g. [3]) are called high–delta or cobweb fibers, depending on the cross section geometry.

Field confinement in an air core (hollow–core fibers), based on the band gap effect, requires a periodic arrangement of air holes on a wavelength scale with a sufficiently high air filling fraction in the cladding, to obtain an in–plane band gap for off–plane propagation in a certain wavelength range. Light guidance in air of such a hollow–core PBGF has been demonstrated using a hexagonal pattern of air holes in silica as cladding, surrounding a core formed by removing seven of the constituting capillaries [2, 4]. This also allows for light guidance in gases. However, the guided mode may not be concentrated in the air core completely, and part of the power may still pass through solid material.

An alternative approach towards air–guidance of light is periodically stacking alternating cylindrical layers of different materials to form a cylindrical Bragg mirror [5–7]. In contrast to PBGFs, many such layers are required with high geometric precision for low–loss guidance.

---

[1] Corresponding author: e-mail bartelt@ipht-jena.de

Photonic Crystals. Edited by K. Busch, S. Lölkes, R. B. Wehrspohn and H. Föll
Copyright © 2004 Wiley-VCH Verlag GmbH & Co. KGaA
ISBN: 3-527-40432-5

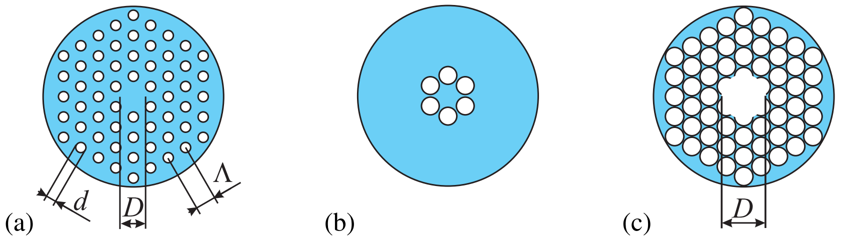

Figure 14.1: Cross sections of photonic crystal fibers: (a) holey fiber, (b) high–delta microstructured optical fiber, (c) photonic band gap fiber. Geometrical parameters: d – hole diameter, Λ – pitch, D – core diameter

In this work we focus on the modeling and fabrication technology of PCF, which are the main challenges. For details of applications arising from the unique properties of PCF, we refer to the excellent review by P. Russell [2].

14.2 Modeling of photonic crystal fibers

Due to their complex transverse structure, the modeling of light propagation in photonic crystal fibers requires new algorithms or at least the modification of established techniques. There are essentially two key modeling tasks for such fibers: the eigenvalue problem for obtaining the mode profile and propagation constant β for a given frequency ω of an ideal photonic crystal fiber, and the propagation problem to monitor the evolution of an arbitrary field launched into the fiber. Here we restrict ourselves almost exclusively to the first of these tasks. Propagation methods are concisely reviewed provided that they can also be used for obtaining mode profiles and propagation constants.

The versatile plane wave expansion and localized functions methods frequently used as standard mode solving techniques will be presented in some detail. Other approaches such as the finite element method (FEM) and the multipole expansion method are particularly well adapted to specific configurations and tasks. It will be reviewed in brief.

An ideal fiber is defined by translational invariance in the propagation direction, thus excluding all longitudinal inhomogeneities. Any transverse inhomogeneity can be included in mode calculations, e. g., by supercell approaches. Longitudinal variations can be accounted for by using propagation methods, depending on the smoothness of the variations.

Due to the extremely high index contrast across the fiber, compared to standard single mode fibers, the weak guidance approximation (scalar approximation) usually ceases to be valid. However, unless the air–filling fraction is too high, the scalar approximation can still be applied [8]. The group velocity dispersion as a quantity mainly defined by the air–silica interfaces of the fiber, is a sensitive detector of the vectorial nature of a fiber mode. Hence, to demonstrate the influence of vectorial effects we compare the results obtained for a PCF with hexagonal cladding of air holes pitched at 2.3 μm and for four different hole diameters, calculated by the scalar and vectorial methods (Figure 14.2). The core is formed by a silica-filled central hole as in the first holey fibers [1]. It is evident that for higher wavelengths, the

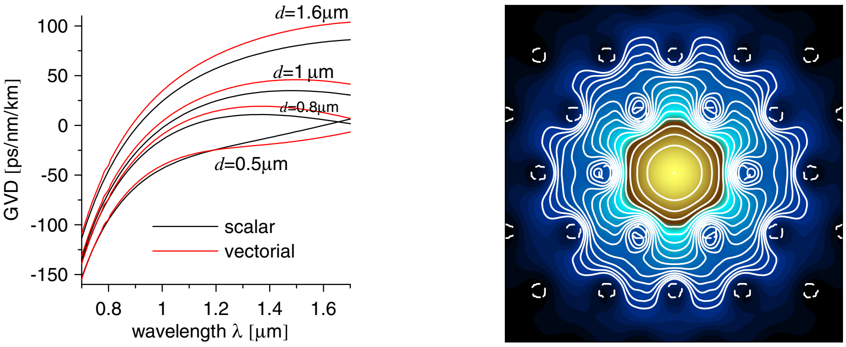

Figure 14.2: Comparison of the group velocity dispersion D for varying hole diameter d and fixed lattice pitch $\Lambda = 2.3\,\mu$m, calculated with the localized functions method in the scalar approximation and in the full-vectorial case (left) and x component of $\vec{H}$ of the mode for $d = 0.5\,\mu$m at $\lambda = 1.75\,\mu$m, taken from [9]. The contour line spacing is 2 dB.

difference between vectorial and scalar calculations increases and that for certain parameter regions of the fiber, the scalar approach can only provide the qualitative behavior of the dispersion curve. But for quantitative calculations, such as the determination of the zero dispersion wavelength required for experiments with solitons, vectorial equations have to be solved.

The starting point is the vectorial wave equation for the magnetic field in the frequeny domain

$$\vec{\nabla} \times \frac{1}{\varepsilon(x,y,\omega)} \vec{\nabla} \times \vec{H}(x,y,z,\omega) = \frac{\omega^2}{c^2} \vec{H}(x,y,z,\omega)\,. \tag{14.1}$$

The advantage of using the magnetic field is that the corresponding operator is Hermitian. Following the usual approach in waveguide theory [3] for solving the eigenvalue problem, the electric and magnetic fields of the waveguide mode in the Fourier domain are separated into a transverse and a longitudinal dependence, where we assume that the fiber index profile is translationally invariant in the propagation direction z:

$$\vec{H}(\vec{r},\omega) = \vec{H}(x,y,\omega)\exp(\imath\beta(\omega)z)\,, \quad \vec{E}(\vec{r},\omega) = \vec{E}(x,y,\omega)\exp(\imath\beta(\omega)z)\,. \tag{14.2}$$

Now the modeling task consists of calculating the bound eigenfunctions (modes) $\vec{H}_n(x,y,\omega)$, $\vec{E}_n(x,y,\omega)$ and the corresponding eigenvalues (propagation constant) $\beta_n(\omega)$ of the discrete part of the spectrum of the linear operator resulting from Maxwell's equations. Modeling of lossy PCFs requires additional efforts. Losses can occur due to material absorption (complex dielectric function $\varepsilon(x,y,\omega)$) or as radiation losses in PCFs with a finite cladding. The modes arising then, are leaky modes with a complex propagation constant. The solution of this problem is much more involved than in the case of real $\beta(\omega)$.

14.2.1 Plane wave expansion methods

A very robust and flexible method for solving the eigenvalue problem is expanding the magnetic field of the fiber into a truncated Fourier series. This implies 2D periodic boundary conditions for the fields of the fiber, i.e., the original structure is modeled as a periodic lattice of supercells. Essentially, there are two approaches for recasting Maxwell's equations into an algebraic linear eigenvalue system.

The solid–state approach calculates the possible frequencies $\omega_n(\beta)$ and all three components of the magnetic field for a previously fixed propagation constant β [10]. The equation eventually to be solved is derived from Equations (14.5) and (14.2) as

$$\left(\vec{\nabla}_\perp + \imath\beta\vec{n}_z\right) \times \frac{1}{\varepsilon(x,y,\omega_0)} \left(\vec{\nabla}_\perp + \imath\beta\vec{n}_z\right) \times \vec{H}_n(x,y,\beta) = \frac{\omega_n^2}{c^2}\vec{H}_n(x,y,\beta)\,, \tag{14.3}$$

with $\vec{\nabla}_\perp$ being the transverse Nabla operator. The dielectric constant has to be taken at a frequency chosen a priori, ω_0, because ω^2 is the eigenvalue to be determined. Thus, inclusion of dispersion into the plane wave approach is by no means a straightforward task. The field expansion intrinsically accounts for the constraint $(\vec{\nabla}_\perp + \imath\beta) \cdot \vec{H}(x,y,\beta) = 0$ following from Maxwell's equations if $\{\vec{G} + \beta\vec{n}_z, \vec{u}_{\vec{G}}, \vec{v}_{\vec{G}}\}$ is chosen as an orthogonal triad:

$$\vec{H}(x,y,\beta) = \sum_{\vec{G}\in\mathcal{G}} \left(h^{(1)}_{\vec{G}}\vec{u}_{\vec{G}} + h^{(2)}_{\vec{G}}\vec{v}_{\vec{G}}\right)\exp(\imath\vec{G}\vec{r}_\perp) \quad \text{with } |\vec{u}_{\vec{G}}| = |\vec{v}_{\vec{G}}| = 1\,. \tag{14.4}$$

Here $\mathcal{G}$ represents the subset of the reciprocal lattice of the underlying two dimensional supercell obtained by truncating the infinite Fourier series to N plane waves and the $h^{(i)}_{\vec{G}}$ are the unknown Fourier coefficients. For an efficient calculation of the matrix coefficients, the inverse dielectric constant $\varepsilon^{-1}(x,y)$ is expanded into a similar Fourier series $\vec{G}' \in \mathcal{G}$, which leads to simple sums of products of the Fourier coefficients of the index profile and of the respective $\vec{G}$ and $\vec{G}'$ [11] for the coefficients. The calculation of the Fourier coefficients can be performed very efficiently, by using a 2D Fast Fourier Transform (FFT) after smoothening the discontinuities in the dielectric constant by proper averaging [10].

The second approach solves the equation for the transverse fields, the standard waveguide eigenvalue equation [3], by expanding these fields into a series of plane waves [12] without additional constraints:

$$\left[\vec{\nabla}_\perp^2 + \frac{\omega^2}{c^2}\varepsilon(x,y,\omega) + (\vec{\nabla}_\perp \log\varepsilon)\times(\vec{\nabla}_\perp\times\circ)\right]\vec{H}_{n\perp}(x,y,\omega) = \beta_n^2\vec{H}_{n\perp}(x,y,\omega)\,. \tag{14.5}$$

Then the z–component can be calculated from $\vec{\nabla}_\perp \cdot \vec{H}_{n\perp}(x,y,\omega) + \imath\beta_n H_z = 0$. As in the solid–state approach, the overlap integrals with the dielectric constant can be obtained by FFT. The major advantage over the solid–state approach is that for a fixed wavelength of interest, the propagation constant is the eigenvalue to be determined. Hence it is easily possible to include the material dispersion $\varepsilon(x,y,\omega)$ into the eigenvalue equation.

Both approaches lead to rather extensive linear algebraic eigenvalue equations. For a mirror symmetric fiber cross section, the memory required to store the coefficient matrix can

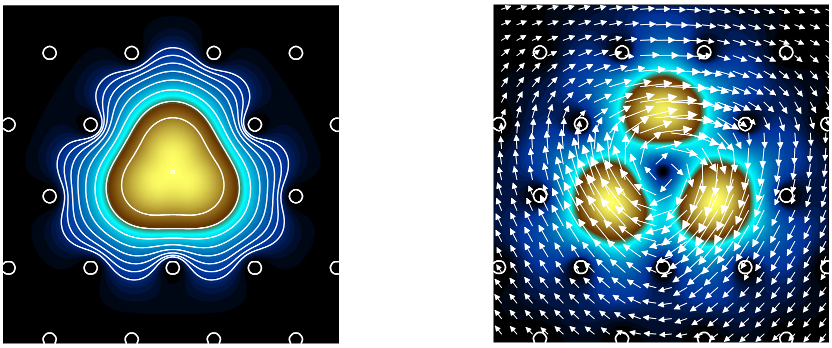

Figure 14.3: Intensity distribution of the (nearly) linearly polarized fundamental (HE_{11}, left, contour spacing 2dB) and the TM_{01} mode (right, with superimposed $\vec{H}_{\perp}$) of a PCF with three doped–silica filled holes as core. The lattice pitch is $\Lambda = 11.5\,\mu$m and hole diameter $d = 1.84\,\mu$m at $\lambda = 1.07\,\mu$m.

be reduced by a factor of 16, which makes the problem tractable with a direct eigensolver and allows the natural inclusion of the material dispersion.

For large systems, an iterative approach is more appropriate. This yields a certain number of the lower eigenvalues where the computational efforts increase with that number. In the case of index–guiding PCFs (holey fibers, large delta or cobweb fibers), where the guiding relies on modified total internal reflection, only the lowest eigenvalues are required because the guided modes correspond to the lowest frequencies for a fixed β. But it is also possible to determine the higher eigenvalues, which may correspond to guided modes in PBG fibers, without computing the underlying bands by introducing a shifted operator [10].

The solid–state approach has the advantage that, due to the particular form of the operator on the left hand side of Equation (14.3), this operator can numerically be applied very efficiently to a given field by transformation from original space to the Fourier domain and back. As a consequence, only vectors of size $2N$ rather than $2N \times 2N$ matrix elements need to be stored. Recasting the eigenvalue equation into a minimization problem of the Rayleigh quotient that is solved, e.g., by using conjugated–gradient like methods, finally gives a previously fixed number of eigenvalues in ascending order [10]. The efficiency of this method crucially depends on the fact that the mentioned operator is Hermitian. The performance of this method is demonstrated by the results of the mode calculations shown in Figure 14.3. There the fields of the fundamental (HE_{11}) and one higher order mode (TM_{01}) are displayed for a configuration where high–index contrast air–silica and low index contrast doped silica–silica are combined in the fiber cross section of a high–power fiber laser [13].

The inclusion of material dispersion into this method leads to a second iteration process deteriorating the method's efficiency. Recently, a perturbative approach was proposed [14] to tackle this issue fast and accurately by the plane wave method (PWM). In addition, by the artificial introduction of a properly chosen transverse wavevector, the mutual interaction of the modes in the lattice of supercells was minimized for a given mode [14], which further increases the efficiency of the algorithm.

14.2.2 The localized functions method

As the modes of interest are localized around the fiber core, the expansion of the fields into a set of orthogonal localized basis functions may be a more appropriate choice than using plane waves, as far as efficiency and convergence are concerned. Two–dimensional Hermite–Gaussian functions can serve as such a set [8, 15, 16]:

$$h_{x/y}(x,y) = \sum_{i=0}^{N_x-1} \sum_{j=0}^{N_y-1} h_{ij}^{x/y} \phi_i^w(x) \phi_j^w(y) \tag{14.6}$$

with

$$\phi_i^w(x) = \frac{2^{-\frac{i}{2}} \pi^{-\frac{1}{4}}}{\sqrt{i! w}} H_i\left(\frac{x}{w}\right) \exp\left(-\frac{x^2}{2w^2}\right). \tag{14.7}$$

As before, to facilitate the calculation of the coefficient matrix of the algebraic eigenvalue system with integrals involving the field and the refractive index distribution, the dielectric function has to be expanded into basis functions, which are easier to integrate. A reasonable expansion that avoids the supercell approximation consists in dividing the transverse dielectric function into a periodic part and a localized defect. The periodic part is expanded into a Fourier series and the localized defect into the set of Hermite–Gaussian functions in order to reduce the computational effort needed to calculate the overlap integrals with the fields. For fibers with two orthogonal mirror planes, the expansion reduces to even terms:

$$\epsilon(x,y) = \sum_{i=0}^{M_x-1} \sum_{j=0}^{M_y-1} a_{ij} \cos\left(\frac{2\pi i x}{l_x}\right) \cos\left(\frac{2\pi j y}{l_y}\right) + \sum_{i=0}^{L_x-1} \sum_{j=0}^{L_y-1} b_{ij} \phi_{2i}^d(x) \phi_{2j}^d(y) \,. \tag{14.8}$$

Here d denotes the potentially different widths of the basis functions, and l_x, l_y define the size of the unit cell of the periodic cladding. Due to the presence of the vectorial terms, an analogous decomposition for $\log \varepsilon(x,y)$ must be performed. In contrast to the periodic part, the calculation of the coefficients for the defect is critical because high order Hermite-Gaussian functions have to be integrated in two dimensions over nontrivial areas. As usual for modal expansion methods, the algebraic eigenvalue equations resulting from the waveguide Equation (14.5) read as

$$\beta^2 h_{kl}^x = \sum_{i,j} h_{ij}^x I_{ijkl}^{(1)} + \frac{\omega^2}{c^2} \sum_{i,j} h_{ij}^x I_{ijkl}^{(2)} + \sum_{i,j} h_{ij}^x I_{ijkl}^{(3)} + \sum_{i,j} h_{ij}^y I_{ijkl}^{(4)} \tag{14.9}$$

and a similar one for h_{kl}^y. Here, $I_{ijkl}^{(1)}$ represent integrals of the field basis functions containing the Laplace operator, $I_{ijkl}^{(2)}$ contains the dielectric functions, $I_{ijkl}^{(3)}$ the semivectorial differential terms and $I_{ijkl}^{(4)}$ the vectorial cross coupling terms from Equation (14.5).

The choice of a localized basis system eventually leads to smaller matrices compared to the plane wave method and may result in reduced CPU time. As a rule of thumb CPU time reduces more for large mode areas (small holes) and modes of PBG fibers. For example, using PWM to calculate the mode and its effective index, shown in Fig. 14.2, with a comparable accuracy required twice the CPU time of the localized function method. Due to the intrinsically infinite cladding with an effectively lower index, this method cannot be applied to finite structures, which may exhibit radiation losses. On the other hand, it is appropriate for fibers with infinite cladding because no supercell approximation has to be used, and the material dispersion can be included. Using this method, we obtained the results depicted in Figure 14.2.

14.2.3 The finite element method (FEM)

In the framework of the plane wave, the localized functions and other decomposition methods, as, e.g., the polar coordinate Fourier decomposition method [17], the field has to be expanded in terms of global basis functions, taking into account the discontinuities of the refractive index at the air holes via the derivatives in the wave equation (14.5) instead of using the transition conditions at interfaces. These conditions would lead to a jump in the normal derivative of the tangential components of the $\vec{H}$ field and to jumps of the normal components of the $\vec{E}$ field. A sufficiently accurate description of this behavior with planes waves or other basis functions may require a huge number of functions and lead to convergence problems.

Instead, in the FEM [18,19] the fiber cross section is divided into homogeneous subspaces where Maxwell's equations are solved by accounting for the adjacent subspaces. Usually, these subspaces are triangles allowing for a good approximation of circular structures. The boundaries of the triangles approximate the interfaces of the dielectrics well, and the fields at the boundaries of the triangles can be connected with the help of the transition conditions just mentioned. This scheme leads to a matrix eigenvalue system, which can be solved numerically. Because the system inherently fulfills the transition conditions and the mesh of triangles can be chosen (in principle) arbitrarily, and hence adapted to the system, the method of discretization can be very efficient, compared to expansion methods. In particular, this method is superior to other methods if the transverse structure exhibits big index differences. Thus it meets the requirements well of PCF modeling [18] where the index difference is substantial and, hence vectorial effects will matter(see Figure 14.2). Even leaky modes can be calculated by means of the FEM by introducing perfectly matched layers (PML) as boundary conditions [20].

14.2.4 The multipole method

The multipole method is particularly suited for PCF fibers featuring a finite arrangement of circular holes in a silica matrix surrounded by some other, possibly absorptive jacket. In general, the modes of such a configuration will be leaky. Similarly to FEM, the multipole method [21] divides the fiber cross section into homogeneous subspaces where the wave equation (14.5) reduces to two scalar Helmholtz equations. In addition, a circular jacket of appropriate optical properties surrounds the holey domain. Here these subspaces are the circular air holes. The solutions in local coordinates are Bessel and Hankel functions. So, similar to step index fibers, the z components of the $\vec{e}$ and $\vec{h}$ field in the vicinity (outside) of cylinder l, are written in terms of its local coordinates (r_l, θ_l)

$$e_z(x,y) = \sum_m \left[A_m^{el} J_m(k_\perp^e r_l) + B_m^{el} H_m^{(1)}(k_\perp^e r_l) \right] \exp(\imath m \theta_l), \tag{14.10}$$

with $k_\perp^e = \sqrt{\omega^2 \varepsilon_e / c^2 - \beta^2}$ being the silica transverse wave vector, and the potentially complex eigenvalue β. A similar expansion holds for the jacket. Then, consistency is demanded with a physically motivated Wijngaard expansion for the global field. The field transition conditions are accounted for by the use of cylindrical reflection coefficients obtained from the respective decomposition (14.10) with $k_\perp^i$ for the interior of the cylinder, which leads to a coupling of the individual field components. Eventually, a matrix equation is obtained where the coefficients are rather involved functions, composed of Bessel and Hankel functions with the eigenvalue β_n as argument. To obtain the nontrivial solutions, the zeros of the determinant of this matrix are computed by an iterative technique.

Using the multipole method, leaky modes of PC fibers with a finite number of air holes can be calculated very accurately [21]. For finite structures with cylindrical inclusions, therefore, this approach is very well suited.

14.2.5 Propagation methods

In contrast to mode solvers, propagation methods can be applied to model light propagation in configurations with longitudinal inhomogeneities of the refractive index. Adapted to PCFs, propagation methods usually discretize the (vectorial) wave equation in Fresnel approximation after separating a previously appropriately chosen index n_0,

$$\vec{H}(\vec{r}, \omega) = \vec{h}(\vec{r}) \exp\left(\imath \frac{\omega}{c} n_0 z\right), \tag{14.11}$$

in order to avoid fast oscillations in the propagation direction. Often the magnetic field is the preferred choice because of its smoothness at dielectric discontinuities and the slightly easier vectorial terms in the wave equation. Usually, backtravelling waves are neglected and the diffraction terms are directly discretized on an equidistant mesh. In our context the field depends on two transverse coordinates and has two vectorial components coupled via the wave equation. That is why the numerically stable Crank–Nicolson discretization scheme does not lead to banded, though at least sparse matrices. If there are longitudinal inhomogeneities, the large resulting linear system must be solved for every propagation step. Additionally, appropriate boundary conditions must be applied to prevent spurious reflection at the boundaries of the computing window. The challenge is an efficient numerical implementation. This can be achieved, e.g., by utilizing an iterative solver (GMRES) [22] or finite–difference schemes consisting of tridiagonal matrices, as ADI [23].

To only obtain the lowest order modes of a given fiber, the imaginary distance beam propagation [24] can be used. By this method, modes of microstructured optical fiber have been calculated [25] up to order 4.

Another particularly powerful and accurate propagation method is the finite difference time domain method (FDTD) [26], in which a three–dimensional field distribution is propagated in time. Here Maxwell's equations are directly discretized without additional approximations as, e.g., the Fresnel approximation exploited in the previous methods. This method

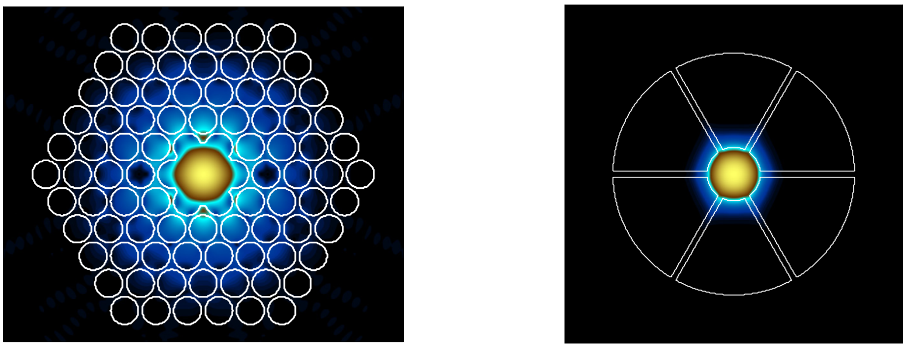

Figure 14.4: Square root of the intensity distribution of the fundamental air-guided mode of a PCF with six completely removed capillaries as air core, surrounded by four rings of holes calculated with FDTD (left). The lattice pitch is $\Lambda = 2.27\,\mu$m and the hole diameter $d = 1.98\,\mu$m at $\lambda = 1.55\,\mu$m. The effective index is 0.977. The right figure shows a cobweb fiber with a web thickness of 220 nm and an inner diameter of $2.2\,\mu$m calculated with FDTD.

is extremely time–consuming and requires huge memory capacities. Usually it is preferred for visualizing light propagation in two or three dimensional photonic crystals on at most a millimeter scale. Thus for PCFs of some meters or even kilometers in length, this approach seems to be inappropriate. But the approach can be used for efficiently determining the PCF modes, in particular as an alternative to the multipole method for leaking structures.

In pursuance of this goal, the problem can be reduced by one dimension by separating a propagation constant fixed a priori in z as in Equation (14.2). In the remaining 2D plane, then, an initial field is propagated in time [27]. Due to the nonvanishing z–dependence of the fields, a separation into TE and TM polarized fields cannot be performed. Thus, Maxwell's equations have to be solved for all six field components simultaneously. Using PML [26] as boundary conditions for terminating the computing window one can even study leaky structures. The leaky modes obtained are characterized by an imaginary frequency, which provides the temporal decay rate related to the radiation losses. Due to the propagation constant fixed a priori, material dispersion cannot be included directly. This method was used for calculating the modes of a genuine band gap fiber (see Figure 14.4) where the air core serves as the guiding area. For this configuration, the application of e.g., the PWM is hardly feasible because the guided modes are not the lowest ones but are situated within the band gap. Thus, many modes must be calculated to find the desired air–guided mode. So the advantage of the iterative solver is practically lost. With the FDTD instead, one launches an initial pulse and after a short time of propagation, a steady state formed by the modes is reached with moderate computational efforts. Using the same spatial mesh (Yee's mesh) in Fourier domain, on the other hand, one can obtain an eigenvalue equation for mode calculations [28] based on finite differences, in contrast to the expansion methods described in the previous section.

In conclusion, we have shown that various standard methods for calculating the guided modes of photonic crystal fibers can be applied. Each method has its own advantages and disadvantages; the choice is determined by the definition of the specific problem to be solved.

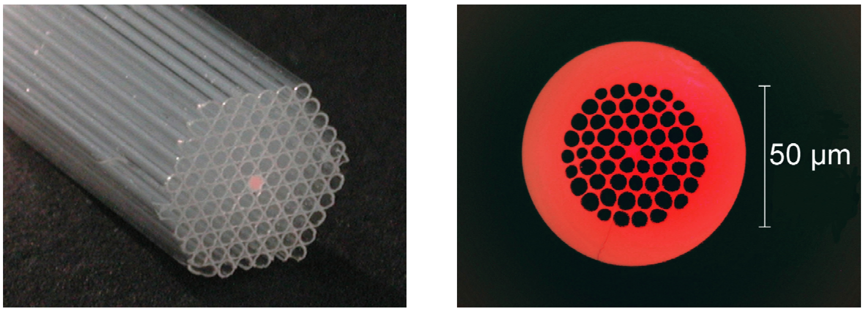

Figure 14.5: Fiber preform as a stack of glass capillaries with a central glass rod (left) and cross section of an implemented holey PCF (right).

14.3 Fiber technology

14.3.1 Preparation of photonic crystal fibers

The usual way to prepare optical fibers with a microstructured cross section is to stack capillaries and solid rods to form a compound structure, which resembles the desired fiber cross section. The final diameters are implemented during the following draw down. In this step, the capillaries have to be fused with each other, however, without closing the holes completely. The capillaries can be small–diameter tubes or specially prepared canes of hexagonal outer shape in order to facilitate precise stacking (in the latter case, however, with increased preparation efforts as far as grinding and polishing is concerned). Due to the small and complex structures, as far as hole diameters, spacing and geometric arrangement are concerned, in most cases, the preparation cannot be accomplished in a single process step but comprises the preparation of intermediate preforms, which must be elongated, jacketed and combined and processed again to yield the final fiber. These preparation steps can be performed vertically in normal fiber drawing towers, but in part also horizontally on glass working lathes, where compound formation, jacketing, pre–collapsing or moderate elongation and compression are possible.

The equipment just mentioned is standard in optical fiber technology. Beyond this, however, arrangements applying a precisely defined inner pressure in the holes (usually a slight overpressure relative to the atmosphere, but sometimes a vacuum) is required for the lathe as well as for the draw tower. This is a consequence of the large internal surface of the PCF, where surface tensions play a much more important role than in solid fiber technology. For instance, starting from a single preform, the hole–pitch relation of the fiber can be adjusted in a wide range by varying pressures.

14.3.2 Fluid–dynamic aspects in the preparation of photonic crystal fibers

All steps in the preparation of photonic crystal fibers depend on the viscous flow of glasses heated to high temperatures. At the processing temperature, glasses and especially quartz glass behave as incompressible Newtonian liquids. Since the Reynolds number is much smaller than 1, the inertia can be neglected. Therefore, the fluid mechanics can be described and simulated on the basis of the Navier–Stokes equations in Stokes–Flow approximation ("creeping flow") [30]. As driving forces of the flow, the mechanical drawing force applied must be considered, but also the surface tension σ and atmospheric pressure differences $p_i - p_a$. They are introduced via boundary conditions at the surfaces of the solid fiber part where the pressures generated by the driving forces are equal to the sum of frictional tension and isotropic pressure. A further simplification is often applied in the treatment of fiber drawing and denoted as quasi "one–dimensional flow". Referring to a cylindrical coordinate system (ρ, ϕ, z), the one–dimensional flow approach implies that the axial velocity component v_z depends only on the axial coordinate z, independent of the radial and azimuthal coordinates [31–33]. For a smooth neck–down region, the simplification of a plane flow is validated by theoretical and experimental investigations [34], but in cases with a very steep neck–down region, certain deviations have been reported [35]. On the basis of "one–dimensional flow", the velocity field can be assumed to be a superposition of two fields expressing in the first case the pure "drawing" (no collapsing effect, preserving the relative cross sectional shape), and in the second case the pure "collapsing" (change of the cross sectional shape without any length change). Considering a small cylindrical volume element, the drawing time step follows immediately from the continuity relation in the form of a homogeneous elongation. In the collapsing step, the axial velocity is zero and the radial and azimuthal velocity components have to be calculated, which can become an intricate problem for complex inner structures of the fiber. For the simplest case of a PCF, a hollow cylinder with inner radius r_i, outer radius r_a and length Δz, the time dependent differential equations were derived [36]. In the real drawing process, we have to allow for the movement of the volume element through the heating zone of the drawing apparatus as shown schematically in Figure 14.6, expressed by a variation of the viscosity η in consequence of an axial temperature profile.

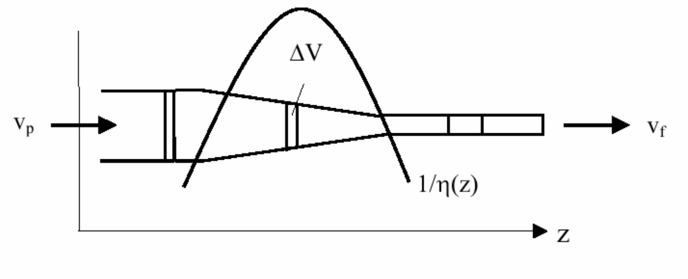

Figure 14.6: Scheme of the heating zone (preform with volume element ΔV, preform feed rate v_p, fiber drawing velocity v_f, position dependent viscosity $\eta(z)$).

With the axial velocity of the volume element relative to the heating zone, v_z, the time coordinate is transformed into the axial space coordinate z

$$\mathrm{d}z = v_z(z)\mathrm{d}t\,. \tag{14.12}$$

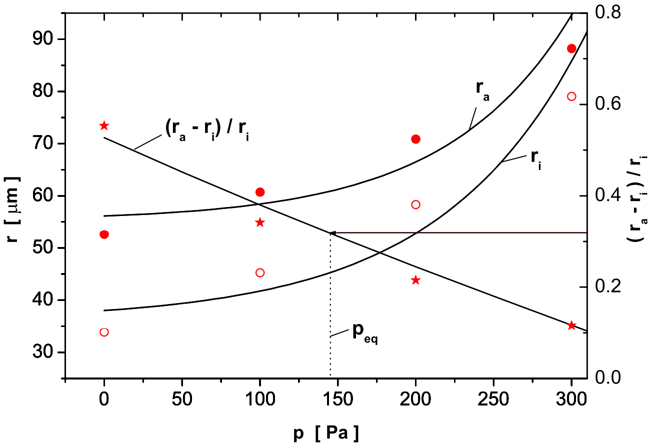

Figure 14.7: Hollow fiber dimension, experimental results in comparison with calculations (solid lines) r_{ap}: 12.50 mm, r_{ip}: 9.50 mm, v_p: 0.5 mm/min, v_f: 19.8 m/min, drawing force F: 0.38 N.

The steady state where the distribution in the heating zone remains temporarilly unchanged is relatively simple. Here $v_z(z)$ is inversely proportional to the cross section area a. In the case of the non–stationary formation of the drawing process, the total temporal change of a is given by

$$da/dt = \left(\partial a/\partial t\right)_z + \left(\partial a/\partial z\right)_t v_z \,, \tag{14.13}$$

where v_z has to be calculated by spatial integration over $\Delta z/t$. The partial differential Equation (14.12) can be solved by suitable numerical methods.

On the basis of the equations derived for the hollow fiber it can be shown, that the "equilibrium" pressure for the drawing process, where the ratio of outer and inner radius remains constant, can be expressed to a good approximation by the preform radii r_{ap} and r_{ip}

$$\left(p_i - p_a\right)_{eq} \approx 2\sigma \left(r_{ap}^{-1} + r_{ip}^{-1}\right) , \tag{14.14}$$

this pressure being just twice the value derived for the case of collapsing without length change [36].

Figure 14.7 shows hollow fiber dimensions calculated for different preform geometries, drawing forces and inner pressures differences in comparison with experimental results. A good agreement is found with regard to both the equilibrium pressure and the variation of fiber dimensions with the pressure.

Little attention has been paid up to now to the non–stationary transient phenomena, which are especially crucial in the case of PCF, because of the increased number of process parameters. As an example, Figure 14.8 shows diameter changes that appear in the elongation of tubes on the glass lathe and can be simulated by the equations derived above.

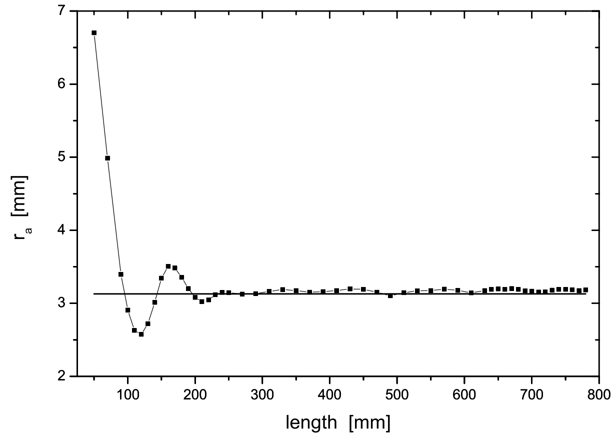

Figure 14.8: Diameter oscillations of an elongated silica tube (r_{ap}: 7 mm, r_{ip}: 5.7 mm, v_p: 2 mm/min, v_f: 10 mm/min).

14.4 Special properties of photonic crystal fibers

In the following sections we study some characteristic properties of holey fibers prepared from different materials and with various structures. Besides such properties like effective mode area and dispersion, which are a result of the particular microstructure and can be derived from numerical modeling, see Section 14.2, other properties originating from the glass material used and the fabrication process, as e.g., attenuation and mechanical strength, are also discussed.

14.4.1 Spectral transmission

Transmission properties of non–silica PCF

PCFs made from heavy metal oxide and chalcogenide glasses are interesting for modulation and switching applications, because of their high nonlinear refractive index, and for evanescent field spectroscopy, because of their transmission in the near and mid IR range [37, 38]. Here, the attenuation properties of multicomponent glass PCFs were studied for lead oxide silicate holey fibers. The preform was fabricated by stacking lead glass tubes (28 % lead oxide) hexagonally with seven solid lead glass rods as the core. For mechanical stabilization and better handling, an outer ring of glass rods was applied (Figure 14.9). The geometric parameters of two multimode fiber types implemented are listed in Table 14.1. Figure 14.10 shows the attenuation spectra of the total fiber and the core region. Both curves are quite similar, but curve 2 displays higher losses in the wavelength range of 450 and 700 nm. For comparison, a solid fiber of the same material was measured. The peak at 1400 nm is related to OH–groups. It is supposed that the peaks at 650 nm and 1100 nm are caused by transition metal impurities of the glass, probably Ni^{2+} and Fe^{2+} impurities, respectively. Despite the homogeneous structural arrangement supported by low melting temperatures and lower surface tension of the heavy metal oxide PCF, high attenuation values (compared to silica PCF) limit the applications to a length of several meters.

Table 14.1: Parameters for lead oxide silicate holey fibers as shown in Fig. 14.9.

Fiber	a)	b)
hole diameter d	6.2 μm	2.5 μm
pitch Λ	9.2 μm	10.1 μm
core diameter	26.2 μm	39.0 μm
d / Λ	0.67	0.25

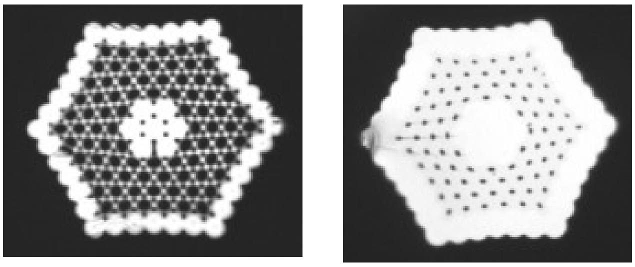

a) b)

Figure 14.9: Cross sections of lead oxide silicate holey fibers with different hole diameters (a) drawn at 840 °C with pressure applied (b) drawn at 880 °C without pressure.

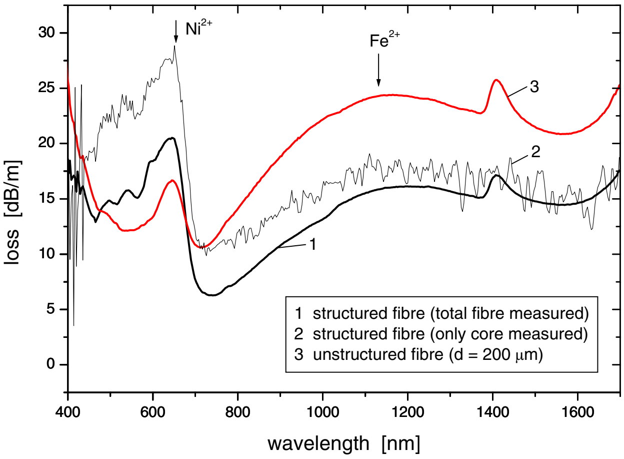

Figure 14.10: Loss spectra of structured and unstructured lead glass fibers (the loss value fluctuations of core light measurement (2) are caused by the low power intensity in relation to total fiber measurement).

Losses due to preform preparation and drawing procedure for silica fibers

Typically, the basic material for the preparation of PCF preform components is high purity–silica. The different silica materials for lightguide preparation are distinguished by their defect and OH–group concentrations, originating from different production processes. Usually, the concentration of transition metal ions is at the ppb level due to the sophisticated purification processes. In practice, it is of no relevance to additional material losses. Figure 14.11 shows the loss spectrum of a four–ring solid–core fiber (air hole diameters 6 μm, pitch of 7 μm) made of the typical fiber material F300, and the spectrum of a fiber, fully collapsed during the drawing procedure. The capillaries for the PCF preform were prepared by precollapsing with a hydrogen oxygen torch and subsequent elongation. The four-ring holey fiber as well as the collapsed holey fiber show an OH–absorption peak intensity at 1395 nm of about 0.4 dB/m, corresponding to an OH–content of 10 ppm. However, the unstructured fiber shows an absorption intensity of approximately 20 dB/km at 1395 nm, which matches with the material absorption level of the glass material (see Figure 14.11). The similarity of the OH absorption of holey and a completely "collapsed" PCF, shows that OH groups were mostly included during capillary preparation by hydrogen–containing flame treatment. A high OH concentration within a small outer layer of about a hundred micrometers, due to flame treatment of a tube has already been investigated and described [39]. Obviously the OH absorption effects caused by atmospheric humidity on the porous holey structure play a negligible role. By subsequent etching with hydrofluoric acid it is possible, in principle, to remove this layer and to re-establish the low OH level of the untreated tube material. Another effective method is the "torch free" PCF preparation procedure. The result is shown in Figure 14.12. All elongation and drawing steps were implemented by heat treatment in a dry inert gas atmosphere. Consequently an OH peak level of approximately 16 dB/km was obtained, corresponding to an OH concentration of only 0.4 ppm. In the same way, the background loss at 1.3 μm decreases to 2.9 dB/km. These high transmissivity fibers may be used for applications where interaction lengths in the kilometer range are essential. Beside the OH, the attenuation of holey fibers shows some peculiarities in their spectral loss behavior compared to solid fibers (Figure 14.11, Figure 14.12), e.g., additional losses in the red and NIR spectral ranges. Possibly, these loss effects are caused by drawing–induced atomic defects in the pure silica material. The relevance of the special PCF structure with its large inner surface area for the formation of atomic defects is still unknown. Typical process–induced atomic defect bands are in the wavelength range of 630 nm [40] and in the NIR at about 850 nm [41].

14.4.2 Variation of the numerical aperture and the mode profil

The effective refractive index of the cladding can be adjusted by varying the air filling fraction (determined by the ratio d/Λ) of the holey fibers. As a result, the numerical aperture (NA) of PCFs may vary over a wide range from less than 0.1 to more than 0.5. To estimate the effect of structural changes on the numerical aperture, the sample fibers in Table 14.2 were prepared (see also Figure 14.13). Increasing penetration of the evanescent light into the air holes for higher wavelengths leads to a reduced effective index of the cladding, and hence additionally to a strong wavelength dependence of the numerical aperture. Consequently, for a suitable air filling fraction, one can obtain single mode behavior over a wide wavelength range [42].

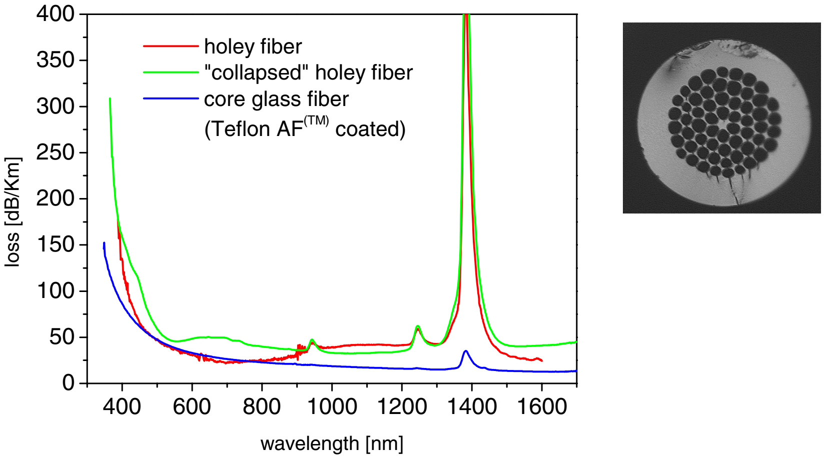

Figure 14.11: Micrograph and loss spectrum of four–air–ring holey fiber (red line) compared with “collapsed” holey fiber (green line) and pure core glass fiber (blue line).

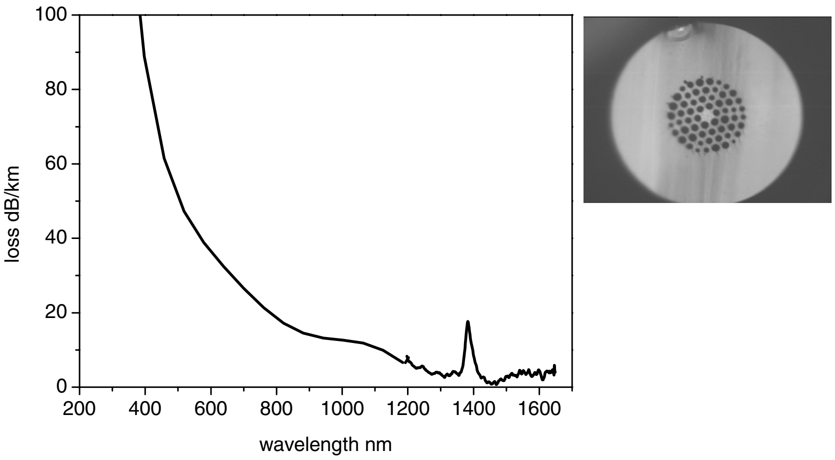

Figure 14.12: Micrograph and loss spectrum of a four–air–ring solid core PCF, prepared by dry inert gas heat treatment processing.

We also observed changes in the bending losses due to the variation of the numerical aperture. Also, the mode field distribution is mainly determined by the air filling fraction of the cladding and the core dimensions, and reflects the symmetry of the regular arrangement of the air holes in the cladding. Typically the microstructured cladding supports guiding of the fundamental mode and shows increasing losses for higher modes, if any. The influence of the dimensions of the holey cladding structure is illustrated in the following examples. The low aperture fiber

Table 14.2: Geometric and optical properties of implemented PCF (core diameter as inner hole distance).

fiber	ring number	mean core diameter	mean hole diameter	wall thickness	NA	MFD
c	2	14 μm	4.0 μm	3.2 μm	0.04	12.0 μm
d	2	13 μm	6.6 μm	2.4 μm	0.08	14.7 μm
e	2	4.5 μm	12.0 μm	0.4 μm	0.66	10.5 μm

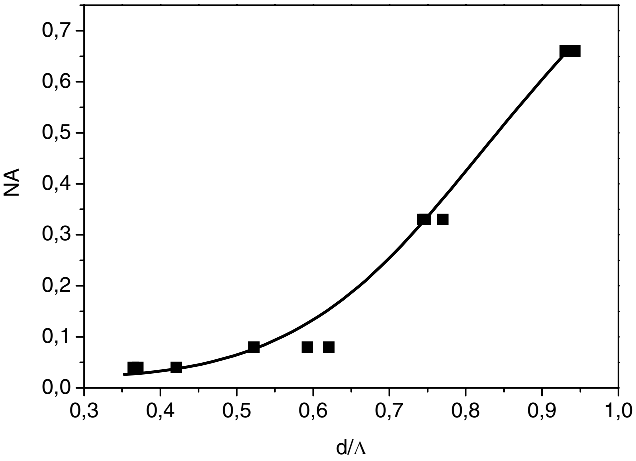

Figure 14.13: Influence of structural modifications of the fibers on the NA.

shown in Figure 14.14 is characterized by a hexagonal near–field pattern of $11\,\mu\mathrm{m} \times 13\,\mu\mathrm{m}$. This fiber only allows propagation in the fundamental mode at wavelengths above 0.85 μm and exhibits an extremely high sensitivity to bending. By increasing the air filling fraction (see Figure 14.15), the numerical aperture increases to 0.08 and the mode field diameter to 14.7 μm. The fiber has two guided modes and is also sensitive to bending. Increasing the internal pressure during the fiber drawing process leads to a PCF with a cobweb structure with extremely small wall thickness as shown in Figure 14.16. Due to the core diameter of about 4.5 μm, a large part of the evanescent field intensity is located in the first ring of air holes, which is useful, e.g., for evanescent wave sensing.

14.4.3 Dispersion properties

In contrast to conventional step–index fibers with very low index difference where the zero dispersion point is primarily defined by the glass material and occurs at wavelengths around 1280 nm, it is usually the waveguide dispersion that prevails in PCFs due to the air–silica interfaces in the cladding [43]. This allows for a dispersion tailoring by altering the PCF cross section. An extreme example is the cobweb structure with large air–filled portions, where the zero dispersion wavelength can be shifted down to visible wavelengths [44]. With holey fibers, a proper design allows for an ultra–flattened curve over a wide wavelength range [45]. This can be used, e.g., for the transmission of ultrashort pulses.

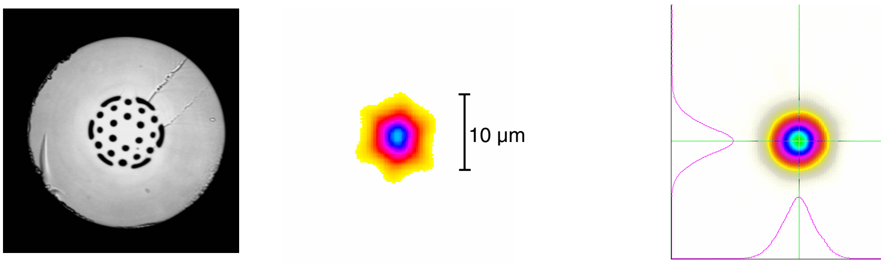

Figure 14.14: Micrograph of two–air–ring solid–core PCF, near–field and–far field patterns (fiber sample c).

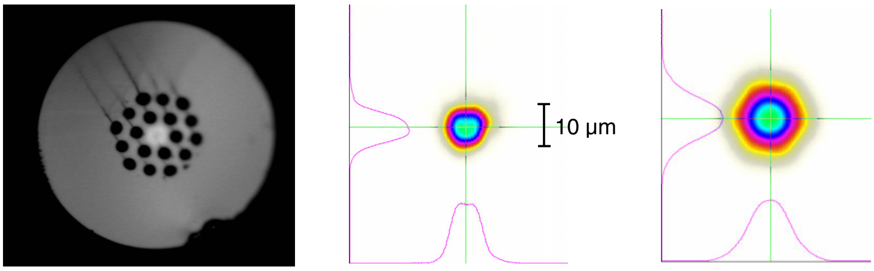

Figure 14.15: Fiber micrograph, near–field and far–field patterns of two–air–ring fiber with increased hole dimensions (fiber sample d).

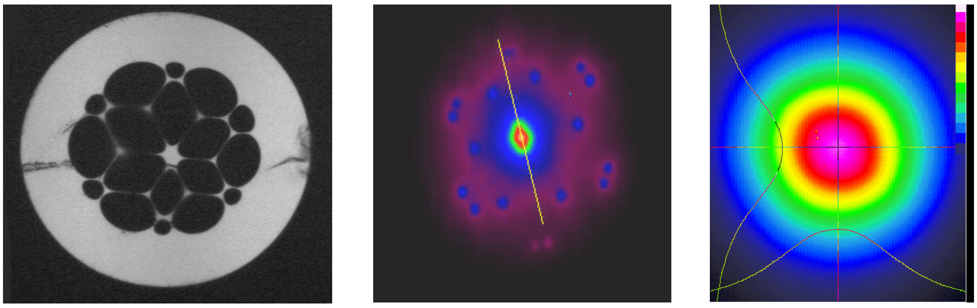

Figure 14.16: Micrograph, near–field and far–field patterns of a structured cobweb PCF (fiber sample e).

14.4.4 Mechanical properties

Until now, the mechanical properties of PCF have been investigated but sparsely. Due to the increased inner surface, enhanced corrosion effects caused by environmental conditions could influence the mechanical stability of the fiber. We have shown that the mean tensile strength

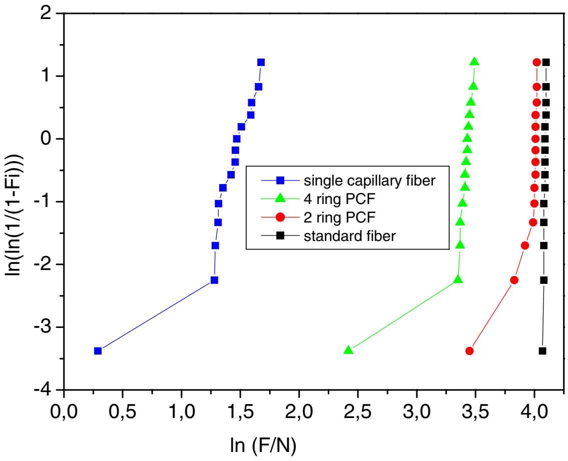

Figure 14.17: Weibull plots of holey fibers in comparison to compact silica fiber.

of holey fibers actually depends on the cross section structure and is lower than that for standard silica fibers. In Figure 14.17, Weibull plots (fracture probability vs. tensile strength) of different solid core PCFs with similar hole/pitch dimensions show the reduced mean tensile strength as well as decreased Weibull slope parameters compared to a compact standard silica fiber. Surprisingly, however, their mechanical parameters exceed those of single capillary fibers by far. The corrosion effect on the inner surface of a four–ring PCF was investigated by water loading of capillaries with liquid and vaporous water. According to these results, the tensile strength does not decrease by more than 3 % after 4 days at room temperature (treatment with liquid water) and at 70 °C (treatment with vaporous water).

14.5 Overview of applications

Within a short time, PCFs have found a wide range of applications. A first group of obvious applications is related to the improved flexibility in achieving specific optical parameters and mostly concerns holey or cobweb fibers. The adjustment of the effective refractive index of the cladding via the air filling fraction has been used for the implementation of extremely large and extremely small index steps. In the case of a large refractive index difference between the core and the cladding either a strong guiding or small mode areas were achieved. In the opposite case of very small index variations, fibers with large mode areas resulting in relatively low energy densities are possible. The flexibility in adjusting the effective mode area and the high power densities achieved by these means, greatly facilitates the generation of nonlinear effects in fibers (small solid glass core and high air filling fractions in the cladding). Highly nonlinear fibers with zero–dispersion at 1.55 μm are generally very attractive for a range of telecommunication applications such as parametric amplifiers, wavelength conversion and all-optical switching [46]. A very impressive example for the application of nonlinear effects is the generation of light with a supercontinuum spectrum.

Large mode areas, on the other hand, allow nonlinear effects to be avoided and are therefore interesting for high power transmission. The flexibility to modify the geometric properties in PCFs provides a simple way to deviate from cylindrical geometries. As a result, highly birefringent fibers may easily be designed. In a similar way, double–core ring structures or dual–clad PCFs combining the advantage of a large mode area for the laser field in the inner holey cladding with a rare–earth doped central core and the guidance with good pump absorption by an air–silica cobweb outer cladding, have been used successfully for constructing efficient fiber lasers [47], even with high output powers [13,50]. Finally, the possible variation in the effective refractive index results in different bending properties.

A second group of applications is related to the more specific light guiding properties in PCFs and concerns holey or cobweb as well as photonic band gap fibers. Due to the microstructure in the fiber, the dispersion properties are strongly affected. New properties such as strongly anomalous, flattened or shifted dispersion curves have been achieved. For example, such fibers may exhibit a single mode characteristic over an extended range of wavelengths (endlessly single mode) [1], even for an unusually large mode area [49]. The dispersion can be tailored to be nearly zero ultra-flattened [45] or anomalous for wavelengths well below 1270 nm [25]. Highly enhanced normal dispersion for dispersion compensation at 1550 nm has also been achieved [8]. Cobweb [2, 51] or high–delta air–silica microstructured optical fibers [25] have novel optical properties concerning better confinement of the electric field compared to holey fibers. Due to their high air filling fraction, those fibers are often multimode, but guiding can be achieved with only a few rings of air holes [25]. Due to the peculiar dispersion properties and the small core diameter, soliton formation at 850 nm [52], broadband continuum generation extending from near–infrared to the visible [53, 54] via efficient four–wave mixing, Raman scattering and soliton effects [55], efficient third harmonic generation [56, 57], pulse compression at 800 nm, and other strong nonlinear interactions have been observed in such PCFs with a pure silica core [58].

For photonic band gap fibers, non–glass materials such as fluids, gases or vacuum may be used as light guiding medium, which opens up new wavelength ranges and possibly high power levels for light guiding. However, the guided mode may not be concentrated in the air core completely, and part of the power may still pass through solid material. Light guidance in air of such a hollow–core PBGF has been demonstrated using a hexagonal pattern of air holes in silica as cladding, surrounding a core formed by removing seven of the constituting capillaries [2,4]. Potential applications involve guiding of high intensities without nonlinear or damage effects. Gas–based nonlinear optics with high efficiencies such as Raman scattering or generation of higher harmonics up to x–ray wavelengths becomes possible [60]. Such concepts will also enable new applications for optical fiber sensing.

In a third group, one may summarize applications based on a combination of effects or of specialized applications. The generation of a supercontinuum light source mentioned before is actually based on a combination of nonlinear effects and single mode transmission. The resulting spectrum, consisting of an extremely large number of discrete individual frequencies, can be used as a highly accurate standard for measuring frequencies [59]. Other applications are envisaged in optical coherence tomography, spectroscopy and metrology. A combination of fiber gratings and photonic crystal fibers has successfully been used to implement a new range of grating–based optical devices. These fibers may be used for long–period grating devices, where light is coupled to non–leaking cladding modes [46]. As a very unconventional application, hollow core fibers have been used for levitation and guidance of microparticles by light forces within the hollow core [29].

This short overview cannot give more than an incomplete impression of some of the major applications, but it shows how PCF technology can go well beyond the known and accepted limits of conventional optical fibers and expands our horizons in optical light guiding techniques.

14.6 Conclusions

Nowadays, conventional optical fibers are optimized in that they exhibit a delicate balance between losses, nonlinearity, dispersion and polarization properties. Photonic crystal fibers may revolutionize fiber–optical system design for there are much more degrees of freedom in varying these parameters independently. Holey and large delta fibers permit the control of nonlinearity and dispersion just by changing their transverse structure. However, most spectacular applications may be anticipated for PBG or hollow core fibers because of the flexibility in choosing the core material. PCF design and modeling is challenging but well understood nowadays. These mature modeling techniques are the prerequisite for an effective fiber manufacturing being still the biggest challenge. The field of PCFs is just coming of age, having the consequence that losses approach those of conventional fibers. It may be anticipated that considerable progress will be achieved within the next years and PCF can then unfold their full spectrum of exciting properties.

Acknowledgement

Funding of this work by the German Science Foundation (DFG) and the Federal Ministry of Education and Research (BMBF) is gratefully acknowledged.

References

[1] J. C. Knight, T. A. Birks, P. St. J. Russell, and D. M. Atkin, Opt. Lett. **21**, 1547 (1996).
[2] P. Russell, Science **299**, 358-362 (2003).
[3] A. W. Snyder and J. D. Love, Optical Waveguide Theory (Chapman and Hall, London, 1983).
[4] R. F. Cregan, B. J. Mangan, J. C. Knight, T.A. Birks, P. St. J. Russel, P. J. Roberts, and D. C. Allan, Science **285**, 1537-1539 (1999).
[5] P. Yeh, A. Yariv, and E. Marom, J. Opt. Soc. Am. **68**, 1196-1201, (1978).
[6] F. Brechet, P. Roy, J. Marcou, and D. Pagnoux, Electron. Lett. **36**, 514-515 (2000).
[7] B. Temelkuran, S. D. Hart, G. Benoit, J. D. Joannopoulos, and Y. Fink, Nature **420**, 650 (2002).
[8] D. Mogilevtsev, T. A. Birks, and P. St. J. Russell, Opt. Lett. **23**, 1662 (1998).
[9] R. Iliew and F. Lederer, in OSA Trends in Optics and Photonics (TOPS) Vol. 57, Quantum Electronics and Laser Science Conference (QELS 2001), Technical Digest, Postconference Edition (Optical Society of America, Washington DC, 2001), p. 146.
[10] S. G. Johnson, J. D. Joannopoulos, Opt. Express **8**, 173-190 (2001).
[11] S. John and K. Busch, J. Lightwave Technol. **17**, 1931-1943 (1999).
[12] A. Ferrando, E. Silvestre, J. J. Miret, P. Andrés, and M. V. Andrés, Opt. Lett. **24**, 276-278 (1999).
[13] J. Limpert, T. Schreiber, S. Nolte, H. Zellmer, A. Tünnermann, R. Iliew, F. Lederer, J. Broeng, G. Vienne, A. Petersson, and C. Jakobsen, Opt. Express **11**, 818 (2003).
[14] J. Lægsgaard, A. Bjarklev, and S. E. Barkou Libori, J. Opt. Soc. Am. **B 20**, 443 (2003).

[15] T. M. Monro, D. J. Richardson, N. G. R. Broderick, and P. J. Bennett, J. Lightwave Technol. **17**, 1093-1102 (1999).

[16] T. M. Monro, D. J. Richardson, N. G. R. Broderick, and P. J. Bennett, J. Lightwave Technol. **18**, 50-56 (2000).

[17] L. Poladian, N. A. Issa, and T. M. Monro, Opt. Express **10**, 449 (2002).

[18] F. Brechet, J. Marcou, D. Pagnoux, and P. Roy, Opt. Fiber Technol. **6**, 181-191 (2000).

[19] K. Saitoh, M. Koshiba, T. Hasegawa, and E. Sasaoka, Opt. Express **11**, 843 (2003).

[20] D. Ferrarini, L. Vincetti, M. Zoboli, A. Cucinotta, and S. Selleri, Opt. Express **10**, 1314 (2002).

[21] T. P. White, B. T. Kuhlmey, R. C. McPhedran, D. Maystre, G. Renversez, C. Martijn de Sterke, and L. C. Botten, J. Opt. Soc. Am. **B 19**, 2322-2340 (2002).

[22] F. Fogli, L. Saccomandi, P. Bassi, G. Bellanca, and S. Trillo, Opt. Express **10**, 54-59 (2002).

[23] J. W. Thomas, Numerical partial differential equations: finite difference methods (Texts in Applied Mathematics; 22) (Springer-Verlag New York, Inc., 1995).

[24] D. Yevick, W. Bardyszewski, Opt. Lett. **17**, 329-330 (1992).

[25] J. K. Ranka, R. S. Windeler, and A. J. Stentz, Opt. Lett. **25**, 796-798 (2000).

[26] A. Taflove and S. C. Hagness, Computational Electrodynamics–The Finite-Difference Time-Domain Method (Artech House, Norwood, Mass., 2000).

[27] M. Qiu and S. He, Phys. Lett. **A 278**, 348-354 (2001)

[28] Z. Zhu and T. G. Brown, Opt. Express **10**, 853 (2002).

[29] F. Benabid, J. C. Knight, and P. S. J. Russell, Opt. Express **10**, 1195-1203 (2002).

[30] A. Sommerfeld, Mechanik der deformierbaren Medien, Akademische Verlagsgesellschaft Geest & Portig K.-G., Leipzig 1970

[31] F. T. Geyling, Bell Syst. Tech. J. **55**, 1011 (1976).

[32] S. D. Sarboh, S. A. Milinkovic, D. L. J. Debeljkovic, Glass Technol. **39**, 53 (1998).

[33] A. D. Fitt, K. Furusawa, T. M. Monro, C. P. Please, D. J. Richardson, J. Engineering Math. **43**, 201 (2002).

[34] F. T. Geyling, G. M. Homsy, Glass Technology **21**, 95 (1980).

[35] H. R. Clark, M. Viriyayuthakorn, J. Lightwave Technol. **4**, 1039 (1986).

[36] J. Kirchof, K. Gerth, J. Kobelke, K. Schuster, 6th ESG Conference, Montpellier, France, 2002.

[37] T. M. Monro, Y. D. West, D. W. Hewak, N. G. R. Broderick, D. J. Richardson, Electron. Lett **36**, 1998-200 (2000).

[38] V. V. R. K. Kumar, A. K. George, W. H. Reeves, J. C. Knight, P. St. J. Russell, F. G. Omenetto, A. J. Taylor, Opt. Express **10**, 1520-1525 (2002).

[39] J. Kirchhof, G. Braun, Mat. Res. Soc. Proc. Vol. **244**, 15-20 (1992).

[40] P. Kaiser, J. Opt. Soc. Am. **64**, 475 (1974).

[41] H. Bauch, V. Paquet, W. Siefert, J. Opt. Commun. **8**, 140-142 (1987).

[42] T. A. Birks, J. C. Knight, and P. St. J. Russel, Opt. Lett. 22, 961-963 (1997).

[43] D. Mogilevtsev, T. A. Birks, and P. St. J. Russell, Opt. Lett. **23**, 1662 (1998).

[44] W. J. Wadsworth, A. Ortigosa-Blanch, J. C. Knight, T. A. Birks, T.-P. Martin Man, and P. St. J. Russell, J. Opt. Soc. Am. **B 19**, 2148 (2002).

[45] A. Ferrando, E. Silvestre, J. J. Miret, and P. Andres, Opt. Lett. **25**, 790-792 (2000).

[46] A. Bjarklev et al., ECOC 2002, Copenhagen (Denmark), Paper S.1.1

[47] K. Furusawa, A. N. Malinowski, J. H. Price, T. M. Monro, J. K. Sahu, J. Nilsson, and D. J. Richardson, Opt. Express **9**, 714-720 (2001).

[48] W. J. Wadsworth, J. C. Knight, W. H. Reeves, P. St. J. Russell and J. Arriaga, Electron. Lett. **36**, 1452-1454 (2000).

[49] J. C. Knight, T. A. Birks, R. F. Cregan, P. St. J. Russell, P. D. de Sandro, Electron. Lett. **34**, 1347-1348 (1998).

[50] W. J. Wadsworth, R. M. Percival, G. Bouwmans, J. C. Knight, and P. St. J. Russell, Opt. Express **11**, 48-53 (2003).

[51] A. Efimov, A. J. Taylor, F. G. Omenetto, J. C. Knight, W. J. Wadsworth, and P. St. J. Russell, Opt. Express **11**, 910-918 (2003).

[52] W. J. Wadsworth, J. C. Knight, A. Ortigosa-Blanch, J. Arriaga, E. Silvestre, and P. St. J. Russel, Electron. Lett. **36**, 53-55 (2000).

[53] S. Coen, A. H. Lun Chau, R. Leonhardt, J. D. Harvey, J. C. Knight, W. J. Wadsworth, and P. St. J. Russell, J. Opt. Soc. Am. **B 19**, 753 (2002).

[54] J. M. Dudley, L. Provino, N. Grossard, H. Maillotte, R. S. Windeler, B. J. Eggleton, and S. Coen, J. Opt. Soc. Am. **B 19**, 765 (2002).

[55] J. Herrmann, U. Griebner, N. Zhavoronkov, A. Husakou, D. Nickel, J. C. Knight, W. J. Wadsworth, P. St. J. Russell, and G. Korn, Phys. Rev. Lett. **88**, 29 (2002).

[56] A. N. Naumov, A. B. Fedotov, A. M. Zheltikov, V. V. Yakovlev, L. A. Mel'nikov, V. I. Beloglazov, N. B. Skibina, and A. V. Shcherbakov, J. Opt. Soc. Am. **B 19**, 2183 (2002).

[57] L. Tartara, I. Cristiani, V. Degiorgio, F. Carbone, D. Faccio, M. Romagnoli, and W. Belardi, Opt. Comm. **215**, 191-197 (2003).

[58] J. K. Ranka, R. S. Windeler, and A. J. Stentz, Opt. Lett. **25**, 25-27 (2000).

[59] Th. Udem, R. Holzwarth, and T. W. Hänsch, Nature **416**, 233 (2002).

[60] F. Benabid, J. C. Knight, G. Antonopoulos, and P. S. J. Russell, Science **298**, 399-402 (2002).

15 Photonic crystal optical circuits in moderate index materials

Markus Augustin, Gummar Böttger, Manfred Eich[1]*, Christoph Etrich, Hans–Jörg Fuchs, Rumen Iliew, Uwe Hübner, Marcus Kessler, Ernst–Bernhard Kley, Falk Lederer, Christian Liguda, Stefan Nolte, Hans–Georg Meyer, Wolfgang Morgenroth, Ulf Peschel, Alexander Petrov, Detlef Schelle, Markus Schmidt, Andreas Tünnermann, and Waltraud Wischmann*

15.1 Motivation

During the past several years, considerable experimental effort has been devoted to the investigation of light propagation in photonic crystals (PhCs). In this context photonic crystal films have attracted particular attention, where in–plane–light propagation is controlled by a 2D PhC, usually a lattice of air holes, and vertical confinement relies on total internal reflection. In contrast to genuine 3D crystals, there is a mature fabrication technology for these transversally periodic structures.

Most studies on PhC waveguides have concentrated on high index materials such as Si, InP or GaAs, which lead to propagation losses in PhC waveguides of 11–30 dB/mm [1,2]. As PhC devices are typically very small in size, even high intrinsic losses of slab waveguides seem not to be a major issue. For real applications, the fan–out has to be considered which covers an area of several square millimeters and thus the intrinsic loss becomes important again. Slab waveguide materials known for low propagation losses are silica, glass and polymers. Silica for example is commercially applied in a diversity of integrated optical components with slab losses less than 0.05 dB/cm at 1550 nm.

These low loss materials all possess a low index of refraction ($n = 1.5 - 2.1$). This is advantageous with respect to scattering effects: the presence of holes in the slab material induces coupling of guided modes to radiating modes, mainly due to incoherent Rayleigh scattering [3]. By reducing the air filling fraction of the structure, i.e. by etching smaller holes, it is possible to minimize these losses, but only at the expense of bandgap width. On the other hand, a lower dielectric contrast at the interface reduces the scattering. It has been shown that these losses scale with $\Delta\epsilon^2$, where $\Delta\epsilon$ is the difference between the dielectric constant of the slab material and that of the surrounding dielectric material [3,4].

The effect described above is strongly superimposed by losses due to imperfections at the side walls of the etched holes. The optical wavelength and the dimensions of PhC structures in moderate index materials are generally larger compared to those in higher index materials.

---

[1] Corresponding author: e-mail: m.eich@tu-harburg.de, Tel.: ++49-(0)40-42878-3247 Fax : ++49-(0)40-42878-2229

Photonic Crystals. Edited by K. Busch, S. Lölkes, R. B. Wehrspohn and H. Föll
Copyright © 2004 Wiley-VCH Verlag GmbH & Co. KGaA
ISBN: 3-527-40432-5

This reduces the influence of the surface irregularities for moderate index materials and thus the loss. Recently, this has been shown for PhC films with a low substrate refractive index (high vertical contrast) [5]. Hence, the moderate refractive index approach offers the potential of a greater design robustness [6–8].

As a consequence of the lower refractive indices, mode volumes in moderate refractive index optical waveguides are larger than in semiconductor materials. Thus, the coupling to external fibers should be facilitated. Because of the large mode volume, the PhC waveguides can be potentially monomode. At 60° bends in hexagonal lattices, the notorious multimodal field pattern might be easier to suppress in favor of a smooth transition of the wavefronts, accompanied by smaller radiation losses.

Inevitably, the moderate index approach has its drawbacks. The most severe one is the relatively narrow stop gap overlap for ΓK and ΓM directions in hexagonal lattices. It is therefore impossible to obtain 60° TE bends in finite 2D hexagonal hole slabs for base materials with refractive indices well below 1.8. However, for more specialized applications such as resonator based filters and optical functions that make use of the high nonlinear dispersion of photonic crystal waveguides or of ultrarefractive and superprism effects [9, 10], a large in-plane refractive index contrast is not a prerequisite.

In addition to the argument that PhC devices may provide new functionalities [11], which cannot be easily obtained with more conventional technologies, there are two approaches for them to become an economical success: either they perform better and/or they cost less than already existing optical components. The performance of commercially available optical components is excellent, e.g., state of the art optical devices like arrayed waveguide gratings (AWG) offer an excess loss less than 3 dB, including coupling loss, and total crosstalk levels better than –25 dB [12]. That PhC devices – the corresponding device for a AWG would be a superprism – can compete with integrated optical devices is rather questionable. The need for further improvement of performance has to be discussed as well.

Thus cost reduction remains as a central argument in favor of photonic crystal devices. The size of PhCs is orders of magnitude smaller than that of their counterparts based on standard technologies and the number of devices per wafer is drastically increased. In view of the production costs, the advantage of the size of PhCs is presently foiled by the need of very costly methods like e–beam lithography for the definition of the etching masks. As a consequence, a lot of effort is dedicated to the development of less costly production methods for medium to big quantities of wafers with 2D PhC structures (e.g. [13]). Admittedly, the necessary waveguide fan–in and fan–out does not only add substantial losses as described above, it also cancels most of the size advantage of the PhC structure. For both reasons, the integration of several PhC components with different functionalities on one chip is not only a possibility, it is mandatory. Since a waveguide fan–in and fan–out is only needed once for such a device, the excess loss for each single PhC function decreases and by adding further functions the over all size of the whole device will not grow rapidly. Anyway, a real PhC component with connections to standard optical networks is not really a small-sized one and will surely benefit from low loss slab materials.

Summarizing all the arguments for moderate index materials, we can conclude that they have a high potential for PhC applications, because they promise low loss devices. Additionally, their integration into existing photonic circuits based on silica technology seems to be less critical. Even low index materials which do not exhibit direction independent stopgaps bandgaps, and hence cannot be used in a 2D connected device architecture, are of great use in applications in which unusually high nonlinear dispersion is needed, as in superprisms or dispersion compensators [9, 10].

The next section will give a concise survey on band structure calculations for moderate index PhC films. In the ensuing sections, the current state of the experimental studies for two moderate index material classes, Niobiumpentoxide and Polymers, will be reviewed.

15.2 Design of the PhC films

We start with a PhC structure based on a slab system consisting of a waveguiding film made of Niobiumpentoxide (Nb_2O_5) (500 nm, $n = 2.17$), a 300 nm cladding layer and a 2000 nm buffer layer, both made of SiO_2 ($n = 1.43$) (Fig. 15.1).

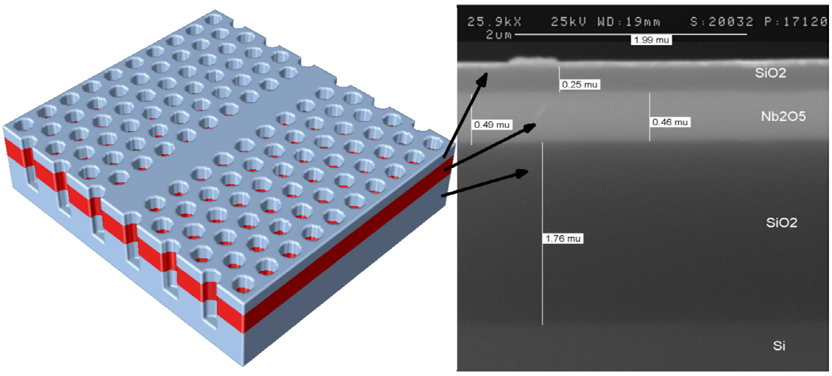

Figure 15.1: The quasi–symmetric $SiO_2/Nb_2O_5/SiO_2$ slab system. A 500 nm thick waveguiding layer of Nb_2O_5 is sandwiched between a 300 nm SiO_2 cladding and a 2000 nm quartz buffer.

The quasi–symmetric structure allows for well–separated TE and TM–like Bloch modes. It was designed for single mode waveguiding at 1.55 μm in the vertical direction. The lattice was optimized by band structure calculations using preconditioned conjugate–gradient minimization of the block Rayleigh quotient in a plane wave basis, using a freely available software package [14] to get a maximum in–plane gap. To obtain a sufficiently large 2D TE bandgap, a hexagonal arrangement of air holes [15] was used for the PhC lattice which, on the other hand, does not allow for a gap between the lowest two TM bands. For a hole diameter of 370 nm, a pitch of 595 nm and an etching depth of 1100 nm, the structure showed a complete in–plane band gap for TE polarization (see Fig. 15.2).

As anticipated this 2D–gap is noticeably smaller (gap–to–midgap ratio: 13 %) than that in semiconductor PhCs (gap-to-midgap ratio: 20 %). The supercell calculations for the embedded waveguide were performed on the basis of an effective–index model for the vertical dimension in order to be able also to model modes inside the light cone. The dispersion relation, shown in Fig. 15.2, reveals that modes of the PhC–waveguide (PhCWG) are situated inside the light cone and can in principle scatter into the substrate. Only a very small part of higher order modes close to the band edge lies below the light line. Due to the low group velocity and hence low transmission in real structures, these modes were not investigated in

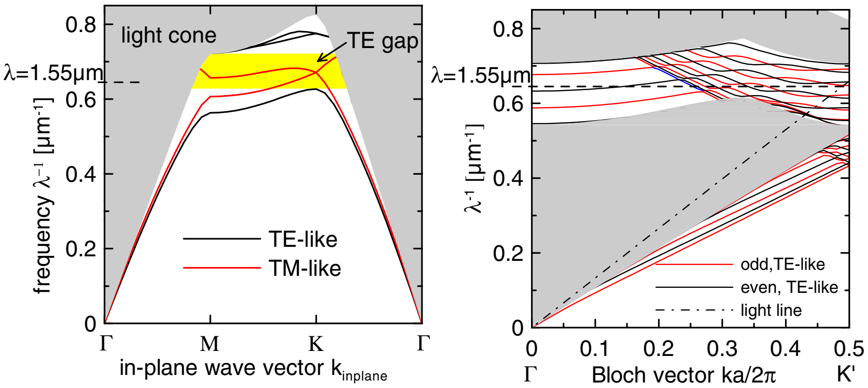

Figure 15.2: 3D band structure (left) of the PhC slab system and 2D dispersion relation (right) of the W9–PhCWG of Fig. 15.1. The blue line indicates the fundamental mode.

this context. The notation even and odd indicates the symmetry of the modes with respect to the plane vertical to the slab system and along the waveguide.

The etching depth of the holes into the substrate, being an important parameter of out–of–plane losses loss reduction for modes inside the light cone [16, 17], was investigated simultaneously utilizing 3D FDTD and 3D band structure calculations. A substrate etching depth, required for a considerable reduction of losses of an unetched substrate, was found to be 300 nm compared to 700 nm or more for semiconductor heterostructures. So the necessary aspect ratio is reduced to 3:1 compared to 6:1 for heterostructures [1].

Due to the well established layer deposition and structuring process of polymers, in particular with regard to etching depth and mass production with stamp techniques, polymers are also attractive materials for PhC slabs with a spectrum of low to moderate refractive indices. Here for low index polymers such as BCB [7] with a refractive index of 1.54, deposited on a silica substrate, no TE band gap exists in a slab system due to fundamental limits of a minimum index contrast, but all effects relying on the unique refraction and/or diffraction phenomena are possible as well as the exploitation of directional stop bands. However, using a high–index polymer (n =1.8) a band gap can also exist for a proper design of the slab system. Here we compare the band structure for the case where this material is put either on a *conventional* silica substrate or on mesoporous silica ($n = 1.14$) [18]. In Fig. 15.3 we see that even for a relatively thick guiding layer, there is no gap for the silica substrate, but a gap of roughly 9 % opens up for the low–index substrate for TE polarized light for wavelengths around 1.33 μm. Here the light cone lies substantially higher than the first TE air bands which offers better access to defect modes of larger bandwidth and group velocity.

15.3 Photonic crystal waveguides in niobiumpentoxide

Large scale PhCWGs (lengths ~ 4.6 mm) in Nb_2O_5 have been fabricated to measure propagation losses. Based on our experience with sub–wavelength high aspect gratings [19, 20], the PhCWGs were fabricated by e–beam lithography by means of a three–layers–resist. In a first

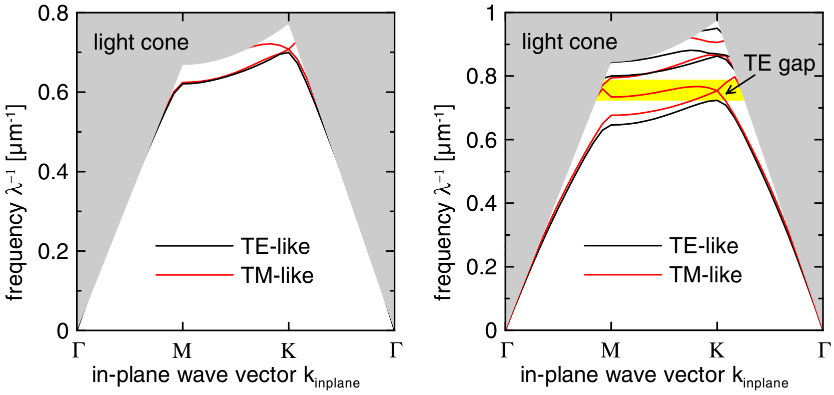

Figure 15.3: Three–dimensional band structures for a high index polymer with index $n = 1.8$ as guiding layer on a silica substrate ($n = 1.44$, left) and on a substrate of mesoporous silica with index $n = 1.14$ (right) for a pitch of the hexagonal lattice of 600 nm and a hole diameter of 400 nm.

fabrication step, the three–layers–resist (Fig. 15.4) was sputtered onto the samples. The topmost resist was then exposed with an electron beam. For the following etching steps, reactive ion beam etching (RIBE) was used. First, the chromium layer was etched. This chromium layer acts as etch mask for structuring of the second, much thicker resist layer. This resist layer was then in turn used as an etching mask for the last and final etching step of the slab system itself. After reaching the necessary etching depth, the remaining resist layer was stripped. Due to the very resistant Nb_2O_5 layer the etching depth was restricted to 1100 nm (aspect ratio 1:3).

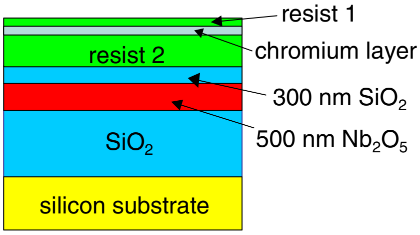

Figure 15.4: Slab system with three-layers-resist on top.

To define a W9 WG channel, nine rows of holes were omitted (see Fig. 15.5). SEM images of the W9 PhCWG show that it consists of holes with a diameter of 370 nm and a depth of 1100 nm (aspect ratio of 1:3). The wall angle in the holes amounts to 85°. For characterization, optical facets are needed which were produced by cleaving the sample.

The optical response of the PhCWGs was analyzed to determine the propagation losses. Due to the small transverse dimensions of the PhCWG ($\sim 5\,\mu$m by $0.5\,\mu$m), microscope objectives with short focal distances and high numerical apertures had to be used for efficient in (80x, NA = 0.95) and out (63x, NA = 0.85) coupling of the beam of a CW–OPO operating at $1.55\,\mu$m. A polarizer and a half wave plate were used to separately excite TE and TM modes.

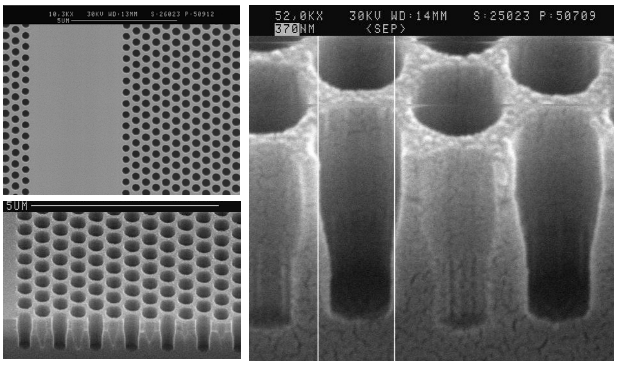

Figure 15.5: SEM images of the fabricated W9–PhCWG consisting of holes with a diameter of 370 nm and a depth of 1100 nm (aspect ratio of 1:3) in a hexagonal lattice of period 595 nm. The wall angle in the holes amounts to 85°.

To determine the propagation loss of the PhCWG, the cut–back method was utilized. By comparing the transmission measurements for the different sample lengths the coupling loss and the propagation loss can be obtained. For the W9–PhCWG, a coupling efficiency of -10 dB and propagation losses of 1.7 dB/mm have been measured. The latter value is surprisingly low compared with previous measurements of high index PhCWGs but can be related to the waveguide width [1, 2]. For comparison, we measured damping losses of 2.6 dB/mm for a W5–PhCWG, while the losses for a W3–PhCWG amount to 8.5 dB/mm. However, the most surprising effect was the effective single mode behavior of this wide PhCWG. Monitoring the near field distribution at the exit we only found the fundamental mode of the 5 μm wide PhCWG. In contrast, conventional ridge waveguides with comparable width and index contrast are highly multi–mode. Mode field and band structure calculations show that the W9-PhCWG is indeed multi-mode (four even and four odd modes in the bandgap, cf. Fig. 15.6 and Fig. 15.2).

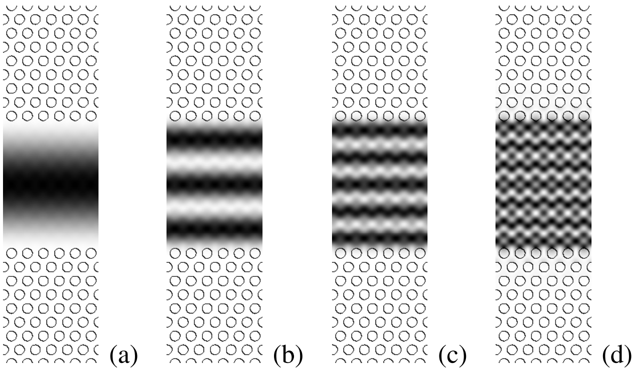

Figure 15.6: Odd guided modes of a W9–PhCWG. While the fundamental mode (a) is primarily located inside the PhCWG higher order modes (b–d) penetrate into the PhC region.

However, there are remarkable differences between these modes. The fundamental mode (Fig. 15.6a) is mainly located inside the PhCWG–region and thus only weakly interacts with the PhC structure resulting in small losses. By contrast, the higher order modes penetrate deeply into the PhC lattice. Because all modes are located inside the light cone, an interaction with the lattice results in an efficient scattering, mainly into the substrate. As the interaction with the PhC structure is weakest for the fundamental mode it survives upon propagation whereas higher order modes are suppressed. Thus, the conclusion can be drawn that propagation within the light cone can be advantageous with regard to single mode operation.

In addition to straight waveguides, we also studied PhCWG bends. In this case the length was reduced to 59 μm in order to monitor the dynamics of higher order modes as well. Furthermore, the PhCWG width was reduced to W5 (5 rows of holes missing), which is expected to perform better at the bend [21, 22]. Theoretical estimates of the mode fields (Fig. 15.6, Fig. 15.7) show that the W5 and W9–PhCWGs behave very similarly indeed.

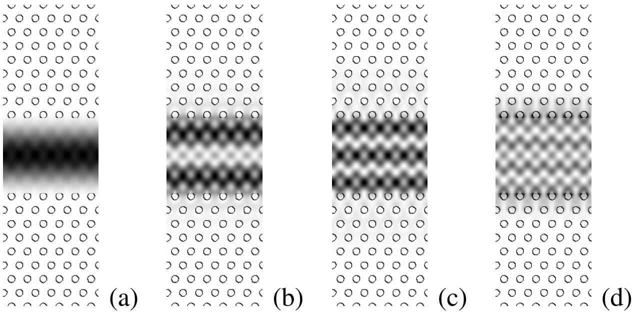

Figure 15.7: Guided modes of a W5–PhCWG. While the fundamental mode (a) is mainly located inside the PhCWG higher order modes (b–d) penetrate into the PhC region.

Thus a W5–PhCWG (width: 2.8 μm) with a period of 595 nm and a diameter of 260 nm was fabricated. To enhance the coupling efficiency, ridge waveguide tapers have been used to couple light into and out of the PhCWG. Compared to an untapered ridge waveguide, almost twice the light intensity could be inserted into the PhCWG. The near field distribution after 59 μm of propagation shows that the PhCWG is indeed multi–mode. Based on the same design, a W5–PhC waveguide double bend ($2\times\ 60^\circ$), also with ridge waveguide tapers for coupling, was realized (Fig. 15.8).

Figure 15.8 shows the W5–PhCWG bend under investigation. The spectral response of the PhCWG bend was characterized by tuning a CW–OPO in the range between 1490 nm and 1830 nm. The near field distribution of the transmitted light was observed with the help of the output microscope objective and an infrared camera.

The overall transmission (TE polarization) for the PhCWG double bend (including coupling, in and out coupling into the taper, propagation and bend losses) shows a peak of $\sim$ 1 % at 1677 nm (see Fig. 15.9). By comparing the TE transmission of a bend and a straight PhCWG, bend losses can be deduced to amount to $\sim$ 3 dB at 1677 nm.

Although the straight W5–PhCWG was observed to be multimode for short propagation distances the near field distribution of the W5–PhCWG bend shows only a fixed field distribution in varying the transverse position of the incident beam (see inset in Fig. 15.9).

First theoretical analyses of a W5–PhCWG with a hole diameter of 260 nm and a period of

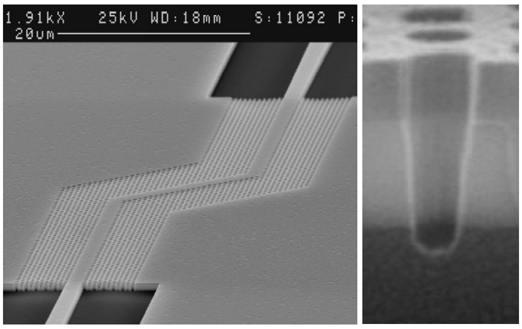

Figure 15.8: SEM–image of the fabricated PhC–structure with a W5 double bend (left). Cleaved facet of a similar photonic crystal shows wall angles of 85° (right).

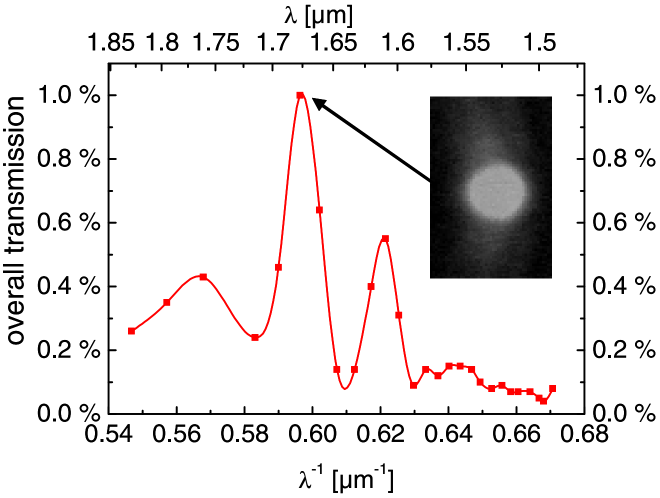

Figure 15.9: Overall transmission (TE polarization) of the W5 photonic crystal device shown in Fig. 15.8).

595 nm were performed. Band structure calculations (see Fig. 15.10) reveal that the bandgap almost vanishes and that at 1677 nm, four index guided modes are lying inside the light cone.

This clearly shows that the W5–PhCWG is indeed multi–mode as has been observed experimentally. However, as described above, due to the very narrow gap higher order modes are primarily scattered into the substrate at bends and upon propagation.

In addition, the dispersion curves of the higher order (even) modes exhibit a mini stop band close to this wavelength (see Fig. 15.10) and the higher order odd modes also show a flat dispersion curve meaning a low group velocitiy and also leading to enhanced propagation losses in straight sections. This dominance of the fundamental mode is confirmed by 3D finite–difference time–domain (FDTD) calculations (see Fig. 15.11).

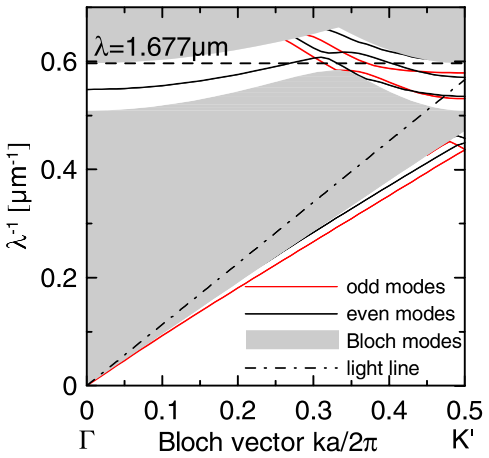

Figure 15.10: Band structure of a W5–PhCWG (diameter 260 nm, pitch 595 nm) in a $SiO_2/Nb_2O_5/SiO_2$ slab system. This structure has four guided modes lying inside the light cone.

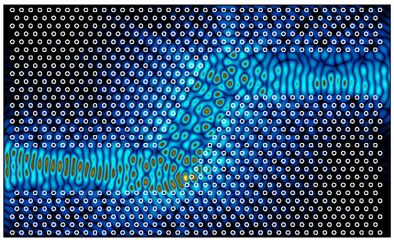

Figure 15.11: Field distribution in a W5 double bend (3D FDTD calculation), $\lambda = 1653$ nm, PhC parameters as in Fig. 15.7.

15.4 Photonic crystals in polymer films

In addition to the simple waveguide preparation, an additional and highly attractive feature of certain organic polymers is their ability to undergo changes in the refractive index upon temperature variations and due to external electromagnetic interaction. For instance, a non-permanent index change is observed in high field poled second–order nonlinear optical polymer films that, besides their tendency to generate optical harmonics, exhibit the linear electro–optical effect [23]. In addition, calamitic molecular side groups can be synthesized that are both highly polarizable and photochemically sensitive at the same time. Amorphous polymers functionalized with such side groups therefore offer the potential of optically induced irreversible refractive index alterations by means of irradiation with UV photons [24]. We have recently started to investigate such tuning and trimming capabilities in highly resonant photonic crystal structures, which may be used to shift both band edges as well as defect peak frequencies [18]. Another approach uses free carrier injection with femtosecond pulses into semiconductors [25].

As waveguide core material moderate refractive index polymer materials BCB Cyclotene 3022 from Dow, PMMA–DR1, and APC/DHANS with low optical losses of one to a few dB/cm were used. Core thicknesses were $t = 1.5\,\mu$m and refractive indices for BCB and PMMA–DR1 are $n = 1.54$, for APC/DHANS $n = 1.57$ at 1300 nm excitation wavelength. Whereas BCB is a thermoset optical polymer, PMMA–DR1 is a thermoplastic covalently functionalized polymethacrylate side chain polymer that carries 10 Mol% of Disperse Red chromophore as side groups and exhibits a glass transition temperature of 120 °C. APC/DHANS is an amorphous polycarbonate that has been doped with 25 wt% of 4–(N,N–dihexylamino)–4'–nitrostilbene. These noncentrosymmetric chromophore groups make the polymer both optically nonlinear and sensitive to UV–irradiation of wavelengths around 300 nm. The polymeric materials listed here can be spin coated from solution. As substrate, we used a low refractive index amorphous polymer (Teflon AF from Dupont, $n = 1.30$ at 1300 nm excitation wavelength). This substrate polymer was spun on from solution to final thicknesses of 3 μm on oxidized silicon wafers (thickness of SiO_2 $t = 2.3$ μm). Optical losses were determined to be 1.6 dB/cm at 1300 nm for the asymmetric Teflon AF–BCB–air waveguide and to be 2.2 dB/cm at 1300 nm for the asymmetric Teflon AF–PMMA–air waveguide. Nearly identical loss figures are observed for TE and TM polarizations.

The fabrication of the PhC structures was performed by electron beam lithography and reactive ion etching (RIE) as described in Section 15.3 and published elsewhere [7]. The PhC slab dimensions were: 8000 lattice constants (4 mm) perpendicular and 10 or more lattice constants parallel to the direction of propagation. Scanning electron microscopy (SEM) images of the fabricated PhC slabs are shown in Fig. 15.12. The holes have radii of 125–150 nm and the etching depth was chosen between 1.5 μm and 3 μm, resulting in aspect ratios between 6:1 and >10:1. Deep etching into the substrate improves vertical confinement and hence reduces radiation losses to the substrate.

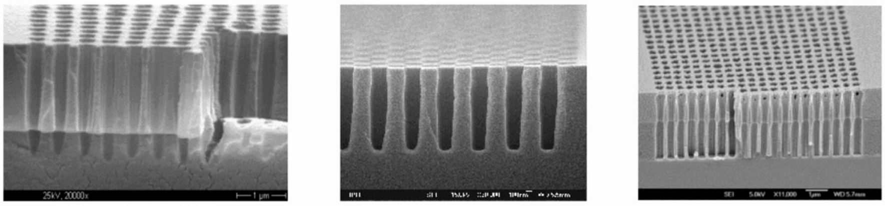

Square lattice of air colums in BCB/Teflon
lattice constant: 500nm
hole radius: 150nm
aspect ratio: 6:1

Triangular lattice of air colums in BCB
lattice constant: 650nm
hole radius: 150nm
aspect ratio: 6:1

Square lattice of air colums in PMMA-DR1-Teflon
lattice constant: 500nm
hole radius: 125 nm
aspect ratio: >10:1

Figure 15.12: Left/Center: Square and triangular lattices of air holes etched into BCB layer. Right: Square lattice etched into PMMA–DR1 guiding layer and into Teflon substrate.

The optical characterization of the 2D PhC slabs was performed using the waveguide prism coupling technique using broadband and fiber coupled high resolution tunable laser sources. This experimental setup allows mode selective polarization and wavelength dependent transmission measurements. In order to obtain the transmission characteristics of either bulk or defect PhC structures, the transmission spectra of the patterned waveguides were divided by the spectra of the unpatterned waveguides. Photobleaching experiments were performed using a 1 kW Xe high pressure lamp, and guided to the sample via an UV fiber. UV–VIS power densities were about 440 mW/cm^2 leading to doses of effective 3 kJ/cm^2 for maximum bleaching effects at exposure times of approximately 2 hours.

As a first example, we present the transmission characteristics of a bulk PhC which consists of a square lattice of air holes ($a = 500\,\text{nm}$, $r = 150\,\text{nm}$) etched into an APC/DHANS on Teflon slab waveguide. Propagation length was varied from $7a$ over $14a$ to $40a$. The transmission spectrum was taken from frequencies of 190THz to 300THz corresponding to vacuum excitation wavelengths from 1–1.6 μm.

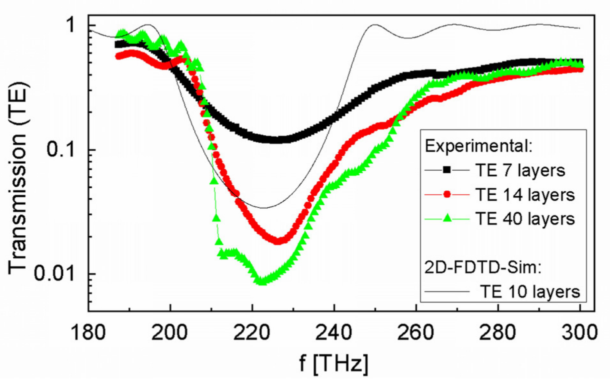

Figure 15.13: Experimental intensity transmission as a function of excitation frequency of bulk square lattice PhC of amorphous polycarbonate APC/DHANS – Teflon into which holes ($r = 150\,\text{nm}$, $a = 500\,\text{nm}$) have been etched. Shown are TE transmission spectra of three different propagation lengths (black: 7a, red:14a, green:40a). For comparison, the transmission spectrum as obtained from 2D FDTD simulations is shown as solid black curve. Propagation was along ΓX direction.

In Fig. 15.13, the existence of a stop gap for propagation in ΓX direction is clearly seen which extends about 50 THz. As expected, the increase in propagation length strongly reduces the transmission in the stop gap minimum. Typical values between 1.2 and 1.5 dB/a are achieved, comparable to values achieved for the BCB-Teflon PhC system [7]. The transmission at high frequencies is considerably reduced as compared to what is expected from 2D simulations. This phenomenon has also been observed for BCB-Teflon bulk PhC [7]. Since on the high frequency side of the spectra, the electric field is mainly concentrated in the air holes (air band) the guided mode propagates in a medium of a lower effective refractive index. Thus vertical confinement will be weaker and radiation losses to the substrate are facilitated. Because of the inherent assumption of infinitely deep holes, the 2D model, of course, does not predict such losses. However, real slabs of limited and sometimes inhomogeneous etching depth are expected to show this behavior which is also observed experimentally [3, 17, 26], as shown below.

We have analyzed the transmission characteristics in detail as a function of the etching depth. The 3D–FDTD simulation volume consisted of an air superstrate of thickness 1.5 μm, a waveguiding BCB polymer layer of 1.5 μm and a Teflon substrate of 3 μm. Propagation through the ΓX–oriented photonic crystal was modelled. As PhC slab we assumed a square lattice of 10 layers of air holes embedded in a 9 μm long conventional slab waveguide. The only parameter changed in the simulations was the etching depth.

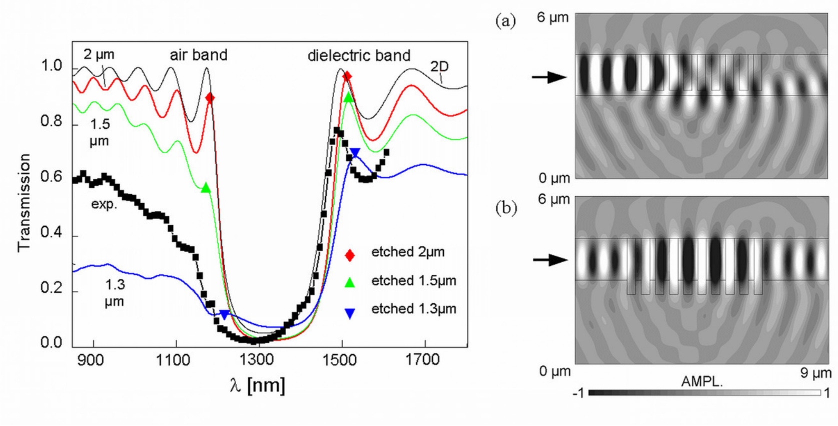

Figure 15.14: Left: 3D FDTD simulated TE transmission intensity T of a PhC slab waveguide of length $10a$ consisting of 1.5 μm air superstrate, 1.5 μm BCB core and 3 μm Teflon substrate ($a = 500$ nm, $r = 150$ nm). Etching depth varied from 1.3 μm (blue), 1.5 μm (green) to 2.0 μm (red). The black curve represents the transmission obtained from 2D calculations. Right: Amplitudes of E_y-field for monochromatic excitation from the left with a TE-polarized fundamental slab mode are shown at first maximum of transmission on air band side with λ around 1200 nm. (a): Etching depth 1.3 μm ($T \approx 0.12$), (b): Etching depth 2 μm ($T \approx 0.90$).

The simulated TE transmission curves are shown in Fig. 15.14, left side. Full transmission at the maxima is observed for 2D–FDTD simulations (using effective mode index) of the infinitely high photonic crystal structure only, as there can be no out–of–plane losses. Overall transmission through the photonic crystal slab in air and the dielectric band strongly improves as the etching depth is increased. As the losses subside, the amplitudes of the oscillations outside the stop gap also get larger, approaching those of the 2D–simulated infinitely thick photonic crystal. Monochromatic simulations were performed on the expected first maxima outside the stop gap, as indicated in Fig. 15.14 (left) by symbols. Increasing the etching depth beyond 2 μm did not significantly enhance the transmission for the simulated structure. Transmission is especially improved for TE excitation on the air band side with electrical fields localized in the air regions of the photonic crystal. On the dielectric band side, etching depth has less influence as electrical fields are concentrated in the dielectric material anyway. Experimental data for the BCB/Teflon system are also included in Fig. 15.14. The positions of the dielectric band edges are well reproduced by the simulations.

Figure 15.14 (right) depicts the distribution of E_y–field amplitudes at the first maxima on the air band side for TE excitation and etching depths 1.3 μm and 2 μm. With an etching depth of 1.3 μm, the incoming light is pulled toward the remaining unstructured 200 nm of the core and subsequentially radiates into the substrate (Fig. 15.14 right (a)). For TE excitation there is an obvious mode mismatch between the exciting fundamental slab mode and photonic crystal air band mode. This leads to a significant reflection back into the exciting waveguide mode of $R = 0.28$. Transmission into the unstructured slab is $T = 0.12$. Intensities not accounted for with R and T are not guided into the respective waveguide ports, and are mainly radiated into the substrate and absorbed at the boundaries of the simulation volume. Etching 500 nm into the substrate as pictured in Fig. 15.14 right (b), leads to a very good mode match between unstructured and structured parts of the slab waveguide, corresponding to low insertion losses and $T = 0.90$. Coupling to and from the photonic crystal structure is much improved. There are also visibly less radiation losses into the substrate, light is much better confined to the core and guided almost symmetrically in the waveguide. Therefore we conclude that for low vertical index contrasts, deep etching is mandatory to minimize out–of–plane radiation losses. Alternatively, a strong vertical index contrast also results in a sufficient vertical confinement, thus representing an airbridge–type membrane structure.

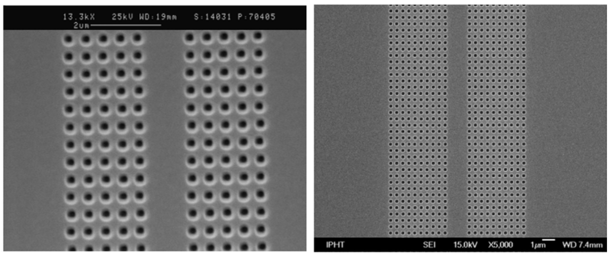
13.3kX 25kV WD:19mm S:14031 P:70405
2um
IPHT SEI 15.0kV X5,000 1μm WD 7.4mm

Figure 15.15: Left: SEM picture of linear defect square lattice PhC resonator in BCB-Teflon ($a = 500$ nm, $r = 150$ nm). Defect of width $2a$ between boundaries of $5a$ each (5_2_5). Length of defect is $8000a$. Right: SEM picture of linear defect square lattice PhC resonator in PMMA-DR1 on Teflon. Defect of width $3a$ between boundaries of 10a each (10_3_10). Length of defect is $8000a$. Light propagation is perpendicular to the defect from left to right.

In this part, we present first realizations of polymer PhC waveguide defect resonators. The achievable quality factor Q in finite PhC slabs is limited by additional out–of–plane losses to either substrate or cladding. Deep etching or increased vertical refractive index contrast is therefore a prerequisite to increased quality factors. Figure 15.15 shows two examples of bulk PhC slab waveguides into which, by missing rows, linear defects have been introduced.

Transmission spectra were taken from linear defect resonators of different defect geometries varying from two to four missing rows (Fig. 15.16).

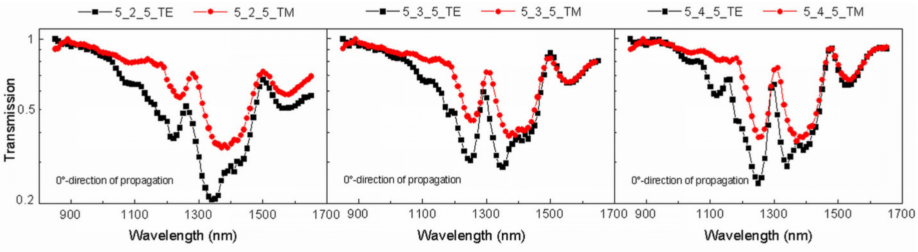

Figure 15.16: Experimental transmission spectra of linear defect resonators as shown in Fig. 15.15. Left: 5_2_5, middle: 5_3_5, right: 5_4_5. Red circles denote TM–like, black squares indicate TE–like polarizations.

Compared to bulk PhC spectra, the appearance of a peak for both polarizations is clearly seen. Its center frequency, which is strongly dependent on the defect size, indicates the position of the defect state inside the stop gap. As the defect width is increased from $2a$ to $4a$, the center frequency shifts towards the center of the stop gap. This behaviour and the dependence of the transmission spectra on the angle of propagation with respect to the ΓX direction of the lattice, are in accordance with our 2D–FDTD simulations.

The width of the defect peaks reveals quality factors Q of about 50. This experimental Q–value is governed both by the low reflectivity of the two Bragg mirrors of depth 5a and by additional out–of–plane losses. Therefore, two measures were taken to increase the quality factors and hence the spectral resolution of such moderate refractive index–based PhC defect strutures. First, increasing the reflectivity by increasing the number of lattice constants adjacent to the defect and/or enhancing the refractive index contrast inside the waveguide core. Second, minimizing the out–of–plane radiation losses by using deeply etched high aspect ratio PhC slabs or, alternatively, by improving the vertical mode confinement. Keeping the core refractive index constant, the latter can be achieved by reducing the substrate and cladding indices or, ultimately, by using air bridge type PhCs.

An example of a polymer–based PhC defect resonator which both employs a large aspect ratio of >10:1 and an increased number of lattice constants right and left of the defect, is shown in Fig. 15.15 right. A significantly higher Q–value of about 260 was obtained for the TE–like mode as is depicted in Fig. 15.17. A smaller Q–value is observed for the TM–like mode which is attributed to the smaller gap size, hence reduced Bragg mirror reflectivity. However, 3D–FDTD simulations had predicted a higher Q–value of about 800 for the TE–like polarization. This substantial deviation is attributed to the fact that the experimental hole sizes are larger (about 400 nm) and etching depth is expected to be inhomogenous, thus incurring higher radiation losses. In addition, Rayleigh scattering losses from roughness are not taken into account. Nevertheless, a Q–value of 260 in a moderate refractive index PhC is a promising result, given the many parameters to improve.

For wavelength division multiplexing technology (WDM) state of the art channel distances are 100 GHz or even 50 GHz, equivalent to wavelength separations of 0.8 or 0.4 nm at 1,55 μm respectively. In order to separate a particular channel in a PhC based drop filter, unrealistically high atomic resolution on manufacturing would be demanded. Given the fact that the nanofabrication of PhCs will always be associated with the bringing in of systematic and statistical errors in geometry, the development of tools to trim or tune PhCs is a mere necessity. Therefore, we have investigated the potential of PhCs based on molecular entities that are sensitive to UV radiation and undergo a substantial change in the effective refractive index during this treatment called UV photobleaching [18].

We present a new concept to adjust the transmission properties of a two dimensional photonic crystal by UV photobleaching the structure. A square lattice bulk PhC slab waveguide from PMMA–DR1 on Teflon ($a = 500$ nm, $r = 150$ nm) was investigated. Upon UV irradiation, the DR1 molecules which are covalently attached to the PMMA polymer backbone undergo photodegeneration, their molecular fragments easily diffusing out of the polymer layer at elevated temperatures. Because of the reduction of the charge transfer band of the DR1 chromophore, this process leads to a substantial reduction of the refractive index of the order of 0.04 as shown in Fig. 15.18 [23].

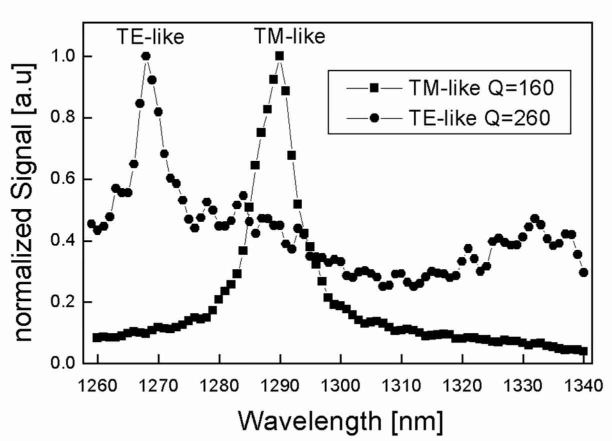

Figure 15.17: Experimental transmission spectra around the resonance peak of a linear 10_3_10 PhC defect resonator (see Fig. 15.15 right) realized in PMMA-DR1 on Teflon for both TE–like and TM–like polarizations. Aspect ratio of >10:1 was achieved.

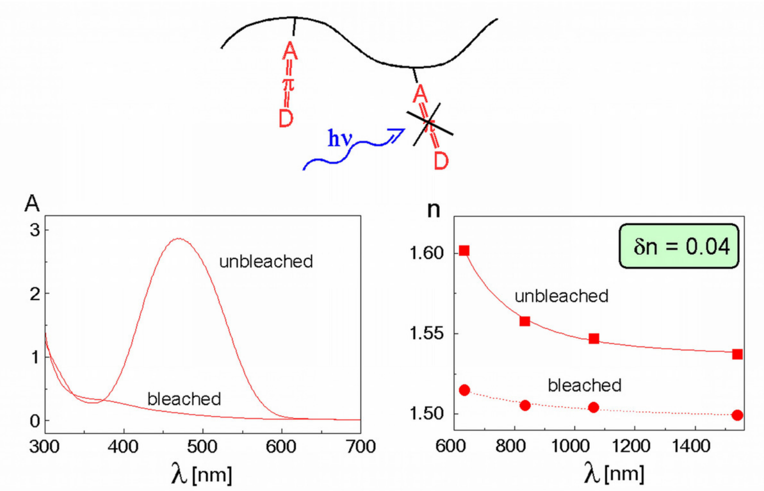

Figure 15.18: Top: Schematics of UV photobleaching of PMMA–DR1. Left: Absorption spectrum before (upper curve) and after bleaching (lower curve), showing the reduction of the DR1 charge transfer band. Right: Refractive index dispersion of the unbleached and bleached film (lower refractive indices).

This photoinduced modification of the refractive index, together with the reduction of the core layer thickness from 1.45 μm to 1.28 μm, which is accompanying the out gassing of DR1 molecular fragments, was utilized to induce a very strong shift of the PhC band edge.

Figure 15.19 shows the dielectric edge of the stop gap of the 2D PhC structure described above for the TE–like ($\vec{E}$–field parallel to the slab plane) and TM–like polarization after different bleaching times. The raw transmission data was divided through an unbleached reference spectrum, measured at an unstructured position of the slab between two PhC structures. This reference method extracts the changes resulting from the PhC structure only. One can see a significant spectral shift of the TE stop gap dielectric edge of approximately 35 nm to higher wavelengths. We attribute the smaller shift of about 27 nm in the TM–like polarization to a smaller change in the refractive index for this polarization, which we believe to be a consequence of photoselection induced birefringence during the bleaching process. The observed shifts are in accordance with our 3D–FDTD simulations which took into account the reduced refractive index and the decreased slab waveguide thickness. The reduced transmission on the right side of the dielectric stop gap edge is related to an enhanced surface roughness, which most likely is a result of the chromophore fragments gassing out of the waveguide core. This surface roughness, however, can be eliminated by proper annealing the sample close to the glass transition temperature of PMMA–DR. The observed wavelength shift of 35 nm is two orders of magnitude larger than the width of a single WDM channel. Therefore, much smaller refractive index changes, hence UV doses, will be necessary in actual manufacturing processes.

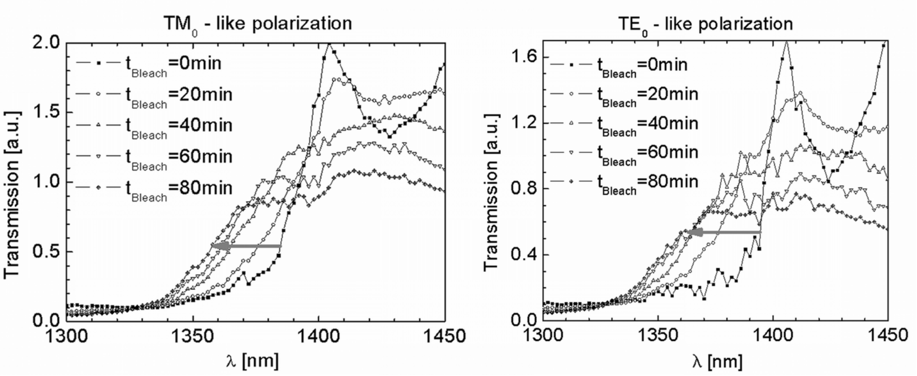

Figure 15.19: Transmission spectra of a PMMA/DR–1 / Teflon square lattice PhC slab waveguide (a: 500 nm, r: 150 nm) for TM–like (left) TE–like (right) polarizations in the ΓX direction. Different curves in one graph refer to different bleaching times. A shift of the dielectric edge in both polarizations is observed.

15.5 Conclusions

By means of 3D–band structure calculations (using a freely available software package [14]) and 3D–FDTD calculations, we have investigated the potential of moderate index materials to exhibit complete in–plane band gaps for TE polarisation. For the Niobiumpentoxide–silica sandwich system a PhC lattice was designed that allows for an in–plane band gap at 1.55 μm with a gap–to–midgap ratio of 13 %. As anticipated, this is reduced compared to semiconductor PhCs (gap–to–midgap ratio 20 %). For polymer systems BCB and APC/DHANS on teflon, no complete TE bandgap exists due to fundamental limits of low index contrast. For a higher index contrast between the polymer ($n = 1.8$) and an ultra low index substrate with $n = 1.14$, a gap of roughly 9 % opens up for TE polarisation at 1.33 μm. To minimize losses in PhCWG the reduction of out–of–plane loss for modes inside the light cone has been theoretically investigated by variation of the depth of the air holes.

Based on an optimized design, straight waveguides in Nb_2O_5 have been fabricated. A W9 PhCWG with a width of 5 μm leads to a coupling efficiency of -10 dB and low propagation loss of 1.7 dB/mm at 1677 nm. The observed single mode behaviour could be explained by an efficient scattering of the higher order modes mainly into the substrate. Hence the conclusion can be drawn that propagation within the light cone can be advantageous with respect to single mode operation.

In addition, 60° PhCWG bends with a total device length of 59 μm were studied, to the best of our knowledge for the first time in such moderate index systems. Ridge waveguide tapers have been used to couple light efficiently into these structures. The PhC waveguide bends show high transmission of -3 dB per bend. Furthermore, the near field distribution of these bends indicates that higher order modes which exist in straight W5–PhCWGs are suppressed at the bends and single mode behavior is obtained. Therefore wide PhCWG and bends in moderate–index materials with guided modes lying inside the light cone show very promising properties regarding propagation loss and single mode behavior.

For low loss polymer 2D bulk PhC slabs ($n = 1.54$), waves with frequencies inside the stop gap are effectively suppressed with typically 1.5 dB per lattice constant for TE–like modes. Transmission of waves with frequencies outside the stop gap is significantly improved by etching the air holes deep into the substrate. FDTD simulations show that both radiation losses into the substrate and transmission losses due to insufficient coupling are strongly reduced.

Photonic crystal defect resonator structures were shown, for which etching depths critically determine quality factors and transmission at defect frequencies. For a deeply etched polymer PhC defect resonator, we experimentally observed a quality factor Q of 260.

Finally, we have presented a new concept to trim and adjust the transmission properties of 2D photonic crystal slab waveguide structures after fabrication. This method relies on the UV photobleaching technique which irreversibly transforms organic chromophore molecules and hence leads to a substantial reduction of the effective refractive index. In PMMA–DR1 bulk PhC waveguides, we could demonstrate a very large spectral shift of the dielectric band edge of $\lambda = 35$ nm in TE polarization, much larger than ever needed for device trimming.

The demonstrated low loss properties of moderate index materials in basic PhC elements such as straight waveguides and bends are promising for future device applications. A further challenge will be a predictable and reproducible fabrication process for PhC devices which can be simplified by using trimming effects.

Acknowledgements

We acknowledge the financial support from the Deutsche Forschungsgemeinschaft (DFG) in the framework of the Schwerpunktprogramm *Photonische Kristalle* and the Bundesministerium für Bildung und Forschung (BMBF), Germany, within the project *Photonic Crystal Optical Circuits* (PCOC). We also acknowledge support from CST, Darmstadt, Germany, with their finite integration software Microwave Studio.

References

[1] C.J.M. Smith, H. Benisty, S. Olivier, M. Rattier, C. Weisbuch, T.F. Krauss, R.M. De La Rue, R. Houdré, U. Oesterle, Low-loss channel waveguides with two-dimensional photonic crystal boundaries, App. Phys. Lett. **77**, 2813 (2000).

[2] A.Talneau, L.Le Gouezigou, N.Bouadma, Quantitative measurement of low propagation losses at 1.55 μm on planar photonic crystal waveguides, Opt. Lett. **26**,1259 (2001).

[3] H. Benisty, D. Labilloy, C. Weisbuch, C. J. M. Smith, T. F. Krauss, D. Cassange, A. Beraud and C. Jouanin, Radiation losses of waveguide-based two-dimensional photonic crystals, Appl. Phys. Lett. **76**, 532 (2000).

[4] R. Ferrini, R. Houdré, H. Benisty, M. Qiu, J. Moosburger, Radiation losses in planar photonic crystals: two dimensional representation of hole depth and shape by an imaginary dielectric constant, J. Opt. Soc. Am. B, Vol. **20** No. 3, 469 (2003).

[5] W. Bogaerts, P. Bienstman, and R. Baets, Scattering at sidewall roughness in photonic crystal slabs, Opt. Lett. **28**, 689-691 (2003).

[6] R. Ferrini, B. Lombardet, B. Wild, R. Houdré, G. H. Duan, Hole depth- and shape-induced radiation losses in two-dimensional photonic crystals, Appl. Phys. Lett. **82**, 1009 (2003).

[7] C. Liguda, G. Böttger, A. Kuligk, M. Eich, H. Roth, J. Kunert, W. Morgenroth, H. Elsner, H. G. Meyer, Polymer photonic crystal slab waveguides, Appl. Phys. Lett. **78**, 2434 (2001).

[8] S. Foteinopoulou, A. Rosenberg, M. M. Sigalas, C. M. Soukoulis, In- and out-of-plane propagation of electromagnetic waves in low index contrast two dimensional photonic crystals, J. Appl. Phys. **89**, 824 (2001).

[9] S. Foteinopoulou, E. N. Economou and C. M. Soukoulis, Refraction in Media with a Negative Refractive Index, Phys. Rev. Lett. **90**, 107402-1 (2003).

[10] H. Kosaka, T. Kawashima, A. Tomita, M. Notomi, T. Tamamura, T. Sato, and S. Kawakami, Superprism phenomena in photonic crystals, Phys. Rev. B **58**, R10096 (1998).

[11] S. John, O. Toader and K. Busch, Photonic Band Gap Materials: A Semiconductor for Light, Encyclopedia of Science and Technology, Vol. **12**, Academic Press (2001).

[12] Alcatel Optronics, Alcatel 1941 AWG - Gaussian 40 x 100 GHz Datasheet, http://www.alcatel.com/telecom/optronics/products/datasheets/A1941AWG.pdf (2001).

[13] J. Seekamp, S. Zankovych, A. H. Helfer, P. Maury, C. M. Sotomayor Torres, G. Böttger, C. Liguda, M. Eich, B. Heidari, L. Montelius, Nanoimprinted passiv optical devices, Nanotechnology, Vol. **13** No. 5, 581 (2002).

[14] Steven G. Johnson and J. D. Joannopoulos, Block-iterative frequency-domain methods for Maxwell's equations in a planewave basis, Opt. Expr. **8**, 173-190 (2001).

[15] S. G. Johnson, S. Fan, P. R. Villeneuve, J. D. Joannopoulos and L. A. Kolodziejski, Guided modes in photonic crystal slabs, Phys. Rev. B **15**, 5751 (1999).

[16] Ph. Lalanne, Electromagnetic Analysis of Photonic Crystal Waveguides Operating Above the Light Cone, IEEE J. Quantum Electron. QE-**38**, 800 (2002).

[17] G. Böttger, C. Liguda, M. Schmidt, and M. Eich, Improved transmission characteristics of moderate refractive index contrast photonic crystal slabs, Appl. Phys. Lett. **81**, 2517 (2002).

[18] M. Schmidt, G. Böttger, F. Marlow and M. Eich, unpublished results

[19] T. Glaser, S. Schröter, H. Bartelt, H.-J. Fuchs, E.-B.Kley, Diffractive optical isolator made of high efficiency dielectric gratings only, Appl. Opt. **41** (18), 3558-3566 (2002).

[20] E.-B. Kley, H.-J. Fuchs, A fabrication technique for high aspect ratio gratings, Micromachining and microfabrication, SPIE Vol. **3879**, Santa Clara USA, (1999).

[21] A.Talneau, L.Le Gouezigou, N.Bouadma, M. Kafesaki, C. M. Soukoulis and M. Agio, Photonic-crystal ultrashort bends with improved transmission and low reflection at 1.55 μm, App. Phys. Lett. **80**, 547 (2002).

[22] S. Olivier, H. Benisty, C. Weisbuch, C. J. M. Smith, T. F. Krauss, R. Houdré, and U. Oesterle, Improved 60° Bend Transmission of Submicron-Width Waveguides Defined in Two-Dimensional Photonic Crystals, J. Lightwave Technol. **20**, 1198 (2002).

[23] D. M. Burland, R. D. Miller, and C. A. Wlash, Second-order nonlinearity in poled-polymer systems, Chem. Rev. **94**, 31 (1994).

[24] J. Vydra, H. Beisinghoff, T. Tschudi, and M. Eich, Photodecay mechanisms in side chain nonlinear optical polymethacrylates, Appl. Phys. Lett. **69**, 1035 (1996).

[25] S. W. Leonard, H. M. van Driel, J. Schilling, and R. B. Wehrspohn, Ultrafast band-edge tuning of a two-dimensional silicon photonic crystal via free-carrier injection, Phys. Rev. B **66**, 161102 (2002).

[26] H. Benisty, P. Lalanne, S. Olivier, M. Rattier, C. Weisbuch, C. J. M. Smith, T. F. Krauss, C. Jouanin, and C. Cassagne, Finite-depth and intrinsic losses in vertically etched two-dimensional photonic crystals, Optical and Quantum Electronics **34**, 205 (2002).

16 Planar high index-contrast photonic crystals for telecom applications

Reinhard März[1], *Sven Burger, Sebastian Golka, Alfred Forchel, Christian Hermann, Cecile Jamois, Dirk Michaelis, and Klaus Wandel*

16.1 Introduction and motivation

The pioneering work on photonic crystals dates back to 1987 when Yablonovitch aimed at the concept of a zero-threshold laser based on the suppression of spontaneous emission into unwanted directions by studying the Yablonovite, a microwave equivalent of the desired photonic structure. A long period of great progress in modeling, patterning, etching and characterization, was required to demonstrate photonic crystals of sufficient quality showing fundamental gaps in the visible and near infrared region. In parallel to the fundamental research, the spectrum of proposed applications offering new and attractive features of photonic crystals, has been and is still enlarging. It includes microwave antennas, photonic crystal fibers, cosmetic and food colors, car lacquers, various types of sensors, high–brightness LEDs as well as active and passive components for telecommunications reported in the following. The assessment of their feasibility is currently the subject of numerous research projects all over the world.

For telecommunications, photonic crystals offer the following attractive features which are mainly utilizing two medium–term aspects, compactness and photonic mode engineering:

- strong interaction between light and matter allowing for on–chip resonators of high finesse and optical components/circuits being orders of magnitude smaller than currently fabricated devices.
- reduction of the group velocity by orders of magnitude allowing optimizing the chromatic dispersion and its slope.
- enhancement of tunability by concentrating the optical field in regions infiltrated with tuning agents (especially for high–contrast photonic crystals).
- reduced number of fabrication steps (e.g. mask layers and epitaxial steps) easing the integration of active and passive photonic functions (e.g. laser, waveguides, filters, switches) on a single chip on the basis of simplified processing.

This chapter, we describe ongoing work on telecom–oriented components based on high–contrast photonic crystals with a refractive index steps $\Delta n > 2$ between air holes and dielectric. Photonic crystals of that type exhibit very large photonic bandgaps for both polarizations. The materials systems under investigation include the two group III–V compounds

---

[1] Corresponding author: e-mail: reinhard.maerz@infineon.com

Photonic Crystals. Edited by K. Busch, S. Lölkes, R. B. Wehrspohn and H. Föll
Copyright © 2004 Wiley-VCH Verlag GmbH & Co. KGaA
ISBN: 3-527-40432-5

InGaAsP/InP and InGaAs/GaAs allowing both for active and passive components as well as the silicon–on–insulator (SOI) material system, which is well suited for the realization of tunable passive components.

Photonic crystals with an average refractive index $\bar{n} > 2$ operated at $1.55\,\mu\mathrm{m}$ require elementary cells with a minimum feature sizes in the sub–$100\ \mathrm{nm}$ range. The in–plane diameters of the eigenmodes of a defect waveguide with one missing row $(W1)$ are also in the $100\ \mathrm{nm}$ range. The vertical index contrasts, i.e. between refractive index of core and cladding layers, differ from one high–contrast material system to another. The photonic crystal components based on the III–V compounds are based on a moderate vertical index contrast ($\Delta n_V < 0.5$) in order to be compatible with both optical and optoelectronic components whereas those in the SOI material system rely on the high refractive index contrast ($\Delta n_V \approx 2$) between silica and silicon. As a consequence, photonic crystals based on SOI discussed in the following can be (and are always) operated below the light–line whereas the III–V based photonic crystals have to be operated above the light–line, where the components and their propagation losses are much more sensitive to the shape and depth of the photonic crystal structures. The challenges with respect to the aspect ratios and surface quality require the development of novel etching technologies and equipment for all material systems. We selected the set of active and passive components presented in the following such that the feasibility of the key features from the telecommunication point of view – compactness, integrability, dispersion management, tunability – can be assessed. Special focus is also given to fiber–to–chip coupling which is of particular importance for applications in telecommunications.

The organization of this chapter reflects the above discussion. We start with an investigation of theoretical aspects, including the light–cone problem and derive from that theoretical losses for both types of material systems. In addition, new modeling tools allowing for tolerancing of photonic crystal components are presented. Great emphasis will be put on crucial patterning steps such as lithography and etching and the required equipment. The second part of this chapter deals with the concepts of the most important components as well as component–oriented characterization techniques are presented. The chapter ends with a discussion of fiber–chip coupling of photonic crystals and the chips and basic components required for it.

16.2 Waveguide losses

Waveguide losses due to out–of–plane radiation represent one of the major issues of planar photonic crystals. A waveguide based photonic crystal with reciprocal lattice vectors $\mathbf{Q}_1$ and $\mathbf{Q}_2$ stimulated at k_0 by an input mode with an (in–plane) wave vector $\mathbf{q}_p^{(\mathrm{in})}$ can – just as a conventional Bragg grating – radiate optical power into a background material (sub– or superstrate) with a permittivity ϵ_B. The radiation process via an outgoing plane wave ($\mathbf{q}^{(\mathrm{out})}$) requires the conservation of the in–plane components of the wave vectors, i.e., $\mathbf{q}_p^{(\mathrm{in})} + \mathbf{q}_p^{(\mathrm{out})} = l\mathbf{Q}_1 + m\mathbf{Q}_2$, and of the optical power, i.e., $|\mathbf{q}^{(\mathrm{out})}|^2 = k_0^2\epsilon_B$. In the terminology of photonic crystals, regions in the bandstructure where both conditions cannot be satisfied concurrently are called ”below light–line”, the other regions being called ”above light–line”. The efficiency of the radiation process in regions above the light–line is driven by the layout of the elementary cell and by the density of photonic states close to the actual point of operation. Therefore,

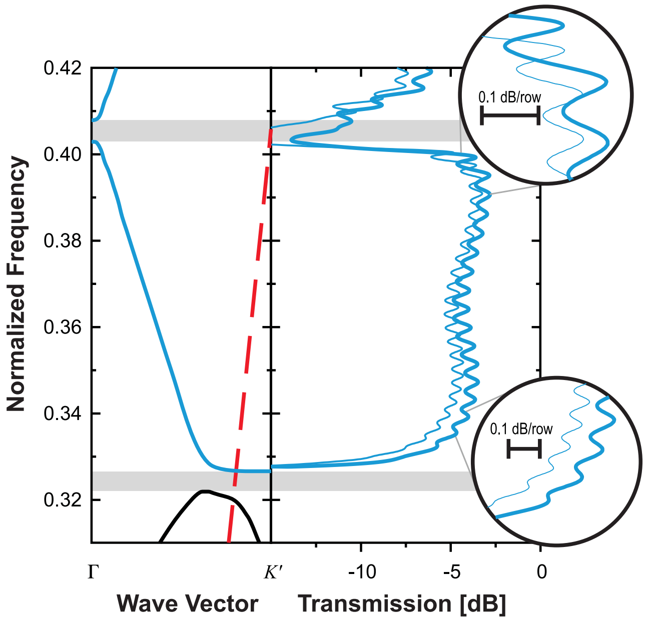

Figure 16.1: Band structure showing the fundamental odd mode (Ez is odd) of a W1–waveguide (blue) running into the Γ-M direction of a hexagonal photonic crystal (black) for the a SOI layer system ($n_{\text{core}} = 3.4$, $d_{\text{core}} = 0.4a$, $n_{\text{cladding}} = 1.45$, $d_{\text{cladding}} = \infty$, $r_{\text{hole}} = 0.366a$), and transmittance through a PhC–bar with 30 (thick) and 40 (thin) lattice constants. The red dashed line shows the light–cone, the grey regions correspond to the remaining bandgaps.

a quantitative numerical analysis of the radiation efficiency, which allows the derivation of realistic propagation losses obtained for a perfectly fabricated device, requires a full three–dimensional approach.

The numerical results were obtained using a three–dimensional Finite–Difference Time–Domain (3D–FDTD) simulation method using hybrid boundary conditions. For the computation of the bandstructure of bulk PhCs, periodic boundary conditions were applied at all in–plane boundaries, for embedded defect waveguides, only at the front and back boundaries. The remaining boundaries were in both cases equipped with Perfectly Matched Layers (PMLs). The simulations of transmission through a W1–waveguide[2], in contrast, are based on a computational window which is fully embedded by PML boundaries. The calculations apply to photonic crystal bars with 30 and 40 rows excited by the fundamental TE–mode of the outside slab waveguide. The hole structures are always assumed perfect, i.e., the cladding layers and the holes have "infinite" depth and the holes exhibit completely vertical, perfectly etched walls. The results of these simulations can be regarded as a benchmark which can be achieved at best by real devices. The transmittance was "measured" by using a numerical detector at the end of the structure. The waveguide losses are derived by comparing the transmittance of

---

[2] A Wn–waveguide is a defect waveguide with n missing rows.

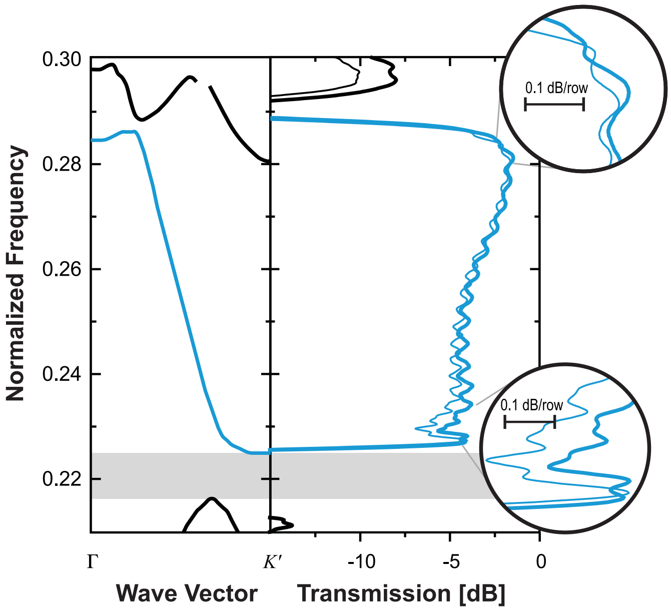

Figure 16.2: Band structure showing the fundamental even mode (Ez is odd) of a W1–waveguide (blue) running into the Γ-M direction of a hexagonal photonic crystal (black) in the InGaAsP material system ($n_{\text{core}} = 3.45a$, $d_{\text{core}} = 0.737a$, $n_{\text{cladding}} = 3.17$, $d_{\text{cladding}} = \infty$, $r_{\text{hole}} = 0.288a$), and transmittance through a PhC–bar with 30 (thick) and 40 (thin) lattice constants. The the grey region corresponds to the remaining bandgap.

bars of different length. This method can be regarded as a numerical equivalent to established cut–back measurements to derive the losses of optical fibers.

The design of the slab waveguide responsible for the vertical guiding differs between the strongly guiding silicon–on–insulator (SOI) material system ($\Delta n \approx 2$) and the weakly guiding III–V material systems ($\Delta n < 0.5$) investigated here. As a consequence, the PhCs in the SOI material system are (at least partially) operated below light–line, the weakly guiding PhC devices in the III–V compounds must be operated above light–line.

Figures 16.1 and 16.2 show the relevant part of the band structure and the calculated transmittance for two PhC–bars of different lengths. The insufficient adaption of the outside waveguides results in reflections at the input and output interfaces and in clearly visible Fabry–Perot oscillations. To ease the estimation of propagation losses, both figures zoom into the transmittance at the lower and upper ends of the transmission band of the W1–waveguide. The estimated losses for the InGaAsP W1–waveguide (1 row $\approx 650\,\text{nm}$ at $1.3\,\mu\text{m}$) which is always operated above the light–line vary between $\approx 0.02\,\text{dB}/\text{row}$ at $\omega_N = 0.280$ and $\approx 0.12\,\text{dB}/\text{row}$ at $\omega_N = 0.225$. For the SOI W1–waveguide (1 row $= 710\,\text{nm}$ at $1.55\,\mu\text{m}$) the losses above the light–line vary between $\approx 0.05\,\text{dB}/\text{row}$ at $\omega_N = 0.395$ and $\approx 0.11\,\text{dB}/\text{row}$ at $\omega_N = 0.330$, i.e., the losses of the SOI waveguides above the light–line are slightly higher than those in the InP material system. On the basis of a purely kinematic analysis, the propagation losses below light –line should vanish. The computation of the propagation losses of the SOI W1–waveguides by the 3D–FDTD method turned out to be difficult, since the group velocity of the W1–waveguide is – with respect to its use within a dispersion compensator – intentionally extremely small (see Section 16.7).

16.3 Efficient analysis of photonic crystals

The use of photonic crystals in an application–oriented environment makes it necessary to understand the influence of manufacturing deviations on the device properties such as local defects, deformations of the elementary cell, displacements, and inhomogeneities. Obviously, the majority of tolerancing relies on modeling tools which allow the investigation of multiscale structures with both high (at least relative) accuracy and good time complexity.

Simulators used for tolerancing and backtracking must be able to resolve small deviations, which are typically orders of magnitude smaller than the device under investigation. The approach used here is based on a family of finite element solvers which compute eigenvalues $\Omega_m = k_0^2(m)$ and eigenmodes, i.e.,

$$\frac{1}{\epsilon(\mathbf{r}_t)}(\nabla_t + i\mathbf{q}_t)^2 e_z^{(m)}(\mathbf{q}_t, \mathbf{r}_t) = \Omega_m \, e_z^{(m)}(\mathbf{q}_t, \mathbf{r}_t) \tag{16.1}$$

$$(\nabla_t + i\mathbf{q}_t) \cdot \frac{1}{\epsilon(\mathbf{r}_t)}(\nabla_t + i\mathbf{q}_t)\, h_z^{(m)}(\mathbf{q}_t, \mathbf{r}_t) = \Omega_m \, h_z^{(m)}(\mathbf{q}_t, \mathbf{r}_t) \tag{16.2}$$

for two–dimensional photonic crystals[3] and

$$(\nabla + i\mathbf{q}) \times \left(\frac{1}{\epsilon(\mathbf{r})}(\nabla + i\mathbf{q}) \times \mathbf{h}^{(m)}(\mathbf{q}, \mathbf{r}\,)\right) = \Omega_m \, \mathbf{h}^{(m)}(\mathbf{q}, \mathbf{r}) \tag{16.3}$$

with the divergence condition $(\nabla + i\mathbf{q}\,) \cdot \mathbf{h}^{(m)}(\mathbf{q}, \mathbf{r}) = 0$ for the full 3D–case [1].

The use of Arnoldi algorithms for tackling the sparse FE–matrices results in a time complexity of $O(N^{3/2})$ instead of $O(N^3)$ for 3D–solvers acting on dense matrices. We also use multi–grid algorithms [2] with an even better time–complexity of $O(N)$. In contrast to plane wave methods, the periodic boundary conditions are implemented by solving the differential equation on a compact manifold (e.g., on a torus for the 2D square lattice). The divergence condition is satisfied by implementing an additional restriction to the numerical solution within the algorithm. The use of adaptive (locally refined) irregular grids is crucial for the numerical analysis of multiscale structures without significant additional effort.

Figure 16.3 shows a benchmarking of the accuracy vs. computational effort for eigenmode computations of a 2D photonic crystal with and without a small perturbation in its elementary cell using three different solvers – two finite element solvers using linear and quadratic finite elements and an optimized implementation (MPB) [3] of the Plane Wave Method (PWM). For the unperturbed case (Fig. 16.3a), the quadratic FE-solver delivers an accuracy gain of three orders of magnitude when compared to the same number of sampling values, i.e., plane waves, for the PWM or, alternatively, a reduction in CPU time by more than two orders of

---

[3] Here and in the following, the z–axis runs parallel to the holes forming the 2–dimensional photonic crystal. The vectors $\mathbf{r}_t$ and $\mathbf{q}_t$ designate positions and wave vectors in the plane transverse to z.

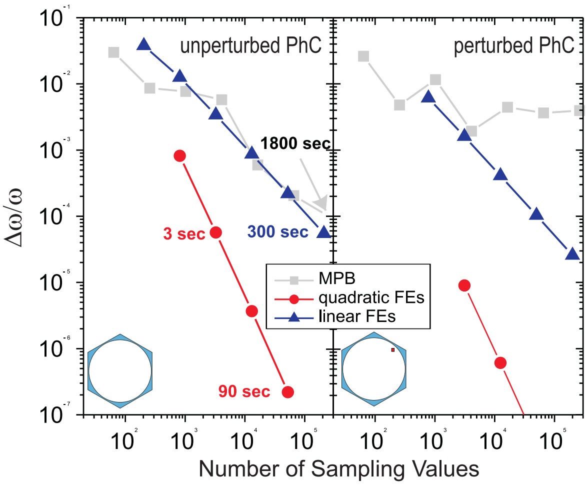

Figure 16.3: Relative error $\Delta\omega/\omega$ of the lowest eigenvalue at the M–point vs. number of sampling values computed by two FE–solvers with quadratic and linear elements in comparison to an optimized PWM–solver [3] for an unperturbed (left) and perturbed (right) 2D hexagonal photonic crystal with air holes ($2r = 0.96\,a$, $\varepsilon = 13$). All results were computed by using the same computer and operating system.

magnitude. For the more challenging, perturbed case (Fig. 16.3b), the PWM cannot resolve the perturbation and fails to converge for the investigated numbers of unknowns. The behavior of both FE–solvers remains stable.

The analysis of many relevant properties of optical devices, including losses, transmission, reflection, group delay, dispersion, and thresholds, relies on the time–harmonic quasi–steady state, which is obtained when all transient phenomena fade away. Based on the time domain propagation method described in Section 16.2 of this article, the analysis of the time–harmonic state requires running computational experiments over long periods, especially for the particularly interesting case of low group velocities, i.e., frequency domain methods are often much more efficient than time domain methods. Like the time domain methods, the frequency domain methods rely on an effective suppression of the reflections at the boundary of the computational window.

The Beam Propagation Method (BPM), a workhorse used for frequency domain propagation in integrated optics, turns out to be inadequate to model photonic crystals since it does not allow the modeling of omnidirectional propagation and it is generally limited to low–contrast waveguide structures. The more sophisticated approach presented here relies on the following considerations. For lossless media, the asymptotic optical field is governed by Sommerfeld's radiation condition. By using this result, it is possible to divide the optical field at infinity into two parts, the scattered field leaving the computational domain forever and an incoming field entering the computational domain at its boundaries. By making assumptions on the refractive index profile outside the computational window, such as waveguides entering the computational domain and photonic crystals forming a periodic background, it becomes possible to separate both contributions also on the boundary of the computational domain [4].

Figure 16.4 illustrates the propagation of an optical field in the 2D computational window, containing a PhC–bar operated in the regime of an apparent negative refractive index [5]. The optical field consists of an incoming Gaussian beam, the field propagating inside the PhC slab, and of reflected and transmitted outgoing beams. This result demonstrates that an accurate frequency-domain modelling of light propagation in PhCs is feasible. Frequency domain methods will be more efficient in case of one–wavelength propagation and be required in case of problems exhibiting slowly running modes and/or high spectral resolution.

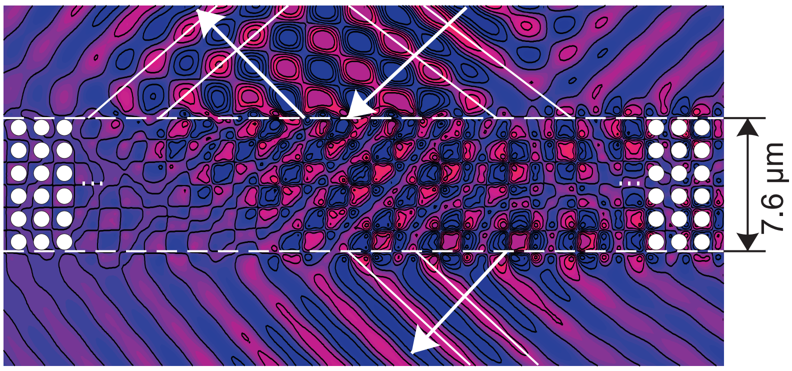

Figure 16.4: Frequency domain propagation of a plane wave through a PhC–bar operated in the regime of apparent negative refractive index. The propagation directions of the essential beams are indicated by white arrows.

16.4 Patterning of photonic crystals

Two–dimensional PhCs for the telecom wavelength windows are realized as air hole patterns in InP/InGaAsP, GaInNAs/AlGaAs or silicon–on–insulator (SOI) material systems. Whereas SOI is limited to passive PhCs, GaInNAs/AlGaAs quantum wells and GaInAs quantum dots on GaAs/AlGaAs also allow the realization of light emitting PhC–devices preferably in the $1.3\,\mu\mathrm{m}$ window. The InP based material systems are used for both wavelength windows. High–contrast photonic crystals operated in the $1.3/1.5\,\mu\mathrm{m}$ wavelength regions exhibit periods of about 250 to $400\,\mathrm{nm}$. Air filling factors of ≈ 0.3, which are used to maintain sufficient waveguiding in the heterostructure layers, result in hole diameters of about 140 to $250\,\mathrm{nm}$. For all of the above material systems, the current patterning process consists of three major steps:

- definition of a resist pattern by lithography,
- transfer of the resist pattern into the dry etch mask by RIE–etching,
- transfer of the dry etch mask into the waveguide layers by anisotropic etching.

The transfer of the resist patterns into the thick dry etch mask forces the use of such resist layers, which in turn, results in a demand for high resolution lithography on thick resists (resist thickness: $500\,\mathrm{nm}$, minimum feature size: $100\,\mathrm{nm}$ or less). Most research and development projects currently use modern electron beam lithography systems. The high accelerating voltages (50 – 100 kV) result in backscattering into areas much larger than the typical elementary cell of a PhC. The additional dose resulting from backscattered electrons is therefore almost constant over a PhC cell, i.e., the proximity effects can easily be corrected. Extreme UV exposure scanners already used for sub–$100\,\mathrm{nm}$ DRAMs as well as large–area imprint processes are promising candidates for a future production phase. Overall, lithography for photonic crystals is challenging, but not considered a roadblock.

The etching of 2D PhC hole patterns into the heterostructures turns out to be crucial with respect to propagation losses [6,7]. True two–dimensional PhCs require infinitely deep holes. The depth of holes in waveguide–based quasi–2D PhCs must be sufficient to ensure that the guided modes interact with a perfect hole pattern and that scattering losses into the substrate are sufficiently suppressed. The required PhC hole depths therefore depend on the refractive index contrast between the layers forming the core and cladding layers of the waveguides. For SOI, the index contrast is $\Delta n \approx 2$. Due to the strong vertical confinement of light, it is generally assumed that the holes do not need to penetrate deeply into the lower cladding layer (rule of thumb in literature: $d = 2xd_{\mathrm{cladding}} + d_{\mathrm{core}} + 0.6\mu m$). However, since working below the light–line is mandatory, bulk modes can have a significant extension in the vertical direction. This is relevant, in particular, for modes close to the light–line. The III–V heterostructures provide much smaller refractive index contrasts of about 0.3–0.4 (GaAs/AlGaAs) and of about 0.2 (InP/InGaAsP) resulting in hole depths which are – especially for InP – significantly deeper than the waveguide thickness (GaAs about $1 - 1.5\,\mu\mathrm{m}$, InP about $3 - 4\,\mu\mathrm{m}$). From the fabrication point of view, a high aspect ratio of the distance between adjacent holes and their depths represents the most important figure of merit of patterning. III–V compounds based on slab waveguides require aspect ratios > 10. In addition, the shape of the holes has to be well–defined over the entire interaction length with the guided mode. Variations of the parameters over the photonic crystal area, especially close to their boundary, have to be kept small. Due to the importance of the PhC hole etching process, we focus on this step in the next subsections.

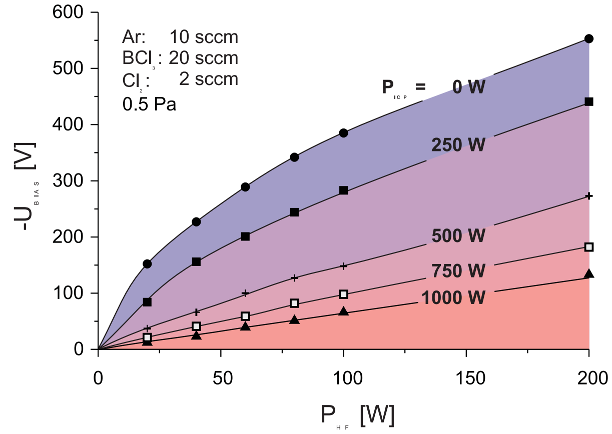

Figure 16.5: Self bias voltage U_{BIAS} vs. radio frequency power P_{HF} applied to the substrate for various RF–powers P_{ICP} fed into the ICP–antenna.

The fabrication of planar PhCs with a high aspect ratio forces the use of massively directional etching technologies. This prevents the use of wet chemical etching as well as that of partially isotropic dry etching processes, e.g., reactive ion etching (RIE). Appropriate options include the inductively coupled plasma based reactive ion etching (ICP–RIE), the electron cyclotron resonance enhanced RIE (ECR–RIE), and the chemically assisted ion beam etching (CAIBE) applied within the HiPhoCs–consortium. In order to gain directivity, all processes are attacking the PhC-wafer by ions accelerated in an electrical field. The required selectivity between the etch rates of mask and PhC is achieved by using reactive etch gases ($Cl_2, CH_4/H_2$). With an increasing depth of the etched holes, the transport of the non–volatile reactants from the bottom and the sidewalls becomes increasingly difficult.

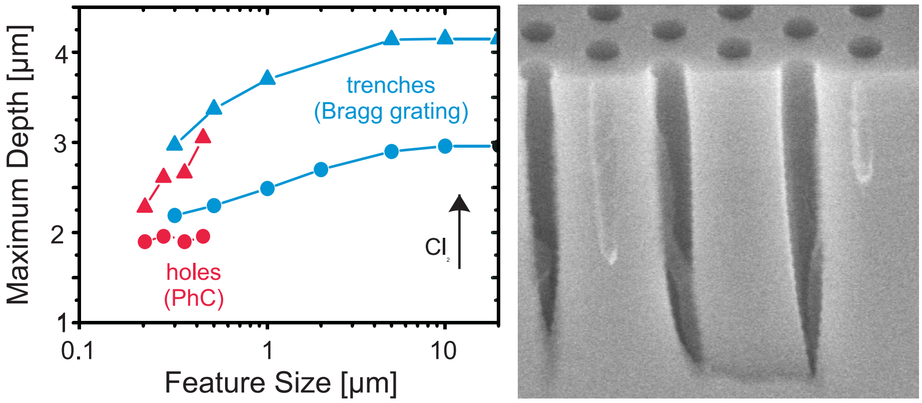

Figure 16.6: a) Maximum depth vs. diameter of holes and trenches for two Cl_2 flow rates (1 sccm and 3 sccm). Trenches allow for greater aspect ratios. b) SEM photograph of a typical InP/InGaAsP PhC (pitch $a = 270\,\mathrm{nm}$).

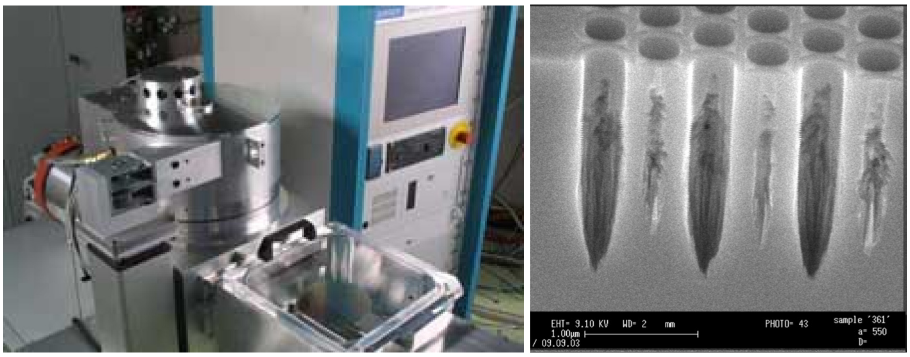

Figure 16.7: (a) Photonic crystal dry etch system using an inductively coupled plasma (ICP) source (Sentech Instruments SI 500). The system allows the use of Cl_2 and CH_4 based etch processes with high ion densities. The wafers can be heated or cooled to improve the process. (b) Hexagonal PhC (pitch $550\,\mathrm{nm}$) in InP etched with a Cl_2/N_2 process at $190°\mathrm{C}$.

ICP systems (see Fig. 16.7 for a system developed within the HIPhoCs–consortium) are currently used for PhC–etching in SOI as well as in the GaAs and InP material systems. Figure 16.5 shows the self bias voltage vs. RF–power fed into the ICP–substrate for different RF–powers applied to the ICP–antenna. The RF–power delivered to the ICP–antenna controls the density of the accelerated ions. Screening effects lead to a decreasing self bias voltage with increasing ion, i.e., plasma density. An increasing RF–power at the substrate leads to an increasing separation of electrons and ions in the plasma and thus to an increasing self bias voltage. The ICP, as well as the ECR sources, create a high–density plasma at low pressures. The generated ion energy is independently controlled by the bias on the substrate electrode. This allows the acceleration of both the chemically active and the inert ions on the substrate and thereby combines chemical and physical etch mechanisms. The CAIBE process combines a highly anisotropic physical etching component with a chemical, isotropic component which can be tuned independently. This allows, in principle, the etching of PhC–holes with a well controlled cylindrical shape. Since the chemical component determines the overall etch rate, a fairly aggressive chemistry is typically used, for III–V materials mostly based on chlorine.

Amorphous high–density $\mathrm{SiO_x}$ and $\mathrm{SiN_x}$ are good masking materials for III–V compounds, because they offer a low resistance against the fluorine–based mask etching, and a high resistance against chlorine–based etching used to transfer the etch mask. This combination of processes results in selectivities (etch rate mask layer : etch rate PhC) of approximately 1:10 and smooth facets after deep etching. The SOI patterning which have to be transfered to a fluorine plasma–chemistry relies on chromium masks. The masking materials are usually deposited by PECVD (plasma enhanced chemical vapor deposition) where layer density, surface damage, composition and strain can be well controlled by selecting appropriate process parameters.

For high aspect ratio holes in III–V materials and in SOI, specific etching recipies have been developed by different groups in the consortium based on ECR – RIE, ICP – RIE, and CAIBE. Etching of hole patterns differs from etching extended structures such as ridge waveguides. In the case of the ridge waveguide, the etched atoms can leave the surface into a large solid angle, which results in large etch rates and good selectivity. In contrast, the transport of material out of deep holes is limited to small solid angles. Therefore, the etch rates and the selectivity of the mask versus semiconductor decrease with increasing etch depth.

For a useful etching process, all atomic species have to be removed at the same rate. In contrast to Si and GaAs, where this condition is satisfied to a good approximation, the etching of InP–based semiconductor layers is affected by PCl_x etching products of varying vapour pressure. In addition, one component ($\mathrm{InCl_3}$) is non–volatile at room temperature. Due to the very different vapor pressure of PCl_x products, slight surface roughness is caused by InCl_x–islands which are present, that result in rough hole bottoms (fig. 16.6b center hole) at depths $> 2\,\mu\mathrm{m}$. To remove etch products of low volatility, the desorption can be promoted by Argon ion beam sputtering. This keeps the process anisotropic at a speed which is still as fast as that of chemical etching. The sidewalls are protected as long as they are not hit by Ar atoms. The balanced removal of the InCl_x and PCl_x material can be obtained at higher temperatures when the desorption of reaction products is no more a limiting step. A precise control of this operating point ($180 - 200 \pm 5^\circ\mathrm{C}$ for InP) requires a precise control ($\pm 5^\circ\mathrm{C}$) of the wafer temperature, i.e., the use of wafer cooling and heating systems. Figure 16.6b shows the geometry dependence of CAIBE etching for trenches and holes of varying diameters for

$\mathrm{Ar/Cl_2}$, with low and high Cl_2 content. Wide trenches ($w = 20\,\mu\mathrm{m}$) allow for maximum etch depths of $4\,\mu\mathrm{m}$. The depth of holes with a diameter of $200\,\mathrm{nm}$, in contrast, is limited to less than $2.5\,\mu\mathrm{m}$ which is still sufficient for InP based PhCs. Figure 16.8 shows top and side views of PhCs etched into a GaAs/AlGaAs slab waveguide by ECR – RIE with $\mathrm{Ar/Cl_2}$. The PhCs designed for the $1.3\,\mu\mathrm{m}$, show a period of 380 nm and a hole diameter of about 210 nm (air filling factor: $\approx 30\%$). Optimized ECR – RIE conditions allow for holes with vertical sidewalls up to depths of $1.2\,\mu\mathrm{m}$.

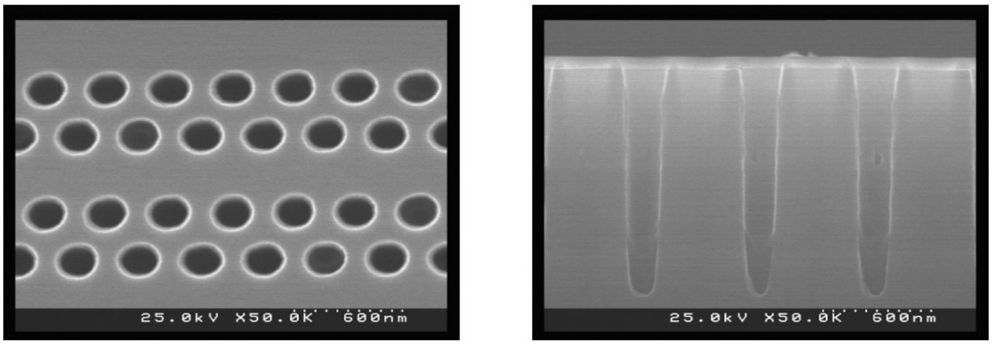

Figure 16.8: (a) Top view of a GaAs/AlGaAs PhC resonator. (b) Cross section of the etched holes.

For SOI photonic crystal structures, the minimum etching depth inside the SiO_2 cladding is still a matter of debate. Therefore, two strategies for etching are pursued in parallel. Silicon on thin SiO_2 layers ($d = 1\,\mu\mathrm{m}$) are structured using a classical photoresist mask only. This process yields a maximum hole depth[4] of about $700\,\mathrm{nm}$ with ICP–plasmas based on $\mathrm{Cl_2/HBr}$ gas mixtures for Si and CF_4/CHF_3–mixtures for SiO_2. The process for etching deep holes is optimized using ICP–RIE and chromium hard masks. The process parameters for etching the chromium mask by an RIE plasma are a gas mixture of Cl_2/O_2 (100:15) at a RF power of $40\mathrm{W}$. The transfer of the mask into the $\mathrm{SiO_2/Si/SiO_2}$ layers is carried out by ICP–RIE with a gas mixture of CHF_3/ SF_6 (see Fig. 16.9 for first results).

16.5 Sources for multi-channel WDM–transmitters

Widely tunable single–mode lasers are key components of advanced optoelectronics, in particular as sources for optical transmission lines and networks using wavelength division multiplexing (WDM). PhC–mirrors can be used with benefit in multi–segment lasers. The approach pursued in this work is based on a two–segment laser with PhC–mirrors, which are combined with multi–wavelength weakly coupled distributed feedback (DFB) gratings. The multi–wavelength gratings are obtained by electron beam lithography on the basis of a numerical superposition of several single wavelength DFB gratings. The reflectance of multi–wavelength DFBs exhibits several peaks with a spacing determined by the wavelengths of the individual DFB gratings. The two laser segments employ two slightly different sets of reflectivity peaks. The laser emits at that wavelength which offers the best overlap of the reflection

---

[4] Done by IMEC in Belgium using DUV lithography [8].

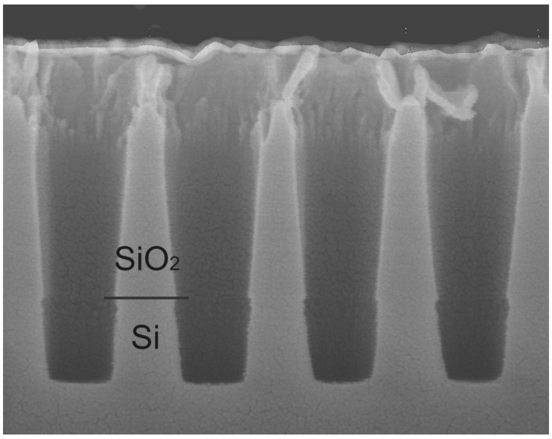

Figure 16.9: SEM photograph of etched holes in an oxidized SOI (hole diameter: 350 nm, period: 650 nm). The embedded silicon layer has a thickness of 470 nm.

peaks of both segments. By varying the drive current of one or both segments, this overlap can be switched to other modes, i.e., the wavelength of the laser can be tuned discontinuously over a wide spectral range. By changing the mean refractive index, e.g., by changing the device temperature, it is possible to provide a continuous tuning over a small spectral range. The separation of the laser segments by a photonic crystal mirror allows for a well–controlled intracavity coupling. The use of two highly reflecting PhC–mirrors, forming the overall laser resonator, allows for widely tunable lasers at the same footprint as conventional DFB lasers. In addition, integrated mirrors enable the monolithic integration with other devices such as optical amplifiers and modulators, to build more complex photonic integrated circuits.

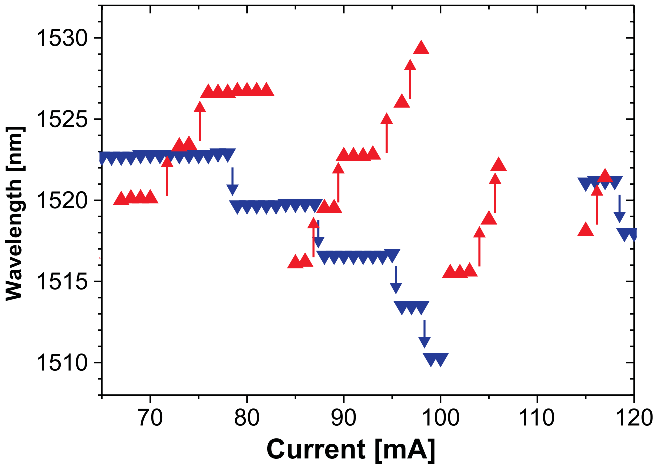

Figure 16.10: Discontinuous tuning of the laser wavelength by changes of the injection current in the front (red) and rear (blue) segment. The current of the other segment is fixed in both cases at 40 mA.

We have produced a two–segment tunable laser with PhC–mirrors, with a hole depth of $3\,\mu\mathrm{m}$ for intracavity coupling and for the rear facet of the resonator. The two binary super–

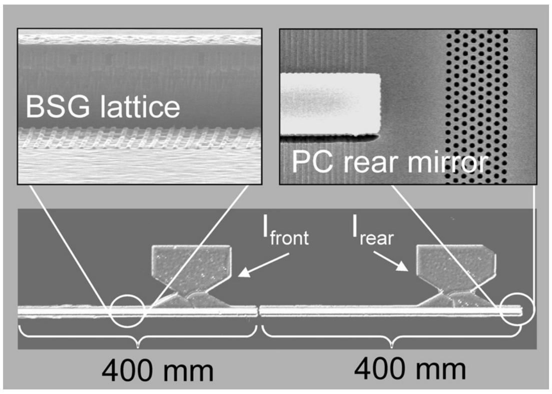

Figure 16.11: Top left: SEM micrograph of ridge waveguide segment with lateral Cr grating that defines the BSG lattice. Top right: SEM micrograph of photonic crystal rear mirror. Bottom: total design with the two segments and two contact pads (I_{front} and I_{rear}) for independent current injection. The two segments are separated by one period of a PhC.

imposed gratings define reflection spectra, each with 10 modes spaced $3.1\,\mathrm{nm}$ and $3.3\,\mathrm{nm}$ apart. The partial cavities are coupled through a photonic crystal segment with only one period in Γ-M–orientation. A PhC–period of $360\,\mathrm{nm}$ and air fill factor of 33% lead to a reflectance of about 65%. The dimensions have been chosen such that the lasing wavelength lies in the center of the photonic bandgap. The rear facet consists of a highly reflective mirror formed by 4 periods of the same PhC, resulting in a reflectance close to 100%. The front facets have been cleaved. Figure 16.11 shows SEM micrographs of the PhC–mirror and of the distributed feedback grating, which is realized as a binary superimposed grating (BSG). The photographs at the bottom give a top view of the structure. By changing the current in the front segment at a constant $(40\,\mathrm{mA})$ applied to the rear segment, it is possible to switch the lasing wavelength in steps of 3.3 nm, towards higher wavelengths corresponding to the wavelength comb of the rear BSG grating (Fig. 16.10). By a further increase of the current, the wavelength switches back to smaller wavelengths and shows a cyclical switching behavior. Changing the current in the rear segment and keeping the current into the front segment at $40\mathrm{mA}$ switches the lasing wavelength cyclically towards smaller wavelengths, from $1523\,\mathrm{nm}$ to $1510\,\mathrm{nm}$ in steps of $3.1\,\mathrm{nm}$, corresponding to the peak wavelenghts of the front BSG grating [9]. By combining the above switching behavior and a temperature controlled continuous tuning, one can tune this device quasi–continuously over a spectral range of $24.5\,\mathrm{nm}$ with 56 wavelength channels, corresponding to a channel spacing as typically required by WDM applications (Fig. 16.12). The laser spectra shows a single mode operation over the entire tuning range with side mode suppression ratios in the range of 20 to $35\,\mathrm{dB}$, at output powers up to several mW fluctuating $< 5\,\mathrm{dB}$ over most of the wavelength channels. Even larger tuning ranges of up to $50\,\mathrm{nm}$ have been realized with similar devices at the expense of reduced side–mode suppression ratios and increasing power fluctuations.

16.6 Photonic crystal superprisms for WDM–applications

Close to the photonic band edge, photonic crystals exhibit chromatic dispersion caused by the gradual change of the apparent refractive index, due to the curvature of the photonic bands. This can be interpreted as the prism effect, i.e., as a change in the diameter of the

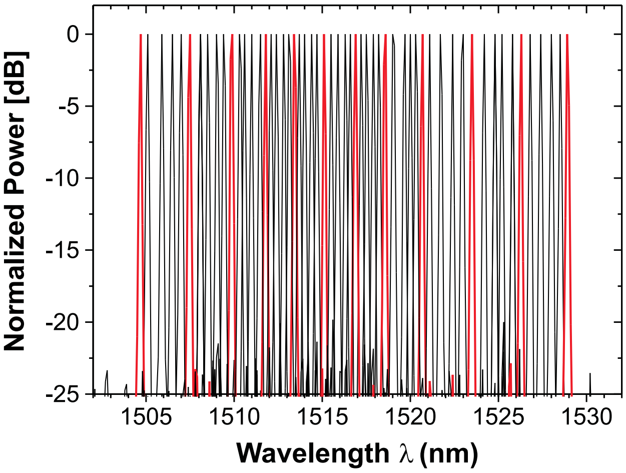

Figure 16.12: Superimposed spectra displaying a tuning range of $24.5\,\mathrm{nm}$ with 56 channels obtained by a combination of current and temperature tuning. Every fifth channel is marked in red.

iso–frequency lines within the bandstructure. If the iso–frequency contours change their shape with the frequency, the dispersion can increase by orders of magnitude. Such ultrastrong dispersive properties called "superprism effects" allow the production of compact optical filters which are highly attractive for WDM applications. Superprisms in two dimensional PhCs studied here, have to be operated close to the K or M–point, i.e., for light with the wavevector primarily in the plane of the epitaxial waveguides. Compared to integrated optical WDM filters such as arrayed waveguide gratings (AWGs), the strong dispersion of PhC–superprisms would allow us to reduce the size of a demultiplexer by a factor of 10 to 100. Obviously, the 2D PhC–superprism approach is fully compatible with planar integration. As for other PhC–components, the minimization of losses is crucial for its success. After a first experimental demonstration of the strong refraction in $\mathrm{Si/SiO_2}$ structures [5], a first superprism in a GaAs–based slab waveguide has already been reported [10]. The authors report on the dispersion of light at wavelengths around $1.3\,\mu\mathrm{m}$ by a GaAs–based device consisting of an input waveguide, the PhC–superprism, and output waveguides at different angles, each separated by 10°. The achieved wavelength resolution is $20\,\mathrm{nm}$, which fits to the requirements of coarse WDM–systems. Channel crosstalk attenuations $> 25\,\mathrm{dB}$ and insertion losses $< 0.3\,\mathrm{dB}$ should become feasible by optimizing the etching processes and by using "Bloch tapers" [11] to suppress the reflections at the interfaces.

Figure 16.13 shows calculated iso–frequency contours in the plane of the waveguide layer for TE modes $(\mathbf{H}\|\mathbf{i}_z)$. The FE–calculations have been carried out for a 2D PhC with a hole diameter of $2r = 0.8a$ and a permittivity $\epsilon = 10.341$ $(n = 3.216)$ for the voids corresponding to the effective index of the InP–based slab waveguide ($d = 400\,\mathrm{nm}$, $\lambda_G = 1.3\,\mu\mathrm{m}$). The iso–frequency contours show considerable anisotropy close to the boundary of the Brillouin zone, in particular at the M and K–points. The propagation direction of the refracted beams

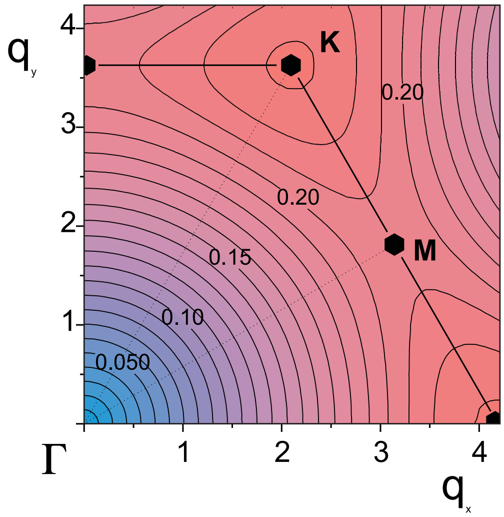

Figure 16.13: Calculated iso–frequency contours for the TE–modes ($\mathbf{H}\|\mathbf{i}_z$) for the envisaged superprism (hexagonal lattice, $2r = 0.8a$, $\epsilon = 10.341$).

in a superprism can be determined graphically in momentum space, by providing momentum conservation with respect to the wavevector component parallel to the entrance facet of the PhC. The Poynting vector of the refractive beam, which has the same direction as the group velocity, is then given by the gradient of the iso–frequency contours. The desired angular dispersion ($> 1^\circ/\,\mathrm{nm}$ close to the M–point) is achieved by choosing the angle of incidence and crystal pitch such that the operating point lies in a region of high curvature and non–circularity of the iso–frequency contours.

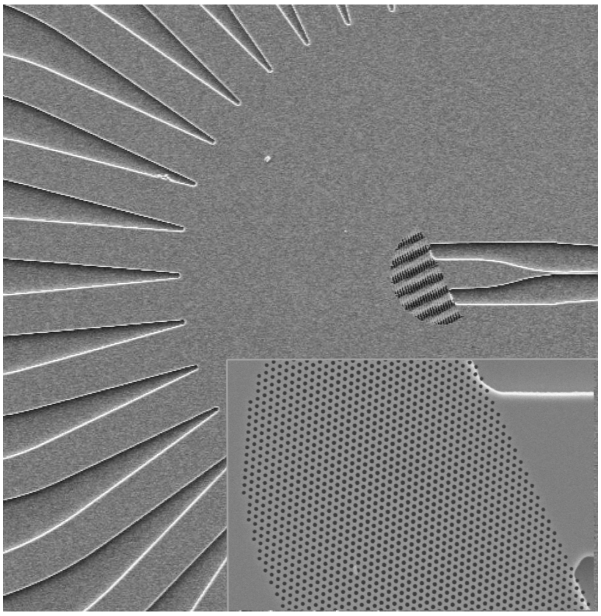

Figure 16.14: SEM photograph showing the superprism, the taper on the input side (right), and the output ports (left). The insert zooms into the photonic crystal.

Figure 16.14 shows a SEM micrograph of a planar superprism demultiplexer structure based on InP. Light is coupled into the superprism via the entrance waveguide and a tapered collimator structure. The feed of the fundamental mode of the collimator leads to a quasi plane wave excitation of the superprism. The diffraction at the other end of the superprism is suppressed by a circular facet before the light is collected in multimode waveguides, leaving the superprism at different angles. PhC–based collimators for the output beams could be added in order to further reduce channel crosstalk. The coexistence of beam collimators, tapers, superprism, and waveguides realized as PhC–components illustrates the versatility of the planar PhC–approach.

16.7 PhC–based dispersion compensator

The huge spread of group velocity in photonic crystals leads to spectral regions of very large chromatic dispersion. Therefore, PhC–devices are promising candidates for dispersion compensating filters. To date, there are mainly two different types of dispersion compensators used in telecom applications [12]. The Ge–doped dispersion compensating fibers (DCF) commonly used in optical transmission lines exhibits anomalous dispersion at 1.55 mm [13]. 1 km DCF typically allows to correct the dispersion of 10 km standard single–mode fiber (SSMF, 17 ps/nm/km at $1.55\,\mu\mathrm{m}$) over a wide spectral window ($> 20\,\mathrm{nm}$). Nevertheless, a full correction of several WDM–channels cannot be provided, since the dispersion slope of the SSMF cannot be corrected. Fiber Bragg gratings (FBGs), i.e., fibers whose core consists of a chirped 1D photonic crystal with a small refractive index contrast $\Delta n < 10^{-2}$, have emerged during the last years. The dispersion compensation of these devices is obtained by a gradually blue–shifted photonic band gap along the fiber (chirp), in order to let the short wavelength components travel longer before being reflected than the long wavelength components. Typically, about 1 m FBG is necessary to compensate for 10 km SSMF, i.e., the anomalous chromatic dispersion is by three orders of magnitude larger at the expense of a small spectral window ($< 1\,\mathrm{nm}$) which limits its application to a single WDM–channel. In addition, FBG need a circulator to drop the reflected signal [12, 14].

Dispersion compensators based on photonic crystal waveguides have to exhibit an anomalous chromatic dispersion, which must again be several orders of magnitude higher in order to allow the compensation of residual dispersion of 10 km standard single–mode fiber, within a compact device ($< 10\,\mathrm{mm}$). Furthermore, fine tuning of the chromatic dispersion after fabrication is possible by different means, in order to adjust the filters to the desired operating points. By tuning the overall material properties of either the dielectric (e.g., by carrier injection) or of an infiltrated material inside the pores (e.g., electro–optic or birefringent materials), the residual dispersion of a WDM–channel can be continuously adjusted.

Until now, only few dispersion compensators based on photonic crystals have been proposed or fabricated. Hosomi et al. proposed [15] a coupled cavity waveguide (CCW) which exhibits dispersion properties suitable for dispersion compensation. This type of waveguide can yield a linear dispersion of about $-10\,\mathrm{ps/nm/mm}$ in the wavelength range $1550 \pm 5\,\mathrm{nm}$, being more than five orders of magnitude larger than the dispersion achieved in DCF. First experimental results indicate that the predicted chromatic dispersion can be achieved at the expense of very large insertion losses [16]. The large impedance mismatch between a con-

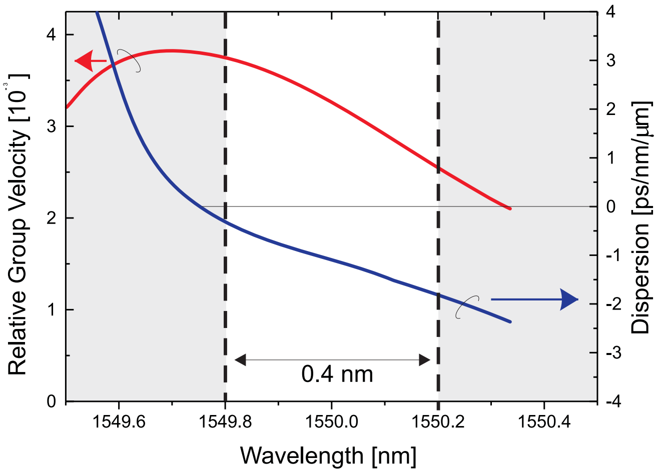

Figure 16.15: Relative group velocity (v_g/c) and dispersion of a W1–waveguide (W1) running into the Γ-M direction of a hexagonal photonic crystal in a SOI layer system ($a = 500\,\mathrm{nm}$, $n_{\mathrm{core}} = 3.4$, $d_{\mathrm{core}} = 0.38$, $n_{\mathrm{cladding}} = 1.5$, $r_{\mathrm{hole}} = 0.366a$).

ventional ridge waveguide and PhC waveguides with extremely low group velocities makes an appropriate tapering of the eigenmodes to reduce the coupling losses indispensable.

Our design operates close to the band edge of a mini–stopband of a photonic crystal waveguide with one missing row (W1) without relying on backward traveling waves. It takes advantage of the low group velocities close to the band edge which results in an increase of the group delays and thus of the differential chromatic dispersion. The calculated group velocity and the dispersion are shown in Fig. 16.15. The relative group velocity can be adjusted in the range of $v_g/c = 2 \ldots 4 \cdot 10^{-3}$. The dispersion runs quasi–linearly over a wavelength range of $0.4\,\mathrm{nm}$ ($40\,\mathrm{GHz}$ at $1.55\,\mu\mathrm{m}$) and delivers an expected chromatic dispersion of about $-1.5\mathrm{ps/nm/}\,\mu\mathrm{m}$, i.e., the dispersion of a 40 GB/s communication channel running over 10 km SSMF is proposed to be compensated within less than $100\,\mu\mathrm{m}$ of photonic crystal waveguide. By using W1–waveguides in the SOI layer system, a variation of the group index n_G from 5 to 90 could be experimentally demonstrated [17].

To date, tuning and trimming of dispersion compensators used for residual dispersion is carried out by mechanical stress. However, this represents an issue with respect to reliability. Photonic crystals offer the unique possibility that their dispersion properties can be tuned after fabrication. Indeed, the particular location of the field intensity within the dielectric (here silicon) as within the pores (Fig. 16.9) permits different ways of tuning the chromatic dispersion of the photonic crystal waveguides after fabrication. Electrical or optical injection allows the adjustment of the refractive index of the dielectric in use [18]. Tuning can also be achieved by infiltration of electro–optic [19] or birefringent materials [20] into the holes of the dielectric structure. In particular, liquid crystals can lead to a significant change of the dispersion properties.

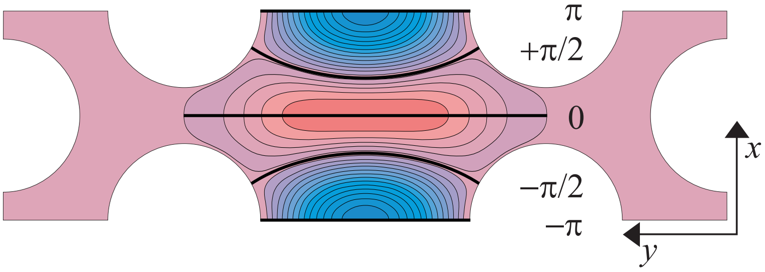

Figure 16.16: Fundamental TE–mode ($\Re\left(H_z\right)$) and and the corresponding phase fronts (thick lines) for a hexagonal W1 waveguide in SOI at $k_x = 0.3$ (parameters: Fig. 16.9).

16.8 Fiber–to–chip coupling of photonic crystals

The efficient, i.e., low–loss and low–reflectance coupling from a single–mode fiber to a chip containing planar photonic crystals, represents one of the major challenges in introducing photonic crystal devices into telecommunication systems. The use of high index–contrast material systems, offering a broad photonic bandgap complicates the coupling by requiring spot magnifications beyond those of laserdiodes in III–V compounds.

The natural starting point of analysis is the coupling between a photonic crystal waveguide with n missing rows and a conventional waveguide compared to the coupling of two conventional waveguides. To decompose the optical field, it is necessary to consider the orthogonality relation[5] of two Bloch modes

$$\int\limits_A d\mathbf{a}\cdot[\mathbf{E}_t(\mathbf{q}_1)^*\times\mathbf{H}_t(\mathbf{q}_2)+\mathbf{E}_t(\mathbf{q}_2)\times\mathbf{H}_t(\mathbf{q}_1)^*]=\delta(\mathbf{q}_1,\mathbf{q}_2)S_z(\mathbf{q}_1), \tag{16.4}$$

where $\mathbf{q}_1$ and $\mathbf{q}_2$ represent wave vectors of the two modes at the interface A, $\mathbf{E}_t(\mathbf{q}_l)$ and $\mathbf{H}_t(\mathbf{q}_l)$ the corresponding electric and magnetic field projected onto the interface, $\delta(\mathbf{q}_1, \mathbf{q}_2)$ is Kronecker's symbol, and $S_z(\mathbf{q}_1)$ describes the vector component of the energy flux perpendicular to the interface. By using the orthogonality relations and keeping in mind that the tangential components of electric and magnetic fields are always continuous at a dielectric interface, it is possible to derive expressions for the coupling coefficients. For two single–mode waveguides, the approximation formula for the reflection coefficient

$$r=-\frac{\int\limits_A d\mathbf{a}\cdot\left[\mathbf{E}_t|_{\text{left}}\times\mathbf{H}_t|_{\text{right}}-\mathbf{E}_t|_{\text{right}}\times\mathbf{H}_t|_{\text{left}}\right]}{\int\limits_A d\mathbf{a}\cdot\left[\mathbf{E}^*_t|_{\text{left}}\times\mathbf{H}_t|_{\text{right}}+\mathbf{E}_t|_{\text{right}}\times\mathbf{H}^*_t|_{\text{left}}\right]} \tag{16.5}$$

is given by a generalization of the expression widely used in integrated optics [22]. Due to the rather complex nature of the modes propagating through photonic crystal waveguides, the coupling of PhC–waveguides is much more involved than that of conventional waveguide coupling:

---

[5] A similar orthogonality relation holds for conventional waveguides of integrated optics [21].

- **Phase Matching**
  The reflection coefficient is sensitive to the shape of the phase fronts (see Eq. (16.5)). A photonic crystal waveguide, in contrast to a conventional waveguide, guides by refocusing, i.e., the phase fronts of its eigenmodes run only at certain cuts (planes of mirror symmetry) through the elementary cell perpendicular to direction of the waveguide. As a consequence, the coupling between a conventional and a photonic crystal waveguide, relies sensitively on the position of the interface within the elementary cell of the photonic crystal.

- **Spot Size and Shape Matching**
  The spot size and the roll–off of a defect mode of a photonic crystal waveguide depends on the number of missing rows and on the size and layout of the elementary cell of the underlying photonic crystal. Like the phase fronts, spot size and shape vary along the elementary cell.

- **Impedance Matching**
  An efficient coupling of conventional waveguides relies on a reasonable matching of the wavevector at the interface [22]. As suggested by (16.5), the matching of the main and tributary impedances ($E_{\mathrm{main}}/H_{\mathrm{main}}$, $E_{\mathrm{tributary}}/H_{\mathrm{tributary}}$) represents the analogue of wavevector matching for PhC–to–waveguide coupling. These values vary like the shape of the phase fronts within a elementary cell of the photonic crystal waveguide.

For realistic examples, all effects together result in significant changes of the reflectance (up to 300%) along an elementary cell.

The optical system for fiber–to–chip coupling can contain both micro–optical elements located outside the chip and integrated spot transformers based on conventional or photonic crystal waveguide structures. Candidates for micro–optical elements are conventional ball lenses of high refractive index in glass, spherical and aspherical planoconvex lenses in silicon and various types of lensed fibers. Proposed schemes for the on–chip transformation of the eigenmode of a conventional ridge waveguide into the defect mode of a photonic crystal include parabolic waveguide mirrors [23], tapered dielectric waveguides [24, 25], and tapers within the photonic crystal medium [26,27]. Tapers, in particular, are intended to tackle an essential problem of the on-chip transformation, i.e., the suppression of reflections by realizing a ”smooth” transformation of the eigenmodes.

Figure 16.17 shows a schematic diagram of a compact fiber–to–chip coupling unit, based on a silicon plano–convex lens with a high numerical aperture (NA) and a silicon optical bench (SiOB) [28]. The fabrication processes for the Si–lenses allow for non–circular surfaces, i.e., for a stigmatic mapping of the nearfields which is at least adequate for the coupling of fundamental modes. The typical distance of the Si–lens to the PhC–chip is as for edge emitting laser diodes, a few $10\,\mu\mathrm{m}$. Due to the periodic variation of the shape of phase fronts and impedances mentioned above, the coupling of the optical field from fiber to PhC–waveguide, via an intermediate conventional waveguide, avoids the preparation of the endfaces of the PhC–chips on a nanometer scale. As long as the requirements of amplitude transformation do not devaluate the conventional PhC–to–waveguide coupling, it seems superior to use an intermediate conventional waveguide to couple between a PhC–waveguide and the outside world. The adjustment requirements of high–index contrast waveguides are still noticeably higher than those for conventional fiber optics. However, modern nano–positioning equipment is available which allows for the accuracies needed to assemble hybrid fiber–to–PhC–waveguide coupling optics. For IOSOI waveguide structures, e.g., coupling efficiencies of approximately 30% seem therefore realistic.

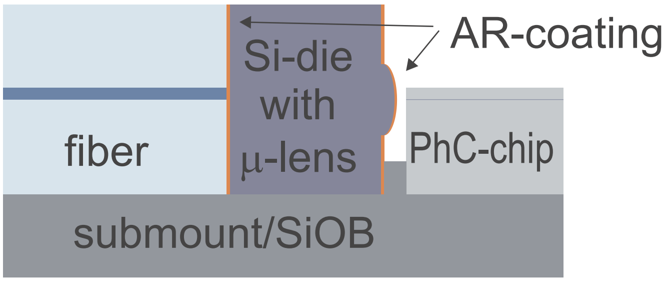

Figure 16.17: Fiber–to–chip coupling unit using a silicon optical bench (SiOB) equipped with a Si plano–convex lens (not to scale).

Acknowledgements

The authors gratefully acknowledge the support of the German Federal Ministry of Education and Research (BMBF) under the grants 13N8245, 13N8252, 13N8248, 13N8246, 13N8251, 13N8247, 13N8249, and 13N8250.

References

[1] K. Sakoda. *Optical Properties of Photonic Crystals*, volume 80 of *Optical Sciences*. Springer, Berlin, 2001.

[2] P. Deuflhard, F. Schmidt, T. Friese, and L. Zschiedrich. Adaptive Multigrid Methods for the Vectorial Maxwell Eigenvalue Problem for Optical Waveguide Design. In W. Jäger and H. J. Krebs, editor, *Mathematics - Key Technology for the Future*, page 279. Springer, Berlin, 2003.

[3] S. G. Johnson and J. D. Joannopoulos. Block-iterative frequency-domain methods for Maxwell's equations in a planewave basis. *Opt. Express*, 8:173, 2001.

[4] F. Schmidt. *A New Approach to Coupled Interior-Exterior Helmholtz-Type Problems: Theory and Algorithms*. Postdoctoral Thesis, Freie Universität Berlin, Berlin, 2002.

[5] H. Kosaka, T. Kawashima, A. Tomita, M. Notomi, T. Tamamura, and T. Sato. Superprism phenomena in photonic crystals: Towards microscale lightwave. *IEEE J. Lightwave Technol.*, 17:2032, 1999.

[6] B. D'Urso, O. Painter, J. O'Brien, T. Tombrello, A. Yariv, and A. Scherer. Modal reflectivity in finite depth two-dimensional photonic-crystal microcavities. *J. Opt. Soc. Am.*, B15:1155, 1998.

[7] H. Benisty, P. Lalanne, S. Olivier, M. Rattier, C. Weisbuch, C.J.M. Smith, T.F. Krauss, C. Jounain, and D. Cassagne. Finite-depth and intrinsic losses in vertically etched two-dimensional photonic crystals. *Opt. Quant. Electron.*, 34:205, 2001.

[8] W. Bogaerts, V. Wiaux, D. Taillaert, S. Beckx, B. Luyssaert, P. Bienstman, and R. Baets. Fabrication of photonic crystals in silicon-on-insulator using 248-nm deep UV lithography. *IEEE J. Sel. Top. Quant.*, 8:928, 2002.

[9] S. Mahnkopf, M. Kamp, A. Forchel , and R. März. Tunable distributed feedback laser with photonic crystal mirror. *Appl. Phys. Lett.*, 82:2942, 2003.

[10] L. Wu, M. Mazilu, T. Karle, and T. F. Krauss. Superprism phenomena in planar photonic crystals. *IEEE J. Quant. Elect.*, 38:915, 2002.

[11] T. Baba, D. Ohsaki, T. Iwai, and M. Nakamura. Transmission-type photonic crystal devices with efficient input/output interfaces. *Proc. Conference on Lasers and Electro-Optics (CLEO)*, I:280, 2001.

[12] J.F. Brennan. Dispersion compensation gratings for the C-band. *Photon. Spectra*, 159/6:159, 2001.

[13] A. Othonos. Fiber Bragg gratings. *Rev. Sci. Instrum.*, 68:4309, 1997.

[14] V. A. Semenov, A. V. Belov, E. M. Dianov, A. A. Abramov, M. M. Bubnov, S. L. Semjonov, A. G. Shchebunjaev, V. F. Khopin, A. N. Guryanov, and N. N. Vechkanov. Broadband dispersion-compensating fiber for high-bit-rate transmission network use. *Appl. Opt.*, 34:5331, 1995.

[15] K. Hosomi and T Katsuyama. A dispersion compensator using coupled defects in a photonic crystal. *IEEE J. Quant. Elect.*, 38:825, 2002.

[16] Y. Chai, C. Morgan, R. Penty, I. White, T. Karle, and T. Krauss. Compression of picosecond pulses using photonic crystals. *Proc. European Conference on Integrated Optics (ECIO)*, 1:29, 2003.

[17] M. Notomi, K. Yamada, A. Shinaya, J. Takahashi, C. Takahashi, and J. Yokohama. Extremely large group velocity dispersion of line-defect waveguides in photonic crystal slabs. *Phys. Rev. Lett.*, 87:253902–1, 2001.

[18] S. W. Leonard, H. M. Van Driel, H. Schilling , and R. B. Wehrspohn. Ultrafast band edge tuning of a two-dimensional silicon photonic crystal via free carriers. *Phys. Rev. B*, 66:161102–1, 2002.

[19] Y. Luo, I. Szafraniak, A. Nagarajan, R. B. Wehrspohn, M. Steinhart, N. D. Zhakarov, R. Ramash, and M. Alexe. Nanoshell tubes of ferroelectric lead zirconate titanate and barium titanate. *Appl. Phys. Lett.*, 83/2:in press, 2003.

[20] S. W. Leonard, J. P. Mondia, H. M. Van Driel, O. Toader, S. John, K. Busch, A. Birner, U. Gösele, and V. Lehmann. Tunable two-dimensional photonic crystals using liquid-crystal infiltration. *Phys. Rev. B*, 61:R2389, 2000.

[21] R. März. *Integrated Optics: Design and Modeling*. Artech House, Boston, 1994.

[22] D. Marcuse. *Theory of Dielectric Optical Waveguides*. Academic Press, New York, 1974.

[23] D. W. Prather. Photonic crystals: An engineering perspective. *Opt. Photonics News*, 6/2002:16, 2002.

[24] Y. Xu, R. K. Lee, and A. Yariv. Adiabatic coupling between conventional dielectric waveguides and waveguides with discrete translational symmetry. *Opt. Lett.*, 25:755, 2000.

[25] A. Mekis and J. D. Joannopoulos. Tapered couplers for efficient interfacing between dielectric and photonic crystal waveguides. *IEEE J. Lightwave Technol.*, 19:861, 2001.

[26] M. Palamaru , and Ph. Lalanne. Photonic crystal waveguides: Out-of-plane losses and adiabatic modal conversion. *Appl. Phys. Lett.*, 78:1466, 2001.

[27] T. D. Happ, M. Kamp, and A. Forchel. Photonic crystal tapers for ultra-compact mode conversion. *Opt. Lett.*, 26:1102, 2001.

[28] T. Possner, B. Höfer, G. Leibeling, B. Messerschmidt, and G. Tittelbach. Fabrication of optical subsystems for hybrid integration in microsystems. *Proc. Conference on Micro System Technologies (MST)*, page 579, 1996.

17 Photonic crystal based active optoelectronic devices

Martin Kamp[1], *Thomas Happ, Sven Mahnkopf, Alfred Forchel, Srinivasan Anand, and Guang–Hua Duan*

17.1 Introduction

Modern electronic devices, such as semiconductor lasers, microwave transistors or highly integrated circuits, all rely on the ability to control the properties of the constituent semiconductor materials to a very high degree. Often a combination of different semiconductor materials with layer thicknesses on the order of a few nm is used to tailor the electronic properties. An extreme example is the quantum cascade laser, where the wavefunctions in the active region are designed to obtain intraband transitions with the desired emission wavelength.

A possibility to control the optical properties of the materials with a similar accuracy is the use of photonic crystals. Photonic crystals (PhCs) are artificial dielectric materials which modulate the refractive index on a scale of the wavelength. Similar to the formation of energy bands in the periodic potential of the crystal lattice, optical bands and bandgaps emerge in photonic crystal structures. Light propagation is suppressed in the gaps between the bands. These properties enable the control of light propagation and generation on a very small scale. Furthermore, the similarity of the fundamental equations allows one to transfer a number of concepts from solid state physics, such as defects, doping, bloch states, etc. to optical systems.

After the first proposal of photonic crystals by John [1] and Yablonovich [2], a wide range of possible PhC based devices was proposed. The strong interaction of the light with the photonic crystals enables the miniaturization of optoelectronic components as well as the application of novel designs.

Optical resonators can be produced with PhCs by removing one or several holes from a uniform PhC lattice. The resulting defect localizes light with a very small mode volume and high Q–values of several thousand. This has led to the demonstration of ultra–small laser sources with a size below 1 μm [3]. Although some issues such as electrical injection and thermal management have to be solved, these devices demonstrate the capabilities of PhC–based devices. PhC–based resonators also allow the design of very compact filters, which consist of one or several coupled cavities [4, 5].

Another application of photonic crystals in optoelectronic devices is their use in bent waveguides with a very small radius of curvature, which are key elements for highly integrated photonic circuits. If the bending radius of classical index guides becomes too small, the transmission losses increase drastically. These losses can (at least theoretically) be suppressed completely in PhC based waveguides, where the light is not allowed to propagate in the PhC

---

[1] Corresponding author: e-mail: martin.kamp@physik.uni-wuerzburg.de

Photonic Crystals. Edited by K. Busch, S. Lölkes, R. B. Wehrspohn and H. Föll
Copyright © 2004 Wiley-VCH Verlag GmbH & Co. KGaA
ISBN: 3-527-40432-5

surrounding the bend. Compact PhC based curved waveguides with high transmission have first been proposed by Mekis et al. [6]. As a final example, PhCs or PhC–based waveguides can be designed to have a very large spectral dispersion. The dispersive properties of PhCs are utilized in the superprism [7], which could be the key for the realization of small size wavelength multiplexers.

This article describes results on the integration of photonic crystals with active optoelectronic devices. Starting from the use of photonic crystals as mirrors in semiconductor lasers, more and more functionality is moved to the PhC part of the devices. The most complex example is a tunable PhC based light source.

17.2 Waveguide based 2D photonic crystals

Although three dimensional crystals would be the preferred choice since they control the light propagation in all three directions and are ideally lossless, they are difficult to integrate with optoelectronic devices. The technology developed so far for the fabrication of 3D crystals often only allows the fabrication of homogeneous PhC blocks without any functional elements such as mirrors, waveguides or resonators. A more suitable approach is the use of two–dimensional crystals, which are based on a planar waveguide structure [8]. This planar waveguide is similar to that used in semiconductor lasers or integrated optics devices, hence the integration of PhC structures is a relatively easy task. A common implementation of this type of crystal is a hexagonal lattice of air holes, which are etched into the planar waveguide. A schematic view of this basic PhC structure is shown in Figure 17.1.

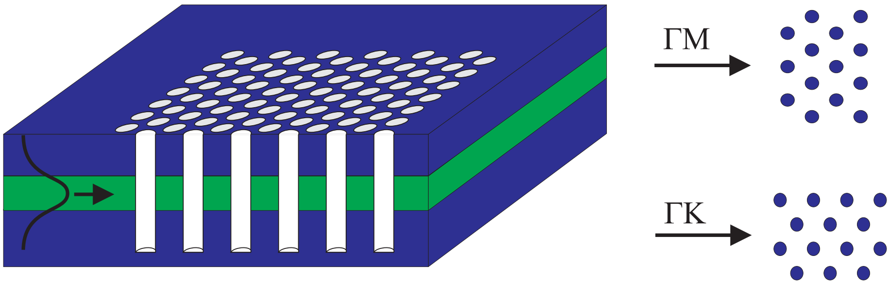

Figure 17.1: 2D photonic crystal based on planar waveguide structure.

The planar waveguide consists of a guiding layer (shown in green) with a high refractive index and a lower and upper cladding layer, with a lower refractive index. The width of the guided mode depends on the thickness of the core layer and the difference of the refractive index between core and cladding. All devices discussed in this chapter were fabricated from InP based waveguides, which have an index difference of about 0.2. The width of the core layer is determined by the requirement of a single guided mode. If the thickness of the core layer is too large, more than one mode can be guided by the planar guide. Typically, a thickness between 300 and 400 nm is used. The intensity profile of the guided mode has a bell shape and penetrates into the cladding layer, with a total width of 600 – 800 nm. Since the photonic crystals have to intersect the guided mode completely in order to avoid scattering losses, the depth of the holes has to be much larger than the width of the mode. For the geometry described above, this translates into a minimum etch depth of at least 2 μm. In this regime, the losses can be described with a perturbative model [9, 10]. There are two contributions to the losses: The first one is caused by the diffraction of the light in the holes, where no vertical waveguiding is present. The second one is proportional to the part of the exponentially decaying tail of the mode which does not overlap with the PhC.

Due to the presence of losses, a complete description of devices based on this structure would require full 3D simulations. For a couple of properties, such as the spectral position and size of the bandgap, one can look at a corresponding 2D system, where the dielectric material has the effective refractive index of the fundamental guided mode of the planar waveguide. The second important parameter besides the dielectric constant, is the air filling factor of the crystal. In this approximation, the losses caused by out of plane scattering can be taken into account by assigning a small imaginary part to the refractive index in the holes.

A plot of the bandstructure for TE–polarized light (E–vector in the plane) as obtained by a plane wave expansion technique [11] is shown in the left of Figure 17.2. The k–vector is varied from the center of the Brillouin zone (Γ point) to the two directions of high–symmetry, named ΓM and ΓK.

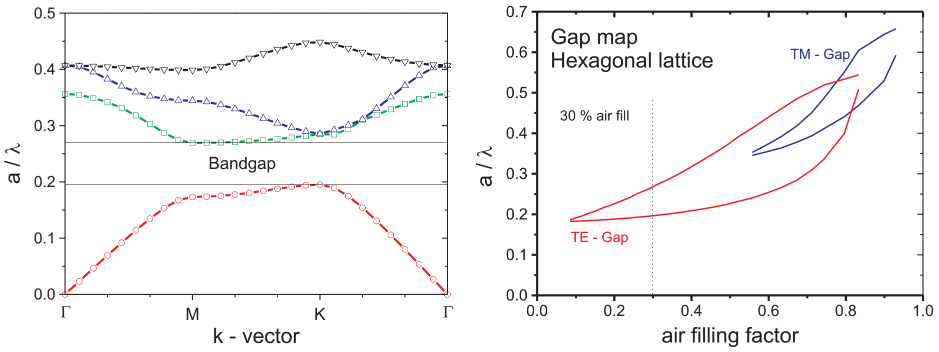

Figure 17.2: Left: Bandstructure of a 2D PhC for TE polarized light. The air filling factor was 30 %, the refractive index of the dielectric 3.2. Right: Spectral position of the TE and TM gap as a function of the air filling factor.

The energies of the states are plotted in units of a/λ where a is the lattice constant and λ the wavelength. The bandgap for light propagating in the ΓM direction extends from 0.2–0.27. For propagation in ΓK direction, the gap ranges from 0.22–0.3. This results in a bandgap for all in–plane k–vectors for a/λ values between 0.2 and 0.27. For applications at 1.55 μm, this translates into lattice periods between 310 and 420 nm. If the bandstructure is calculated for different air filling factors, one can obtain a 'gap map' as shown in the right plot of Figure 17.2. For small air filling factors, only a gap for TE polarized light is present, the TM gap opens at high filling factors of 60 %. A complete gap is present for filling factors between 60 and 85 %. Since the emission of a semiconductor laser is usually TE polarized, one can use a broad range of air filling factors for the PhC structures. However, the losses are going to increase with the air filling factor due to out of plane diffraction. Usually an air filling factor around 30 % is chosen as a good compromise between width of the gap, losses and fabrication capability.

17.3 Semiconductor lasers with photonic crystal mirrors

Due to their high efficiency, large bandwidth and compact size, semiconductor lasers have become indispensable for optical fiber transmission, sensing, optical storage, metrology and a vast number of other applications. The cross section of a very common laser structure, the ridge waveguide laser [12], is shown in Figure 17.3.

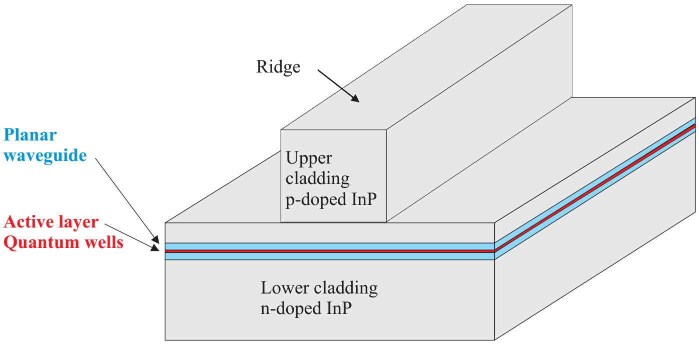

Figure 17.3: Cross section of a ridge waveguide laser.

It consists of several epitaxially grown layers on a semiconductor substrate, which are partially etched in order to form a ridge structure. The planar waveguide layer together with the ridge forms the so called waveguide. In order to operate in a single lateral mode regime, the width of the ridge is kept around 2–5 μm. The gain is provided by the active region where the light is amplified by stimulated recombination of electrons and holes. The active region consist of one or several quantum wells inside the waveguide. Holes are injected into the structure from a top p–contact, whereas electrons are injected from the bottom. The carriers are captured in the quantum wells, which have the lowest electronic bandgap in the layer stack. The vertical layer structure is called separate confinement heterostructure (SCH), since the planar waveguide confines the optical mode and the quantum wells the carriers. The gain spectrum of the active region in a semiconductor laser has a width of a several 10 nm. Optical feedback in a ridge waveguide laser is provided by the cleaved facets, which have a reflectivity of around 30 %.

Standard semiconductor lasers have a length between 300 and 1000 μm, which is reasonable if the lasers are operated individually, but clearly too large for highly integrated optoelectronic circuits. In this type of application, there is a clear need for the miniaturization of the lasers. Besides high integration density and a small parasitic capacitance, the reduction of the threshold currents is an important aspect for the integration. A low threshold leads to a decrease of the thermal load of each laser source, which is a critical parameter in densely integrated circuits. If one reduces the length of the laser resonator, the reflectivity of the mirrors has to be increased at a certain point, in order to compensate the increasing optical losses. Cleaved facets are not suitable for this purpose. Besides their reflectivity of only 30 %, they cannot be placed at arbitrary positions on the chip. This is a severe restriction of freely positioned on the chip.

A possible solution proposed by several groups is the use of deeply etched Bragg mirrors. Very short lasers with this design were demonstrated in a number of material systems [13–15]. Another possibility is the use of photonic crystals as mirrors. Figure 17.4a and b show two possible szenarios. In the first design, one facet has been replaced by a high–reflection PhC mirror. The second design uses PhC mirrors at both sides of the ridge waveguide. This allows immediate integration with further PhC elements such as PhC waveguides, combiners or filters. Ridge waveguide lasers with PhC mirrors were first produced for GaAs based lasers [16, 17] and later on for InP lasers at 1.55 μm wavelength. For the production of semiconductor lasers with 2D PhC mirrors, the combination of a ridge waveguide structure with PhC mirrors has the advantage of relaxed requirements concerning the fabrication of the PhC structures.

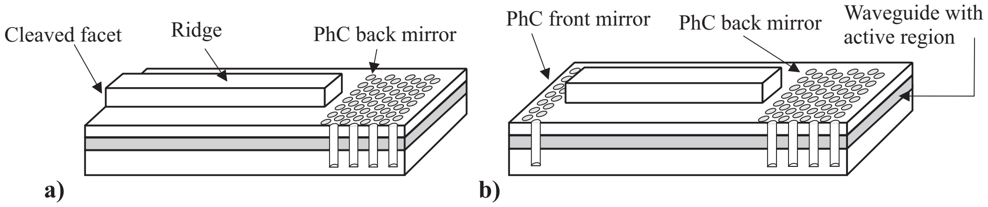

Figure 17.4: a) Ridge waveguide laser with PhC back mirror b) Laser with PhC front and back mirror.

The upper cladding layer has a thickness of about 1.5–2 μm in order to keep the absorbing upper metal in contact at a certain distance from the guided mode. For a PhC etched directly from the unpatterned surface, the thickness of the cladding layer adds to the depth of the holes required by the overlap with the guided mode. In this case, a total depth of 4–5 μm would be required. The use of a ridge waveguide, which is etched to a distance of 300–500 nm from the waveguiding layer, relaxes the demands on the depth of the holes. Calculations of the modal reflectivities for this geometry indicate that holes with a depth of 1 μm have a sufficient reflectivity to serve as mirrors for a semiconductor laser [18].

17.3.1 Fabrication

The process used for the fabrication of the devices is shown in Figure 17.5. The fabrication of the lasers starts with the processing of 2.5–3 μm wide ridge waveguide lasers. The sample is coated with a layer of optical resist and the ridge waveguide pattern is exposed by optical lithography. After development of the resist, an etch mask consisting of a 290 nm $\mathrm{BaF_2}$ and 210 m thick Cr layer, is evaporated on the sample. Etching of the ridge waveguides is performed in an ECR/RIE (Electron cyclotron resonance – reactive ion etching) tool in a

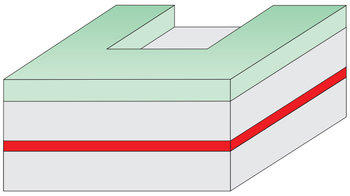

1. Definition of ridge pattern in optical resist

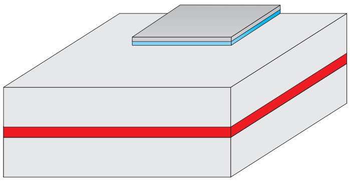

2. Evaporation of BaF$_2$/Cr mask and lift off

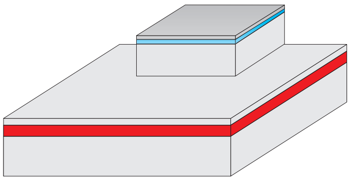

3. ECR/RIE etching of ridge

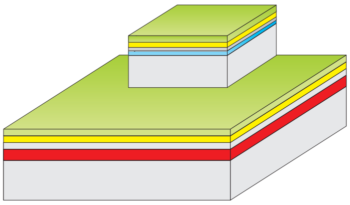

4. Deposition of 250 nm Si$_2$O and 500 nm PMMA resist

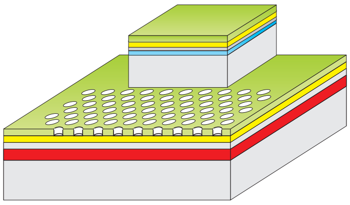

5. E-beam exposure of PhC pattern and resist develoment

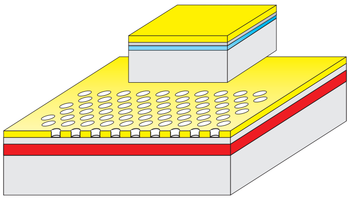

6. Pattern transfer in SiO$_2$ mask with CHF$_3$/Ar based RIE

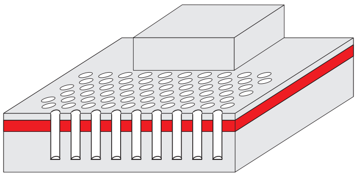

7. Etching of the semiconductor with Cl$_2$/Ar ECR/RIE

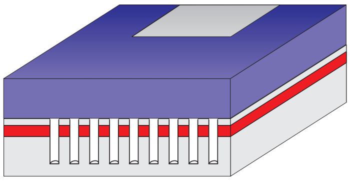

8. Planarization and subsequent contact formation

Figure 17.5: Fabrication scheme of ridge waveguide laser with PhC mirrors.

Cl_2/Ar based plasma. The ridges are etched down to a distance of 300–500 nm from the SCH waveguide. In order to protect the waveguide during the PhC etching, the etch mask is left on the sample.

Since the E–beam resist used to define the PhC pattern has a poor etch resistance, it cannot be used directly as a mask for the etching of the holes. Instead, an intermediate mask has to be used. Common choices are Si_xN_y or SiO_2 layers. In the process described here, a layer of 250 nm thick SiO_2 is used, which is deposited by a sputter process. The PhC patterns are exposed with E–beam lithography in a 500 nm thick PMMA layer on top of the SiO_2. A high accelerating voltage, 100 kV in this case, is useful because the electrons undergo only a little forward scattering in the resist. Since the diameter of the holes increases a little during the subsequent etch processes, the holes are exposed with 80–90 % of their final size. After the exposure, the sample is developed in a 1:3 mixture of Methyisobutylketon (MIBK) and Isopropanol (IPA). A CHF_3/Ar reactive ion etch (RIE) step is now used to transfer the pattern in the SiO_2 mask.

The following etch step transfers the holes into the semiconductor. A ECR/RIE process with a Cl_2/Ar mixture is used [20]. Etching of In containing compounds with a Cl_2 plasma, usually requires an elevated sample temperature, since the vapour pressure of the reaction product $InCl_3$ is very low at room temperature. In the process used here, a high microwave power of 1kW is applied, which leads to a high density plasma and substantial heating of the sample. This ensures a sufficiently high desorption rate of the $InCl_3$. After the etching of the holes, the BaF_2 and SiO_2 layers are removed in 1% HF. The thick BaF_2 layer allows a complete removal of the Cr and remaining SiO_2 layer on top of it. The lasers are now planarized with a polymer layer, which is etched back until the top of the ridge is open. The last step is the formation of p– and n–contact to the sample. The SEM micrograph in Figure 17.6 shows a top view of the PhC mirror at the end of the ridge waveguide after the etching.

There are several degrees of freedom in the design of the PhC mirrors, which can be used

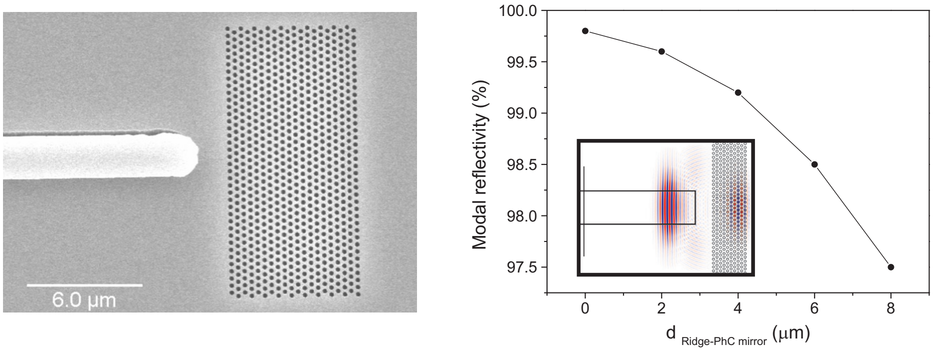

Figure 17.6: Left: SEM micrograph of a ridge waveguide with a PhC mirror. Right: Modal reflectivity of a PhC mirror versus the distance from the ridge. A snapshot of a FDTD simulation is shown in the inset.

to optimize their performance. The orientation of the mirror has to be chosen along the ΓM direction, otherwise the first column of holes acts as a very efficient diffraction grating and very little light is reflected back into the waveguide [19]. If the air filling factor is very small, the holes might not reach a sufficient etch depth. For a large air filling factor, the losses due to diffraction become large, eventually reducing the reflectivity of the mirror. An air filling factor between 30 and 40 % turns out to be a reasonable compromise between depth and losses.

The position of the PhC mirror with respect to the end of the waveguide is another design issue. For a PhC mirror very close to the end of the ridge, resist non–uniformity and proximity effects related to the E–beam exposure can lead to a strong variation of the hole size and depth, resulting in poor performance of the PhC mirror. On the other hand, diffraction losses due to the lack of lateral guiding will reduce the modal reflectivity for a mirror placed far away from the waveguide. A finite difference time domain (FDTD) simulation can be used to calculate the modal reflectivity of the PhC mirror. The result of the simulation as a function of the distance between the PhC mirror and the end of the waveguide, is displayed in Figure 17.6. A slight decrease of the reflectivity is seen as the mirror is moved further away, but the overall effect is less than one percent for a distance less than 2μm. This distance is a reasonable compromise between losses and fabrication requirements.

17.3.2 Device performance

All measurements of the lasers were performed on a temperature controlled heat sink at room temperature. The left plot in Figure 17.7 shows the output power characteristic of a 100 μm and 200 μm long laser with a highly reflecting PhC back mirror and a cleaved front facet. The PhC mirror has a lattice period of 325 nm and an air filling factor of 40 %. The 100 μm long laser has a threshold current of 13 mA; the threshold of the 200 μm long device is 16 mA. The maximum output power is 4.6 mW for the 100 μm and 9 mW for the 200 μm laser. In both cases, the output power is limited by the increased temperature at higher currents, which reduces the efficiency of the device.

The right plot in Figure 17.7 shows the threshold current and external efficiency as a function of the laser length L. There is a clear improvement for shorter cavities of both the threshold and the efficiency. This trend indicates that even shorter lasers should be possible, with a further improvement of the device parameters.

As a next step, both facets can be replaced by PhC mirrors. The left plot in Figure 17.8 shows the output power characteristic of a 100 μm long laser with a highly reflecting PhC back mirror and a front mirror consisting of 4 rows PhC. The threshold is now only 7.6 mA, which is a clear reduction compared to the devices with only one PhC mirror. Due to the high reflectivity of the front mirror, the output power is reduced to 600 μW. The spectrum of the device is displays in the right plot of Figure 17.8. It consist of a series of Fabry–Perot modes with a spacing of 3.2 nm. The reflectivity of the PhC mirror is basically constant over the wavelength range plotted here, so it does not provide any wavelength selectivity.

17.3.3 Single mode photonic crystal based lasers

All lasers discussed so far, show a Fabry–Perot like emission which is a result of the broad reflectivity of the PhC mirrors. A number of applications, however, require single mode emitting lasers. This task is easily accomplished with the introduction of a PhC mirror inside the laser cavity. The additional mirror results in the formation of two coupled cavities with a different mode spacing [21]. Figure 17.9 shows a schematic of this device.

The laser resonator consists of a highly reflective PhC back mirror, an intermediate mirror which is patterned laterally to the ridge waveguide and a cleaved facet as output mirror. The PhC pattern of the intermediate mirror is exposed directly across the ridge waveguide, resulting in a self–aligned definition of the intermediate mirror. The fabrication benefits from the 100 kV accelerating voltage of the E–beam lithography system, which allows the exposure of a PhC pattern in the immediate vicinity of the ridge. The intermediate mirror interacts with the evanescent part of the guided mode. Assuming a complete reflection of the part overlapping with the PhC mirror, the reflectivity turns out to be 12 %.

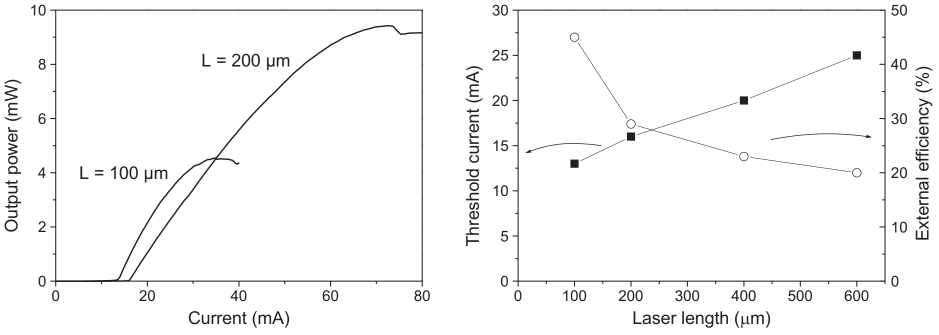

Figure 17.7: Left: Power characteristic of lasers with one PhC mirror and different lengths L. Right: Threshold current and external efficiency as a function of the laser length.

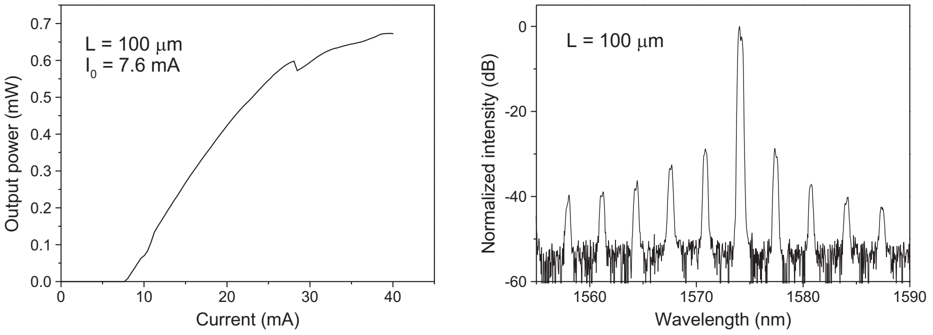

Figure 17.8: Left: Output power characteristics of a 100 μm long laser with two PhC mirrors Right: Emission spectrum of a 100 μm long laser.

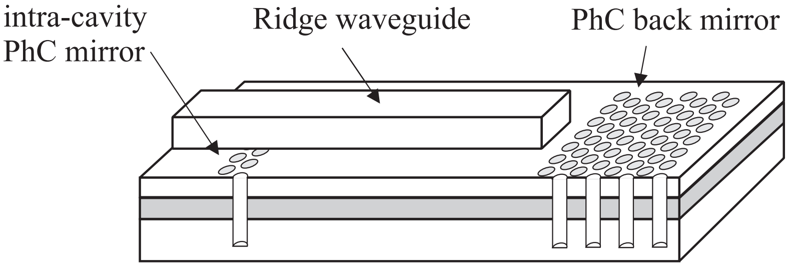

Figure 17.9: Ridge waveguide laser with intracavity PhC mirror.

Figure 17.10 shows the output power characteristic of three lasers with different length. The short cavities result in low threshold currents from 13 mA for the 100 μm long device up to 22 mA for the 400 μm long laser. The output power is thermally limited to values of around 4 mW for the 100 μm long laser and to over 9 mW for the 200 μm long laser. Differential quantum efficiencies of 44 %, 32 % and 26 % are measured for the three length of 100 μm, 200 μm and 400 μm, respectively.

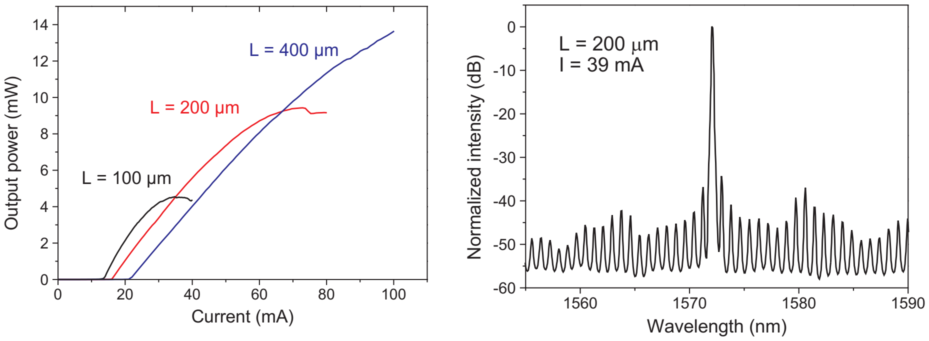

Figure 17.10: Left: Output power characteristic of three lasers with different length
Right: Emission spectrum of a 200 μm long laser at a bias of 39 mA.

As expected, the lasers show single mode emission with a sidemode–suppression ratio (SMSR) of 35 dB. The mechanism of the mode selection is clearly visible in the spectrum of the sidemodes: the coupling of the two resonators with their different mode spacing results in a beating. The devices show a good stability of the single mode emission over a wide range of currents and temperature. Figure 17.11 shows the wavelength and sidemode suppression of the laser emission as a function of the drive current. The sidemode suppression is over 30 dB for a large range of drive currents. Due to the temperature dependence of the refractive index, the emission shifts to larger wavelengths as the current and with it, the device temperature is increased.

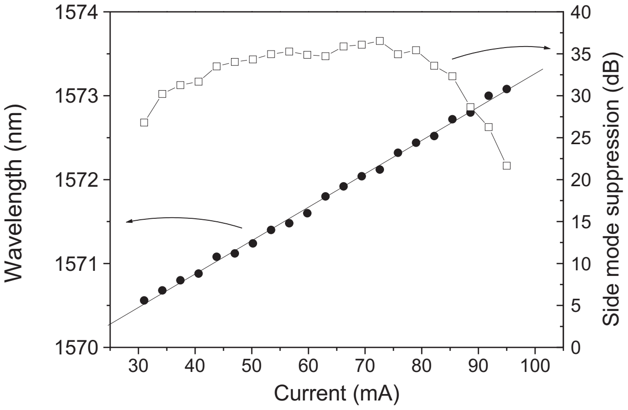

Figure 17.11: Wavelength and sidemode suppression ratio of the device as a function of drive current.

17.4 All photonic crystal lasers

One of the drawbacks of the combination of a ridge waveguide laser with a PhC waveguide is the large modal mismatch between the two components. Although taper structures have been described in the literature, they add unnecessary complexity to the devices. The coupling issue can be avoided completely by using 'all PhC' lasers, where the laser resonator is formed by a PhC waveguide. A simple PhC waveguide would be sufficient, but this laser would operate multi–mode with a Fabry–Perot like emission spectrum. In order to obtain single mode operation, one has to introduce a wavelength selective element into the resonator. We found that a design with a chain of coupled hexagonal resonators (CROW) [22] is suitable for the production of a single mode, all PhC laser device. A CROW based on H6 cavities was used (6 missing holes along one side of the hexagon), and is shown schematically in Figure 17.12.

The coupling of the cavities leads to the formation of minibands within the photonic bandgap. The origin of the minibands is shown in the right plot of Figure 17.12, which compares transmission spectra obtained from a FDTD simulation of a single cavity and a chain of two, four and eight coupled cavities. The main contribution to the transmission comes from equally spaced Fabry–Perot modes across the photonic bandgap. These modes are favored in this transmission calculation over the about 75 other cavity eigenmodes due to their preferential coupling to the plane wave used to excite the structure. However, these are the modes which are also relevant for the experiment, since they show the strongest coupling in the CROW geometry. This coupling leads to a spectral splitting of the Fabry–Perot resonances in a number of peaks which is proportional to the number of cavities in the chain. In the limit of an infinite series of coupled resonators, the discrete modes merge into a miniband. In this case, the dispersion of the mode can be expressed analytically by:

$$v_g = \frac{d\omega_k}{dk} = -\Omega \, R \, \kappa \, \sin{(kR)} \tag{17.1}$$

Where Ω is the resonance frequency of a single cavity, R is the center–to–center spacing of two resonators and κ the coupling constant, describing the overlap of two neighbouring cavity modes. The group velocity becomes zero at the edges of the miniband at k = 0 and π/R. In case the of an active resonator, the modal gain is inversely proportional to the group velocity, so lasing is expected to occur at the edge of the minibands. Due to the wide spacing of the minibands (approximately 100 nm), only one miniband will be a spectral region with substantial gain, so the lasing operation will be restricted to this particular miniband. The degeneracy of the two edges of the miniband is lifted by a different overlap with the active area of the device, as will be explained later on. Together, these effects will ensure a stable single mode operation of the device at a well defined wavelength [23].

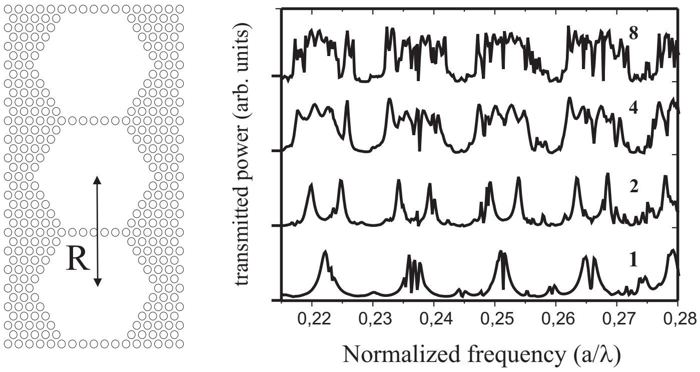

Figure 17.12: Left: Schematic of a coupled resonator optical waveguide (CROW). The distance between the resonators is R. **Right:** Transmitted power through a CROW consisting of one, two, four and eight cavities.

The fabrication starts with an unpatterned laser layer and uses a PhC structure to define both the waveguide and the mirrors of the laser. This approach puts high demands on the etching, since the holes have to penetrate the complete upper cladding (thickness 1.5–2 μm), the waveguide of laser and extend into the lower cladding. The devices were processed from an InGaAsP/InP laser structures. The photonic crystal patterns have an air fill factor of f = 28 % and lattice constants in the range of $a = 350$–400 nm. Figure 17.13 shows a top view micrograph and a cross section of the CROW laser. An etch depth of about 3.8 μm is achieved for the PhCs.

In order to achieve more selective current injection, a contact strip is defined in a second lithography step and the highly p–doped contact and the cladding layer are etched back by approximately 400 nm, outside this area. The region where the top InGaAs layer is still present appears as a bright stripe in the SEM image. After removal of the masks, the structure

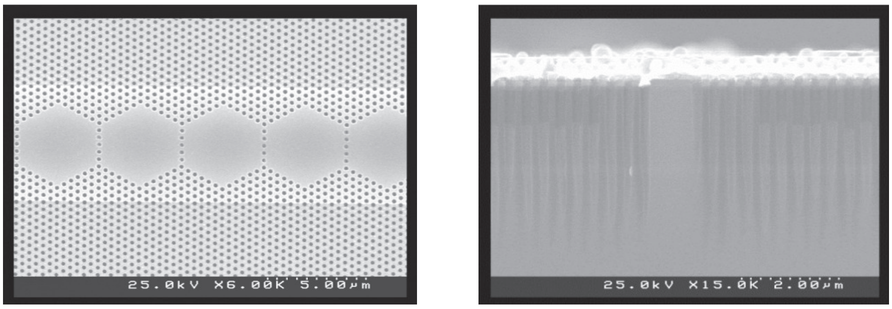

a) **b)**

Figure 17.13: Left: SEM top image of CROW laser. Right: Cross section of the PhC.

is planarized and insulated with benzo–cyclobutene and electrical contacts are formed. For characterization, the lasers are cleaved at the end of the PhC waveguides.

The left plot in Figure 17.14 shows the output power, characteristic of a 135 μm long CROW laser with a PhC lattice period of a = 350 nm. The threshold current is 17 mA and the maximum output power within the investigated current range is 2.6 mW. The right plot shows a superposition of emission spectra from lasers with a = 350, 375 and 400 nm period plotted versus the normalized frequency (a/λ).

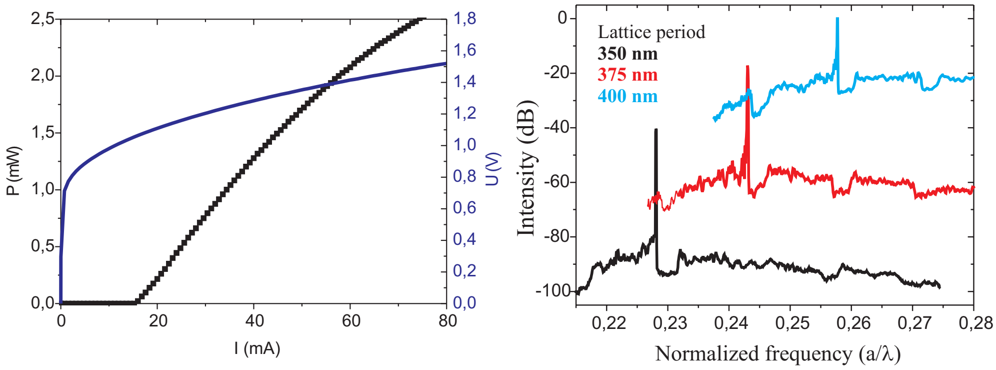

Figure 17.14: Left: Output power characteristic of a CROW laser.
Right: Emission spectra of three CROW lasers with lattice periods a of 350, 375 and 400 nm plotted versus the normalized frequency a/λ. The curves are offset by 30 dB for clarity.

The CROW minibands and stopbands are clearly visible in the spectra. Each CROW laser shows an emission spectrum with a single emission line and a high sidemode suppression of over 40 dB. One minigap of the CROW can be seen as a dip in the emission spectrum to the right of the lasing mode. The selection of the right or left mode adjacent to the minigap is caused by a different overlap with the air holes separating the cavities. In our case, the mode on the long–wavelength side of the minigap has a node of the field distribution along the row of air holes separating the cavities. This results in a lower loss compared to the mode on the short wavelength side of the minigap. Figure 17.15 shows the emission wavelength and sidemode suppression ratio of the laser as a function of the device temperature at a fixed drive current of 50 mA.

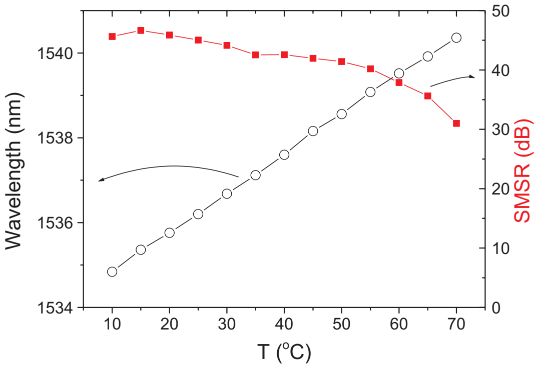

Figure 17.15: Wavelength and sidemode suppression ratio of a CROW laser versus operation temperature.

A SMSR of over 40 dB is achieved for temperatures up to 50 °C. The laser is still in operating single mode at 70 °C, also with a reduced SMSR of 30 dB. The emission wavelength shifts without mode jumps from 1534.8 nm at 10 °C to 1540.2 nm at 70 °C. The wavelength shift of 0.09 nm/K is caused by the temperature dependence of the refractive index, and similar to that of other single mode lasers based on InP.

17.5 Tunable photonic crystal lasers

The basic principle of tuning a single–mode semiconductor laser is based on a change of the refractive index, which in turn leads to a change of the emission wavelength. This can be achieved by an increase of the temperature (which increases the index) or the carrier density (which decreases the index). Even a combined change of both parameters leads to a maximum relative shift of around 1 % only, for realistic ranges of temperature and carrier density. This corresponds to a tuning range of 15 nm for a device operating at 1.55 μm. In order to obtain a larger tuning range, some sort of leverage has to be used which translates a small shift of the refractive index into a larger shift of the emission wavelength. One possible principle is the use of two coupled cavities with a slightly different length. Both cavities support a set of Fabry–Perot modes with a spacing inversely proportional to the cavity length. Since the mode spacing of the two cavities is not equal, the mode combs only overlap at one particular wavelength within the gain curve of the laser. This is shown schematically in the central plot of Figure 17.16. The modes of the shorter cavity are displayed in blue and have a spacing of λ_1, the modes of the longer cavity are shown in red and have a spacing of λ_2.

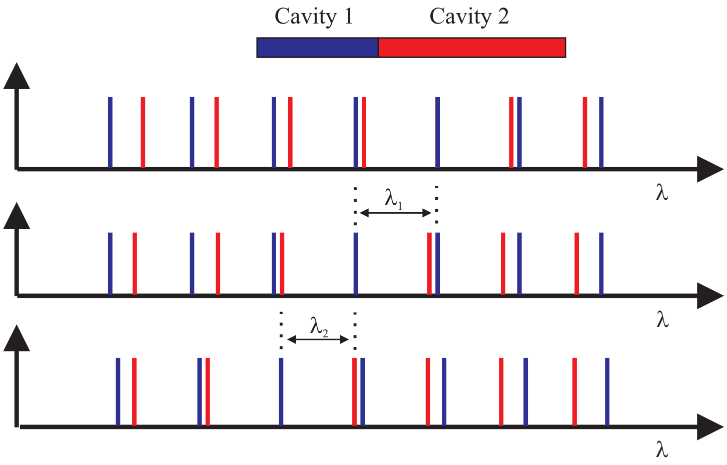

Figure 17.16: Tuning principle of a coupled cavity laser.

Coarse tuning can be achieved by a variation of the drive current in one segment. The heating associated with the increased current results in a higher refractive index for this particular segment. This leads to a shift of one set of modes, and the emission switches to the next overlap of modes. If the current in the longer cavity is increased, a red shift of the emission by λ_1 is observed, as shown in the upper plot of Figure 17.16. On the other hand, an increased current in the shorter cavity results in a blue tuning by λ_2. If the spacing of the modes is large, only a few selected wavelengths are accessible. However, due to the large spacing of the neighbouring modes, the emission is very stable and a high sidemode suppression ratio can be achieved. A fine spacing has the advantage of a closely spaced set of available wavelength. The drawback is the very small spectral difference of the modes next to the main mode, which usually lead to a small sidemode suppression ratio. We found that mode spacings in the range of 2–5 nm (which corresponds to cavity length in the range 70–120 μm) are a reasonable compromise. Fine tuning of the emission to a wavelength can be achieved by a simultaneous variation of both drive currents. In our case, the cavities are formed by two PhC waveguides along the ΓM direction with a width of 3–7 missing rows. A PhC lattice period of 380 nm was used, with an air filling factor of 40 %. The cavities are separated by an intermediate mirror consisting of PhC, with one lattice period. The front mirror is also produced by a PhC with one period. Figure 17.17 shows SEM micrographs of the three mirrors and the PhC waveguide.

The orientation of the PhC waveguides is chosen to be ΓM in order to have ΓM–oriented PhC boundaries as mirrors. ΓK–oriented mirrors mainly diffract the light and have a low specular reflectivity.

As explained in the introduction, a coarse set of wavelengths, defined by the Fabry–Perot modes of the cavities, can be accessed when one current is held fixed and the second one is varied. Figure 17.18 shows the emission spectra of the device for the two different tuning configurations. The temperature of the heat sink was kept at 21 °C. The plot on the left side shows the emission as the current in the rear section is varied; the plot on the right side shows the corresponding tuning of the front section.

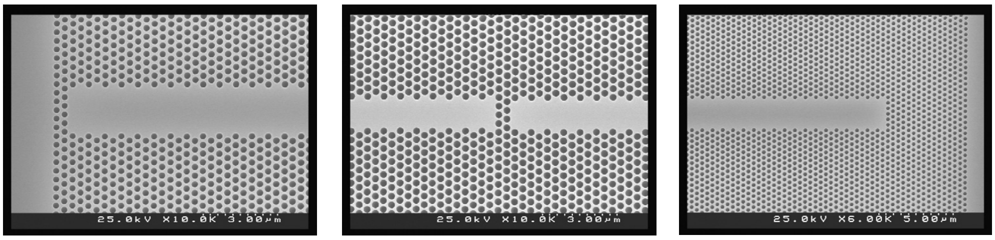

Figure 17.17: SEM micrographs of the three PhC mirrors in the tunable laser. Left: Front mirror. Center: Intra–cavity mirror. Right: High reflectivity mirror at the back of the rear cavity.

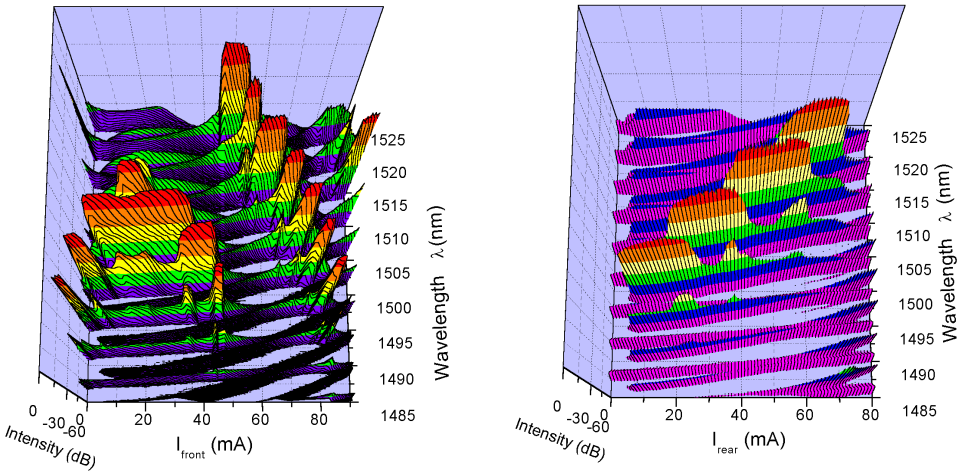

Figure 17.18: Tuning characteristic of coupled cavity laser. Left: Constant current (40 mA) in front section, variation of current in rear section. Right: Constant current (40 mA) in rear section, variation of current in front section.

Two sets of modes can be distinguished in the plots: the modes of the cavity where the current is increased, shift to longer wavelength as the refractive index increases. The other set of modes stays at a fixed position or show only a slight shift with increasing current. In this case, the cavities had a length of 76 μm (rear cavity) and 70 μm (front cavity). The corresponding mode spacings are 4.3 and 4.7 nm. If the current in the rear cavity is increased, the emission shifts to longer wavelength. For currents below 20 mA, an increase of the current in the front cavity also results in a shift towards longer wavelengths. At higher currents, a shift towards shorter wavelengths is observed. In the region below 20 mA, the change of the refractive index is most likely dominated by the increasing carrier density, which reduces the index. At higher current levels, thermal effects take over and the sign of the wavelength shift changes.

Figure 17.19 shows the fine tuning of the laser emission, which can be achieved by a simultaneous variation of both currents. This results in a smooth shift of the emission wavelength, filling the gaps between the set of modes defined by the two cavities. The wavelength is changed in steps of 0.8 nm over a total range of 30 nm with a sidemode suppression ratio larger than 20 dB. The tuning was achieved at constant temperature of the heat sink. If an additional variation of the temperature is allowed, the tuning range or the sidemode suppression ratio can be increased.

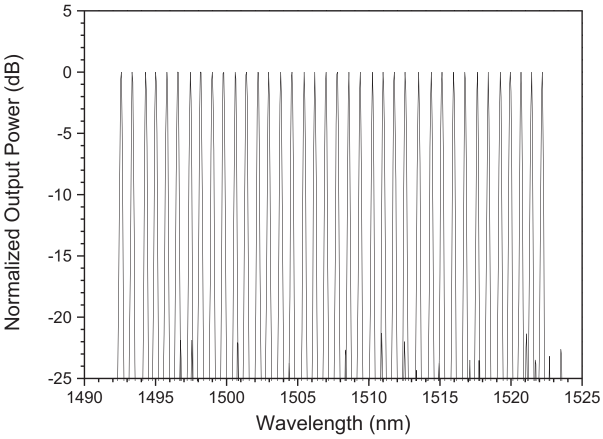

Figure 17.19: Fine tuning by simultaneous variation of the two drive currents. A wavelength span of almost 30 nm is covered in steps of 0.8 nm.

17.6 Conclusion

We have described a number of ways to integrate photonic crystals with active optoelectronic devices. PhCs can be used as mirrors in semiconductor lasers where their high reflectivity allow the fabrication of lasers with small cavity length. Lasers with a length down to 100 μm and two PhC mirrors have been demonstrated. Single mode emission can be achieved by the introduction of an intracavity PhC mirror. The mode interference in this coupled cavity lasers leads to a stable single mode operation at high sidemode suppression ratios. As a further step, lasers entirely based on photonic crystals have been discussed. Devices with resonant optical waveguides show single mode emission and low threshold currents. The most complex device presented is a tunable, all PhC based laser source.

Acknowledgements

The authors would like to acknowledge the financial support of the state of Bavaria and the EU under Project No. IST–PCIC.

References

[1] S. John, Strong localization of photons in certain disordered dielectric superlattices, Phys. Rev. Lett **58**, 2486-2489, 1987

[2] E. Yablonovitch Inhibited spontaneous emission in solid-state physics and electronics Phys. Rev. Lett **58**, 2059-2062, 1987

[3] O. Painter, R.K. Lee, A. Scherer, A. Yariv, J.D. O'Brien, P.D. Dapkus and I. Kim, Two-dimensinal photonic band-gap defect mode laser, Science **284**, 1819-1821, 1999

[4] S. Fan, P.R. Villeneuve, J.D. Joannopoulos and H.A. Haus, Channel drop tunneling through localized states, Phys. Rev. Lett. **80**, 960-963, 1998

[5] J.S. Foresi, P.R. Villeneuve, J. Ferrara, E.R. Thoen, G. Steinmeyer, S. Fan, J.D. Joannopoulos, L.C. Kimmerling, H.I. Smith and E.P. Ippen, Photonic-bandgap microcavities in optical waveguides, Nature **390**, 143-145, 1998

[6] A. Mekis, J.C. Chen, I. Kurland, S. Fan, P.R. Villeneuve and J.D. Joannopoulos, High transmission through sharp bends in photonic crystal waveguides, Phys. Rev. Lett. **77**, 3787-3790, 1996

[7] H. Kosaka, T. Kawashima, A. Tomita, N. Notomi, T. Tamamura, T. Sato and S. Kawakami, Superprism phenomena in photonic crystals, Phys. Rev. B **58**, R10096-R10099, 1998

[8] T.F. Krauss, R.N. De La Rue and S. Brand, Two-dimensional photonic-bandgap structures operating at near-infrared wavelength, Nature, **383**, 699-702, 1996

[9] H. Benisty, D. Labilloy, C. Weisbuch, C. J.M. Smith, T. F. Kraus, D. Cassagne, A. Beraus and C. Jouanin, Radiation losses of waveguide-based two-dimensinal photonic crystals: positive role of the substrate, Appl. Phys. Lett. **76**, 532-534, 2000

[10] H. Benisty, P. Lalanne, S. Olivier, M. Rattier, C. Weisbuch, C. J.M. Smith, T. F. Kraus, C. Jouanin and D. Cassagne, Finite-depth and intrinsic losses in vertically etched two-dimensional photonic crystals, Opt. Quant. Electron. **34**, 205-215, 2001

[11] S.G. Johnson and J.D. Joannopoulos, Block-iterative frequency-domain methods for Maxwells's equations in a planewave basis, Opt. Express **8**, 173, 2001

[12] L.A. Coldre and S.W. Corzine, Diode Lasers and Photonic Integrated Circuits, Wiley, New York, 1995

[13] M. Kamp, J. Hofmann, A. Forchel and S. Lourdudoss, Ultrashort InGaAsP/InP lasers with deeply etched Bragg mirrors, Appl. Phys. Lett **78**, 4074-4075, 2001

[14] S. Rennon, K. Avary, F. Klopf, A. Wolf, M. Emmerling, J.P. Reithmaier and A. Forchel, Quantum dot microlasers, Electron. Lett. **36**, 1548-1550, 2000

[15] J. Wiedmann, M.M. Raj, Y. Saka, S. Tamura and S. Arai, Singlemode operation of deeply etched coupled cavity laser with DBR facet, Electron. Lett. **36**, 1211-1212, 2000

[16] J. O'Brien, O. Painter, R. Lee, C. C.Cheng, A. Yariv and A. Scherer, Lasers incorporating 2D photonic bandgap mirrors, Electron. Lett. **32**,2243-2244, 1996

[17] T.D. Happ, M. Kamp and A. Forchel, Ridge waveguide lasers with 2D photonic crystal mirror, Inst. Phys. Conf. Ser **166**, Proceedings of 26th Int. Sym. Compound Semiconductors, Berlin (Germany), pp. 411-414, 2000

[18] B. D'Urso, O. Painter, J. O'Brien, T. Tombrello, A. Yrib and A. Scherer, Modal reflectivity in finite depth two-dimensinal photonic-crystal microcavities, J. Opt. Soc. Am B **15**, 1155-1159, 1998

[19] D. Labiloy, H. Benisty, C. Weisbuch, T. F. Krauss, D. Cassagne, C. Jouanin,R. Houdre, U. Oesterle and V. Bardinal, Diffraction efficiency and guided light control by two-dimensional photonic-bandgap lattices, IEEE J. Quant. Electron. **35**, 1045-1052, 1999

[20] T. D. Happ, A. Markard, M. Kamp, J. L. Gentner, and A. Forchel, Nanofabrication of 2D photonic crystal mirrors for $1.5\mu m$ short cavity lasers, J. Vac. Sci. Technol B **19**, 2775-2778, 2001

[21] T. D. Happ, A. Markard, M. Kamp, S. Anand and A. Forchel, Single-mode operation of coupled-cavity lasers based on two-dimensional photonic crystals, Appl. Phys. Lett. **79**, 4091-4093, 2001

[22] A. Yariv, Y. Xu, R. K. Lee and A. Scherer, Coupled resonator optical waveguide: a proposal and analysis, Opt. Lett **24**, 711-713, 1999

[23] T.D. Happ, M. Kamp, A. Forchel, J.L. Gentner and L. Goldstein, Two-dimensional photonic crystal coupled-defect laser diode, Appl. Phys. Lett. **82**, 4-6, 2003

A List of abbreviations

1D	one-dimensional
2D	two-dimensional
3D	three-dimensional
BPM	beam propagation method
BSG	binary superimposed grating
BZ	Brillouin zone
CAIBE	chemically assisted ion beam etching
CCW	coupled cavity waveguide
CVD	chemical vapour deposition
DFB	distributed feedback
DOS	density of states
DUT	device under test
EM	electromagnetic
FDTD	finite difference time domain
FE	finite element
FIB	focused ion beam
GVD	group velocity dispersion
IBZ	irreducible Brillouin zone
ICP	inductively coupled plasma
LDOS	local density of states
LbL	layer-by-layer
NC	nanocrystal
PBG	photonic band gap
PECVD	plasma enhanced chemical vapor deposition
PL	photo luminescence
PML	perfectly matched layer
PW	plane wave
PWM	plane wave method
PhC	photonic crystal
QED	quantum electrodynamics
RI	refractive index
SEM	scanning electron microscope
SIPS	solvent evaporation-induced phase separation
SWG	strip waveguide
TEM	transmission electron microscope
TIPS	thermally induced phase separation
WDM	wavelength division multiplexing
WSC	Wigner-Seitz cell

Photonic Crystals. Edited by K. Busch, S. Lölkes, R. B. Wehrspohn and H. Föll
Copyright © 2004 Wiley-VCH Verlag GmbH & Co. KGaA
ISBN: 3-527-40432-5

B Conventions

Lattices

hexagonal lattice

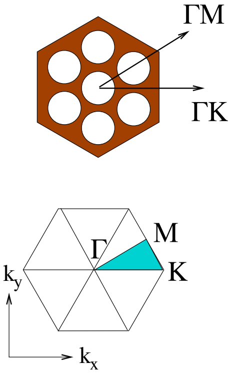
ΓM
ΓK
M
Γ
K
k_y
k_x

square lattice

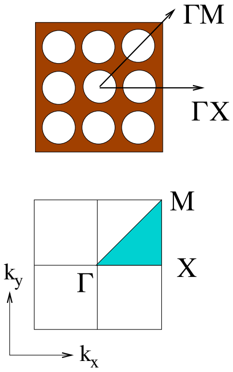
ΓM
ΓX
M
X
Γ
k_y
k_x

Mode nomenclature

TE-mode = H – polarization

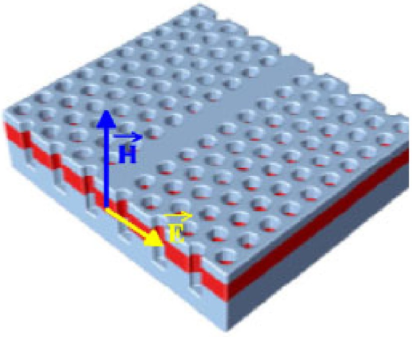

TM-mode = E – polarization

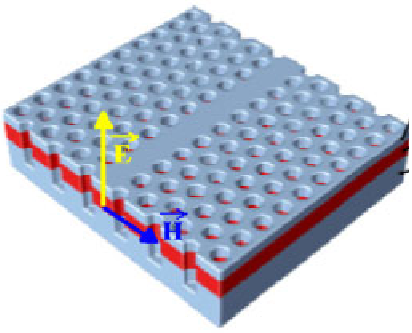

Waveguide naming

Waveguide with e.g. 1 missing row (e.g. in picture above) = W1 - waveguide
Waveguide with e.g. 3 missing row = W3 - waveguide
etc.

Photonic Crystals. Edited by K. Busch, S. Lölkes, R. B. Wehrspohn and H. Föll
Copyright © 2004 Wiley-VCH Verlag GmbH & Co. KGaA
ISBN: 3-527-40432-5

Index

1D, 2D, 3D photonic crystal *see* photonic crystal

absorbing crystal 27
AlGaAs
    etching 318
alumina, porous 63, 67, 78
    10%–porosity rule 67
anchoring of liquid crystals 178, 179, 183, 194
angle–resolved transmission 245
angular dispersion 141, 143, 144
anisotropy
    dielectric 178, 181
    magnetic 178
    optical *see* birefringence
arrayed waveguide grating 290
autocorrelation 101

backtracking 312
ball lens 326
band diagram
    2D infinite–height PhC 211
    strip waveguide 204
band gap
    dispersion 147
    width for moderate index slab materials 291
    width for semiconductor slab materials 291
band structure 2
    iso-frequency contours 322
    Niobiumpentoxide PhC slab 292, 296, 297
    polymer PhC slab 292, 293
basis element 156
beam propagation method (BPM) 313
binary superimposed grating (BSG) 320
birefringence 177, 178, 180, 183, 192
bleaching 56
Bloch taper 321
blue phases 179–182
blue shift 56
Bragg diffraction gap 134, 141, 144–146, 150, 151

cavity 16
chemically assisted ion beam (CAIBE) etching 316
cholesteric phase 179–181
cobweb fiber 266
colloidal crystal 174, 180, 183, 192
colloids with different surface charges 115
core shell structures 115
Coulomb interaction 46, 49
coupling prism 160
crosslinked colloids 114
crystallization
    into opaline structures 120
    on a fluid matrix 122

defect
    lasing 181
    structures 12
defect mode 28
density of states 4
density–dependent absorption 56
dephasing 58
dephasing time 101
DFB laser 103
dielectric anisotropy 178, 181
dielectric constant *see* microwave material
    complex 199
dipole emission 24, 29, 33
disordered crystal 27
dispersion 89, 91, 93, 282

Photonic Crystals. Edited by K. Busch, S. Lölkes, R. B. Wehrspohn and H. Föll
Copyright © 2004 Wiley-VCH Verlag GmbH & Co. KGaA
ISBN: 3-527-40432-5

  - chromatic 323
  - compensator 323
  - slope 323
  - W1–waveguide (SOI) 324
- dispersion relation
  - strip waveguide 204
- distributed feedback resonators 254
- DOS
  - anisotropic model 26
  - band edge singularities 26
  - projected LDOS 24

- effective 2D model 260
- effective Hamiltonian 99
- effective mass approximation 26
- effective nonlinearity 7
- effective parameters 256
- elastic properties of liquid crystals 178
- electrochemical deposition 171
- electron beam lithography 187–189
- electron cyclotron resonance (ECR) enhanced etching 316
- electron population 51, 54
- electron–beam lithography 125
- EM field continuity 134, 144
- emission spectra 105
- empty-lattice approximation 89, 93
- equations
  - Maxwell–Bloch 256
- etching 186, 188, 189
  - AlGaAs 318
  - chemically assisted ion beam (CAIBE) 316
  - electrochemical 63
  - electron cyclotron resonance (ECR) enhanced 316
  - inductively coupled plasma (ICP) 316
  - large area 65
  - SOI 318, 319
- etching depth 291–293, 298–300, 302, 305
- exciton 44, 53
  - binding energy 47
- extinction 91

- Fabry–Perot–resonances 74, 140, 142
- FDTD *see* finite–difference–time–domain calculation
- ferroelectric liquid crystals 194
- fiber technology 275
- fiber–to–chip coupling 325
- field computation
  - boundary elements 34
  - frequency domain 33
- filling factor 157, 160
- filter PL 136, 145–147
- finite difference time domain 142–144, 273
- finite element method 267
- finite element solvers 312
- finite–difference–time–domain calculation 36, 310
  - out–of–plane losses 292, 300, 305
  - PhC slab waveguide transmission 299, 300
  - PhC waveguide bend 296, 297
- finite–height PhC *see* photonic crystal
- fluorescent dyes 114
- focal point 150
- form factor 157
- frequency domain propagation 313
- full band gap 109, 127
- functional colloids 114

- GaAs, porous 64, 68, 81
- gain 56
- gas sensor 238
- generalized Coulomb potential 46
- gold nanodisks 87, 94, 104
- grating
  - binary superimposed (BSG) 320
- gratings
  - surface relief 247
- group velocity 5, 239
  - dispersion 5

- heterojunction 132, 134, 135, 142–144, 149, 151
- heterostructures 125
- high–delta fiber 266
- hole population 51, 54
- holey fiber 266
- holographic lithography 154

- ICP etching system 316
- III–V semiconductors, porous 63, 68, 78
- impedance matching 326
- inductively coupled plasma (ICP) etching 316
- InGaAsP
  - W1–waveguide 311

InGaAsP/InP
    superprism 320
inhomogeneous carrier populations 54
inifinite–height PhC *see* photonic crystal
inorganic colloids 110
InP, porous 64, 68, 78
interband polarization 49, 51
interconnectivity conditions 158
interface gap 132, 141, 143
interface minimum 141–144
interference lithography 247
interference pattern 155
inverted opal 37, 176, 183, 185
isophote 163
ITO 86

kp perturbation theory 5

laser 39
    direct writing 161
    multi-segment 318
    semiclassical theory 256
    widely tunable 318
lateral patterning 125
lattice
    bcc 156
    Bravais 156
    fcc 156, 158
    hexagonal 66, 67, 79
    honeycomb 67
    real space 156
    reciprocal 156
    simple cubic 76
    square 67
layer-by-layer
    deposition 138, 151
    structure 165
LDOS 24, 35, 38
leaky modes 268
light cone 93
light–matter interaction 44, 49
linear absorption 47, 53
local density of states 5
localized functions 267
loss *see* microwave material, 280
    factor 199
    measurement 209
    per medium wavelength 199
    scattering 209
losses
    W1–waveguide 309
low loss materials 289, 290, 305

macroporous silicon 228, 241
Markov approximation 30
matching
    phase, spot, impedance 326
material *see* microwave material, dielectric constant
Maxwell's equations 199
    scaling the dielectric constant 200
    scaling the structure 198, 200
metallo–dielectric
    grating 10
    photonic crystal 85
microcavity 75, 176, 190, 193
microreplication 247
microresonators
    and fabrication quality 230
    and SNOM 228, 233
microwave 198
    coaxial feeder 205
    equipment 203
    material 201
    measurement 203, 204, 207, 210, 211
    vector network analyser 203
mirror
    scattering matrix 208
mode field 281
modes 268
moving meniscus 123
multi–photon
    absorption 163
    polymerization 162
multi–scale
    analysis 256
    approach 7
multipole expansion 267

nanoimprinting 67
nanoparticle arrays 87, 94
nanowire arrays 90, 97
nematic phase 179, 187
Niobiumpentoxide, Nb_2O_5 291–293, 304, 305
non–silica 278
nonlinear absorption 56
nonlinear polarization 6

nonlinear Schrödinger equation 7
numerical aperture 280
numerical modeling 135
numerics
    FDTD 202
    FE 202

opal, artificial 109

particle plasmon 86
patterned substrates 125
PDLC *see* polymer-dispersed liquid crystals
perfectly matched layer (PML) 272, 310
permittivity *see* microwave material, dielectric constant
phase matching 326
photobleaching 298, 302, 303, 305
photoinitiator 155
photonic band gap
    complete 76, 77
photonic band gap fiber 266
photonic crystal 189, 190, 241
    1D 26, 78
    2D 69, 70, 78, 79
    2D crystal 33
    2D finite–height
        line–defect waveguide 210
        line–defect waveguide loss 212
        measurement 212
        microwave model 210
    2D inifinite–height
        band diagram 211
        measurement 211
        microwave model 211
        transmission 211
    3D 75, 81
    bulk 70
    circuit 19
    finite 72
photonic crystal fiber 266
photoresist (SU–8) 155
PL intensity ratio 146, 149
planar defect 133, 134
planar photonic crystals 187, 193
plane wave expansion 267
plane wave method 3
plano-convex lens (Si) 326
plasma enhanced chemical vapor deposition (PECVD) 317
polariton splitting 96, 97
polyelectrolyte multilayers 117
polymer 297–299, 301, 302
polymer colloids 111
polymer–dispersed liquid crystals 185
polymerization
    cationic 155
    radical 155
polymers
    conjugated 247
pore
    crystallographical 79
    currrentline 79
    diameter modulation 75, 81
post–exposure bake 158
preform 275
propagation constant 268
propagation loss of slab waveguides 289

quantum cascade lasers 245
quantum electrodynamics (QED) 24, 29
quantum optics 23
    multiphoton states 32
    strong coupling 28
    weak coupling 24
quantum well 47, 53
quantum wire 55

radiated power 148
radiation losses 290, 305
Rayleigh
    anomalies 87, 92
    scattering 289
reflection 11
reflection spectrum 167
refractive index 112
    high 289
    moderate to low 289, 290, 297, 299, 302, 304, 305
    negative 314
    tuning of 297, 305
replica 127
resonance fluorescence 28, 32
resonant condition 133
resonator 290, 301–303
rotating wave approximation 29

saturation threshold 132, 147–149
scaling *see* Maxwell's equations

scattering matrix 8, 90, 99, 203
  mirror 208
  transmission line 208
sedimentation 120
self energy 49
self–organization 66, 67, 79, 81, 109, 132, 133, 151
semiconductor 174, 186, 187
  Bloch equations 50
  laser 57
  organic 247
sensor 238
shrinkage 158
silica 280
silicon
  macroporous 63, 64, 70, 75, 185–187, 192
  mesoporous 64, 66
Silicon CVD 169
silicon optical bench (SiOB) 326
slowly varying envelope approximation 8
SNOM
  and interferometry 222
  and manipulation of sample 234
  and pulse tracking 223
  influence of probe 233
  modes 218
  principle 216
  prism 219
  resolution 229
  shear force control 218
  whispering-gallery resonators 220
SNOM and photonic crystals
  comparison to FDTD models 230
  fabrication quality 230
  measuring waveguide loss 228
  scattered light 225
  theoretical treatments 225
  waveguide bends 227
soft bake 158
SOI
  etching 318, 319
  W1–waveguide 310
source PL 136, 145–148, 150
spontaneous emission 24
  nonexponential decay 29, 32
  optical tuning 28
spot 326
strong coupling 94
superprism 290, 291
  InGaAsP/InP 320
surface-plasmon polaritons 85
surfactant free emulsion polymerization 112

taper 240, 326
template infiltration 168
thermal stability 112, 114
thermalization 58, 61
thin opal film 133, 135
threshold
  dose 155, 157
  irradiation 155
time–dependent Hartree–Fock approximation 50
time-harmonic analysis 313
tolerancing 312
transition
  between strip and PhC waveguide 209, 212
translational symmetry 156
transmission 11, 278
  line *see* scattering matrix, transmission line
  spectrum 161, 167
trigonal structure 158
tunable
  band gap 174
  laser 318
  resonance 190
tuning 28, 245
two dimensional crystallization 121

ultrafast dynamics 101
umbrella–like configuration 158
uncoupled bands 12

voxel 163

W1–waveguide 309
  dispersion (SOI) 324
  InGaAsP 311
  SOI 310
Wannier functions 13
wave packet dynamics 61
waveguide 17, 74, 94
  bend 20, 290, 295–297, 305
  coaxial feeder 205
  dispersion of strip 204

  line–defect 210
  loss measurement 209
  modes 205
  resonator 208
  strip 205
  transmission 226, 228
waveguide, PhC
  Niobiumpentoxide 291–295
  propagation loss 289
waveguide–plasmon polariton 94
wavelength division multiplexing (WDM) 318
Wigner–Seitz cell 156
woodpile structure 165

Yablonovite 65, 77